MEMS GYROSCOPES

FOR TACTICAL-GRADE INERTIAL MEASUREMENT APPLICATIONS

A THESIS SUBMITTED TO

THE GRADUATE SCHOOL OF NATURAL AND APPLIED SCIENCES

OF

MIDDLE EAST TECHNICAL UNIVERSITY

BY

SAİD EMRE ALPER

IN PARTIAL FULFILLMENT OF THE REQUIREMENTS

FOR

THE DEGREE OF DOCTOR OF PHILOSOPHY

IN

ELECTRICAL AND ELECTRONICS ENGINEERING

SEPTEMBER 2005

Approval of the Graduate School of Natural and Applied Sciences

<div style="text-align: right;">
Prof. Dr. Canan ÖZGEN

Director
</div>

I certify that this thesis satisfies all the requirements as a thesis for the degree of Doctor of Philosophy.

<div style="text-align: right;">
Prof. Dr. İsmet ERKMEN

Head of Department
</div>

This is to certify that we have read this thesis and that in our opinion it is fully adequate, in scope and quality, as a thesis for the degree of Doctor of Philosophy.

<div style="text-align: right;">
Prof. Dr. Tayfun AKIN

Supervisor
</div>

Examining Committee Members:

Prof. Dr. Cengiz BEŞİKÇİ (Chairman) (METU, EEE) _____

Prof. Dr. Tayfun AKIN (METU, EEE) _____

Prof. Dr. Mehmet Ali Sahir ARIKAN (METU, ME) _____

Asst. Prof. Dr. Haluk KÜLAH (METU, EEE) _____

Dr. Tarık REYHAN (Bilkent University, EEE) _____

I hereby declare that all information in this document has been obtained and presented in accordance with academic rules and ethical conduct. I also declare that, as required by these rules and conduct, I have fully cited and referenced all material and results that are not original to this work.

Said Emre ALPER

ABSTRACT

MEMS GYROSCOPES FOR TACTICAL-GRADE INERTIAL MEASUREMENT APPLICATIONS

Alper, Said Emre

Ph. D., Department of Electrical and Electronics Engineering

Supervisor: Prof. Dr. Tayfun AKIN

September 2005, 301 pages

This thesis reports the development of high-performance symmetric and decoupled micromachined gyroscopes for tactical-grade inertial measurement applications. The symmetric structure allows easy matching of the resonance frequencies of the drive and sense modes of the gyroscopes for achieving high angular rate sensitivity; while the decoupled drive and sense modes minimizes mechanical cross-coupling for low-noise and stable operation. Three different and new symmetric and decoupled gyroscope structures with unique features are presented. These structures are fabricated in four different micromachining processes: nickel electroforming (NE), dissolved-wafer silicon micromachining (DWSM), silicon-on-insulator (SOI) micromachining, and silicon-on-glass (SOG) micromachining. The fabricated gyroscopes have capacitive gaps from 1.5μm to 5.5μm and structural layer thicknesses from 12μm to 100μm, yielding aspect ratios up to 20 depending on the

fabrication process. The size of fabricated gyroscope chips varies from 1x1mm^2 up to 4.2x4.6mm^2.

Fabricated gyroscopes are hybrid-connected to a designed capacitive interface circuit, fabricated in a standard 0.6μm CMOS process. They have resonance frequencies as small as 2kHz and as large as 40kHz; sense-mode resonance frequencies can be electrostatically tuned to the drive-mode frequency by DC voltages less than 16V. The quality factors reach to 500 at atmospheric pressure and exceed 10,000 for the silicon gyroscopes at vacuum. The parasitic capacitance of the gyroscopes on glass substrates is measured to be as small as 120fF.

The gyroscope and interface assemblies are then combined with electronic control and feedback circuits constructed with off-the-shelf IC components to perform angular rate measurements. Measured angular rate sensitivities are in the range from 12μV/(deg/sec) to 180μV/(deg/sec), at atmospheric pressure. The SOI gyroscope demonstrates the best performance at atmospheric pressure, with noise equivalent rate (NER) of 0.025(deg/sec)/Hz$^{1/2}$, whereas the remaining gyroscopes has an NER better than 0.1(deg/sec)/Hz$^{1/2}$, limited by either the small sensor size or by small quality factors. Gyroscopes have scale-factor nonlinearities better than 1.1% with the best value of 0.06%, and their bias drifts are dominated by the phase errors in the demodulation electronics and are over 1deg/sec. The characterization of the SOI and SOG gyroscopes at below 50mTorr vacuum ambient yield angular rate sensitivities as high as 1.6mV/(deg/sec) and 0.9mV/(deg/sec), respectively. The NER values of these gyroscopes at vacuum are smaller than 50(deg/hr)/Hz$^{1/2}$ and 36(deg/hr)/Hz$^{1/2}$, respectively, being close to the tactical-grade application limits. Gyroscope structures are expected to provide a performance better than 10 deg/hr in a practical measurement bandwidth such as 50Hz, provided that capacitive gaps are minimized while preserving the aspect ratio, and the demodulation electronics are improved.

Keywords: Gyroscope, Angular Rate Sensor, Micromachining, Capacitive Interface Circuit, Microelectromechanical Systems (MEMS).

ÖZ

TAKTİK AMAÇLI ATALETSEL ÖLÇÜM UYGULAMALARI İÇİN MEMS DÖNÜÖLÇERLER

Alper, Said Emre

Doktora, Elektrik ve Elektronik Mühendisliği Bölümü

Tez Yöneticisi: Prof. Dr. Tayfun AKIN

Eylül 2005, 301 sayfa

Bu tez taktik amaçlı ataletsel ölçüm uygulamaları için yüksek performanslı simetrik ve etkileşimsiz dönüölçerlerin geliştirilmesini anlatmaktadır. Simetrik yapı, yüksek açısal hız hassasiyeti için dönüölçerlerin sürüş ve algılama modlarının rezonans frekanslarının kolaylıkla eşleştirilebilmesi amacıyla, etkileşimsiz sürüş ve algılama modları ise düşük gürültü ve kararlı çalışma için mekanik etkileşimin en aza indirilmesi amacıyla kullanılmaktadır. Üç farklı ve yeni simetrik ve etkileşimsiz dönüölçer yapısı sunulmaktadır. Bu yapılar dört farklı mikroişleme teknolojisi ile üretilmiştir: aşındırılmış-pul silisyum mikroişleme, nikel elektrokaplama, yalıtkan-üzeri-silisyum mikroişleme, ve cam-üzeri-silisyum mikroişleme. Üretilen dönüölçerlerin sığasal açıklıkları 1.5µm'den 5.5µm'ye, yapısal katmanlarının kalınlıkları ise 12µm'den 100µm'ye kadar değişmekte olup yapıların derinlik-açıklık oranları üretim sürecine bağlı olarak 20'ye kadar çıkabilmektedir. Dönüölçer yongalarının alanları 1x1mm^2'den 4.2x4.6mm^2'ye kadar değişmektedir.

Üretilen dönüölçerler, standart 0.6µm CMOS sürecinde üretilen kapasitif okuma devrelerine hibrit olarak bağlanmıştır. Dönüölçerlerin rezonans frekansları 2kHz ile 40kHz aralığında olup, algılama modlarının rezonans frekansları 16V'dan daha düşük DC gerilimler yardımıyla sürüş modunun rezonans frekansına eşleştirilebilmektedir. Dönüölçerlerin kalite faktörleri atmosfer basıncında 500'lere ulaşırken, bu değer vakumda silisyum dönüölçerler için 10,000'i aşmaktadır. Cam taban üzerinde üretilen dönüölçerlerin parazitik sığalarının 120fF kadar düşük olabildiği görülmüştür.

Arabirim devresine bağlı dönüölçerler daha sonra açısal hız ölçümleri yapmak üzere standart entegre devre elemanlarından kurulmuş elektronik kontrol ve geri-besleme devreleri ile birleştirilmiştir. Üretilen dönüölçerlerin açısal hız hassasiyetleri atmosfer basıncında 12µV/(der/sn)'den 180µV/(der/sn)'ye kadar değişmektedir. SOI dönüölçer atmosfer basıncında $0.025(der/sn)/Hz^{1/2}$'lik bir gürültü-eşdeğer-dönü (GED) değeri ile en iyi performansı göstermiş, diğer dönüölçerlerin GED değerleri küçük duyarga boyutları veya düşük kalite faktörleri nedeniyle $0.1(der/sn)/Hz^{1/2}$ ile sınırlı kalmıştır. Dönüölçerlerin orantı katsayısı hataları %1.1'den daha iyi olup, en iyi değer %0.06 olarak elde edilmiştir. Dönüölçerlerin sabit kaymaları demodulasyon elektroniğindeki faz hataları sebebiyle 1der/sn'nin üzerindedir. SOI ve SOG dönüölçerler 50mtorr'un altındaki vakum ortamında sırasıyla 1.6mV/(der/sn) ve 0.9mV/(der/sn) açısal hız hassasiyeti göstermişlerdir. Bu dönüölçerlerin GED değerleri ise taktik uygulama limitlerine yaklaşarak sırasıyla $50(der/saat)/Hz^{1/2}$ ve $36(der/saat)/Hz^{1/2}$ olarak ölçülmüştür. Derinlik-açıklık oranları korunarak sığasal açıklıkların küçültülmesi ve demodulasyon elektroniğinin iyileştirilmesi ile dönüölçer yapılarının 50Hz gibi pratik bir ölçüm bandı içerisinde 10der/saat'ten daha iyi bir performans sergilemeleri beklenmektedir.

Anahtar Kelimeler: Dönüölçer, Açısal Hız Duyargası, Mikroişleme, Sığasal Arabirim Devresi, Mikroelektromekanik Sistemler (MEMS).

"Every careful mankind recognizes the perfect ingenuity in the universe…"

Dedicated to;

The Greatest Artist and the Greatest Artwork

ACKNOWLEDGEMENTS

I am very grateful to my wife Nuray for her eternal patience and great support, and to my son İbrahim Ethem, "The sweet". I also appreciate my parents Serpil and Ahmet Alper, as well as Nuran and Halil Karagöz, Fazilet and Eyüp Alper, Semahat and Hacı Gedikli, Meliha and (to the late of) İbrahim Özdemir, and all of my dear seniors and friends, who give continuous moral support to me.

TABLE OF CONTENTS

LIST OF FIGURES

FIGURE

xviii

LIST OF TABLES

TABLE

CHAPTER 1

INTRODUCTION

Evolutionary development of integrated circuit (IC) and micromachining technologies in the past few decades is the key factor in the development of today's high-technology systems. Integrated circuits have provided compact, reliable, low-power, and low-cost solutions for complex electronic systems by miniaturization techniques. These techniques are then adapted to the fabrication of miniaturized actuators and sensors allowing miniaturization of the complete electromechanical systems. Such advanced systems have physical dimensions in the range of micrometers and classified as Micro-Electro-Mechanical Systems (MEMS). MEMS technologies enabled the construction of micro electromechanical transducers for most of the high-technology sensor systems, replacing bulky components in certain well-known sensor applications and even introducing novel applications. Inertial navigation of a moving frame is one of the well-known applications, in which the exact position and orientation of a moving or rotating frame is continuously monitored by tracking linear and angular motions of the frame within a certain time-period. Yet another application is the stabilization of the position and the orientation of the frame by continuously monitoring its inertia. The examples of conventional applications for which bulky inertial transducers are being replaced by MEMS transducers are airplane and submarine navigation, camera stabilization in helicopters, guided-missile control, spacecraft and satellite control, and unmanned air vehicle stabilization. The novel applications for which micromachined inertial transducers are the unique solutions include automotive safety systems, handheld camera stabilization, personal navigation, and high-g munitions.

Inertial transducers are classified in two categories: 1) accelerometers that sense linear acceleration and 2) gyroscopes that sense angular rate of an inertial frame. Automotive-grade micromachined accelerometers are already in high-volume production, whereas micromachined accelerometers capable of sensing micro-g accelerations are also started to appear in the military applications providing the most satisfactory solutions for inertial-grade acceleration sensing [1]. Gyroscopes, on the other hand, have more complex structures and operation principles compared to the accelerometers; therefore, conventional mechanical and optical gyroscopes are still widely used especially in military applications that require navigation-grade performances better than 0.01 degrees per hour (0.01deg/hr). Although the performance of micromachined gyroscopes is not competitive with very-high-performance conventional gyroscopes, there is extensive research on increasing the performance of micromachined gyroscopes. Today, micromachined quartz gyroscopes with 0.1deg/sec performance in a 50Hz bandwidth, classified as rate-grade, are widely used in automotive industry and several consumer applications, owing to low unit costs and small size, while silicon counterparts are on the way [2, 3]. Improved micromachined gyroscopes with performances approaching to 10deg/hr (~0.0025deg/sec) in a similar bandwidth, intended for tactical-grade applications, are also reported within the past few years [4-7]. In the long-term, it is expected that the performance of micromachined gyroscopes reach to 0.1deg/hr, replacing most of the conventional ring laser, fiber-optic, and mechanical gyroscopes that are currently used in tactical-grade applications [8]. In addition, high-g survivability of micromachined gyroscopes make them unique solutions for applications including high-g guided munitions.

The need for tactical-grade micromachined gyroscopes force the research towards dedicated mechanical designs, improved microfabrication technologies, high-sensitivity electronics, and high-quality packaging. This thesis reports the development of a unique micromachined gyroscope structure fabricated with four different micromachining technologies in order to determine the limits associated with each process. In addition, high-performance CMOS readout electronics as well as control electronics are developed and hybrid connected to the fabricated

gyroscopes, constructing complete angular rate sensors. Performances of the developed angular rate sensors are measured to be in the range from rate-grade to tactical-grade depending on the fabrication process. It is verified that the improved gyroscope structures developed throughout this research together with their electronic readout circuits are capable of sensing angular rates approaching to 1deg/hr in 1Hz bandwidth, when fabricated with advanced micromachining technologies.

The organization of this chapter is as follows; Section 1.1 includes a brief introduction to the micromachined vibratory gyroscopes, Section 1.2 summarizes the basic performance criteria for gyroscopes and tactical-grade requirements, and Section 1.3 lists the challenges for increasing the performance of micromachined gyroscopes. Then, Section 1.4 provides an overview of micromachined gyroscope structures reported in the literature. Next, Section 1.5 introduces the symmetric and decoupled micromachined gyroscope structures developed in this research, and finally, Section 1.6 presents the research objectives and the organization of the thesis.

1.1 Micromachined Vibratory Gyroscopes

The motion of a body with respect to a stationary coordinate frame can be described by using Newton's Second Law of Motion for an observer located on the stationary coordinate frame. However, if the coordinate frame in which the body moves is not stationary but rotating about one of its coordinate axes, then the motion of the body on the rotating frame with respect to the stationary coordinate frame cannot be simply described by Newton's Second Law for an observer located on the rotating frame. Towards the mid-19th century, French scientist Gustave Gaspard de Coriolis found that *the classical laws of motion could be used in a rotating frame of reference if a fictitious force is added to the equations of motion* [9]. This fictitious force is named as Coriolis force and governs the operation of Coriolis rate gyroscopes.

Basically, a mechanical rate gyroscope consists of a continuously rotating or vibrating element mounted on a frame, called the gyro frame. A separate sense

element mounted on the gyro frame continuously monitors the motion of this rotating or vibrating element. If the gyro frame is rotated about the sensitive axis of the gyroscope, which is perpendicular to the plane of motion of the rotating or vibrating element, the motion of the rotating or vibrating element detected by the sense element can only be defined by a fictitious acceleration term. This acceleration term is called Coriolis acceleration, and it is proportional to the angular velocity of the gyro frame about its sensitive axis. The presence of the rotating or vibrating element is therefore necessary for the sense element to detect the angular rate. For a rotating mechanical element, friction is inevitable, which definitely cause wear-out problems in the long-term operation. Friction is much more dominant in determining the lifetime of micrometer sized mechanical elements, such as in micromachined gyroscopes, since the atomic destruction caused by friction is comparable to the micromachining structure tolerances [10]. As a result, using vibrating mechanical elements are mostly preferred instead rotating components in micromachined gyroscopes. For this reason, most of the micromachined gyroscopes today include vibrating mechanical structures, for which the dominant energy dissipation mechanism is air friction instead of inter-atomic friction.

Figure 1.1 describes the Coriolis Effect in vibratory gyroscopes. A movable mass attached to the gyro frame is driven into sustained oscillations along the drive axis of the gyro frame. If an angular rate, Ω, is applied to the gyro frame about the sensitive axis that is orthogonal to the drive axis, a secondary oscillation is induced on the proof mass along the so-called output axis orthogonal to both the drive axis and the sensitive axis as observed by an observer $O2$ sitting on the gyro frame. Therefore, the observer $O2$ on the gyro frame sense the motion of the movable mass as if it tracks an elliptic path, whereas the observer $O1$ on the stationary frame sense the same motion as a superposition of rotation and linear oscillation, i.e., tracking a complex helical path. The frequency of the induced secondary oscillation sensed by the observer $O2$ on the gyro frame is identical to that of the sustained drive oscillations. On the other hand, the amplitude of the induced secondary oscillation is proportional to the angular velocity applied to the gyro frame.

4
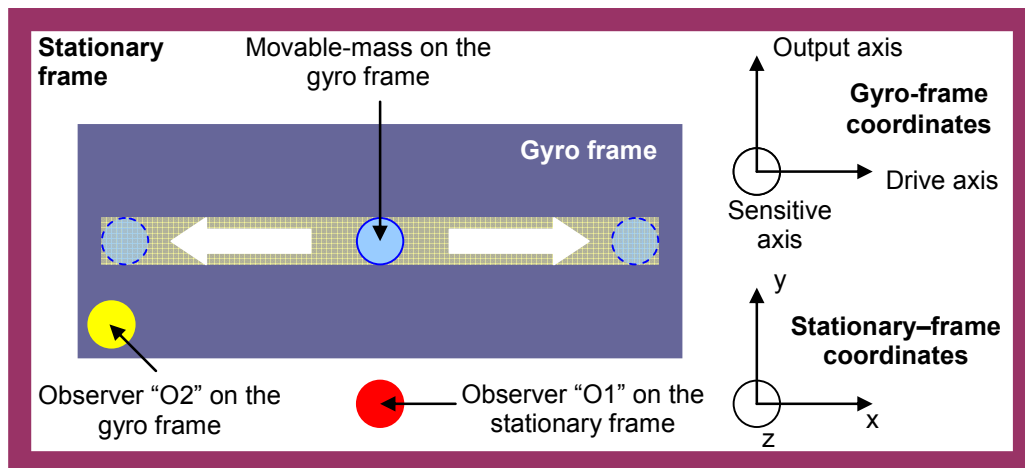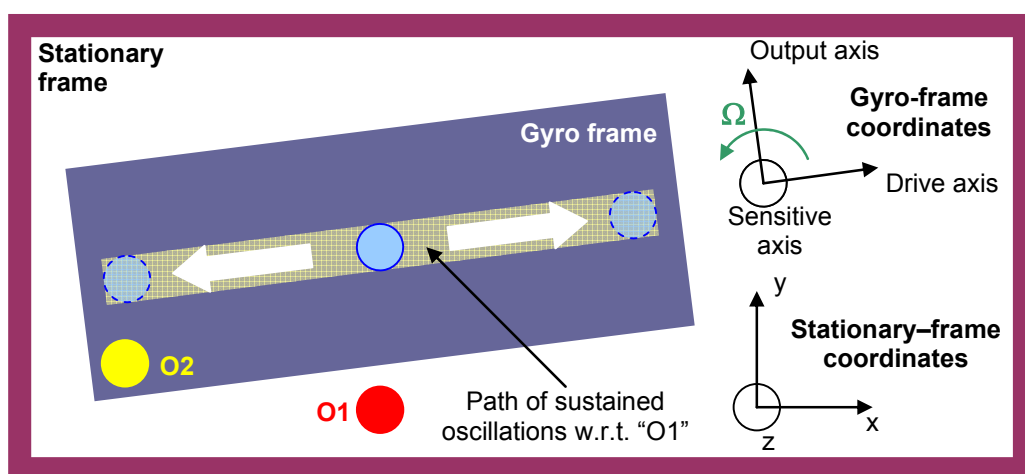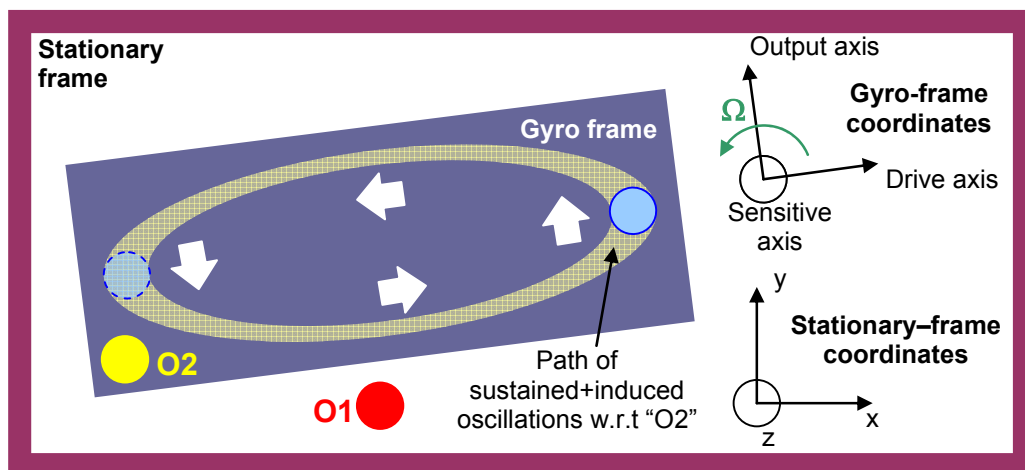
Figure 1.1: Coriolis-effect in a vibratory gyroscope. (a) Movable mass on the gyro-frame is driven into sustained oscillations. (b) Gyro-frame is rotated by a constant angular velocity Ω with respect to the stationary frame. The observer O1 senses the motion of the mass as a superposition of the rotation and the sustained oscillations (c) However, the observer O2 senses the motion of the mass as a superposition of the sustained oscillations and the induced oscillations as a result of fictitious Coriolis forces.

In general, electrostatic, piezoelectric, or electromagnetic actuation mechanisms are used to generate the sustained drive oscillations of the proof mass, whereas the induced oscillations of the proof mass is detected mostly by means of capacitive or piezoresistive sensing mechanisms mounted on the gyro frame, though there is a number of different sense mechanisms exist. The amplitude of Coriolis vibration in response to input angular velocity is very small compared to the sustained drive oscillations, and any crosstalk between the drive and sense modes of a vibratory gyroscope highly disturbs the measurements. Therefore, it is essential to precisely define the motion axes of the proof mass defining its degrees-of-freedom with respect to the gyro frame and to keep these axes orthogonal to each other. In practice, the mechanical structure of a vibratory gyroscope is much more complicated than a simple oscillating mass shown in Figure 1.1, and it includes dedicated flexures and anchor points that accurately define the degrees-of-freedom for the movable components of a vibratory gyroscope.

1.2 Performance Criteria and Tactical-Grade Requirements

The minimum detectable angular rate is not the only performance parameter for an angular rate sensor, and there are a number of other criteria that determines the overall quality of the sensor within various applications. These parameters include, but not limited to, the rate noise density, bias stability, measurement range, scale-factor linearity, input bandwidth, power supply requirements, operation temperature range, and g-sensitivity. Increasing the number of performance parameters also increases the design complexity and the number of possible trade-offs. Rate noise density and bias stability are the most important parameters among the list, which determines the performance grade of the gyroscope, whereas the significance of the remaining parameters varies for different applications. The complete definitions and terminology of performance parameters of vibratory gyroscopes can be found in [11], some of which are also described below:

Rate noise density is defined by the power spectral density of the self-generated noise from the gyroscope, representing the noise power at the output of the

gyroscope in a unit bandwidth. Both the mechanical-thermal noise from the sensor's mechanical structure and the electrical noise from the interface and control electronics contribute to this noise density, which determines the minimum detectable angular rate for the rate sensor. It is expressed in $(deg/sec)/Hz^{1/2}$, and it determines the measurement resolution in a given bandwidth.

Bias stability: All of the rate sensors provide a non-zero output in the absence of a rate input, called gyroscope rate bias or zero-rate output (ZRO). The stability of this bias in a particular time period is very important for many applications, since the bias point is the only reference for the gyroscope's output signal. Bias usually drifts in time due to a number of sources, including sensor architecture, fabrication process tolerances, post-process variations, packaging, and ambient temperature. It is expressed in deg/sec or deg/hr.

Measurement range: It is the specified as the maximum input rate over which the full performance will be provided. Expressed in ±deg/sec for positive and negative angular rate inputs.

Scale-factor and linearity: The output of an angular rate sensor is an analog DC signal proportional to the applied rate input. The scale-factor of the gyroscope is determined by the slope of the least-squares best-fit-straight-line drawn through the plot of the gyroscope output vs. applied input rate within the measurement range. It is expressed in V/(deg/sec). Linearity (R^2) is a measure of how successful the fit is in explaining the variation of the measured data in percent (%) full scale range. The maximum deviation of the measured output from a specified output function (not necessarily the best-fit straight line) determines the composite error, due to hysteresis, non-linearity, and non-repeatability, and it must not be confused with linearity.

Input bandwidth is determined by the maximum frequency of a time-varying angular-rate input, for which there is a 90° phase shift occurs between gyroscope output and the applied rate input. It can also be considered as the frequency of the

input rate for which the gyroscope output drops to $1/\sqrt{2}$ of the specified scale-factor value. Expressed in Hertz (Hz).

Power supply: Though the mechanical resonators used for creating drive-oscillations in a micromachined vibratory gyroscope requires high DC voltages, the power supplies of the sensor must lay within practical limits in terms of power dissipation and availability.

Temperature range: It is necessary to identify the parameters of the sensor that vary with temperature, such as rate bias and scale-factor, for practical use in many applications.

G-sensitivity: Minimizing the variation of the gyroscope output bias in response to acceleration inputs (g-sensitivity: $1g=9.8m/s^2$, gravitational acceleration) along the sensing axis is important for applications where there is no external accelerometer is employed for compensation purposes.

It is important to consider all of the criteria listed above in order to develop a complete rate sensor product, which is beyond the scope of this research. In this research, the parameters that determine the performance grade of the gyroscope are concerned primarily. Performance grades of gyroscopes can be classified in four major categories regarding these performance grades; rate-grade, tactical-grade, navigation-grade, and space-grade. Table 1.1 provides various requirements for these grades, including the rate-noise density, bias, scale-factor linearity, measurement range, and bandwidth requirements for these grades [1, 8].

Table 1.1: Rate noise density, bias, scale-factor linearity, measurement range, and bandwidth requirements for gyroscopes for different performance grades.

Parameter	Rate Grade	Tactical Grade	Navigation Grade	Strategic Grade
Rate noise density, $(deg/hr)/Hz^{1/2}$	>30	3-30	0.06-3	<0.06
Bias stability, deg/hr	>150	0.15-150	0.001-0.15	<0.001
Scale Factor Linearity, % FS	0.1-1	0.01-0.1	0.001-0.01	<0.001
Full scale range, deg/sec	50-1000	>500	>500	>400
Bandwidth, Hz	>70	~100	~100	~100

The progress of micromachined vibratory gyroscopes starting from 1990s enabled their use in newborn rate-grade applications where low-cost is essential. The performance of MEMS gyroscopes is not limited to rate-grade, and it is expected that most of the tactical-grade applications would be dominated by micromachined sensors by 2020 [8], though the performance of the best ones meet the specifications of only few tactical-grade applications today. Section 1.3 provides a list of challenges in the development of high-performance micromachined vibratory gyroscopes.

1.3 Challenges for Micromachined Vibratory Gyroscopes

Increasing the performance of a micromachined vibratory gyroscope for satisfying tactical-grade requirements needs careful assessment of several facts associated with vibratory gyroscope operation principles as well as micromachining technologies. A vibratory gyroscope consists of a movable proof mass, as described in Section 1.1, which has at least two-degrees-of-freedom along driving and sensing axes respectively. Figure 1.2 illustrates the simplest spring-mass-damper model describing such a proof mass structure. The drive and sense (output) axes are orthogonal to each other and to the sensitive axis of the gyroscope, which is set as the out-of-plane axis in the coordinate system of the figure. Kinematics of the given model is described by the second-order force-displacement characteristics along drive and sense axes separately as follows:

$$F_{actuation} = m_{drive}\ddot{x} + b_{drive}\dot{x} + k_{drive}x \tag{1.1a}$$

$$F_{Coriolis} = m_{sense}\ddot{y} + b_{sense}\dot{y} + k_{sense}y \tag{1.1b}$$

where F, m, k, and b in the above equations correspond to the force acting along that particular mode, mass, damping, coefficient, and the spring constant associated with a particular mode of the gyroscope, respectively. $\dot{x}, \dot{y}$ and $\ddot{x}, \ddot{y}$ corresponds to the first and second derivatives, respectively, of the displacement vectors x and y. The

mechanical resonance frequency for the given second-order systems are defined as follows in radians:

$$\omega_{resonance} = \sqrt{\frac{k}{m}} = 2 \cdot \pi \cdot f_{resonance} \qquad (1.2)$$

The amplitude of displacement of a vibrating system is maximized at the resonance frequency of the system, at which the amplitude is only limited by the energy losses through the damper. Efficient use of actuation energy is a key point for any micromachined gyroscope, and therefore, the resonance frequency associated with the drive axes motion of the proof mass, i.e., drive-mode of the gyroscope, is the most suitable selection for the frequency of the driving force applied to the proof mass for generating sustained drive-mode oscillations. This way, it is possible to generate the maximum vibration along the drive mode, which is necessary to increase the gyroscope output response to input angular rates by using minimum necessary actuation force.
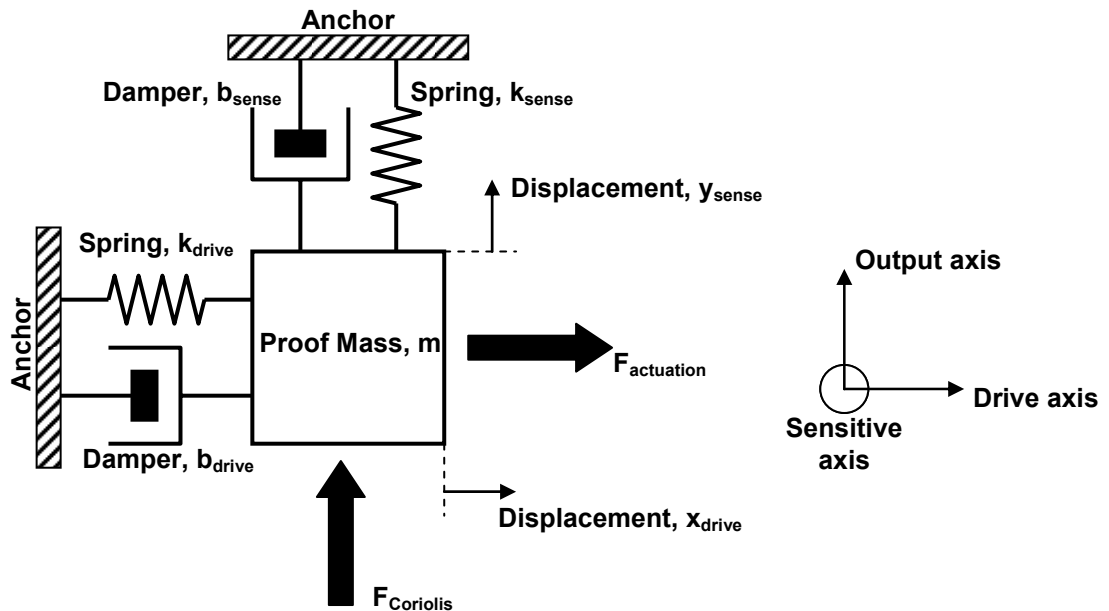
Figure 1.2: The simplest spring-mass-damper model for describing a single-proof-mass gyroscope structure having two-degrees-of-freedom. $F_{actuation}$ and $F_{Coriolis}$ correspond to generated actuation force along the drive mode and the induced Coriolis force along the sense mode, respectively.

After driving the proof mass of the gyroscope into sustained oscillations along the drive-mode, the sensor is ready for rate detection. As the gyro frame is rotated about the sensitive (out-of-plane) axis, the sense mechanism of the gyroscope detects the induced oscillations along the sense axes of the gyroscope in response to the applied input rate. Induced oscillations arise due to fictitious Coriolis forces along the sense axis, whose frequency is identical to the sustained drive oscillations for a constant rotation, i.e., a time-invariant angular rate input. As the Coriolis force acting along the sense axis of the proof mass is a time-varying force with a frequency identical to the drive-mode mechanical resonance frequency, the response obtained from the sense output of the gyroscope is maximized if the sense-mode mechanical resonance frequency is set close to the drive-mode mechanical resonance frequency. Figure 1.3 illustrates the effect of matching the resonance frequencies of the drive and sense modes of a vibratory gyroscope on the angular rate sensitivity of the gyroscope. When the resonance frequencies of the two modes are identical, the sense mode response of the gyroscope is theoretically amplified by the mechanical quality factor of the sense mode, which can be as high as few thousands at vacuum ambient for high-quality structural materials.

Vacuum is necessary to obtain very high mechanical quality factors, since air is the dominant damping mechanism for vibrating microsensors operating at atmospheric pressure [12]. Eliminating air molecules in the ambient increase the quality factor to a limit defined by the mechanical damping of the structural material, which is much smaller for high-quality materials compared to the air damping. Vacuum operation with high mechanical quality factors improves the signal-to-mechanical-noise ratio of the gyroscope significantly, maximizing the sense mode response to the applied angular rates. Maximizing the angular rate response is essential for reaching to the ultimate resolution limits, with the trade-off between resolution and input bandwidth. Analyzing Figure 1.3, it is clear that the bandwidth of the gyroscope shrinks as the resonance frequencies of the drive and sense modes move close to each other, since the Coriolis force now acts along the steepest edge of the sense mode response characteristics. This trade-off is usually handled by keeping the resonance frequencies of the two modes of the gyroscope close to each other, but not perfectly

matched, since perfect matching of the frequencies is also not practical in terms of mechanical cross-coupling as described next.
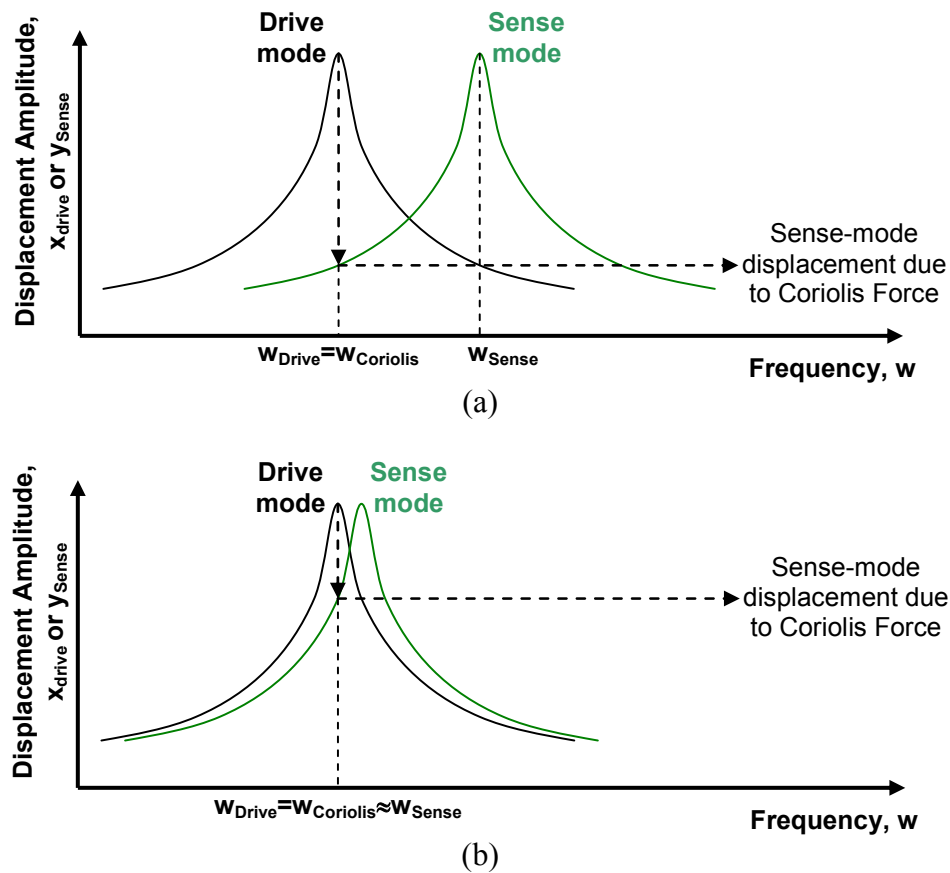
Figure 1.3: The effect of matching the resonance frequencies of the drive and sense modes of a vibratory gyroscope on the angular rate sensitivity of the gyroscope. Sense-mode displacement in response to an angular rate input increases as the drive and sense modes of the gyroscope are closely matched as in (b) compared to the case where the modes are separated as in (a).

Mechanical cross-coupling or crosstalk between the drive and sense modes is one of the major problems facing micromachined vibratory gyroscopes. In practice, drive and sense axes of a vibratory gyroscope are not perfectly aligned orthogonal to each other, due to micromachining tolerances. These tolerances are poor for micromachining [13], comparing them to the fine feature sizes used in micromachined structures. The width of a few-micrometer-wide beam structure cannot be defined with a tolerance better than 10% using standard microlithography processes. In addition, imbalanced mass distribution in the movable gyroscope components, misalignment of driving actuator with respect to drive axis, and

12

misalignment of sensing mechanisms with respect to the sense axis all result in a false output response from the sensing mechanism in the absence of a rate input. This response is defined as the zero-rate output (ZRO) or rate bias of the gyroscope. As a striking example, 0.1° misalignment of a driving actuator with respect to the pre-defined drive axis could result in a mechanical quadrature signal as high as several hundred deg/sec, which is difficult to suppress below few deg/sec even using phase sensitive detection algorithms. The high quadrature signal causes an offset at the gyroscope output, and even it may saturate the readout electronics. A high rate bias is also susceptible to higher drift, which is a vital parameter for many applications.

Micromachined gyroscope structures employ different decoupling mechanisms as well as precision processes for achieving a minimum rate bias and bias drift characteristics. Figure 1.4 describes three basic approaches in decoupling the driving actuator, the proof mass, and the sensing mechanism of a vibratory gyroscope. Figure 1.4-a shows the simplest configuration similar to the spring-mass-damper model of Figure 1.3, neglecting the damper for convenience. Here, the driving actuator, proof mass, and sensing mechanism of the gyroscope are all attached to each other and have 2DOF motion capability; any misalignment associated with the drive axis and the driving actuator force is directly detected by the sense mechanism as a false rate signal. Figure 1.4-b shows an improved decoupling mechanism, in which the driving actuator motion is limited to 1DOF along the pre-defined drive-axis only. Now, the non-ideal actuation forces cannot excite false vibrations along the sense axis, provided that the drive-axis is perfectly orthogonal to the sense axis. In addition, there is no back-interaction from the rate-induced sense motion to the drive oscillations, resulting in linear and balanced drive oscillations all the time. However, the sensing mechanism is still in continuous motion along the drive-axis in the absence of a rate input. This continuous motion makes the sense output susceptible to drift in time. Figure 1.4-c shows the advanced decoupling mechanism, in which the driving actuator and the sensing mechanism are separated from the proof mass and restricted to 1DOF motion along drive and sense axes, respectively. This configuration keeps the sense mechanism stationary while

13

the proof mass oscillates along the drive-mode. This way, the interaction between the driving actuator and sensing mechanism is further suppressed, if not cancelled, due to process variations.
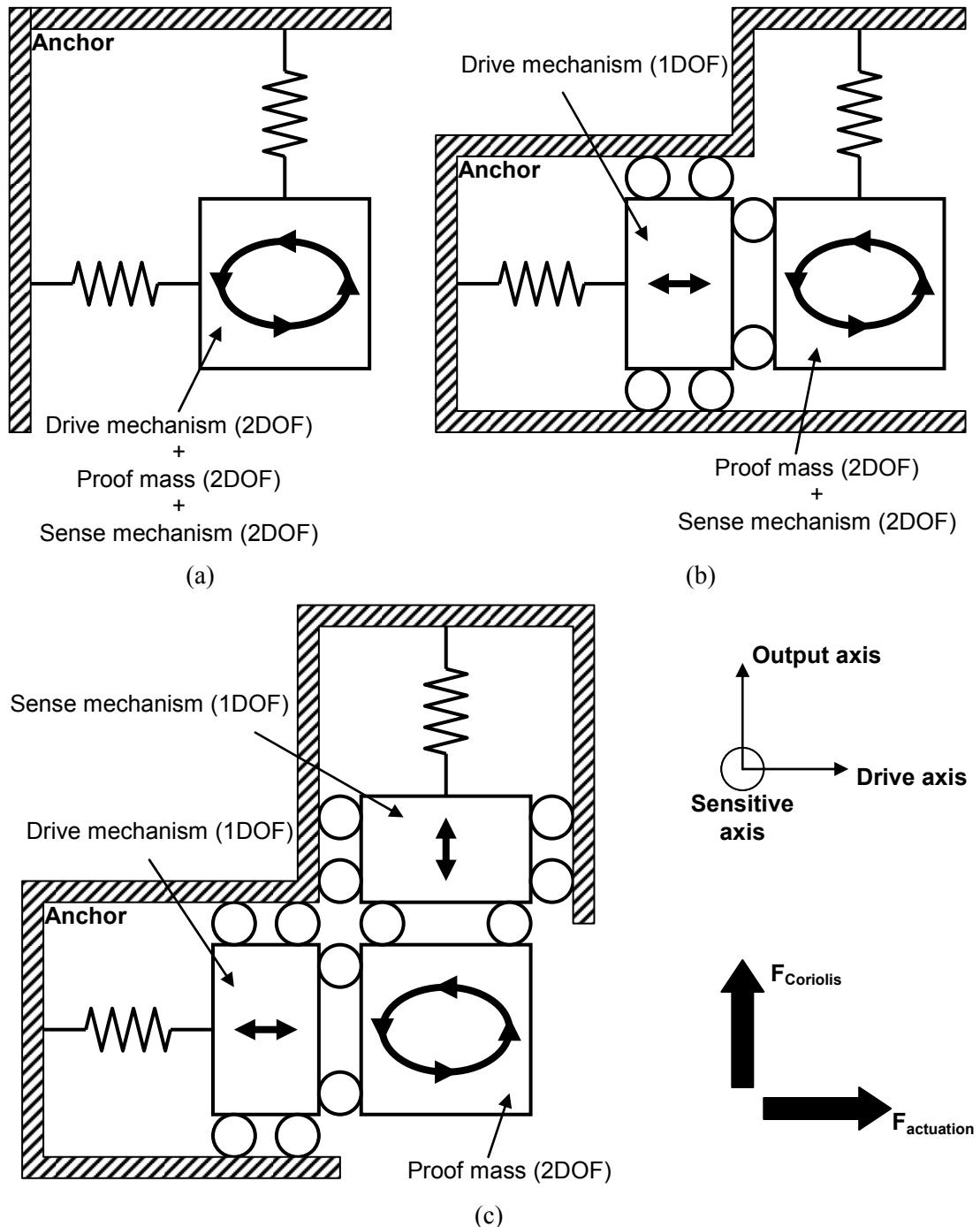
Figure 1.4: Basic decoupling approaches for vibratory gyroscopes. (a) Single-mass configuration with no special decoupling treatment. (b) Decoupling the drive mechanism from the rest of the system suppress mechanical crosstalk between drive and sense modes. (c) Sense mechanism is stationary in the fully decoupled configuration, unless an angular rate input is applied to the gyro frame.

The ideal rollers in Figure 1.4 are implemented using lengthy flexible beams in order to eliminate possible friction, which have finite mechanical stress during drive-mode motion causing a non-zero mechanical crosstalk. Clearly, the precision of the fabrication process is still the dominant factor in any of the implemented decoupling mechanisms, but advanced decoupled structures such as in Figure 1.4-c with dedicated flexure designs reduce the burden on the fabrication tolerances.

Symmetric design of the flexures for the drive and sense modes of a micromachined vibratory gyroscope is another important challenge in terms of both mode matching and reduced temperature-dependent drifts. Symmetric flexures induce similar mechanical stresses during operational vibrations, ambient temperature variations, and package-induced bending. The resembling behavior of the flexures along the drive and sense modes help keeping the matching between the resonance frequencies of the drive and sense modes during the regular operation of a micromachined vibratory gyroscope. Obviously, this may not be a critical issue for rate-grade vibratory gyroscopes operating with highly-separated drive and sense mode resonance frequencies, but it is essential for tactical-grade gyroscopes where closely-matched drive and sense frequencies are required in order to maximize the efficiency of both actuation and sensing energies.

The energy loss in a gyroscope can be minimized by a proper electromechanical design and an optimized fabrication process. Various dampers dissipate energy in micromachined vibratory gyroscopes. The well-known energy dissipating mechanisms are damping due to air molecules, soft anchors, thermo-elastic damping, and damping due to electronics [14, 15]. Air damping is usually reduced by operating the gyroscope in vacuum ambient. Truly rigid anchors depend on multi-step optimization during the design phase, material selection, and fabrication process. Thermo-elastic damping of the structural material is again a material selection problem. Metals and polycrystalline silicon have amorphous structure, rather than regular crystallographic orientation, and exhibit higher damping. Single-crystal silicon, on the other hand, has a much smaller damping and has superior mechanical properties compared to amorphous structural materials. For this reason, it is one of

the most preferred structural materials for micromachined vibratory gyroscopes together with single-crystal quartz. The performance obtained by minimizing the energy losses is further improved by minimizing electronic damping [14].

Noise is the key factor determining the resolution of micromachined transducers. Careful consideration of the random noise generated by the mechanical sensor and the readout electronics is essential to improve the overall performance. Two major random noise components in micromachined vibratory gyroscopes are the mechanical-thermal noise (Brownian noise) and the electronic noise around the operating frequency of the gyroscope.

Brownian motion is a well-known mechanical-thermal noise mechanism that is dominant in determining the sensitivity of micromachined transducers including gyroscopes, accelerometers, and microphones [12]. Any micromachined structure is subject to a random agitation caused by molecular collisions from a surrounding gas or liquid, where the agitation is directly related to the fluid's viscosity. The agitations caused by Brownian motion of air molecules can be the dominant noise source for a micromachined vibratory gyroscope, since the sense mode output vibrations of a micromachined vibratory gyroscope in response to a 1deg/sec angular rate input is usually smaller than an Angstrom (10^{-10}m or equivalently 10^{-4}μm). Brownian motion associated with the sense mode of a micromachined gyroscope can be three to four orders of magnitude smaller than this value, if the gyroscope is operated at vacuum ambient around 100mTorr. In this case, the noise of the preamplifier and remaining readout electronics become the dominant noise sources. Low-noise preamplifier design, optimum selection and construction of readout and control circuits, and electronics packaging play important role in determining the overall resolution of the gyroscope.

A preamplifier is used as an interface circuit between micromachined angular rate transducer and the associated electronics. This interface circuit must be carefully designed depending on the type of sensing mechanism of the gyroscope, like capacitive, piezoresistive, or magnetic sensing. Capacitive sensing is popular due to

16

several attractive features: it has high-sensitivity, requires minimal or no additional process steps, has dual use as an actuator or sensor, and robust against ambient temperature variations [16]. Highly-sensitive buffer-type capacitive interface circuits require very small input capacitances for buffering the high-impedance outputs of the micromachined capacitive gyroscopes. The challenges facing capacitive interfaces are parasitic capacitances, electronic noise, and input-node biasing.

Micromachined capacitive vibratory gyroscopes usually have sense capacitances ranging from few tens of femtofarads (1fF=10^{-15}F) up to few picofarads (1pF=10^{-12}F). The output signal generated from a capacitive gyroscope with 1pF sense capacitance in response to a 1deg/sec angular rate would typically require detection of capacitance changes less than few attofarads (1aF=10^{-18}F). Such small capacitance changes are easily affected from parasitic capacitances around the gyroscope structure and the readout electronics. Parasitic capacitances originates from routing of signal-carrying interconnect lines of the gyroscope and the electronics chips, conductivity of the substrates on which the gyroscope is fabricated, and wirebonding used for hybrid connection of gyroscope and preamplifier electronics chips. These parasitic capacitances cause spurious electrical feed through between the electronic signals used to generate electrostatic forces for drive oscillations of the gyroscope and the sensing mechanism. It may not be possible to differentiate such an electrical feed through from the rate output signal, even by phase-sensitive detection, for a micromachined gyroscope with matched drive and sense modes. This adversely affects the sensitivity of the gyroscope.

The challenges listed above are part of a diverse list including repeatability of the fabrication process, stress-free and reliable packaging and assembly of sensor and readout chips, and shock-survival characteristics. Improvements in micromachining technologies combined with novel sensor architectures demonstrate an increase in the overall performance of micromachined vibratory gyroscopes in recent years. The next section provides an overview of micromachined vibratory gyroscopes reported in the literature.

1.4 Overview of Micromachined Vibratory Gyroscopes

Commercial success of micromachined acceleration sensors in automotive and then in military industries in the past twenty years has pushed the research on micromachined vibratory gyroscopes for constructing micro inertial measurement units for both commercial and military applications. The Charles Stark Draper Laboratory reported one of the first micromachined vibratory gyroscopes, having a gimbal structure [17]. The fabrication process of this gyroscope is compatible for batch fabrication together with the use of on-chip electronics. Fabricated through a high-concentration boron doping and EDP anisotropic etching steps, the gyroscope resolves only 4deg/sec in 1Hz measurement bandwidth due to its small size and 10μm-spaced capacitive sense gaps. Similar designs are also reported with electroplated copper and nickel into deep photoresist molds [18] and circularly gimbaled structures with electromagnetic actuation and detection [19]. The performance and reliability of gimbaled micromachined vibratory gyroscopes are limited by large capacitance gaps, thin structural layers, nonlinearities associated with torsion-based displacements, high mechanical cross-talk between the modes.

Contrary to torsional movement of gimbaled gyroscope structures, research is also conducted on linearly actuated vibrating mass gyroscopes. Toyota reported a three-layer polysilicon surface-micromachined vibrating mass gyroscope, employing linear comb-drive electrostatic actuation and parallel-plate differential capacitive sensing [20] and then encapsulated in vacuum ambient [21]. This structure exhibits a resolution of 1deg/sec, limited by the sense electrode areas that are kept small due to residual stress of the surface-micromachined polysilicon deposit. The advances in dry etching of silicon allowed the researchers to construct much thicker structural layers using bulk micromachining, in order to increase the response from the vibrating mass [22]. Still, it was difficult to have the overall performance of vibrating beam gyroscopes below 1deg/sec, due to excessive mechanical-crosstalk between the drive and sense modes, small capacitive areas, temperature-dependent-drifts of piezoresistive detection mechanisms, and the sensitivity of the single vibrating mass to external acceleration inputs.

18

An improved version of the vibrating beam structure, called tuning-fork, has twin-mass architecture, where two masses are oscillated in opposite directions along the drive axis. Figure 1.5 shows the tuning-fork structure. The tines of the structure are driven into anti-phase oscillations along the drive axis. The oscillating tines response to angular rate inputs in directions opposite to each other, due to opposite Coriolis forces acting on them. Anti-phase Coriolis response from the tines are then detected by a differential readout scheme. The tuning-fork configuration is robust against spurious responses due to external acceleration inputs, since the acceleration inputs cause a common deflection of the tines in the same direction, being rejected by differential readout. Daimler-Benz demonstrated a tuning-fork rate gyroscope for demanding automotive applications using piezoelectric actuation and piezoresistive detection [23]. The actuation direction of the tines is designed to be vertical to the substrate plane, allowing the fabrication of large-area tines that generate significant output signals. Temperature sensitivity of pizeoresistive detection is still a concern for such designs. Robert Bosch GmbH also reported a yaw rate sensor for automotive applications [24], with minimized mechanical crosstalk using precision stepper lithography and relaxed packaging requirements due to high-Q of the structural material as well as low operating frequencies (2kHz).
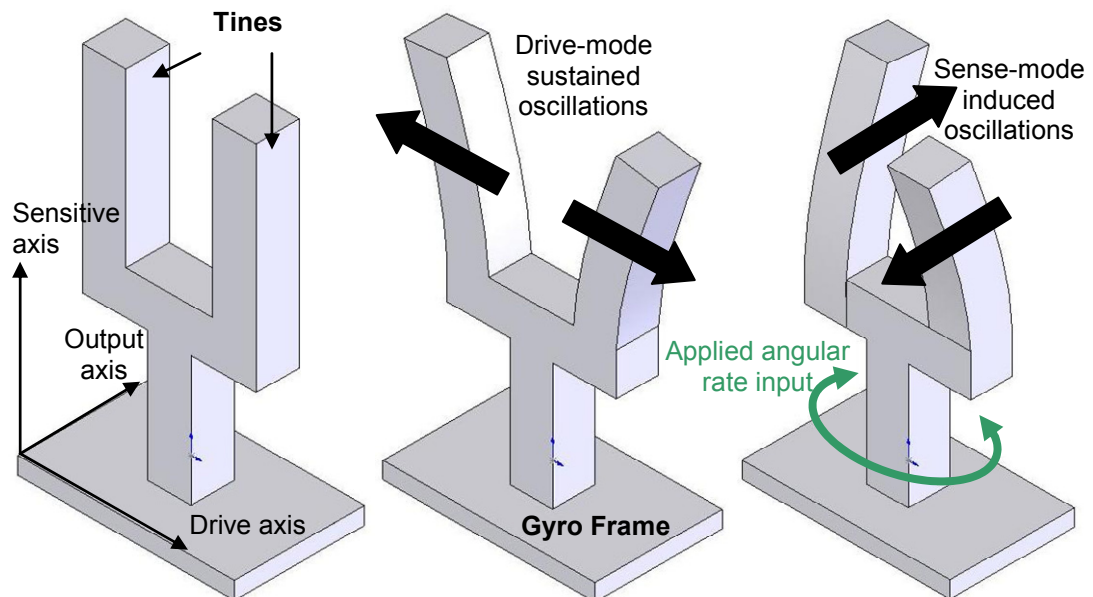
Figure 1.5: Tuning-fork vibratory gyroscope structure (Left). The tines are oscillated anti-phase along the drive-axis (middle) and respond to angular rate inputs applied about sensitive axis (right). The output response has also anti-phase nature and detected by differential readout, while rejecting common-mode response of the tines to spurious accelerations.

There are also resonating disk structures developed for micromachined gyroscopes for automotive applications. In 1999, Bosch reported another surface micromachined gyroscope fabricated of 11μm-thick low-stress polysilicon structural layer [25]. The sensor structure extends to 1.6mm without experiencing stress-induced buckling. Figure 1.6 shows the fabricated sensor hermetically sealed using a silicon cap. Targeting batch production for automotive applications, this sensor provided a noise equivalent rate as small as 0.4deg/sec in 1Hz bandwidth. A similar structure fabricated using a dissolved wafer process is reported in [26]. Obviously, size and unit-cost limitations of the automotive-grade rate sensors limit their performance for use in military applications that require higher performance.
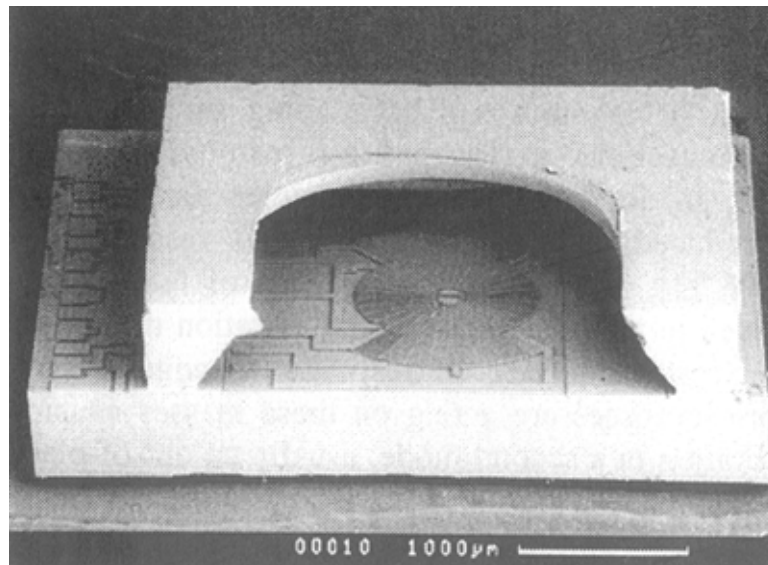
Figure 1.6: Bosch's angular rate sensor fabricated using a thick polysilicon structural layer and encapsulated using a silicon cap for hermetic sealing purposes [26].

Draper Labs reported their first micromachined tuning-fork vibratory rate gyroscopes for high-performance military applications in 1993 [27]. The gyroscope is fabricated using different structural materials including electroformed nickel, single-crystal silicon, and polysilicon, and it employs electrostatic actuation for large drive-mode vibration amplitudes up to 10μm using linear comb electrodes and stress-relieving folded flexures. The performance of the gyro is reported to be 0.19deg/sec in 1 Hz bandwidth, when operated at vacuum ambient. The tuning fork gyroscope showed an increasing performance from 5000deg/hr (1.4deg/sec) in

20

60 Hz bandwidth to an impressive performance of 25deg/hr in 60Hz bandwidth after collaboration of Draper Lab with Boeing North American [28]. Undesired crosstalk between the drive and sense modes of this tuning-fork design requires precision micromachining in a proprietary fabrication process and complicated nonlinear drive electronics in order to reach the tactical-grade performance.

BEI Systron Donner Inertial Division also develops high-performance tactical-grade tuning-fork microgyroscopes for aerospace and defense applications, fabricated by micromachining of single-crystal quartz [6]. The output noise-equivalent-rate of the quartz tuning-fork rate sensor is very good, approaching to 30deg/hr in 1Hz bandwidth. However, micromachined quartz rate sensors lost their popularity due to complicated electronics required for temperature compensation of quartz structural material, special micromachining techniques for fabricating quartz sensors, recent advances in silicon micromachining technologies, and integration of the silicon rate sensors with readout electronics on the same chip. Quartz rate sensor manufacturers also target lower performance applications, such as automotive applications for the future market [6, 29].

High-performance microgyroscopes with thicker structural layers, smaller capacitive gaps, and larger drive-mode vibration amplitudes are also implemented using LIGA process, which employs electroplating inside an ultra-thick photoresist mold. Rate resolution as small as 0.04deg/sec is achieved in 27Hz bandwidth with such a gyroscope [30], by electroforming nickel into a 250μm-thick PMMA mold patterned by deep X-ray lithography and by actuating the drive mode to vibration amplitudes as high as 70μm. The major disadvantages of this approach are the limited availability of very-high-cost deep X-ray lithography and possible reduction of the long-term reliability of the nickel structural material.

The ring geometry is proven to be a promising structure for high-performance micromachined vibratory gyroscopes. Figure 1.7 shows the three-dimensional model and corresponding actuation, input, and detection axes of the gyroscope as well as the scanning electron microscope (SEM) picture of a fabricated ring

structure. The inherent symmetry of the drive and sense vibration modes in a ring structure allows easy matching of the resonance frequencies of the drive and sense modes as well as electrostatic control of stiffness and mass imbalances resulting from fabrication tolerances [31]. Matching the resonance frequencies improves the gyroscope resolution by the mechanical quality factor of the sense mode, whereas the symmetry of the flexures of the ring design keeps the frequencies closely matched for varying ambient temperatures.

An electroformed version of ring gyroscope integrated with CMOS readout and control electronics demonstrated a noise floor of 0.5deg/sec in 25 Hz bandwidth with its 15μm-thick nickel structural layer and 7μm capacitive gaps [31, 32]. An improved version of the vibrating ring structure is fabricated using a high-aspect ratio combined poly and single-crystal silicon MEMS technology [33]. The performance of the gyroscope is improved by an order of magnitude with this technology, since 80μm-thick structural layer combined with 1.4μm-wide capacitive gaps carried the performance of the initial ring gyro design to about 0.01deg/sec (36deg/hr) in 1Hz bandwidth. The complexity of the fabrication process is the major limitation for this design. Later in 2002, University of Michigan reported a new ring gyroscope fabricated through a much simpler process using deep reactive ion etching of silicon [34]. A 150μm-thick single-crystal silicon structural layer together with 12,000 mechanical quality factor of the sense mode at vacuum provided a resolution better than 11deg/hr in 1Hz bandwidth. Inherently the symmetric structure of the ring gyroscope allows very small resolutions due to high mechanical quality factors, although the actuation amplitude and linearity of the ring design is highly limited compared to classical tuning-fork-based designs. A recent study reports a star-shaped gyroscope similar to the ring gyroscope [35]. This latest design is expected to resolve angular rates as small as 8.5deg/hr in 1Hz bandwidth, if fabricated with single-crystal silicon. There is also a research on implementing a three-axis angular rate sensor using the vibrating ring structure [36]. Current limitations of the vibrating-ring structures are basically due to the small drive-mode vibrations, limited to sub-micron amplitudes in general, and hybrid connection of the gyroscope to the interface and control electronics.
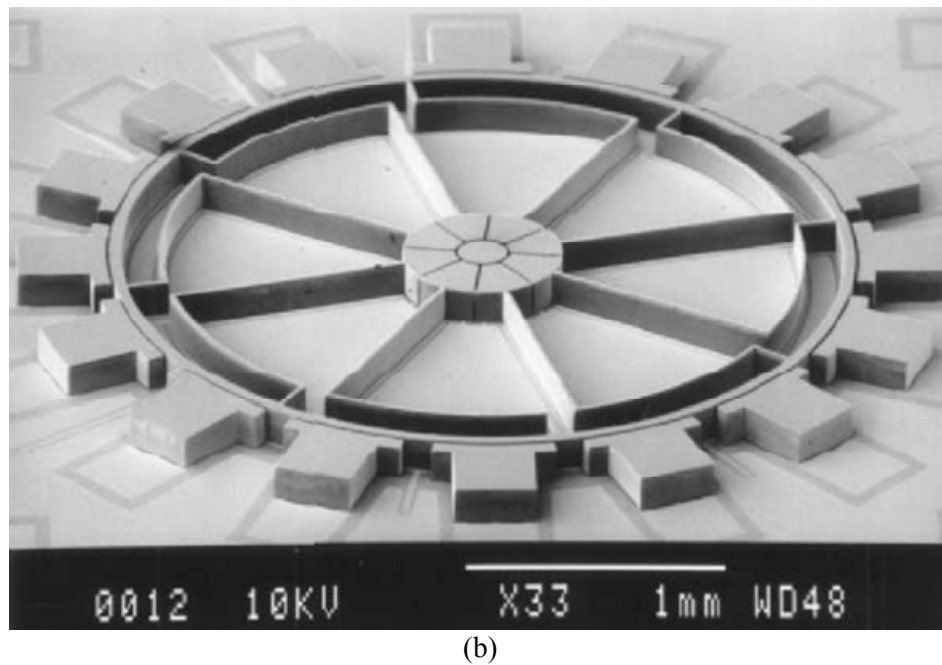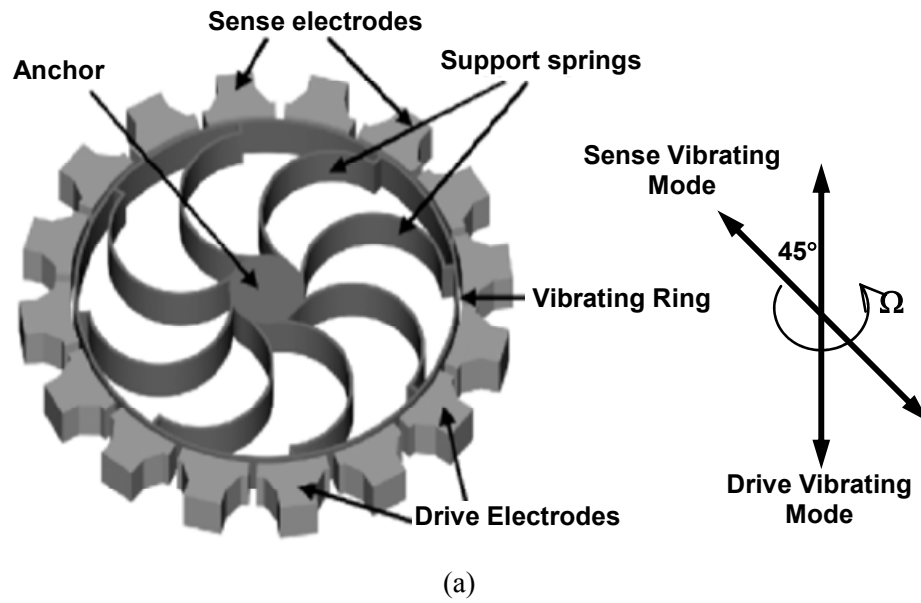
Figure 1.7: Vibrating ring gyroscope. (a) Three-dimensional model describing the major components and measurement axes. (b) SEM picture of a fabricated ring gyroscope structure [35].

There is also research continues on the development of CMOS-integrated micromachined vibratory gyroscopes. Other than the ring gyroscope reported in [32], there are different approaches for the integrated rate sensor development [37-43]. Carnegie Mellon University developed a micromachined vibratory gyroscope by post-processing a CMOS substrate containing readout and control electronics of the gyroscope [37]. First a CMOS substrate is processed to construct

the integrated electronics as well as the structural features of the gyroscope that would be defined by DRIE following the CMOS process. Deep reactive ion etching of silicon sensor features defined on the CMOS substrate followed by isotropic silicon undercut process forms the gyroscope on the same substrate with CMOS electronics. An improved version of the same structure fabricated with post-CMOS processing of a 0.18μm six-copper-layer CMOS wafer, demonstrated a resolution of 0.5deg/sec in 1Hz bandwidth [38]. Obviously, the thickness and structure of the gyroscope is defined by a stack of CMOS metal and isolation layers, which cause curling of the fabricated structure after release. This is expected since the residual stress of the layers in a standard CMOS process does not meet the requirements of mechanical sensor element.

Analog Devices reported a surface micromachined integrated microgyroscope in 2002, using their state-of-the-art BiCMOS technology with micromachining of polysilicon structural layer [39]. Figure 1.8 shows the gyroscope together with surrounding integrated electronics. This process is used to produce tens of millions of single-chip integrated airbag sensors within the past decade. Gyroscope has a twin-mass structure as in tuning-fork designs and provide a small crosstalk between the drive and sense modes using mechanical-leverages. Although the thickness (4μm), size (2mm x 1mm), and capacitance (~1pF) of the gyroscope are all quite small compared to the devices fabricated with advanced micromachining technologies, the sensor provided an impressive noise equivalent rate of 0.05deg/sec in 1Hz bandwidth and currently in batch fabrication, owing to the mature polysilicon surface micromachining technology, high-quality monolithic readout electronics with temperature compensation, and decoupled sensor architecture.

The limited performance of surface-micromachined integrated gyroscopes leads the researchers to study on bulk micromachining of CMOS-substrates. Backside thinning of the CMOS substrate from 500μm down 80μm and then front-side deep etching of silicon results in a bulk-micromachined gyroscope structure integrated with CMOS electronics [40, 41]. The resolution of the gyroscope is measured to be 0.01deg/sec in 1Hz bandwidth. A similar structure with competitive performance is

also reported in [42]. Beside the significant advantages of integrating micromachined gyroscopes with CMOS electronics, the major concerns of this approach are the long-term reliability of CMOS layers in continuous motion and difficulties with the handling of high-cost CMOS substrates.
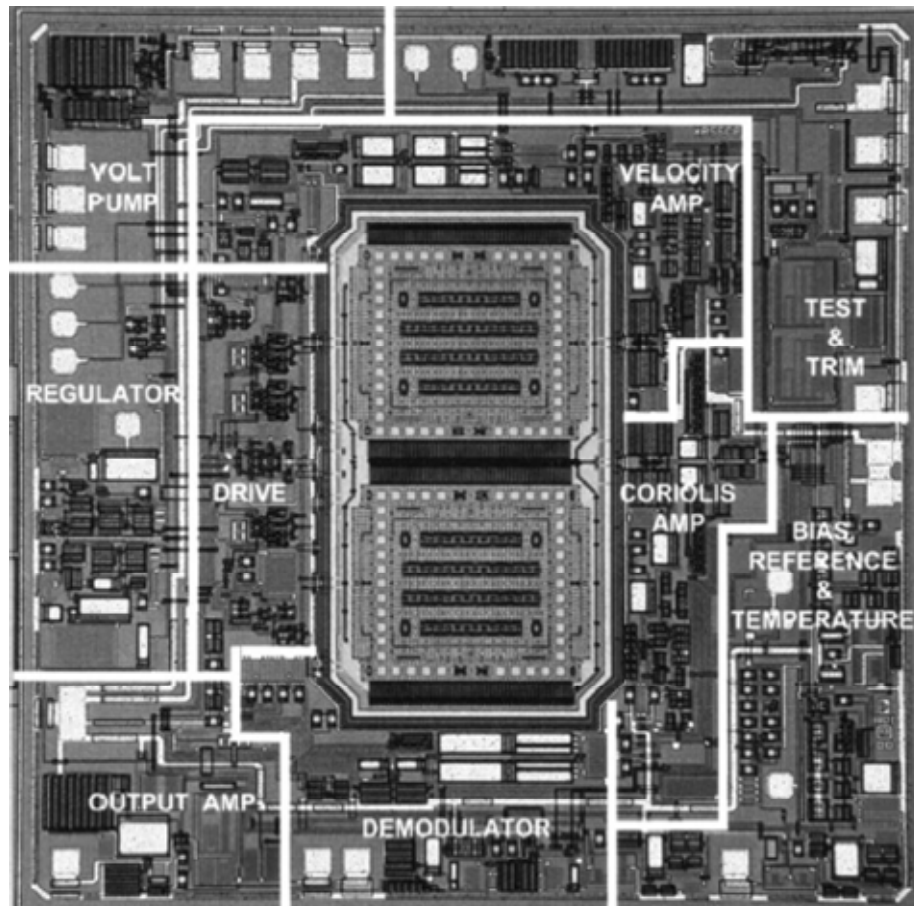
Figure 1.8: Analog Devices ADXRS gyroscope together with surrounding integrated electronics [39].

A simple and reliable micromachining process combined with advanced micromechanical designs is yet another approach in the development of high-performance micromachined angular rate sensors. Samsung reported a single-mask z-axis micromachined gyroscope with a noise-equivalent rate of 0.01deg/sec in 5Hz bandwidth [44]. The gyroscope is fabricated by anodic bonding of silicon and glass wafers followed by polishing and front-side DRIE etching of silicon wafer until silicon-glass interface, and finally the structures are released by glass wet etch. A similar process including anodic bonding of silicon and glass wafers in addition to

deep etching of silicon from both sides is also reported in [45], providing a bulk silicon gyroscope with very low mechanical noise floor. Murata reported another structure with mechanical decoupling of drive and sense modes fabricated on a silicon-on-insulator (SOI) substrate with a performance of 0.07deg/sec in 10Hz bandwidth [46]. Later in 2001, Murata reported a similar structure with a resolution better than 15deg/hr in 1Hz bandwidth [47]. The importance of reducing mechanical crosstalk between the vibration modes of micromachined gyroscopes drew a lot of attention in constructing high-performance gyroscopes [48-55]. Samsung reported a decoupled microgyroscope with a resolution better than 10deg/hr in 1Hz bandwidth [50]. HSG-IMIT also developed decoupled vibratory microgyroscopes with resolutions close to 10deg/hr, fabricated on SOI substrates, and they rely on both torsional and linear vibrations [51]. Figure 1.9 shows an SEM picture of a fabricated gyroscope with torsional flexures for the drive and sense modes.
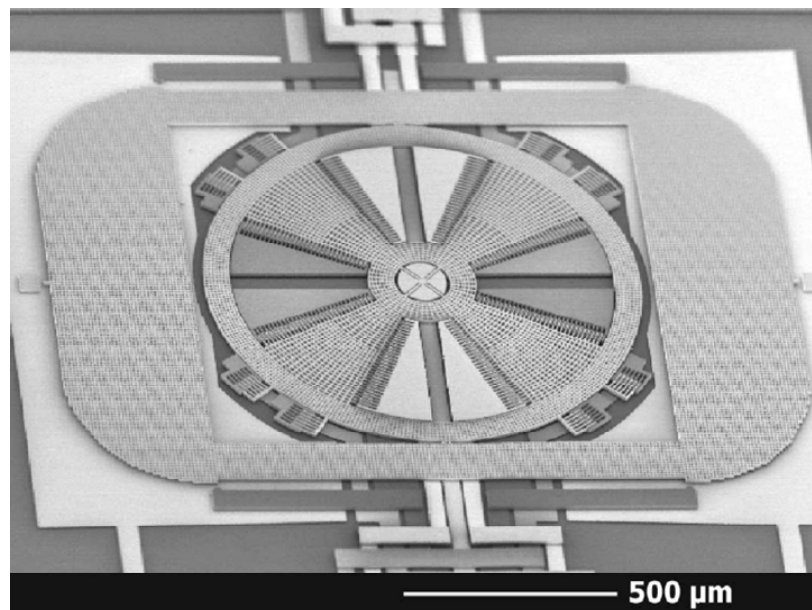
Figure 1.9: Decoupled microgyroscope with torsional oscillation modes, developed by HSG-IMIT [51].

Researchers at Berkeley Sensor and Actuator Center (BSAC) and Analog Devices also studied mechanical coupling on different drive and sense configurations [52]. Complicated mechanical designs are also reported for reducing mechanical crosstalk [53-55], though the rate measurement resolutions are still limited due to electronics

26

[54, 55]. In addition, SensoNor's butterfly-shaped gyroscope [56], Seoul National University's metal-interlaid silicon-on-glass gyroscope [57, 58], out-of-plane [59] and in-plane [60] silicon microgyroscopes fabricated using a surface/bulk micromachining (SBM) process, and a recently reported SOI tuning-fork gyroscope [61] all show remarkable performance approaching to tactical-grade limits. Figures 1.10 and 1.11 show the SEM pictures of SensoNor's butterfly gyroscope and Seoul National University's silicon-on-glass gyroscope, respectively. Different approaches to reach tactical-grade micromachined gyroscopes include linked gyroscope arrays [62] as shown in Figure 1.12, NASA JPL's clover-leaf structure [63], BSAC's dual-axis gyroscope [64], and reduced-damping structures [65]. There are also studies on the development of absolute angle gyroscopes instead of rate gyroscope [66]. Most of these structures have dedicated mechanical designs, are implemented through standard micromachining processes, rely on basic tuning-fork or vibrating-beam principle, and use electrostatic actuation and capacitive detection.
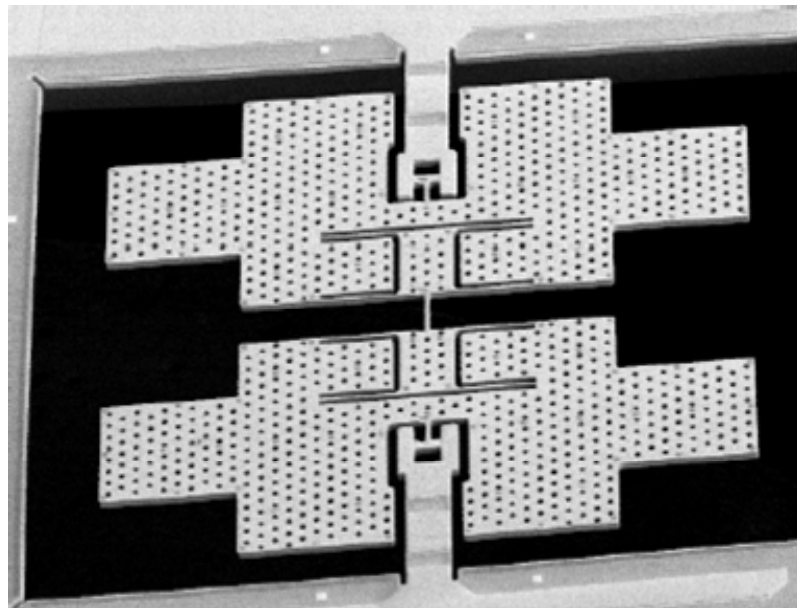
Figure 1.10: SensoNor's butterfly-shaped gyroscope structure [56].

Finally, there are micromachined gyroscopes that use different transduction methods. Micromachined gyroscopes with electromagnetic actuation and piezoresistive detection [67, 68], electrostatic actuation and optical detection [69], electrostatic actuation and piezoresistive detection [70] are such examples. BSAC's resonant output gyroscope [71], dual-axis quartz angular rate sensor [72], magnetically-

suspended spinning-wheel MEMS gyroscope [73], as well as micromachined gyroscopes based on thermal convection [74] and microfluidics [75] are examples of various approaches used for angular rate sensing with micromachined sensors.

(a)   (b)
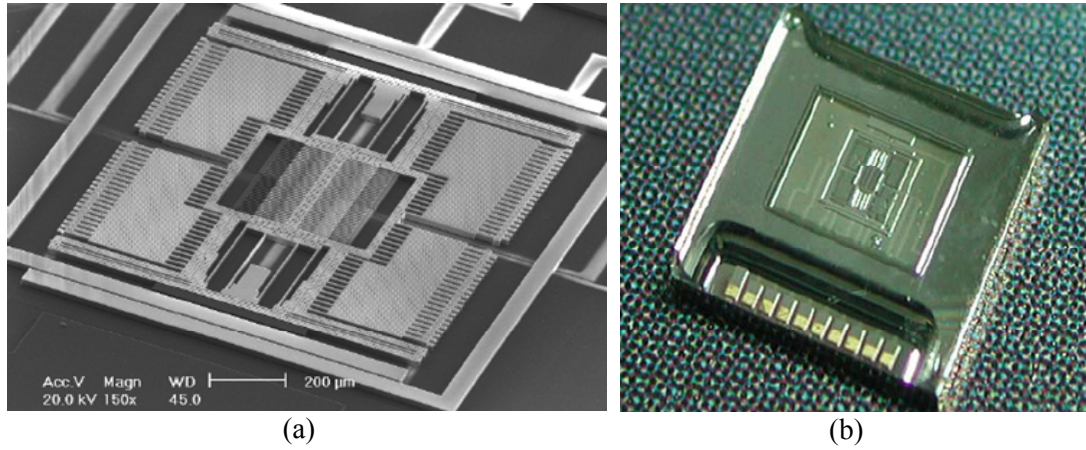
Figure 1.11: (a) Silicon-on-glass gyroscope developed by Seoul National University. (b) Vacuum-encapsulation of the fabricated gyroscope [57].
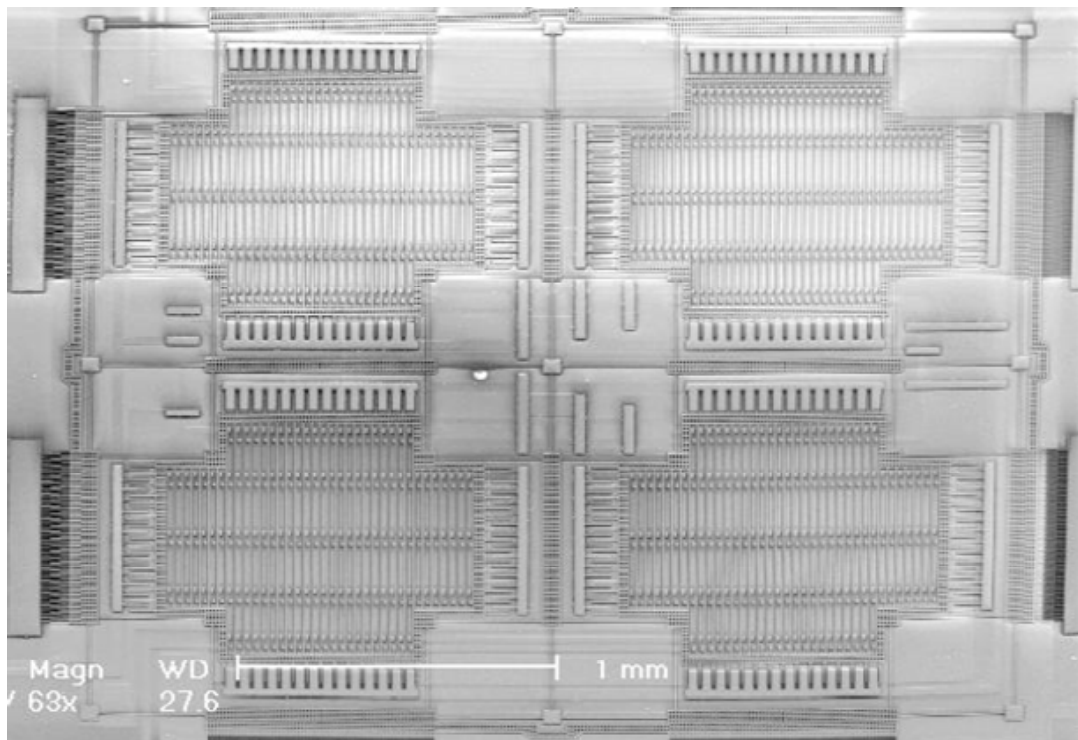
Figure 1.12: Linked 2 x 2 gyroscope array for the reduction of output noise [62].

In conclusion, it is difficult to classify micromachined gyroscopes in strict categories as there are variety of transduction principles, mechanical structures, structural

materials, micromachining processes, packaging and integration concepts, and the target applications makes it difficult classifying micromachined vibratory gyroscopes in strict categories. Clearly, the vast majority of the research on high-performance micromachined vibratory gyroscopes is focused on improving the rate resolution of the gyroscope by means of decoupling the drive and sense modes of the gyroscope, operating with closely-matched drive and sense mode resonance frequencies, incorporating large drive-mode vibration amplitudes, using thicker structural layers, constructing high-aspect-ratio capacitive gaps, and the development of high-quality electronics and packaging strategies. Still, there is a need for a comprehensive study trying to overcome these challenges with a dedicated gyroscope structure fabricated with a variety of standard micromachining technologies.

1.5 Symmetric and Decoupled Micromachined Gyroscopes Developed at METU

The research on micromachined vibratory gyroscopes started at Middle East Technical University (METU) in 1998, through a series of micromachined gyroscope designs for the standard three-layer polysilicon surface micromachining process (POLYMUMPs) [76], offered by MEMSCAP (formerly Cronos Integrated Microsystems and the MCNC MEMS Technology Applications Center) located in The United States. Among these designs, the gimbaled designs and the symmetrical and decoupled design are proved to be the best in terms of both production yield and reliability. Large sense capacitances, frequency tuning of the modes, and capacitive pick-off techniques are first applied in the preliminary gimbaled gyroscope design [77]. The buckling problems due to the residual-stress of the thin polysilicon structural layer and the mechanical crosstalk between the drive and sense modes limit the fabrication and performance of gimbaled gyroscopes, respectively. Having addressed the basic problems of the gimbaled gyroscope associated with the fabrication process and the structural geometry, the research is then focused on the symmetric and decoupled gyroscope structure [78, 79]. Figure 1.13 shows the structure of the developed symmetric and decoupled gyroscope structure. The

29

structure employs a symmetric design of the suspension beams as well as identical actuation and detection mechanisms, while the anchors of the structure are located in such a way that the drive and sense modes of the gyroscope is mechanically decoupled from each other, as described previously in Fig1.4-c. The symmetry of the gyroscope allows both matched resonance frequencies for the drive and sense modes for improved rate resolution and robustness of the mode-matching against ambient temperature variations. In addition, mechanically decoupled drive and sense modes prevent unstable operation due to mechanical crosstalk. However, the structure has no electrostatic tuning capability for post-production fine-tuning of the resonance frequencies. The performance of this first symmetrical and decoupled gyroscope structure is estimated to be only 1.6deg/sec at vacuum ambient, limited by the fabrication precision of the POLYMUMPs, small sense capacitances, large parasitic capacitances, small drive-mode vibration amplitude, and the readout electronics.
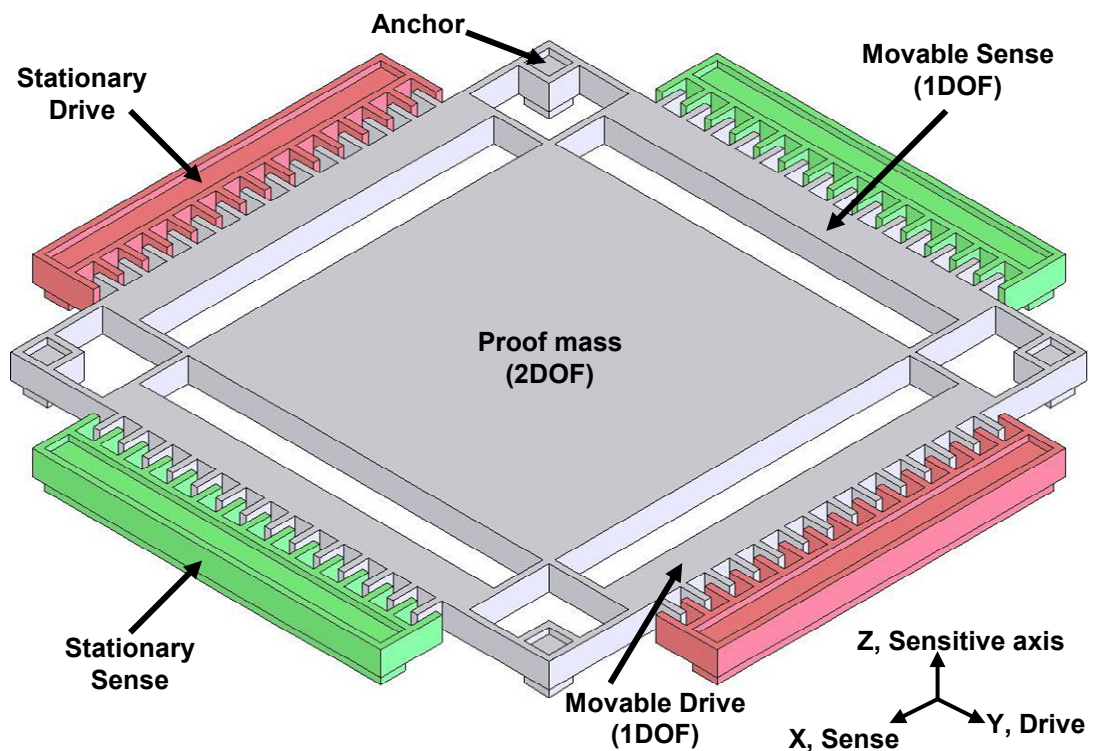
Figure 1.13: Original symmetric and decoupled gyroscope architecture. The symmetry of the gyroscope allows both matched resonance frequencies for the drive and sense modes for improved rate resolution and robustness of the mode-matching against ambient temperature variations. In addition, mechanically decoupled drive and sense modes prevent unstable operation due to mechanical crosstalk [78].

The work presented in this thesis reports the development of the original, improved, and advanced symmetric and decoupled vibratory gyroscopes. These gyroscopes are fabricated in four different micromachining technologies;   1) dissolved wafer silicon micromachining, 2) nickel electroforming, 3) silicon-on-insulator (SOI) micromachining, and 4) silicon-on-glass (SOG) micromachining with deep reactive ion etching (DRIE). The first phase in this research is the development of the original symmetrical and decoupled gyroscope in nickel electroforming [80-82] and dissolved wafer silicon micromachining [83, 84] processes, which has significant advantages over the polysilicon surface micromachining process in [78, 79]. Characterization of the original symmetric and decoupled design of [78, 79] fabricated in nickel electroforming [80-82] and dissolved wafer silicon micromachining [83, 84] processes reveal that tactical-grade performance can be achieved with structural modifications in the original design.

In the second phase of this research, the required structural modifications are realized on the original structure of [78-84], developing an improved symmetric and decoupled gyroscope. Figure 1.14 shows the simplified model of the improved gyroscope structure developed in this research. The drive mode of the gyroscope is optimized for large amplitude and linear driving oscillations, whereas the sense mode is optimized for increased rate sensitivity and for electrostatic tuning. Suspension flexures are designed symmetric along the drive and sense modes for minimizing possible temperature-dependent drift. Undesired mechanical cross-talk between the drive and sense modes is minimized by proper design of suspension flexures and anchorage of the structure for restricting the motion of the movable drive and sense electrodes to one degree-of-freedom (DOF), while allowing the two DOF motion only for the proof mass. The advantages of the new structure include large sense capacitances, large drive mode vibration amplitude, and electrostatic tuning capability, while the symmetry of the suspension beams and mechanical decoupling of the drive and sense modes are still preserved in this highly modified gyroscope architecture. This improved gyroscope is then fabricated in nickel electroforming [85] and SOI micromachining technologies.

31
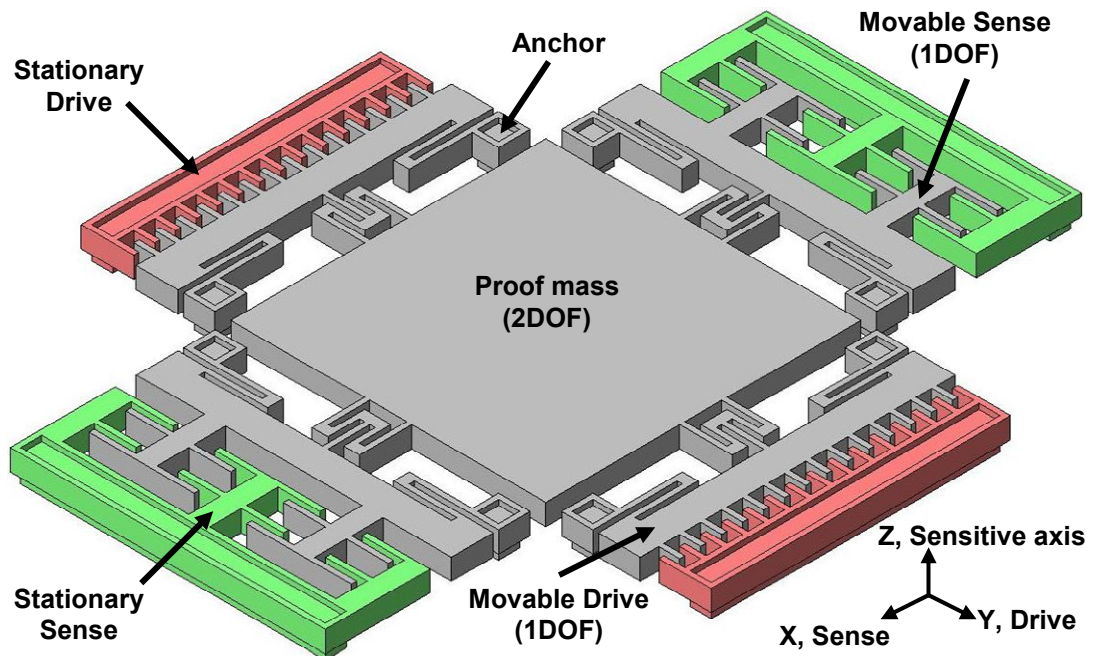
Figure 1.14: Improved symmetrical and decoupled gyroscope architecture using linear combs for drive electrodes, large sense capacitances with electrostatic tuning capability, and folded flexures for large drive-mode vibration amplitudes, while preserving the advantages of the original design in Figure 1.13.

The third phase of this research includes the development of an advanced symmetric and decoupled gyroscope, minimizing the mechanical cross-coupling between the drive and sense modes by using a single and rigid sense-frame instead of isolated dual sense frames of the structures developed in the first two phases. Figure 1.15 shows the model of the advanced symmetric and decoupled gyroscope developed in this research. This advanced design has many common features with the improved design, such as large sense capacitances, large drive mode vibration amplitude, electrostatic tuning capability, and the symmetry of the suspension beams. In addition, the sense electrodes are connected by rigid trusses constructing a single sense-frame in the advanced design, increasing the stiffness of the sense electrodes against the spurious deflections caused by the large vibration amplitudes along the drive-mode. Also the flexures of the sense frame are located such that the sense frame is highly robust against rotary oscillations.

Fabricated gyroscopes are hybrid-connected to a capacitive interface circuit fabricated in a 0.6μm standard CMOS process. The hybrid gyroscope/interface assemblies are then combined with external feedback and readout electronics on

printed-circuit boards for performance characterization of the complete angular rate sensor system. The original and improved symmetric and decoupled microgyroscopes fabricated with dissolved wafer silicon micromachining and nickel electroforming processes, respectively, achieve rate-grade performance. The improved symmetric and decoupled microgyroscope fabricated with SOI micromachining, and the advanced symmetric and decoupled microgyroscope fabricated with SOG micromachining processes demonstrate much impressive performance figures with angular rate sensitivities approaching to tactical-grade performance. The advanced SOG gyroscope structure is verified to be capable of sensing angular rates smaller than 10deg/hr in 1Hz bandwidth, provided that the SOG process is further improved by including hermetically-sealed vacuum cap and the sensor is properly packaged together with its interface and readout electronics.

Table 1.2 summarizes the measured angular rate resolutions of different types of symmetric and decoupled gyroscopes developed at METU in various fabrication processes, since year 2000.
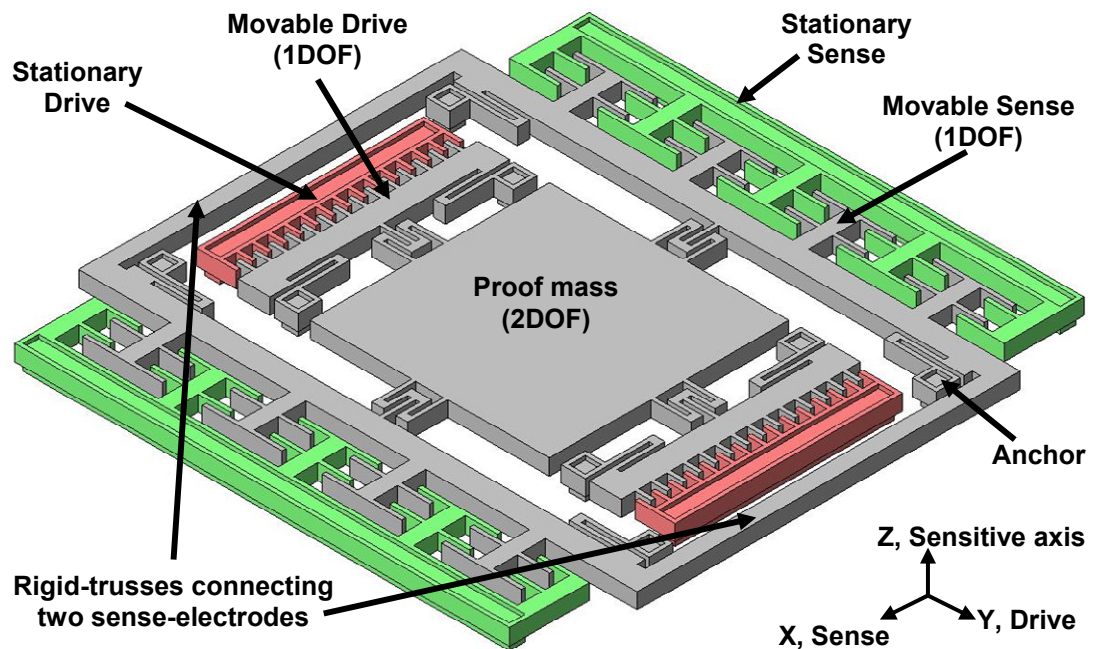
Figure 1.15: Advanced symmetrical and decoupled gyroscope architecture preserving the advantages of the improved design in Figure 1.14 and has additional features such as a single rigid sense frame and improved robustness against rotary vibrations, which minimize the mechanical cross-coupling between the drive and sense modes.

Table 1.2: The measured angular rate resolutions of different types of symmetric and decoupled gyroscopes developed at METU in various fabrication processes, since year 2000.

Fabrication process	Angular Rate Resolution, (deg/sec)/Hz$^{1/2}$		
	Original Design (Figure 1.13)	Improved Design (Figure 1.14)	Advanced Design (Figure 1.15)
POLYMUMPs	1.6 (at atmosphere)	-	-
Nickel electroforming	N/A*	0.1 (at atmosphere)	-
Dissolved wafer silicon micromachining	0.06 (at atmosphere)	-	-
SOIMUMPs	-	0.025 (at atmosphere) 0.014 (in vacuum)	-
Silicon-on-glass micromachining	-	0.1 (at atmosphere)	0.09 (at atmosphere) 0.01 (in vacuum)

* Gyroscope fabricated but resolution not measured due to the fabrication problems.

1.6 Research Objectives and Thesis Organization

The goal of this research is to develop micromachined angular rate sensors for tactical-grade applications. Rate sensors consist of micromachined gyroscopes fabricated through a number of different technologies, a CMOS capacitive interface circuit, and additional feedback and readout electronics. The specific objectives of this research are listed as follows:

1. Electromechanical design and development of symmetrical and decoupled gyroscope structures. The gyroscope should have symmetric suspension designs, and should be capable of matching the resonance frequencies of the drive and sense modes for high rate sensitivity, while minimizing mechanical crosstalk between the modes. The effects of mode matching, flexure geometry, damping, electrostatic actuation, capacitive sensing, and fabrication tolerances on the gyroscope performance should be analyzed together with secondary effects such as quadrature error, frequency-doubling, and mechanical-thermal noise.

2. Fabrication of the designed symmetrical and decoupled micromachined gyroscopes in different micromachining technologies including dissolved wafer silicon micromachining, nickel electroforming, silicon-on-insulator (SOI) micromachining, and silicon-on-glass (SOG) micromachining. The

problems associated with each fabrication technology should be analyzed, and corrective actions should be developed in order to overcome these problems.

3. Development of a CMOS capacitive interface circuit for the fabricated gyroscopes. The circuit should be compatible with hybrid-connection to the fabricated gyroscopes. It should be capable of buffering the high-impedance outputs of the fabricated capacitive gyroscopes. Therefore, the circuit should have high input impedance and should convert the charge output from the gyroscope to a raw voltage signal, which would then be processed by the feedback and readout electronics.

4. Development of feedback and readout electronics for the construction of a complete angular rate sensor system. The feedback electronics should be capable of finding the mechanical resonance frequency of the drive mode automatically and starting self-oscillation of the drive-mode. Automatic amplitude control loop should also be investigated for the precise control of the drive-mode vibration amplitude at vacuum ambient and/or at varying ambient temperatures. On the other hand, the readout electronics should accept the buffered raw output signal from the CMOS capacitive interface circuit and process it in order to generate a useful output voltage signal proportional to the applied angular rate input. The closed-loop force-feedback configuration for the rate output of the gyroscope should also be investigated.

5. Characterization of the constructed angular rate sensors in terms of angular rate sensitivity, quadrature error, zero-rate output offset (bias), bias stability, dynamic range, scale-factor and its linearity. The performances of the gyroscopes fabricated in different micromachining technologies should be compared, and the performance limits of different sensors should be identified. The most suitable gyroscope architecture and micromachining technology for achieving tactical-grade performance should be determined.

The organization of this thesis and the contents of the following chapters are summarized as follows:

Chapter 2 introduces the theory behind the micromachined vibratory gyroscopes and the electromechanical design issues. Then it briefly describes the construction of the mechanical model for decoupled vibratory gyroscope, extraction of the mechanical model parameters, the design in electrical domain, and the construction of the electromechanical models are briefly described. In addition, it explains the second-order effects such as levitation, side instability, and mechanical-thermal noise. The chapter also includes examples of finite-element, analytical, and system-level simulations performed during the design of the symmetric and decoupled gyroscopes.

Chapter 3 describes the fabrication of the symmetric and decoupled gyroscope structures in four different micromachining technologies: dissolved wafer silicon micromachining, nickel electroforming, silicon-on-insulator (SOI) micromachining, and silicon-on-glass (SOG) micromachining. All of these fabrication processes are completed at the in-house cleanroom facilities of METU except the SOI micromachining process, which is conducted through the commercially available SOIMUMPs process of MEMSCAP. The chapter provides the details of each fabrication process, including the problems encountered and the improvements achieved. It also presents the technical information about the fabricated symmetric and decoupled gyroscope prototypes.

Chapter 4 provides information on the capacitive interface circuit designed for the micromachined vibratory gyroscopes developed in this study. It explains the interface requirements and presents the architecture of the designed circuit. It also presents the results of the simulations performed on the designed circuit together with the lumped electrical model of the gyroscope, verifying the operation of the capacitive interface.

Chapter 5 presents the results of the preliminary characterization performed on the fabricated gyroscopes and the hybrid-connected gyroscope/interface assemblies. The characterization work includes the determination of the sensor capacitances, resonance frequencies, sensitivity parameters, frequency-tuning characteristics, the effect of capacitive interface circuits, and the effects of vacuum ambient. The measured parameters of the fabricated gyroscopes are compared with the design values, for evaluating the design process, the capacitive interface circuit, and the fabrication tolerances.

Chapter 6 explains the design of the primitive electronic feedback and control circuits required for constructing a complete angular rate sensor system powered from a single DC power supply and providing a DC output voltage proportional to the applied angular rate input. In addition, it briefly describes the construction of the electronics for the self-resonance excitation and automatic amplitude control of the drive-mode vibrations, as well as the open-loop and closed-loop rate sensing configurations. It also presents the results of the behavioral simulations performed on the designed circuits including the electromechanical models of the fabricated gyroscopes.

Chapter 7 presents the result of the final tests performed on the fabricated angular-rate sensors constructed by combining the fabricated gyroscope/interface assemblies and the developed electronic control and feedback circuits. The presented results include the angular rate sensitivity, noise-equivalent rate, quadrature error, scale-factor, linearity, and the bias instability of each rate sensor. The chapter compares the demonstrated performances with the expected results and briefly assesses the factors limiting the overall performance of each gyroscope.

Finally, Chapter 8 summarizes this research and draws conclusions in the light of achieved results. It also suggests a possible research path for the related studies in the future.

CHAPTER 2

VIBRATORY GYROSCOPE THEORY

This chapter introduces the theory behind the electromechanical design of micromachined vibratory gyroscopes. Transduction of the physical effect of angular rotation to electrical charge in a vibratory gyroscope demands combined analysis of both mechanical and electrical parameters associated with the sensor structure. Section 2.1 constructs the mechanical model for the decoupled vibratory gyroscope developed in this research and analyzes the transduction mechanism in detail. Section 2.2 briefly provides the extraction of basic lumped model parameters for the symmetric and decoupled vibratory gyroscope, including the spring constant, the mass, and the damping factor of the structure. It also discusses several possible non-idealities in estimating these parameters. Section 2.3 describes the design of electrical domain parameters such as parallel-plate capacitors and electrostatic actuation, conversion of the mechanical sensor model to an electrical equivalent circuit, capacitive sensing, and electrostatic springs. Section 2.4 discusses second-order effects to be considered in the design of micromachined vibratory gyroscopes, such as electrostatic levitation, side-instability for large-drive-mode vibration amplitudes, quadrature signal, double-frequency motion, and mechanical-thermal noise. Section 2.5 presents sample simulations performed during the design, including finite-element, analytical, and system-level simulations for predicting the performance of the micromachined symmetrical and decoupled vibratory gyroscope prior to fabrication. Finally, Section 2.6 provides a summary of this chapter.

2.1 Mechanical Model of Decoupled Vibratory Gyroscope

Mechanical decoupling of the drive and sense modes of a vibratory gyroscope is essential for minimizing the crosstalk between the modes, unless otherwise a large output offset is generated by the gyroscope even in the absence of a rate input. Therefore, the gyroscope structures developed in this research all have fully-decoupled structures, as described in Figure 1.4-c. Figure 2.1 shows a fully-decoupled and balanced vibratory gyroscope structure, highlighting the masses moving along the drive and the sense modes, separately. The figure illustrates the degrees-of-freedom (DOF) of the movable electrodes and the proof mass for both drive and sense mode of the gyroscope. The DOF of the movable components are assigned by increasing the rotational stiffness of the structures about any three coordinate axes as well as increasing the linear stiffness along out-of-plane ("sensitive") axis. Clearly, the proof mass is the only component with 2-DOF, whereas the drive and the sense electrodes all have 1-DOF with the help of flexible beams and rollers. In practice, the rollers shown in the figure are also implemented by flexible beams in order to avoid friction. The flexible beam structure is an energy storing mechanism and act as mechanical spring. Together with the inertia of the movable masses and the viscous damping of the surrounding gas in the ambient, the structure represents a second-order spring-mass-damper system in either the drive or the sense mode. It is appropriate to consider the drive mode as a mechanical resonator actuated at its resonance frequency, while the sense mode acts as an acceleration sensing mechanism that detects Coriolis acceleration in response to an angular rate input. The drive mode resonator, the Coriolis acceleration, and the sense mode output response to Coriolis acceleration are analyzed in separate subsections below.

2.1.1 Drive-Mode Resonator

The mechanical structure of the driving actuator of the vibratory gyroscope consists of drive electrodes, proof mass, and a number of flexible beams. Together with the effect of viscous damping of the gas surrounding the mechanical structure, the

overall system can be modeled by a spring-mass-damper system, as described in Figure 1.2.
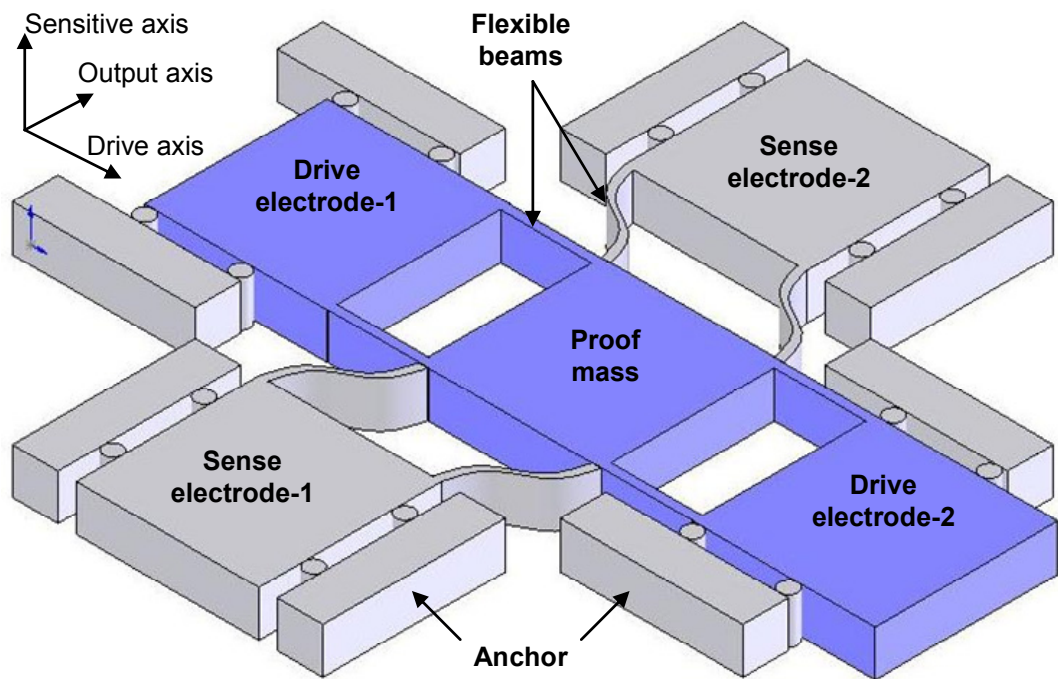
(a)
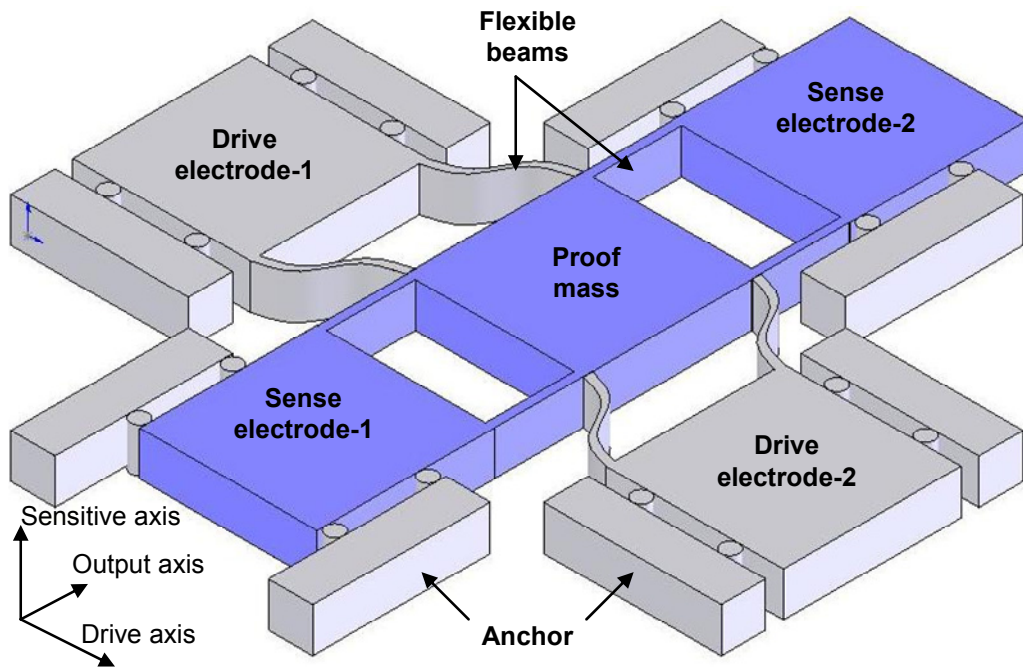
(b)

Figure 2.1: Fully-decoupled and balanced vibratory gyroscope structure, highlighting the masses moving along (a) the drive and (b) the sense modes by blue color whereas the stationary or quasi-stationary (bending) parts are shown in gray color.

As the name implies, the purpose of the drive-mode is to overcome the inertia of the proof mass, which is the component responsible for coupling the Coriolis acceleration to the sense-mode. Continuous motion is necessary to generate Coriolis acceleration effect on the proof mass in response to an angular rotation input, which will then be coupled to the sense mode electrodes. The continuous motion of the proof mass is generated by the oscillations created by the drive-mode resonator. The force-deflection characteristic of the drive-mode resonator is defined by the second-order differential equation below:

$$f_D(t) = m_D \cdot \frac{\partial^2 x(t)}{\partial t^2} + b_D \cdot \frac{\partial x(t)}{\partial t} + k_D \cdot x \qquad (2.1)$$

where f_D is the force acting on the system along the drive axis, x is the resulting deflection, m_D is the mass, b_D is the damping coefficient, and k_D is the spring constant all associated with the drive-mode, and t represents the time. The time-varying nature of the applied force requires the first and the second time derivatives of the deflection x appear in the expression above. The time-domain expression of Equation 2.1 can be converted to frequency-domain by using Fourier transformation in order to have an explicit expression between the applied force and the resulting deflection,

$$F_D(j\omega) = -\omega^2 \cdot m_D \cdot X(j\omega) + j\omega \cdot b_D \cdot X(j\omega) + k_D \cdot X(j\omega) \qquad (2.2)$$

where ω is the frequency of the applied time-varying force as well as the resulting deflection and j is the imaginary unit. Now, it is possible to express the relation between the applied force and the resulting deflection in terms of the mechanical system parameters and the frequency of the applied force as follows,

$$\frac{X(j\omega)}{F_D(j\omega)} = \frac{1}{m_D \cdot \left[\left(\dfrac{k_D}{m_D} - \omega^2\right) + j \cdot \dfrac{\omega \cdot b_D}{m_D}\right]} = \frac{1}{k_D \cdot \left[\left(1 - \left(\dfrac{\omega}{\omega_D}\right)^2\right) + j \cdot \dfrac{\omega}{Q_D \cdot \omega_D}\right]} \qquad (2.3)$$

where ω_D is the mechanical resonance frequency of the drive-mode resonator and is defined as $\sqrt{k_D/m_D}$, and Q_D is the mechanical quality factor of the drive-mode and is defined as $\sqrt{k_D \cdot m_D}/b_D$. If the frequency of the actuating force is set equal to ω_D, then Equation 2.3 simplifies to

$$\frac{X(j\omega_r)}{F_D(j\omega_r)} = \frac{1}{j} \cdot \frac{Q_D}{k_D} \qquad (2.4)$$

The equation above corresponds to the maximum deflection of a resonator with minimum actuating force and states that the deflection of the system lags the actuating force by 90°. The magnitude of the vibrations is only limited by the energy dissipation mechanisms in the resonator system, defined by the mechanical quality factor of the drive-mode. For this reason, the driving actuator is continuously oscillated at its mechanical resonance frequency for maximum energy efficiency. High stability of the structural materials used in microfabrication technologies allows long-term use of resonating micromechanical components.

2.1.2 Coriolis Coupling

Consider a particle on the gyro frame moving with respect to the gyro frame with a time-dependent position vector, *r*. If the gyro frame is rotated with respect to a stationary reference frame, then an observer on the gyro frame cannot describe the motion of the moving particle only by applying Newton's Second Law of motion. Rather, this observer can only describe the motion of the particle by using additional fictitious forces acting on the particle. Consider the gyro frame rotates about the z-axis of the stationary reference frame with angular rotation rate of magnitude Ω_z, then the position vector of the particle is on the xy-plane that is perpendicular to the axis of rotation, as defined in Equation 2.5 below, for simplifying the analysis.

$$\overline{\Omega}_s = \Omega_z \hat{k} \qquad (2.5a)$$

42

$$\bar{r}_i = x(t)\hat{i} + y(t)\hat{j} \tag{2.5b}$$

The velocity and acceleration of the particle are given as,

$$\bar{v}_g = \dot{\bar{r}}_g = \dot{x}(t)\hat{i} + \dot{y}(t)\hat{j} \tag{2.6a}$$

$$\bar{a}_g = \dot{\bar{v}}_g = \ddot{\bar{r}}_g = \ddot{x}(t)\hat{i} + \ddot{y}(t)\hat{j} \tag{2.6b}$$

where v_g and a_g are the velocity and acceleration of the particle, respectively, with respect to the gyro frame and subscript "g" denotes the gyro frame. However, the velocity and acceleration of the particle with respect to the stationary frame take into account the rotation of the gyro frame also,

$$\bar{v}_s = \dot{\bar{r}}_g + \overline{\Omega}_s \times \bar{r}_g \tag{2.7a}$$

$$\bar{a}_s = \dot{\bar{v}}_s + \overline{\Omega}_s \times \bar{v}_s = \left[\ddot{\bar{r}}_g + \left(\dot{\overline{\Omega}}_s \times \bar{r}_g\right) + \left(\overline{\Omega}_s \times \dot{\bar{r}}_g\right)\right] + \overline{\Omega}_s \times \left[\dot{\bar{r}}_g + \overline{\Omega}_s \times \bar{r}_g\right] \tag{2.7b}$$

where subscript "s" denotes the stationary frame. Rearranging Equation 2.7b results in

$$\Rightarrow \bar{a}_s = \underbrace{\bar{a}_g}_{\substack{Acceleration \\ w.r.t.gyro \\ frame}} + \underbrace{2\left(\overline{\Omega}_s \times \bar{v}_g\right)}_{\substack{Coriolis \\ Acceleration}} + \underbrace{\overline{\Omega}_s \times \left(\overline{\Omega}_s \times \bar{r}_g\right)}_{\substack{Radial \\ Acceleration}} + \underbrace{\dot{\overline{\Omega}}_s \times \bar{r}_g}_{\substack{Tangential \\ Acceleration}} \tag{2.8}$$

Equation 2.8 states that the motion of the moving particle on the gyro frame with respect to the stationary coordinate frame can be defined by the linear, radial, and tangential acceleration terms plus the fictitious Coriolis acceleration term. Replacing the acceleration and the velocity terms of Equation 2.6 in Equation 2.8 results in

$$\bar{a}_s = \begin{bmatrix} \left(\ddot{x}(t)\hat{i} + \ddot{y}(t)\hat{j}\right) + 2\left(\Omega_z\hat{k} \times \left(\dot{x}(t)\hat{i} + \dot{y}(t)\hat{j}\right)\right) \\ + \left(\Omega_z\hat{k} \times \left(\Omega_z\hat{k} \times \left(x(t)\hat{i} + y(t)\hat{j}\right)\right)\right) \\ + \left(\Omega_z\hat{k} \times \left(\left(\dot{x}(t)\hat{i} + \dot{y}(t)\hat{j}\right) + \left(\Omega_z\hat{k} \times \left(x(t)\hat{i} + y(t)\hat{j}\right)\right)\right)\right) \end{bmatrix} \tag{2.9}$$

Simplifying Equation 2.9, applying Newton's Second Law on the gyro frame, and collecting the components along *x* and *y* axes together provides

$$m_D \cdot \ddot{x}(t) = F_{s,x} + 2 \cdot m_D \cdot \Omega_z \cdot \dot{y}(t) + m_D \cdot \Omega_z^2 \cdot x(t) + m_D \cdot \dot{\Omega}_z \cdot y(t) \qquad (2.10a)$$

$$m_D \cdot \ddot{y}(t) = F_{s,y} - 2 \cdot m_D \cdot \Omega_z \cdot \dot{x}(t) + m_D \cdot \Omega_z^2 \cdot y(t) - m_D \cdot \dot{\Omega}_z \cdot x(t) \qquad (2.10b)$$

where $F_{s,x}$ and $F_{s,y}$ are the force components along *x* and *y* directions, respectively, with respect to the stationary frame that give rise to acceleration $\overline{a}_s$. Equation 2.10b states that the Newton's Law of Motion is valid in the gyro frame by using fictitious force components other than the applied forces $F_{s,x}$ and $F_{s,y}$.

The particle described here is similar to the proof mass of a vibratory gyroscope. There, the proof mass is actuated along the drive-mode only, let be the x-direction, i.e., $\overline{r}_i = x(t)\hat{i}$. Let the gyro frame rotates about z-axis by a constant (time-independent) Ω_z. Then, the forces acting on the oscillating proof mass would be approximated as follows:

$$m_D \cdot \ddot{x}(t) = F_{s,x} + m_D \cdot \Omega_z^2 \cdot x(t) \qquad (2.11a)$$

$$m_D \cdot \ddot{y}(t) = -2 \cdot m_D \cdot \Omega_z \cdot \dot{x}(t) \qquad (2.11b)$$

Here, $F_{s,x}$ corresponds to electrostatic actuating force applied to the drive-mode resonator along the *x*-direction. The proof mass would experience the fictitious force along the sense-mode direction (*y*-direction), which is nothing but the force due to Coriolis coupling to the sense mode. This force would act on the sense mode spring-mass-damper system causing a deflection of the proof mass along the sense mode pushing the sense-electrodes, the motion of which are then detected by the sense electronics. Next section describes the sense mode response to the generated Coriolis force.

2.1.3 Sense-Mode Response to Angular Rate Input

The mechanical structure of the sense-mode of the decoupled vibratory gyroscope resembles that of the drive mode, and Equation 2.1 is also valid for the sense mode spring-mass-damper system by replacing the subscript "D" by subscript "S", denoting the parameters associated with the sense mode. Contrary to the electrostatic actuation force applied to the drive mode resonator for deflecting it, no external force is applied to the sense mode except the self-induced Coriolis force of Equation 2.11b, which states that the Coriolis force acting along the sense mode is directly proportional to the mass and the velocity of the drive mode. This statement is mostly correct, but remembering that it is valid only for the masses common to both the drive and the sense modes, i.e., the proof mass. This is because of the fact that the drive-electrodes of Figure 2.1 also experience a Coriolis force associated with their drive-mode oscillations and the input rotation, however, this force is absorbed by the roller mechanism of these electrodes causing no coupling effect to the sense electrodes. Similarly, there would be no Coriolis force induced on the sense electrodes, since they are already stationary during the drive-mode oscillations. In conclusion, proof mass is the only element that couples the Coriolis force resulting from the drive-mode actuation and the input angular rate to the sense electrodes. Therefore, one should be careful about constructing the sense-mode dynamics of the symmetrical and decoupled microgyroscope, which is expressed as,

$$-2 \cdot m_{PM} \cdot \Omega_z \cdot \dot{x}(t) = m_S \cdot \ddot{y}(t) + b_S \cdot \dot{y}(t) + k_S \cdot y(t) \tag{2.12}$$

where m_{PM} is the proof mass and m_S is the sum of proof mass and the mass of sense electrodes.

Up to this point, the angular rate input applied to the gyro frame is considered as a constant rotation, which is not true for many practical applications. In practice, the angular rate input can also a time-varying function. Let the time-varying electrostatic actuating force applied to the drive mode, the resulting drive mode

displacement at drive-mode resonance, and the time-varying angular rate input be expressed as

$$F_x(t) = -F_D \cdot \sin(\omega_D t) \qquad (2.13a)$$

$$x_D(t) = x_D \cdot \cos(\omega_D t) \qquad (2.13b)$$

$$\Omega_z(t) = \Omega_z \cdot \cos(\omega_z t) \qquad (2.13c)$$

where ω_z is the frequency of the time-varying angular rate input. The negative sign in front of time-varying electrostatic force is set for convenience and would be clear after reviewing Section 2.3 of this chapter. With time-varying angular rate inputs, the expression in Equation 2.12 must be extended to include the time-derivative of the angular rate signal expressed in Equation 2.10b.

$$-2 \cdot m_{PM} \cdot \Omega_z \cdot \dot{x}(t) - m_{PM} \cdot \dot{\Omega}_z \cdot x(t) = m_S \cdot \ddot{y}(t) + b_S \cdot \dot{y}(t) + k_S \cdot y(t) \qquad (2.14)$$

Inserting the expressions of Equation 2.13 into the modified Equation 2.14 results in

$$\frac{m_{PM}}{m_S} \cdot \Omega_D \cdot x_D \cdot \left[\left(\omega_D + \frac{\omega_z}{2} \right) \cdot \sin((\omega_D + \omega_z)t) + \left(\omega_D - \frac{\omega_z}{2} \right) \cdot \sin((\omega_D - \omega_z)t) \right]$$
$$= \ddot{y}(t) + \frac{\omega_S}{Q_S} \cdot \dot{y}(t) + w_S^2 \cdot y(t) \qquad (2.15)$$

Equation 2.15 shows that the Coriolis force acting along the sense mode of the gyroscope has two components equally separated from the drive-mode resonance frequency, w_D, in the frequency domain. The left-hand side (LHS) of Equation 2.15 is indeed a sum of the imaginary parts of complex sinusoids as

$$LHS = \text{Im} \left\{ \Omega_D \cdot x_D \cdot \left(\omega_D + \frac{\omega_z}{2} \right) \cdot e^{j(\omega_D + \omega_z)t} + \Omega_D \cdot x_D \cdot \left(\omega_D - \frac{\omega_z}{2} \right) \cdot e^{j(\omega_D - \omega_z)t} \right\} \qquad (2.16)$$

Taking the Fourier transform of the complex expression above and applying it to the Fourier transform of the equations describing the sense mode dynamics provide the sense mode response to the angular rate inputs as

$$2 \cdot \pi \cdot \frac{m_{PM}}{m_S} \cdot \Omega_D \cdot x_D \cdot H(\omega) = \left(-\omega^2 + j\omega \frac{\omega_S}{Q_S} + \omega_S^2 \right) \cdot Y(\omega) \qquad (2.17a)$$

$$H(\omega) = \left[\left(\omega_D + \frac{\omega_z}{2} \right) \cdot \delta(\omega - \omega_D - \omega_z) + \left(\omega_D - \frac{\omega_z}{2} \right) \cdot \delta(\omega - \omega_D + \omega_z) \right] \qquad (2.17b)$$

where $\delta(\omega)$ is the impulse function. Simplifying Equation 2.17 and separating the sense mode response into its frequency components gives

$$Y(\omega_D + \omega_z) = \frac{2 \cdot \pi \cdot \Omega_z \cdot x_D \cdot \dfrac{m_{PM}}{m_S} \cdot \left(\omega_D + \dfrac{\omega_z}{2} \right)}{\left(\omega_S^2 - (\omega_D + \omega_z)^2 \right) + j(\omega_D + \omega_z) \cdot \dfrac{\omega_S}{Q_S}} \qquad (2.18a)$$

$$Y(\omega_D - \omega_z) = \frac{2 \cdot \pi \cdot \Omega_z \cdot x_D \cdot \dfrac{m_{PM}}{m_S} \cdot \left(\omega_D - \dfrac{\omega_z}{2} \right)}{\left(\omega_S^2 - (\omega_D - \omega_z)^2 \right) + j(\omega_D - \omega_z) \cdot \dfrac{\omega_S}{Q_S}} \qquad (2.18b)$$

Clearly, the sense mode output of the gyroscope in response to a time-varying angular rate input has two components, one at frequency $\omega_D + \omega_z$ and the other at $\omega_D - \omega_z$, and having slightly different weights. The general expression of Equation 2.18 can be analyzed for special cases, regarding whether the mechanical resonance frequencies of the drive mode and the sense mode are close to each other or highly separated from each other.

If the resonance frequencies of the drive and the sense modes are very close to each other, i.e., $\omega_D \cong \omega_S$, and if the applied angular rate is constant ($\omega_z = 0$), then Equation 2.18 simplifies to

$$Y(\omega_D + \omega_z) + Y(\omega_D - \omega_z) \approx \frac{2 \cdot \Omega_z \cdot x_D \cdot Q_S}{\omega_D} \cdot \frac{m_{PM}}{m_S} \tag{2.19}$$

Matching the resonance frequencies of the drive and sense modes of the gyroscope amplifies the sense mode deflection by the mechanical quality factor of the sense mode, in response to the applied constant angular rate inputs. This is the idea behind maximizing the sensitivity of a vibratory gyroscope, since the mechanical quality factors can be as high as few thousands at vacuum for micromachined resonators. For time-varying angular rate inputs, Equation 2.19 cannot be used directly, since the denominators of Equations 2.18a and 2.18b would not be identical. The sensitivity can be highly degraded in this case, for large ω_z values. Even a few Hertz may reduce the gyroscope sensitivity to half its value at constant angular rate input, due to the response bandwidth of the sense mode. Response bandwidth is approximated as

$$\Delta f_{BW} = \frac{f_D}{2 \cdot Q_S} \tag{2.20}$$

where Δf is the separation between the drive and the sense mode resonance frequencies and f_D is the drive mode resonance frequency, all in Hertz. Obviously, higher the sense mode mechanical quality factor, Q_S, smaller the response bandwidth. This trade-off usually limits the matched operation of the drive and the sense modes of the gyroscope, but the mode frequencies are set to values having a slight mismatch with each other, in practice. Another fact related to Equation 2.19 is that the sense mode displacement, $Y(\omega)$, is in-phase with the drive mode motion $X(\omega)$, which must be considered during phase-sensitive detection of the sense-mode response.

If the resonance frequencies of the drive and sense modes are highly-separated from each other, i.e., $\omega_D \ll \omega_S$, and if the applied angular rate is constant ($\omega_z=0$), then Equation 2.18 simplifies to

$$Y(\omega_D + \omega_z) + Y(\omega_D - \omega_z) \approx j \cdot \frac{\Omega_z \cdot x_D}{(\omega_S - \omega_D)} \cdot \frac{m_{PM}}{m_S} \tag{2.21}$$

Here, the sensitivity is significantly reduced for highly-separated resonance frequencies, as expected. Taking the ratio of Equation 2.19 to Equation 2.21 yields,

$$\frac{Y_{sense-matched}}{Y_{sense-mismatched}} = \frac{2 \cdot Q_S \cdot (\omega_S - \omega_D)}{\omega_D} \tag{2.22}$$

Considering the drive and sense mode resonance frequencies 10kHz and 11kHz, respectively, and the sense mode quality factor be 500 at vacuum, the resulting sense mode response for mismatched frequencies would be two orders of magnitude smaller than the response with matched frequencies. However, the mismatched operation is less sensitive to the frequency of time-varying angular rate inputs than the matched operation is, as the response bandwidth is large for mismatched operation. Finally, it should be noted that there is a 90° phase difference between the sense mode and the drive mode displacements for the mismatched operation of the gyroscope.

It is beneficial to put quantitative limits for the matched and mismatched operations. As a rule of thumb, the drive and the sense mode resonance frequencies of the gyroscope can be considered as matched for the separation between the drive and the sense mode resonance frequencies being smaller than 1/10 of the response bandwidth. For this case, Equation 2.19 can be used for the sense mode output response. Similarly, the mode frequencies can be considered as mismatched for the separation between them being 10 times larger than the response bandwidth. For this case, Equation 2.21 can be used for the sense mode output response. In between these ranges, the general expressions of Equation 2.18 must be used. Table 2.1 summarizes the sense-mode response and the limits for matched and mismatched operation.

Table 2.1: Sense-mode response and the limits for matched, mismatched mode operations as well as the transition mode in which the gyroscope cannot be considered either matched or not.

Mode	Condition (using Δf_{BW} in Equation 2.20)	Output Expression
Matched-mode	$f_D - f_S < (0.1) \cdot \Delta f_{BW}$	Equation 2.19
Mismatched-mode	$f_D - f_S > (10) \cdot \Delta f_{BW}$	Equation 2.21
Transition-mode	$(0.1) \cdot \Delta f_{BW} < f_D - f_S < (10) \cdot \Delta f_{BW}$	Equation 2.18

2.2 Model Parameters for Decoupled Vibratory Gyroscope

The analysis in Section 2.1 requires the identification of the mechanical model parameters of the gyroscope, in order to have analytical solutions. These parameters are simply the spring constant, mass, and the damping factor associated with the dynamics of the gyroscope, as stated for the drive mode in Equation 2.1 or for the sense mode in Equation 2.12. Extraction of the mechanical model parameters is discussed in separate subsections below, together with possible disturbances introduced to the ideal case assumptions.

2.2.1 Flexure Design and Spring Constant Estimation

Flexures are used in the vibratory gyroscopes for identifying the degrees-of-freedom of the movable components without introducing any friction mechanisms to the structure. The bending of flexures with various cross-sections under different applied forces and boundary-conditions are analyzed in detail in [86]. Although there are a large variety of geometries for constructing a bending flexure, the number of alternatives is greatly limited for standard microfabrication technologies. Typical flexures used in micromachined inertial sensors have rectangular cross-sections, are subject to concentrated loads instead of distributed loads, and usually have clamped-guided or clamped-free boundary conditions.

Force-deflection characteristics of a bending flexure can be defined by the equation

$$F_x = k_x \cdot \delta x \tag{2.23}$$

50

where F_x is the force applied along x-axis, δx is the deflection along x-axis, and k_x is a proportionality constant called the mechanical spring constant of the bending flexure along x-axis. The relation between the applied force and resulting deflection is linear for a limited deflection range, depending on the structure of the flexure. Physically, bending a flexure induces stress inside the beam that is linearly proportional to the amount of bending up to a certain limit, over which more force is required to achieve the same amount of displacement. In that case, the force-deflection characteristics cannot be modeled by the first-order expression of Equation 2.23, but a higher order equation with displacement-dependent spring stiffness must be considered as follows

$$F_x = k_x \cdot \left\{ \delta x + \alpha \cdot (\delta x)^3 \right\}$$ (2.24)

where α is a constant depending on the mechanical properties of the structural material as well as the stress-relieving capability of the flexure. Nonlinear stiffness disturbs the overall linearity of the vibratory gyroscopes and therefore it is a common practice to keep the deflection of the flexures below the limit that cause nonlinear stiffness. This limit is usually identified through finite element simulations. For the rest of the analysis in this section, it is assumed that the flexures are deflected within their linear range and have constant spring stiffness.

Figure 2.2 shows a typical beam structure with rectangular cross-section intended for use as a bending flexure and the possible deflections caused by the forces applied at the tip of the beam along different axes of the coordinate frame. The movable face of the beam with free-end boundary condition in Figure 2.2-a follows a rotary deflection while the movable face of the beam with guided-end in Figure 2.2-b is restricted to perform a linear deflection. The force-deflection characteristics and resulting stiffnesses of these two cases are different from each other, except for axial loading (x-axis in the Figure). Detailed analysis of calculating the mechanical spring constant is beyond the scope of this thesis, but related information is available in [86, 87].
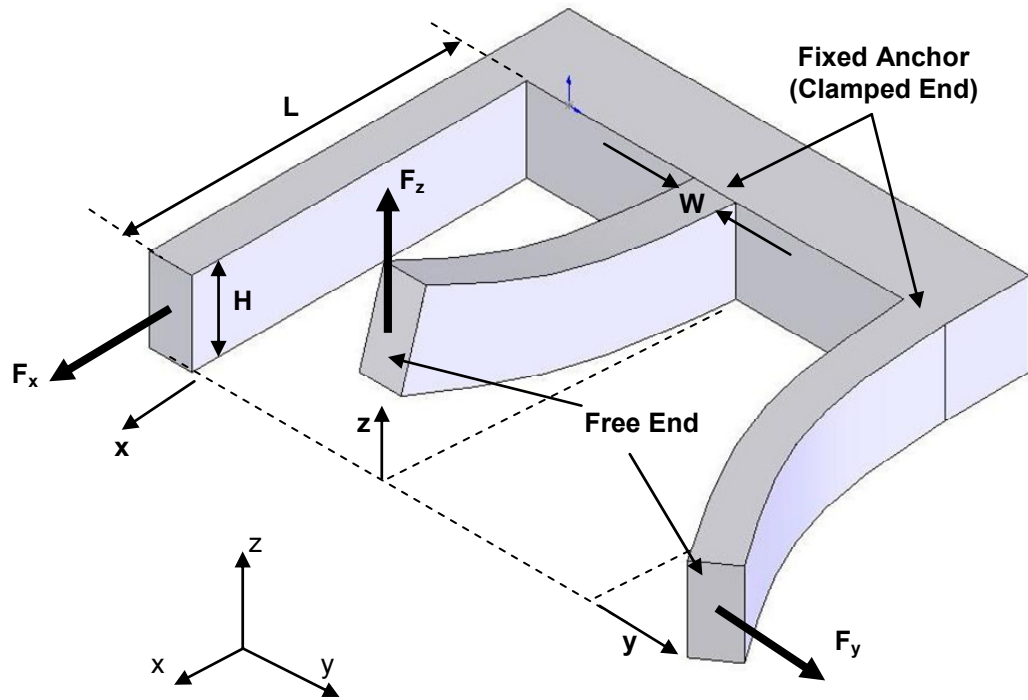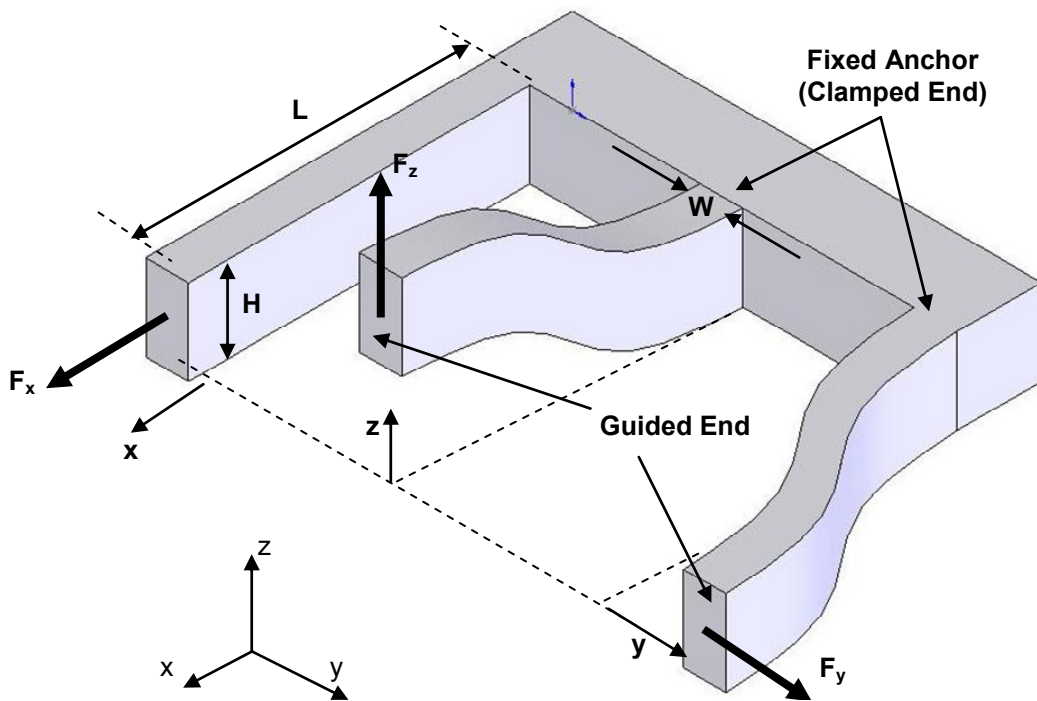
Figure 2.2: Typical beam structure with rectangular cross-section intended for use as a bending flexure and the possible deflections caused by the forces applied at the tip of the beam along different axes of the coordinate frame. (a) Cantilever beam with clamped-free boundary condition. (b) Beam with clamped-guided boundary condition.

Table 2.2 provides the spring constants associated with the clamped-free cantilever beam and clamped-guided beam of Figure 2.2. *E*, *H*, *W*, and *L* are the elasticity modulus of the beam's structural material, beam height, beam width, and beam length, respectively. Axial loading of both types of the beams would cause elongation of the loaded beam creating huge amounts of axial stress, which limits the linear axial deflection to very small values. Indeed, the high stiffness of the beams along axial direction is used to determine the degree-of-freedom of the rigid parts by their proper attachment to the flexures. For the displacements along the horizontal (y-axis) and vertical (z-axis) directions on the plane of beam-cross-section, the cantilever beam does not elongate since its movable end is free to change its orientation. However, the change in the orientation of the movable face of the cantilever beam can be modeled by the linear deflection expressions of Table 2.2 only for small deflections. Finally, the displacements along the horizontal (y-axis) and vertical (z-axis) directions on the plane of beam-cross-section, the clamped-guided beam structure tends to elongate, since the orientation of its movable face is restricted to stay parallel to its original orientation. As a result, the single-beam flexures of Figure 2.2 have limited use in practice, due to their small linear deflection range.

Table 2.2: Spring constants associated with the clamped-free cantilever beam and clamped-guided beam of Figure 2.2. *E*, *H*, *W*, and *L* are the elasticity modulus of the beam's structural material, beam height, beam width, and beam length, respectively.

Spring Constant	Clamped-Free End (Cantilever)	Clamped-Guided End
K_x	$\dfrac{E \cdot H \cdot W}{L}$	$\dfrac{E \cdot H \cdot W}{L}$
K_y	$\dfrac{E \cdot H \cdot W^3}{4 \cdot L^3}$	$\dfrac{E \cdot H \cdot W^3}{L^3}$
K_z	$\dfrac{E \cdot W \cdot H^3}{4 \cdot L^3}$	$\dfrac{E \cdot W \cdot H^3}{L^3}$

Instead of the simple beams in Figure 2.2, more sophisticated flexure structures are used for the decoupled vibratory gyroscopes in this study. The aim of using these sophisticated flexures is to reduce mechanical stresses induced in the beams during displacement, in order to increase the linear deflection range of the flexures. Figure 2.3 shows two sample flexure designs having advanced geometries for reducing

mechanical cross-coupling between the drive and the sense modes of the developed gyroscopes and for increasing the linear deflection range of the drive mode. The intended direction of motion is along y-axis, whereas the stiffness along x and z axes are much higher compared to the stiffness along y-axis. K_i denote the spring constant of each beam along y-axis. These dedicated flexure design consist of several clamped-guided end flexures, connected in parallel or in series, and attached via rigid trusses. Once the clamped-guided or clamped-free beams are identified, the basic expressions of Table 2.2 can be used to closely predict the overall spring constant of more sophisticated flexure structures, provided that the attachment trusses are much more rigid compared to the beams themselves. The dual-folded flexure design of Figure 2.3 consists of four beams with spring constants K_1, K_2, K_3, and K_4 along y-axis. The total spring constant between the fixed anchor node and the movable rigid node is the series combination of $K_1//K_4$ and $K_2//K_3$. Similarly, the overall spring constant of the triple-folded flexure design along y-axis can be through the parallel combination of K_5&K_6 and K_8&K_9, which is then in series with K_7. In other words,

$$K_{y\_Dual-Folded} = \left(\frac{1}{K_1 + K_4} + \frac{1}{K_2 + K_3} \right)^{-1} = K \quad if \quad \forall K_i = K \qquad (2.25a)$$

$$K_{y\_Triple-Folded} = \left(\frac{1}{\left(\frac{1}{K_5} + \frac{1}{K_6} \right)^{-1} + \left(\frac{1}{K_8} + \frac{1}{K_9} \right)^{-1}} + \frac{1}{K_7} \right)^{-1} = 2K \quad if \quad \forall K_i = K \qquad (2.25b)$$

In conclusion, it is possible to extract the spring constants of sophisticated flexure designs by careful identification of boundary conditions and intended degrees-of-freedom for the movable rigid parts of the gyroscope. In practice, the cross-section of the flexures is not perfectly rectangular, but may be trapezoidal or even triangular due to insufficient control on the fabrication process. In addition, the stresses induced inside the beams, concentrated stress regions, and linear deflection ranges of the flexures must be simulated using finite element analysis for an accurate flexure design.
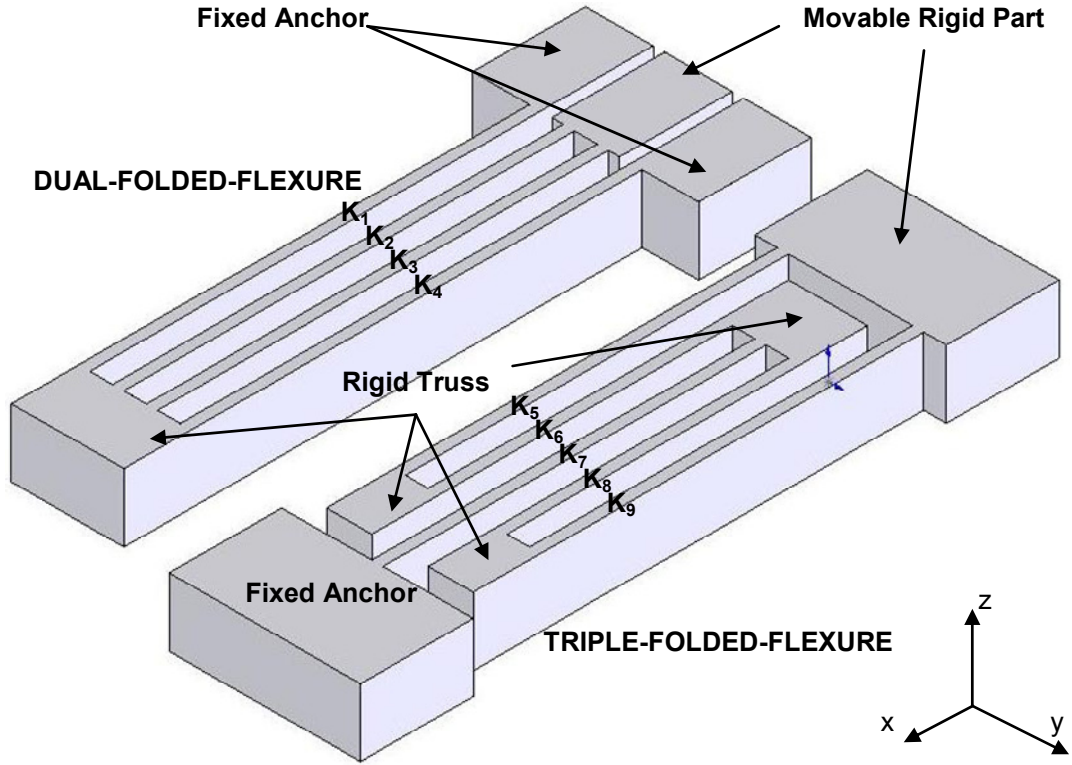
Figure 2.3: Two sample flexure designs having advanced geometries for reducing mechanical cross-coupling between the drive and the sense modes of the developed gyroscopes and for increasing the linear deflection range of the drive mode. The intended direction of motion is along y-axis, whereas the stiffness along x and z axes are much higher compared to the stiffness along y-axis. Ki denote the spring constant of each beam along y-axis.

2.2.2 Mass Estimation

Mass estimation is straightforward for the moving rigid parts in a vibratory gyroscope, once the volume of the object, *V*, and mass per unit volume (density) of the structural material, *d*, is known,

$$m = d \cdot V \tag{2.26}$$

where *m* is the mass of the movable part. However, this expression must be extended to take into account the mass of bending flexures. The mass of the flexures cannot be directly added to the overall mass associated with a particular vibration mode of the gyroscope, since the motion associated with a bending flexure is not constant throughout the flexure length. The amount of mass added by the

55

flexures to the overall mass of the movable rigid parts can be considered by using Rayleigh energy method [88, 89], which concludes that only a fraction of the mass of the flexure is added to the effective mass of a certain mode depending on the bending characteristics of the flexure. The effect of this fractional mass may not be ignored for small-size resonators; however, it is safely negligible for the vibratory gyroscopes developed in this study since the mass of rigid movable parts are more than two orders of magnitude larger than those of the flexures. In addition, the volume errors introduced by the fabrication tolerances during etching or deposition of structural materials usually dominates the overall estimation error for the mass.

2.2.3 Damping Factor Estimation

The term damping refers to the dissipation of vibration energy. The dissipation mechanisms vary for micromachined vibratory sensors, including viscous air damping, thermoelastic damping, anchor damping, and electronics damping. Viscous air damping is typically the dominant mechanism over the others for the micromachined vibratory gyroscopes operated at atmospheric pressure. There, the interaction between the surface of the movable structure and the surrounding gas molecules dissipate significant amounts of energy for micromachined sensors. Figure 2.4 illustrates two major sources of viscous air damping, the slide and the squeeze actions between the microstructure surface and the surrounding gas. The slide action refers to the slipping of the moving structure in a gas ambient causing a surface friction, whereas the squeeze action refers to compressing the gas molecules in between two structures causing a push-back effect. Accurate modeling of the gas flow through the narrow channels is essential for precise estimation of the damping factor due to the interaction between the structure surface and the air molecules. Constructing such models requires a deep background on microfluidics, extending beyond the scope of this research. Rather, a more general discussion on estimating the approximate damping factors for viscous fluid damping is enough for estimating the approximate quality factor of the sensor at atmospheric pressure. In contrary, the viscous air damping is usually negligible for determining the overall quality factor

of the sensor at vacuum ambient, where the thermoelastic damping usually becomes the dominant dissipative mechanism thereafter.
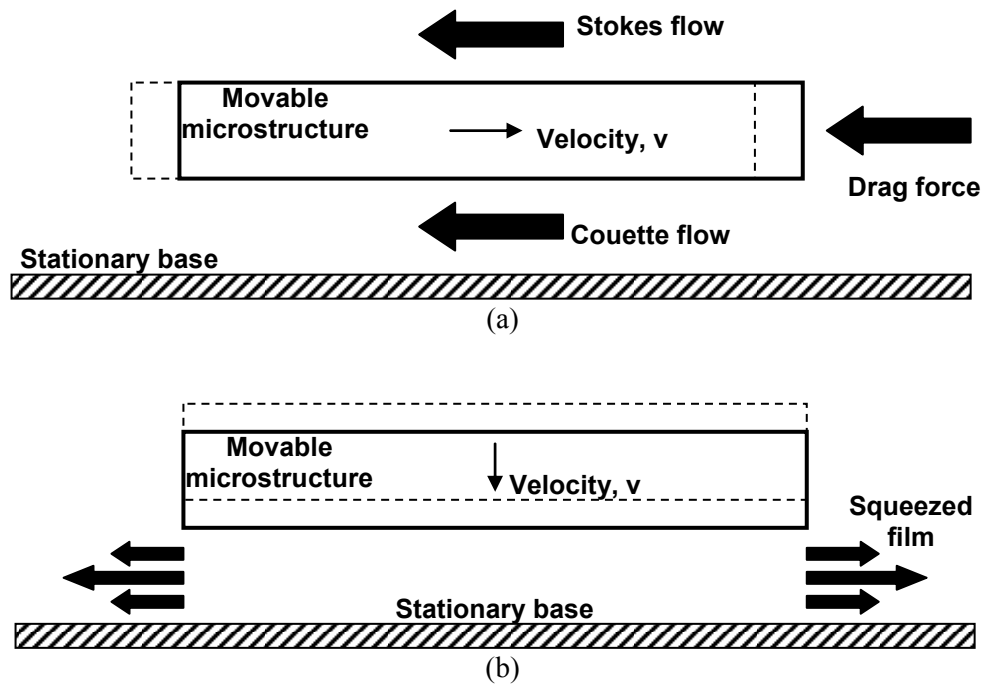
Figure 2.4: Illustration of the two major sources of viscous air damping; a) Slide-film damping, b) squeeze film damping.

Slide action of viscous damping is observed for a gas surrounded by two parallel surfaces, the distance between which is constant. In contrast, the distance between the parallel surfaces vary for the squeeze damping action. The drive and the sense mode directions of the gyroscopes developed in this research lay on a plane parallel to the substrate plane, and the offset height of the movable structure over the substrate surface does not vary with time. Therefore, the squeeze action is negligible for the proof mass and the substrate surfaces. Rather a slide film action is dominant for the proof mass and the bulk of the movable drive and sense electrodes. On the other hand, slide film damping is dominant for the linear comb structure of the driving actuator and squeeze film damping is dominant for the varying-gap type comb structure of the sensing actuator. The overall damping coefficient associated with the drive or the sense mode of a micromachined gyroscope can only be extracted by estimating the damping coefficients associated with the components of the gyroscope having different geometries. In general, Navier-Stokes equations are

used for describing the viscous, pressure, and inertial effects of such geometries within the fluid [90]. If inertial effects in Navier-Stokes equations are dominated by viscous and pressure effects, which is true for slow viscous motion conditions, then the equations can be simplified to what is known as Reynolds Equation. Under several assumptions such as small gaps, isothermal film, uniform pressure distribution, and small amplitude motion, linearized Reynolds equation can be used for estimating the squeeze film damping for rectangular plates as follows:

$$b_{squeeze} = \frac{64 \cdot \beta \cdot P_0 \cdot A}{\pi^6 \cdot \omega \cdot h_0} \cdot \sum_{m,n=odd} \frac{m^2 + c^2 n^2}{(m \cdot n)^2 \cdot \left[m^2 + c^2 n^2 + \frac{\beta^2}{\pi^2} \right]} \tag{2.27}$$

where P_0 is the undisturbed pressure of the gas, A is the area of the plane of the rectangular plate normal to the direction of motion, ω is the oscillation frequency of the plate, h_0 is the static gap spacing between the plate and the stationary surface, c is the ratio of the width of the plate W to its length L, m and n are odd integers, and β is the squeeze number defined as

$$\beta = \frac{12 \cdot \mu_{eff} \cdot L^2 \cdot \omega}{P_0 \cdot h_0} \tag{2.28}$$

Here, μ_{eff} is the effective viscosity of the surrounding gas, which is expressed by

$$\mu_{eff} = \frac{\mu}{1 + 9638 \left(\frac{P_0}{P} \cdot \frac{\lambda}{L_c} \right)^{1.159}} \tag{2.29}$$

where μ is the viscosity of the fluid, and the ratio of mean free path of the molecules, λ, to the characteristics length scale, L_c, of the system is defined as the Knudsen number, which is used to identify the flow regime of the fluid. The above equations are valid for the free molecular flow regime, for which the Knudsen number is above 3.

The conventional Navier-Stokes equations can also be used to estimate the approximate damping factors for the slide film damping mechanisms. The damping factors for the Couette flow and Stokes flow illustrated in Figure 2.4-a are then expressed by

$$b_{Couette} = \frac{\mu_{eff} \cdot A}{h_0} \tag{2.30a}$$

$$b_{Stokes} = \frac{\mu_{eff} \cdot A}{\delta} \tag{2.30b}$$

where A is the area of the plane of the rectangular plate sliding parallel to the direction of motion and δ is the penetration depth at which the fluid motion amplitude decrease by a factor of natural logarithm base, e (e=2.718281828…). It should be noted that the penetration depth is also a frequency dependent parameter, defined as

$$\delta = \left(\frac{2 \cdot \mu}{\rho \cdot \omega} \right)^{1/2} \tag{2.31}$$

where ρ is the density of the fluid.

The equations above may provide a rough estimate of the overall damping factor for a complex microstructure, however, it is clear that the above equations still require a high computational power with accurate knowledge of fluid viscosity, density, pressure, etc. although they are derived for simple geometries such as rectangular plates. Obviously, the damping characteristics of the surrounding gas may significantly vary from the expressions provided above for non-trivial geometries as in micromachined vibratory gyroscopes, which contain perforated proof masses, non-planar offset between the movable structure and the substrate, and different types of comb fingers for the drive and the sense electrodes. In addition, the quality factors estimated from the viscous fluid damping may vary with ambient temperature and pressure of the surrounding gas, which are difficult to stabilize in practice. Fortunately, the damping factor associated with viscous fluid damping is dominant for operation at atmospheric pressure in general, with its effect being

highly suppressed for operation at vacuum ambient, where the mean-free path of the gas molecules increases and the effective viscosity of the fluid decreases. Then, the other dissipation mechanisms such as thermoelastic damping, anchor damping, or electronics damping become the limiting factors in determining the overall damping coefficient of the microstructure.

Thermoelastic damping refers to the dissipation of vibration energy through an increase in the entropy due to the coupling between the heat transfer and the strain rate [14, 91]. Anchor damping is yet another dissipation mechanism caused by soft anchors, which are not perfectly rigid and cause finite energy loss through the substrate [92]. Finally, the readout electronics of the sensor also dissipates vibration energy due to their resistance against charge accumulation proportional to the velocity of the vibrating structure [14]. The analytical expressions for these damping effects are still subject to research and vary for different geometries as in viscous fluid damping.

In conclusion, there is a number of dissipation mechanisms associated with microstructures, and it is difficult to keep these mechanisms stable in time and repeatable from sensor to sensor. Therefore, it is a good practice to keep the operation of micromachined vibratory gyroscopes away from depending on the variable damping factors. Rather closed-loop systems with appropriate feedback architectures associated with both the drive and the sense modes of the gyroscopes are usually employed, introducing controlled electronic damping mechanisms for removing the dependency on the described damping mechanisms, which makes the sensor operation more predictable and controllable.

2.3 Design in Electrical Domain

The mechanical model of a micromachined vibratory gyroscope is essential for predicting its dynamic behavior; however, this is not sufficient for realizing a practical sensor. In practice, the generation of the drive-mode actuation force, transduction of the physical rotation rate to an electronic signal, and the electrostatic

control and feedback mechanisms of the sensor all require a complete electromechanical model of the gyroscope. This model includes the effects of both mechanical and electrical domain parameters, and the analysis is usually performed by converting the mechanical domain parameters to their electrical equivalent circuits. This section describes the basic principle of electrostatic actuation for generating drive-mode oscillations, conversion of the mechanical domain parameters to electrical domain equivalents, capacitive sensing of the sensor output, and electrostatic springs.

2.3.1 Electrostatic Actuation using Parallel-Plate Capacitors

The electrical charges in two closely-spaced but isolated conductors biased at different potentials repel each other due to their neutralization tendency. The repel energy induces a net force on the conductors towards each other. If the conductors are fixed then the repel energy is stored between the capacitor plates, and it may then be dissipated by generating a reverse charge flow through a dissipating system such as an electrical resistor. However, if at least one of the conductors has one or more degrees-of-freedom for motion then the repel energy can also be dissipated by the physical displacement of the movable capacitor plate. This is the basic principle that lies behind the electrostatic actuation in microstructures. Figure 2.5 shows a typical parallel-plate capacitor configuration together with parametric dimensions that allows us to generate expressions for the electrostatic energy and force for the given configuration. The reason for selecting the parallel-plate configuration is not only due to its simple geometry, but also due to the fact that it is the most suitable and widely used configuration for manufacturing by standard micromachining technologies, for which there is limited process control in all three dimensions simultaneously.

The capacitance of the parallel-plate capacitor in Figure 2.5 is given as

$$C = \alpha \cdot \varepsilon_0 \frac{L(x) \cdot H(z)}{D(y)} \qquad (2.32a)$$

61

$$L(x) = L_0 + x \qquad\qquad (2.32\text{b})$$

$$D(y) = D_0 - y \qquad\qquad (2.32\text{c})$$

$$H(z) = H_0 - z \qquad\qquad (2.32\text{d})$$

where α is the correction factor for fringing electric fields, ε_0 is the permittivity of free air, $L(x)$ is the overlap length, $H(x)$ is the overlap height, $D(x)$ is the gap spacing between the capacitor plates, and x-y-z defines the coordinate system of the movable capacitor plate with respect to the origin shown in Figure 2.5. Electrostatic fringe-field factor α is assumed constant for simplifying the analysis, although it slightly varies by displacement. The energy stored in the capacitor has the well-known expression

$$E = \frac{1}{2} \cdot C \cdot V^2 \qquad\qquad (2.33)$$

where V is the potential difference applied across the capacitor plates. The position gradient of energy provides the electrostatic force acting on the conductors,

$$F_e = \frac{\partial E}{\partial r} = \frac{1}{2} \cdot \frac{\partial C}{\partial r} \cdot V^2 \qquad\qquad (2.34)$$

where r is the position vector along either coordinate axis. Equation 2.34 assumes that the potential difference, V, does not change with position of the capacitor plates. Inserting Equation 2.32-a into 2.34 results in

$$F_{e,x} = \frac{\partial E}{\partial x} = \frac{1}{2} \cdot \frac{\partial C}{\partial L} \cdot \frac{\partial L(x)}{\partial x} \cdot V^2 = \frac{1}{2} \cdot \alpha \cdot \varepsilon_0 \cdot \frac{H_0}{D_0} \cdot V^2 \qquad\qquad (2.35\text{a})$$

$$F_{e,y} = \frac{\partial E}{\partial y} = \frac{1}{2} \cdot \frac{\partial C}{\partial D} \cdot \frac{\partial D(y)}{\partial y} \cdot V^2 = \frac{1}{2} \cdot \alpha \cdot \varepsilon_0 \cdot \frac{H_0 \cdot L_0}{(D_0 - y)^2} \cdot V^2 \qquad\qquad (2.35\text{b})$$

$$F_{e,z} = \frac{\partial E}{\partial z} = \frac{1}{2} \cdot \frac{\partial C}{\partial H} \cdot \frac{\partial H(z)}{\partial z} \cdot V^2 = -\frac{1}{2} \cdot \alpha \cdot \varepsilon_0 \cdot \frac{L_0}{D_0} \cdot V^2 \qquad\qquad (2.35\text{c})$$

Analyzing the polarities of the electrostatic force expressions in Equation 2.35, it can be concluded that the electrostatic force tends to increase the energy stored in the system, by forcing the movable plate to a position that would maximize the overall capacitance. Another point is that, the electrostatic force components in x and z directions, $F_{e,x}$ and $F_{e,z}$, are constant with displacement of the movable capacitor plate, while the force component in y direction, $F_{e,y}$, depends on the position of the movable plate, being nonlinear with respect to displacement. However, note that $F_{e,y}$ generates the highest electrostatic force among the other force components, provided that L_0 and H_0 are greater than D_0, which is typical for many standard micromachining technologies.
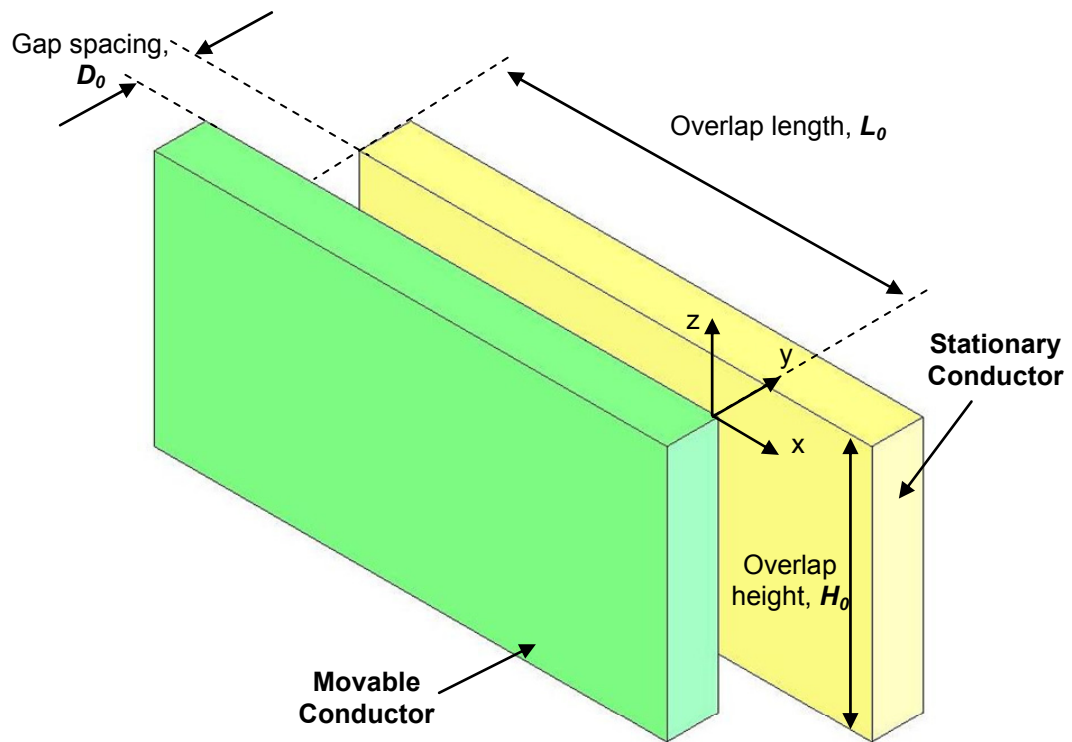
Figure 2.5: Typical parallel-plate capacitor configuration together with parametric dimensions that allows us to generate expressions for the electrostatic energy and force for the given configuration.

The electrostatic actuation force expression in Equation 2.34 is also a function of the applied potential, V. Remembering the discussion in Section 2.1, the drive-mode resonator of the micromachined vibratory gyroscope is entered into oscillations at its mechanical resonance frequency by electrostatic actuation. Therefore the frequency

of the electrostatic force must match with the resonance frequency of the drive-mode resonator. This is achieved by applying a time-varying potential difference between the capacitor plates of Figure 2.5. The electrostatic force component then becomes

$$F_e = \frac{\partial E}{\partial r} = \frac{1}{2} \cdot \frac{\partial C}{\partial r} \cdot (V_{ac} \cdot Sin(\omega t))^2 = \frac{\partial C}{\partial r} \cdot \left\{ \underbrace{\frac{V_{ac}^2}{4}}_{DC\,Component} - \underbrace{\frac{V_{ac}^2}{2} \cdot Cos(2\omega t)}_{AC\,Component\ at\ 2\omega} \right\} \qquad (2.36)$$

where V_{ac} is the amplitude of the time-varying potential difference. Examining Equation 2.36 indicates that there are two electrostatic force components, one being constant and the other being time-varying. The constant force component may only cause a static deflection of the movable capacitor plate. On the other hand, the time-varying component of the force can be used to excite the drive-mode of the gyroscope into resonance, provided that the mechanical resonance frequency of the drive-mode resonator is at 2ω. This can be achieved by setting the frequency ω of the input time-varying potential difference to half of the mechanical resonance frequency of the drive mode, but this approach requires dedicated electronic control of the frequency of the actuation force in the oscillator feedback loop, which complicates the drive-mode electronics. In addition, the generated force in Equation 2.36 is nonlinear with respect to the amplitude of the applied potential difference, which may cause problems in the overall linear operation of the system. Instead, a constant DC offset potential can be added to the time-varying potential difference, which would generate an electrostatic force of

$$F_e = \frac{\partial E}{\partial r} = \frac{1}{2} \cdot \frac{\partial C}{\partial r} \cdot (V_{DC} + V_{ac} \cdot Sin(\omega t))^2 \qquad (2.37)$$

where V_{DC} is the amplitude of the offset component of the applied time-varying potential difference. Expanding the squares in Equation 2.37 and re-arranging the terms yields

$$F_e = \frac{\partial E}{\partial r} = \frac{\partial C}{\partial r} \cdot \left\{ \underbrace{\frac{1}{2} \cdot \left[V_{DC}^{\ 2} + \frac{V_{ac}^{\ 2}}{2} \right]}_{DC\,Component} + \underbrace{V_{DC} \cdot V_{ac} \cdot Sin(\omega t)}_{AC\,Component\,at\,\omega} - \underbrace{\frac{V_{ac}^{\ 2}}{2} \cdot Cos(2\omega t)}_{AC\,Component\,at\,2\omega} \right\} \qquad (2.38)$$

Equation 2.38 shows the advantage of using a potential difference having both constant and time-varying components. This way, the electrostatic force would have an AC component at frequency ω, which can be set to the mechanical resonance frequency of the drive-mode. The AC component at frequency 2ω would be filtered by the mechanical resonator, provided that the drive-mode resonator has a sharp quality factor around its resonance frequency, which is usually the case.

Having analyzed the generation of the electrostatic force in a parallel-plate capacitor, the results can be applied to the drive mechanism of a micromachined vibratory gyroscope. Considering the parallel-plate configuration in Figure 2.5 and the expression in Equation 2.35, there are two basic configurations for the drive-mode actuation mechanism: 1) Varying-gap actuation, 2) Varying-overlap-area actuation. The displacement of the movable electrode in Figure 2.4 along the *y* direction corresponds to a varying-gap actuation whereas the displacement along *x* or *z* directions corresponds to a varying-overlap-area actuation. The configuration of the drive-mode actuation mechanism is determined by the capacitor geometry and the assigned DOF of the drive electrode. Figure 2.6 shows typical drive electrodes for varying-gap and varying-overlap-area actuation mechanisms. For the varying-gap type electrode, there is a net force along the direction of drive oscillations, which is set by suspension beams not shown in the figure. This force is given by,

$$F_{y,1} - F_{y,2} = \frac{1}{2} \cdot N \cdot \alpha \cdot \varepsilon_0 \cdot H_0 \cdot L_0 \cdot \left[\frac{1}{(D_0 - y)^2} - \frac{1}{(D_{anti-gap} + y)^2} \right] \cdot V^2 \qquad (2.39)$$

where *N* is the number of capacitor pairs on the electrode and $D_{anti-gap}$ is the distance from the movable capacitor plate to the stationary plate of the neighboring capacitor pair.
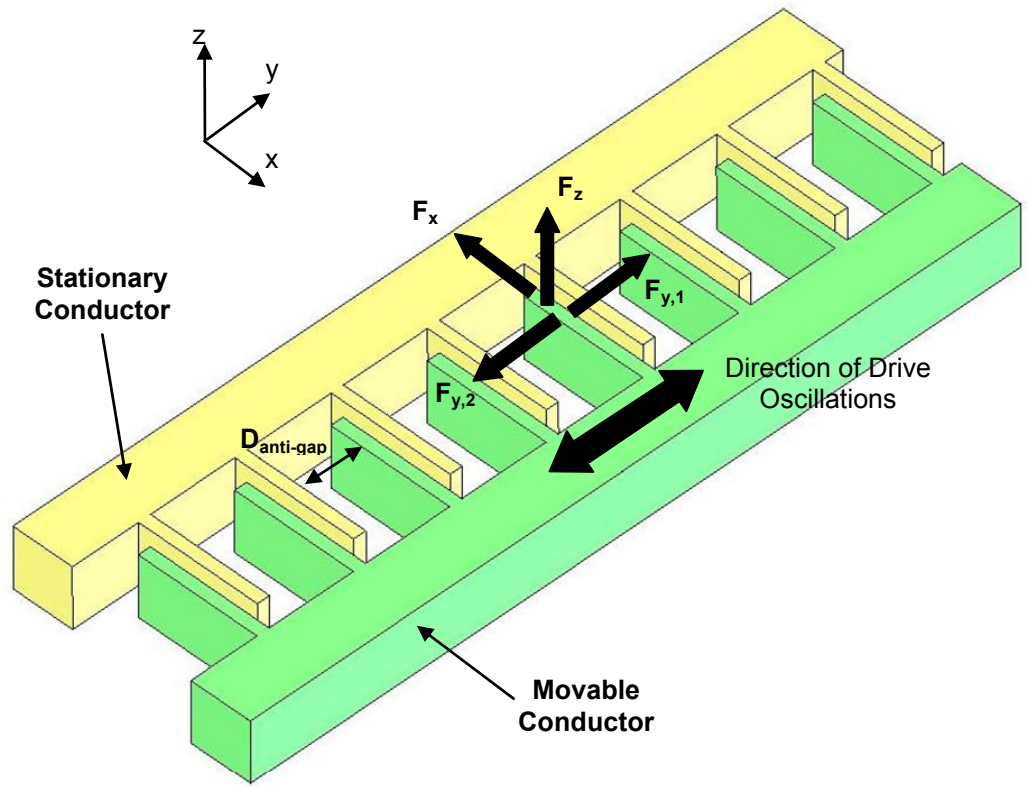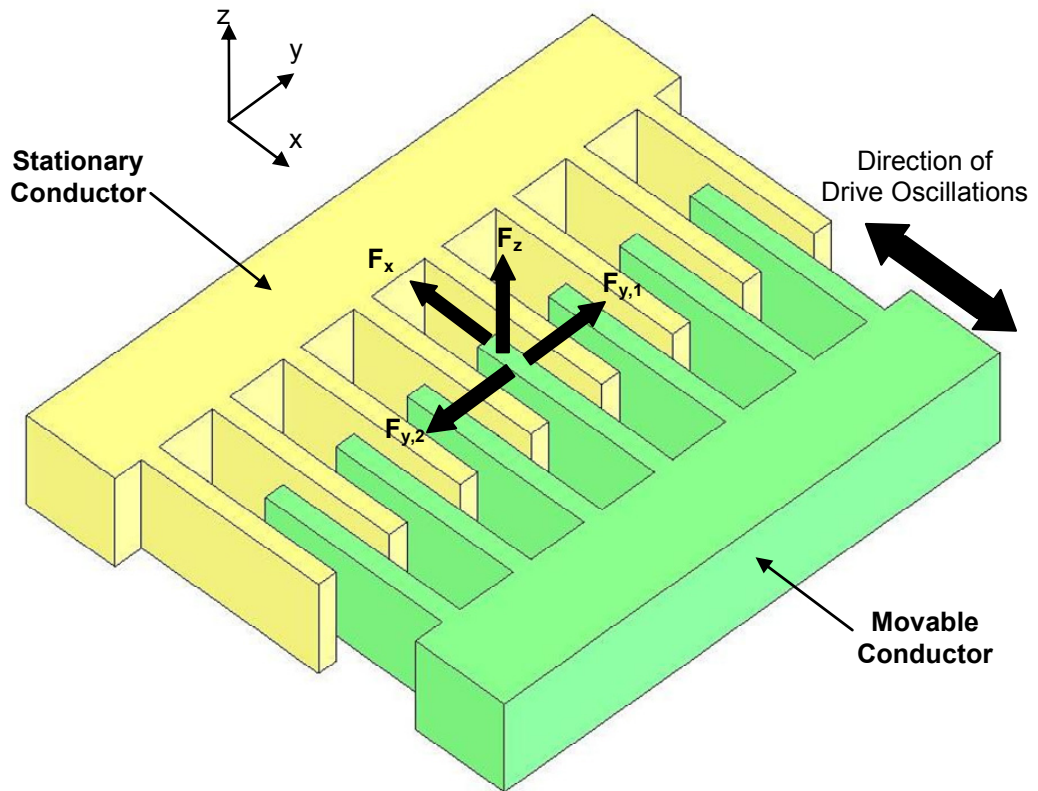
Figure 2.6: Typical drive electrodes for (a) varying-gap and (b) varying-overlap-area actuation mechanisms.

Assuming small displacements so that $y \ll D_0$, Equation 2.39 simplifies to,

$$F_{y,1} - F_{y,2} = \frac{1}{2} \cdot N \cdot \alpha \cdot \varepsilon_0 \cdot H_0 \cdot L_0 \cdot \left[\frac{1}{D_0^{\,2}} - \frac{1}{D_{anti-gap}^{\,2}} \right] \cdot V^2 \qquad (2.40)$$

which is independent of the displacement. The effect of anti-gap capacitor can be decreased by selecting $D_{anti-gap}$ larger than D_0, which has the trade-off for reduced capacitance per unit electrode length. For the varying-overlap-area capacitor in Figure 2.6b, the net force along the drive-mode oscillation direction would be

$$F_x = N \cdot \alpha \cdot \varepsilon_0 \cdot \frac{H_0}{D_0} \cdot V^2 \qquad (2.41)$$

which is virtually independent of the drive-mode displacement. However, the $F_{y,1}$ and $F_{y,2}$ forces significantly vary by changing the drive-mode displacement of the varying-overlap-area type electrode. Although these two forces act along opposite directions with equal magnitudes, they potentially cause stability problems for large drive-mode displacements as will be discussed in Section 2.4.

Although varying-gap electrodes generate larger electrostatic forces, their nonlinear dependence on the displacement limits their operation to small displacements. Equation 2.40 would be in more than 10% error for drive-mode displacements of only 5% of the static gap spacing, D_0. Since, large drive-mode oscillations is desirable for better rate sensitivity, as described in Section 2.1, varying-overlap-area type drive electrodes are selected for the drive-mode actuation of the designed vibratory gyroscopes. This selection allows drive-mode oscillation amplitudes as high as 15μm, instead of 5% of the static gap spacing which would be less than 0.25μm for the gyroscopes developed in this research. Next section describes the use of electrostatic force in generating drive-mode oscillations.

2.3.2 Electrical Equivalent Circuit Representation

Conversion of the mechanical domain parameter to their electrical equivalents allows the use of combined design and simulation for the overall electromechanical system. This conversion is performed by establishing an analogy between a mechanical system and its electrical representation, where the behavior of both systems being represented by identical mathematical models. Figure 2.7 shows a serial RLC circuit, for which the following relation holds

$$V_S = R \cdot i(t) + L \cdot \frac{\partial i(t)}{\partial t} + \frac{Q(t)}{C} \qquad (2.42)$$

where V_S is the potential of the voltage source, $i(t)$ is the loop current, $Q(t)$ is the charge stored in the capacitor, R is the resistance, L is the inductance, and C is the capacitance of the components in the loop. Re-arranging the terms and remembering that $i(t) = \partial Q(t) / \partial t$,

$$V_S = L \cdot \frac{\partial^2 Q(t)}{\partial t^2} + R \cdot \frac{\partial Q(t)}{\partial t} + C \cdot Q(t) \qquad (2.43)$$

which has the same form as in Equation 2.1. Therefore, it is possible to predict the behavior of the mechanical system by converting the mechanical model parameters to their electrical analogues. Table 2.3 provides the mechanical model parameters for the second-order spring-mass-damper system and their electrical equivalents. Figure 2.8 shows the electrical equivalent circuit representation of the mechanical system describing the drive-mode resonator of a vibratory gyroscope.
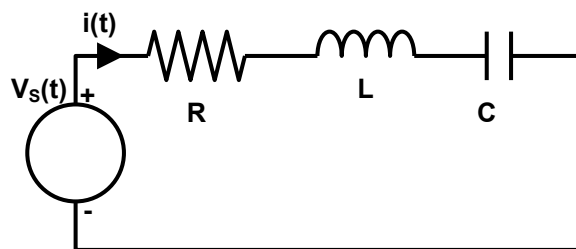
Figure 2.7: Series RLC circuit.

Table 2.3: The mechanical model parameters for the second-order spring-mass-damper system and their electrical equivalents.

Mechanical Model Parameter		Electrical Analogue	
Mass	m	L	Inductance
Damping coefficient	b	R	Resistance
Spring constant	k	1/C	Reciprocal of capacitance
Displacement	x	Q	Electronic charge
Velocity	v	i	Current
Force	F	V	Voltage
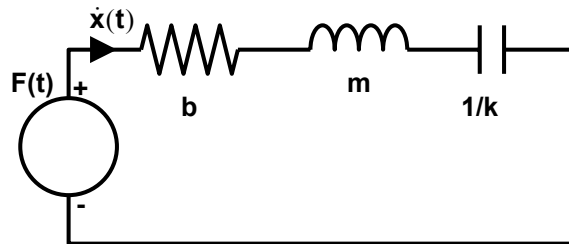
Figure 2.8: Electrical equivalent circuit representation of the mechanical system describing the drive-mode resonator of a vibratory gyroscope.

Figure 2.9 shows the electrical port and the mechanical port of the drive-mode actuation electrode of the gyroscope, which are coupled to each other by using an equivalent transformation coefficient, n. i_e represents the electrical current pumped to the variable capacitor of the drive electrode, $C_{drive,in}$. The model describes that the time-varying potential applied across variable capacitor would cause a displacement of the resonator due to electrostatic force generated across the plates of the capacitor [93].
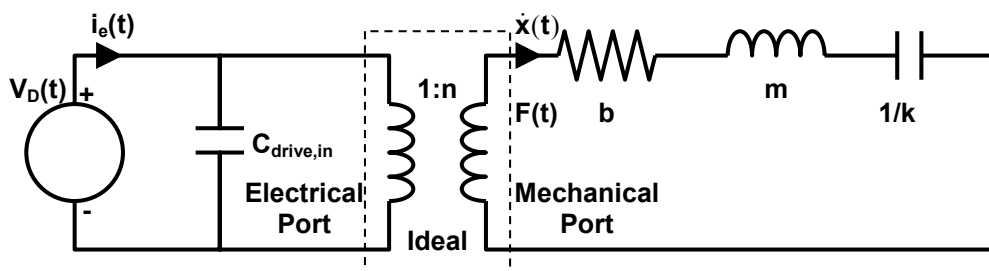
Figure 2.9: The electrical and the mechanical ports of the drive-electrode of the gyroscope. The ideal transformer in the model converts the mechanical domain parameters to their electrical domain equivalents.

Figure 2.10 shows the combined electromechanical model of the actuation portion of the drive mode resonator, where the mechanical domain parameters are replaced by their electrical equivalents and the resulting circuit connected to the electrical port of the drive-electrode. i_e pumped through the gyroscope is divided into two parts: 1) i_f denotes the electrical feedthrough current passing through the electrical capacitance $C_{drive,in}$ and 2) i_m is the portion of the input current used to generate a motion of the capacitor plates and hence the drive mode resonator. i_m is known as the motional current proportional to the velocity of the resonator, and R_m, C_m, and L_m represents the electrical equivalents for the damper, spring, and the mass of the drive-mode resonator.
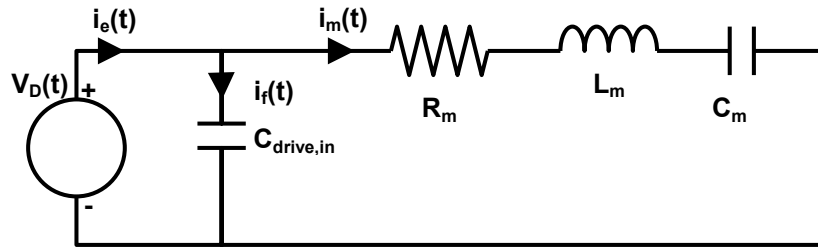
Figure 2.10: The combined electromechanical model of the actuation portion of the drive mode resonator, where the mechanical domain parameters are replaced by their electrical equivalents and the resulting circuit connected to the electrical port of the drive-electrode.

The analysis of the drive-mode electrical equivalent model of the gyroscope starts with assigning a time-varying capacitance at one of the drive electrodes shown in Figure 2.1.

$$C_{Drive,in}(t) = \begin{cases} C_0, off\ resonance \\ C_0 + C_D(t), at\ resonance \end{cases} \qquad (2.44a)$$

$$C_D(t) = x(t) \cdot \frac{\partial C_{Drive,in}}{\partial x} \qquad (2.44b)$$

where C_0 is the static overlap capacitance of the drive-electrode and $C_D(t)$ is the time-varying capacitance when the drive-mode of the gyroscope oscillates at its mechanical resonance frequency. The input electrical current, $I_e(t)$ can be expressed as

$$i_e(t) = \underbrace{C_{Drive,in}(t) \cdot \frac{\partial V_D(t)}{\partial t}}_{i_f(t)} + \underbrace{V_D(t) \cdot \frac{\partial C_{Drive,in}(t)}{\partial t}}_{i_m(t)} \qquad (2.45)$$

Where $V_D(t)$ is the applied input potential to the drive-mode capacitor plates, and has the form $V_{DC} + V_{ac}(t)$ as described in Section 2.3.1. Expanding Equation 2.45 at mechanical resonance of the drive mode yields

$$i_e(t) = (C_0 + C_D(t)) \cdot \frac{\partial (V_{DC} + V_{ac}(t))}{\partial t} + (V_{DC} + V_{ac}(t)) \cdot \frac{\partial (C_0 + C_D(t))}{\partial t} \qquad (2.46)$$

Remembering Equation 2.44b and after rearranging the terms in Equation 2.46

$$i_e(t) = \left[C_0 + x(t) \cdot \frac{\partial C_{Drive,in}}{\partial x} \right] \cdot \frac{\partial V_{ac}(t)}{\partial t} + \left[\frac{\partial C_{Drive,in}}{\partial x} \cdot \frac{\partial x}{\partial t} \right] \cdot (V_{DC} + V_{ac}(t)) \qquad (2.47)$$

Equation 2.47 can now be converted to a more convenient phasor notation by using Laplace transform and arranged as

$$I_e(t) = j\omega \cdot C_0 \cdot V_{ac}(j\omega) + 2j\omega \cdot \frac{\partial C_{Drive,in}}{\partial x} \cdot V_{ac}(j\omega) \cdot X(j\omega) + j\omega \cdot V_{DC} \cdot \frac{\partial C_{Drive,in}}{\partial x} \cdot X(j\omega) \qquad (2.48)$$

The first term in right-hand-side of Equation 2.48 gives the feed-through current flowing through the static overlap capacitance between the movable and stationary capacitor plates. The second term represents the modulation current at twice the excitation frequency, ω. The final term is the motional current, which indeed transforms to a physical motion in mechanical domain. If $V_{DC} \gg |V_{ac}(t)|$, then the effect of modulation current can be neglected, otherwise it would try to actuate the resonator at a frequency twice the resonance frequency, ω, which can be filtered by the mechanical resonator if the quality factor around the resonance frequency is high enough and there are no resonance modes in the close vicinity of *2ω*.

The results obtained in Equation 2.48 can be used to predict the vibration amplitude of the drive-mode resonator at mechanical resonance. Remembering the models of Figure 2.9 and 2.10,

$$i_m(t) = n \cdot \dot{x}(t) \tag{2.49a}$$

$$j\omega \cdot V_{DC} \cdot \frac{\partial C_{Drive,in}}{\partial x} \cdot X(j\omega) = I_m(j\omega) = n \cdot j\omega \cdot X(j\omega) \tag{2.49b}$$

$$V_{DC} \cdot \frac{\partial C_{Drive,in}}{\partial x} = n \tag{2.49c}$$

where Equation 2.49b shows the phasor domain representation of the expression in Equation 2.49a, and **n** is called the electromechanical coupling coefficient that is used to transform the mechanical domain parameters to their electrical domain equivalents. Note that, this coefficient is constant for varying-overlap-area type actuation electrodes. The electrical domain equivalents of the drive-mode resonator can also be expressed in terms of the observable parameters **m**, **b**, **k**, and **n** as follows:

$$L_m = \frac{m}{n^2} \tag{2.50a}$$

$$R_m = \frac{b}{n^2} \tag{2.50b}$$

$$C_m = \frac{n^2}{k} \tag{2.50c}$$

and the admittance of the electrical equivalent circuit in Figure 2.10 is then found as

$$Y_{in}(j\omega) = j\omega \cdot C_0 + \frac{1}{j\omega \cdot L_m + R_m + \dfrac{1}{j\omega \cdot C_m}} \tag{2.51}$$

which defines the actuation characteristics of the electromechanical drive-mode resonator of the gyroscope. Once the electromechanical conversion factor, **n**, is

72

known, it is possible to find an expression for the drive-mode vibration amplitude in response to an applied input potential. The phasor representation of Equation 2.1 is

$$F_D(j\omega) = \left\{-\omega^2 \cdot m_D + j\omega \cdot b_D + k_D\right\} \cdot X_D(j\omega) \qquad (2.52)$$

Using the transformer model of Figure 2.9,

$$F_D(j\omega) = n \cdot V_{ac}(j\omega) \qquad (2.53)$$

Inserting the force expression of Equation 2.52 into Equation 2.53 and re-arranging the terms yield,

$$\frac{X_D(j\omega)}{V_{ac}(j\omega)} = \frac{n}{k_D \cdot \left[\left(1 - \left(\dfrac{\omega}{\omega_D}\right)^2\right) + j \cdot \dfrac{\omega}{Q_D \cdot \omega_D}\right]} \qquad (2.54)$$

and if the frequency of the applied time-varying signal, ω, is at the mechanical resonance frequency, ω$_D$, of drive-mode resonator, then Equation 2.54 simplifies to

$$X_D(j\omega) = \frac{V_{ac}(j\omega) \cdot V_{DC} \cdot \dfrac{\partial C_{Drive,in}}{\partial x} \cdot Q_D}{k_D} \qquad (2.55)$$

which express the vibration amplitude of the drive-mode resonator at resonance, in terms of the mechanical and electrical model parameters. Next section describes the capacitive sensing mechanism in response to a displacement either at the drive-mode resonator output or at the sense-mode output of the micromachined vibratory gyroscope.

2.3.3 Capacitive Sensing

The actuation mechanism described in Sections 2.3.1 and 2.3.2 for a second-order spring-mass-damper system illustrates the actuation of the mechanical system using electrostatic forces. Capacitive sensing refers to the detection of the physical displacement of the mechanical sensor element, in response to any kind actuation mechanism; either electrostatic or inertial. Basically, there are two motions to be sensed for a micromachined vibratory gyroscope: 1) The drive-mode oscillations for constructing a self-resonance actuation of the drive-mode and 2) the sense-mode displacements in response to angular rate inputs. Both motions are detected using capacitive sensing mechanisms for the gyroscopes developed in this research. Figure 2.11 shows the mechanical model for the detection port of the capacitive sensor output. The model is very similar to that of Figure 2.9, except the polarities of the currents flowing in the loop are reversed and the source generating these currents is the displacement of the mechanical element in response to an actuation force $F(t)$. Z_o at the output of the electrical port defines the complex impedance at the input of an electronic detection mechanism to be connected at the output port of the sensor, such as a capacitive interface circuit. It should be noted that any of the parameters in the model of Figure 2.11 are not necessarily be identical to those given in Figure 2.9.
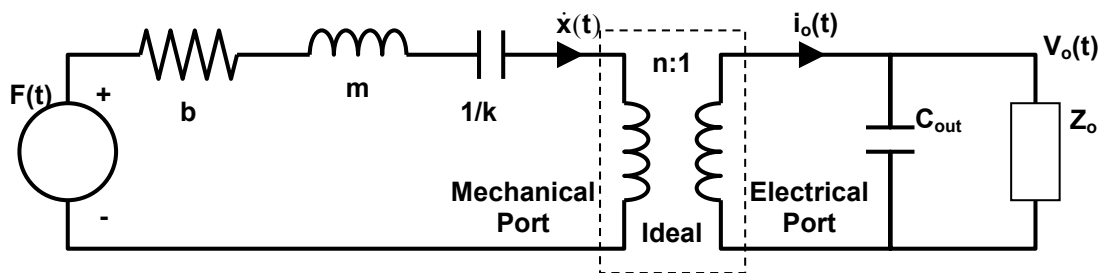
Figure 2.11: Mechanical model for the detection port of the capacitive sensor output.

The output current, $I_o(t)$, in the model of Figure 2.11 denotes the current generated at the output of an oscillating capacitor plate, having biased at a constant offset potential with respect to its stationary counter capacitor plate. C_{out} is the static

74

overlap capacitance of the variable capacitor plates. The general expression of Equation 2.45 is again valid while changing the labels of the parameters

$$i_o(t) = C_{out}(t) \cdot \frac{\partial V_o(t)}{\partial t} + V_o(t) \cdot \frac{\partial C_{out}(t)}{\partial t} \tag{2.56}$$

where $V_o(t)$ has the form $V_{DC,out} + V_{ac,out}(t)$. Obviously, $V_{ac,out}(t)$ is the generated time-varying output of the voltage in response to the displacement, and is much smaller than $V_{DC,out}$, which is an externally set offset potential across the sensor output capacitor C_{out}. $C_{out}(t)$ has the form similar to that of Equation 2.44,

$$C_{out}(t) = \begin{cases} C_0, \text{off resonance} \\ C_0 + C_S(t), \text{at resonance} \end{cases} \tag{2.57a}$$

$$C_S(t) = x(t) \cdot \frac{\partial C_{out}}{\partial x} \tag{2.57b}$$

Assuming $V_{DC,out} \gg V_{ac,out}(t)$ so that $V_o(t) \approx V_{DC,out}$, and using the expressions in Equation 2.57, Equation 2.56 simplifies to

$$i_o(t) = V_{DC,out} \cdot \frac{\partial C_{out}(t)}{\partial x} \cdot \frac{\partial x(t)}{\partial t} \tag{2.58a}$$

$$I_o(j\omega) = j\omega \cdot \underbrace{V_{DC,out} \cdot \frac{\partial C_{out}(t)}{\partial x}}_{n} \cdot X(j\omega) \tag{2.58b}$$

This output current generates the time-varying output voltage, $V_{ac,out}(t)$, through the complex impedance at the output port of the sensor,

$$V_{ac,out}(j\omega) = I_o(j\omega) \cdot \left[\frac{1}{j\omega \cdot C_{out}} // \underbrace{Z_o}_{R_o // \frac{1}{j\omega \cdot C_o}} \right] = \frac{j\omega \cdot n \cdot R_o \cdot X(j\omega)}{1 + j\omega \cdot R_o \cdot (C_{out} + C_o)} \tag{2.59}$$

where R_o and C_o are the resistance and impedance of the electronic network interfacing the sensor output. Typically, $V_{ac,out}(t)$ does not exceed several tens of millivolts, about three orders of magnitude smaller than $V_{DC,out}$, therefore the assumptions in deriving Equation 2.59 safely holds. This equation provides an efficient method to estimate the output voltage in response to a displacement of the sensor element.

The displacement-induced current generation capability of the varying-gap type electrodes is larger than that of varying-overlap-area type electrodes, as in the case of their use as actuation mechanisms. However, the capacitive sensing mechanism for the drive-mode resonator must be varying-overlap-area type structure, since the amplitude of drive-mode oscillations typically exceeds the minimum allowable gap spacing, which is essential both for the most efficient actuation and sensitive detection. This does not affect the operation of the drive-mode resonator because of the fact that the output current detected from the drive-mode resonator using varying-overlap-area type detection mechanism is still much higher than the current noise of the drive-mode resonator. Once the drive-mode output exceeds the noise threshold, it is possible for the drive-mode to construct a self-oscillating system using feedback electronics. The situation is somewhat more challenging for the sense-mode of the gyroscope. The Coriolis force acting along the sense-mode of the gyroscope in response to an applied 1deg/sec angular rate input result in sense-mode oscillations in the order of a few Angstroms for a sense-mode quality factor of 100 and resonance frequency of 4kHz. Therefore, sensing the fractions of 1deg/sec may require the detection of displacements in the sub-atomic range. Since the sense-mode displacements are already small in a Coriolis vibratory rate gyroscope, the use of varying-gap sensing mechanism is much more sensitive for the sense mode of the gyroscope, compared to the varying-overlap-area type sensing mechanism. In conclusion, drive-mode resonator displacements are sensed with varying-overlap-area type detection mechanism due to the large vibration amplitude of the drive-mode and the linear drive requirements, whereas the sense-mode displacements are detected using a very sensitive varying-gap type detection mechanism. Another advantage of the varying-gap type detection mechanism is its capability of tuning

the overall spring constant along its direction of motion, which is described in the next section.

2.3.4 Electrostatic Spring Effect

Electrostatic actuation and detection mechanism in a micromachined vibratory gyroscope allows generating the drive-mode oscillations with a closed-loop frequency lock network, and the sensitive detection of sub-atomic displacements at the sense-mode output due to angular rate inputs. The small sense-mode output displacements are maximized by using matched resonance frequencies for the drive and the sense modes of the vibratory gyroscope. The resonance frequency of the spring-mass-damper model of either the drive or the sense mode is a function of the mechanical spring constant and the amount of mass vibrating along with a particular mode. The spring constant expressions shown in Table 2.2 for the flexure structures used in micromachining contain cubic dependence on the structure dimensions. Unfortunately, the micromachining tolerances are quite poor; it is quite difficult to define the width of a flexure beam with a tolerance better than 10% in standard micromachining processes. The poor tolerance in defining the minimum features may cause spring constant errors more than 30% and resonance frequency shifts as high as 20%, combined with the tolerances in estimating the proof mass. Therefore, the matching of the mechanical resonance frequencies of a micromachined vibratory gyroscope for high sensitivity is typically not possible without the use of post-process tuning. Mechanical tuning is a solution, which requires precise machining capability, long tuning periods, and high tuning costs. Instead, electrostatic tuning of the resonance frequencies is also possible by using varying-gap type capacitors, which provides an efficient and reliable way of tuning the mechanical resonance frequencies based on the fact that the varying-gap structures can act as electrostatic negative springs. Taking the derivative of electrostatic force expression in Equation 2.35b with respect to position results in

$$\frac{\partial F_{e,y}}{\partial y} = \frac{\partial^2 E}{\partial y^2} = \frac{1}{2} \cdot \frac{\partial^2 C}{\partial y^2} \cdot V^2 = \alpha \cdot \varepsilon_0 \cdot \frac{H_0 \cdot L_0}{(D_0 - y)^3} \cdot V^2 = \delta k_{electrostatic} \qquad (2.60)$$

77

where $\delta k_{electrostatic}$ is the instantaneous spring constant across the plates of the capacitor. Note that, the polarity of the spring constant is positive, stating that the electrostatic spring tends to enhance the motion of the capacitor plates towards each other, trying to maximize the energy stored in it contrary to classical mechanical springs that tends to minimize the energy stored in them. Electrostatic negative springs is very useful in practice for fine tuning the overall spring constant associated with the mode that oscillates along the direction of changing the capacitor gap. The parameters in Equation 2.60 are all defined by the geometrical structure of the capacitor and can be assumed constant for small displacements, and the electrostatic spring constant can be varied by adjusting the voltage across the capacitor plates. It must be noted that, the squared voltage, V^2, in Equation 2.60 still have the form shown in Equation 2.38, with a constant DC term plus the higher order harmonics. If $V_{DC} \gg V_{ac}(t)$ is satisfied during the operation, then the constant DC term dominates in determining the electrostatic spring, which can still be assumed constant for small displacements as being typical for the sense-mode dynamics. If the displacement amplitude is large, the cubic relation between the displacement and the electrostatic spring constant would cause errors in assuming a fixed spring constant. Therefore, the electrostatic spring constants are used to tune the sense-mode resonance frequency of the designed micromachined gyroscopes. In practice, the mechanical resonance frequency of the sense-mode is set to be higher than the drive-mode mechanical resonance frequency, and it is tuned-down using electrostatic negative springs for matching with the drive-mode frequency using the relation

$$\omega_S = \sqrt{\frac{k_S - \delta k_{electrostatic,S}}{m_S}} \qquad (2.61)$$

where ω_S, k_S, m_S, and $\delta k_{electrostatic,S}$ are the resonance frequency in radians, mechanical spring constant, amount of oscillating mass, and electrostatic spring constant, respectively, all associated with the sense mode as denoted by the subscript "S".

78

As it is possible to reduce the overall spring constant of a particular mode by using electrostatic negative springs, it should be noted that the system would be unstable if the overall spring constant drops to zero by applying sufficiently high negative spring constant. At this limit, the mechanical spring constant cannot withstand the electrostatic forces, which results in the collapse of the movable capacitor plates called pull-in. The condition for pull-in is reached when the electrostatic force reaches and then overdrives the restoring mechanical spring force along the sense direction, k_S.

$$\frac{1}{2} \cdot \alpha \cdot \varepsilon_0 \cdot \frac{H_0 \cdot L_0}{(D_0 - y)^2} \cdot V^2 = k_S \cdot y \tag{2.62}$$

The equilibrium point is then found after taking the derivative of both sides with respect to the displacement, y,

$$\alpha \cdot \varepsilon_0 \cdot \frac{H_0 \cdot L_0}{(D_0 - y)^3} \cdot V^2 = k_S \tag{2.63}$$

where the left hand side is nothing but the expression for the electrostatic spring constant derived in Equation 2.60. The critical displacement for reaching unstable equilibrium is then found by replacing the result in Equation 2.63 into Equation 2.62 and solving for y as

$$y_{critical} = \frac{1}{3} \cdot D_0 \tag{2.64}$$

meaning that the varying-gap system enters pull-in following a displacement of one third of the original gap spacing. From there, it is also possible to find an expression for the pull-in voltage that cause such a displacement by inserting the result in equation 2.64 into equation 2.62 and solving for V yields

$$V_{Pull-in} = \sqrt{\frac{8 \cdot k_S \cdot D_0}{27 \cdot \alpha \cdot \varepsilon_0 \cdot H_0 \cdot L_0}} \tag{2.65}$$

Once this voltage is exceeded, the movable electrode of the varying gap capacitor collapses to the stationary electrode, called pull-in state.

2.4 Second-Order Effects

The electromechanical theory presented up to this point considers the ideal operation of a micromachined vibratory gyroscope, providing well-defined expressions for the sensor operation but ignoring most of the limits associated with the sensor operation. This section introduce the second-order effects that defines the performance limits of micromachined vibratory gyroscopes, including electrostatic levitation, side-instability for large-drive-mode vibration amplitudes, quadrature signal, double-frequency motion, mechanical-thermal noise, and manufacturing process tolerances.

2.4.1 Electrostatic Levitation

Applying a potential difference across the plates of a parallel plate capacitor generates electrostatic forces along all coordinate axes. The displacement caused by these force, however, can be limited to a single axis by proper arrangement of flexures, which have a low stiffness along the desired direction of motion but a high stiffness along the remaining directions orthogonal to the direction of motion. The electrostatic forces tend to maximize the capacitance of the system, due to their inherent tendency of neutralizing the potential across the capacitor electrodes. Examining Equation 2.35c and Figure 2.6, any displacement along the out-of-plane (z-axis) direction of the movable comb finger generates a negative electrostatic force, trying to restore the original position of in the z-direction. This is because of the fact that, the configuration shown in Figure 2.6 already has the maximum capacitance regarding the out-of-plane displacements only, since the capacitive overlap height equals to the comb finger height for the given configuration. Any further displacement along out-of-plane direction would decrease the capacitance of the system. This discussion is valid if there are no neighboring conductive plates in the close vicinity of the movable and stationary comb fingers. Figure 2.12 shows a

configuration, where there is a conductive ground plane or a conductive substrate lay under the comb fingers. Such a configuration would destroy the symmetry of electric fields between the top and the bottom surfaces of the comb fingers, generating spurious electrostatic forces. These spurious forces tend to levitate the movable rotor comb in order to maximize the energy stored in a varying-overlap-area type comb electrode.

(a)

(b)
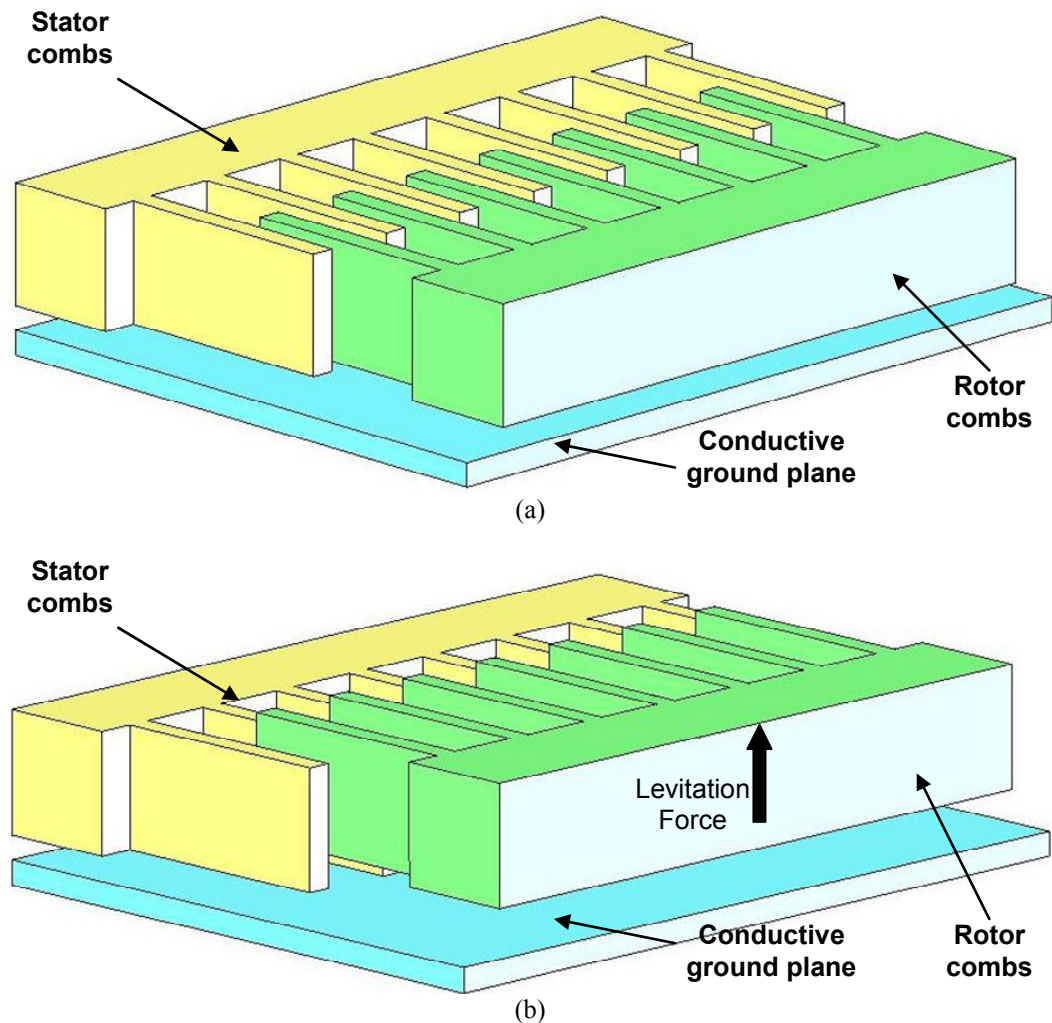
Figure 2.12: If there is a conductive ground plane lay under the movable rotor combs, as in (a), then the system tends to maximize the stored energy in the system by exerting an out-of-plane force to the rotor combs. The result is the levitation of the rotor combs as in (b), the actual amount of vertical displacement depends on the out-of-plane stiffness of the suspensions carrying the rotor electrode (not shown in the figure).

A method to prevent the levitation effect is described in [94], when using a conductive ground plane. However, this method proposes applying differential

biasing of the stator comb fingers in Figure 2.12, which requires electrical isolation of neighboring stator fingers. Fabrication of such kind of stator fingers has some limitations especially when using advanced high-aspect-ratio micromachining processes. In addition, the use of a conductive ground plane increase the parasitic capacitances associated with the capacitive detection port, reducing the overall sensitivity. For this reason, insulating substrate materials are used for most of the gyroscope structures developed in this study, except for the ones fabricated in silicon-on-insulator (SOI) micromachining technology, in which the levitation is cancelled using a different method to be described in Chapter 3.

2.4.2 Side Instability for Varying-Overlap-Area Type Comb Drives

The varying-overlap-area type actuation mechanism discussed in Section 2.3.1 and used for the drive-mode resonator of the micromachined gyroscopes in this research, generates an electrostatic force along the drive-mode direction, which is virtually independent of the displacement. Applying this constant force expression to the force-displacement characteristics of the drive-mode resonator expressed in Equation 2.52 states that there is no limit evident for the maximum achievable displacement. In practice, however, the $F_{y,1}$ and $F_{y,2}$ components of the force shown in Figure 2.6 put some limit to the drive-mode displacement together with the fabrication tolerances [95].

For a varying overlap-area type comb finger shown in Figure 2.6b, the capacitance between the movable and the stationary electrode of the gyroscope would be

$$C = \alpha \cdot \varepsilon_0 \frac{L(x) \cdot H(z)}{D_1(y)} + \alpha \cdot \varepsilon_0 \frac{L(x) \cdot H(z)}{D_2(y)} \tag{2.66a}$$

$$D_1(y) = D_0 - y \tag{2.66b}$$

$$D_2(y) = D_0 + y \tag{2.66c}$$

where $D_1(y)$ and $D_2(y)$ denote the gap spacing from a rotor comb to its neighboring stator combs. Ideally, the rotor comb in a linear varying-overlap-area type comb

82

electrode is located just at the middle of two stator combs, meaning that $y=0$ and $D_1(y)=D_2(y)$. Indeed, this assumption is true to an extent described by the fabrication tolerances for the capacitive gaps. The electrostatic forces $F_{y,1}$ and $F_{y,2}$ in Figure 2.6b, being vertical to the direction of motion are also expressed by

$$F_{y,1} = \frac{1}{2} \cdot \frac{N \cdot \alpha \cdot \varepsilon_0 \cdot H_0 \cdot L_0 \cdot V^2}{(D_0 - y)^2} \tag{2.67a}$$

$$F_{y,2} = \frac{1}{2} \cdot \frac{N \cdot \alpha \cdot \varepsilon_0 \cdot H_0 \cdot L_0 \cdot V^2}{(D_0 + y)^2} \tag{2.67b}$$

stating that $F_{y,1}$ and $F_{y,2}$ vanish each other if the rotor combs are located exactly at the middle of the stator combs along y-direction. If $y \neq 0$ due to fabrication tolerances, the net force acting on the rotor finger in the direction vertical to the rotor displacement would be

$$F_{y,1} - F_{y,2} = \frac{1}{2} \cdot N \cdot \alpha \cdot \varepsilon_0 \cdot H_0 \cdot L_0 \cdot V^2 \cdot \left[\frac{1}{(D_0 - y)^2} - \frac{1}{(D_0 + y)^2} \right] \tag{2.68}$$

At equilibrium, this electrostatic force would be balanced by the mechanical spring constant of the drive-mode rotor electrode in y-direction, $k_{D,y}$,

$$F_{y,1} - F_{y,2} = k_{D,y} \cdot y \tag{2.69}$$

Ideally, the stiffness $k_{D,y}$ is too high compared to the stiffness along the drive-mode direction, $k_{D,x}$, which does not allow a significant displacement along y-direction. The equilibrium point is again found by taking the derivative of both sides with respect to the displacement of the rotor along y-direction and taking the limit as y approach to 0 (ideal fabrication),

$$\lim_{y \to 0} \frac{\partial (F_{y,1} - F_{y,2})}{\partial y} = \frac{2 \cdot N \cdot \alpha \cdot \varepsilon_0 \cdot H_0 \cdot L_0 \cdot V^2}{D_0^3} - k_{D,y} \tag{2.70}$$

83

The right-hand side of the equation must be negative for being in the stable region, meaning that

$$k_{D,y} \geq \frac{2 \cdot N \cdot \alpha \cdot \varepsilon_0 \cdot H_0 \cdot L_0 \cdot V^2}{D_0^3} \qquad (2.71)$$

Equation 2.71 is valid for a static overlap length, L_0, however, the overlap length would change upon application of a DC offset potential across the capacitor. Therefore, Equation 2.71 must be modified as

$$k_{D,y} \geq \frac{2 \cdot N \cdot \alpha \cdot \varepsilon_0 \cdot H_0 \cdot (L_0 + x_D) \cdot V_{DC}^2}{D_0^3} \qquad (2.72)$$

where x_D denotes the static deflection of the rotor electrode by applying a DC offset potential, V_{DC}. The static deflection x_D would be

$$x_D = \frac{N \cdot \alpha \cdot \varepsilon_0 \cdot H_0 \cdot V_{DC}^2}{k_{D,x} \cdot D_0} \qquad (2.73)$$

Inserting the Equation 2.73 into Equation 2.72 and re-arranging the terms yields the maximum DC offset potential that can be applied to between the stator and rotor combs for static deflections as

$$V_{DC}^2 = \frac{k_{D,x} \cdot D_0^2}{2 \cdot \alpha \cdot \varepsilon_0 \cdot H_0} \cdot \left[-\frac{L_0}{D_0} + \sqrt{\left(\frac{L_0}{D_0}\right)^2 + 2 \cdot \frac{k_{D,y}}{k_{D,x}}} \right] \qquad (2.74)$$

Replacing the V_{DC}^2 term in Equation 2.73 with the result found above yields the maximum static deflection amplitude for the rotor comb as

$$x_{D,\max} = \left[D_0 \cdot \sqrt{\frac{1}{4} \cdot \left(\frac{L_0}{D_0}\right)^2 + \frac{k_{D,y}}{2 \cdot k_{D,x}}} \right] - \frac{L_0}{2} \qquad (2.75)$$

84

As the gap spacing between the combs is smaller, the maximum allowable deflection limit also drops. Note that, the result derived above is valid for static deflections of the varying-overlap-area type drive-mode rotor electrode. The dynamic deflection range can be slightly larger than the expression in Equation 2.75, assuming V_{DC} is much larger than the time-varying input potential $V_{ac}(t)$.

2.4.3 Quadrature Error

The mechanical model described in Section 2.1 assumes the orientation of the drive and sense vibration modes are well-defined and are orthogonal to each other. However, manufacturing tolerances may cause a slight rotation of the drive and sense modes of the fabricated gyroscope from the predefined orientations in the designed layout. Therefore, some of the drive-mode oscillations mechanically couple to the sense mode, generating a false sense output, so called the quadrature signal [31, 39, and 96]. Figure 2.13 describes the situation that would cause quadrature error. Any mismatch in the stiffness of the suspensions, uneven mass distribution, or susceptibility to rotations may add to the quadrature error. The name quadrature comes from the fact that the phase of this undesired output signal is in phase-quadrature with the rate-induced sense output. Considering a fraction of the drive-mode oscillations couple to the sense mode as

$$y_{Quadrature}(t) = \lambda \cdot x_D(t)$$ (2.76)

where λ is the amount of the coupling fraction, depending on the manufacturing tolerances. The coupled quadrature motion cause the differential capacitance change at the sense electrode, which is identical to the response generated by the Coriolis-based rate response, except the signal phase. Clearly, the quadrature displacement in Equation 2.76 is proportional to the drive-mode displacement whereas the Coriolis-based displacement of the sense mode is proportional to the velocity of the drive-mode displacement as given in Equation 2.11b, causing a 90° phase difference between the two output response. This difference in the phase can be used to suppress the false quadrature signal at the gyroscope output by using phase-sensitive

detection techniques. Still, a finite portion of the quadrature signal couples to the sensor output causing an offset. The stability of this offset is very important in determining the bias drift of the gyroscope. Quadrature signals can be as high as few thousand deg/sec, in single-mass gyroscope structures where there is no effective decoupling mechanisms are used, or for the gyroscopes fabricated with processes having large manufacturing tolerances. The quadrature signals for some of the microgyroscopes developed in this research are highly suppressed, due to effective decoupling between the drive and the sense modes.
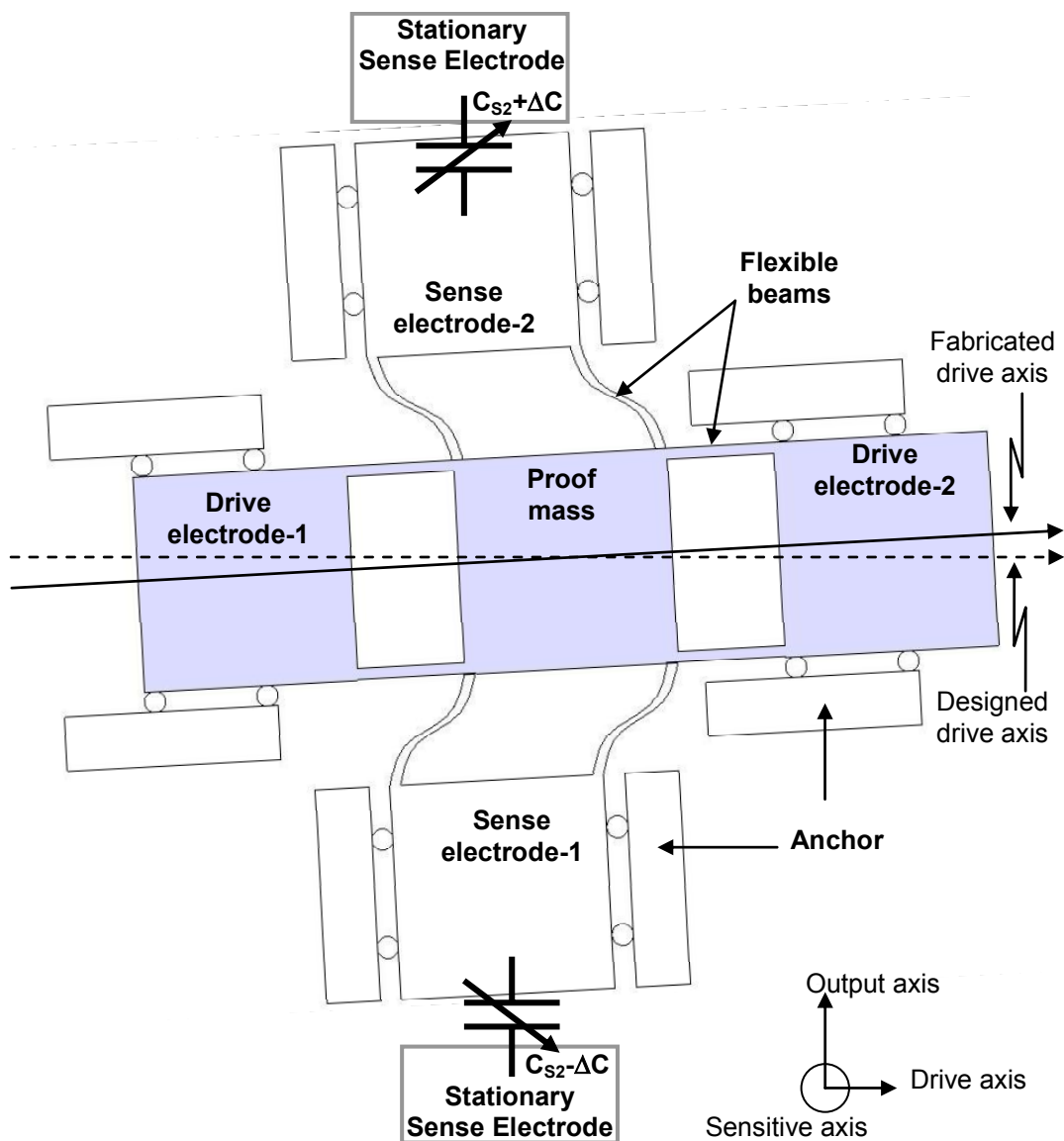
Figure 2.13: The exaggerated view of quadrature coupling. The vibration axes of the drive and sense modes may be rotated due to manufacturing variations, causing a fraction of the drive-mode oscillations couple to the sense mode.

2.4.4 Frequency Doubling

The sense-mode electrodes of the decoupled micromachined gyroscope structure of Figure 2.1 are quasi-stationary during the drive-mode oscillations, except the quadrature signal discussed in the previous section. Though it is possible to suppress the sense-mode output due to the quadrature signal by phase-sensitive detection, there is also another motion coupled from the drive-mode to the sense-mode in the absence of an external rate signal. This motion has a frequency twice that of the drive-mode oscillations and arises due to the axial stresses induced in the flexible beams attached between the sense electrodes and the proof mass. Figure 2.14 illustrates this motion.

The frequency-doubling is due to the fact that the sense-mode electrodes are pulled and released by the flexible beams twice, while the drive-mode oscillation completes only a single cycle. The pulling force exerted on the sense electrodes by the beams are due to internal stresses induced in the beams as a result of their elongation during drive-mode oscillations. This effect may cause drive-mode oscillations as high as a few hundred ppm of the drive-mode vibration amplitude, if the sense electrodes do not have sufficient stiffness against such a motion. If not suppressed, this motion disturbs the readout electronics, causing the saturation of the very sensitive capacitive preamplifier circuits. Fortunately, the double-frequency motion cause a common-mode capacitance change at both sense electrodes, which can be suppressed to a great extent by differential sensing scheme, in contrast to the quadrature signal response. In addition, the phase-sensitive detection of the sense-mode output response further suppresses the signals at twice the frequency of the resonance frequency. Also, using folded flexures instead of clamped flexures help relieving the axial stresses induced in the beams during bending, reducing the coupling of double-frequency vibrations. Finally, combining both of the sense electrodes in a single rigid frame also reduces the effect of double-frequency vibrations. Each of these methods is employed in the micromachined vibratory gyroscopes developed in this research, for evaluating the effectiveness of the proposed solutions.
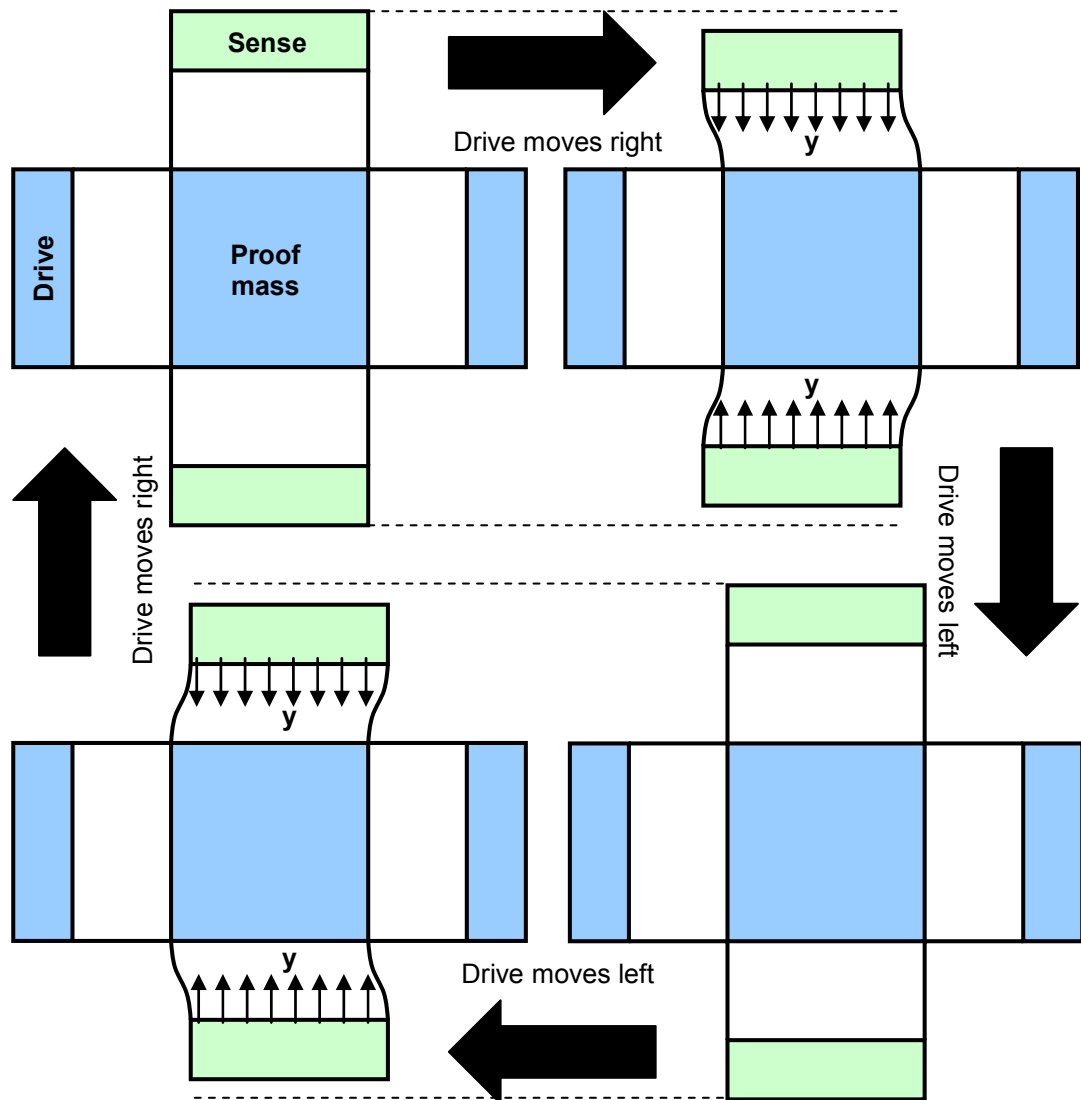
Figure 2.14: Frequency-doubling at the sense-mode. The sense mode electrode is pulled down twice during the completion of a single cycle of drive-mode oscillations.

2.4.5 Mechanical-Thermal Noise

The rate sensitivity of a micromachined vibratory rate gyroscope can be improved by detecting smaller sense-mode displacements. However, the sense-mode displacements in response to rate inputs are already as small as a fraction of the diameter of a silicon atom, being in the range of a fraction of Angstroms (10^{-10}m). Although very sensitive capacitive preamplifiers are capable of detecting the small capacitance changes due to subatomic displacements, if the displacement itself is noisy, then there is no practical electronic solution for detecting displacements

smaller than the average noise displacement. The major source of the noise displacement is the average thermal energy in an energy storage mechanism, such as an electrical capacitor or mechanical spring [12], at thermal equilibrium. Then, the mean-square displacement in a spring-mass system, such as the sense mode of a vibratory gyroscope, can be found by equating the average thermal energy to the energy stored in the spring mass system due to average displacement as

$$\frac{1}{2} \cdot k_B \cdot T = \frac{1}{2} \cdot k_S \cdot \langle y_S \rangle^2 \qquad (2.77)$$

where k_B is Boltzmann constant ($1.38\mathrm{x}10^{-23}$ J/K), T is the ambient temperature in Kelvin, k_S is the mechanical spring constant along the sense mode of the gyroscope, and y_S is the average displacement of the spring-mass system along the sense-mode direction due to the average thermal energy of the atoms. In addition, the spectral density of the fluctuating force associated with any mechanical resistance, such as the viscous fluid damper, is given by

$$F_n = \sqrt{4 \cdot k_B \cdot T \cdot b_S} \qquad (2.78)$$

where F_n is fluctuating force in N/√Hz and b_S is the coefficient of viscous fluid damping along the sense mode of the gyroscope. Applying this fluctuating force to the dynamic system characteristics of the sense-mode resonator described by Equation 2.3 and remembering that $b_S = \sqrt{k_S \cdot m_S}/Q_S = (\omega_S \cdot m_S)/Q_S$, the magnitude of the sense-mode displacements due to the fluctuating noise force, F_n, is found as

$$|Y_S| = \sqrt{\frac{4 \cdot k_B \cdot T \cdot \omega_S \cdot m_S}{Q_S}} \cdot \frac{1}{k_S \cdot \sqrt{\left(1 - \left(\frac{f}{f_S}\right)^2\right)^2 + \left(\frac{f}{Q_S \cdot f_S}\right)^2}} \qquad (2.79)$$

where f_S is the resonance frequency of the sense mode in Hz and Q_S is the mechanical quality factor of the sense mode. For frequencies $f \ll f_S$, Equation 2.79 simplifies to

89

$$|Y_S| = \sqrt{\frac{4 \cdot k_B \cdot T \cdot \sqrt{m_S}}{k_S^{3/2} \cdot Q_S \cdot}} \qquad (2.80)$$

meaning that the noise displacement can be reduced increasing the mechanical spring constant and the quality factor, and by reducing the mass of the sense mode. Increasing the spring constant by reducing mass also increases the mechanical resonance frequency of the gyroscope. Equation 2.80 is valid for f f<<f$_S$, i.e., mismatched mode of operation for the gyroscope. The noise equivalent rate output of the gyroscope for the mismatched operation is then found by dividing Equation 2.80 by the sense-mode displacement of Equation 2.21 in response to a 1deg/sec (0.01745 rad/sec) rate input, resulting in

$$\Omega_{n,mismatched} \approx \sqrt{\frac{4 \cdot k_B \cdot T \cdot (w_S - w_D)^2 \cdot \sqrt{m_S}}{k_S^{3/2} \cdot Q_S \cdot x_D^2 \cdot (0.01745)^2 \cdot A_g^2}} [=] \frac{(\text{deg/sec})}{\sqrt{Hz}} \qquad (2.81)$$

where the angular gain, A$_g$, defines the constant ratio of m$_{PM}$/m$_S$. The above equation states that, increasing the drive-mode vibration amplitude, x$_D$, also reduce the mechanical-noise-equivalent rate.

When the gyroscope is operated with closely matched drive and sense mode resonance frequencies, i.e., f≈f$_S$, Equation 2.79 simplifies to

$$|Y_S| = \sqrt{\frac{4 \cdot k_B \cdot T \cdot Q_S}{\omega_S \cdot k_S}} \qquad (2.82)$$

which states that the noise displacements increase by increasing the mechanical quality factor, in contrary to the result of Equation 2.80. However, the noise equivalent rate of the gyroscope for the matched operation found by dividing Equation 2.82 by Equation 2.19 in response to a 1deg/sec rate input (again assuming m$_S$≈m$_{PM}$) yields,

90

$$\Omega_{n,matched} \approx \sqrt{\frac{k_B \cdot T}{Q_S \cdot \sqrt{k_S \cdot m_S} \cdot x_D{}^2 \cdot (0.01745)^2 \cdot A_g^2}} [=] \frac{(\text{deg/sec})}{\sqrt{Hz}} \qquad (2.83)$$

stating that the noise floor can be reduced by increasing the mechanical spring constant, the sense mode mass, the quality factor, and the drive-mode vibration amplitude. Note that, increasing both the mass and the spring constant does not primarily change the resonance frequency of the system, but a high spring constant would require large electrostatic actuation forces for generating the drive-mode vibrations. Regarding Equation 2.83 the mechanical noise floor is above $10(\text{deg/hr})/\text{Hz}^{1/2}$ for a micromachined gyroscope with a resonance frequency of 5kHz, quality factor of 1, spring constant of 200N/m, drive-mode vibration amplitude of 15μm, and an angular gain of 0.8. This value can be improved by two orders of magnitude if the sense-mode quality factor of the gyroscope reaches to 10000 at vacuum operation, which is typical for high-quality single-crystal silicon structural materials. Therefore, mechanical-thermal noise puts a serious limit to the overall rate sensitivity of micromachined vibratory gyroscopes operated at atmospheric pressure.

A final note about the mechanical-thermal noise is that the ratio of mechanical noise floor of the matched operation in Equation 2.83 to that of the mismatched one in Equation 2.81 yields,

$$\frac{\Omega_{n,matched}}{\Omega_{n,mismatched}} \approx \frac{\omega_S}{2 \cdot (\omega_S - \omega_D)} \qquad (2.84)$$

and remembering the conditions provided in Table 2.1 for mismatched operation results in the fact that,

$$\frac{\Omega_{n,matched}}{\Omega_{n,mismatched}} \approx \frac{Q_S}{10} \qquad (2.85)$$

which states that the performance of the matched operation to the mismatched operation is directly proportional to the mechanical quality factor of the sense mode, for mechanical-noise-limited micromachined vibratory gyroscopes. This result clarifies the reason behind fabricating micromachined gyroscopes using low-damping structural materials with high quality factors and operating the gyroscopes at vacuum.

Electronic noise is another important parameter that limits the overall performance of the micromachined gyroscopes, which is also briefly discussed in Chapter 4 presenting the capacitive interface circuit.

2.5 Simulations and Verification of the Theoretical Analysis

The design of the symmetrical and decoupled micromachined vibratory gyroscopes is based on the theory discussed early in this chapter. However, the approximations, assumptions, and linearizations in the theory for simplifying the preliminary analysis usually introduce errors. It is a good practice to estimate these errors and verify the theoretical analysis by a series of simulations, including finite-element analysis, analytical simulations, and system-level simulations. The approach taken in this research is to perform finite-element analysis for estimating the errors in determining the model parameters initially. The corrected parameters are then fed to the analytical and higher-order system-level models generated for the gyroscopes designed in this research.

2.5.1 Finite-Element Simulations

Finite-element analysis (FEA) is a powerful technique for analyzing the behavior of mechanical, electrical, and fluidic systems. On the other hand, the computational power required for FEA limits its use for analyzing the overall behavior of complex nonlinear systems, such as the micromachined vibratory gyroscopes. Therefore, the method is used for simulating particular nonlinearities associated with separate parts

of the overall nonlinear system, under the assumption that there is minimal interaction between separately simulated parts. The software used for FEA is CoventorWare as it is specifically designed for MEMS applications and its results closely agree with the measurements. FEA simulations performed during the design of symmetrical and decoupled micromachined gyroscopes are the modal frequency and mode shape analyses, extraction of spring constant and its nonlinearity, extraction of electrostatic fringe-field correction factors for the electrode capacitances, rough estimation of the damping factor, quadrature motion, and the double-frequency motion.

2.5.1.1 Modal Frequency and Mode Shape Simulations

Modal analysis is used to identify the resonance frequencies of the drive and the sense modes of the gyroscope, as well as the mode shapes and frequencies of the higher-order modes. Figure 2.15 shows a sample mode shape simulation for the drive and the sense modes of the original symmetrical and decoupled micromachined gyroscope structure shown in Figure 1.14, developed for the silicon-on-insulator (SOI) micromachining process.

Higher order mode shapes are also simulated for the designed gyroscope structures. Figure 2.16 shows another sample modal simulation performed for the same gyroscope structure. Higher-order modes may result in spurious vibrations, increasing the mechanical crosstalk between the drive and sense modes, if their frequencies are close to the frequencies of the drive and the sense modes of the gyroscope.

Table 2.4 shows the simulated resonance frequencies for the drive and the sense modes of the gyroscope, as well as for the higher order modes. Note that, the resonance frequency of the sense mode would be tuned down using electrostatic springs, during the operation of the gyroscope.

93
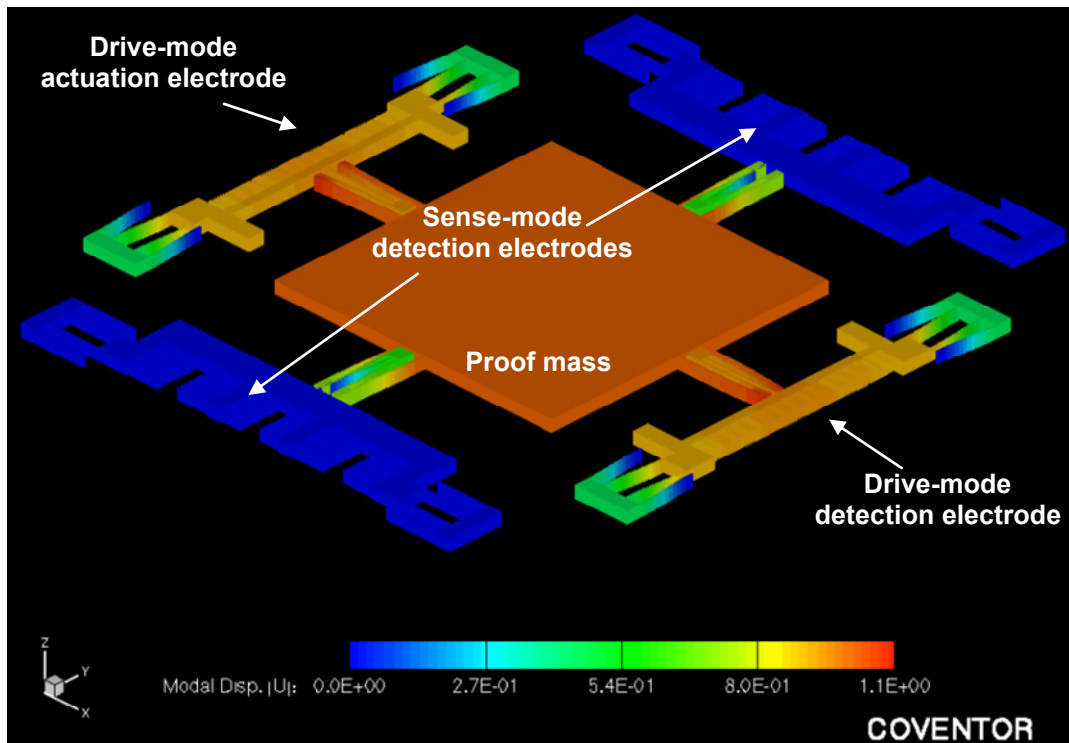
(a)
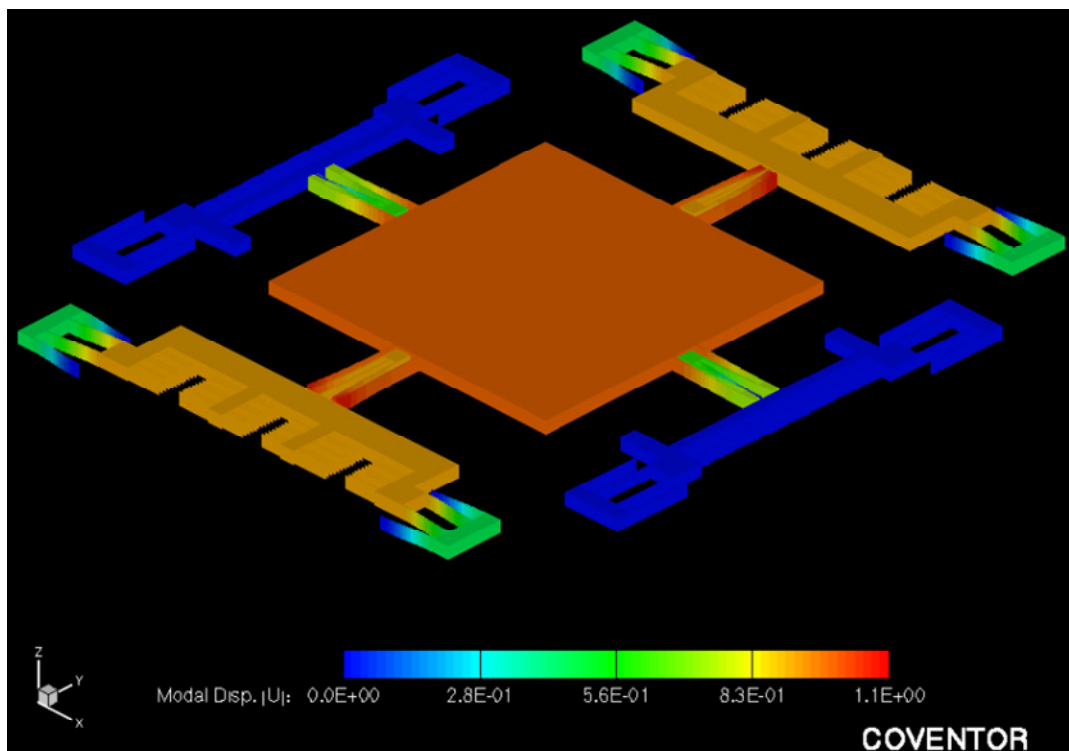
(b)

Figure 2.15: Sample mode shape simulation for (a) the drive and (b) the sense modes of the improved symmetrical and decoupled micromachined gyroscope, developed for the silicon-on-insulator (SOI) micromachining process.
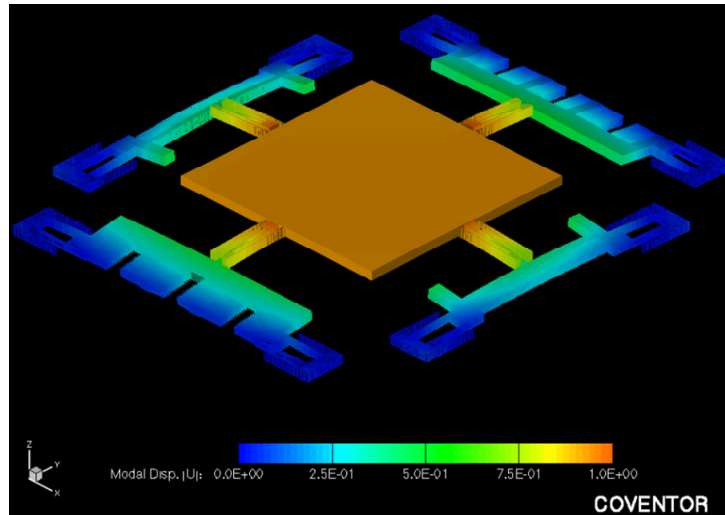
(a)
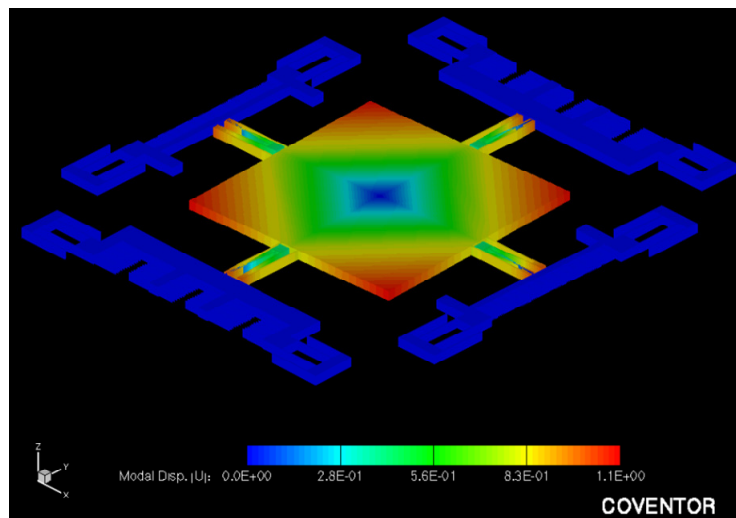
(b)
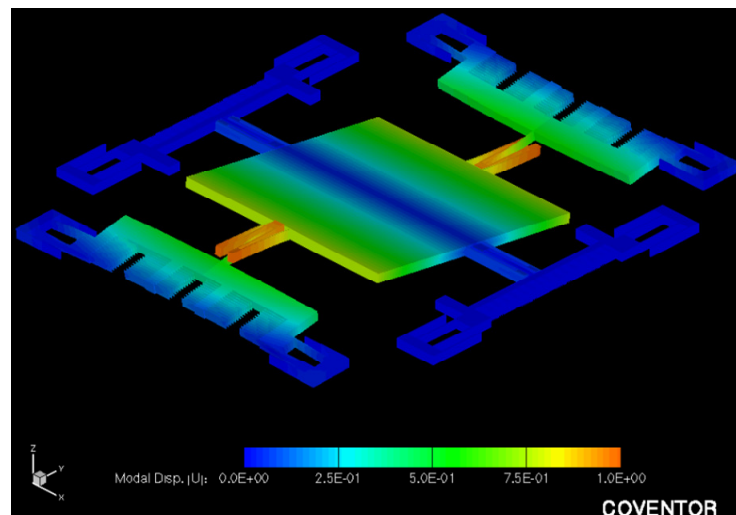
(c)

Figure 2.16: Higher-order mode shapes for the improved SOI symmetrical and decoupled microgyroscope. (a) Out-of-plane mode. (b) Rotary mode. (c) Rocking mode.

95

Table 2.4: The simulated resonance frequencies for the drive and the sense modes of the gyroscope, as well as for the higher order modes.

Mode	Generalized Mass (kg)	Resonance Frequency (Hz)
Drive	6.87×10^{-8}	8,951
Sense	7.81×10^{-8}	9,482
Out-of-plane	5.31×10^{-8}	9,833
Rotary	2.57×10^{-8}	10,776
Rocking	1.53×10^{-8}	15,225

2.5.1.2 Spring Constant Simulations

The force-deflection characteristics of the flexures used for the gyroscopes designed in this research are somewhat more complicated than the simplified expressions derived in Section 2.2.1. It is also possible to find the force-deflection expressions of simple beams in several mechanical engineering handbooks, for various support conditions. However, there is still a need for a detailed FEA analysis for determining the validity of these expressions, especially for large deflections that is necessary for increasing the sensitivity of micromachined vibratory gyroscopes. In addition, the bending stress and the effect of residual material stress on the deflecting flexure structures are considered during the design. Figure 2.17 shows the simulated force-deflection characteristics for a clamped-guided beam structure, used in the original symmetrical and decoupled gyroscope. Simulation shows that the vibration amplitude of the gyroscope must not exceed 2.5μm, in order to keep the spring nonlinearity smaller than 10%.

Table 2.5 presents the results of the spring constant simulations performed for beam lengths ranging from 100μm to 300μm, beam widths ranging from 3μm to 5μm, and beam heights ranging from 6μm to 12μm. The results show that the largest possible deflection range is below 3μm, for nonlinearity to be smaller than 10%. In addition, the simulations show that the bending stresses induced in the clamped-guided beam structure may exceed several hundred MPa even for small deflections, approaching to the yield limit of metal structural materials and brittle limit of silicon. The structure of the clamped-guided beam does not allow relieving the stress induced in it, which also makes it susceptible to the residual stress inside the structural material.

It is possible to get rid of the limitations of the clamped-guided beam structure, by using dual or triple folded beams discussed in Section 2.2.1.
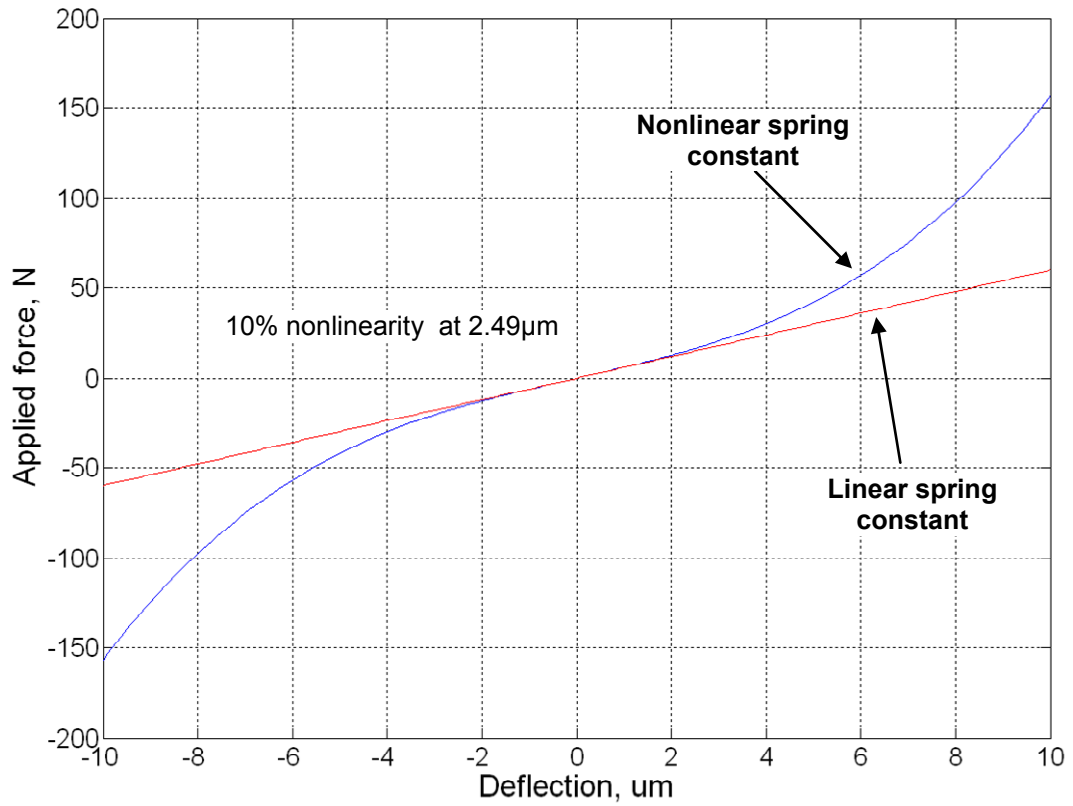
Figure 2.17: The simulated force-deflection characteristics for a clamped-guided beam structure, used in the original symmetrical and decoupled gyroscope.

Table 2.5: The results of the spring constant simulations performed for beam lengths ranging from 100μm to 300μm, beam widths ranging from 3μm to 5μm, and beam heights ranging from 6μm to 12μm.

Height (μm)	Length (μm)	Width (μm)	Analytical Result	Simulated Result	10% nonlinearity
6	100	3	28.26x	$29.29x + 1.45x^3$	1.42μm
		4	59.52x	$60.49x + 2.00x^3$	1.74μm
		5	109.5x	$110.03x + 2.55x^3$	2.08μm
	200	3	6.23x	$5.04x + 0.184x^3$	1.65μm
		4	11.04x	$9.45x + 0.255x^3$	1.93μm
		5	18.19x	$16.01x + 0.32x^3$	2.23μm
	300	5	7.61x	$5.99x + 0.097x^3$	2.49μm
12	100	3	56.52x	$59.05x + 2.92x^3$	1.42μm
	200	5	36.38x	$32.44x + 0.653x^3$	2.22μm
	300	7	31.02x	$26.59x + 0.279x^3$	3.08μm

Figure 2.18 shows the simulated force-deflection characteristics for the dual folded beam structure, having a length of 200μm, width of 5μm, and height of 12μm, used in some of the improved symmetrical and decoupled gyroscopes in this study. Clearly, the nonlinearity predicted by CoventorWare for the folded beam is much smaller compared to that of clamped-guided beam. This is basically due to the stress relieving capability of the folded beam structure. In addition, the simulated and the predicted spring constants agree well, provided that the truss of the folded beam is much stiffer compared to the stiffness of individual beams. The nonlinearity introduced in the force-deflection characteristics of the folded beam is smaller than 5% for deflections up to 20μm. It is also simulated that the residual stress of the structural material has no significant effect on the spring constant.
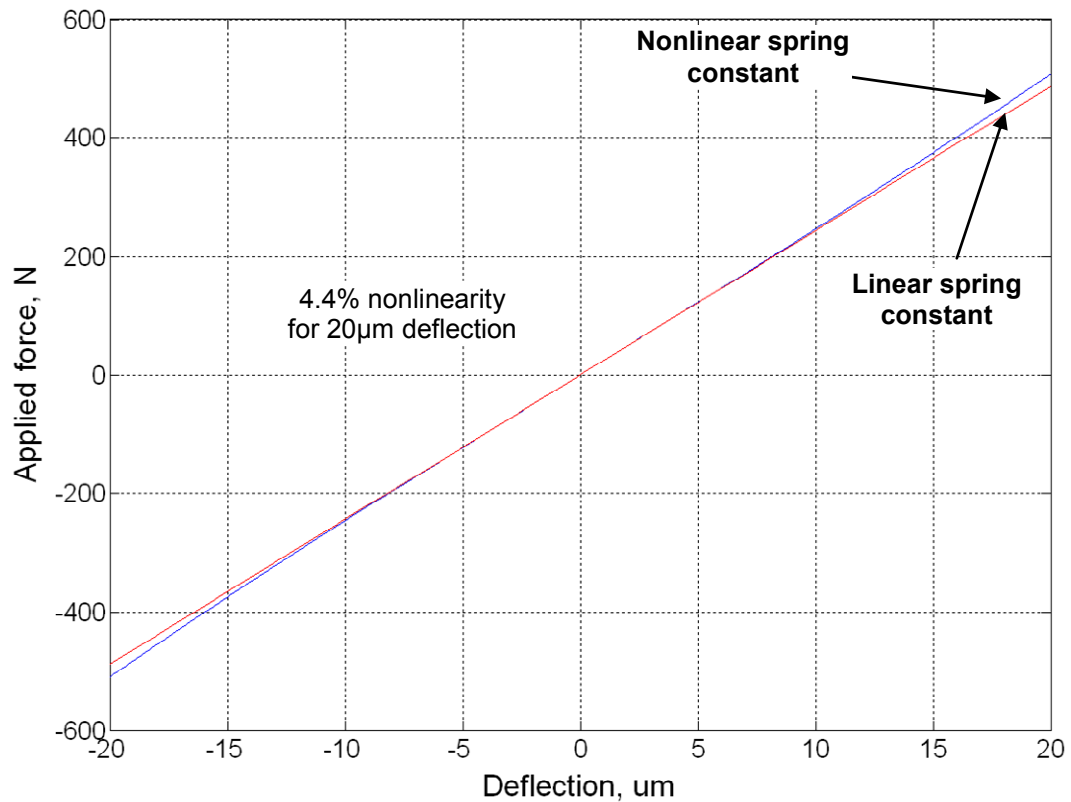
Figure 2.18: The simulated force-deflection characteristics for the dual folded beam structure, having a length of 200μm, width of 5μm, and height of 12μm, used in some of the improved symmetrical and decoupled gyroscopes in this study.

2.5.1.3 Electrostatic Field Simulations

Approximate estimation of the electrode capacitance using standard expressions derived for the parallel-plate capacitors ignore the effects of electrostatic fringe-fields. However, this approximation may result in significant errors, as high as 40% for typical interdigitated comb finger arrays used for the drive and the sense electrodes of the gyroscopes developed in this research. For this reason, the effects of these fringing electrostatic fields are simulated using CoventorWare FEA tool. Figure 2.19 presents the result of field simulations showing the distribution of electrostatic charges on a fractional part of a typical drive-mode actuation/sensing capacitor array used in symmetrical and decoupled gyroscope structures.
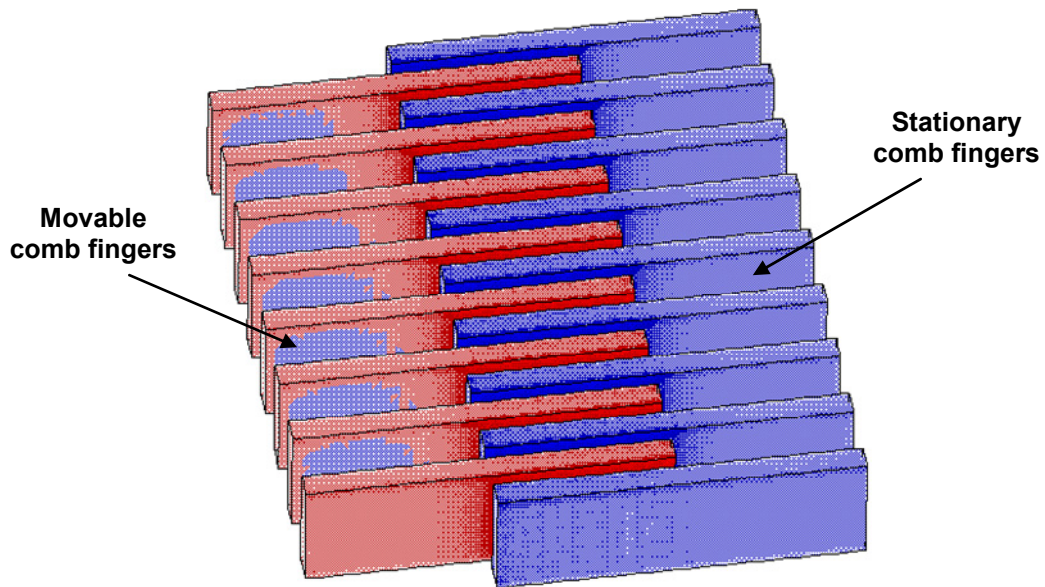
Figure 2.19: The result of field simulations showing the distribution of electrostatic charges on a fractional part of a typical drive-mode actuation/sensing capacitor array used in symmetrical and decoupled gyroscope structures.

In general, the effect of fringing electrostatic fields on the total capacitance of the comb electrode can be taken into account by using a constant correction parameter. Once this correction factor is extracted through the electrostatic field simulations, it can be used to closely estimate the physical capacitances of the interdigitated comb electrodes of the gyroscopes. However, it is necessary to model the electrode array correctly in the simulations; otherwise the extracted correction factor could be different from the measured values. For example, the correction factor of a single

rotor comb surrounded by two stator combs would be highly different from the overall correction factor of an array of interdigitated rotor and stator combs, due to electrostatic field distributions. On the other hand, simulation of the complete comb finger array with tens of comb fingers require very long computation times, making the simulation inefficient for extracting the correction factors for many different electrode geometries. Therefore, a two-step FEA is performed to extract the exact correction factor for an array of comb fingers. Figure 2.20 illustrates the proposed method. In the first step, the capacitance from a single rotor surrounded by two stator combs is simulated. In the second step, the capacitance of an array of interdigitated combs is simulated. Averaging the results of these simulations with proper weight-factors yields accurate extraction of the correction-factors for the fringing electrostatic fields. Table 2.6 shows a sample set of simulation results performed for extracting the correction factor for the drive-mode actuation electrode.

(a)

(b)
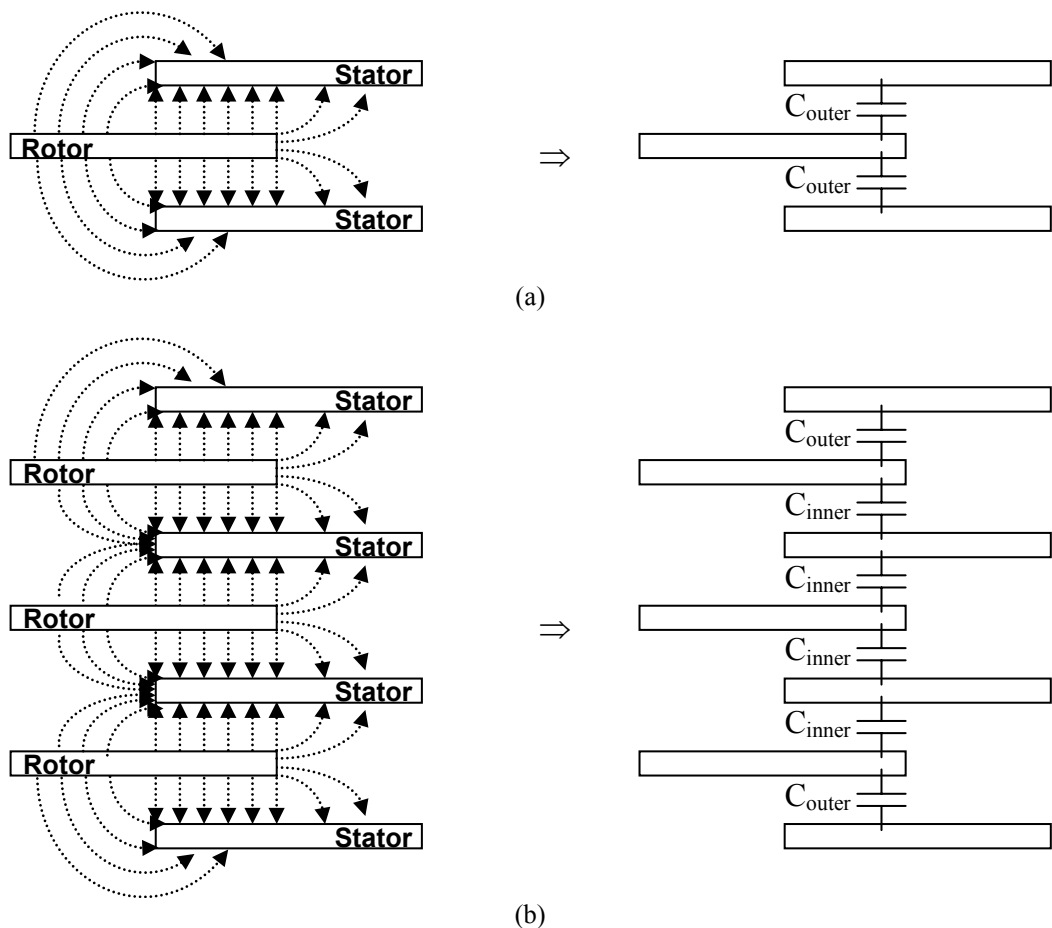
Figure 2.20: Two-step simulation of the electrostatic fringe-field correction factor for a comb capacitor array. (a) First, the correction factor is extracted for C_{outer}. (b) Second, the correction factor is extracted for C_{inner}. The results are then applied to the larger comb arrays, which require very long computational times during FEA otherwise.

100

Table 2.6: Sample set of simulation results performed for extracting the correction factor for the drive-mode actuation electrode.

Length (μm)	Width (μm)	Overlap (μm)	Height (μm)	Gap (μm)	C_{outer} (fF)	C_{inner} (fF)	$C_{analytical}$ (fF)
40	3	20	12	1.5	4.49	3.93	2.83
				0.5	10.51	10.00	8.49
			6	1.5	2.67	2.32	1.42
				0.5	5.79	5.40	4.25
		5		1.5	1.38	0.92	0.35
				0.5	2.25	1.76	1.05
			12	1.5	2.12	1.51	0.70
				0.5	3.83	3.16	2.10
	5			1.5	2.30	-	0.70
				0.5	3.98	-	2.10

Similar method is used for extracting the capacitance gradient with respect to displacement, $\partial C/\partial x$. The correction factors extracted for the capacitance gradients are smaller than the ones found for the capacitance values. This is an expected result, since a large fraction of the fringing electrostatic fields does not vary with displacement especially for the varying-overlap-area type comb finger arrays. Typically, the correction factors for the parameter $\partial C/\partial x$ lie in the range of 1.05-1.1, whereas the correction factors for the capacitance reach to 1.4.

2.5.1.4 Simulations of Damping Factor, Quadrature Motion, and Double-Frequency Motion

Damping factors are also simulated for the designed microgyroscopes, using a particular module of CoventorWare developed for damping analysis. The model for damping simulation is generated by defining a fluid material in the gap between two frames moving relative to each other. The predicted results for viscous air damping are found to be in 20% error with the simulated values for the separate components of the gyroscope, such as the proof mass, comb electrode array, etc. Though it is possible to simulate the damping factor for the overall gyroscope structure, this takes quite a long simulation times, extending to several days. In addition, the damping simulations are limited to viscous fluid damping only, and cannot be used for estimating the gyroscope performance at vacuum. Therefore, only a limited number of damping simulations are performed with CoventorWare. The damping factors are

required for constructing the feedback electronics with an accurate model of the gyroscope, and the simulation results are observed to be insufficient in predicting the actual damping factors. In conclusion, the damping factors of the gyroscopes are extracted during the preliminary tests after fabrication.

The effect of manufacturing variations on the quadrature error is also partially analyzed by FEA. Figure 2.21 shows the simulated behavior of the improved symmetrical and decoupled gyroscope in response to a 0.05° clockwise rotation of the drive-mode vibration axis. The displacement along the sense mode in response to such a disturbance is simulated to generate a common-mode displacement smaller than 0.2% of the drive-mode vibration amplitude. Theoretically, this common-mode signal should correspond to a zero-rate-output smaller than 100deg/sec, provided that there are no higher-order modes with frequencies close to that of the drive-mode. Still, this simulation gives an idea about the approximate quadrature error in response to a known rotation of the drive axis.
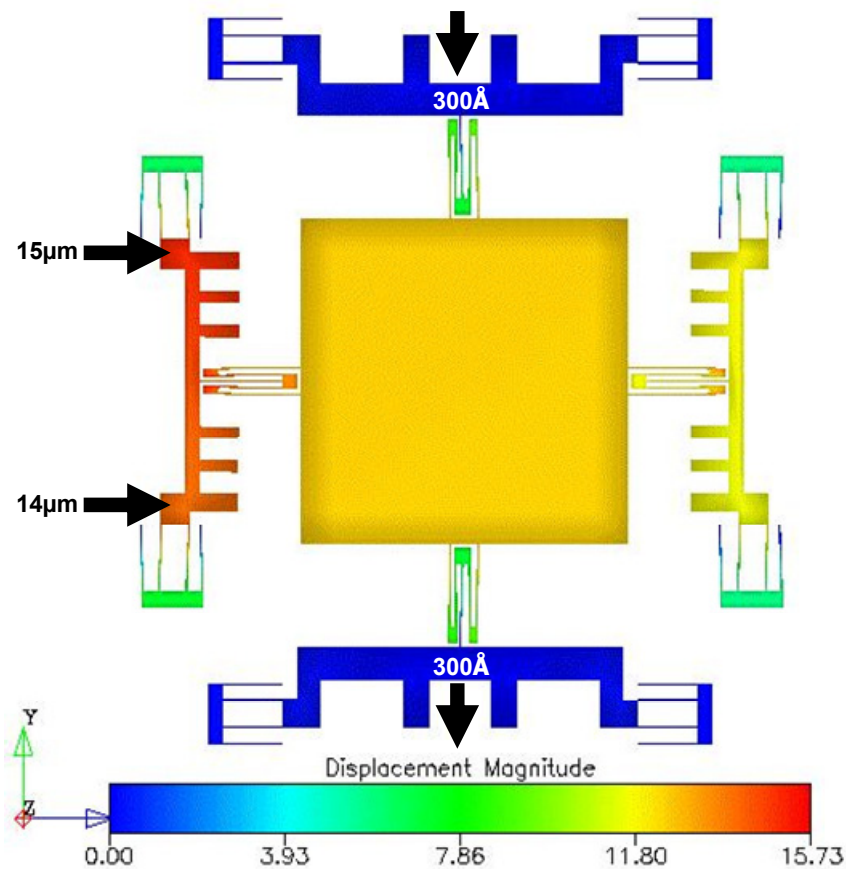
Figure 2.21: Simulated behavior of the improved symmetrical and decoupled gyroscope in response to a 0.05° clockwise rotation of the drive-mode vibration axis.

Finally, Figure 2.22 shows the simulated amplitude for the differential double-frequency displacement along the sense-mode, in response to 15µm drive-mode oscillation amplitude. The simulated displacement of each sense electrode is only 0.14µm, having a frequency twice that of the drive-mode oscillation frequency, which would be suppressed during phase-sensitive detection of the output signal. As discussed earlier in this chapter, this differential displacement would result in a common-mode capacitance change, which would be further suppressed by the readout electronics if a differential preamplifier stage is employed.
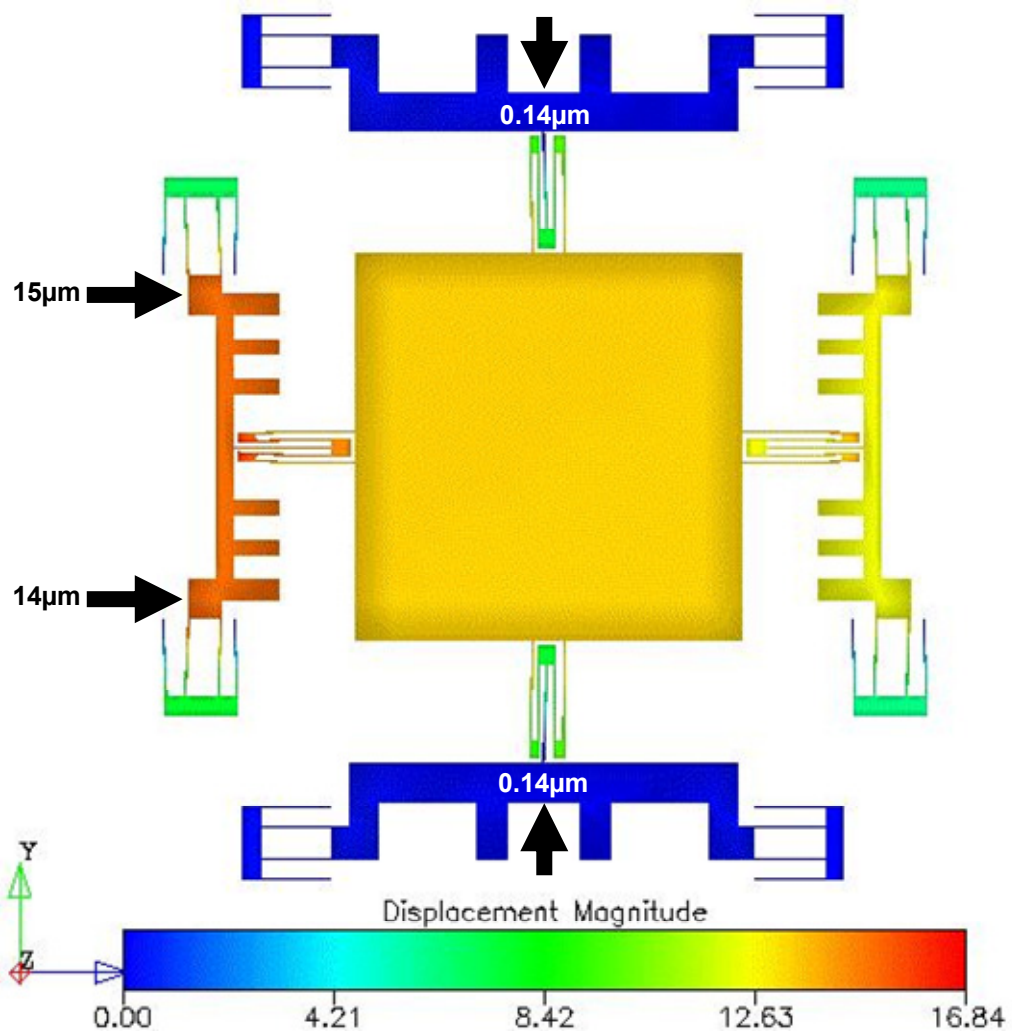
Figure 2.22: Simulated amplitude for the differential double-frequency displacement along the sense-mode, in response to 15µm drive-mode oscillation amplitude.

2.5.2 Analytical Simulations

Finite element simulations presented in the previous section are not sufficient to verify the electromechanical behavior of the gyroscope. Rather, they give an idea about the possible non-ideal behavior of certain mechanical or electrical components of the gyroscope, and help verifying the theory behind designing the gyroscope. After gathering information about these non-idealities, it is possible to proceed with a more complete electromechanical model of the sensor. This model is constructed based on the theoretical background presented in this Chapter, while the simulations performed using finite element method supply complementary parameters for the non-idealities in the electromechanical sensor element. A simulator software is developed for this purpose throughout this research, in order to estimate a number of performance parameters of the designed symmetrical and decoupled gyroscopes. Figure 2.23 shows the sample user interfaces of the developed analytical simulator software. The MATLAB-based code allows the user to input several geometrical and electrical data associated with a selected gyroscope type, and then simulates the mechanical and electrical model parameters associated with the selected gyroscope and the fabrication process. The preliminary results window shown in Figure 2.23b allows the user input values of some of the missing model parameters such as the nonlinear spring constant or electrostatic fringe-field correction factor, from the results obtained from FEA. Figure 2.24 shows the results window, that generate the amplitude of vibrations in response to electrostatic actuation, electrical admittance of the gyroscope for analyzing electrical feed-through characteristics, the currents generated at the drive-mode resonator output and sense-mode output, estimation of the Coriolis force in response to an applied angular rate and the frequency mismatch between the modes, and the bandwidth of the gyroscope for time-varying angular rate inputs.

The analytical simulation software is evaluated for tens of gyroscope prototypes and proved to be a quick and efficient way for simulating the resonance behaviors and the rate-responses of the symmetrical and decoupled gyroscopes prior to fabrication. The results obtained from the analytical simulations are then fed to the behavioral model of the complete rate sensor system, constructed using SIMULINK.
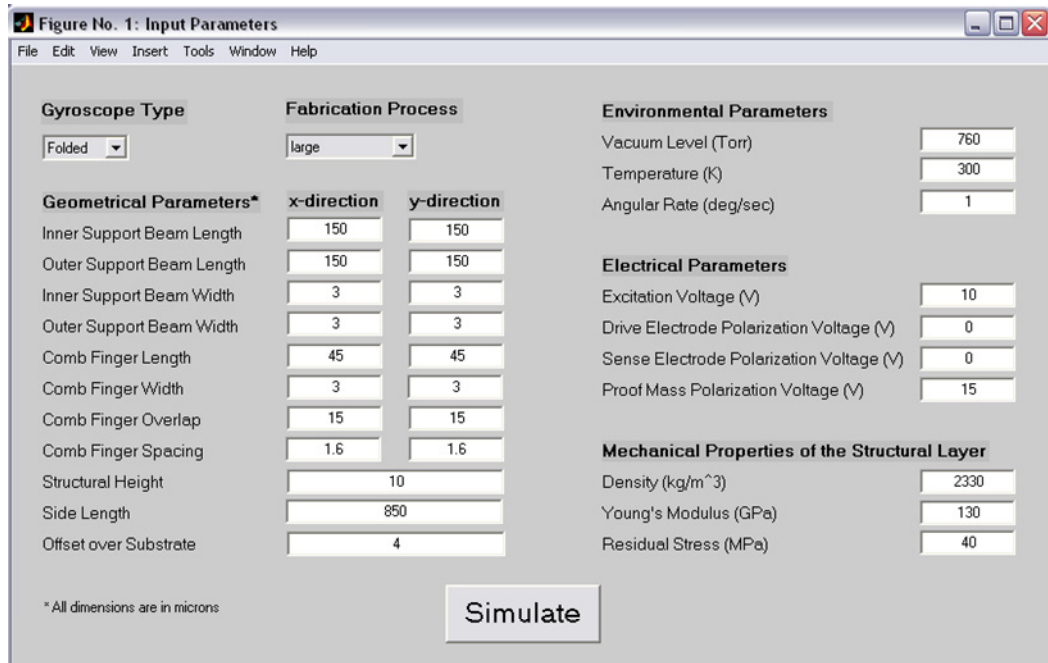
(a)
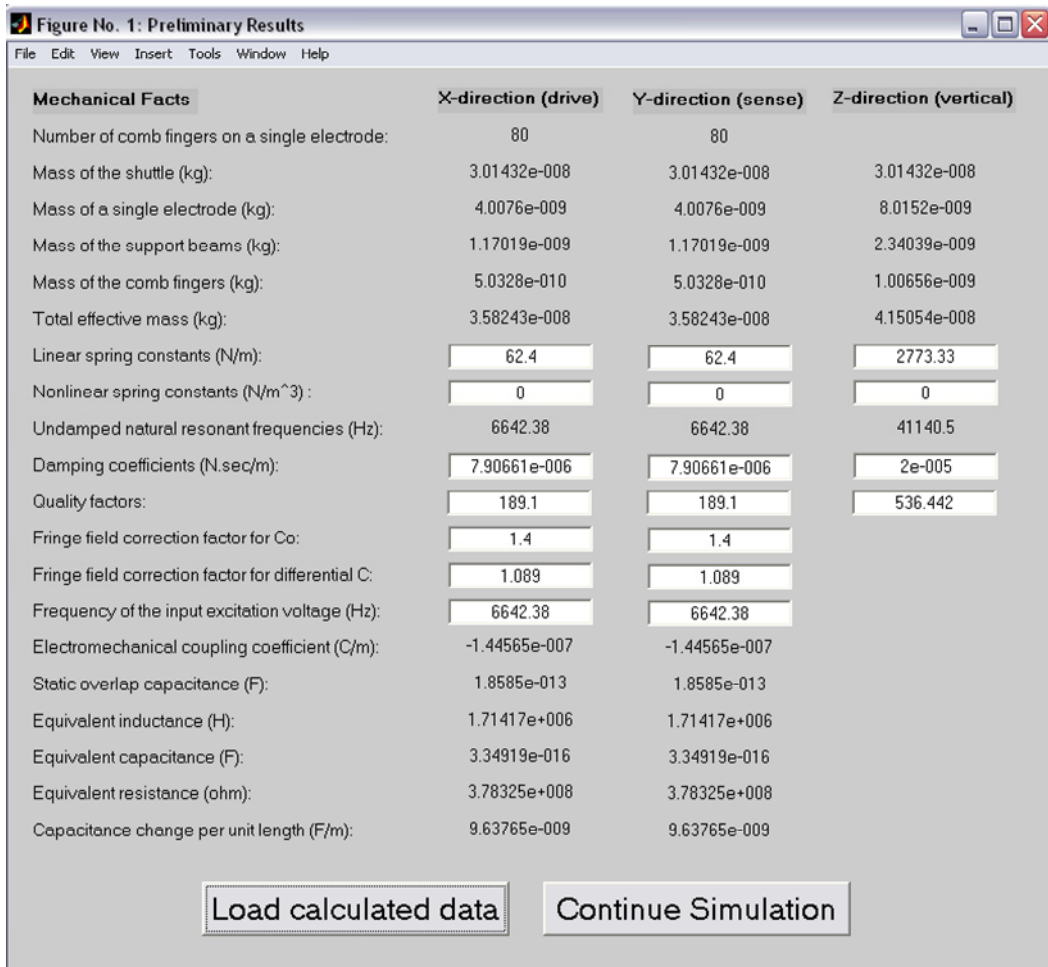
(b)

Figure 2.23: (a) Input and (b) preliminary results windows of the developed analytical simulator software.
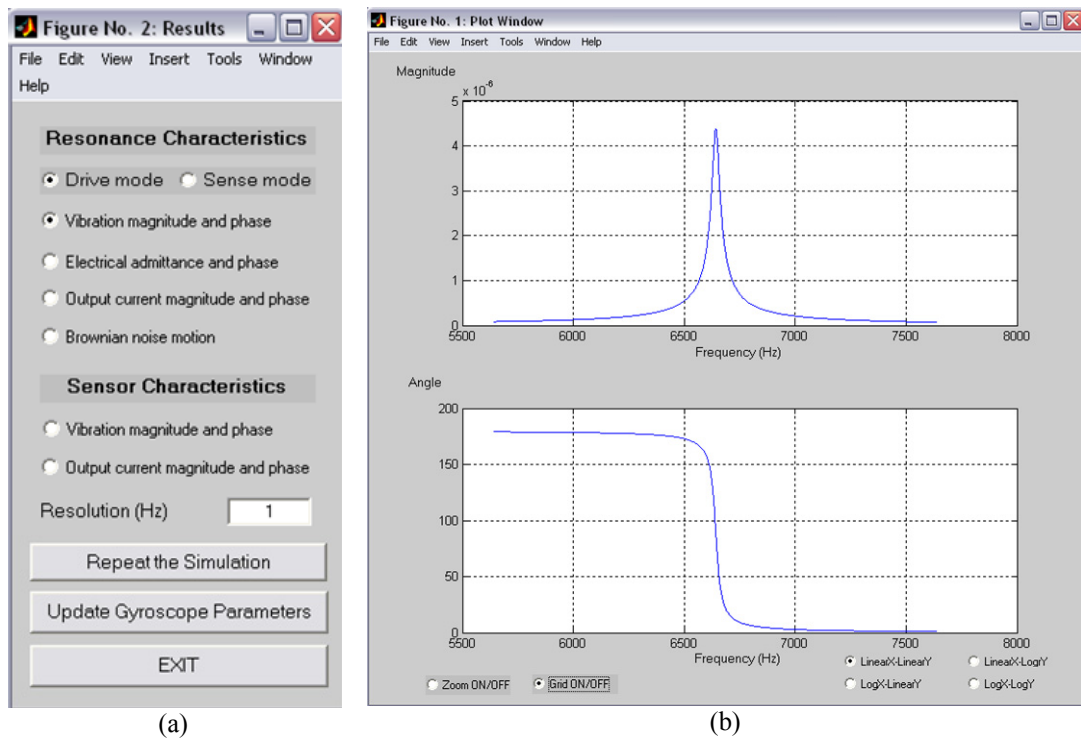
Figure 2.24: (a) Result selection and (b) output plot windows of the developed analytical simulator software.

2.5.3 System-Level Simulations

The behavior of the gyroscope predicted with the analytical simulation software of the previous section is based on the evaluation of the sensor model in the phasor domain. This method helps visualizing the gain-phase characteristics of the nonlinear second-order model developed for the symmetrical and decoupled gyroscope. However, the analytical model cannot predict the transient behavior of the system in time-domain. Therefore, a behavioral model simulator, SIMULINK, is used for predicting the real-time operation of the designed gyroscopes. The behavioral model includes the nonlinear effects such as spring hardening, air damping, electrostatic fringe fields, etc. for accurately modeling the transient behavior of the sensor system. Figure 2.25 shows the behavioral model generated for a symmetrical and decoupled micromachined gyroscope developed in this research for the dissolved wafer silicon micromachining process.
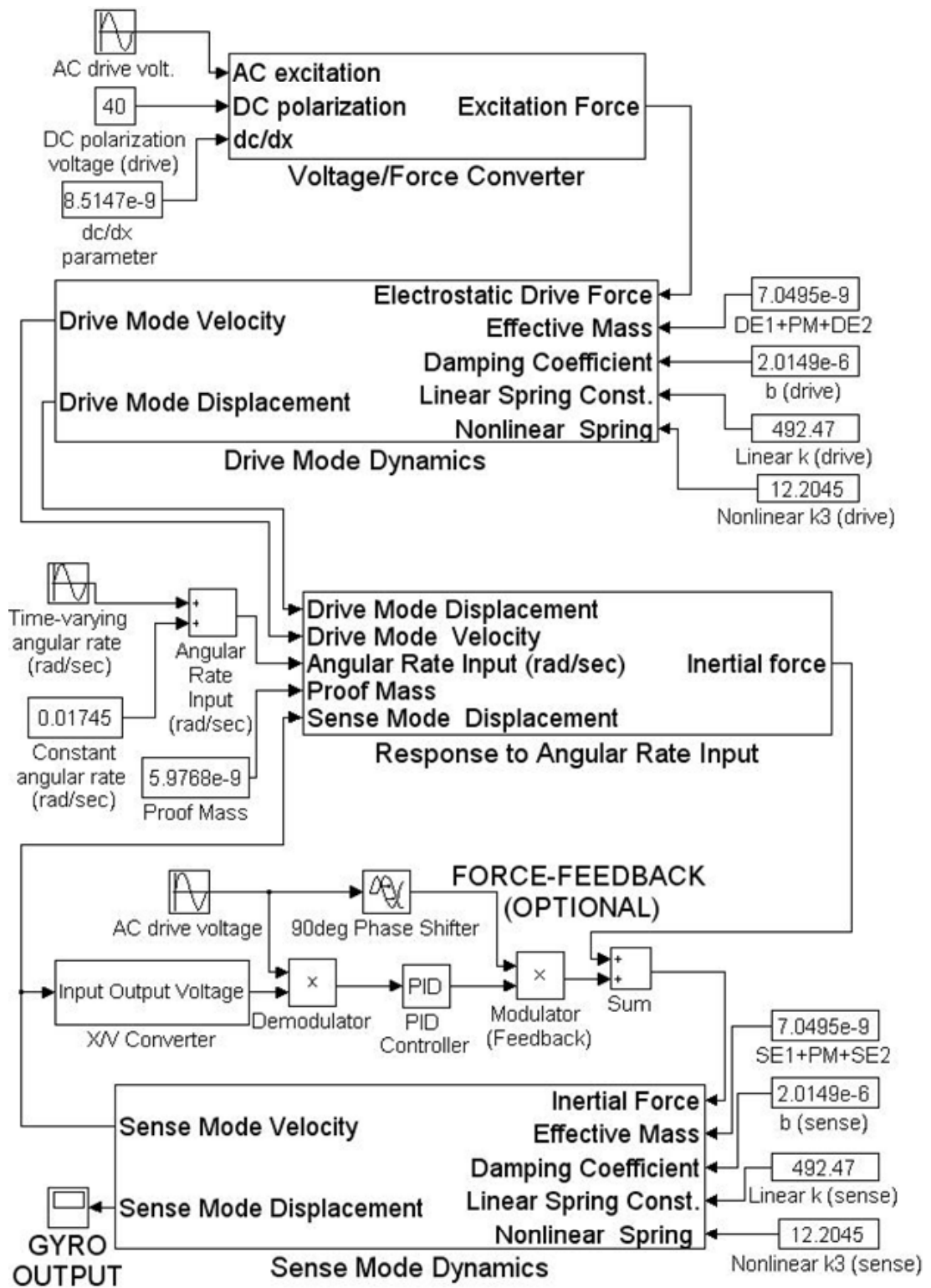
Figure 2.25: The behavioral model generated for a symmetrical and decoupled micromachined gyroscope developed in this research for the dissolved wafer silicon micromachining process.

Figure 2.26 shows the output displacement reached by the drive-mode resonator of an improved symmetrical and decoupled gyroscope developed for nickel electroplating process, simulated using a similar behavioral model. The gyroscope has a start-up period of 0.8sec, required for the drive-mode vibrations to stabilize their set value. The behavioral model of Figure 2.25 is also extended to simulate the closed-loop operation of the gyroscope, including the drive-mode self-resonance excitation and the sense-mode force-feedback. More detailed description of the extended model is provided in Chapter 6 together with the design of electronic control loops.
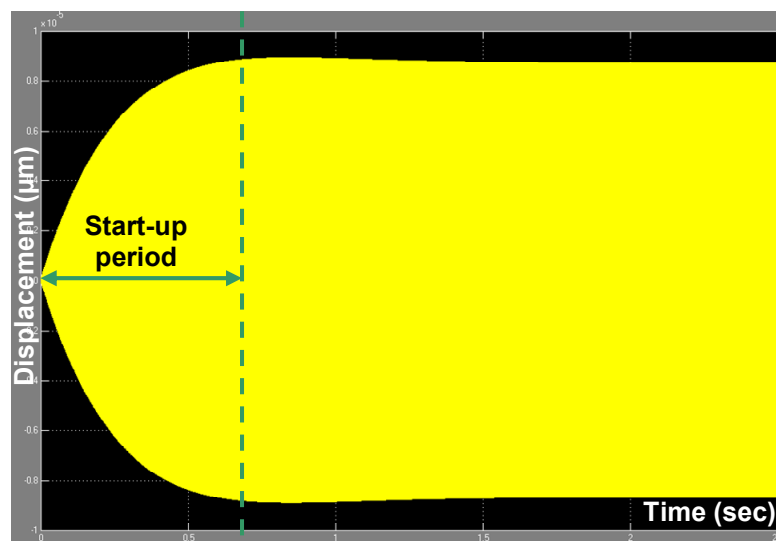
Figure 2.26: The output displacement reached by the drive-mode resonator of an improved symmetrical and decoupled gyroscope developed for nickel electroplating process, simulated using a similar behavioral model.

2.6 Summary

This chapter presented the theory behind the electromechanical design of micromachined vibratory gyroscopes. It described the Coriolis coupling mechanism for sensing angular rates applied to vibratory gyroscopes. Mechanical model of the decoupled vibratory gyroscope is generated from the dynamic equations the drive and sense modes of the proposed gyroscope structure. The effect of operating the gyroscope with or without matched drive and sense mode resonance frequencies is examined in detail. Secondly, the estimation of the mechanical model parameters,

the spring constant, mass, and the damping factor are described, for the structural geometries constructing the designed gyroscopes. Third, the idea behind electrostatic actuation used for actuating the drive-mode of the designed gyroscopes is explained in detail. Next, the electromechanical model of the symmetrical and decoupled gyroscope is constructed both for actuation and sensing ports, for which the capacitive sensing and sensor outputs are described in detail. The use of electrostatic springs in fine-tuning the resonance frequencies is also introduced. Following, the second-order effects, which are not predicted by the simplified theory, are investigated. Electrostatic levitation, side-instability for large drive-mode vibration amplitudes, mechanical quadrature signal, double-frequency signal at the sense electrodes, and mechanical-thermal noise are briefly examined. Finally, some of the finite-element, analytical, and system-level simulations performed during the design of symmetrical and decoupled micromachined vibratory gyroscopes are presented, for illustrating the design methods and verifying the theory discussed in this chapter.

CHAPTER 3

FABRICATION PROCESSES AND PROTOTYPES

This chapter presents the fabrication processes selected for the development of high-performance micromachined vibratory gyroscopes and the specific symmetrical and decoupled gyroscope prototypes designed for each of these processes. Several micromachining processes are selected for evaluation, commonly-used for the fabrication of inertial sensors and require only few mask steps for high yield production. Sections 3.1, 3.2, 3.3, and 3.4 present the details of the fabrication process and the specific gyroscope prototype fabricated with the given process, for dissolved wafer silicon micromachining (DWSM), nickel electroforming (NE), silicon-on-insulator (SOI) micromachining, and silicon-on-glass (SOG) micromachining, respectively. The problems encountered and the improvements achieved in each fabrication process as well as the technical information about the designed and fabricated symmetrical and decoupled gyroscope prototypes together with the specific features of each prototype are also presented separately in each section. Finally, Section 3.5 summarizes the chapter.

3.1 Dissolved Wafer Silicon Micromachining (DWSM)

Dissolved wafer silicon micromachining (DWSM) process is based on fabricating microstructures defined on a highly-doped silicon layer by using deep reactive ion etching (DRIE), silicon-glass anodic bonding, and wet etching of the undoped silicon wafer. The process allows the fabrication of the gyroscopes from a highly-doped silicon structural layer of thickness up to more than 10μm, a structural feature

110

aspect ratio of 10 or more, and an insulating substrate layer for reduced parasitic capacitances. Section 3.1.1 presents an overview of the DWSM process and Section 3.1.2 presents the gyroscope prototype fabricated with the DWSM process, together with the technical specifications in the sensor level.

3.1.1 DWSM Process Overview

The DWSM process requires separate micromachining of the silicon and glass substrates prior to anodically bonding them to each other, and then dissolving the undoped volume of the silicon substrate leaving the highly doped-silicon sensors on glass substrate [97]. The developed process requires only three masks, for pad metallization, anchor layer formation, and structural layer formation. Figure 3.1 illustrates the DWSM process flow. The process starts with deep boron diffusion on the polished surface of a standard (100)-oriented, 500µm-thick, 4-inch silicon substrate at a temperature of 1100°C for a period of 16hours, while protecting the backside of the wafer with thermally-grown silicon dioxide. The depth of the boron diffusion can reach to 12µm, forming a highly p^{++}-doped surface layer on the front-side of the silicon substrate. The front-side of the silicon substrate is then dry-etched to a depth of 20µm using DRIE. A patterned photoresist masking layer (Shipley S1813) is used as the etch-mask during DRIE. The mask pattern contains the structural details of the silicon gyroscopes, the beams, masses, comb electrodes, and anchor areas. After stripping the backside protection oxide layer, the silicon substrate is ready for anodic bonding to the glass substrate.

The glass substrate is machined separately prior to anodic bonding. A 300Å/3000Å-thick chromium/gold (Cr/Au) metal stack layer is evaporated on a 500µm-thick, 4-inch, Corning 7740 Pyrex glass substrate, and patterned using wet chemical etch in selective metal etchants, using the S1813 photoresist (PR) masking layer patterned with the anchor mask. The patterned Cr/Au/PR stack would act as a mask for the wet etching of the glass substrate. The glass substrate is then etched in a 7:3:10 volumetric mixture of hydrofluoric acid (HF), nitric acid (HNO_3), and de-ionized water, to a depth of 5µm. This wet etch step defines the anchor areas of

the gyroscope as well as the offset from the glass substrate to the movable structural silicon layer. Following the completion of glass etching, the Cr/Au/PR stack layer is stripped of the glass surface and a 100Å/1500Å Cr/Au layer is evaporated on the glass surface and patterned using lift-off. The metal layer is allowed to overlap a small fraction of the anchor regions, in order to get electrical contact from the silicon structural layer during anodic bonding of silicon and glass. The machined silicon and glass substrates are then cleaned for 30minutes in a 1:1 mixture of sulphuric acid (H_2SO_4) and hydrogen peroxide (H_2O_2) prior to anodic bonding. The machined surfaces of the substrates are aligned and anodically bonded to each other using EVG520 bonder, at a temperature of 400°C and a potential of 1000V applied between the silicon and glass substrates. The final step in the process is to dissolve the undoped silicon in ethylenediamine pyrocathecol (EDP) solution, until reaching the highly-doped structural silicon layer, at which the etch rate drops drastically. The gyroscopes are then cleaned with deionized water, rinsed in a standard acetone-isopropyl alcohol (IPA)-methanol bath, and dried on hotplate.
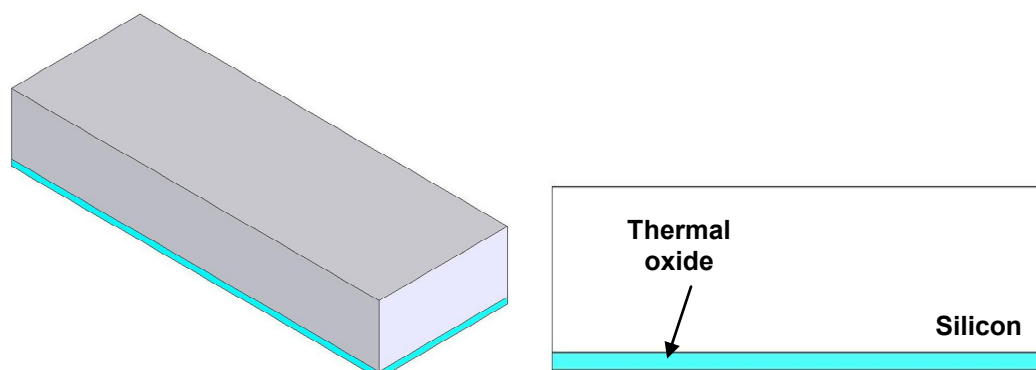
(a) Grow thermal oxide at the bottom surface of a blank silicon substrate.
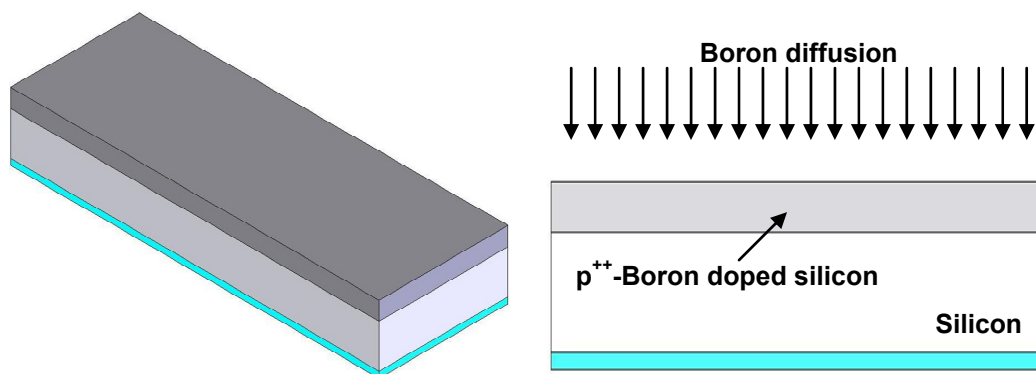
(b) Deep boron diffusion on the front-side, while protecting backside with thermal oxide.

Figure 3.1: Dissolved-wafer silicon micromachining process flow (cont. next page).
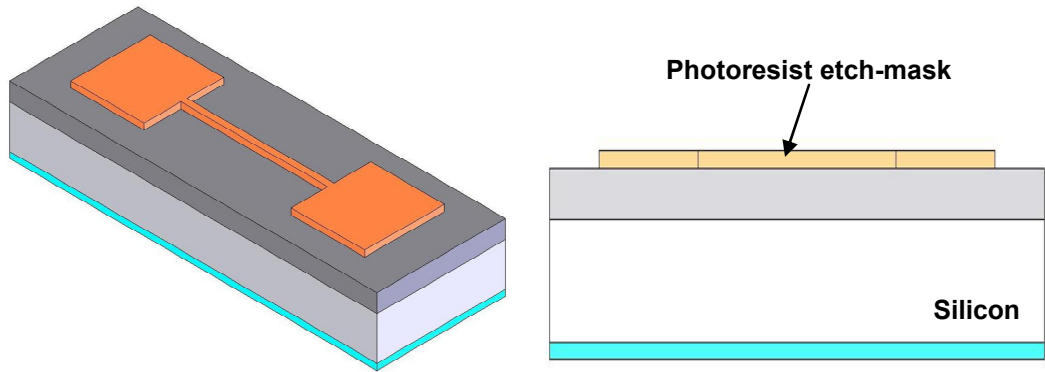
(c) Pattern a photoresist layer on top of silicon using structural layer mask
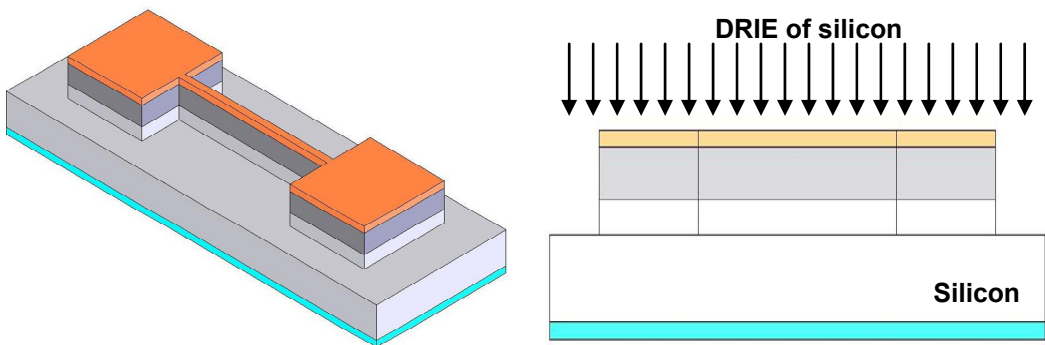
(d) DRIE of silicon to a depth larger than the Boron diffusion depth
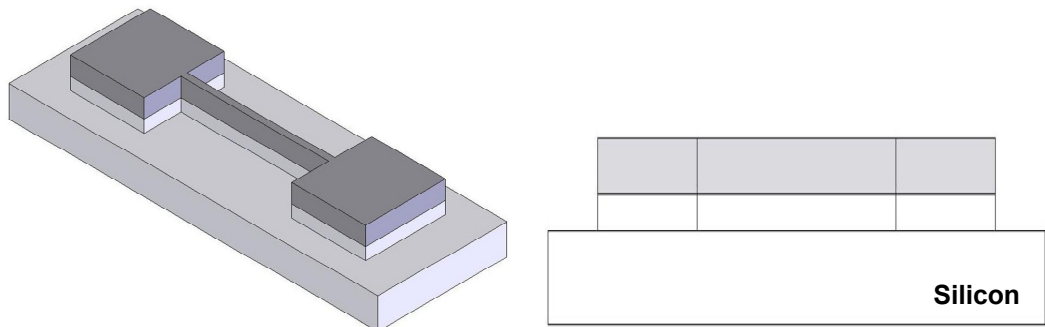
(e) Strip DRIE etch-mask and backside protection oxide
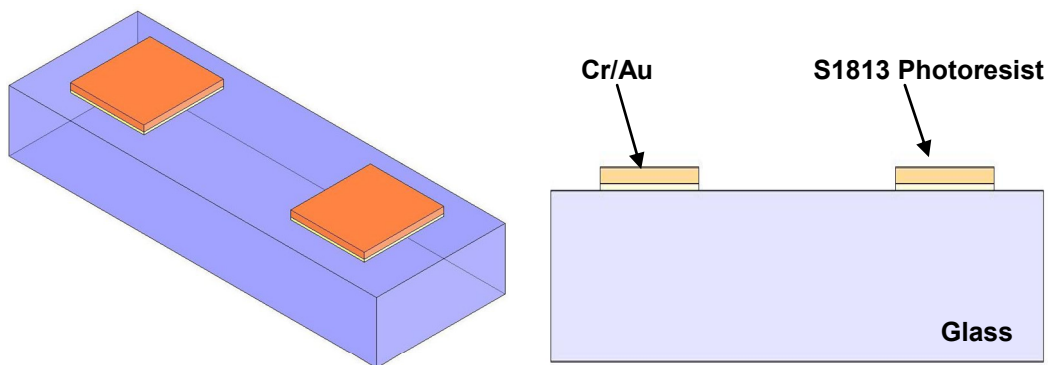
(f) Pattern Cr/Au/PR etch-mask for glass etching using anchor mask.

Figure 3.1: Dissolved-wafer silicon micromachining process flow (cont. next page).

113
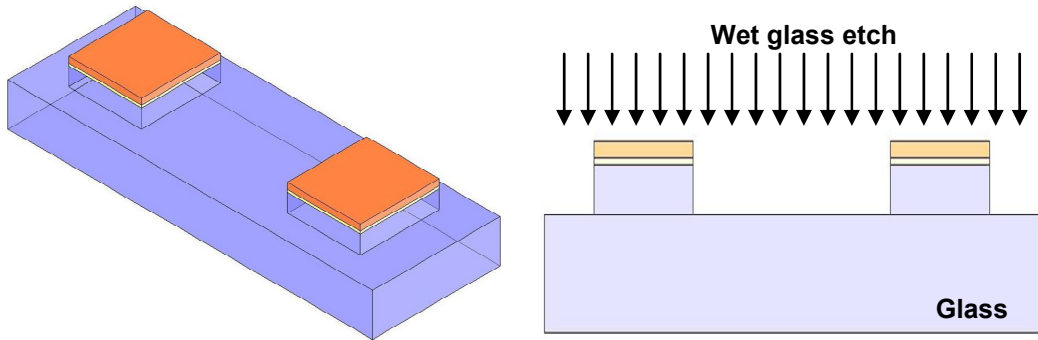
(g) Wet chemical etching of glass substrate forming the anchors
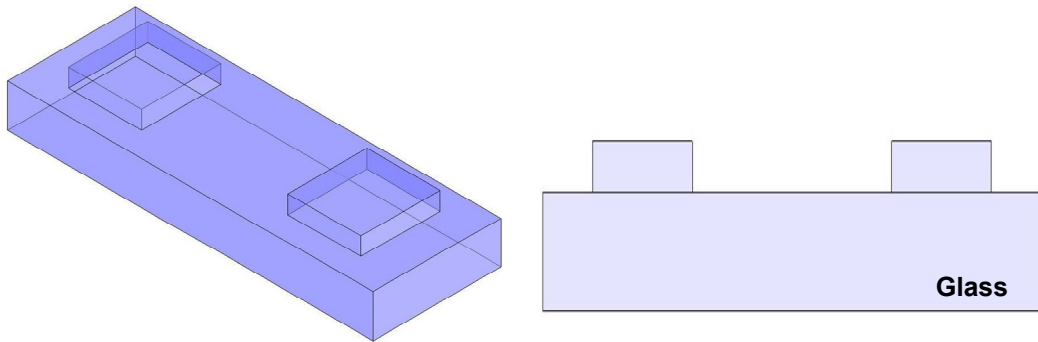
(h) Strip the etch-mask
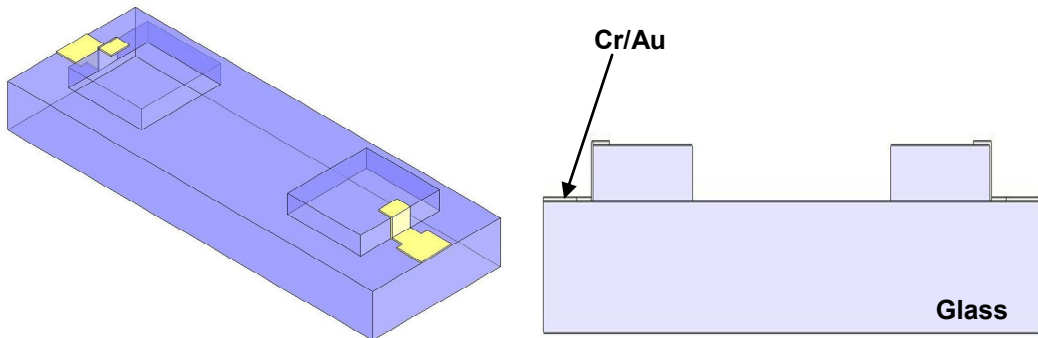
(i) Pattern Cr/Au pad metallization using lift-off
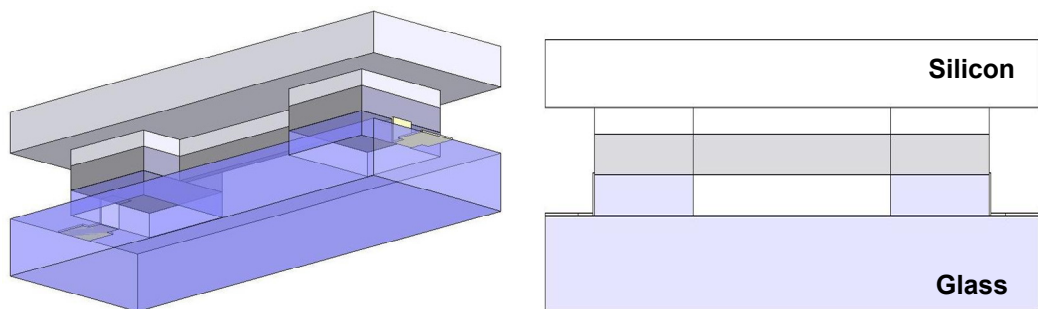
(j) Anodic bonding of machined silicon and glass

Figure 3.1: Dissolved-wafer silicon micromachining process flow (cont. next page).
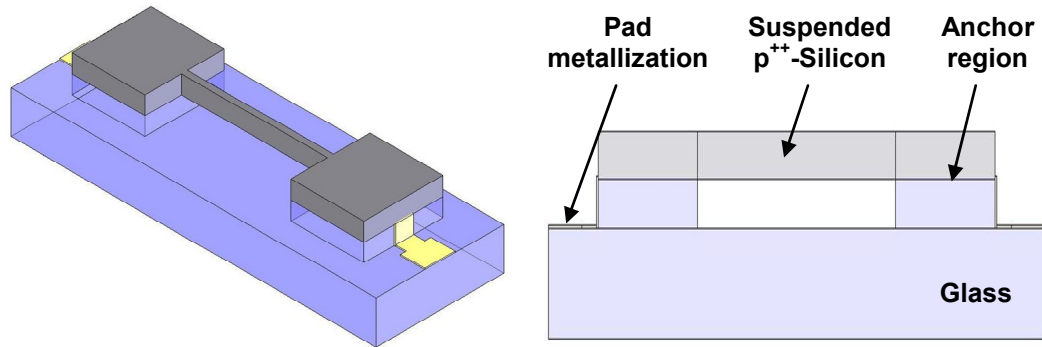
(k) Dissolve undoped silicon in EDP solution and release the structures

Figure 3.1: Dissolved-wafer silicon micromachining process flow. (The drawings are not to scale).

3.1.2 Silicon Angular Rate Sensor Prototype (ARS-DWSM)

The first prototype developed in this research is an original symmetrical and decoupled gyroscope, the structure of which is shown in Figure 1.13, fabricated with dissolved-wafer silicon micromachining process. The gyroscope employs varying-overlap-area type comb electrodes for both the drive and the sense modes, in order to keep the structure completely symmetric along both modes at the cost of reduced sensitivity along the sense-mode. The flexures along the drive and the sense modes are formed as clamped-guided type beams, which limit the vibration amplitudes of the sensor to less than 2µm for keeping the spring non-linearity below 5%.

The fabricated gyroscope prototype is labeled as ARS-DWSM, i.e., "**A**ngular **R**ate **S**ensor fabricated with **D**issolved **W**afer **S**ilicon **M**icromachining process".

Figure 3.2 shows the layout of the gyroscope, drawn in Cadence design environment. Table 3.1 provides the structural dimensions, the number of comb fingers, corresponding capacitance, and $\partial C/\partial x$ parameter for the original symmetric and decoupled gyroscope structure in Figure 3.2. Values for the electrode capacitances are estimated based on 12µm thick structural silicon layer. The gap spacing for the prototype is assumed to be 1µm during the design step, while the actual gap spacing after fabrication is measured to be 1.5µm, due to lithography and DRIE tolerances.
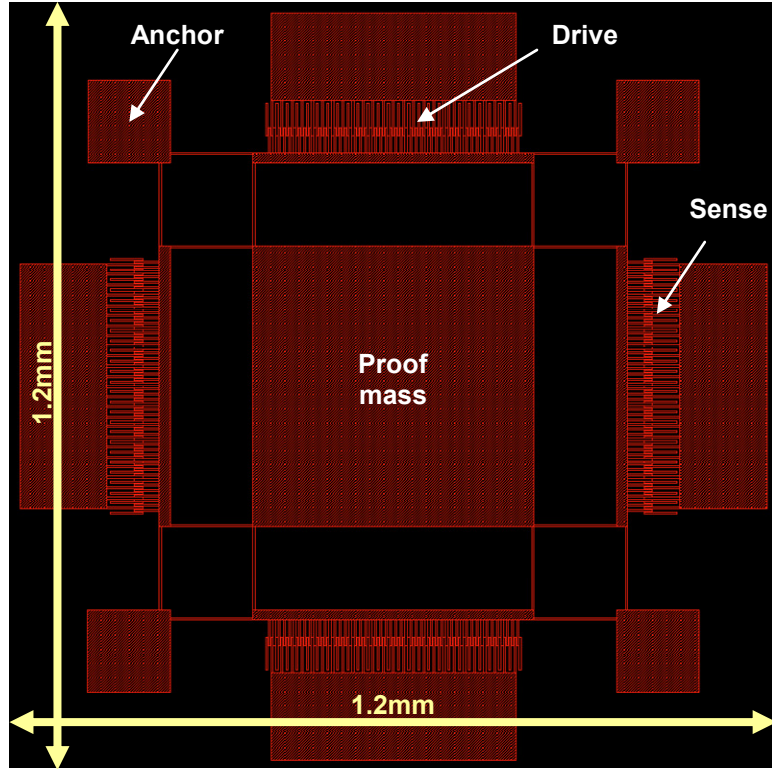
Figure 3.2: The layout of the designed ARS-DWSM symmetrical and decoupled gyroscope prototype.

Table 3.1: Structural dimensions and electrical parameters for the electrodes (including electrostatic fringe-field corrections)of the designed ARS-DWSM prototype.

Electrode	Parameter	Value
DRIVE and SENSE	# of combs	50 x 2
	Capacitance, (fF)	223 x 2
	$\partial C/\partial x$, (F/m)	$(1.17) \times 10^{-8}$ x 2
	$K_E = (\partial^2 C/\partial x^2) \times V^2$, (N/m)	0

The resonance frequencies of the drive and the sense modes are set to about 40kHz, in order to ensure that the resonance bandwidths of the drive and sense modes would be sufficiently large even for the high mechanical quality factors of the single-crystal silicon structural material. This is important since there is no chance for electrostatic tuning of the resonance frequencies for the ARS-DWSM gyroscope after fabrication, due to its varying-overlap-area type comb electrodes. Still, the resonance frequencies of both modes are expected to be close to each other, due to the inherent symmetry of the designed structure. Table 3.2 provides the design parameters for the ARS-NE gyroscope prototype. Young's modulus of 130GPa is used for (100)-oriented single-crystal silicon [98].

116

Table 3.2: The design parameters for the ARS-DWSM gyroscope prototype.

Parameter (Drive and Sense)	Value
M_{PM}, kg	$(6.99)\times10^{-9}$
M_E, kg	$(0.91)\times10^{-9}$
$M_{D\ Total}= M_{S\ Total}$, kg	$(8.81)\times10^{-9}$
K_{inner}, N/m	308
K_{outer}, N/m	308
K_{Total}, N/m	616
F, Hz	42,084

Figures 3.3 and 3.4 show the scanning electron microscope (SEM) photographs of the original symmetrical and decoupled gyroscope prototype fabricated using DWSM process. The gyroscope occupies an area of 1x1mm^2. The height of the structural layer of the gyroscope is measured as 12μm, whereas the electrostatic gap between the fabricated comb fingers is 1.5μm, slightly larger than the mask opening of 1μm due to mask undercut of the DRIE. The aspect ratio of the currently fabricated gyroscope is about 8, but can be increased further by reducing the DRIE mask undercut. The current aspect ratio allows the gyroscope sensor capacitances to be over 100fF. The flexures and the proof mass are suspended 5μm over the substrate reducing the slide-film air damping effects under the suspended structure, when operated at atmospheric pressure.

The major problem with the fabrication process is that the pad metallization layer, which is sandwiched between the silicon and glass surfaces during anodic bonding, reduces the strength of anodic bonds. This causes detachment of the silicon structural material from the glass substrate during long EDP-etch period, as the etchant enters between the silicon and glass surfaces. Therefore, the fabrication of the pad metallization step is ignored for the successful completion of the DWSM process, and the structures could be fabricated without any bonding pads. Electrical contacts to the silicon structures are then established by conductive epoxy applied to the anchors of each individual sensor prior to testing, as described in Chapter 5. The problem encountered during EDP-etch can be solved either by modifying the mask layout in such a way that the EDP solution should only be in contact with the undoped silicon during the long etch, or by reducing the thickness of the silicon substrate for reducing the EDP-etch period.
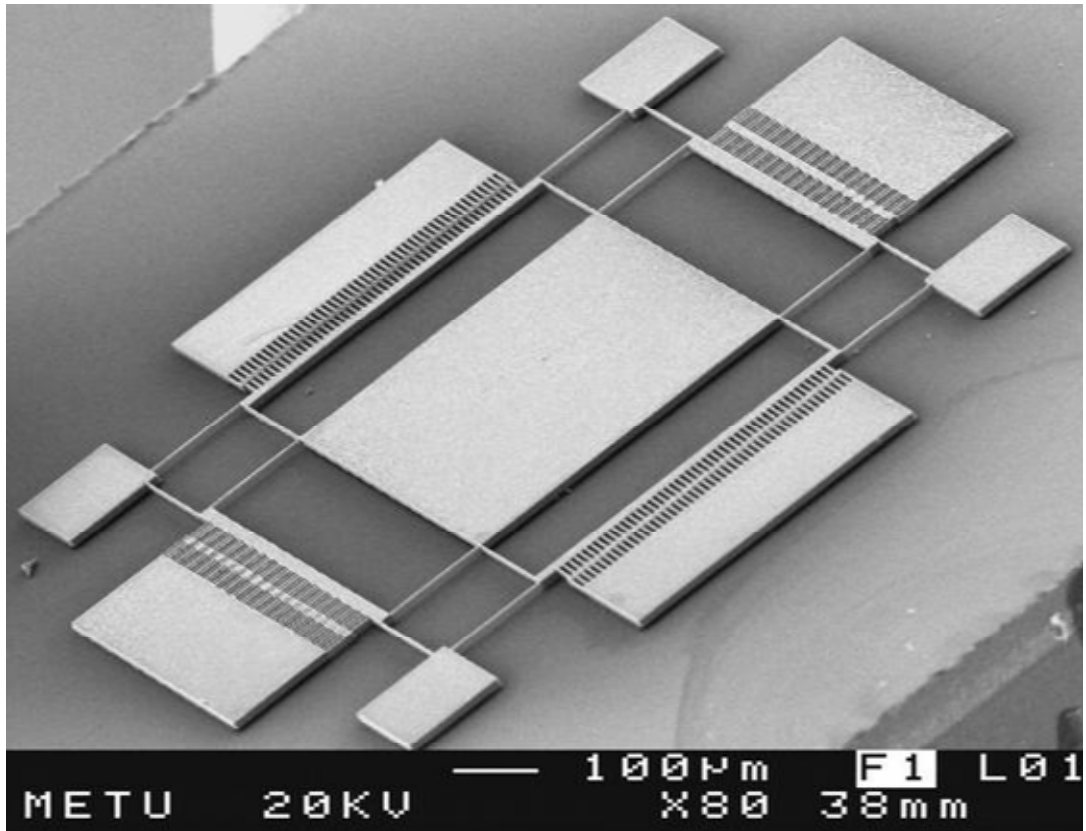
Figure 3.3: SEM photograph of the original symmetrical and decoupled gyroscope prototype, fabricated using DWSM process, ARS-DWSM. The fabricated sensor occupies an area of $1\times1mm^2$.

While the DWSM process has the advantages of fabricating high-quality single-crystal silicon gyroscopes, the structural layer thickness is limited compared to the other fabrication processes involved during this research. The long EDP etch period for dissolving undoped silicon at the end of the fabrication process put severe limitations to the mask design, which could be relaxed by using a thin silicon substrate, which could be very fragile to handle and machine.

DWSM process is run for only a single layout design during this research, because of the requirement of extreme control of the process conditions, which could not be afforded with the available cleanroom environment. Still, the fabricated prototypes are tested and the results of the tests are presented in Chapters 5 and 7. The modification of the mask layout for improved symmetrical and decoupled gyroscope structures is left as a future work, for fabrication with dissolved wafer silicon micromachining process.
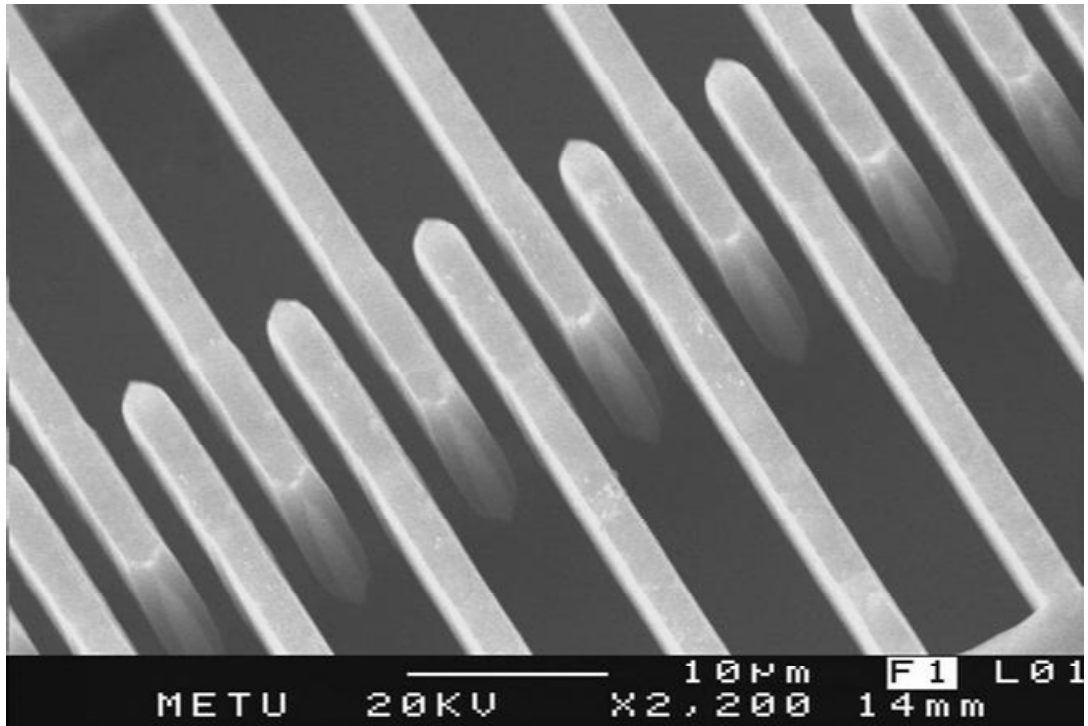
(a)
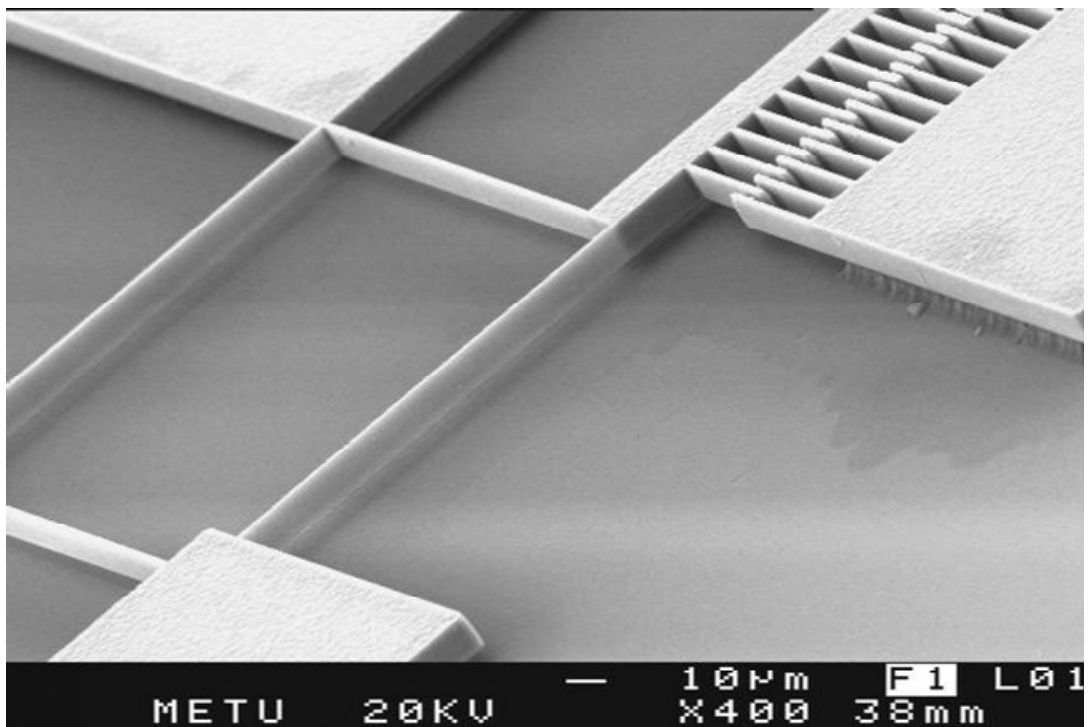
(b)

Figure 3.4: Close-up SEM photographs of the fabricated gyroscope prototype, ARS-DWSM. (a) The high-aspect ratio comb fingers with 12μm height and 1.5μm spacing and (b) the flexures and the proof mass that are suspended 5μm over the glass substrate.

3.2 Nickel Electroforming (NE)

The electrodeposition of metals is well-known for more than a century and is widely used in plating industry for many applications, including non-corrosive decorative coatings of metal equipment.   Electroforming process is based on the electrodeposition of a metal structural layer into an insulating mold, such as lithographically-patterned photoresist polymer. The basics of the electroplating and electroforming can be found in [99-100]. The low-cost, low-temperature processing, and CMOS compatibility of electroforming processes allowed them to be used in several MEMS applications in the past two decades.   The process is used for fabricating suspended microstructures such as inertial sensors, by locating the electroforming mold over a sacrificial layer to be etched at the end of the process, releasing the electroformed structures.   Section 3.2.1 presents an overview of the nickel electroforming process developed in this research and Section 3.2.2 presents the gyroscope prototype fabricated with nickel electroforming, together with the technical specifications in the sensor level.

3.2.1 NE Process Overview

Nickel is found to have superior elastic properties compared to the other well-known electrodeposited metals, such as copper, gold, chromium, etc.   In addition, the residual stress of electrodeposited nickel can be adjusted around zero-stress conditions, by using suitable plating bath chemistries [101]. Therefore, electroformed-nickel is selected as the structural material, whereas electroformed copper is selected as the sacrificial layer in the developed process flow, due to the high-conductivity and easy removal of copper deposits. The type of the photoresist mold defines the aspect ratio and the critical dimensions of the structure to be fabricated. Shipley's SJR5740 photoresist is found to be suitable for this application, due to its high aspect ratio compared to standard photoresist molds within a thickness range up to 20μm in a single-coat. The developed process requires only three masks, for pad metallization, anchor layer formation, and structural layer formation.

120

Figure 3.5 illustrates the NE process flow. The process starts with deposition and patterning of 300/3000Å-thick evaporated Cr/Au metallization layer over a 500µm-thick, 4-inch, Corning 7740 Pyrex glass substrate. Next, 300/3000Å-thick Ti/Cu seed layer is sputter-coated on the whole substrate surface. The Ti/Cu seed layer is then etched away inside the anchor and pad metallization regions, for ensuring the nickel is electroformed on Cr/Au stack rather than on Ti/Cu stack at the structural layer formation step towards the end of the process (Figure 3.5h). Otherwise, nickel structures detach from the substrate surface during long sacrificial layer etch at the final step of the process. Following the patterning of a 5.5µm-thick negative-tone photoresist (Microposit ma-N 440) with controllable-sidewall profile, the copper sacrificial layer is electroformed from copper sulfate chemistry on the whole substrate surface except inside the anchor regions. Next, the negative-tone photoresist is stripped from the substrate surface and Shipley's SJR5740 photoresist is coated to a thickness of about 20µm, and patterned using the structural layer mask. After cleaning the surface of the underlying conductive Ti/Cu and Cr/Au seed layer regions with oxygen plasma and hardbaking the structural photoresist mold, nickel is electroformed inside the thick photoresist mold from a low-stress nickel sulphamate chemistry. Finally, the thick photoresist mold is stripped in SVC175 photoresist stripper, and the copper sacrifical layer and the Ti/Cu seed layer are selectively etched in a mixture 1:1:18 acetic acid (CH_3COOH), H_2O_2, and deionized water. Fabricated nickel gyroscopes are then cleaned in deionized water, rinsed in a standard acetone-isopropyl alcohol (IPA)-methanol bath, and released by drying on hotplate.
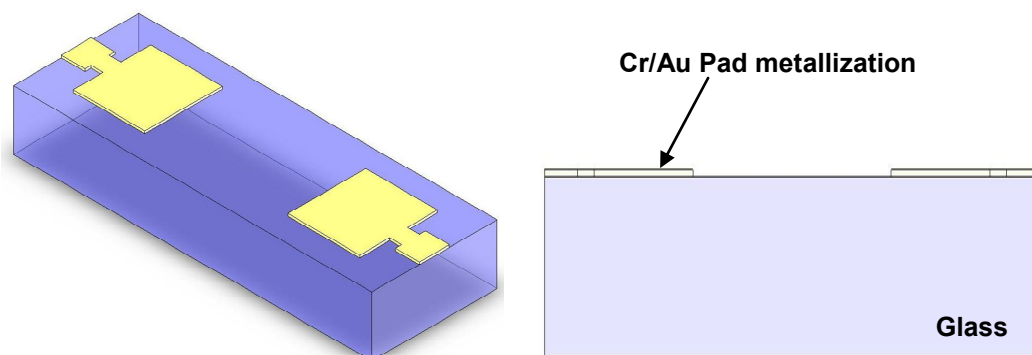
(a) Pattern Cr/Au pad metallization on a blank glass substrate

Figure 3.5: Nickel electroforming process flow (cont. next page).
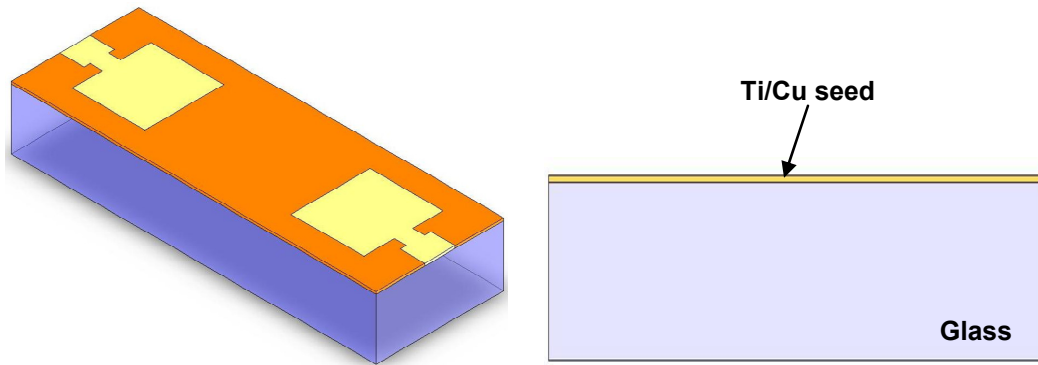
(c) Pattern Ti/Cu on the whole substrate surface as a seed layer for copper electroforming
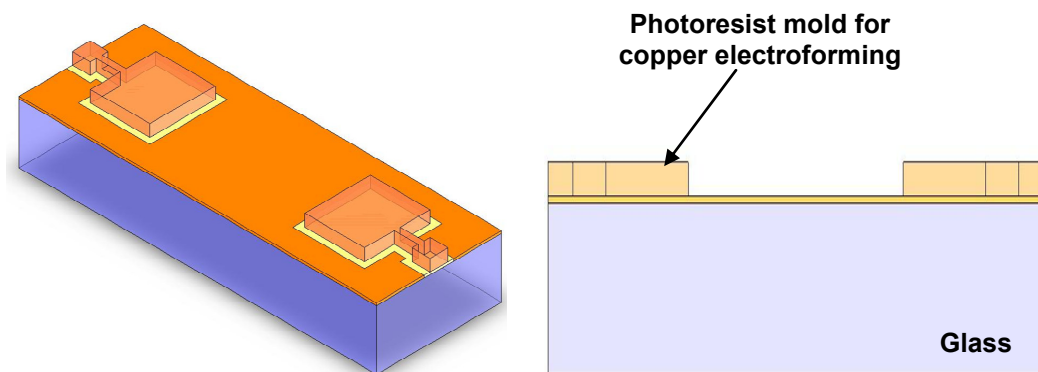
(d) Patterning photoresist as a mold for electroforming sacrificial copper layer
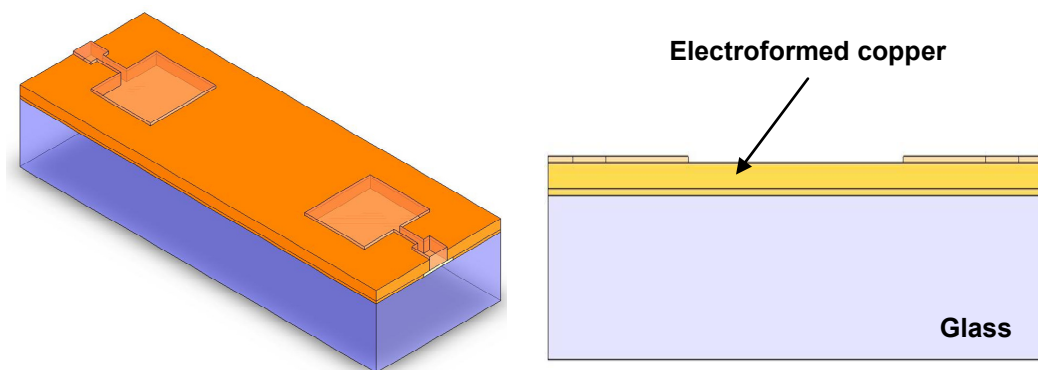
(e) Electroform sacrificial copper into photoresist mold
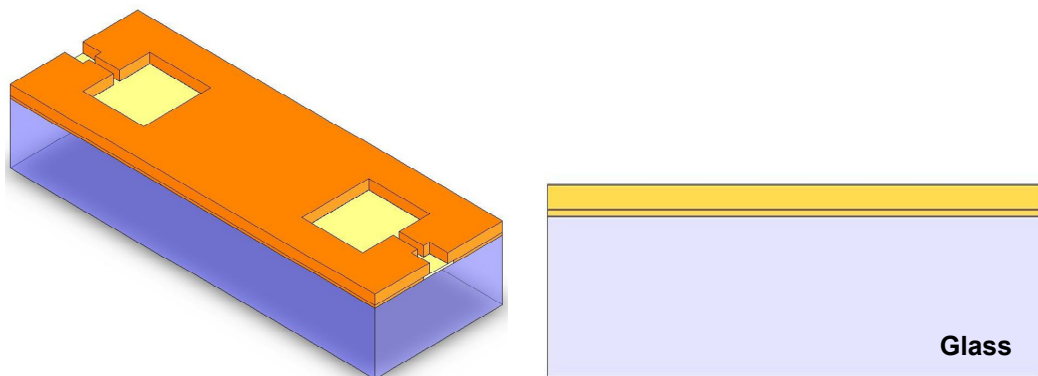
(f) Remove the photoresist mold used for copper electroforming

Figure 3.5: Nickel electroforming process flow (cont. next page).
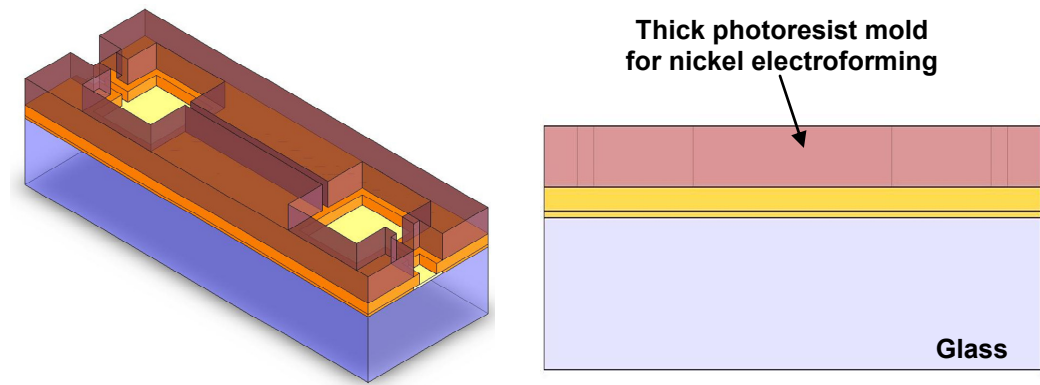
(g) Patterning thick photoresist mold for nickel electroforming
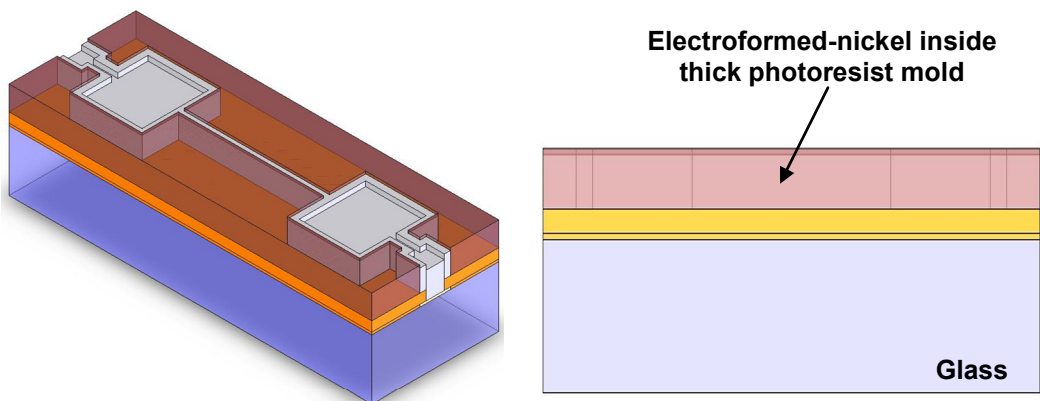
(h) Electroform nickel into the thick photoresist mold
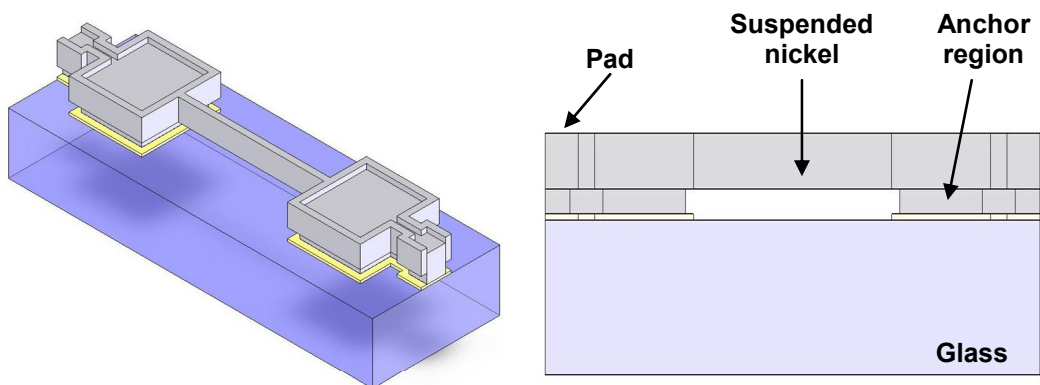
(l) Release nickel microstructures by removing the photoresist, selective etching of copper, and titanium layers.

Figure 3.5: Nickel electroforming process flow (The drawings are not to scale).

Even though the process flow looks straightforward, there are few issues to be considered about nickel electroforming. These issues can be summarized as follows:

1. *High tensile stress of electroformed copper sacrificial layer, buckling the glass substrate*. This usually occurs if the deposition rate of copper is too fast

(greater than 1μm/min) and the thickness of the copper is higher than 2μm. Excessive buckling of the substrate may result in contact problems in the lithography of SJR5740 photoresist mold and makes it impossible to resolve smallest features (<5μm) such as comb finger gaps and thin support flexures of the gyroscopes. In addition, the deposited copper sacrificial layer must be smooth enough to prevent any contact problems in the lithography of SJR5740.

2. *Limited aspect ratio of the photoresist mold for nickel electroforming.* The aspect ratio of the SJR5740 photoresist mold highly depends on the relative humidity of the ambient. The aspect ratio of the mold is much lower (close to 3) than its limits (up to 6) if there is no relaxation period between the softbake and UV exposure.

3. *Change-in feature size during the mold lithography.* Features enlarge and gaps shrink during the development of the mold. For example, 3μm-wide feature turn out to be as wide as 5μm after fabrication and 4μm-wide spacing shrink down to smaller than 2μm. Shrinking of gap spacing is advantageous because it usually increases the sensor capacitance, however, enlargement of the features results in increased beam widths and increased resonance frequencies for the fabricated gyroscopes.

4. *Compatibility of photoresist mold with nickel electroplating bath.* SJR5740 photoresist cannot withstand to plating periods longer than few tens of minutes in nickel sulfamate bath, without hardbaking the developed photoresist mold and operating the nickel sulphamate bath at a temperature close to its lower limits. In addition, the standard plating method using soluble nickel pellets as the anode material are found to be deteriorating for the photoresist mold.

5. *Plating conditions and setup.* The nickel electrodeposition step requires great care and the electroplating solution must be carefully maintained by keeping the concentration of the chemical constituents of the bath within the specified limits. Otherwise, it is very difficult to obtain repeatable characteristics from

electrodeposited nickel, facing roughness, residual stress, and pitting problems. In addition, the plating setup must be properly designed; having constant anode-cathode spacing, sufficient and proper type of agitation, and the plating power supply must provide minimum ripple.

Tensile stress and surface roughness of electroformed copper sacrificial layer is reduced by optimizing the copper electroforming process. Table 3.3 summarizes the bath constituents and operating conditions for copper electroforming process. Figure 3.6 shows the improvement in the surface roughness of the deposited copper after process optimization, measured using Veeco NT1100 optical surface profiler. The improvements in the surface roughness and the residual stress of electrodeposited copper sacrificial layer allowed high-resolution lithography of the SJR5740 photoresist mold. Optimization of SJR5740 lithography in terms of exposure dose, softbake period, and relaxation at controlled-humidity ambient resulted in mold features with aspect ratios approaching to 7. The effect of feature size variation during SJR5740 lithography is taken into account during the mask designs and predicted prior to fabrication. The problem of dissolving photoresist mold during nickel electroforming is cured by using insoluble titanium anodes at a cost of reduced bath life. In addition, the surface roughness, residual stress, and pitting of the electroformed nickel are improved by optimizing the operating conditions for the nickel sulphamate bath and by using an electroplating setup with agitators covered with fibrilic clothing based on a technology for reducing boundary layer thickness [102]. Table 3.4 summarizes the bath constituents and operating conditions for copper electroforming process. Figure 3.7 shows the improvements achieved in the nickel electroforming process, as a result of the process optimization.

Table 3.3: Bath constituents and operating conditions for copper electroforming process.

Constituent	Concentration	Parameter	Condition
Copper sulfate	220 g/L	Plating current type	20% duty-cycle forward-pulse
Sulphuric acid	32 ml/L	Plating current density	2 A/dm^2
Basic brightener	4 ml/L	Deposition rate	0.4 μm/min
Leveling agent	0.4 ml/L	Filter agitation	Off
Wetting agent	20 ml/L	Anode-cathode spacing	5mm
		Anode agitation freq.	3Hz
		Bath temperature	25°C
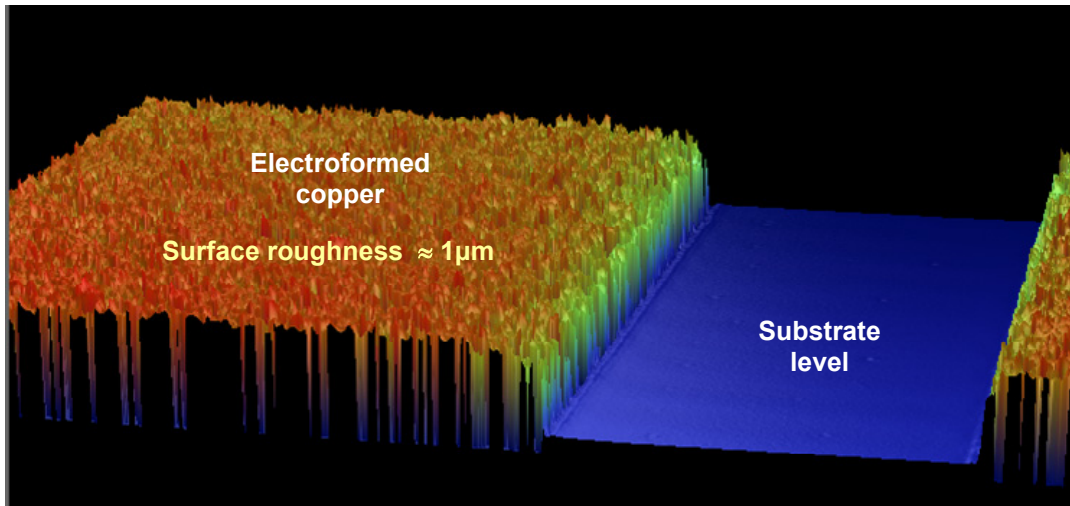
(a)
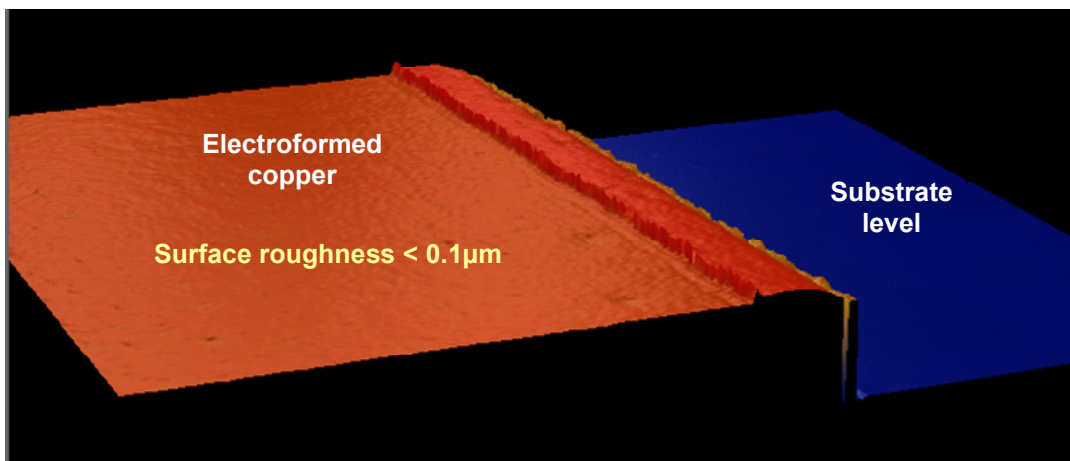
(b)

Figure 3.6: Improvement in the surface roughness of the deposited copper (a) before and (b) after process optimization, measured using Veeco NT1100 optical surface profiler.

Table 3.4: Bath constituents and operating conditions for nickel electroforming process.

Constituent	Concentration	Parameter	Condition
Nickel sulfamate	500 g/L	Plating current type	DC current
Boric acid	30 g/L	Plating current density	0.4-1.1 A/dm^2
Nickel chloride	2 g/L	Deposition rate	0.4-1.1 μm/min
		Filter agitation	On
		Anode-cathode spacing	7.4 mm
		Anode agitation freq.	2.1 Hz
		pH of the solution	3.8-4.2
		Bath temperature	45°C
		Anode-type	Insoluble (titanium)
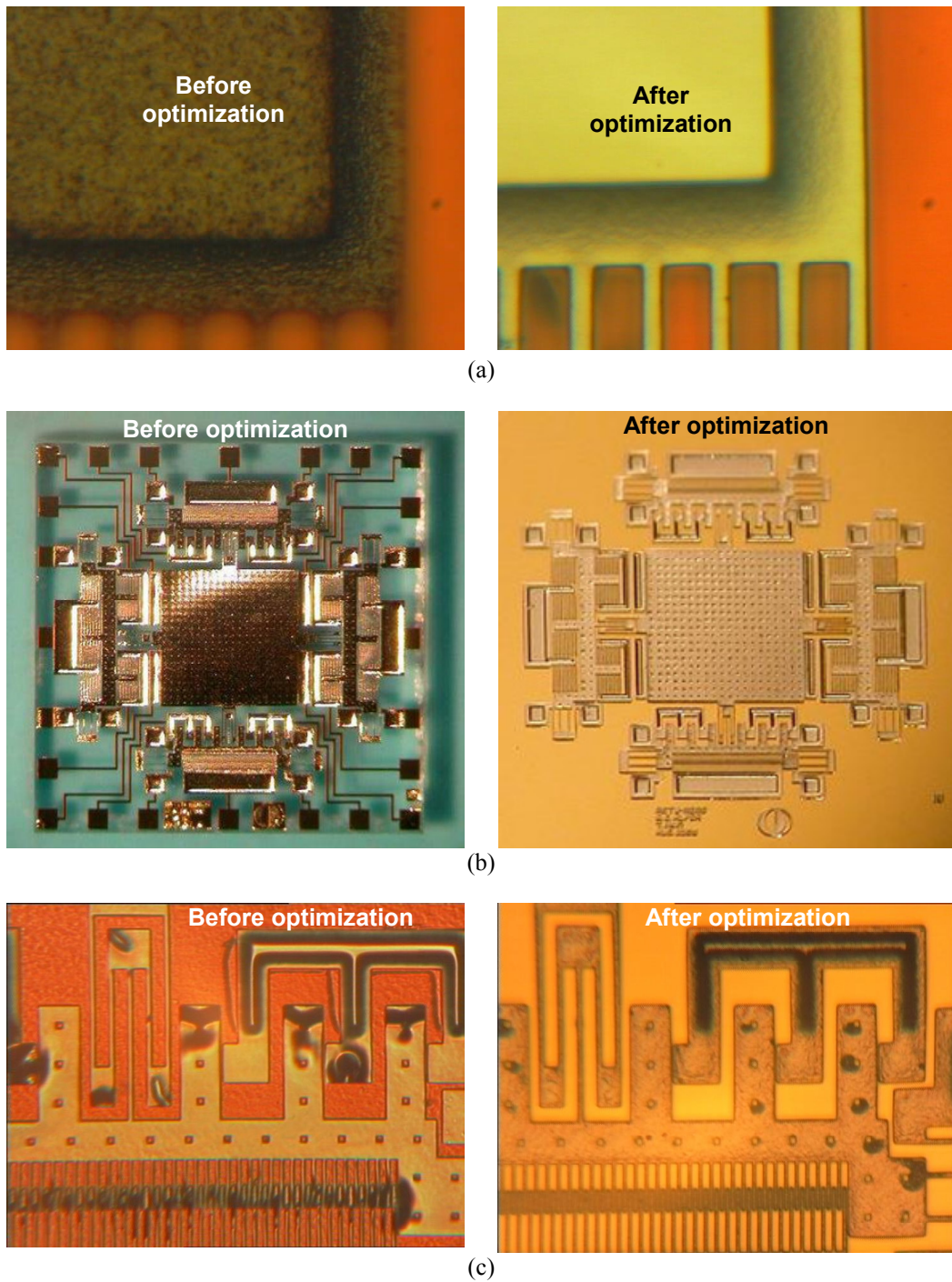
Figure 3.7: The improvements achieved in the nickel electroforming process, as a result of the process optimization. (a) Surface roughness improved from 1μm down to better than 50nm. (b) Residual stress and the resulting buckling of the structural layer is reduced by using insoluble titanium anodes. (c) The pitting observed in the deposited nickel due to hydrogen outgas is removed by optimizing the frequency and strength for the solution agitation.

3.2.2 Nickel Angular Rate Sensor Prototype (ARS-NE)

The second prototype developed in this research is an improved symmetrical and decoupled gyroscope, the structure of which is shown in Figure 1.14, fabricated with the developed nickel electroforming process. The gyroscope employs varying-overlap-area type comb electrodes for the drive mode and varying-gap type comb electrodes for the sense mode. This configuration destroys the symmetry of the gyroscope along the drive and sense modes, however, allows electrostatic tuning of sense-mode resonance frequency for mode matching. In addition, dual and triple-folded type beams are used for the flexures along both the drive and the sense modes in order to avoid spring nonlinearity effects. The gyroscope employs additional electrostatic tuning electrodes around the proof mass for quadrature cancellation and force-feedback electrodes for closed-loop operation of the gyroscope.

The fabricated gyroscope prototype is labeled as ARS-NE, i.e., "**A**ngular **R**ate **S**ensor fabricated with **N**ickel **E**lectroforming process".

ARS-NE gyroscope prototype contains a number of electrodes for actuation, sensing, and electrostatic tuning. Figure 3.8 shows the layout of the gyroscope, drawn in Cadence design environment. Table 3.5 provides the structural dimensions, the number of comb fingers, corresponding capacitance, $\partial C/\partial x$ parameter, and electrostatic spring constant for each type of electrode shown in Figure 3.8. Values for the electrode capacitances are estimated based on 18μm electroplating thickness. The gap spacing for the prototype is assumed to be 3μm during the design step, while the actual gap spacing drawn in the layout is 5μm, in order to take into account the effects of gap narrowing during electroforming process.

After determining the electrical parameters of the gyroscope prototype, the resonance frequencies of the drive and the sense modes are designed. As it is possible to tune-down the resonance frequency of the sense mode by electrostatic springs, the mechanical resonance frequency of the sense mode is tuned slightly higher than that of the drive mode. The drive-mode resonance frequency is selected to be about 5kHz, for achieving a higher sensitivity and smaller actuation force.

However, if the resonance frequency is too small, low-frequency electronic noise disturbs the gyroscope output requiring a modulation-based preamplifier circuit. In addition, the environmental vibrations may also affect the gyroscope performance for very small resonance frequencies (<3kHz). Table 3.6 provides the design parameters for the ARS-NE gyroscope prototype. Young's modulus of nickel is taken to be 150GPa based on previous experiments on nickel electroforming. In addition, the beam width of the prototype is assumed to be 4μm during the design step, while the actual beam width drawn in the layout is 2μm, in order to take into account the effects of feature enlargement during electroforming process.
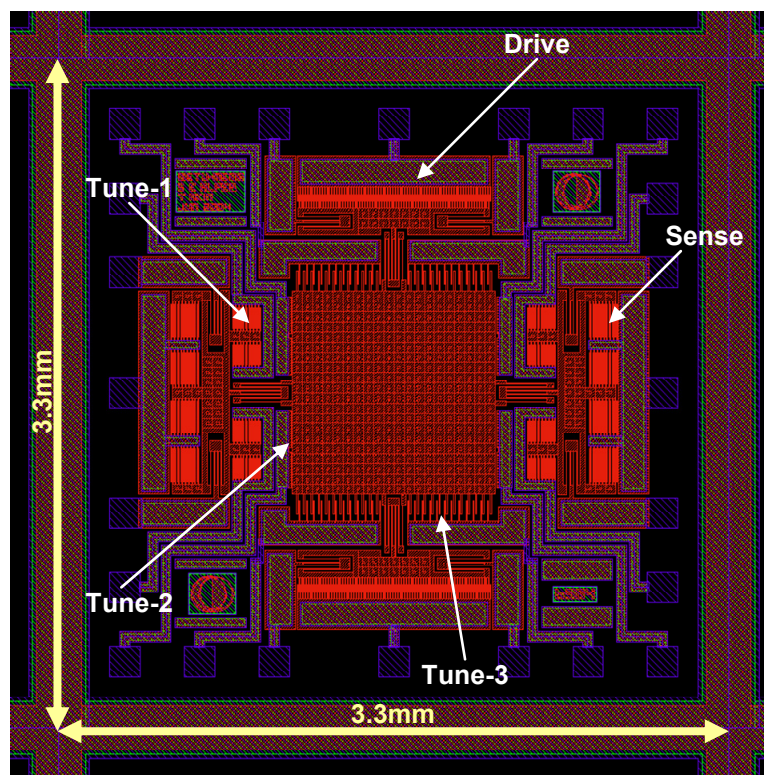
Figure 3.8: The layout of the designed ARS-NE improved symmetrical and decoupled gyroscope prototype.

The design process starts with estimating the approximate mass for the proof mass and drive/sense electrodes (M_{PM}, M_{DE}, M_{SE}, M_{D_Total}, M_{S_Total}) for each mode of the gyroscope. Next, the spring constant associated with drive mode (K_{inner}, K_{D_outer}, K_{D_Total}) is calculated based on an initially determined drive mode resonance frequency (F_D). Then, the sense mode total (mechanical+electrostatic) spring constant (K_{S_On}) is determined in order to have the sense mode resonance frequency

(F_S) equal to that of the drive mode when the gyro is powered ON and operated at the limiting supply voltage. Since the flexures connecting the drive/sense electrodes to the proof mass are fixed by the layout area and identical for both the drive and sense modes, the spring constant of these flexures (K_{inner}) are subtracted from K_{S_On} so as to find the sum of $K_{electrostatic}$ and K_{S_outer}, which are the two parameters that must be properly tuned for adjusting F_S.

Table 3.5: Structural dimensions and electrical parameters for the electrodes (including electrostatic fringe-field corrections) of the designed ARS-NE prototype.

Electrode	Parameter	Value
DRIVE	# of combs	68 x 2
	Capacitance, (fF)	352 x 2
	$\partial C/\partial x$, (F/m)	$(0.88) \times 10^{-8}$ x 2
	$K_E = (\partial^2 C/\partial x^2) \times V^2$, (N/m)	0
SENSE	# of combs	32 x 2
	Capacitance, (fF)	381 x 2
	$\partial C/\partial x$, (F/m)	$(0.09) \times 10^{-6}$ x 2
	$K_E = (\partial^2 C/\partial x^2) \times V^2$, (N/m)	$0.030 \times V^2$ x 2
TUNE-1	# of combs	16 x 4
	Capacitance, (fF)	85 x 4
	$\partial C/\partial x$, (F/m)	$(0.28) \times 10^{-7}$ x 4
	$K_E = (\partial^2 C/\partial x^2) \times V^2$, (N/m)	$0.009 \times V^2$ x 4
TUNE-2	# of combs	1 x 4
	Capacitance, (fF)	11.5 x 4
	$\partial C/\partial x$, (F/m)	$(2.30) \times 10^{-9}$ x 4
	$K_E = (\partial^2 C/\partial x^2) \times V^2$, (N/m)	$0.00046 \times V^2$ x 4
TUNE-3	# of combs	11 x 4
	Capacitance, (fF)	17.5 x 4
	$\partial C/\partial x$, (F/m)	$(0.35) \times 10^{-8}$ x 4
	$K_E = (\partial^2 C/\partial x^2) \times V^2$, (N/m)	$0.0007 \times V^2$ x 4

Finally, the total electrostatic spring constants ($K_{S\_E} + K_{T\_E}$) are determined based on the electrode geometries, remembering that the electrostatic spring constants act as negative springs. The limiting factors in determining the electrostatic spring constants are either the supply voltage or the frequency tuning range. Frequency tuning range is selected based on the fact that the electrostatic spring constants tuning the sense mode frequency are less than 20% of the mechanical spring constant of the sense mode. Note that the sense mode enters pull-in if the magnitude of the electrostatic spring constant equals to the mechanical spring constant. Selecting $K_{S\_Electrostatic} < (0.2) \times K_{S\_Mechanical}$ results in $V_{pull-in} > (2.2) V_{operational}$. If electrostatic spring constant value is selected as $K_{S\_Electrostatic} < (0.5) \times K_{S\_Mechanical}$ then

$V_{pull-in}$ will be only 40% higher than $V_{operational}$. In addition, increasing the frequency tuning range larger makes the $K_{S\_Mechanical}$ and $K_{D\_Mechanical}$ highly different from eachother, destroying the symmetry and increasing the temperature sensitivity of the gyroscope. Having determined the electrostatic spring constants ($K_{S\_E}+ K_{T\_E}$) also determines the K_{S_outer}, the paraemeter to adjust the flexure lengths of the sense mode (L_{Sense_outer}). Calculating the total mechanical spring constant of the sense mode ($K_{S\_Total\_Mech}$) and determining the mechanical resonance frequency (F_{S_Mech}) of the gyroscope completes the design process.

Table 3.6: The design parameters for the ARS-NE gyroscope prototype.

Parameter	Value
M_{PM}, kg	$(1.42) \times 10^{-7}$
M_{DE}, kg	$(0.14) \times 10^{-7}$
M_{SE}, kg	$(0.21) \times 10^{-7}$
$M_{D\ Total}$, kg	$(1.69) \times 10^{-7}$
$M_{S\ Total}$, kg	$(1.84) \times 10^{-7}$
K_{inner}, N/m	29
$K_{D\ outer}$, N/m	117
$K_{D\ Total}$, N/m	146
F_{D}, Hz	4678
$K_{S\ On}$ for $F_{D}=F_{S}$, N/m	159
$K_{S\ On}-K_{inner}$, N/m	130
$K_{S\ E}+ K_{T\ E}$, N/m	$-9.8@10^{V}$
$K_{S\ Outer}$, N/m	140
$K_{S\ Total\ Mech}$, N/m	169
$F_{S\ Mech}$, Hz	4823

Figures 3.9 shows the scanning electron microscope (SEM) photographs of the ARS-NE improved symmetrical and decoupled gyroscope prototype fabricated with nickel electroforming process. The gyroscope occupies an area of $2.9 \times 2.9 mm^2$ including the bonding pads, while the overall chip area is set $3.3 \times 3.3 mm^2$ for dicing tolerances. The movable structure is suspended 5µm over the substrate, defined by the thickness of the copper sacrificial layer.

Figure 3.10 shows the close-up SEM photographs of the varying-overlap-area type drive combs and varying-gap type sense combs. The height of the structural layer of the gyroscope is measured as 18µm, whereas the electrostatic gap between the fabricated comb fingers is 2.5µm. The aspect ratio of the currently fabricated gyroscope is therefore higher than 7, which is actually the physical limit for

electroforming processes using standard UV lithography for patterning a standard thick photoresist.
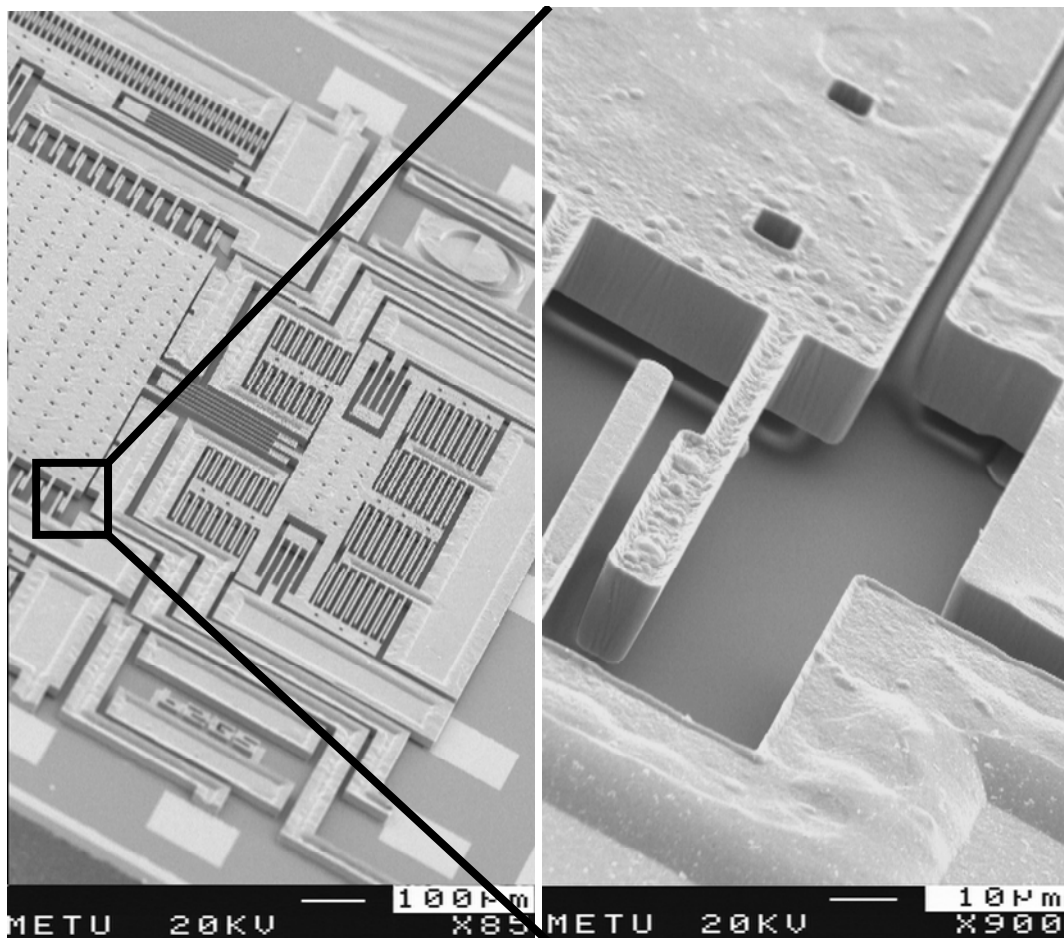
Figure 3.9: SEM photographs of the ARS-NE improved symmetrical and decoupled gyroscope prototype fabricated with nickel electroforming process. The gyroscope occupies an area of 2.9x2.9mm2 including the bonding pads, while the overall chip area is set 3.3x3.3mm2 for dicing tolerances. The movable structure is suspended 5µm over the substrate, defined by the thickness of the copper sacrificial layer.

Figure 3.11 shows the two problems associated with the nickel electroformed gyroscope. The stress-gradient of electroformed nickel cause buckling of the suspended structures, which results in an offset between the movable and stationary comb fingers as in Figure 3.11a. Although the residual stress of electroformed nickel is kept small by process optimization, still there is a finite stress-gradient due to the variation in the plating current density and electric fields inside the plating bath, during 40minute electroforming process. This variation is basically due to the fact that the conductivity of the plated surface decrease in time as nickel is deposited

on the surface, which can be compensated by ramping up the plating current. However, increased plating current is observed to destroy the leveling of the plated surface, as in Figure 3.11b. The problem can be solved by using a different photoresist mold, which is left as a future research topic.

| (a) | (b) |
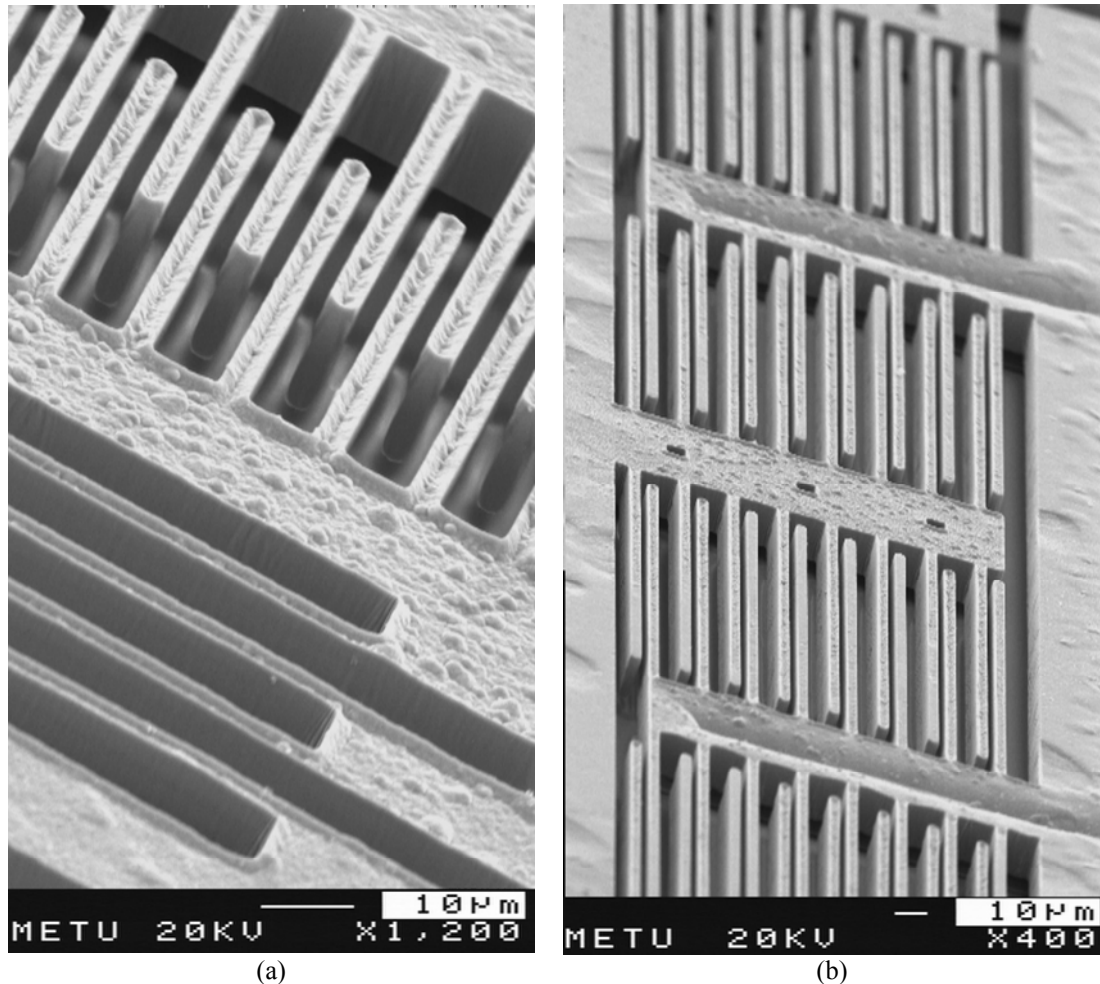
Figure 3.10: SEM photographs of (a) the varying-overlap-area type drive combs and (b) the varying-gap type sense combs.

Four different masks including more than 100 different types of symmetrical and decoupled gyroscopes are designed during the development of nickel electroforming process throughout this research. Beside the cost-effective process runs, the maintenance of the electroforming baths and optimizing the plating conditions are observed to be vital for high-yield manufacturing. In addition, the reliability of electroformed nickel is found to be questionable, which is addressed in Chapters 5 and 7 while discussing the tests performed on fabricated nickel gyroscopes.
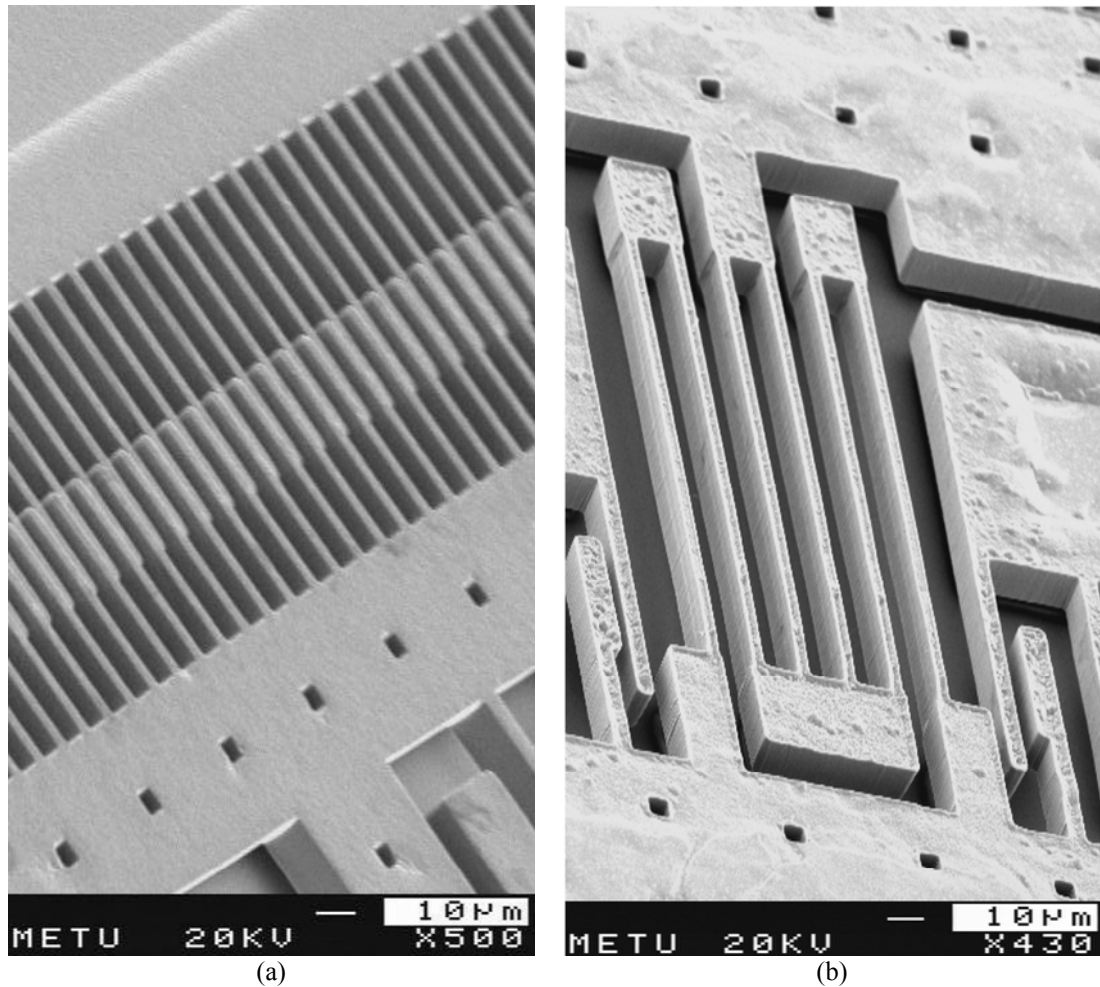
Figure 3.11: The two problems associated with the nickel electroformed gyroscope. (a) The buckling of the suspended structural layer due to residual strerss gradient of electroformed nickel cause an offset between the movable and stationary comb fingers. (b) Ramping up the plating current (and hence the chemical reaction speed) in order to keep stress gradient small cause leveling problems in electroformed nickel due to the dissolving photoresist mold.

3.3 Silicon-On-Insulator (SOI) Micromachining

Silicon-on-insulator technology is widely used in semiconductor industry for producing low-power, low-leakage, and high-performance integrated circuits. The technology gained favor for silicon micromachining, where a high-quality single-crystal-silicon structural layer is deposited on top of a silicon handling substrate with a thin insulating layer in between. This approach serves the advantage of processing a tiny structural layer, while the structural layer is electrically isolated from the handling substrate. The technology is suitable for the fabrication of high-aspect

ratio microstructures together with deep reactive ion etching of the structural layer. The SOI multi-user MEMS process (SOIMUMPs) offered by MEMSCAP company is selected as the third micromachining process in this research, for evaluating the performance of the symmetrical and decoupled vibratory gyroscopes fabricated in a standard SOI micromachining process. Section 3.3.1 presents an overview of the SOIMUMPs process and Section 3.3.2 presents the gyroscope prototype fabricated through SOIMUMPs, together with the technical specifications in the sensor level.

3.3.1 SOIMUMPs Process Overview

SOIMUMPs is a 4-mask process SOI patterning and etching process derived from the work performed at MEMSCAP (formerly Cronos Integrated Microsystems and the MCNC MEMS Technology Applications Center) [103]. Though the detailed process flow is provided in [103], the flow is briefly described here for convenience. The process requires four masks, for pad metallization, trench opening under suspended microstructures, structural layer formation, and an optional second metallization using a shadow mask.

Figure 3.12 illustrates the SOIMUMPs process flow. The process starts with a 4-inch, double-side-polished SOI wafer containing a 25μm-thick epitaxial silicon structural layer, a 1μm-thick silicon dioxide insulating layer, and a 400μm-thick silicon handling substrate. A thin oxide layer also exists at the bottom side of handling substrate, for backside patterning. The structural silicon layer is first doped by depositing phosphor-silicate-glass (PSG) and annealing at 1050°C for 1 hour in Argon, in order to increase the surface conductivity of silicon. Next, PSG is stripped from the surface and a 200/5000Å-thick evaporated Cr/Au pad metallization layer is patterned using lift-off. Following that, the silicon structural layer is patterned using DRIE until the insulating oxide layer is reached. The footing effects of DRIE is minimized using a proprietary SOI etch recipe. Then, the front-side of the wafer is coated with a protective material, the wafer is flipped, and the thin oxide layer at the bottom of the handling substrate is patterned using trench opening mask. The patterned etch mask is then used for DRIE of handling substrate from the backside

until the insulating oxide layer is reached. This etch removes the substrate layer under the microstructures to be suspended. After stripping the bottom-side oxide layer and the front-side protection material, the exposed areas of the insulating oxide are removed using vapor HF, releasing the microstructures. The electrical contact to the handling substrate is then defined by evaporating 500/6000Å-thick Cr/Au metal stack through a shadow mask. The details of the shadow mask are described in [103].
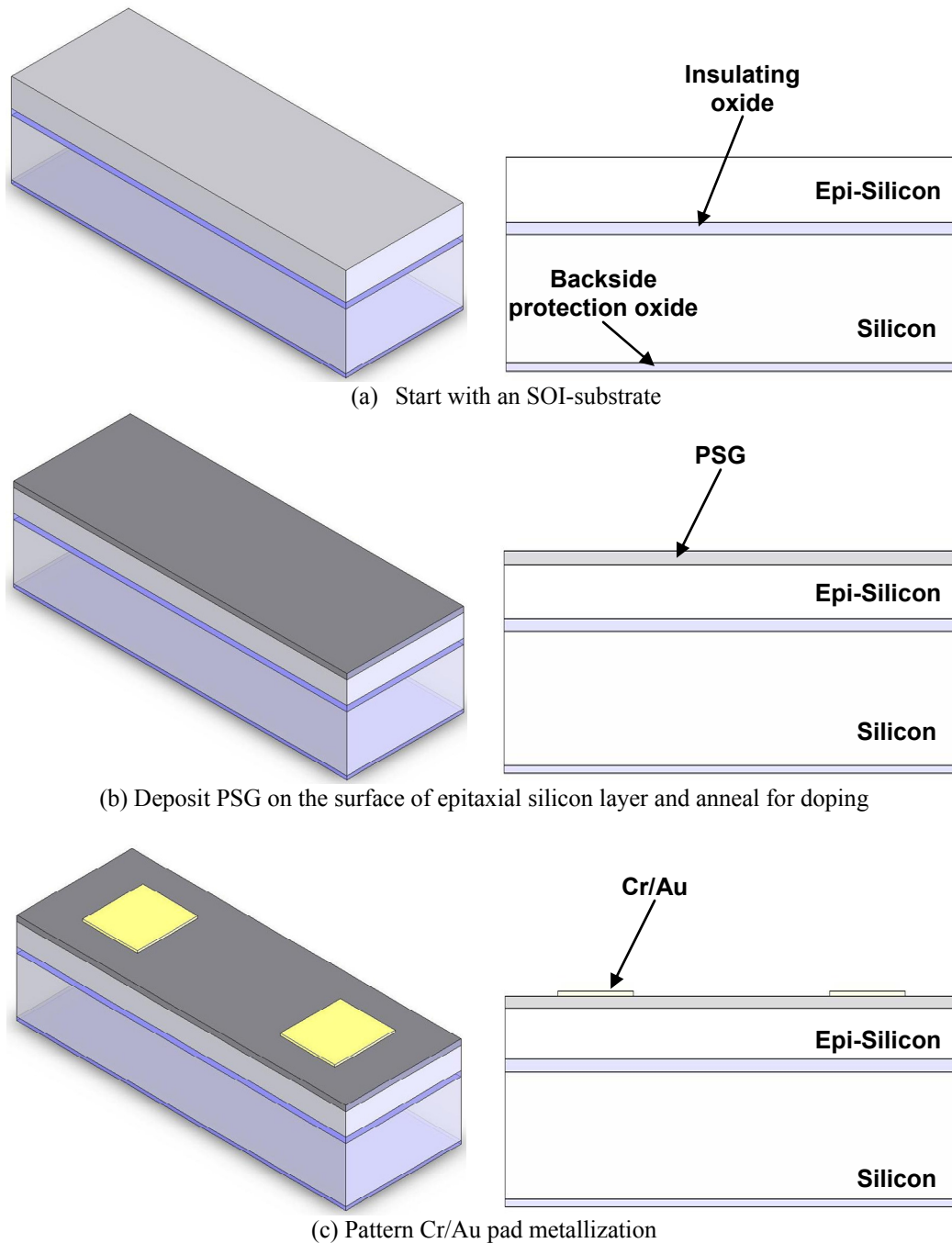
(a) Start with an SOI-substrate

(b) Deposit PSG on the surface of epitaxial silicon layer and anneal for doping

(c) Pattern Cr/Au pad metallization

Figure 3.12: SOIMUMPs process flow (cont. next page).

Etch mask for DRIE

Epi-Silicon

Silicon

(d) Pattern etch mask for DRIE

DRIE

Epi-Silicon
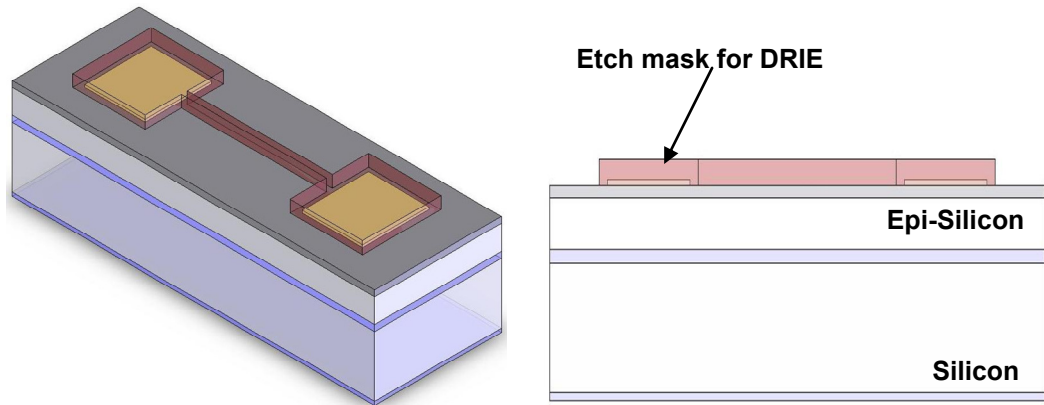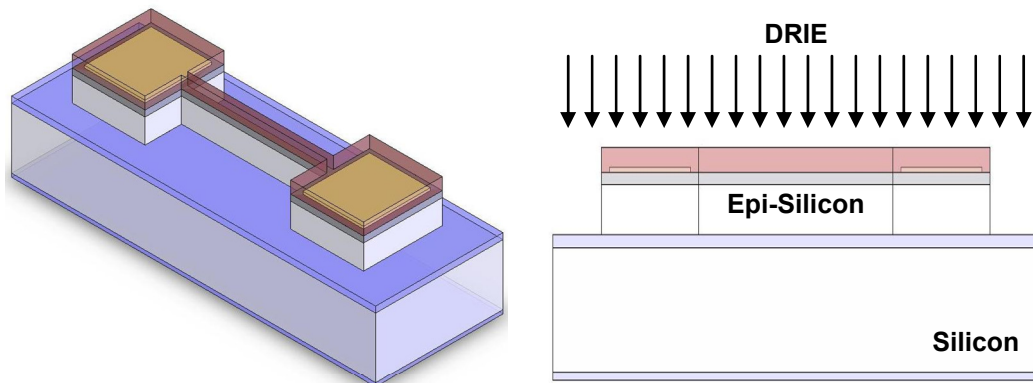
Silicon

(e) Deep reactive ion etching of epitaxial silicon until the insulating oxide

Epi-Silicon
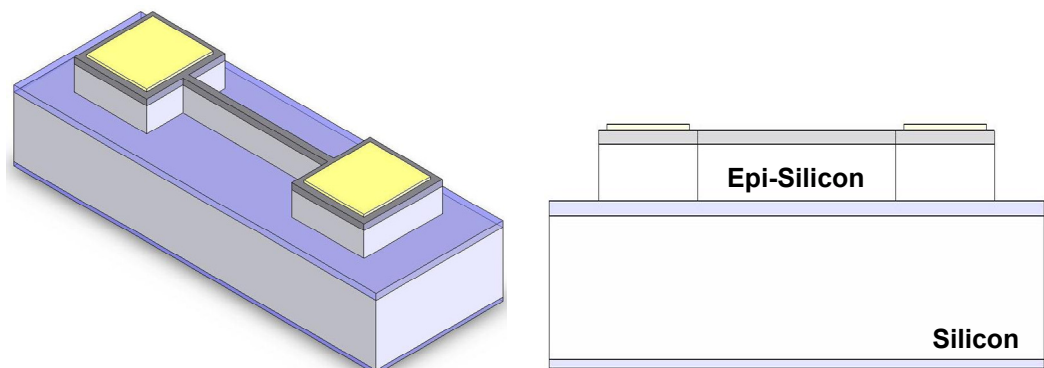
Silicon

(f) Strip DRIE etch-mask

Epi-Silicon
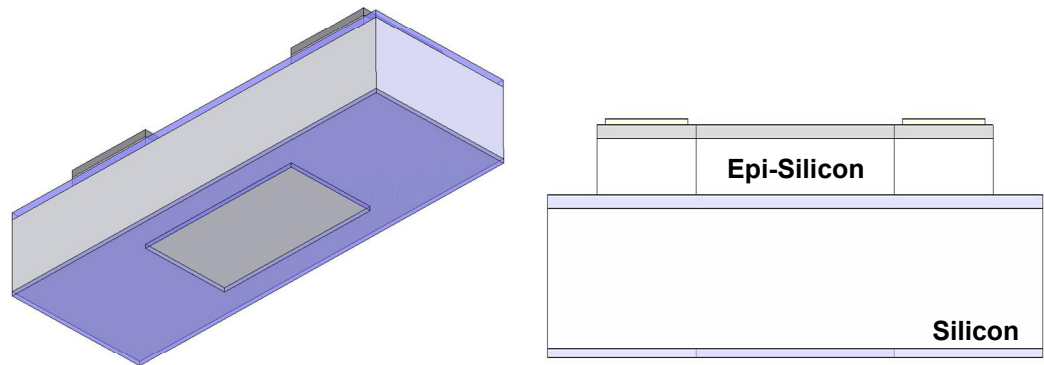
Silicon

(g) Pattern backside-protection oxide

Figure 3.12: SOIMUMPs process flow (cont. next page).

137
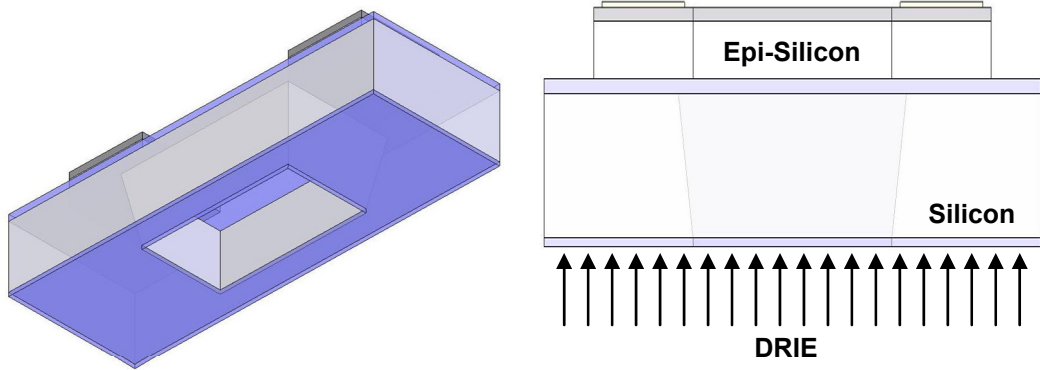
(h) DRIE of handling substrate until insulating oxide layer
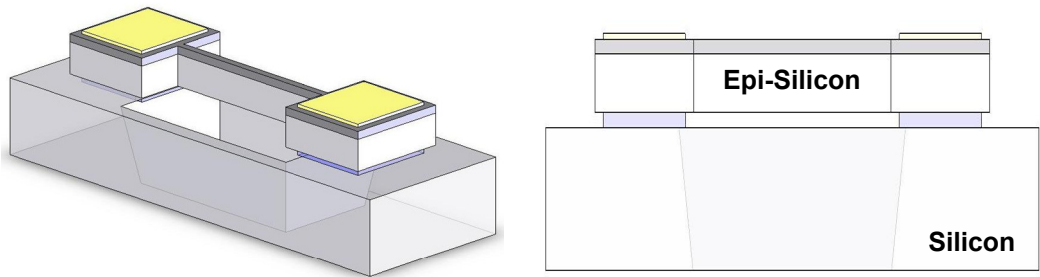
(i) Remove exposed oxide layers on the SOI wafer
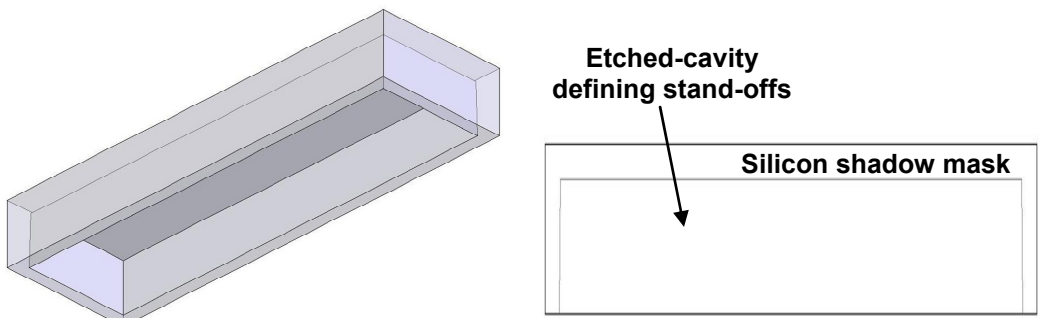
(j) Pattern a blank silicon substrate forming stand-offs for the shadow mask
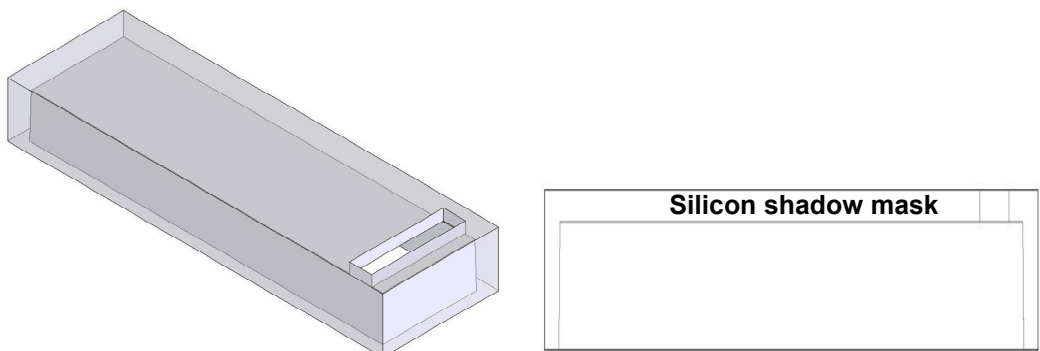
(k) Open a window for optional 2nd-metal deposition on the SOI wafer, using DRIE

Figure 3.12: SOIMUMPs process flow (cont. next page).
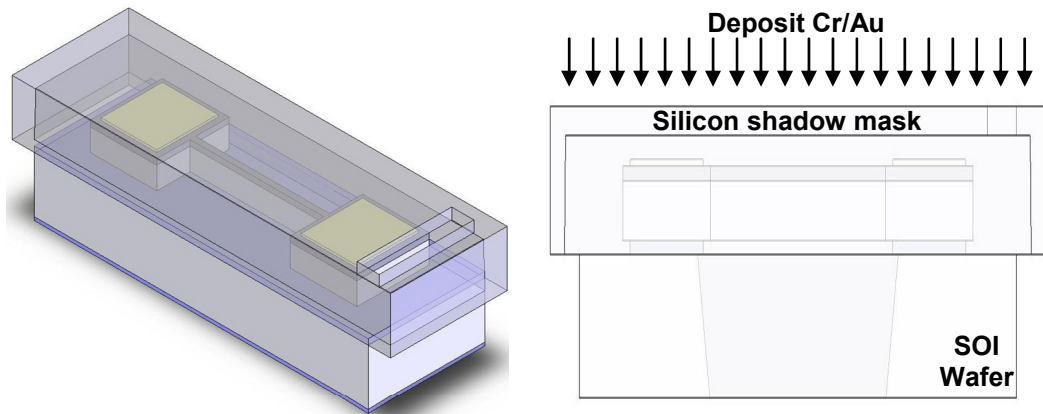
(l) Temporarily bond the shadow mask substrate to the SOI wafer from the stand-off regions and perform 2nd-metal deposition (shadow mask shown transparent for clarifying purposes)
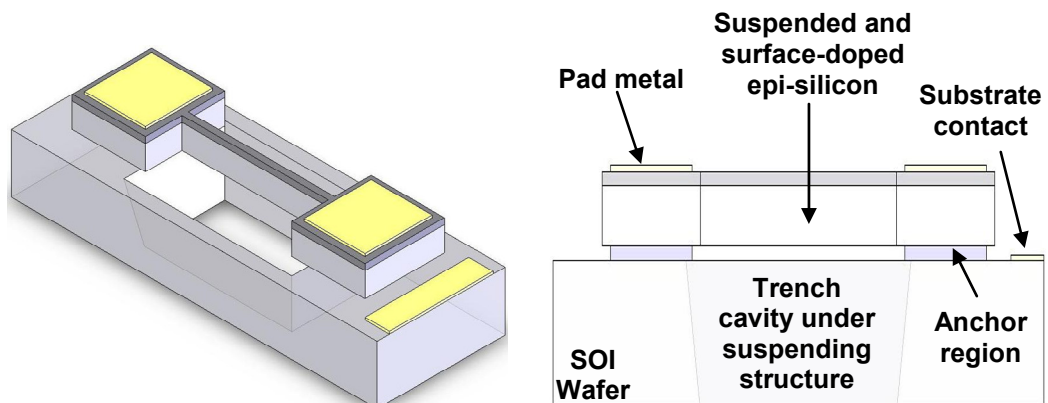
(m) Remove the shadow mask

Figure 3.12: SOIMUMPs process flow (The drawings are not to scale).

SOIMUMPs provides a fast solution to develop an SOI-based design. The major advantage of the SOIMUMPs process is its high-aspect ratio with a small capacitive gap; the 2.5µm minimum gap opening with 25µm-thick structural layer allows an aspect ratio of 10, higher than both DWSM and NE processes. Moreover, the trench opening under the suspending structures minimizes the difference in the viscous air damping for the top and bottom surfaces of the movable structures. Another advantage of the trench opening is that it prevents any electrostatic levitation effects, which creates a big problem especially if there is an electrically-isolated conductor lies under the suspended microstructure.

There are several limitations of SOIMUMPs. First of all, the pad metallization must lay over the epitaxial silicon, since there is no other way to get electrical contact to isolated silicon structures. This requires large anchor regions for wirebonding.

139

Another fact that constraint small anchors is the etch undercut occur during removal of insulating oxide layer (Figure 3.12i). The undercut reduce the rigidness of the anchors and even detach the anchors from the substrate, if the anchor size is small.

Two severe problems observed in SOIMUMPs. One of these problems is the large variation of the trench openings under suspended structures, from the designed values in the layout. Backside DRIE of the SOI substrate is performed using a fast but less-controlled etch recipe, compared to the recipe used for the front-side DRIE. As a result, the trench opening cause a large undercut for the anchors surrounding the trench area. Although the tolerances provided in the design rules of the process are strictly obeyed during the design, the trench undercut sometimes exceed these tolerances causing some of the electrodes falling inside the trench. Figure 3.13a shows a sample situation encountered in the first layout design, causing the electrode of a gyroscope fall into the trench. The destructive effects of this problem are minimized in the second and third layout designs, by using trench-related tolerances much higher than the values stated in the design rules. The second problem of SOIMUMPs is the fracture of slender beams and comb fingers during the fabrication process and the shipment. The source of this problem is again the insufficient tolerances in the design rules and the shipment of microstructures after releasing them. Figure 3.13-b shows a typical comb electrode suffering from broken fingers. This problem is then solved by using round fillets at the inner corners of the joints between the slender structures and the frames attached to them, and by increasing the width of comb fingers to above the minimum feature size stated in the process design rules.

3.3.2 SOI Angular Rate Sensor Prototype (ARS-SOI)

The third prototype developed in this research is another improved symmetrical and decoupled gyroscope, the structure of which is shown in Figure 1.14, fabricated with a commercially available silicon-on-insulator micromachining process (SOIMUMPS) offered by MEMSCAP. The features of the designed gyroscope is similar to the one designed for nickel electroforming process; employing varying-

overlap-area type comb electrodes for the drive mode and varying-gap type comb electrodes for the sense mode, and has additional electrodes for quadrature error cancellation and force-feedback.
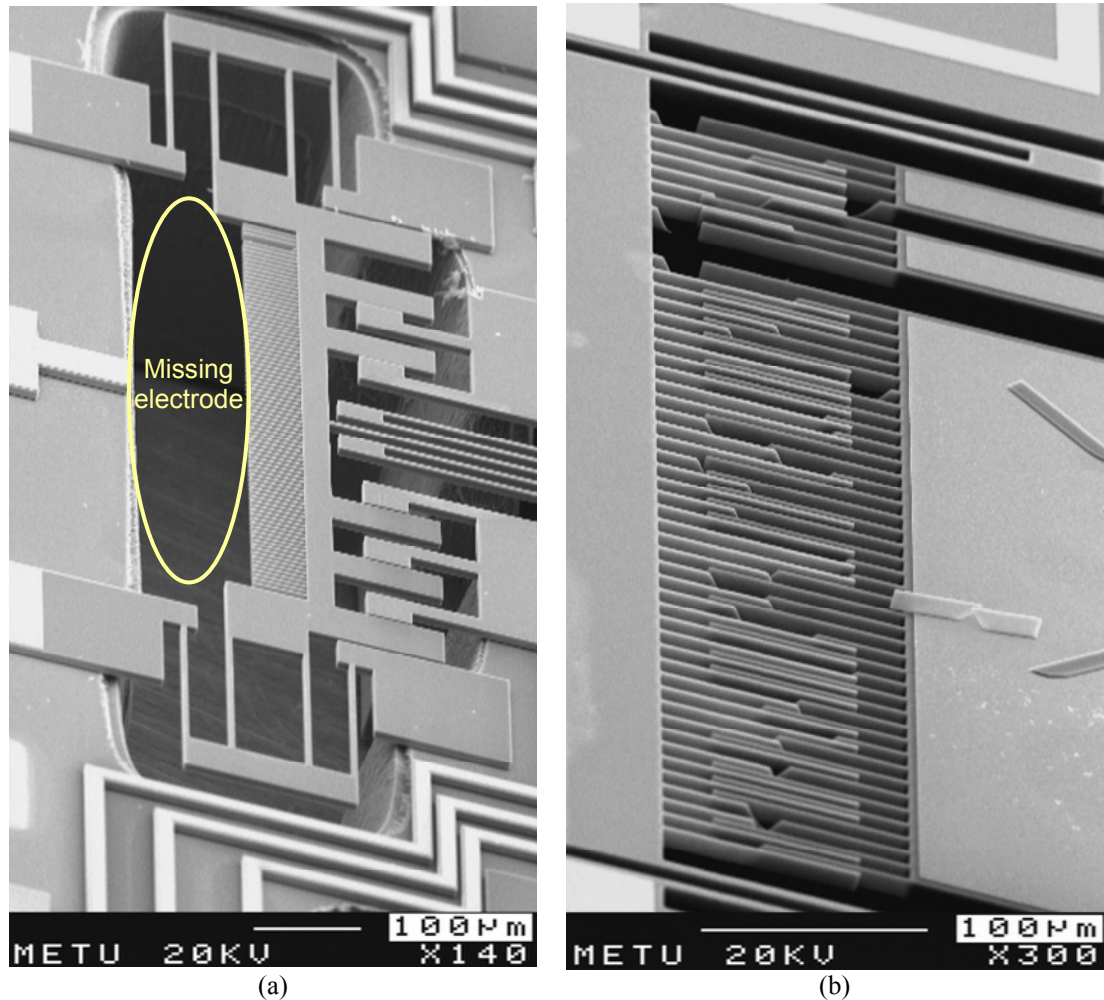
Figure 3.13: The two problems associated with the SOIMUMPs process. (a) The large variation from the design layout for the trench openings under suspended structures, causing some of the electrodes falling inside the trench. (b) Fracture of slender comb fingers during the fabrication process and the shipment.

The fabricated gyroscope prototype is labeled as ARS-SOI, i.e., "**A**ngular **R**ate **S**ensor fabricated with **S**ilicon-**O**n-**I**nsulator micromachining process".

No separate frequency tuning electrodes are used in the ARS-SOI design, since the varying-gap type sense electrode already generates electrostatic spring for frequency-tuning. This configuration increase the effective sense capacitance in a

141

constant footprint, while it has the drawback of the rate sensitivity depending on the DC voltage used for tuning the resonance frequencies. Another difference between the ARS-NE and ARS-SOI prototypes is that the second one has a slightly different flexure layout in order to reduce possible quadrature coupling due to rotary modes.

Figure 3.14 shows the layout of the ARS-SOI, drawn in Cadence design environment. The gyroscope occupies an area of $2.7 \times 2.8 \text{mm}^2$ including the bonding pads, while the overall chip area is about $3.6 \times 3.8 \text{mm}^2$ much larger than the sensor area due to the tolerances of DRIE-based dicing of SOIMUMPs chips.
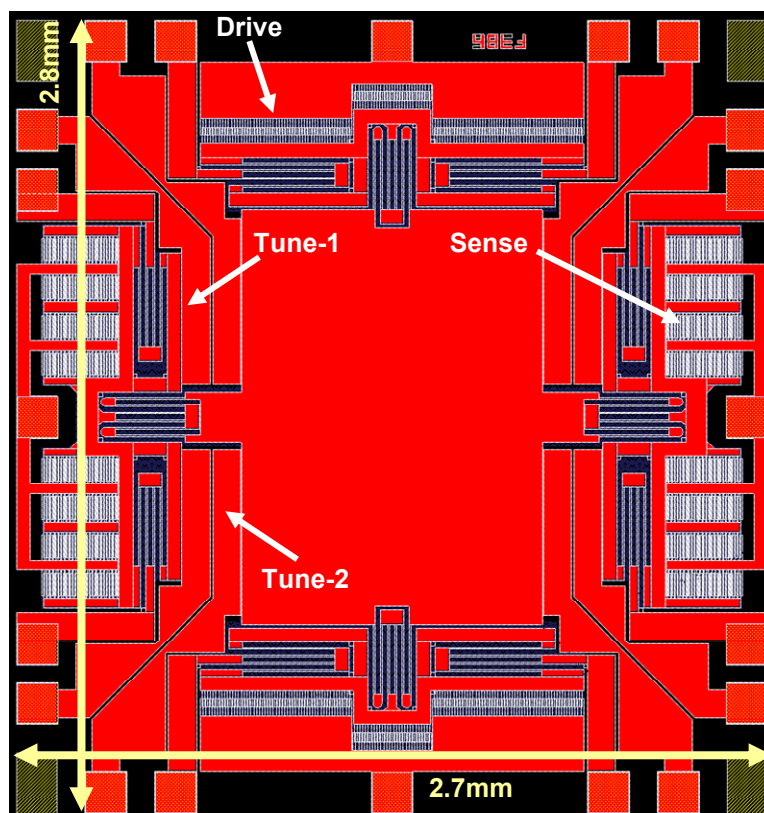
Figure 3.14: The layout of the designed ARS-SOI improved symmetrical and decoupled gyroscope prototype.

Tables 3.7 and 3.8 provide the features of the electrodes of ARS-SOI and the mechanical design parameters, respectively. Figure 3.15 shows the scanning electron microscope (SEM) photographs of the ARS-SOI improved symmetrical and decoupled gyroscope prototype fabricated in SOIMUMPs, showing the varying-gap

type sense and tuning electrodes, folded flexures, and close-up view of varying-overlap-area type linear combs of the drive mode electrode.

Table 3.7: Structural dimensions and electrical parameters for the electrodes (including electrostatic fringe-field corrections) of the designed ARS-SOI prototype.

Electrode	Parameter	Value
DRIVE	# of combs	111 x 2
	Capacitance, (fF)	1036 x 2
	$\partial C/\partial x$, (F/m)	$(2.58) \times 10^{-8}$ x 2
	$K_E = (\partial^2 C/\partial x^2) \times V^2$, (N/m)	0
SENSE	# of combs	144 x 2
	Capacitance, (fF)	1792 x 2
	$\partial C/\partial x$, (F/m)	$(6.72) \times 10^{-7}$ x 2
	$K_E = (\partial^2 C/\partial x^2) \times V^2$, (N/m)	$0.320 \times V^2$ x 2
TUNE-1	# of combs	1 x 4
	Capacitance, (fF)	71 x 4
	$\partial C/\partial x$, (F/m)	$(2.68) \times 10^{-8}$ x 4
	$K_E = (\partial^2 C/\partial x^2) \times V^2$, (N/m)	$0.013 \times V^2$ x 4
TUNE-2	# of combs	1 x 4
	Capacitance, (fF)	91 x 4
	$\partial C/\partial x$, (F/m)	$(3.41) \times 10^{-8}$ x 4
	$K_E = (\partial^2 C/\partial x^2) \times V^2$, (N/m)	$0.016 \times V^2$ x 4

Table 3.8: The design parameters for the ARS-SOI gyroscope prototype.

Parameter	Value
M_{PM}, kg	$(0.95) \times 10^{-7}$
M_{DE}, kg	$(0.119) \times 10^{-7}$
M_{SE}, kg	$(0.16) \times 10^{-7}$
M_{D_Total}, kg	$(1.188) \times 10^{-7}$
M_{S_Total}, kg	$(1.27) \times 10^{-7}$
K_{inner}, N/m	60
K_{D_outer}, N/m	78
K_{D_Total}, N/m	138
F_D, Hz	5424
K_{S_On} for $F_D = F_S$, N/m	148
$K_{S\_On} - K_{inner}$, N/m	88
$K_{S\_E} + K_{T\_E}$, N/m	$-37.0@7.3^V$
K_{S_Outer}, N/m	125
$K_{S\_Total\_Mech}$, N/m	185
F_{S_Mech}, Hz	6074
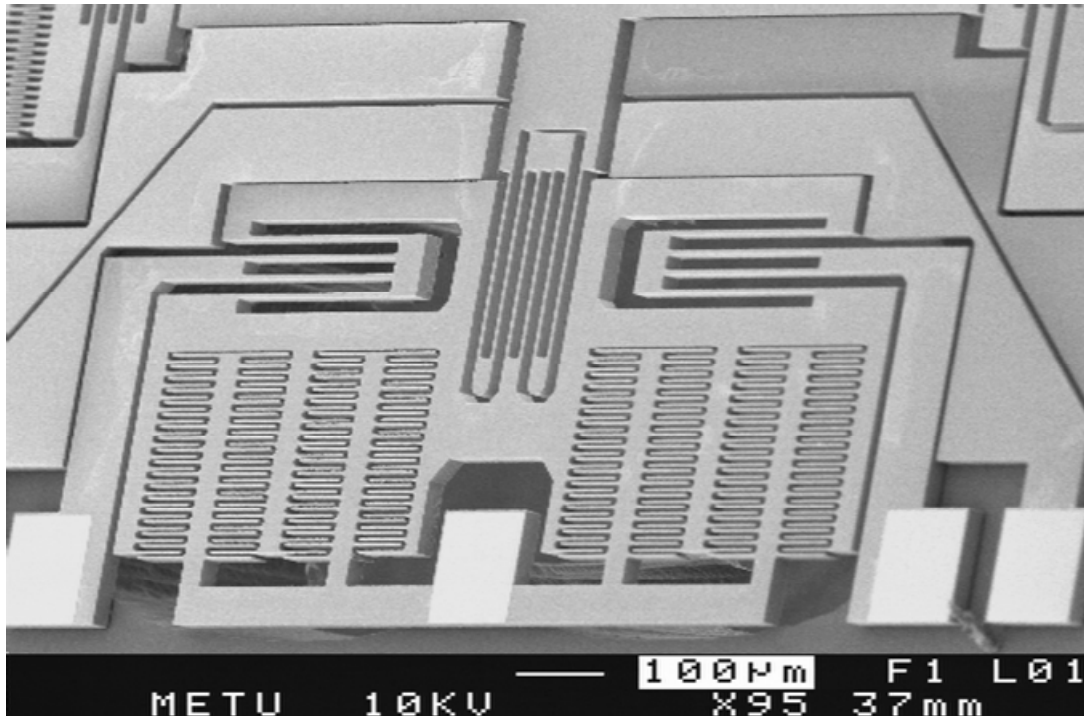
(a)
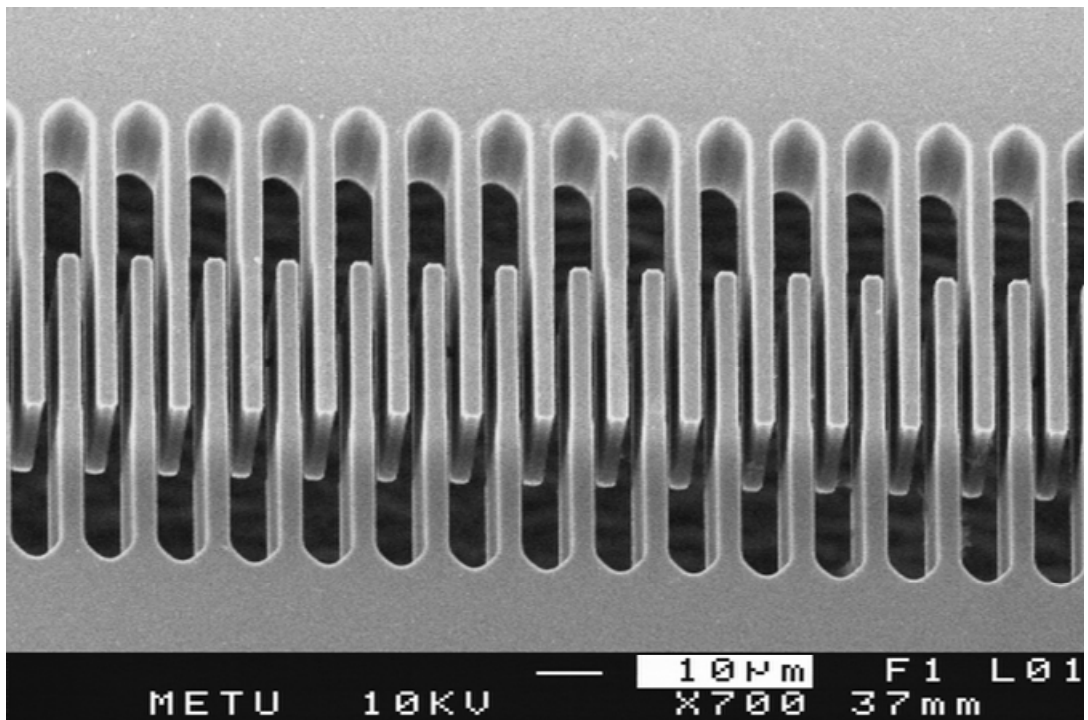
(b)

Figure 3.15: SEM photographs of the ARS-SOI improved symmetrical and decoupled gyroscope prototype fabricated in SOIMUMPs, showing (a) the varying-gap type sense and tuning electrodes and (b) close-up view of varying-overlap-area type linear combs of the drive mode electrode, which has a thickness of 25μm and capacitive gaps of about 2.5m, yielding an aspect ratio of 10.

144

The trench opening under the suspended regions is clear in the SEMs of Figure 3.15. The height of the structural layer of the gyroscope is 25μm, limited by the thickness of the epitaxial silicon on the SOI wafer. The electrostatic gap between the fabricated comb fingers is measured to be about 2.6μm, due to lithography tolerances and initial etch undercut of DRIE. No significant residual stress or stress gradient effects are observed in the fabricated prototypes.

Two different mask designs are submitted to SOIMUMPS process throughout this research. The process-related problems experienced in the first run are minimized by modifications in the second layout design. The fabricated SOI gyroscope prototype demonstrated remarkable performance, as presented in Chapters 5 and 7.

3.4 Silicon-On-Glass (SOG) Micromachining

Silicon-on-glass micromachining is based on fabricating microstructures defined by thorough-etching of a thin silicon substrate anodically-bonded to a machined glass substrate [34, 104]. Thorough-etching of the silicon substrate is performed by DRIE, for which aspect ratios higher than 30 are reported [104]. The SOG micromachining process is appropriate for the fabrication of very-thick and high-aspect-ratio silicon microstructures on low-loss insulating glass substrates, yielding highly-sensitive capacitive inertial sensors with low mechanical-thermal noise and small parasitic capacitances. Section 3.4.1 presents an overview of the three different SOG micromachining processes studied within this research. Section 3.4.2 presents the gyroscope prototype, fabricated using the advanced SOG process, together with the technical specifications in the sensor level.

3.4.1 Overview of the SOG Processes using DRIE

Three different SOG processes are developed using DRIE, an advanced dry silicon etching technology using inductively coupled plasma and patented by Bosch. The process allows deep and anisotropic silicon etching, by switched etching and passivation cycles. Figure 3.16 describes the method for anisotropic silicon etching

using DRIE. The method relies on the successive passivation coating and silicon etching steps. A thin passivation layer is coated on the whole surface following each etch cycle. The passivation on the surface exposed to the ion bombardment is removed in the next etch cycle; while the passivation on the sidewalls protect lateral etching, resulting in highly anisotropic etch profile with a small sidewall roughness.
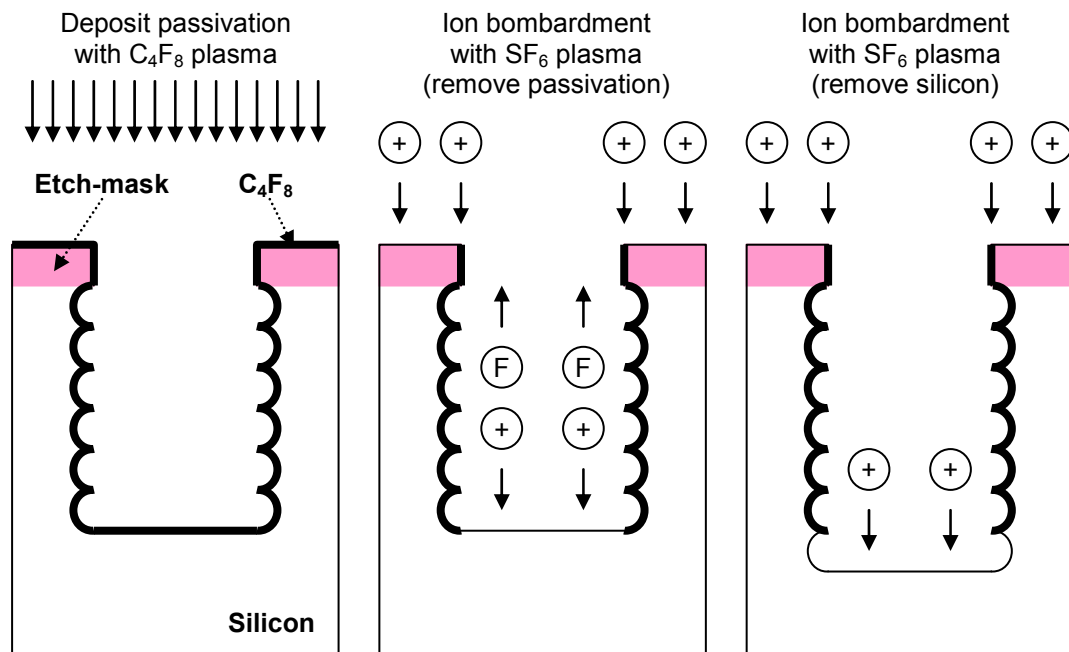
Figure 3.16: Illustration of the method for anisotropic silicon etching using DRIE. Process consists of a passivation cycle (left), followed by an etch cycle (middle and right). The exposed passivation layer is removed at the beginning of the etch (middle) and then silicon is etched (right).

Figure 3.17 illustrates the first SOG process developed in this research, using only 2-mask steps for pad metallization and structural layer formation. The process starts with anodic bonding of a 500μm-thick, 4-inch, blank Corning 7740 Pyrex glass substrate to a 100μm-thick, highly-conductive (Resistivity<0.005ohm.cm), (111)-oriented, 4-inch, p-type, blank silicon substrate, after cleaning the substrates in 1:1 H_2SO_4:H_2O_2 (piranha) solution for 30min. The bonding is performed at 400°C and by applying 1000V across the silicon and the glass substrates. Next, 300Å/3000Å-thick Cr/Au layer is evaporated on the silicon surface and patterned using lift-off, forming the pad metallization. After that, Shipley's SPR220-3 photoresist is spin-coated on the silicon surface, at a thickness of 3.3μm, and patterned using the structural layer mask. After hardbaking the patterned photoresist

at 80°C in convection oven for a period of 15hours, the thorough etching of the silicon substrate is performed using DRIE. Once the etching is completed, the glass substrate is wet etched using %48 HF for 8 minutes, reaching to a depth of approximately 40μm. The isotropic nature of the glass etching allows the release of narrow structures by the etch undercut, while the large-area anchors are still remain bonded to the glass substrate, holding the released features. After removing the DRIE etch mask and the plasma polymer in piranha solution, the structures are released through standard alcohol rinse and drying.

(a) Silicon-glass anodic bonding

(b) Pattern Cr/Au pad metallization

(c) Pattern DRIE etch-mask
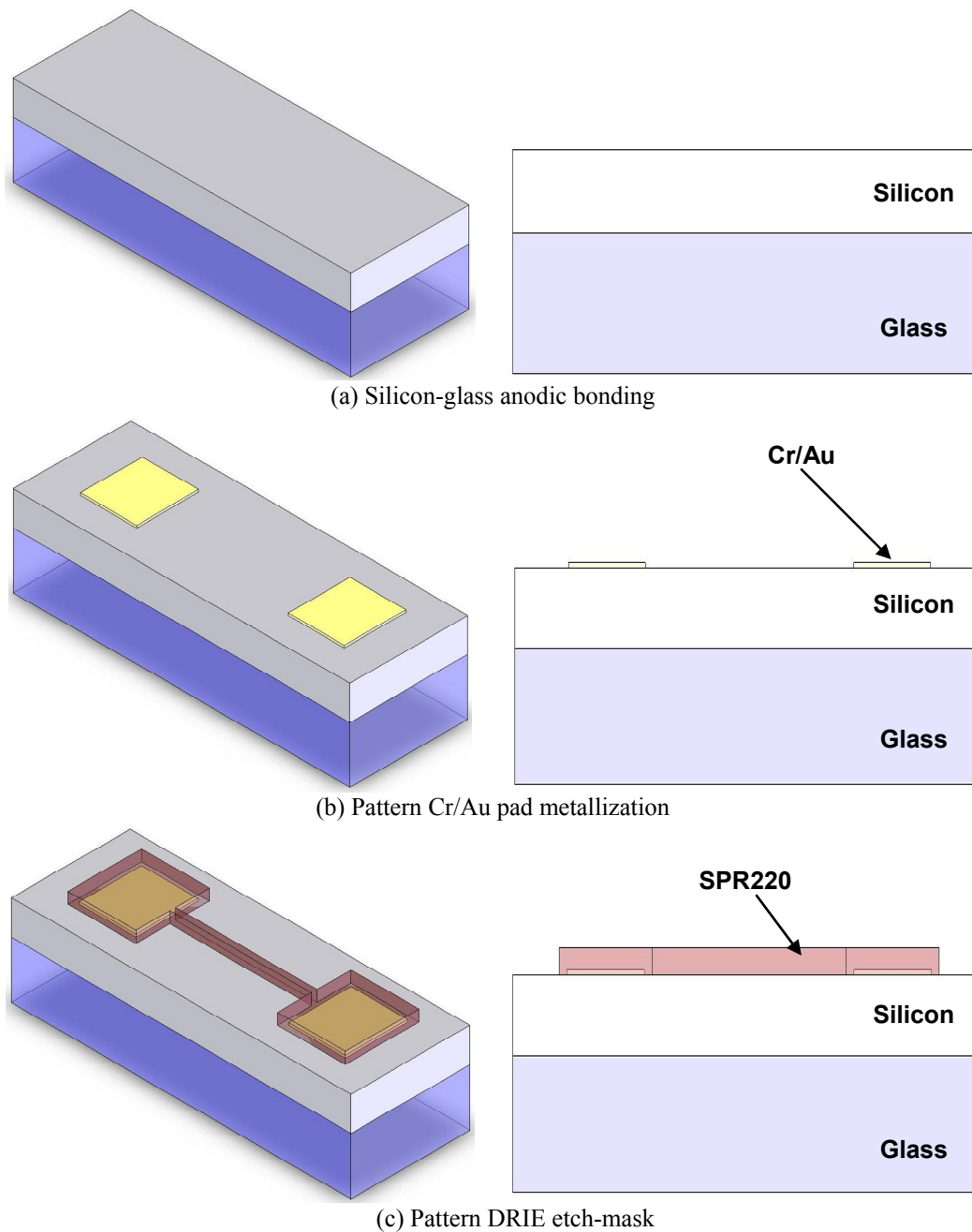
Figure 3.17: The simple 2-mask SOG process flow (cont. next page).
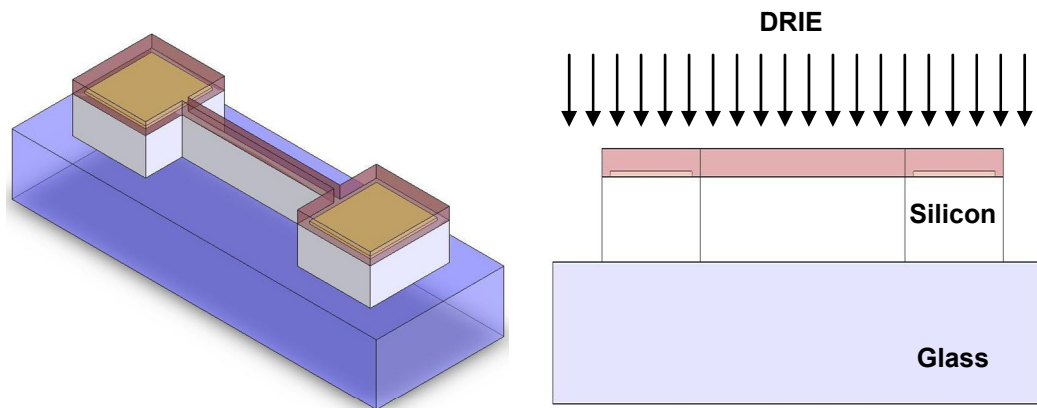
(d) Thorough DRIE etch of silicon substrate until reaching to glass substrate
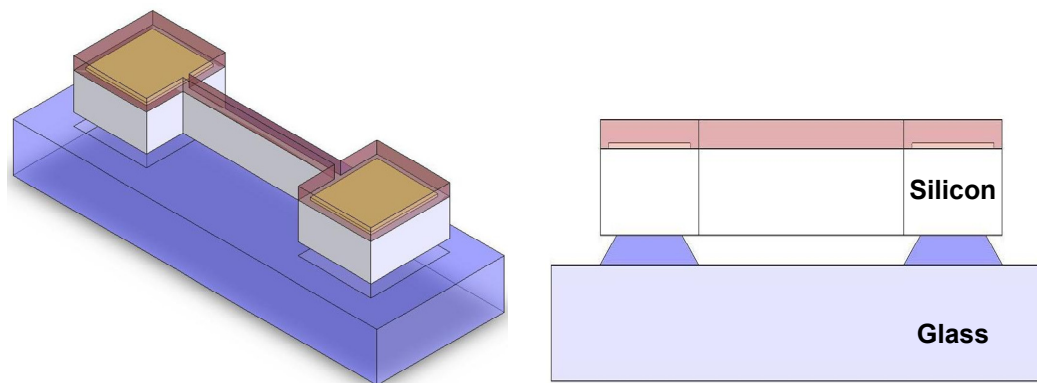
(e) Isotropic glass-etch for releasing the structures
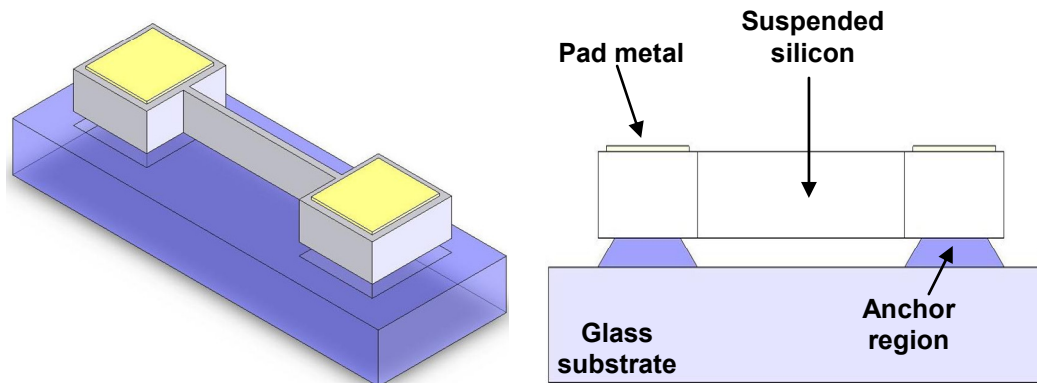
(f) Remove DRIE etch-mask and clean the samples

Figure 3.17: The simple 2-mask SOG process flow (The drawings are not to scale).

The process is quite simple, requiring no tricky processing steps, except the pre-process cleaning of the fragile silicon substrates prior to bonding. Only two masks are necessary for the pad metallization and the structural layer definition. The anchors of the structures are formed by using the patterned silicon as a mask for the glass etching, resulting in self-aligned anchors. The release of the structures

depends on the glass etch undercut, and therefore, the structures to be released must be arranged in such way that the maximum width should not exceed the etch undercut, otherwise structure would remain bonded to the glass substrate. This is achieved by implementing large etch holes on the structures, allowing the diffusion of the etchant through the silicon and removing the glass below the silicon trusses surrounding them.

The problems of microloading and aspect-ratio-dependent etching (ARDE) are encountered in the simple SOG process described above [105], during DRIE of silicon. Microloading refers to the fast etch rate for an isolated trench compared to the etch rate for a dense array composed of similar trenches. Secondly, ARDE effect refers to the fast etch rate for a wide trench compared to the etch rate for a narrow trench. Figure 3.18 illustrates the cross-section of a sample DRIE etch profile, showing the effect of etch rate variation for different-size trench-openings. The effect of the etch-rate-variation becomes apparent for the through etching of a silicon layer located on top of an insulating base. The ions passing through an etched cavity and reaching to the base cause charging of the insulator surface, which can increase the charged potential to several tens of volts [106-108]. The ions are then deflected from the charged insulator surface from the sidewalls, destroying the etch-anisotropy at the bottom of the trench. This effect is called SOI notching, and causes significant destruction of the etched microstructures. In summary, the features surrounded with large trench openings are subject to damage due to notching, while waiting for the completion of the etch of the features surrounded by narrow trench openings. Figure 3.19 describes the mechanism of SOI notch and shows the resulting destruction at the bottom of a comb electrode array, a flexure beam, and an etch hole.

The advanced-silicon-etch (ASE^{TM}) process of the Multiplex ICP-HRM system manufactured by Surface Technology Systems Inc. is used for DRIE of silicon. The system is equipped with a low-frequency platen power supply option for reducing SOI notch, known to be effective for standard SOI wafers. The gyroscope mask layout contains trench openings up to 50μm requiring an over-etch period of more

149

than 50% for the features close to these trenches, in order to complete the etching of the 4µm minimum trenches. This large variation in the trench size combined with the thickness of the glass substrate resulted that the SOI option of the etch tool being insufficient for reducing SOI notch in the through silicon etching of the 500µm/100µm glass/silicon stack.
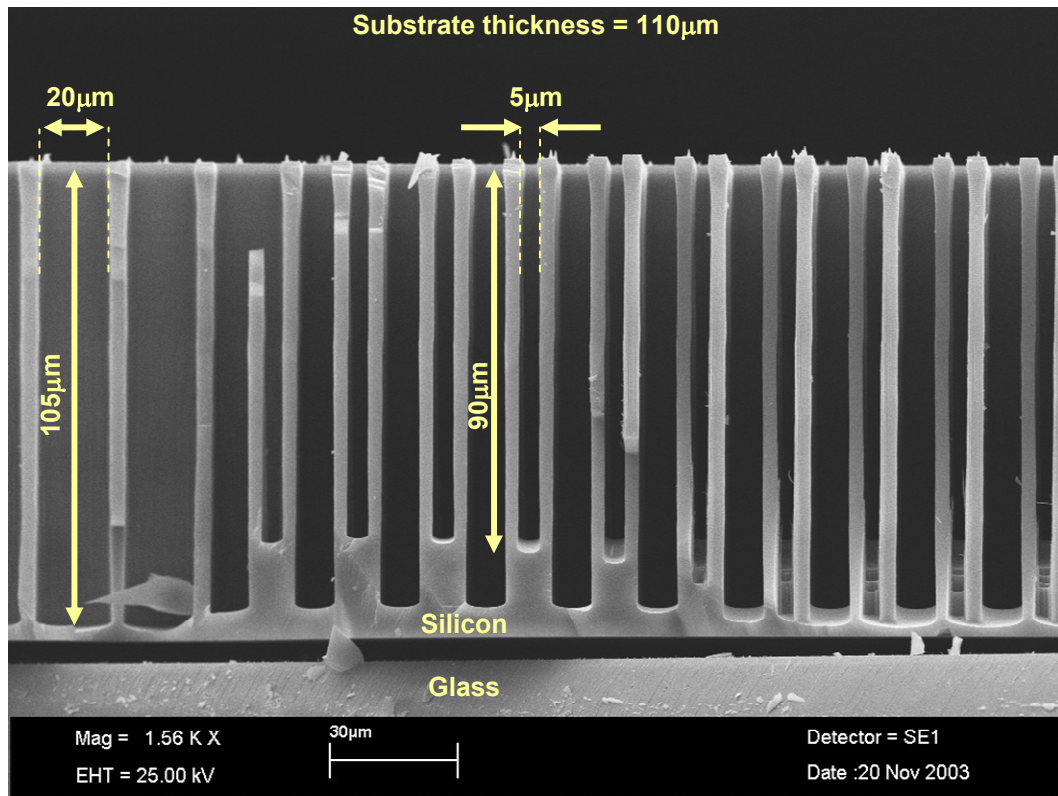
Figure 3.18: Cross section of a sample DRIE etch profile, showing the effect of etch rate variation for different-size trench-openings (aspect-ratio-dependent etching, ARDE).

The gyroscopes fabricated in the simple SOG process showed nonlinear resonance characteristics, reported in Chapter 5. For this reason, an improved SOG process flow is developed, using an additional metal shield layer laid on the glass substrate for preventing notching [109]. Figure 3.20 describes the cancellation of SOI notch using a metal shield laid on the glass substrate under suspended silicon. The metal shield used in the improved SOG process lay on the glass substrate under the suspended silicon structures. The shield is extended inside the anchor regions in order to electrically-short the metal shield to the silicon. This way, the charging of the insulating glass surface by ions passing through the fast-etched trenches is

prevented. The ions are collected by the metal shield, which is electrically short to the silicon substrate, causing no significant damage to the etched silicon during long over-etch periods.

(a)

(b)
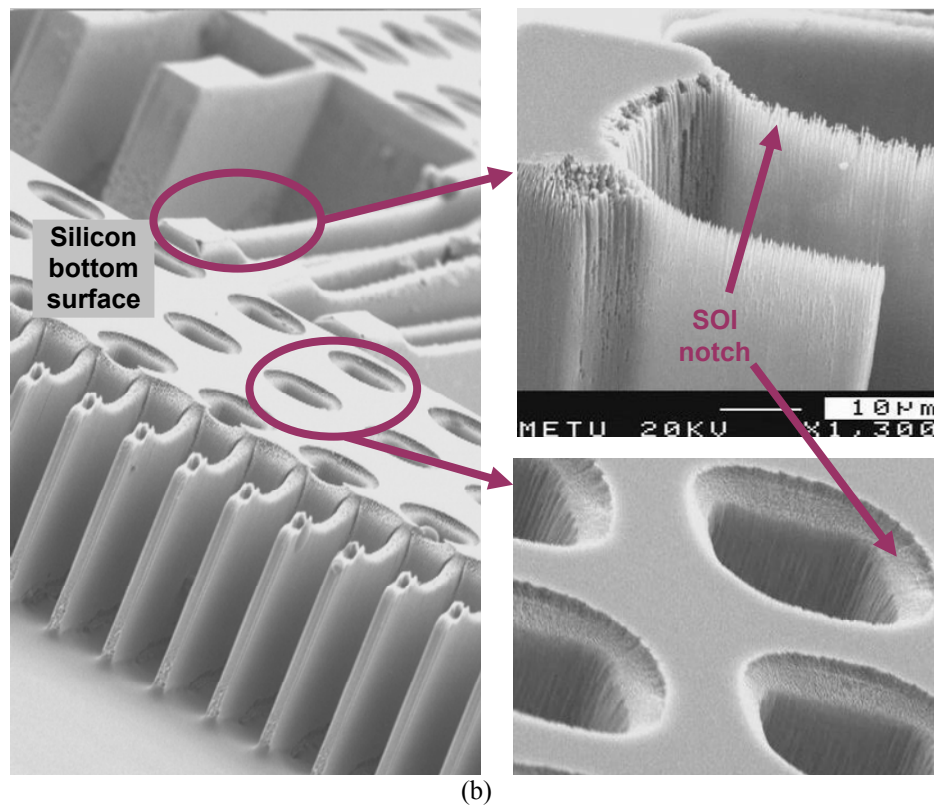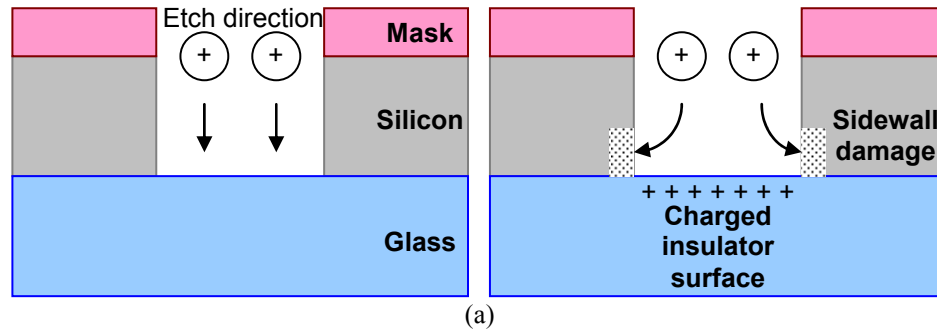
Figure 3.19: (a) Sidewall damage (SOI-notch) as a result of the destruction of directionality of SF6 ions due to the charged insulator surface. (b) The resulting destruction at the bottom of a comb electrode array, a flexure beam, and a rectangular etch hole.

Figure 3.21 illustrates the process flow for the improved SOG process. The process requires 4 masks for anchor formation, shield formation, pad metallization, and structural layer formation. The process starts with machining of the 500μm-thick, 4-inch, blank Corning 7740 Pyrex glass substrate, forming the 5μm-deep anchor

regions as described in the process flow of DWSM process. Next, 300Å/3000Å-thick Cr/Au layer is evaporated on the glass surface inside a 1500Å-deep shallow trench formerly developed by 5 minute etching of the glass surface in buffered-HF, using the lift-off pattern. The Cr/Au metal shield is then developed by lift-off, completing the machining of the glass substrate. Next, the machined glass substrate is anodically bonded to a 100µm-thick, 4-inch, highly-conductive, (111)-oriented p-type blank silicon substrate. The remaining processing of the silicon is identical to that of the simple SOG process, described above. After the completion of DRIE, the metal shield is removed by wet etching of Au and Cr layers in selective etchants. The DRIE etch mask protects the Cr/Au pad metallization during this etch. Finally, the DRIE etch mask is removed and structures are released after cleaning the plasma polymer residues in piranha etchant.
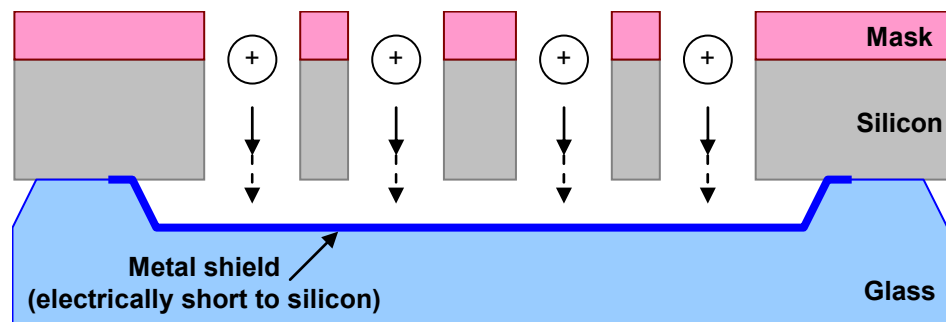
Figure 3.20: Cancellation of SOI notch using a metal shield laid on the glass substrate under suspended silicon. Glass surface is not charged and therefore the directionality of ion bombardment does not change.
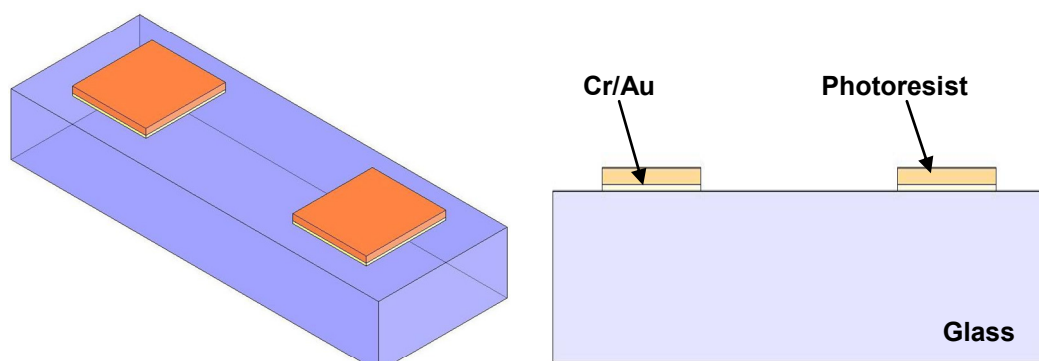
(a) Pattern Cr/Au/PR etch-mask for glass wet etch

Figure 3.21: Improved silicon-on-glass process flow with metal shield (cont. next page).
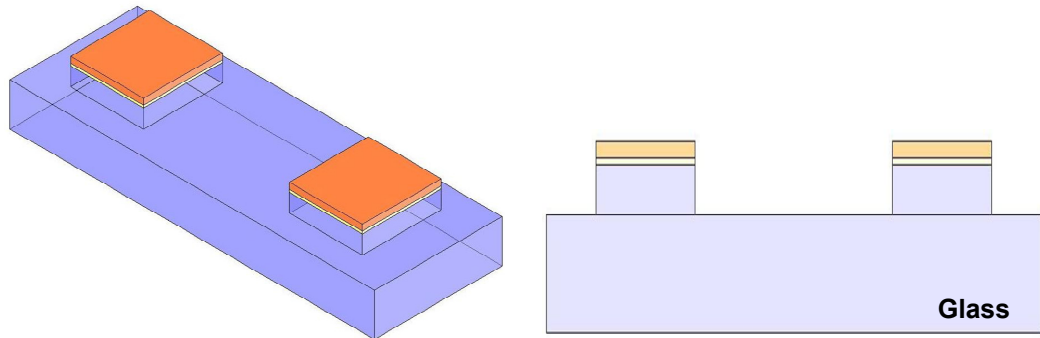
(b) Wet chemical etch of the glass substrate (etch-undercut not shown)
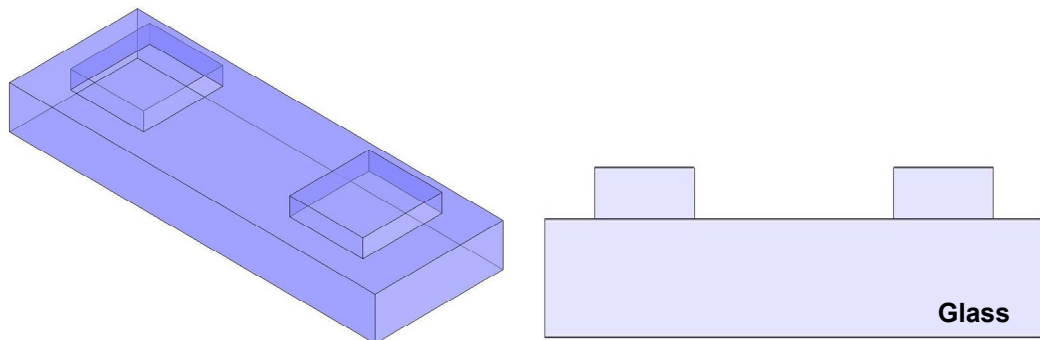
(c) Strip the etch-mask
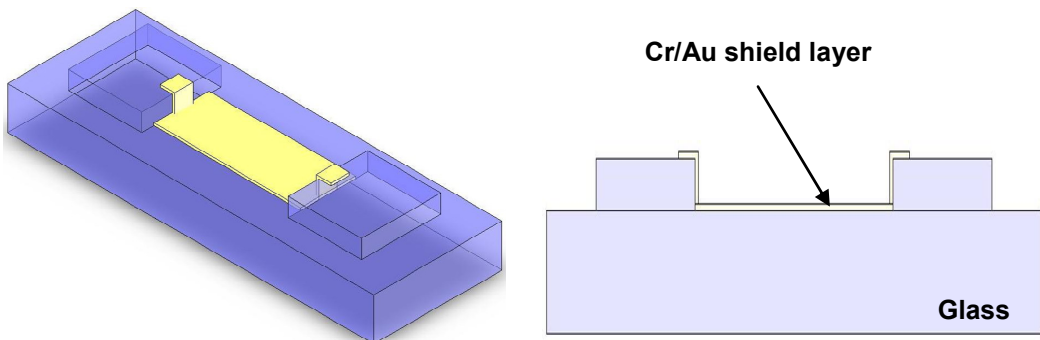
(d) Pattern Cr/Au shield layer metallization covering suspended structure areas
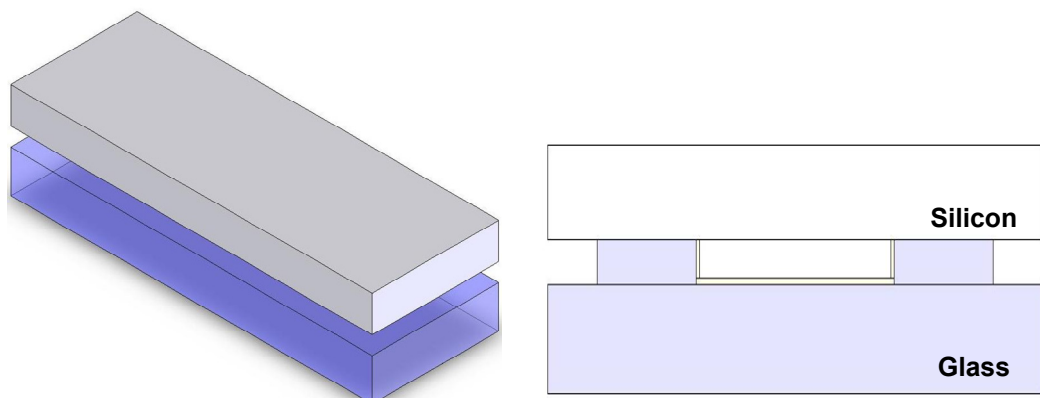
(e) Anodically bond the blank silicon substrate to the machined glass substrate

Figure 3.21: Improved silicon-on-glass process flow with metal shield (cont. next page).
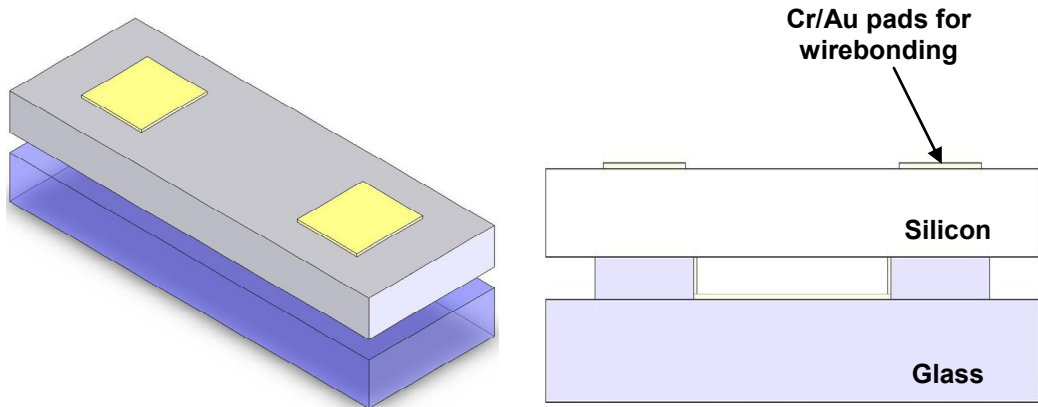
(f) Pattern Cr/Au pad metallization
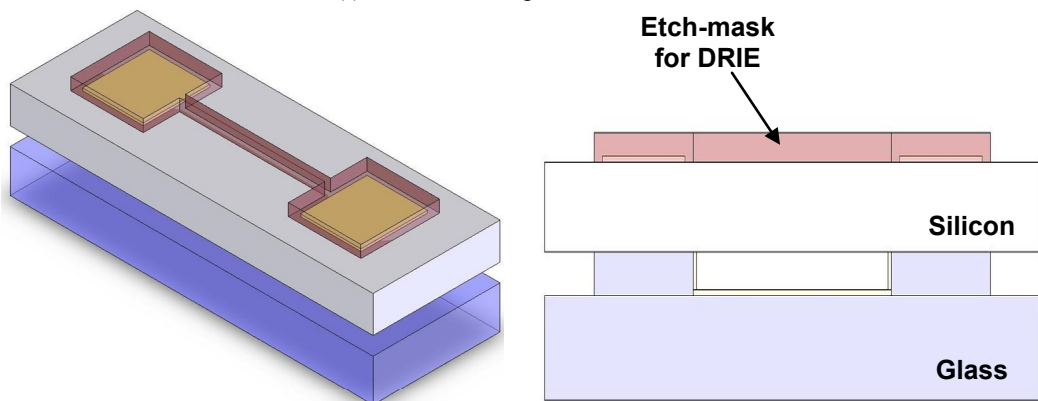
(g) Coat and pattern etch-mask for DRIE
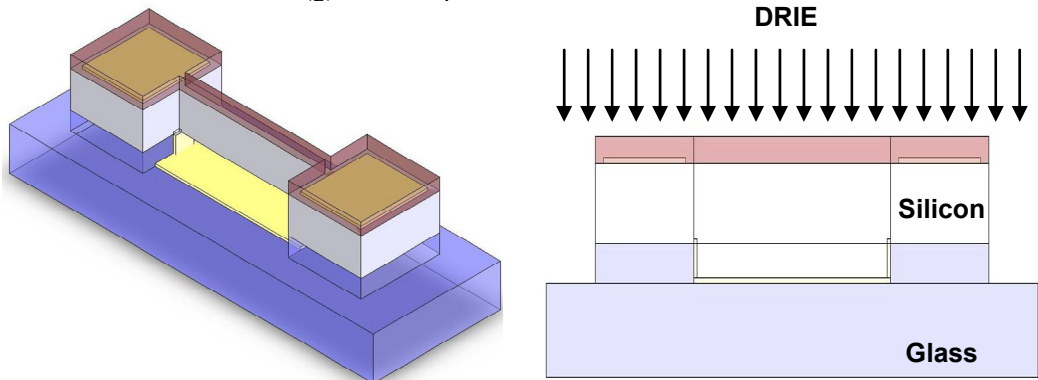
(h) Thorough DRIE etch of the silicon substrate
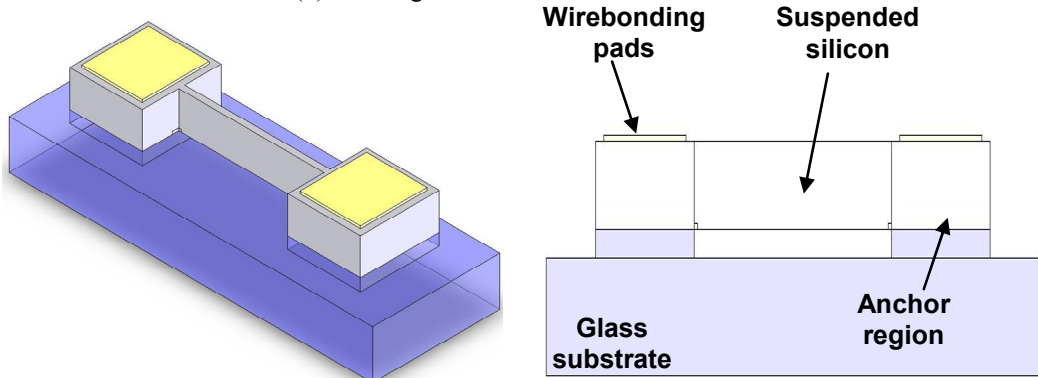
(i) Etch the shield metallization while protecting pad metallization with DRIE etch-mask,
then strip DRIE etch-mask and release the structures

Figure 3.21: Improved silicon-on-glass process flow with metal shield (Not to scale).

Figure 3.22 shows the SEM pictures of a comb electrode array of a gyroscope fabricated with the improved SOG process, showing the improvement achieved using the metal shield layer. Though the improved SOG process is satisfactory in removing SOI notch effects, it suffers from the insufficient cooling of the silicon layer during the long etch period and the release of the structures during DRIE. The smaller contact area between the silicon substrate and the handling glass substrates reduce the heat sink effect around narrow features, resulting in erosion of the photoresist etch-mask and damaging the sidewalls of narrow features. In addition, the structures are partially released during DRIE and are free-to-move before the completion of the etch, which are subject to destruction due to charging-based-displacement of electrically-isolated silicon parts. Figure 3.23 shows the SEM picture showing the results of the sidewall destruction for a beam structure fabricated with the improved SOG process.
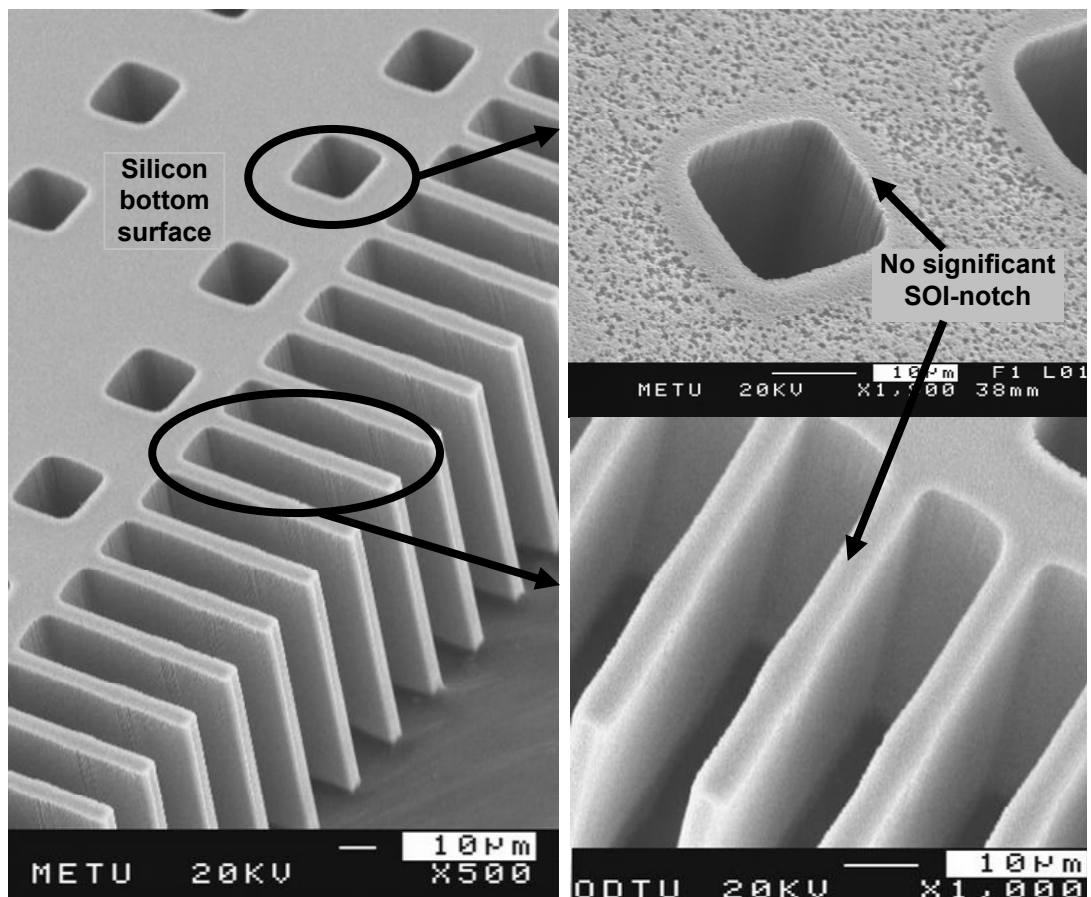
Figure 3.22: The improvement achieved using the metal shield layer under silicon, showing no significant SOI-notch-destruction at the bottom of a comb electrode array of a gyroscope fabricated with the improved SOG process.

155
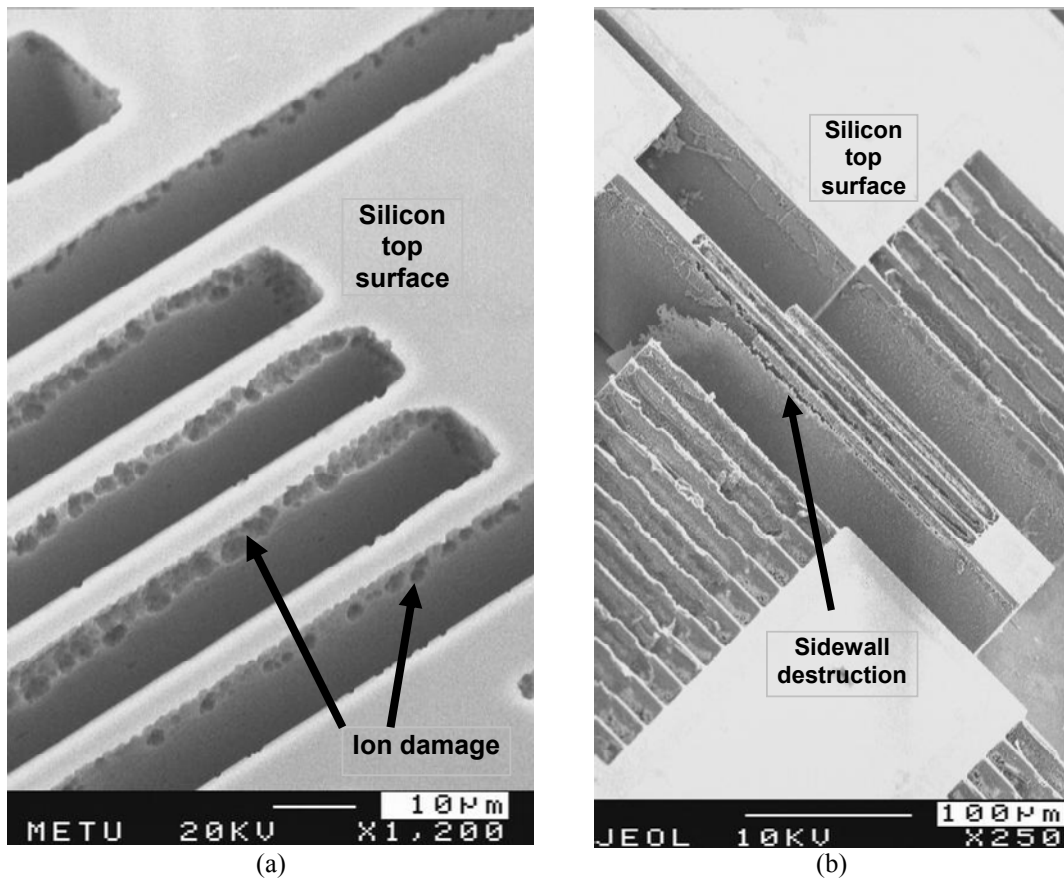
Figure 3.23: SEM pictures showing the problems associated with the overheating of the suspended structures in the improved SOG process. (a) Ion damage at the edges due to reduced mask selectivity. (b) Sidewall destruction.

The sidewall destruction problem in the improved SOG process is eliminated by using an advanced SOG process, for which the metal shield is laid directly at the bottom surface of the silicon substrate instead of the glass surface [110], which acts as a heat sink as well as prevents releasing of the structures during DRIE. Figure 3.24 describes the advantage of the SOG process with metal etch-stop layer.
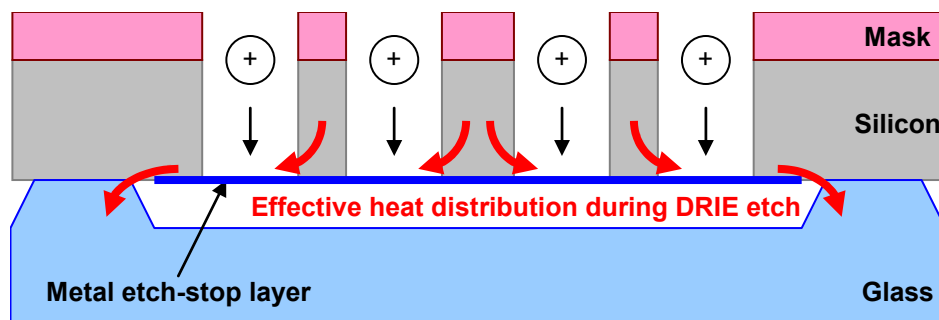
Figure 3.24: Advanced SOG process using a metal-etch-stop layer to prevent SOI-notch and silicon-overheating problems at the same time.

156

Figure 3.25 illustrates the process flow for the advanced SOG process with metal etch-stop layer. The process requires 4 masks, similar to the improved SOG process described above. The advanced SOG process starts with machining of the 500μm-thick, 4-inch, blank Corning 7740 Pyrex glass substrate, forming the anchor regions identical to the ones in the SOG process, except the anchor depth is set to higher than 10μm in order to prevent possible electrical sparks from the glass substrate to the silicon during anodic bonding. Next, 300Å/3000Å-thick Cr/Au layer is evaporated on 100μm-thick, 4-inch, highly-conductive, (111)-oriented, p-type blank silicon substrate and patterned using selective wet etching of Cr and Au, defining the metal shield layer. Then, the machined silicon and glass substrates are aligned and anodically bonded to each other at 300°C, in order to prevent diffusion of the gold shield layer into the silicon. Following the bonding process, the silicon wafer is thoroughly etched until the metal etch-stop layer is reached from the narrowest trench openings in the structural layer mask. Finally, the shield layer is removed by protecting the pad metallization; the structures are cleaned in piranha solution, and released using standard alcohol rinse and dry steps.
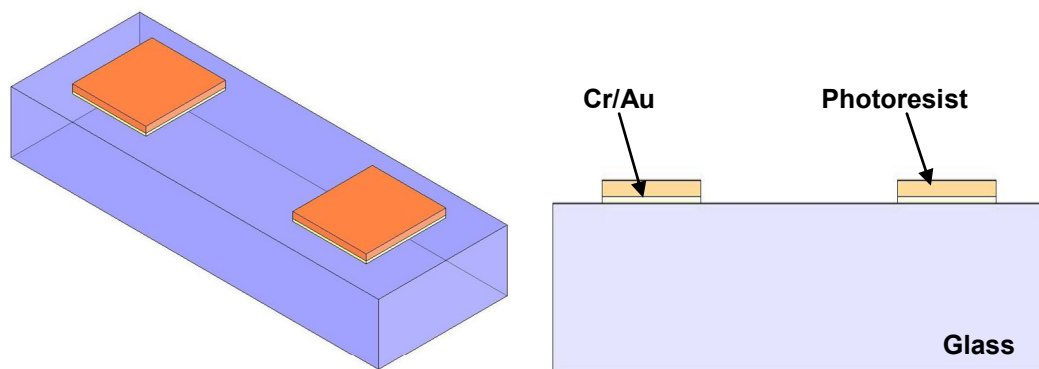
(a) Pattern Cr/Au/PR etch-mask on a blank glass substrate, for glass wet etch
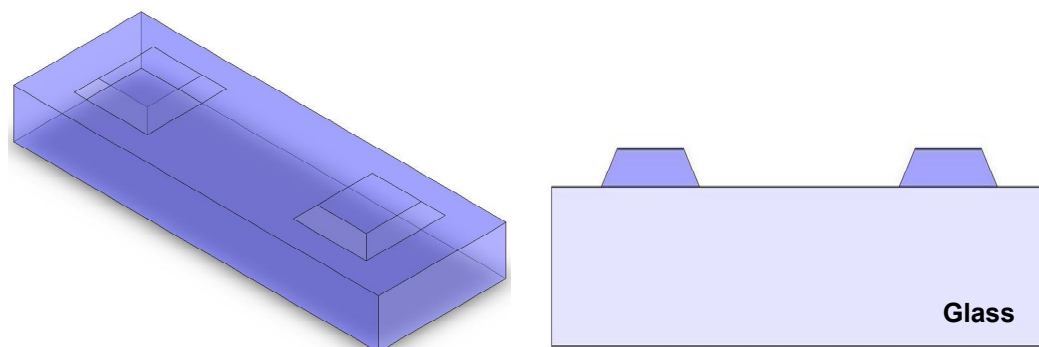
(b) Wet chemical etch of the glass substrate and strip the etch-mask

Figure 3.25: Advanced SOG process flow with metal etch-stop (cont. next page).
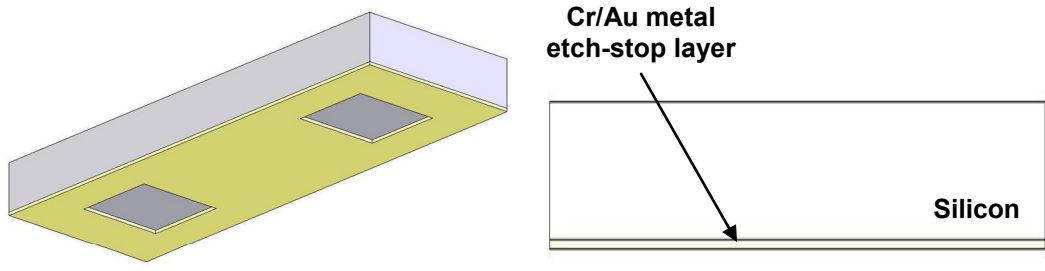
(c) Coat Cr/Au at the bottom surface of the silicon substrate as an etch-stop layer for DRIE.
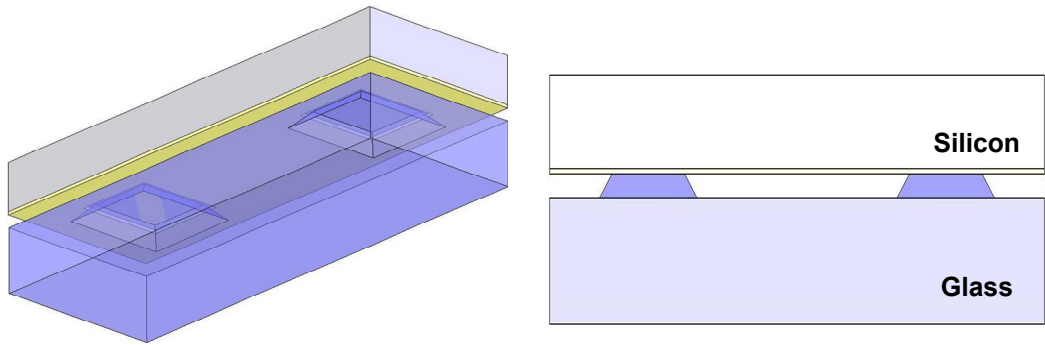
(d) Anodically bond the machined glass and the silicon substrates.
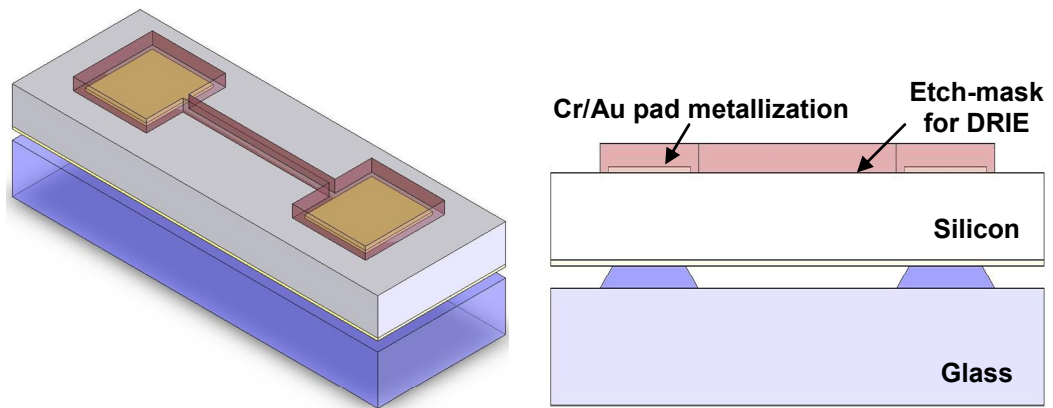
(e) Coat and pattern Cr/Au pad metallization and then the etch-mask for DRIE.
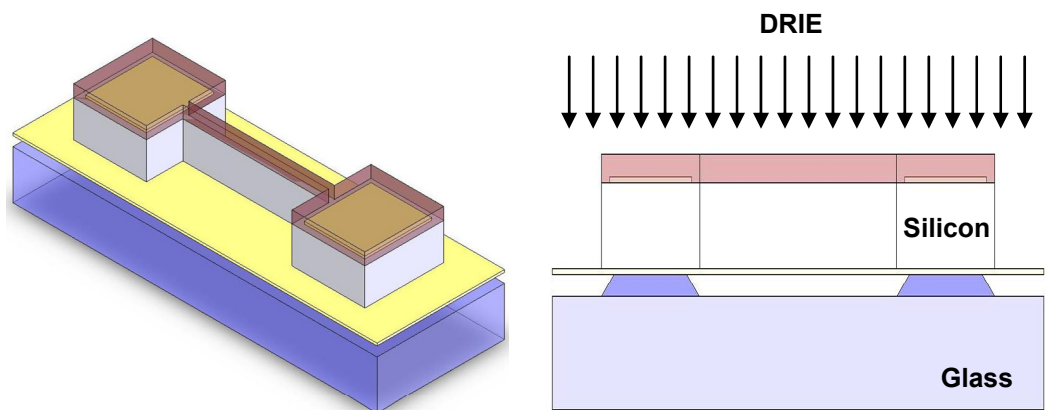
(f) Thorough DRIE etch of the silicon substrate until the metal etch-stop layer.

Figure 3.25: Advanced SOG process flow with metal etch-stop (cont. next page).
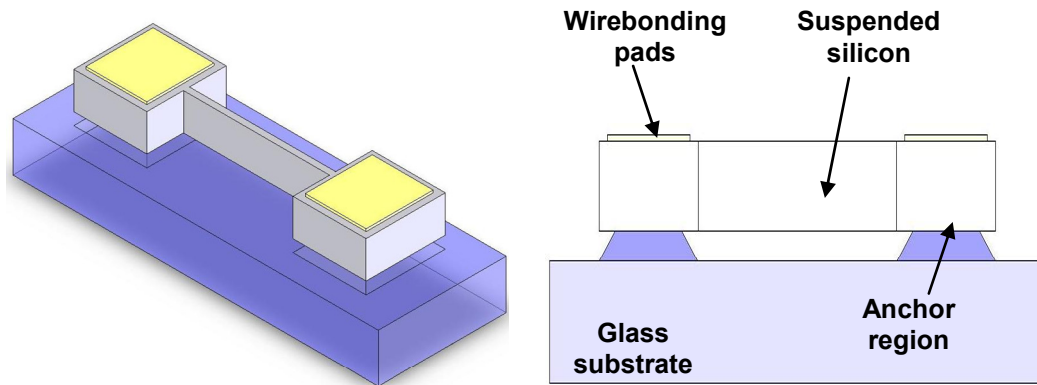
(g) Remove the metal etch-stop layer while protecting pad metallization with DRIE etch-mask, then strip DRIE etch-mask and release the structures

Figure 3.25: Advanced SOG process flow with metal etch-stop (Not to scale).

Figure 3.26 shows the SEM pictures of microstructures fabricated with the advanced SOG process with metal etch-stop layer, demonstrating (a) no damage due to SOI notch at the bottom surface of the etched silicon around a comb electrode array, flexure, and circular etch holes (b) no significant ion damage at the top surface of the etched silicon around a comb finger array.
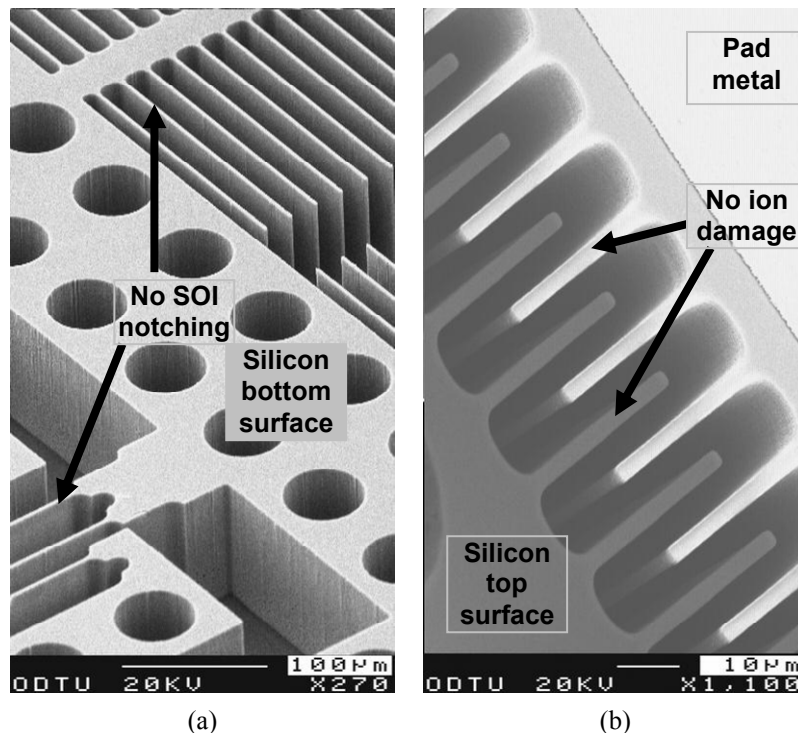
Figure 3.26: SEM pictures of microstructures fabricated with the advanced SOG process with metal etch-stop layer, demonstrating (a) no damage due to SOI notch at the bottom surface of the etched silicon around a comb electrode array, flexure, and circular etch holes (b) no significant ion damage at the top surface of the etched silicon around a comb finger array.

159

Among the three SOG processes studied, the advanced SOG process with metal etch-stop layer proved to be the best with the drawback of extreme handling requirements for the 100μm-thick fragile silicon substrates throughout several process steps. Beside this, the symmetrical and decoupled gyroscope prototypes fabricated with the advanced SOG process demonstrated the best performance among the prototypes fabricated with the other two SOG processes as well as the DWSM, NE, and SOI processes described in the previous sections.

3.4.2 SOG Angular Rate Sensor Prototype (ARS-SOG)

The fourth and the final prototype developed in this research is an advanced symmetrical and decoupled gyroscope, the structure of which is shown in Figure 1.15, fabricated with the developed SOG process with metal etch-stop layer. The basic difference of the advanced decoupled gyroscope structure from the previous designs is that it uses a single sense frame, by connecting the two movable sense electrodes of the previous designs with rigid trusses.

The fabricated gyroscope prototype is labeled as ARS-SOG, i.e., "**A**ngular **R**ate **S**ensor fabricated with **S**ilicon-**O**n-**G**lass micromachining process". Figure 3.27 shows the layout of the ARS-SOG, drawn in Cadence design environment. The gyroscope occupies an area of $3.6 \times 4.0 \text{mm}^2$ including the bonding pads, while the die size is about $4.2 \times 4.6 \text{mm}^2$. Clearly, the structure is not symmetric along the drive and the sense modes except the type of the flexures assigned to each mode, which is indeed the major factor in determining the dynamic characteristics along the drive and the sense modes. The use of a single and rigid movable sense-frame suppresses the double-frequency motion significantly, compared to the gyroscope with isolated dual sense-frames. Figure 3.28 shows the exaggerated visualization of the FEM simulation showing the maximum displacement of the sense-mode fingers is less than 500ppm of the drive-mode displacement. In addition, the separation between the resonance frequencies of the operational modes (the drive and the sense modes) and the higher-order modes is improved by increasing the rotational stiffness of the sense electrodes.

160
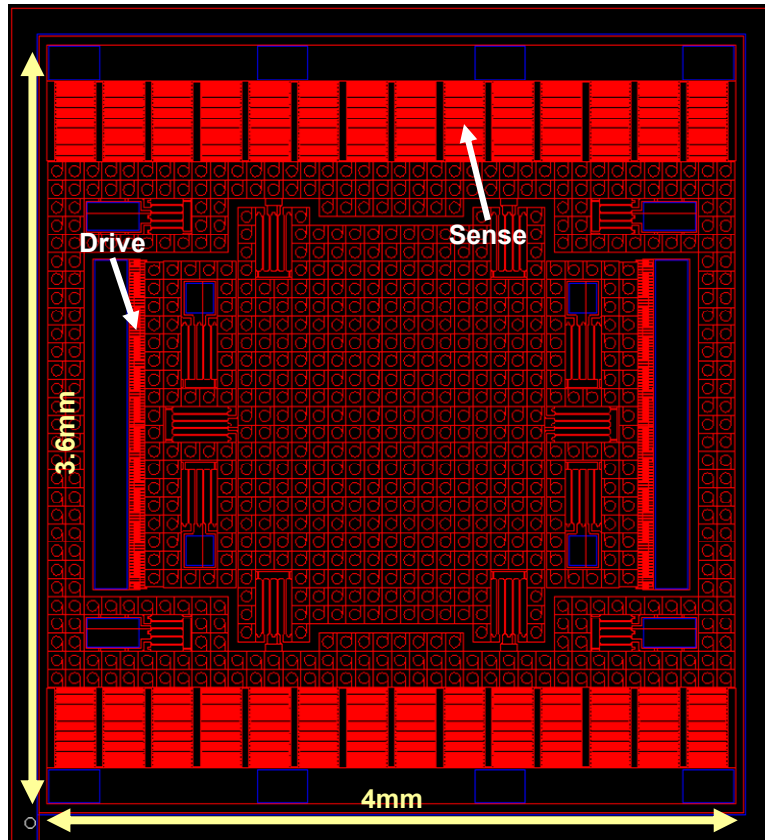
Figure 3.27: The layout of the designed ARS-SOG advanced decoupled gyroscope prototype.
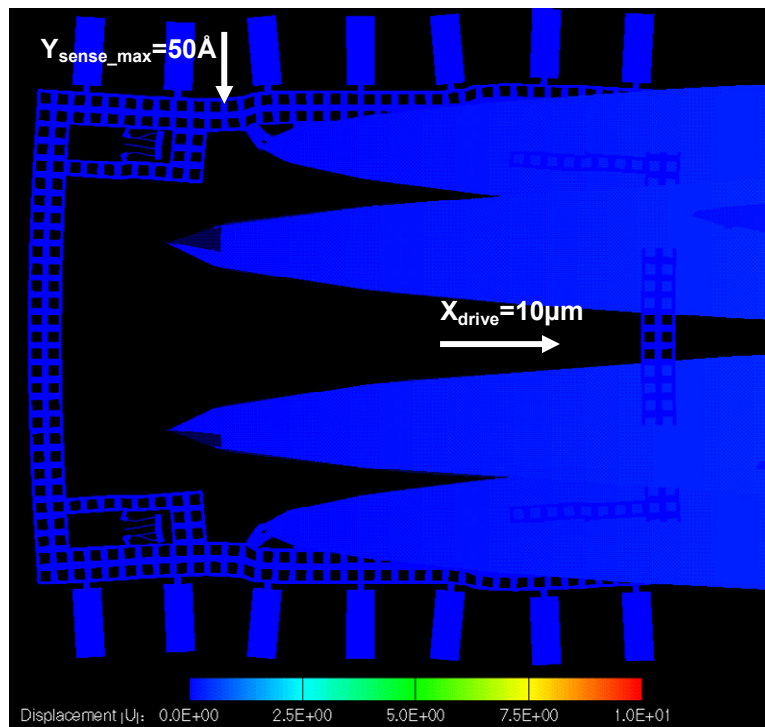
Figure 3.28: FEA performed on ARS-SOG showing the maximum displacement of the sense-mode fingers is less than 500ppm of the drive-mode displacement (10000 times exaggerated).

161

Figure 3.29 shows the first four mode shapes of the designed ARS-SOG prototype including the drive and the sense modes as well as two higher order modes, which have the potential for disturbing the operation in the case of any manufacturing flaws. Table 3.9 provides the resonance frequency associated with each mode. Obviously, the resonance frequencies of the dangerous higher-order modes are highly separated from that of the drive and the sense mode, ensuring a safe operation.

(a)

(b)

(c)

(d)
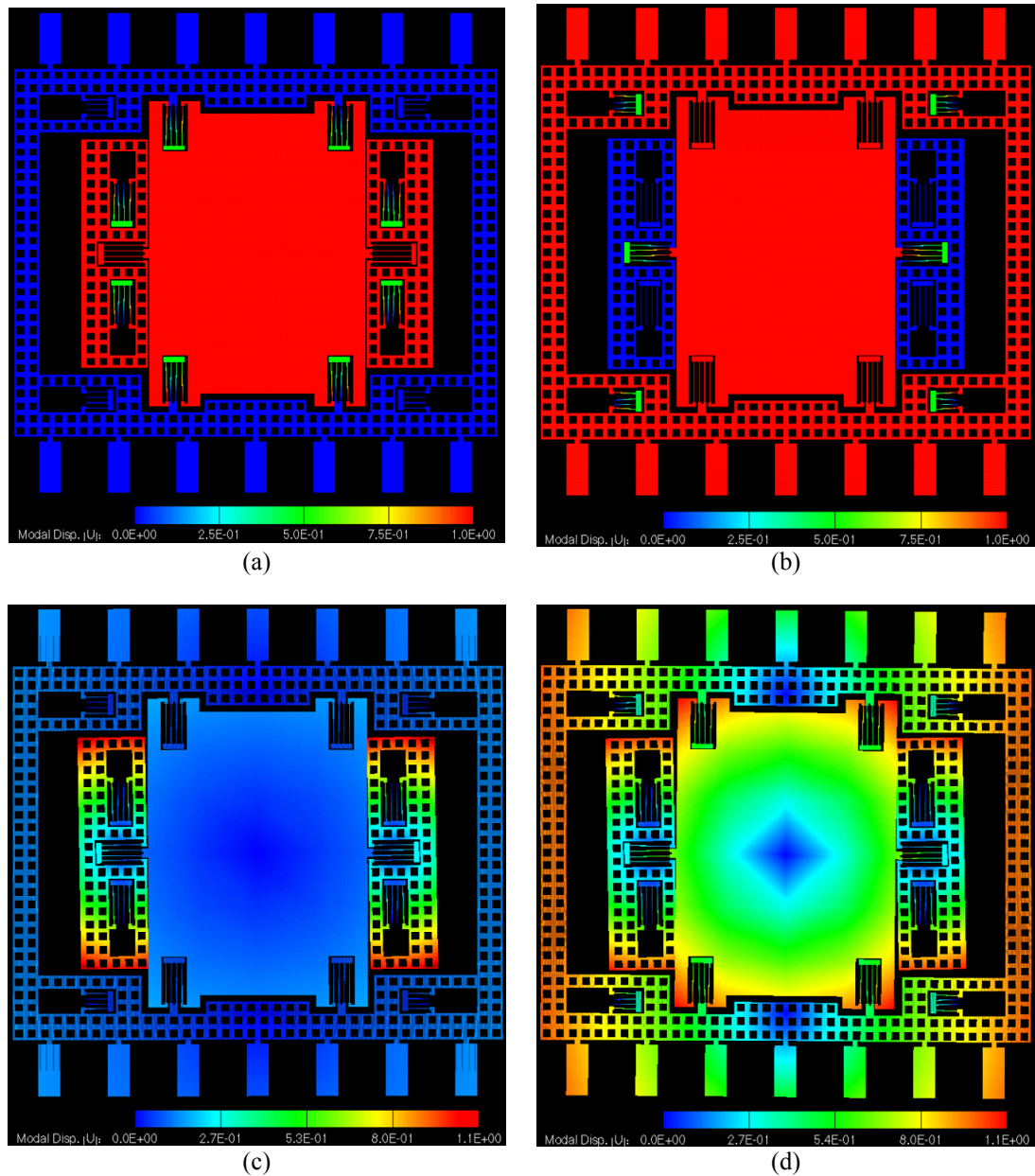
Figure 3.29: First four mode shapes of the designed ARS-SOG prototype. (a) Drive mode, (b) sense mode, (c) rotary mode of the drive-electrodes, and (d) rotary mode of the overall structure.

Table 3.9: Resonance frequency associated with the first four modes of ARS-SOG prototype. Note that the simulated structure in Figure 3.29 employs square etch-holes instead of the circular etch holes of the original design for simplifying the meshing of the model, which cause a slight difference between the simulated and the actual modal frequencies.

Mode	Generalized Mass (kg)	Resonance Frequency (Hz)
Drive	7.49×10^{-7}	5,328
Sense	1.26×10^{-6}	7,168
Rotary (drive-electrodes)	9.39×10^{-8}	20,155
Rotary	6.45×10^{-7}	22,436

ARS-SOG prototype has several other features compared with the ARS-DWSM, ARS-NE, and ARS-SOI prototypes. Dual-folded type beams are used as the inner flexures, instead of the triple-folded design for improved stiffness against axial displacements. Number of the sense fingers is maximized without increasing the footprint, by reducing the dead-zones in the previous prototype designs. The movable masses are perforated with circular etch holes with 60μm-diameter, for easy removal of the underlying metal shield layer at the end of the process. The gyroscope contains no special tuning electrodes except its electrostatic frequency tuning capability using the varying-gap type sense electrodes. Quadrature cancellation electrodes are neglected in the design due to high-immunity of the structure against mechanical quadrature. Also no separate force-feedback electrodes are employed, rather one of the two differential sense electrodes can be used for this purpose.

Tables 3.10 and 3.11 provide the features of the electrodes of ARS-SOG and the mechanical design parameters, respectively.

Table 3.10: Structural dimensions and electrical parameters for the electrodes (including electrostatic fringe-field corrections) of the designed ARS-SOG prototype.

Electrode	Parameter	Value
DRIVE	# of combs	99 x 2
	Capacitance, (fF)	1368 x 2
	$\partial C/\partial x$, (F/m)	$(3.69) \times 10^{-8}$ x 2
	$K_E = (\partial^2 C/\partial x^2) \times V^2$, (N/m)	0
SENSE	# of combs	252 x 2
	Capacitance, (fF)	12119 x 2
	$\partial C/\partial x$, (F/m)	$(1.95) \times 10^{-6}$ x 2
	$K_E = (\partial^2 C/\partial x^2) \times V^2$, (N/m)	$0.37 \times V^2$ x 2

Table 3.11: The design parameters for the ARS-SOG gyroscope prototype. The difference between the calculated resonance frequencies in the table and the simulated ones in Table 3.9 is due to the fact that the calculated results predict a 2μm feature-narrowing due to the expected lithography and DRIE tolerances of the developed SOG process.

Parameter	Value
M_{PM}, kg	$(5.98) \times 10^{-7}$
M_{DE}, kg	$(2.05) \times 10^{-7}$
M_{SE}, kg	$(6.86) \times 10^{-7}$
$M_{D\ Total}$, kg	$(8.03) \times 10^{-7}$
$M_{S\ Total}$, kg	$(1.28) \times 10^{-6}$
K_{inner}, N/m	49.8
$K_{D\ outer}$, N/m	55.4
$K_{D\ Total}$, N/m	421
$K_{S\ outer}$, N/m	296
$K_{S\ Total}$, N/m	1284
F_D, Hz	3644
F_S, Hz	5041
$K_{S\ On}$ for $F_D=F_S$, N/m	671
$K_{S\ electrostatic}$ for $F_D=F_S$, N/m	613
V_{PM} for $F_D=F_S$, V	28.8
$V_{Sense\ Pull-in}$ for $F_D=F_S$, V	41.7

Figures 3.30 and 3.31 shows the SEM photographs of the fabricated ARS-SOG advanced decoupled gyroscope prototype. Fabricated capacitive gaps are 5μm, while the thickness of the structural silicon layer is 100μm, yielding an aspect ratio of 20.
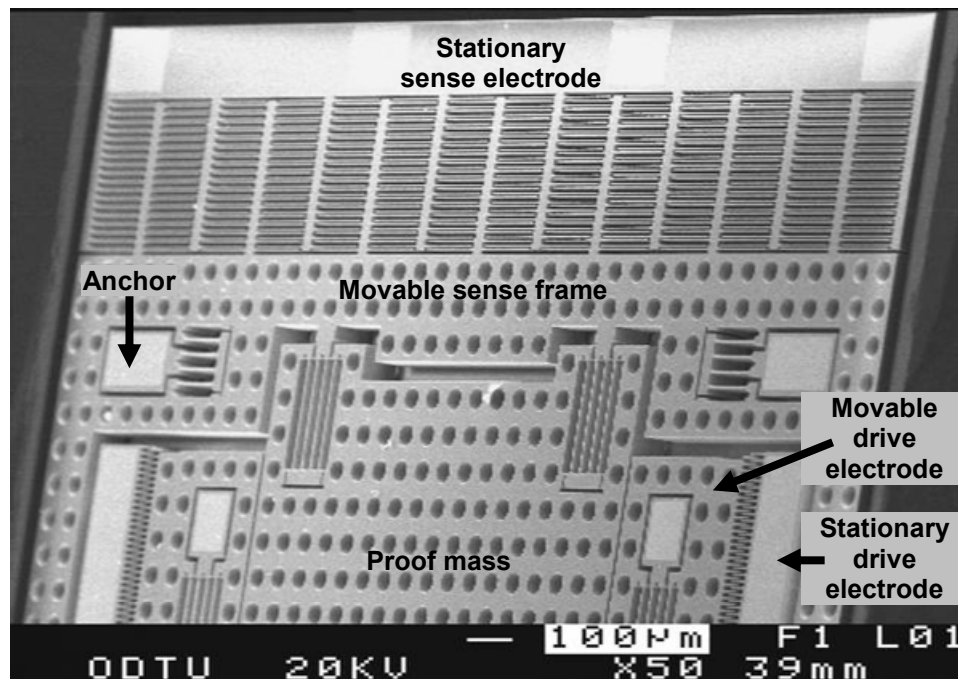
Figure 3.30: SEM picture of the fabricated ARS-SOG showing the drive and the sense electrodes, flexures, perforated suspended frames, and anchors.
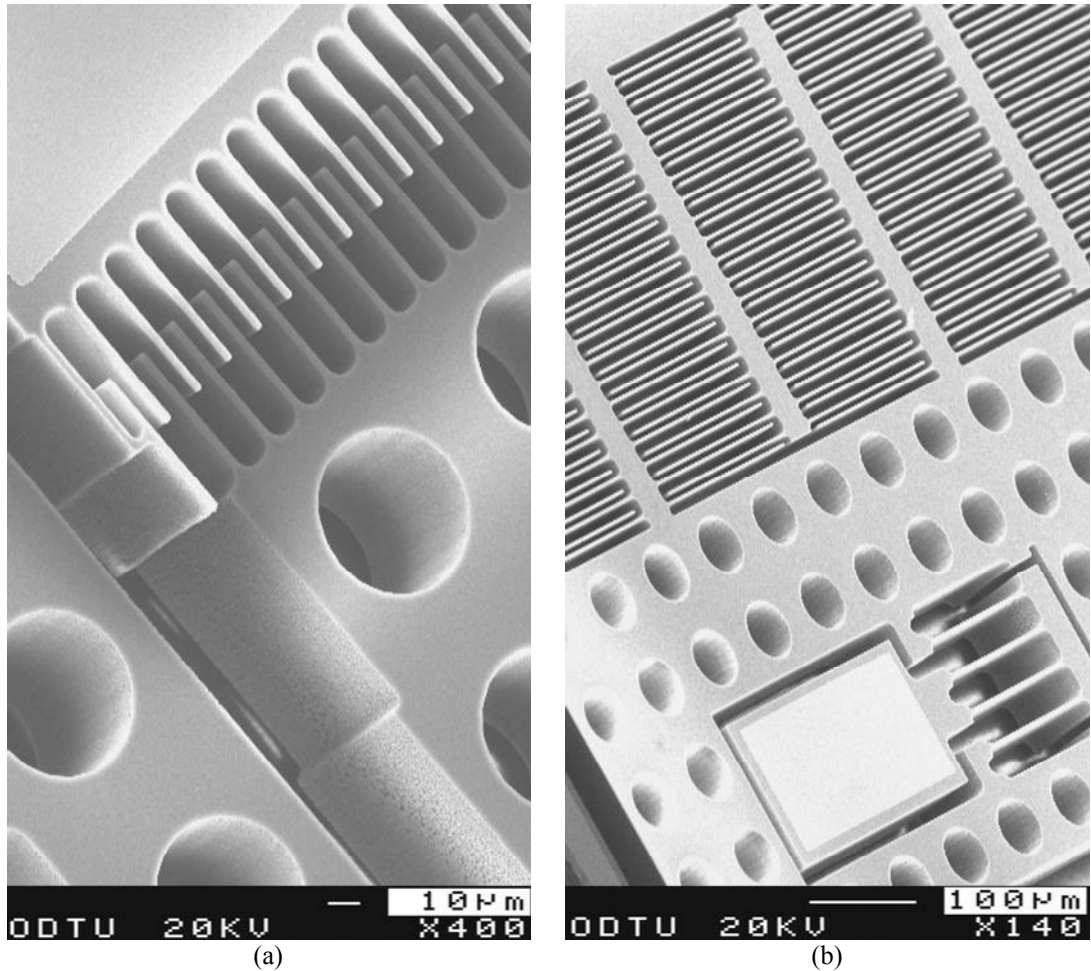
Figure 3.31: Close-up SEM pictures of the fabricated ARS-SOG showing (a) the varying-overlap-area type drive combs and (b) varying-gap type sense combs. Fabricated capacitive gaps are 5μm, while the thickness of the structural silicon layer is 100μm, yielding an aspect ratio of 20.

Three different mask sets are designed throughout the optimization of SOG process and the development of the ARS-SOG prototype. The performance of the fabricated SOG gyroscope prototype is presented in Chapters 5 and 7.

3.5 Summary

This chapter presented the fabrication processes selected for the development of high-performance micromachined vibratory gyroscopes and the specific symmetrical and decoupled gyroscope prototypes designed for each of these processes. The selected fabrication processes are dissolved wafer silicon micromachining (DWSM), nickel electroforming (NE), silicon-on-insulator (SOI) micromachining, and silicon-

on-glass (SOG) micromachining. A comprehensive overview of each of the developed micromachining processes are provided, including the process flows, encountered problems, and developed process solutions. An angular rate sensor (ARS) prototype is designed for each of these micromachining processes and fabricated.

The fabricated ARS-DWSM prototype has a 12μm-thick highly-boron doped silicon structural layer on insulating glass substrate. Its 1.5μm capacitive gaps provide an aspect ratio of 8. It has a completely symmetric structure along the drive and the sense modes, using clamped beams and varying-overlap-area type comb electrodes for both modes.

The fabricated ARS-NE prototype has an 18μm-thick nickel structural layer on insulating glass substrate. The aspect ratio of the 2.5μm capacitive gaps reaches to about 7, in a simple, low-cost, and mature fabrication process based on selective electrodeposition of nickel into a thick photoresist mold. The gyroscope employs varying-overlap-area type comb electrodes for the drive modes allowing large vibration amplitudes. The sense mode, on the other hand, employs high-sensitivity varying-gap type sense electrodes. The gyroscope also has separate electrostatic tuning electrodes for resonance frequency adjustment, quadrature cancellation, and force-feedback. The flexures of the gyroscope are dual or triple folded, with, increased linear deflection range. The number of flexures and their structures are kept symmetric along the drive and the sense modes, for keeping temperature-dependent resonance frequency drifts small.

ARS-SOI prototype is fabricated in a commercially available SOI micromachining process offered by MEMSCAP. The fabricated ARS-SOI prototype has a 25μm-thick surface-doped epitaxial silicon structural layer separated from a silicon handle substrate with a thin insulating oxide layer. The aspect ratio of the structure is 10, with 2.5μm capacitive gaps. The gyroscope structure is very similar to that of ARS-NE, however, the flexures in ARS-SOI are located I such a way that they minimize

the effects of rotary modes on mechanical crosstalk between the drive and the sense modes.

Finally, ARS-SOG prototype is fabricated in an advanced SOG process solving SOI notch and overheating problems associated with typical SOG processes. The fabricated ARS-SOG prototype has a 100µm-thick highly-doped single-crystal silicon structural layer anodically bonded over an insulating glass substrate. Though the 5µm capacitive gap of the fabricated prototype is larger than those of the other prototypes, the overall sensitivity of the gyroscope is much higher due to the high aspect ratio (>20) of the developed process and the advanced structure of the gyroscope. The advanced decoupled gyroscope structure developed for the SOG micromachining process serves the advantages of the large-amplitude linear drive-mode vibrations, high-sensitivity sense electrodes with electrostatic frequency tuning and force-feedback capability, and highly-suppressed mechanical crosstalk between the modes by using a single and rigid sense-frame instead of the isolated dual sense frames of the other symmetrical and decoupled gyroscope prototypes.

The fabrication processes of the designed gyroscope prototypes, except the SOI micromachining process and the DRIE step of the DWSM process, are completed within the Class 100 and Class 1000 cleanroom environment of Middle East Technical University, Microelectronic Technologies (METU_MET) facility. Figure 3.32 shows one of the chemical processing hoods and the lithography area of METU-MET cleanroom.

<div align="center">(a)   (b)</div>

Figure 3.32: (a) Chemical processing hood and (b) lithography area of METU-MET cleanroom, in which the designed gyroscope prototypes are fabricated.

CHAPTER 4

CAPACITIVE INTERFACE CIRCUIT

This chapter briefly presents the capacitive interface circuit designed for the micromachined vibratory gyroscopes developed in this study. A CMOS unity-gain buffer circuit is selected as the capacitive interface, because of its high-sensitivity with a simple architecture. Section 4.1 briefly introduces the interface requirements for micromachined capacitive gyroscopes. Section 4.2 explains the architecture and the operation of the designed unity-gain buffer (UGB) circuit together with the simulation results. Section 4.3 evaluates the designed UGB circuit as a capacitive interface, by simulating its performance together with a lumped element model generated for the drive-mode of a gyroscope prototype. Section 4.4 provides a summary of the chapter.

4.1 Capacitive Interface Requirements

Electronic interfaces play an important role in determining the overall performance of micromachined vibratory gyroscopes. This is because of the fact that the output response of a micromachined vibratory gyroscope is typically smaller than a fraction of the diameter of a silicon atom even for an angular rate input of 1deg/sec. Such a small displacement generates a very small change in the sense capacitance of the gyroscope, in the range of sub-attofarads ($1aF=10^{-18}F$). The variation of the capacitance and hence the charge at the output of the capacitive gyroscope is then detected and converted to a voltage signal by the electronic interface circuit.

Figure 4.1 shows the basic unity-gain buffer configuration as a capacitive interface circuit connected to the sense output of a capacitive gyroscope, where Z_{in} is the effective impedance at the input of the buffer circuit, excluding the sensor capacitance, C_{sense}. The gyroscope output model includes a displacement-controlled current source as described in Section 2.3.3, denoted by I_{out_sensor} in the figure. The effective impedance Z_{in} accounts for the wirebonding/interconnect/input-transistor capacitances, summing to C_{in}, and the resistance of the biasing network, R_{in}, which provides a DC bias to the high-impedance input node of the interface circuit. The DC bias of the input node is important in determining the output current from the gyroscope, by providing a constant DC offset potential between the movable and stationary electrodes of the gyroscope sense capacitance. Floating the input node may cause unpredictable behavior of the system due to the susceptibility of the high-impedance node to leakage currents and coupled noise signals.
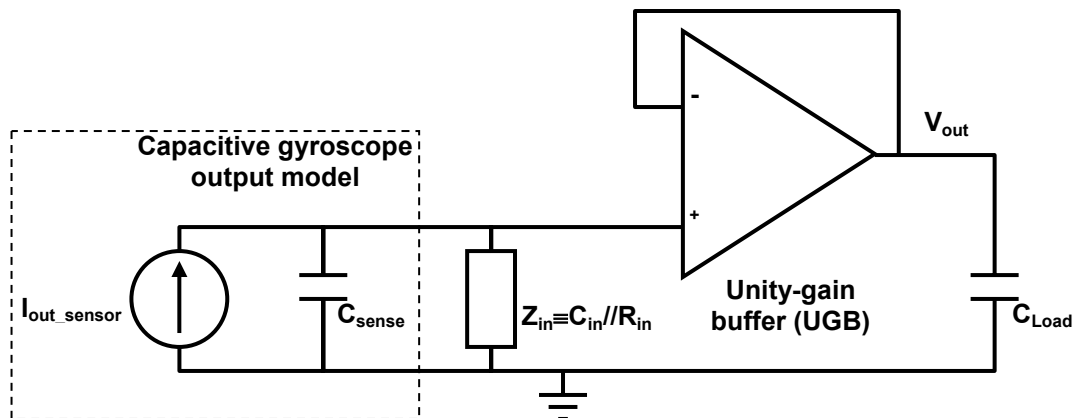
Figure 4.1: The basic unity-gain buffer configuration as a capacitive interface circuit connected to the sense output of a capacitive gyroscope.

Clearly, the voltage V_{out} generated at the output of the buffer circuit of Figure 4.1 is maximized by maximizing the current pumped from the gyroscope and maximizing the impedance at the input of the buffer circuit. The amplitude of the output current pumped from the gyroscope can be increased by increasing the capacitance variation at the sense electrode of the gyroscope, the frequency of capacitance variation, i.e., of the sense-mode vibrations, or the DC potential across the sense capacitance, as described in Chapter 2. Obviously, these parameters depend on the electromechanical design of the gyroscope itself as well as the fabrication process,

169

which can be assumed fixed during the design of the interface circuit. However, there is still some space for generating a higher output voltage, by maximizing the impedance at the input of the buffer circuit. This impedance can be maximized by minimizing the effective capacitance across the high-impedance node and the AC ground, and by maximizing the resistance of the biasing network.

It is possible to minimize the effective capacitance across the high-impedance node and the AC ground by using bootstrapping method [31, 89]. Figure 4.2 illustrates the bootstrapping. The method incorporates the insertion of an electrically conductive shield layer in between the high-impedance node and the grounded substrate of the CMOS chip, dividing the parasitic capacitances from the wirebonding pad and the interconnect metallization to the grounded substrate. The shield layer is driven by the output of the buffer. Although the physical capacitance from the high-impedance node to the shield layer, $C_{in\text{-}shield}$, and from the shield layer to the substrate, $C_{shield\text{-}substrate}$, are both greater than the parasitic capacitance, $C_{in\text{-}substrate}$, the effective capacitance from the high-impedance node to the ground would be

$$C_{effective} = \left[C_{in-shield} \cdot \left(1 - A_{buffer} \right) \right] + C_{UGB} \qquad (4.1)$$

because of the fact that the AC voltage across the shielded capacitance is suppressed by a factor of $1 \big/ \left| 1 - A_{buffer} \right|$, where A_{buffer} approaches to close to unity for a differential amplifier with sufficiently high open-loop gain. In other words, bootstrapping effectively suppress the shielded parasitic capacitances by a factor close to the open-loop gain of the differential stage connected in unity-gain buffer configuration. Remembering that the typical parasitic capacitances associated with wirebonding pads and the interconnects of the high-impedance node may reach to picofarads, bootstrapping method can effectively suppress this value by more than two orders of magnitude using a dedicated buffer circuit design.

Bootstrapping method works well for minimizing the effective parasitic capacitance at the high-impedance node, associated with the CMOS metallization layers.

However, it has no effect on reducing the parasitic capacitance associated with the input transistors of the differential stage or the biasing network. The minimization of the parasitic capacitances associated with the gate of the input FET is a concern related to the design of the buffer circuit and described in Section 4.2. In addition, selecting a proper biasing network is also very important in determining the performance of the capacitive interface circuit. Several methods can be used for biasing the high-impedance node of a unity-gain buffer type capacitive interface circuit. These methods are listed below together with possible problems:

1. *Thin-film resistor*: Consumes very large chip area, considering the fact that the bias impedance should be higher than few tens of megaohms in order to prevent any degradation of the sense output of a gyroscope with a sense capacitance of 1pF and operated at 5kHz.

2. *Low-conductivity diffusion resistor*: Adds parasitic capacitance across the high-impedance node and the CMOS substrate, which cannot be suppressed by bootstrapping.

3. Switched-capacitor resistor: Requires a demanding design in order to prevent glitches at the output signal, which significantly increase the output noise.

4. *MOSFET in sub-threshold region*: High-sensitivity to the subthreshold voltage.

5. *Diode:* Non-linear distortion.
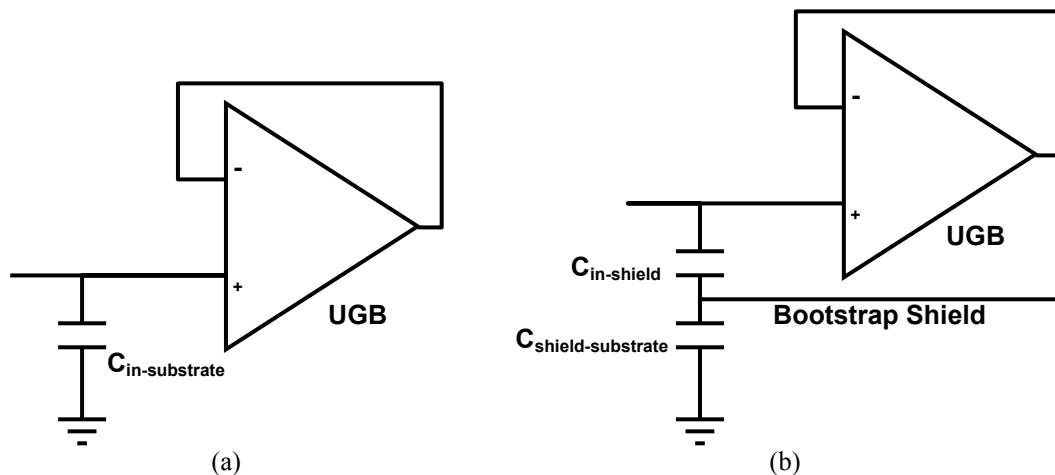
Figure 4.2: The high parasitic capacitance in (a), from the input of the unity-gain buffer (UGB) to the grounded substrate of the CMOS chip can be suppressed with the use of a bootstrap shield layer in (b), dividing the parasitic capacitance in two separate capacitances and driven by the output of the UGB.

171

Due to the area requirements, biasing with a diode or a sub-threshold MOS are found to be appropriate, whereas, the diode biasing have experienced to be unpleasant due to the parasitic BJT effects across the pn-junction and the substrate of the standard CMOS foundry processes. Therefore, sub-threshold MOSFET is selected for the biasing of the high-impedance node. Figure 4.3 illustrates the biasing configuration, which intends to set the DC potential of the high-impedance-node to the ground potential. Connecting the gate and drain of the transistor provides a very-high channel resistance in the range of gigaohms (1Gohm=10^9ohm), so that the overall impedance for the biasing network would be dominated by the transistor capacitances. These capacitances are minimized by using a minimum-size MOS transistor.
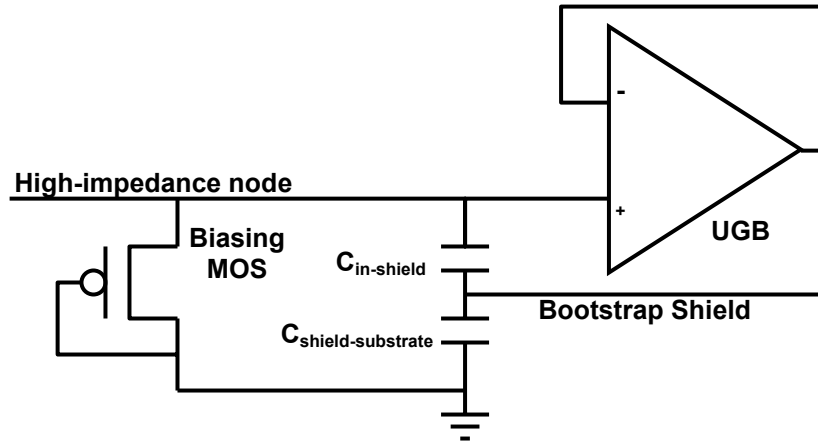
Figure 4.3: The biasing scheme of the high-impedance input node of the UGB.

As a result, the input impedance of the interface circuit would be capacitive rather than being resistive, and the input capacitance is dominated by the pad and interconnect-capacitances, the biasing network capacitance, and the input gate capacitance of the buffer circuit. Then, the approximate output voltage with the UGB interface circuit with capacitive input impedance would be

$$V_{out} = \left(V_{PM} - V_{bias}\right) \cdot \frac{\Delta C_{sense}}{C_{sense} + C_{interface}} \qquad (4.2)$$

where V_{PM} is the DC potential applied to the movable sense electrode (connected to the proof mass of the gyroscope), V_{bias} is the DC bias applied to the high-impedance-

172

node (vanish for the configuration in Figure 4.3), ΔC_{sense} is the differential variation in the sensor capacitance C_{sense}, and $C_{interface}$ is the total parasitic capacitance at the input of the capacitive interface circuit. Equation 4.2 states that, the sensitivity of a capacitive vibratory gyroscope can be maximized by minimizing the parasitic capacitances and by maximizing the ratio $\Delta C_{sense}/C_{sense}$. If the parasitic capacitances of the interface circuit can be kept much smaller than the sensor capacitance, Equation 4.2 provides the ultimate performance limits of the gyroscope as

$$V_{out} \propto \left(V_{PM} - V_{bias}\right) \cdot \frac{Y_{sense}}{d_{gap}} \tag{4.3}$$

which is proportional the electromechanical parameters of the gyroscope.

It is apparent that a unity-gain buffer type interface circuit must be designed for minimizing the sensitivity loss at the output of the capacitive gyroscope. This can be achieved by maximizing the resistance of the biasing network, while minimizing the overall capacitance across the high-impedance node and the substrate. Then, the limiting parameter for the interface circuit in determining the overall performance of the angular rate sensor system would be the electrical noise, which is discussed in Section 4.3.

4.2 Unity-Gain Buffer Type Capacitive Interface Circuit

Maximizing the input impedance of the capacitive interface circuit in order to minimize the sensitivity loss at the gyroscope output requires a dedicated buffer circuit design. Figure 4.4 shows the schematic view of the unity-gain buffer circuit inspired from [89], with a sub-threshold MOS used for biasing the input node. The circuit consists of a single differential stage, where unity-gain feedback is achieved by connecting the output to the negative input of the differential stage. The output of the circuit drives the off-chip loads as well as the on-chip bootstrap shield capacitances.
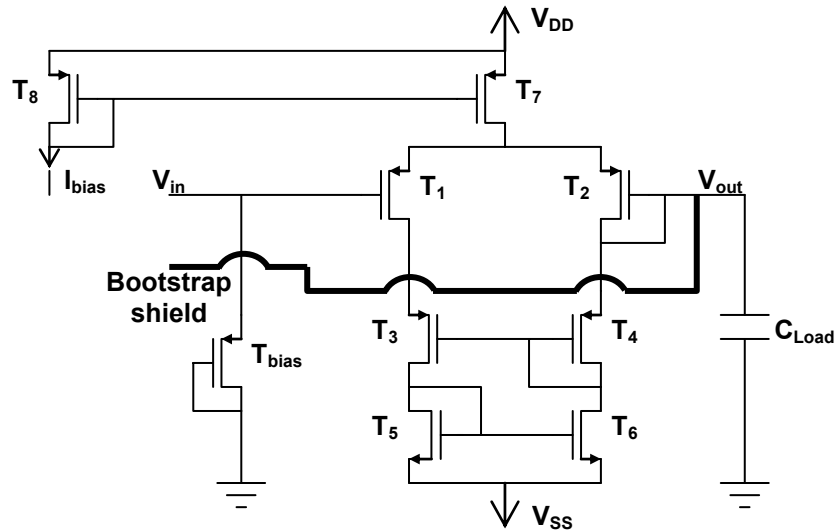
Figure 4.4: The schematic view of the unity-gain buffer circuit inspired from [89], with a sub-threshold MOS used for biasing the input node and a capacitive load, C_{Load}.

The input MOS transistor, T1, adds a parasitic capacitance to the high-impedance node, due to its gate-to-source, gate-to-drain, and gate-to-bulk capacitances. The small-signal voltage across the source and gate of the input transistor is almost identical to the small-signal input voltage, because of the fact that the source of the input transistor can be assumed as virtual ground. This results in a gate-to-source voltage gain close to unity, and therefore, effectively eliminating the large gate-to-source capacitance of the input transistor. Then, gate-to-drain capacitance would be the dominant capacitance. Incorporating a pair of PMOS transistors, T3 and T4, mirrors the output voltage of the differential stage to the drain of the input transistor. If the bulk of the input transistor is also connected to its source terminal, then source-to-gate, bulk-to-gate, and the drain-to-gate signals of the input transistor would all closely track the input AC signal, minimizing the capacitance associated with the input transistor. Table 4.1 provides the transistor dimensions for the designed capacitive interface circuit.

Table 4.1: Transistor dimensions for the capacitive interface circuit designed for the 0.6μm n-well CMOS process of XFAB.

Parameter	T_1	T_2	T_3	T_4	T_5	T_6	T_7	T_8	T_{bias}
Channel width, μm	80	80	40	40	40	40	160	160	2
Channel length, μm	4	4	4	4	8	8	4	4	2

The open-loop gain of the differential stage in Figure 4.4 is given as,

$$A_{open-loop} = g_{m1} \cdot \left(g_{ds6} + s \cdot C_{Load}\right)^{-1} \tag{4.4}$$

neglecting the transistors T3 and T4, which are used to mirror the output voltage to the drain of T1. The gain of the unity gain buffer configuration is then estimated as

$$A_{UGB} = \frac{1}{1 + \left(A_{open-loop}\right)^{-1}} = \frac{g_{m1}}{g_{m1} + g_{ds6} + s \cdot C_{Load}} \tag{4.5}$$

The output resistance of the buffer is expressed as,

$$R_{out} = \left(g_{m1}\right)^{-1} \tag{4.6}$$

Figure 4.5 shows the schematic view of the circuit used to simulate the preliminary performance of the designed unity-gain buffer. Buffer is powered from $\pm 2.5^V$ supplies, whereas its bias current is set to 100µA by using an external 12.1kohm. The figure shows the bootstrap line is fed to a shield, where $C_{in\text{-}shield}$ and $C_{shield\text{-}substrate}$ are both set to 2pF. The input node is biased with a 2µmx2µm PMOS transistor.
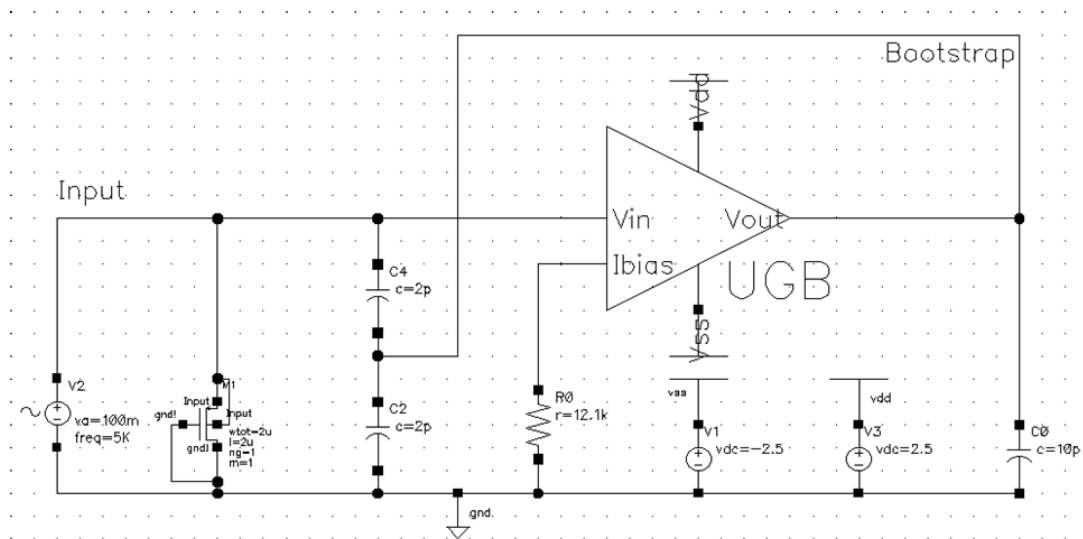
Figure 4.5: The schematic view of the circuit used to simulate the preliminary performance of the designed unity-gain buffer.

Figure 4.6 shows the AC analysis results for the designed UGB, simulated with SpectreS. The DC voltage gain of the buffer is 0.9988 V/V, where the 3dB frequency is at 3.2MHz for an off-chip capacitive load of 10pF. The simulated gain exactly matches with the gain calculated from Equation 4.5, using the simulated transistor parameters. This verifies that, neglecting T_3 and T_4 in deriving the gain of the buffer introduce no significant error to the gain expression. The efficiency of the bootstrap configuration can be calculated by multiplying the $C_{in\text{-}shield}$ capacitance value with $(1-A_{buffer})$, resulting in an effective capacitance of only 2.4fF.

A: (4.98067K −10.8052m)   delta: (3.20125M −3.00345)
B: (3.20623M −3.01426)   slope: −938.212n
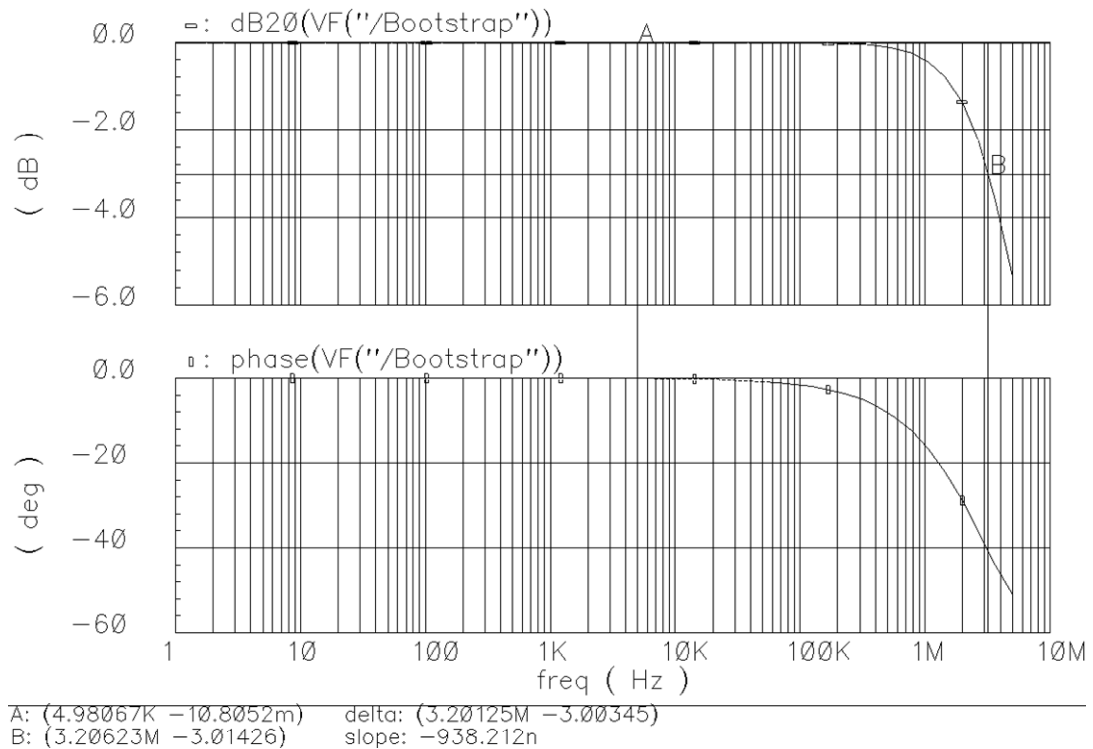
Figure 4.6: AC analysis results for the designed UGB.

The voltage gains from gate-to-source and gate-to-drain of the input transistor of the UGB are simulated to be 0.9954 and 0.9902, respectively. In addition, the physical gate-to-source, gate-to-bulk, and gate-to-drain capacitances are approximately estimated to be 550fF, 21fF, and 27fF, respectively. Multiplying these capacitances with the (1-A) factor using associated voltage gains across each capacitor yields effective gate-to-source, gate-to-bulk, and gate-to-drain capacitances as 2.5fF, 0.1fF, and 0.3fF, respectively. Finally, the capacitance associated with the biasing

176

transistor to the CMOS substrate is simulated to be 7.3fF. This result states that the total effective capacitance seen by the high-impedance node is less than 13fF, excluding the sensor capacitance.

Figure 4.7 shows the input sweep range of the UGB, which is limited to a range of approximately -1.45V and 1.95V. For inputs smaller than -1.45V, the input transistors of the differential stage enters linear region, reducing the open-loop gain of the circuit. Finally, Figure 4.8 shows the transient simulation result for a small input voltage, showing the output has a DC offset of about 0.3mV.
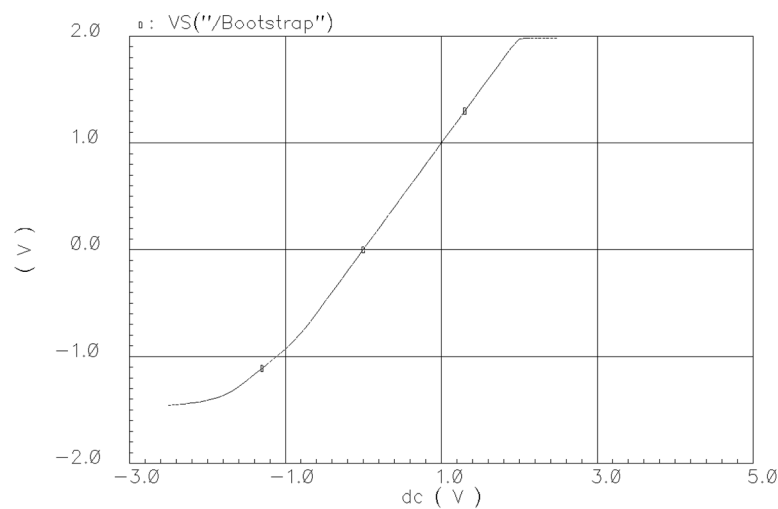
Figure 4.7: Simulated input sweep range of the UGB, which is limited to a range of -1.45V and 1.95V.

Figure 4.9 shows the simulation result for the output resistance of the buffer circuit. The simulation is performed by measuring the gain of the buffer, when a 10kohm resistor is connected to its output. The simulated gain of 0.73 yields an output resistance of 2.7kohm, where the expected result was 3.7kohm using Equation 4.6. The small difference is expected to be due to the shift in the DC operating characteristics when UGB drives a small resistive load.

Figure 4.10 shows the schematic view of the circuit for evaluating the input capacitance of the designed UGB circuit. A time-varying current source is used as the input to the circuit, which pumps charge to the high-impedance node, imitating

the behavior of the gyroscope. The pumped charge is converted to a voltage signal through charging the input capacitance of the buffer. Figure 4.11 shows the simulated output voltages for an input current of 1pA. The buffer circuit converts 1pA input current to an output voltage of 1.85mV, through the effective capacitance at the high-impedance node. The simulated capacitive impedance is about 1.85Gohm, corresponding to a capacitance of 17.2fF at the frequency of the input current signal. This value is close to the expected value of 13fF, verifying that the bootstrapping effectively suppress the parasitic capacitances at the high impedance node.
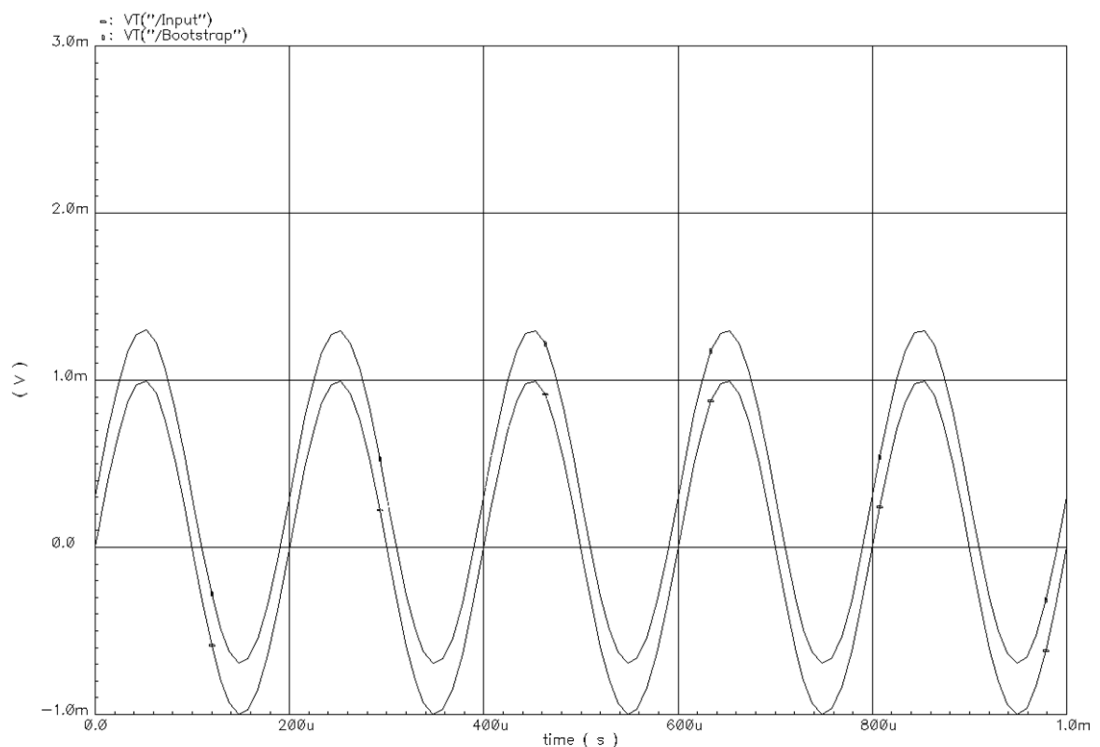
Figure 4.8: The transient simulation result for a small input voltage, showing the output has a DC offset of about 0.3mV.

Figure 4.11b shows the transient response of the output in a larger time-span, showing that the DC offset of the buffer output stabilizes after 40msec. This is expected to be due to the response time associated with the time-constant of the high-resistance sub-threshold biasing transistor. Figure 4.12 shows the effect of removing the bootstrap shield from the circuit of Figure 4.10, which results in a single 1pF parasitic capacitance from the input node to the ground. The output

178

voltage of the UGB drops to about 30μVpeak, corresponding to an input capacitance of about 1.05pF, which aggress with the expected result. In addition, the stabilization time of the output DC offset is increased to about 4sec, verifying the above discussion.
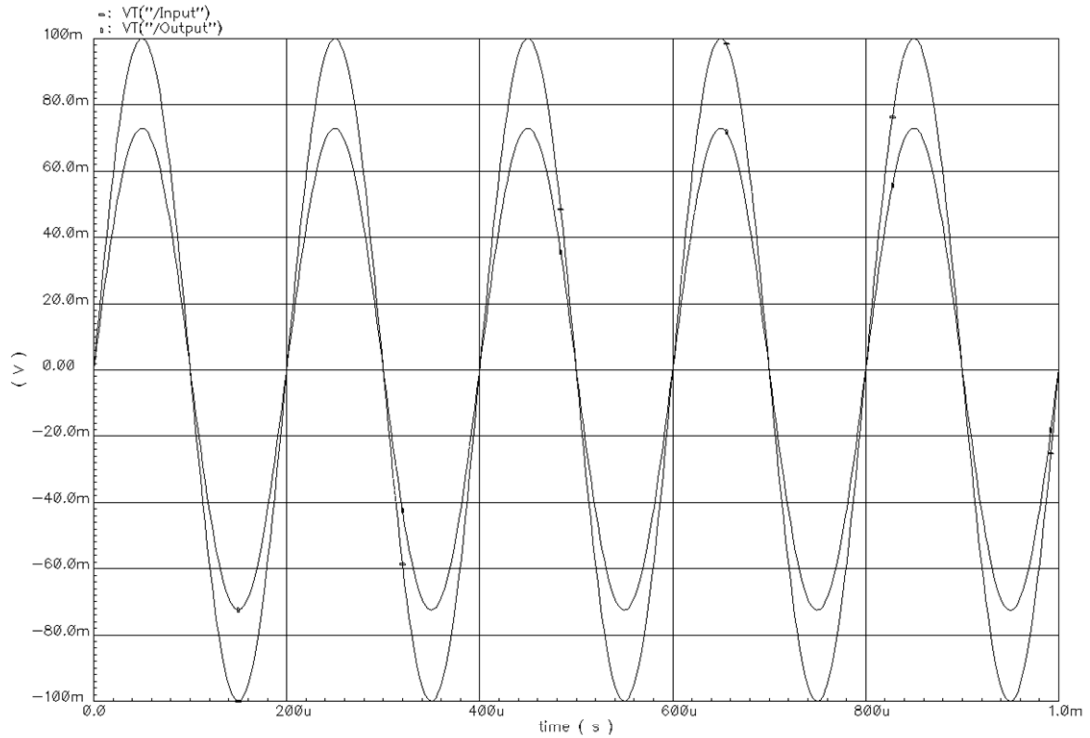
Figure 4.9: The simulation result for the output resistance of the buffer circuit, showing a gain of 0.73 for a 10kohm load resistance yielding 2.7kohm output resistance for the UGB.
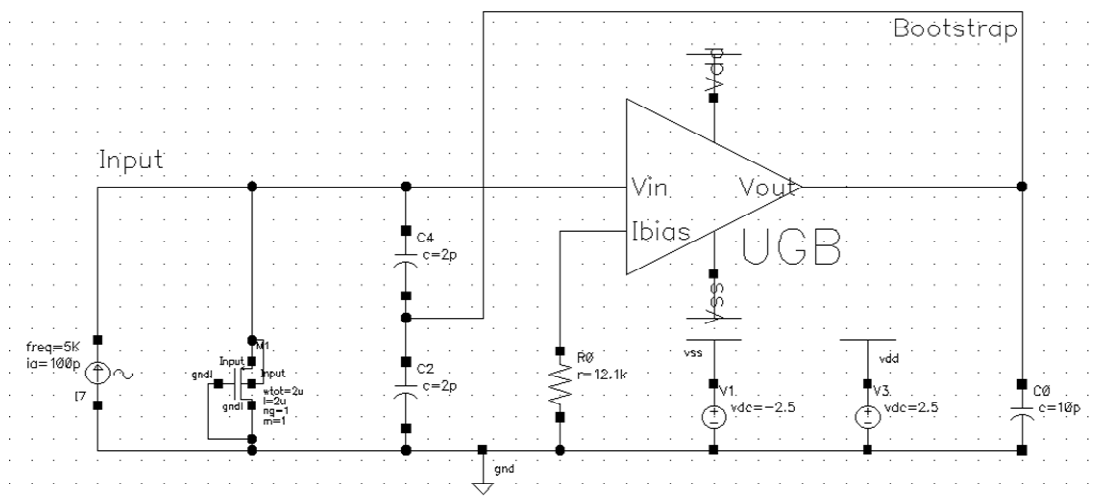
Figure 4.10: The schematic view of the circuit for evaluating the input capacitance of the designed UGB circuit.

179
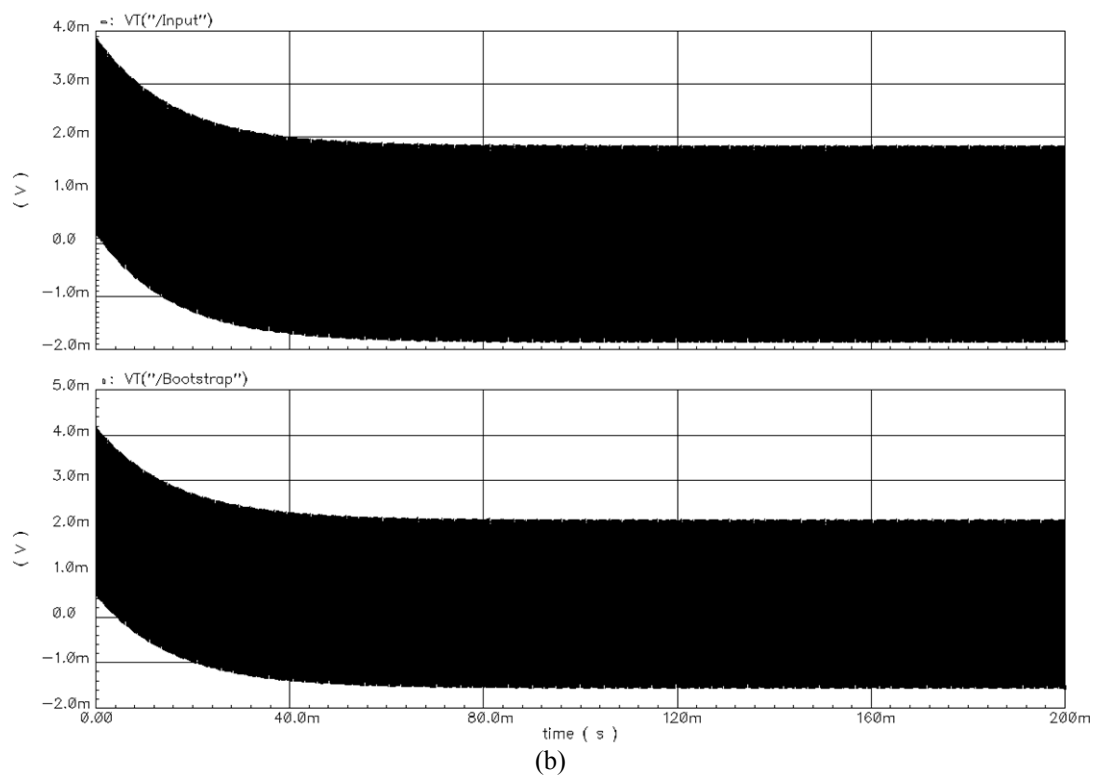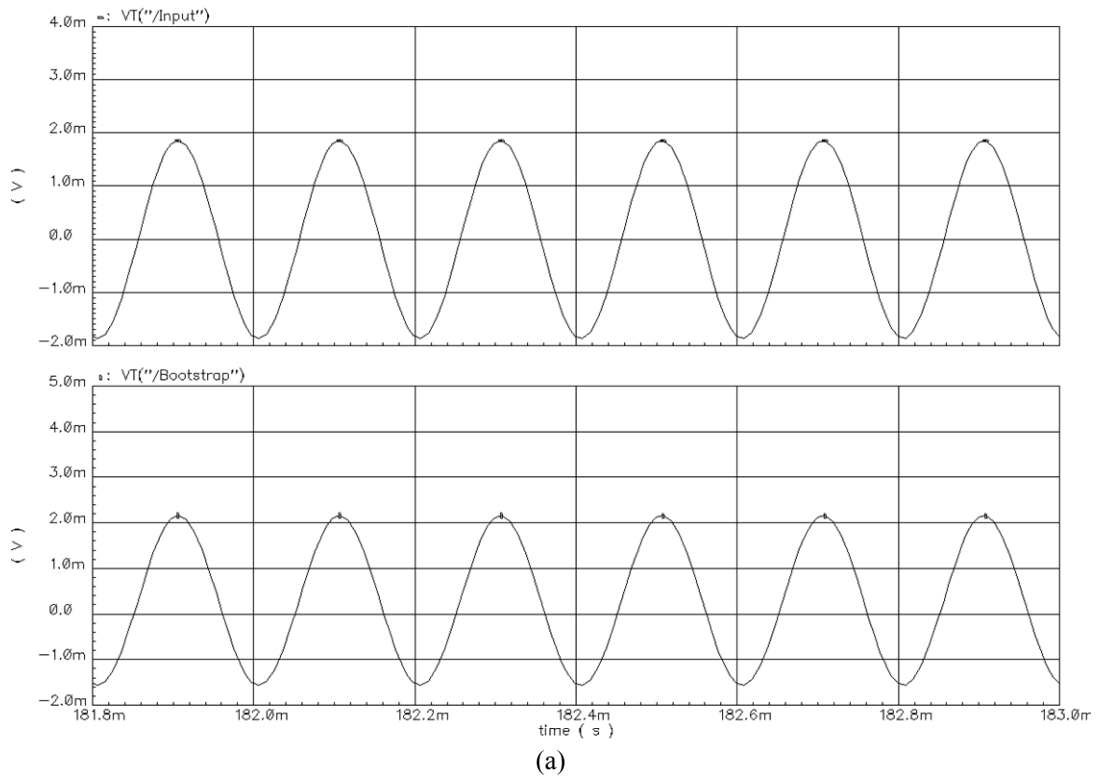
Figure 4.11: The simulated output voltages for the circuit of Figure 4.10, with an input current of 1pA. (a) The UGB acts as a current-to-voltage converter, with a capacitive input impedance about 17.2fF. (b) The high-resistance of the sub-threshold biasing transistor results in a response time of about 40msec for the DC offset of the output.

The effect of the input signal amplitude on the output response is also examined for the designed UGB. Figure 4.13 shows the output voltage for the amplitude of the input current increased by two orders of magnitude, reaching 100pA. The amplitude of the voltage generated from this current input reaches to 215mVpeak, corresponding to an input capacitance of about 15fF. However, the generated voltage has a 50mV DC offset, though it must be kept at 0^V by the biasing transistor. This is because of the fact that the impedance of the biasing transistor vary significantly for positive and negative source-to-gate potentials resulting from large input current signal. As the biasing transistor acts as a voltage-controlled nonlinear resistor, the variations in its resistance results in simultaneous variation of the time-constant for biasing the high-impedance node and results in a DC offset.
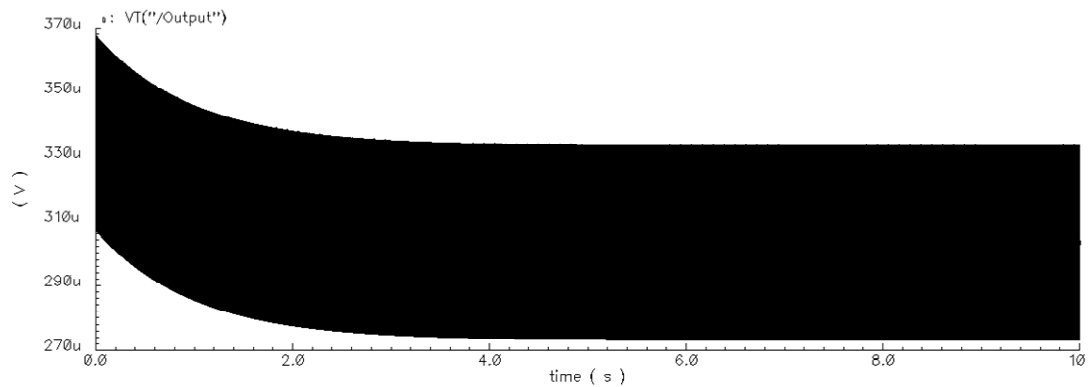
Figure 4.12: The effect of removing the bootstrap shield from the circuit of Figure 4.10, which results in a single 1pF parasitic capacitance from the input node to the ground. The signal amplitude reduced and the response time increased both by a factor of about 60.
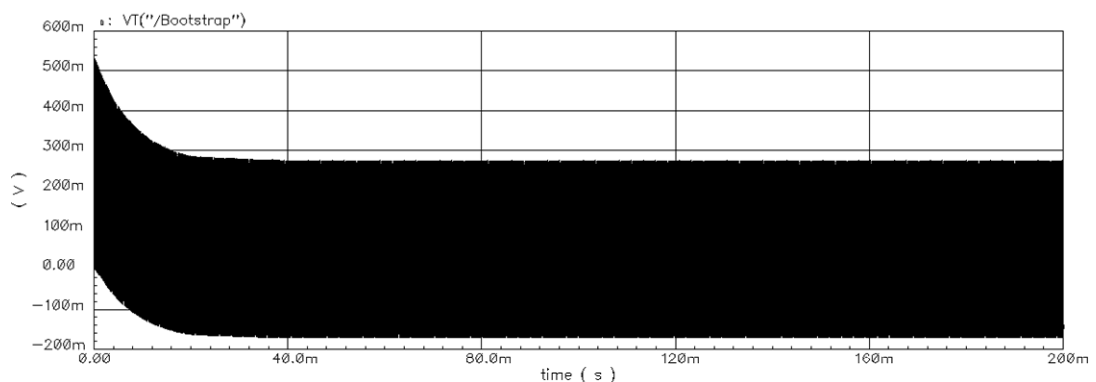
Figure 4.13: The output voltage for the amplitude of the input current increased by two orders of magnitude, reaching 100pA.

181

4.3 UGB Evaluation as a Capacitive Interface Circuit

After determining the performance parameters of the UGB and verifying that it can be used as a capacitive interface circuit for the developed gyroscope prototypes, the UGB circuit is evaluated together with a behavioral gyroscope model constructed using lumped electrical elements. Figure 4.14 shows the lumped element model constructed for the drive-mode of the ARS-SOG prototype, based on the design parameter values listed in Tables 3.10 and 3.11. The constructed model combines the actuation and sensing models described in Figures 2.10 and 2.11, respectively. Gyroscope is actuated along its drive-mode with the time-varying actuation signal V_{in} and the proof mass voltage V_{PM}, applied across the capacitance of the drive-mode actuation electrode, $C_{drive-1}$. The resulting displacement is proportional to the current passing through the RLC equivalent circuit of the second-order spring-mass-damper system of the drive-mode. The displacement-induced current is mirrored to the output port, generating I_{out}, as described in Chapter 2. This current then converted to a voltage through the impedance at the output port, and picked-up by a measurement probe, whose model is also included in Figure 4.14. The impedance at the output port includes the drive-mode sensing electrode capacitance, $C_{drive-2}$, the probe capacitance, C_{probe}, and the probe resitance, R_{probe}. A stray capacitance, C_{stray}, from the input of the drive-electrode to the output is also included in the model, in order to analyze its effects on the measurements.

Figure 4.15 presents the simulated characteristics of the drive-mode resonator of ARS-SOG. The designed resonance frequency of the drive-mode of the ARS-SOG gyroscope is 3644Hz, while the constructed model predicts a frequency of 3654Hz, with a small mismatch due to the rounding errors in the generation of model parameters. The simulated results predict an open-loop gain of about 0.0012 at resonance, without using any capacitive interface circuit. The phase of the transfer function is 5.6degrees, close to 0 degrees due to the resistive nature of the impedance at the output of the gyroscope.

Figure 4.16 shows the effect of stray capacitances on the resonance characteristics of the drive-mode resonator of ARS-SOG. As the stray capacitance from the actuation

node to the sensing node increases, the effect of parasitic anti-resonance becomes dominant in the overall transfer characteristics. In other words, the increase in electrical cross-coupling between the electrically-isolated drive and sense ports of the gyroscope reduces the amplitude of the mechanical resonance peak, which makes it difficult to detect the peak position especially for self-resonance excitation. Capacitive interface circuit improves detection of the resonance peak even if the stray capacitance is too high. Another point with the result of simulation in Figure 4.16 is that the stray capacitance affects the resonance characteristics if the equivalent lumped capacitance, C_D, in Figure 4.14 is much smaller than the stray capacitance. Stray capacitance highly depends on the substrate and packaging, and can be assumed fixed by the manufacturing process. C_D, on the other hand, can be increased by decreasing the mechanical spring constant of the resonator, by increasing the DC polarization voltage applied to the proof mass, or by increasing the $\partial C/\partial x$ parameter of the gyroscope.
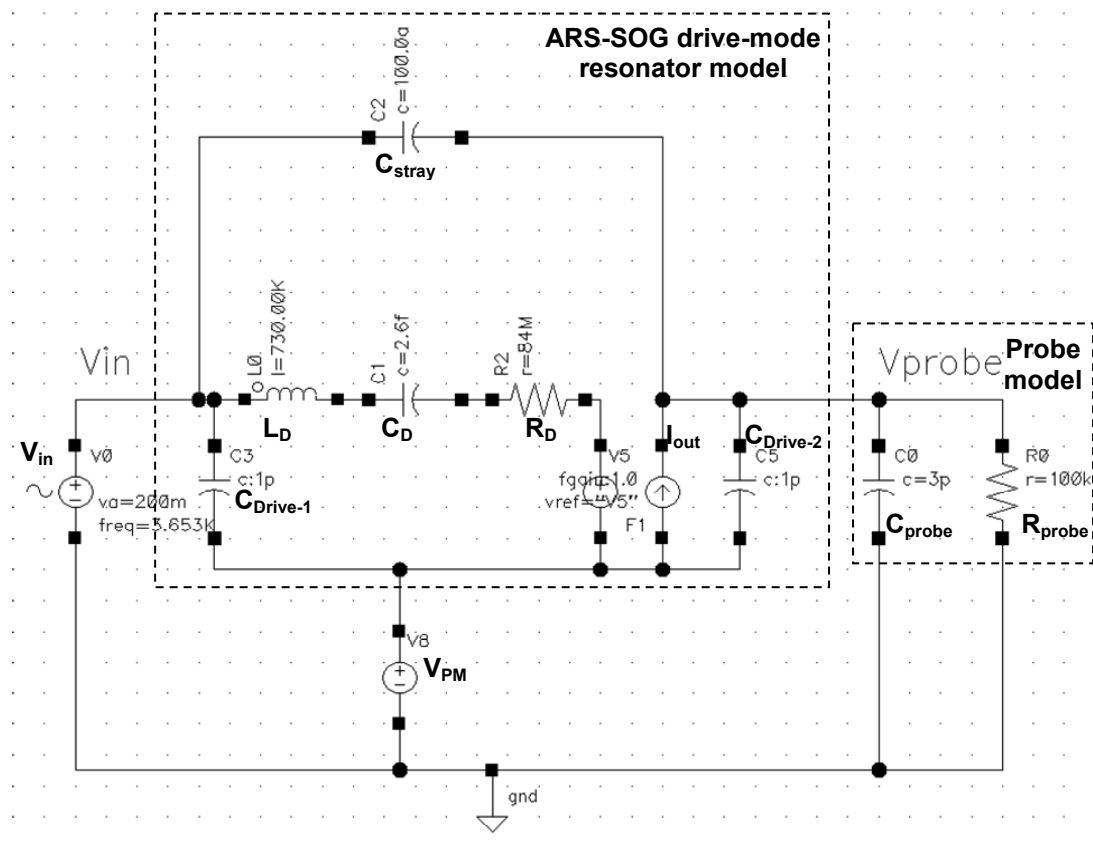
Figure 4.14: The lumped element model constructed for the drive-mode of the ARS-SOG prototype, based on the design parameter values listed in Tables 3.10 and 3.11.
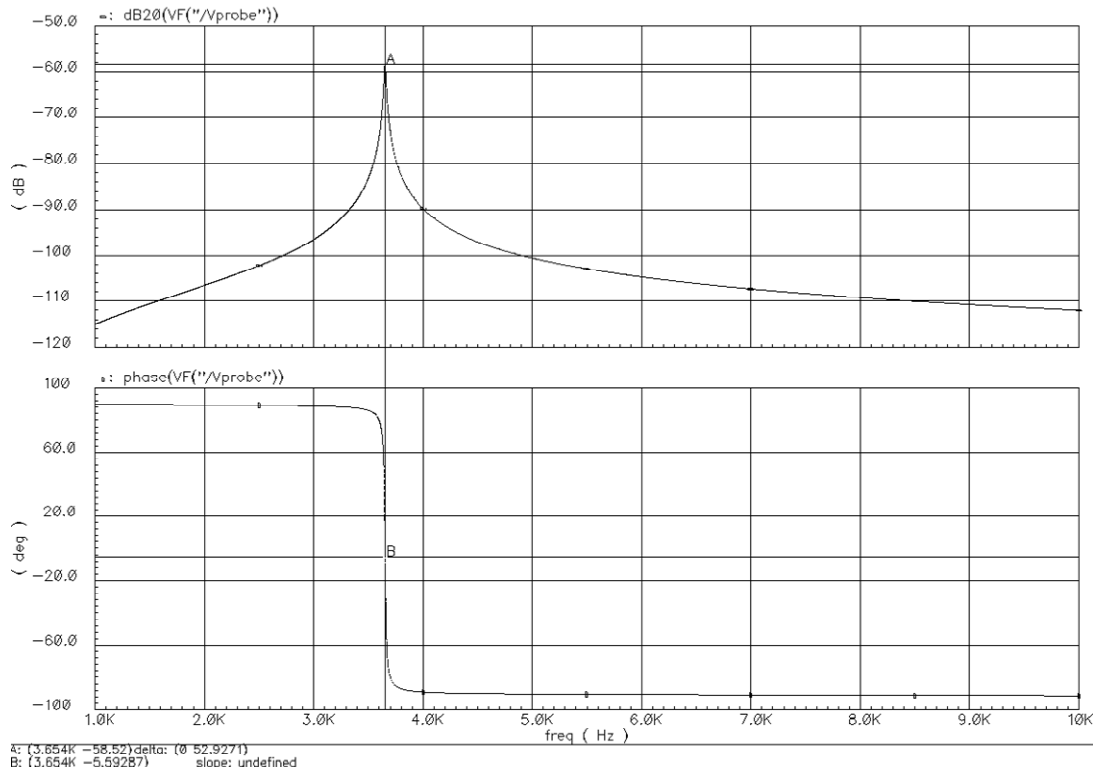
Figure 4.15: The simulated characteristics of the drive-mode resonator of ARS-SOG.

Figure 4.17 shows the schematic view of the lumped-element model of Figure 4.14 with the UGB circuit as a capacitive interface. The circuit is similar to the simulation model of Figure 4.10, where now the gyroscope output connected to the high-impedance node supplies a displacement-induced current signal to the interface circuit. Figure 4.18 shows the simulated characteristics of the drive-mode resonator of ARS-SOG with UGB as the capacitive interface circuit. The resonance frequency of the system remains unchanged, as expected; however, the gain of the system now reaches to 0.45 at resonance, demonstrating an improvement by a factor of about 400 compared to the gain of Figure 4.15 simulated without the capacitive interface circuit. The improvement is simply due to the increase in the impedance seen by the gyroscope output, from 100kohm in Figure 4.14 to about 1.15pF@3.65kHz in Figure 4.17. 1pF of the impedance at the high-impedance node is due to the drive mode output capacitance, while the remaining 150fF is nothing but the effective capacitance of the biasing network, UGB, and bootstrapped parasitic capacitances at the high-impedance node. The reason for increased effective capacitance is due to the reduced gain of the UGB by connecting a resistive pick-up probe at its output. The 100kohm resistance of this probe reduces the open-loop gain of the buffer

184

significantly, resulting in a reduced bootstrap efficiency. Replacing the resistive probe with a 10pF load capacitance is simulated to improve the gain of the overall system from 0.45 to 0.51 corresponding to an effective impedance of only 25fF at the high-impedance node excluding the sensor capacitance, which agrees well with the expected result. Finally, the phase of the overall system is now passing through -95degrees in Figure 4.18, stating that the impedance seen by the gyroscope output is now capacitive when UGB is employed as the interface circuit.

(a)

(b)

(c)

(d)
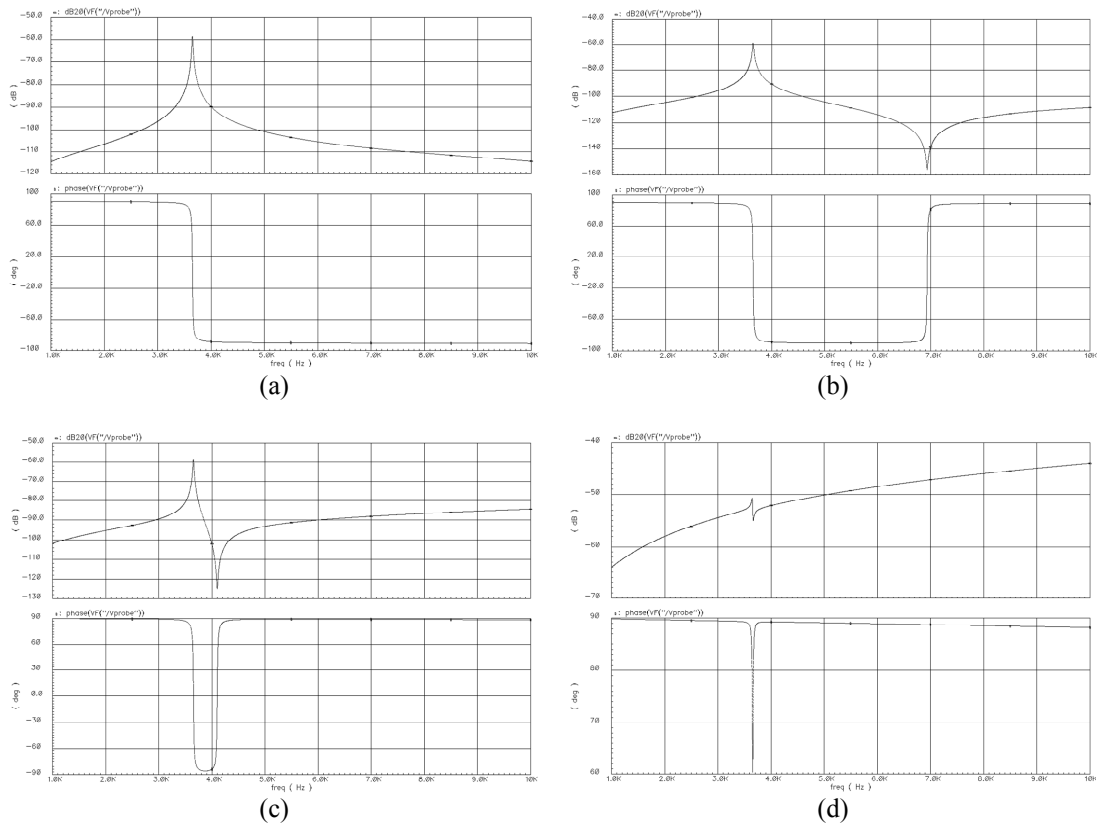
Figure 4.16: The effect of stray capacitances on the resonance characteristics of the drive-mode resonator of ARS-SOG. (a) C_{stray}=100aF, (b) C_{stray}=1fF, (c) C_{stray}=10fF, (d) C_{stray}=1pF. Clearly, the mechanical resonance gets smaller and an anti-resonance peak gets closer to the mechanical resonance, as the electrical cross-coupling through the stray capacitance increases.

Figure 4.19 shows the simulated transient response of the system in Figure 4.17. The simulation use a 200mVpeak sinusoidal input signal at the mechanical resonance frequency of the drive-mode resonator applied to the actuation electrode of the resonator, while the UGB generates a 90mVpeak sinusoidal output signal due

185

to the resulting displacement. The amplitude of the output signal stabilizes within 100msec, due to the large sensor capacitance at the high-impedance node.
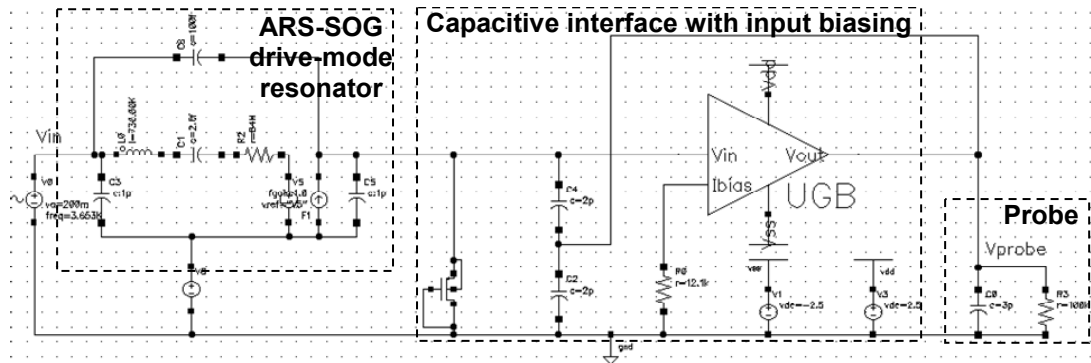
Figure 4.17: The schematic view of the lumped-element model of Figure 4.14 with the UGB circuit as a capacitive interface.
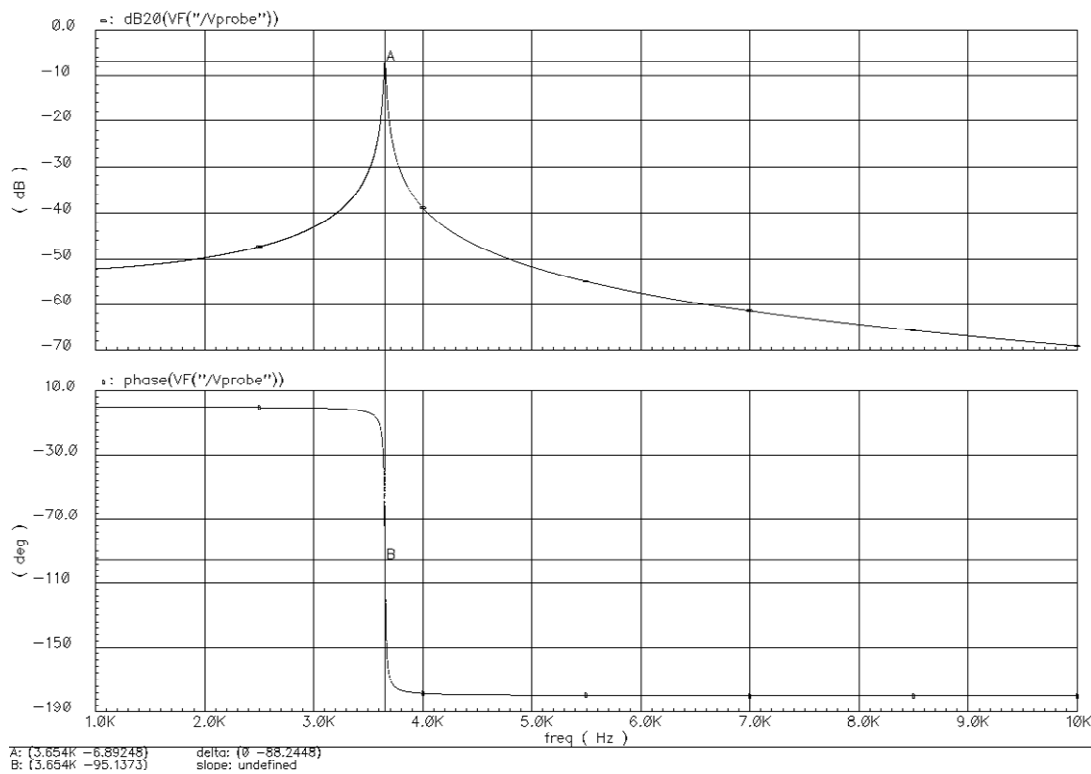
Figure 4.18: The simulated characteristics of the drive-mode resonator of ARS-SOG with UGB as the capacitive interface circuit.

Figure 4.20 shows the improvement achieved by the UGB in recovering the mechanical resonance characteristics of the gyroscope compared to the result of figure 4.17d, when there is 1pF stray capacitance between the input and the output of the drive-mode resonator. UGB achieves to keep the resonance peak over the electrical-coupling out-of-resonance, making the self-resonance excitation feasible.
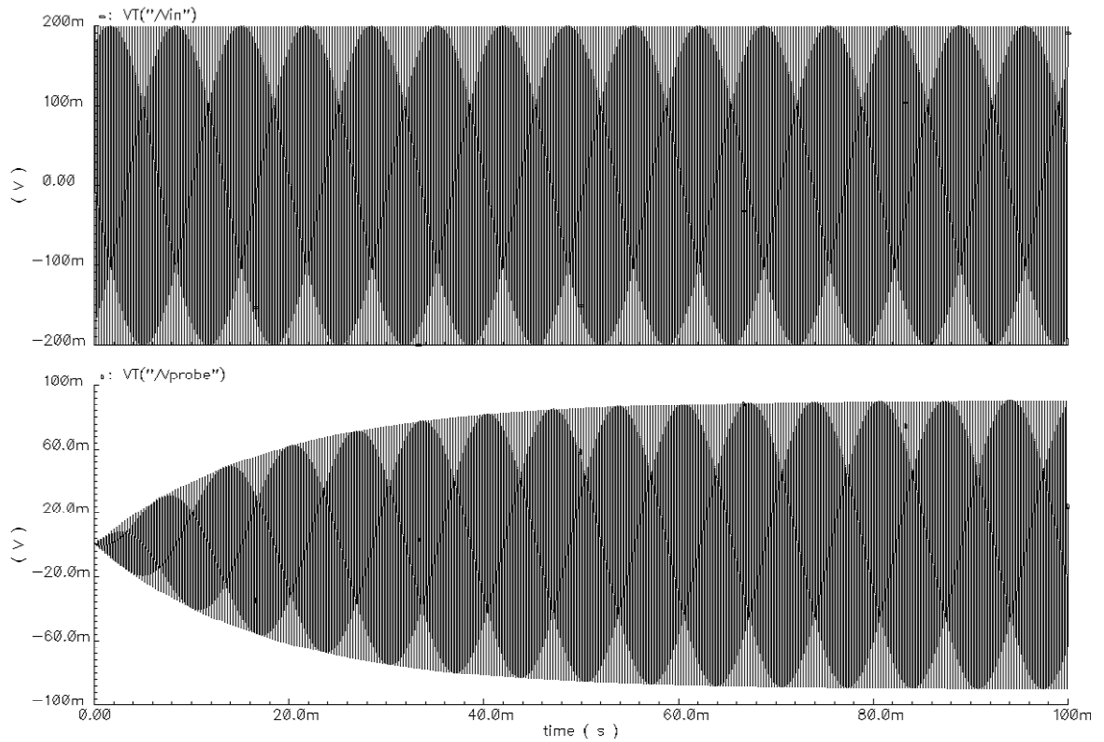
Figure 4.19: The simulated transient response of the system in Figure 4.17.
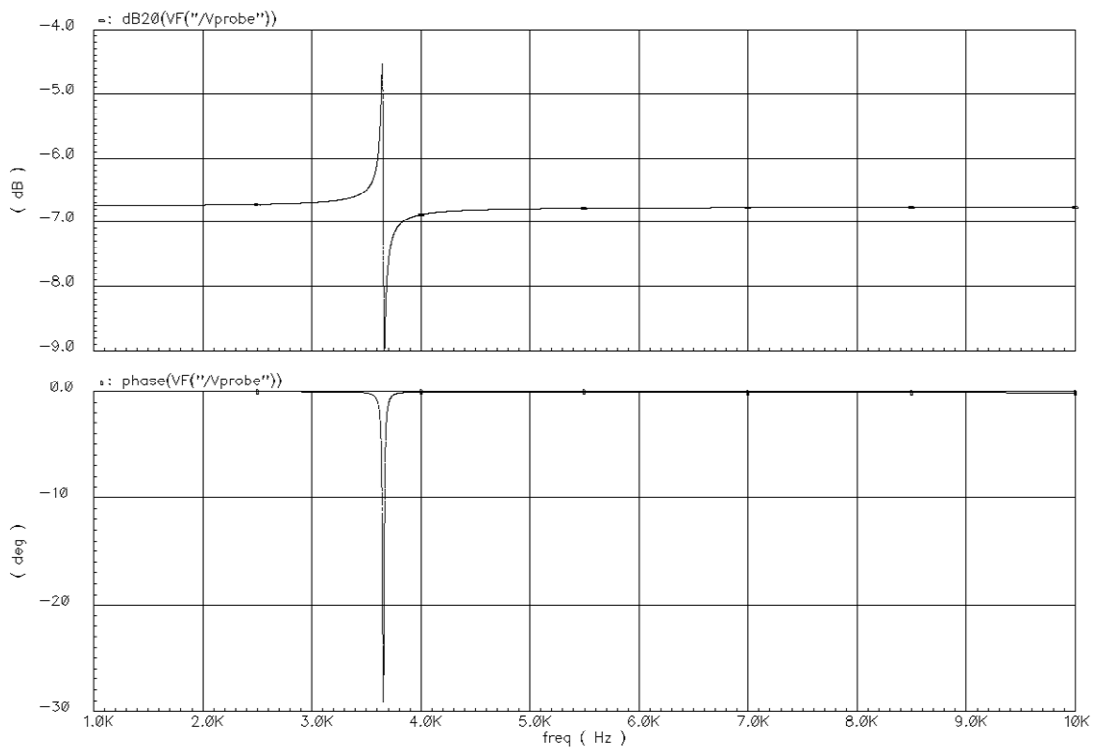
Figure 4.20: The improvement achieved by the UGB in recovering the mechanical resonance characteristics of the gyroscope, with a 1pF stray capacitance between the input and output of the drive-mode electromechanical resonator.

187

The final point about the performance of the designed UGB capacitive interface circuit is the electrical noise. Figure 4.21 shows the simulated spectral-density of output voltage noise of the circuit in Figure 4.10 with a 1pF sensor capacitance is added to the input node. The average output noise density of the UGB circuit is simulated to be less than $64nV/Hz^{1/2}$ in the band from 1kHz to 10kHz, within the typical frequencies of the amplitude-modulated outputs of the designed gyroscopes. The major contribution to the noise is expected to be from the current-noise of the sub-threshold MOS transistor biasing the high-impedance node. Then, the channel resistance of the sub-threshold PMOS transistor is should be 6.5Gohm, sufficiently high for assuming the impedance of the input node is determined by the capacitances, rather than the biasing resistance.
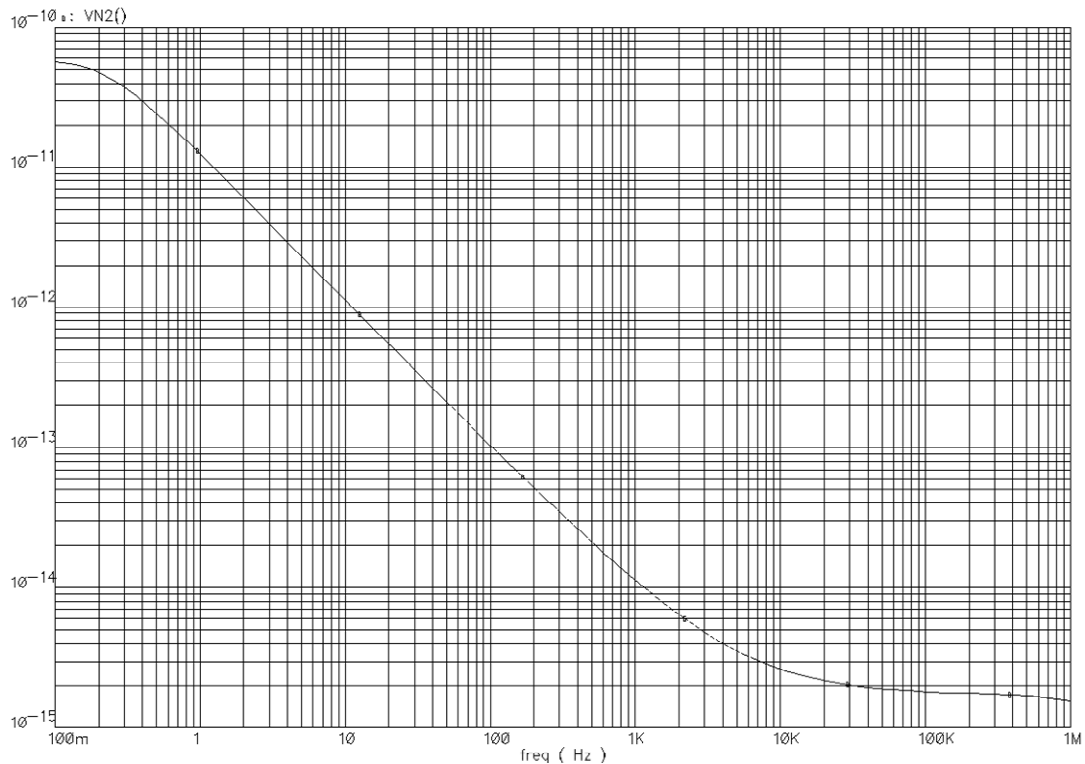
Figure 4.21: The simulated noise-voltage spectral density of the circuit in Figure 4.5. The output noise density of the UGB circuit is simulated to be $64nV/Hz^{1/2}$ in the band from 1kHz to 10kHz.

The UGB capacitive is fabricated in a 0.6μm n-well CMOS process, provided by XFAB. Figure 4.22 shows the Cadence layout of the interface circuit and the photograph of the fabricated CMOS chip, occupying an area of 1.3mm x 0.7mm.

The circuit blocks are all surrounded by substrate contacts, in order to prevent leakage currents between the blocks through the substrate. Bootstrap shield layer is implemented by poly1 layer in the process, in order to prevent possible shorts between the input node and the shield node during wirebonding. The designed interface circuit chip contains three identical buffer circuits for interfacing the single drive-mode output and the two sense-mode outputs of the fabricated gyroscopes. The outputs of each buffer circuit are fed to a gain stage constructed by general-purpose operational amplifiers, for on-chip amplification.

(a)   (b)
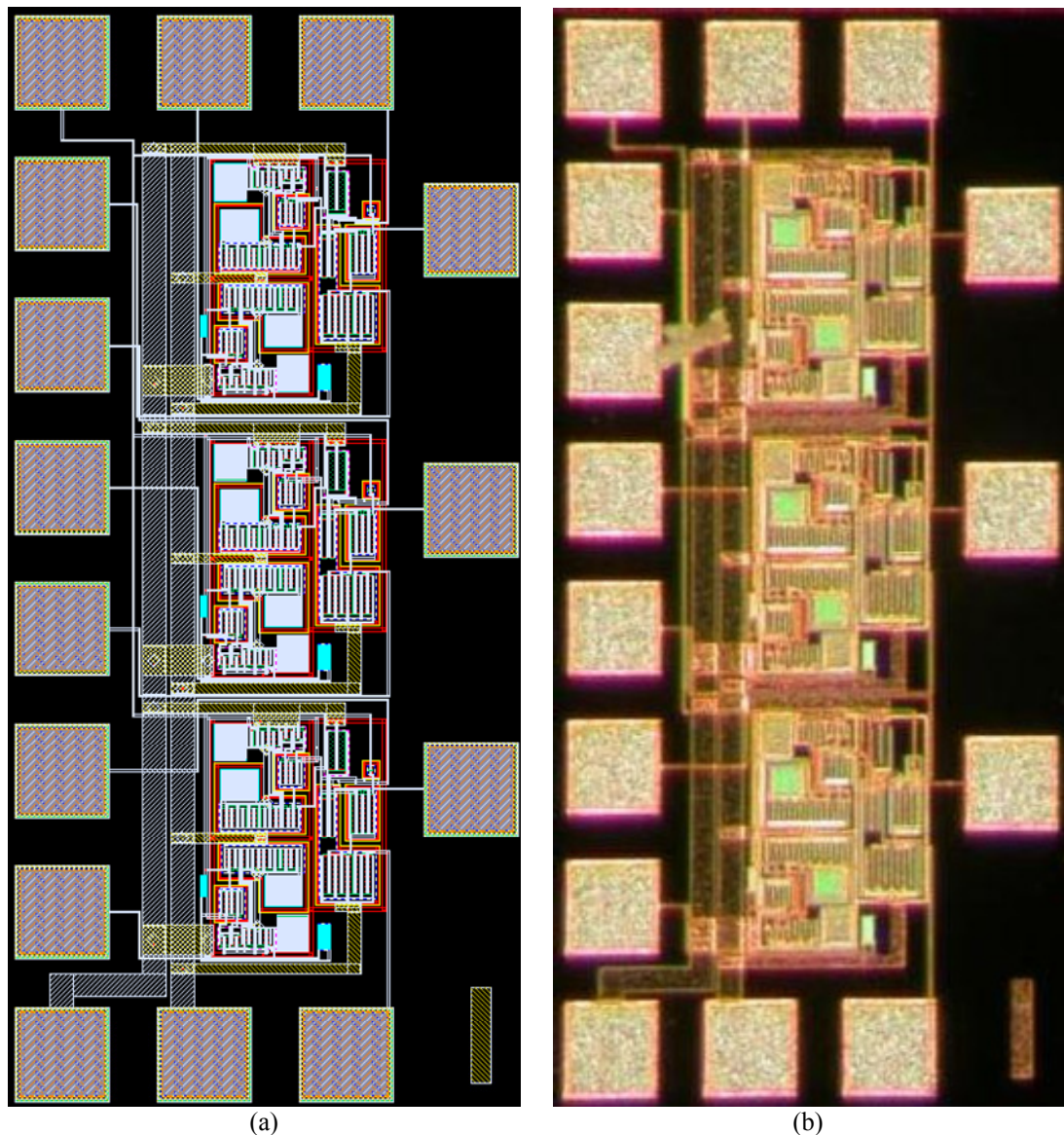
Figure 4.22: The triple-buffer design of the UGB interface circuit chip, occupying a chip area of 1.3mm x 0.7mm, and including on-chip amplification stages. (a) The Cadence layout of the interface circuit chip and (b) the photograph of the chip fabricated in 0.6μm CMOS process of XFAB.

4.4 Summary

This chapter presented the details of the unity-gain buffer (UGB) type capacitive interface circuit designed for the gyroscopes developed in this study. It introduced the basic limitations for the UGB capacitive interface; maximizing the impedance seen by the gyroscope and biasing the high-impedance input of the interface circuit. Next, the designed UGB capacitive interface circuit is introduced. The performance parameters of the circuit such as the open-loop gain, input impedance, output resistance, input sweep range and output DC offset are determined by circuit simulations. The effectiveness of bootstrapping on maximizing the input impedance and the current-to-voltage conversion capability of the UGB are verified by simulations. Finally, UGB performance is evaluated by constructing a lumped-element circuit model is for the drive-mode resonator of the ARS-SOG prototype presented in the previous chapter. The system transfer functions obtained by a standard probe measurement and by the UGB are compared, for verifying the effectiveness of the interface circuit in buffering the high-impedance output of the capacitive resonator. The UGB is also verified to improve the transfer characteristics, when there is huge stray capacitance between the input and the output of the capacitive resonator. Finally, the noise of the UGB capacitive interface circuit is simulated.

CHAPTER 5

PRELIMINARY CHARACTERIZATION RESULTS

This chapter presents the results of the preliminary tests performed on the fabricated gyroscopes as well as for the hybrid-connected gyroscope/interface assemblies. The tests include the measurement of sensor capacitances, resonance frequencies without and with capacitive interface circuit, frequency-tuning characteristics, and resonance at vacuum. The results obtained from the preliminary tests are used for determining the electromechanical model parameters of the fabricated gyroscopes and allows evaluating the design process, the capacitive interface circuit, and the fabrication tolerances. The measured model parameters of the fabricated sensors are then used to proceed with the design of closed-loop feedback electronics, and for predicting the performance of the fabricated sensors accurately.

Four different symmetric and decoupled angular rate sensor (ARS) prototypes are characterized, which are fabricated in dissolved wafer silicon micromachining (DWSM), nickel electroforming (NE), silicon-on-insulator (SOI) micromachining, and silicon-on-glass (SOG) micromachining processes as described in Chapter 3. Sections 5.1, 5.2, 5.3, and 5.4 presents the results of the tests of the fabricated ARS-DWSM, ARS-NE, ARS-SOI, and ARS-SOG gyroscope prototypes together with the fabricated unity-gain buffer (UGB) type capacitive interface circuit. Section 5.5 summarizes the tests and discusses the results.

5.1 ARS-DWSM Prototype Characterization

The preliminary characterization of the fabricated ARS-DWSM gyroscope prototype starts with the measurement of sensor capacitances. Figure 5.1 shows the results of the capacitance measurements for the drive and the sense mode electrodes, performed with AGILENT 4294A precision impedance analyzer. The sensor capacitances are measured to be 139.5fF and 140.6fF for the drive-mode and the sense-mode electrodes, respectively. The small mismatch between the capacitances demonstrates the uniformity of the DRIE patterning from the boron-doped surface of the silicon wafer. The measured capacitances are smaller than the design value of 223fF, which assumed 1µm gap spacing. The actual gap spacing after the fabrication is determined to be 1.5µm, due to lithography tolerance and a small DRIE undercut. The theoretical capacitance for 1.5µm including the simulated fringe-field correction factor of 1.4 yields 149fF, which is quite close to the measured capacitance. The simple geometry and the insulating substrate of the ARS-DWSM gyroscope provide accurate measurement of the electrode capacitances, without being affected from the parasitic capacitances significantly.
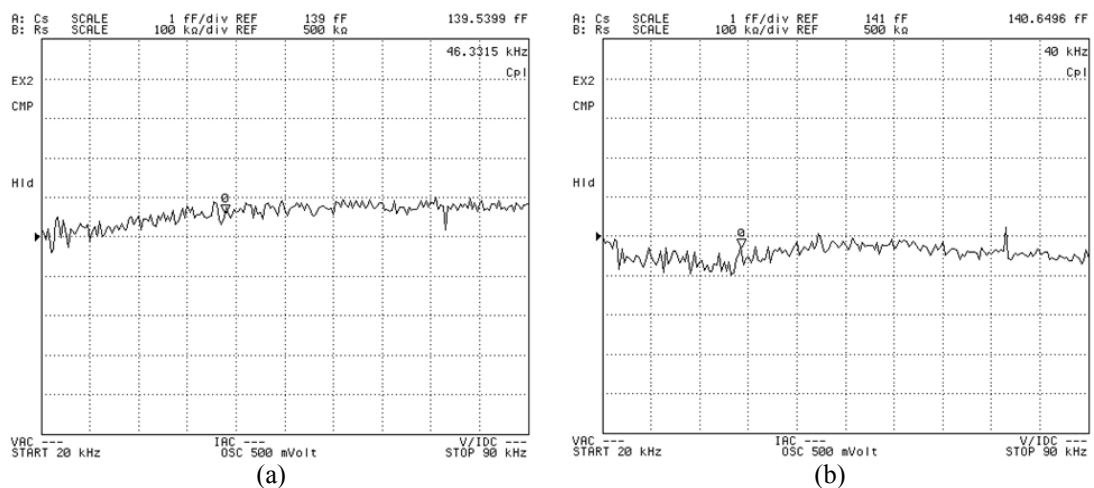
Figure 5.1: The measured capacitances of (a) the drive-mode and (b) the sense-mode electrode of the fabricated ARS-DWSM prototype

Next, the resonance frequencies of the fabricated gyroscope are measured using AGILENT 4395A network analyzer and Karl Suss micromanipulator probe station. Figure 5.2 shows the results of resonance frequency measurements, with 40V DC

192

polarization voltage applied to the proof mass. The drive and the sense mode resonance frequencies are measured to be 41,020Hz and 41,600Hz, respectively. The mismatch between the two frequencies is less than 600 Hz, and it is believed to be mainly due to a thin-layer of undoped-silicon that remained on top of the p++ doped proof mass, causing a non-uniform mass distribution.

Figure 5.2: The resonance frequencies of (a) the drive-mode and (b) the sense-mode of the fabricated ARS-DWSM prototype, measured with a resistive probe, without using capacitive interface circuit.

The resonance frequency measurements of Figure 5.2 provide several electromechanical parameters of the fabricated gyroscope. First, the spring constant of the fabricated gyroscope along the drive and the sense modes are estimated as 585N/m and 602N/m, for the drive and the sense modes, respectively, assuming the mass of the drive and the sense modes are equal to each other and close to the design values. The error introduced by this assumption is very small, since the major error source in estimating the mass is the accuracy of the structural layer thickness, which does not cause a significant variation in the resonance frequency for the designed gyroscope. Next, the quality factor of the resonance modes are identified from the resonance measurements, as about 450 for both modes. Remembering the output signal from the gyroscope is picked by AGILENT 41200A active probe with an equivalent impedance 3pF//100kohm and the sensor capacitances are pretty small; the impedance seen by the gyroscope would be resistive at 40kHz measurement

frequency. Then, combining Equations 2.55 and 2.59 from Chapter 2, the overall gain of the drive or the sense mode resonators for a resistive load would be,

$$A_{D,\,resistive\,load} = \frac{V_{D,out}(j\omega)}{V_{D,in}(j\omega)} = j\omega_D \cdot R_{PROBE} \cdot \frac{V_{DC}^2 \cdot \left(\frac{\partial C}{\partial x}\right)_D^2 \cdot Q_D}{k_D} \tag{5.1}$$

where A_D is the voltage gain from the AC input actuation signal to the displacement-induced AC output signal from the gyroscope, and the subscript "$_D$" denotes the drive-mode, while the above result is also valid for the sense mode resonator. Equation 5.1 is useful in determining the sensitivity parameter, $\partial C/\partial x$, using the measured resonance gain, frequency, quality factor and spring constant, with the known parameters of V_{DC} and R_{probe}. This parameter is evaluated to be 8.17×10^{-9} F/m and 8.37×10^{-9} F/m, for the drive and the sense modes of the fabricated gyroscope. This value is smaller than the design value of 1.17×10^{-8} F/m due to the enlarged capacitive gaps.

The resonance measurements of Figure 5.2 allow determining the spring constant, the damping factor, and the capacitive sensitivity of the fabricated gyroscope, assuming the fabricated mass is close to the designed mass. After determining the important electromechanical model parameters, the gyroscope is hybrid-connected to the designed UGB capacitive interface circuit within a 40-pin DIL package, as shown in Figure 5.3. Figure 5.4 shows the resonance frequency measurements for the drive and the sense modes of the fabricated gyroscope, connected to the fabricated UGB capacitive interface circuit. The overall gain of the system is significantly improved using the UGB capacitive interface circuit. The open-loop gain of both the drive and the sense modes are increased by two orders of magnitude, due to efficient buffering of the high-impedance output node. The phase at the resonance pass through close to -90degrees in the measurements of Figure 5.4, stating that the impedance seen by the gyroscope is now capacitive, as expected. The gain expression of Equation 5.1 is now replaced by the following, for an electromechanical resonator with a capacitive load

$$A_{D,\,capacitive\,load} = \frac{V_{D,out}(j\omega)}{V_{D,in}(j\omega)} = \frac{1}{C_D + C_{UGB}} \cdot \frac{V_{DC}^{\,2} \cdot \left(\dfrac{\partial C}{\partial x}\right)_D^2 \cdot Q_D}{k_D} \qquad (5.2)$$

where C_D and $C_{UGB,D}$ are the drive-mode sensor capacitance and the effective capacitance at the input of the UGB capacitive interface circuit connected to the drive-mode output. From the measured resonance gains in Figure 5.4 and using the extracted model parameters from the probe measurements of Figure 5.2, the total capacitances seen by the drive and sense outputs of the fabricated gyroscope, i.e., $C_D+C_{UGB,D}$ and $C_S+C_{UGB,S}$ are determined to be 265.9fF and 297.4fF, respectively. Subtracting the measured sensor capacitances from the total capacitance leaves 126.4fF and 156.8fF, respectively, for the parasitic capacitance at the input of the UGB capacitive interface circuits connected to the outputs of the drive and the sense modes, respectively. Comparing these values with the simulated input capacitance of less than 20fF, the difference is basically due to the parasitic capacitances associated with hybrid wirebonding and the conductive-epoxy used for getting electrical contact to the electrodes of the ARS-DWSM, whose interconnect metallization is missing as explained in Chapter 3.

<center>(a)</center>

<center>(b)</center>

Figure 5.3: (a) The fabricated ARS-DWSM gyroscope hybrid-connected to the UGB capacitive interface circuit inside a 40-pin DIL package. (b) Close-up view of the fabricated gyroscope.

CH1 B/R log MAG   5 dB/ REF -25 dB   -10.201 dB
                                                 40.85 kHz
                                                 Cpl
Hld   DC SOURCE ON

CH2 B/R phase   20 °/ REF -90 °   -81.461 °
                                               40.85 kHz
                                               Cpl
Hld   DC SOURCE ON
IF BW 30 Hz   POWER 15 dBm   SWP 23.54 sec
START 39 kHz   STOP 43 kHz

CH1 B/R log MAG   10 dB/ REF -40 dB   -11.004 dB
                                                41.25 kHz
                                                Cpl
Hld   DC SOURCE ON

CH2 B/R phase   30 °/ REF -30 °   -82.761 °
                                               41.25 kHz
                                               Cpl
Hld   DC SOURCE ON
IF BW 30 Hz   POWER 15 dBm   SWP 23.54 sec
START 39 kHz   STOP 44 kHz

          (a)   (b)

Figure 5.4: The resonance frequency measurements for (a) the drive and (b) the sense modes of the fabricated ARS-DWSM gyroscope, connected to the fabricated UGB capacitive interface circuit.

The UGB capacitive interface circuit also increased the amplitude of the resonance peak and helped separating the distance between the resonance and anti-resonance peaks, as simulated in Chapter 4, allowing to identify the correct signal phase at resonance, which would be important for self-resonance excitation of the drive-mode.

The varying-overlap-area type comb electrodes of the ARS-DWSM gyroscope theoretically does not allow electrostatic tuning of the mechanical resonance frequencies after fabrication. However, in practice there is a tight range in which the resonance frequencies can be tuned by varying the DC polarization voltages applied across them, due to the nonlinear fringing electrostatic-fields. Figure 5.5 shows the measured resonance frequencies of the drive and the sense modes of the fabricated ARS-DWSM gyroscope, at different DC potential applied across the movable and the stationary comb fingers associated with each mode. The frequency mismatch can be decreased down to 265Hz by applying 15V DC bias to the drive electrode and 40V DC bias to the sense electrode. On the other hand, applying DC bias voltages higher than several tens of volts may cause pull-in of the proof mass to the electrodes or substrate. Also note that keeping the drive mode DC bias at 15V for closing the frequency mismatch would also decrease the drive mode vibration amplitude, as well as the rate sensitivity.

196

Figure 5.5: Measured resonance frequencies of the drive and the sense modes of the fabricated ARS-DWSM gyroscope, at different DC potential applied across the movable and the stationary comb fingers associated with each mode.

The resonance characteristics of the fabricated gyroscope are also measured at vacuum ambient, in order to identify the quality of the p^{++}-doped single-crystal silicon structural material. Figure 5.6 shows the sense-mode resonance characteristics of the fabricated ARS-DWSM gyroscope, measured below 50mTorr vacuum. The quality-factor of the gyroscope exceeds 10,000 for vacuum operation, in accordance with a decrease in the resonance bandwidth. However, the difficulty in matching the resonance frequencies of the drive and the sense modes of ARS-DWSM, limits the operation of the gyroscope to atmospheric pressure.

Table 5.1 presents a comparison of the designed and the measured parameters for the fabricated ARS-DWSM gyroscope. The basic difference between the design and the fabrication is the capacitive gap spacing, which enlarged from 1µm design value to 1.5µm after fabrication. The change in the critical dimensions such as minimum capacitive gaps is typical during fabrication, due to the lithography tolerances and the initial etch undercut of DRIE. However, these effects are not taken into account during the design of the gyroscopes for the DWSM process, because of the fact that only a single fabrication attempt is performed for that process during this research.

197

The future studies should take into account the tolerances for the DWSM process, extracted from a series of well-controlled fabrication runs.
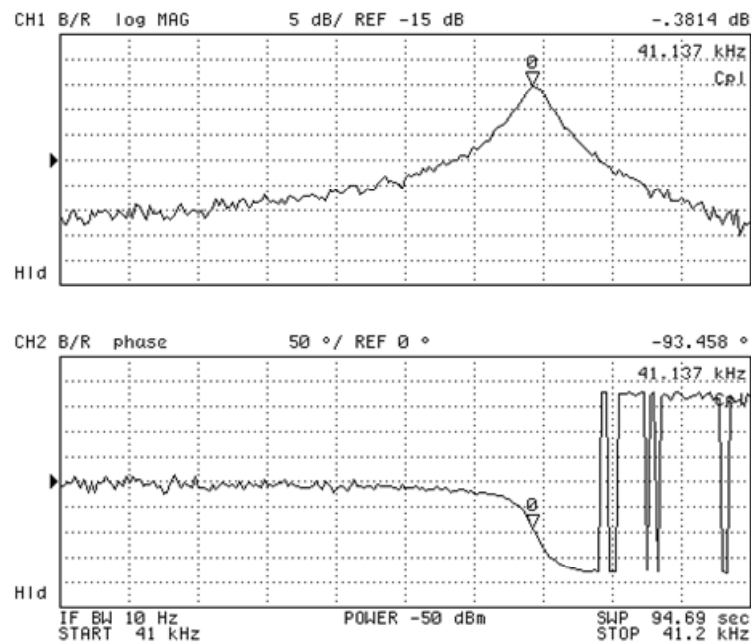
Figure 5.6: The sense-mode resonance characteristics of the fabricated ARS-DWSM gyroscope, measured below 50mTorr vacuum. The gyroscope demonstrates a quality factor above 10,000 for vacuum operation.

Table 5.1: Comparison of the designed and the measured parameters for the fabricated ARS-DWSM gyroscope.

Parameter	Designed		Measured	
	Drive	**Sense**	**Drive**	**Sense**
Capacitive gap, µm	1	1	1.5	1.5
Capacitance, fF	223	223	139.5	140.6
Resonance Frequency, Hz	42,084	42,084	41,020	41,600
Spring constant, N/m	616	616	585	602
$\partial C/\partial x$, F/m	$(1.17) \times 10^{-8}$	$(1.17) \times 10^{-8}$	$(0.82) \times 10^{-8}$	$(0.84) \times 10^{-8}$
Buffer input capacitance, fF	<500*	<500*	126	157

* A 500fF parasitic capacitance is typical for hybrid connection of the sensor chip containing the gyroscope to the CMOS chip containing the capacitive interface circuit, using wirebonding.

The comparison in Table 5.1 shows that the most of the designed parameters agree well with the measured parameters, taking into account the change in the capacitive gap spacing. The measured capacitances of the fabricated gyroscope closely match with the theoretically expected value for a capacitive gap of 1.5µm. The difference between the designed and measured spring constants and resonance frequencies is

due to the fact the width of the flexure beams slightly decreased during the process, as the feature sizes shrink for the gaps enlarging in the process. The change in beam width does not need to match the change in the capacitive gaps, as the effects of lithography and DRIE processes may vary for different geometries in the same mask. Finally, the capacitance seen by the gyroscope outputs connected to the UGB capacitive interface circuit is dominated by the parasitic capacitance associated with the wirebonding between the sensor and interface chips. Another result from Table 5.1 is that the parasitic capacitances associated with the UGB circuits connected to the drive and the sense outputs of the gyroscope are not identical, as expected. This result highlights the importance of monolithic integration of the sensor and the capacitive interface on a single substrate for minimizing the effect of parasitic capacitances, especially for the gyroscopes with small sensor capacitances such as ARS-DWSM.

In conclusion, the preliminary characterization of the fabricated ARS-DWSM gyroscope yield the fabrication tolerances for the single DWSM process conducted in this research, while the measured results agrees well with the expected results taking into account the measured tolerances. In addition, the fabricated UGB capacitive interface circuit functions as designed, while the parasitic capacitances of hybrid wirebonding dominates the input capacitance of the buffer.

5.2 ARS-NE Prototype Characterization

Figure 5.7 shows the results of the capacitance measurements for the drive and the sense electrodes of the fabricated ARS-NE gyroscope prototype, measured as 405fF and 563fF, respectively. The designed capacitances for the drive and the sense are 352fF and 381fF, for 3μm capacitive gaps and including the electrostatic fringe-field effects. The measured gap spacing for the fabricated gyroscope is approximately 2.5μm, which results in theoretical drive and sense electrodes capacitances of 422fF and 457fF, respectively, including fringe-field corrections. Clearly, the measured capacitance value for the drive electrode is very close to the value expected for 2.5μm capacitive gaps. The large difference between the expected and measured

sense capacitances is basically due to the anti-gap capacitance, which is neglected in the design but adds a physical capacitance between the movable and stationary electrodes of the varying-gap type sense capacitance. The fabricated anti-gap is measured as 8.3μm, which add a theoretical capacitance of 108fF, with a simulated fringe-field correction factor of 1.1. Therefore, the total capacitance across the sense electrode of the fabricated ARS-NE gyroscope is expected to be 565fF, for 2.5μm capacitive gap and 8.3μm anti-gap, which is very close to the measured value of 563fF.

Figure 5.7: The measured capacitances of (a) the drive-mode and (b) the sense-mode electrode of the fabricated ARS-NE prototype.

The capacitances of the tuning electrodes of the fabricated ARS-NE prototype are also measured using the precision impedance analyzer. These capacitances are found to be 265fF, 125fF, and 136fF, for tune-1, tune-2, and tune-3 electrodes, respectively, shown in the layout of Figure 3.8. The measured values are observed to be much higher than the expected values of 119fF, 16fF, and 24fF, respectively. The differences between the measured and expected values are 146fF, 109fF, and 112fF, respectively. Analyzing the layout of Figure 3.8, it is obvious that the tuning electrodes are reached through long and bended interconnect paths, laid in between neighboring electrodes, adding significant capacitance to the measurements. Therefore, it is concluded that the accurate measurement of tuning electrode capacitances is not feasible, while the measured results show these capacitances are

implemented as designed, with a common additional offset capacitance due to their interconnect lines.

Figure 5.8 shows the results of the resonance frequency measurements for the fabricated gyroscope using AGILENT 35670A dynamic signal analyzer and Karl Suss micromanipulator probe station. Dynamic signal analyzer having a capacitive input channel is used for verifying the validity of the parameter extraction method described in Section 5.1, instead of the network analyzer having the resistive probe. The resonance frequencies of the drive and the sense modes of the fabricated ARS-NE are measured to be matched at 4090Hz for a DC polarization voltage of 12^V is applied to the proof mass. The measured resonance frequency of the drive mode is slightly smaller than the expected frequency of 4678Hz, primarily due to the fabricated beam widths being 2.75µm instead of the 3µm design value. For the sense mode, it is not possible to measure the pure mechanical resonance frequency due to disturbance of the electrostatic springs across the varying-gap sense electrodes during any electrical measurements. However, the sense-mode resonance frequency is designed to match the drive-mode frequency at a DC voltage of 9.8^V applied to the proof mass, while the measured value for matching is 12^V, close to the design value.

The electromechanical parameters of the fabricated nickel gyroscope are extracted from the measurements of Figure 5.8. The mechanical spring constant of the drive mode is estimated to be 111N/m, while the mechanical+electrostatic spring constant of the sense mode is estimated to be 122N/m @ 12^VDC. The estimated electrostatic spring constant is -9N/m for the sense mode at 12^VDC. Therefore, the mechanical spring constant of the sense mode can be approximated as 131N/m. Comparing the measured mechanical spring constants with the design values of 146N/m and 159N/m, respectively, verifying that the beam widths are estimated to be matching with the design values within 10%, which is typical for many micromachining processes.
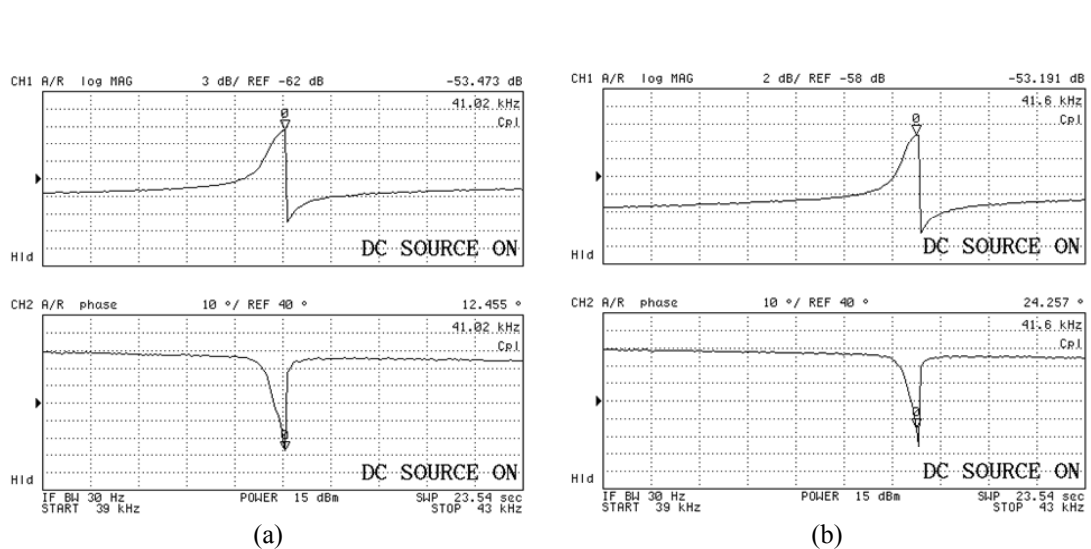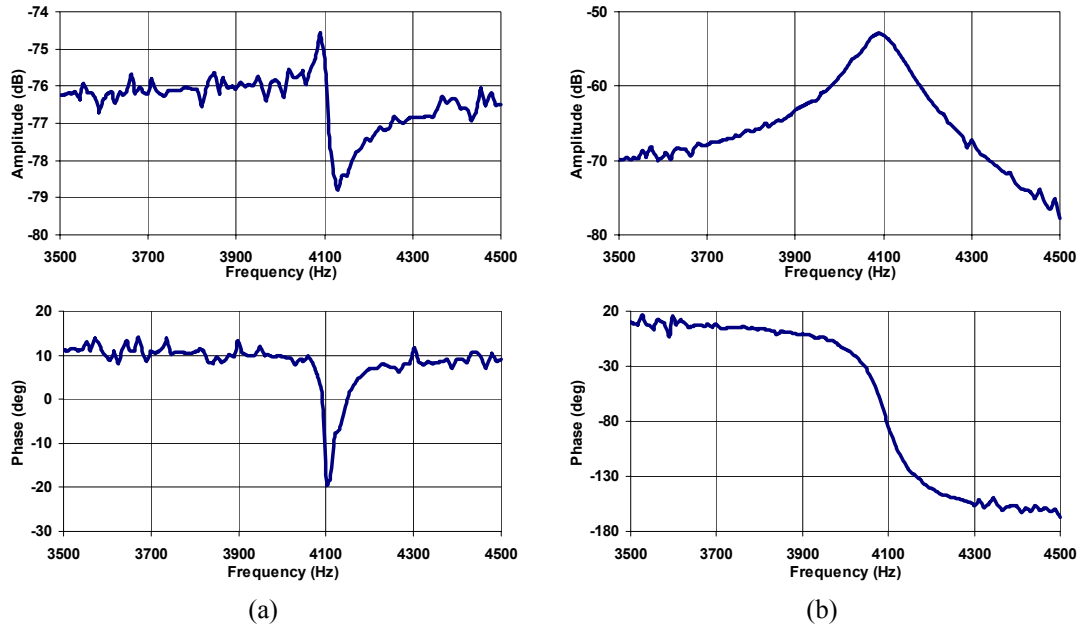
Figure 5.8: The resonance frequencies of (a) the drive-mode and (b) the sense-mode of the fabricated ARS-NE prototype, measured with a dynamic signal analyzer having a capacitive-channel, without using capacitive interface circuit.

The quality factors of the nickel gyroscope for the drive and the sense modes at atmospheric pressure are then measured to be 381 and 55, respectively. The lower quality factor of the sense-mode is a result of higher fluid damping introduced along the sense mode due to the varying-gap type sense electrodes.

The $\partial C/\partial x$ parameters of the fabricated gyroscope are estimated as 6.15×10^{-9}F/m and 5.9×10^{-8}F/m, respectively, using Equation 5.2. The measured values are observed to be smaller than the expected $\partial C/\partial x$ values are 8.88×10^{-9}F/m and 9×10^{-8}F/m, respectively, for 3μm capacitive gaps. This result looks conflicting with the 2.5μm capacitive gap spacing of the fabricated gyroscope. However, remembering that there is a height offset between the movable and stationary electrodes of the gyroscope due to the buckling of the structural layer caused by the stress-gradient of electroformed nickel, the overlapping regions of the comb fingers are reduced. This effect yields insignificant variation of the static overlap capacitance due to the increased density of electrostatic fringe-fields; however, the capacitance gradient is significantly reduced as measured.

Following the probe tests, the fabricated nickel gyroscope is hybrid-connected to the fabricated UGB capacitive interface circuit, as shown in Figure 5.9. Figure 5.10 shows the resonance frequency measurements for (a) the drive and (b) the sense modes of the fabricated ARS-NE gyroscope, connected to the fabricated UGB capacitive interface circuit. The resonance frequencies of the gyroscope after hybrid connection are observed to be different from the results of initial measurements. This is because of the fact that the nickel structure shows a slight deformation during the wirebonding process, for which the chips are heated to a minimum of 60°C. This deformation causes a permanent change in the mechanical characteristics of the gyroscope, which results in shifted resonance frequencies as in Figure 5.10. Fortunately, the variation in the resonance frequencies and the spring constants are small enough so that it is still possible to use the parameters extracted from probe measurements. The measurements of Figure 5.10 together with the probe measurements are then used for identifying the effective capacitances at the high-impedance nodes of the drive and sense mode outputs as 629fF and 642fF, respectively. The parasitic capacitances at the high-impedance drive and sense output nodes are then extracted by subtracting the measured sensor capacitances from these values, which are found as 224fF and 79fF, respectively. These values lie within the range of the expected parasitic capacitances for hybrid wirebonding.

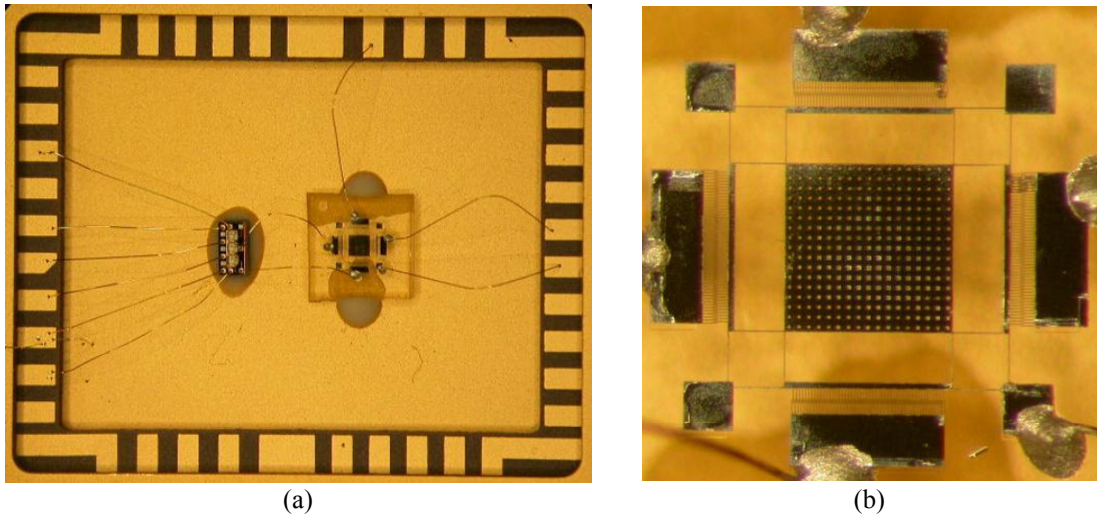(a)   (b)
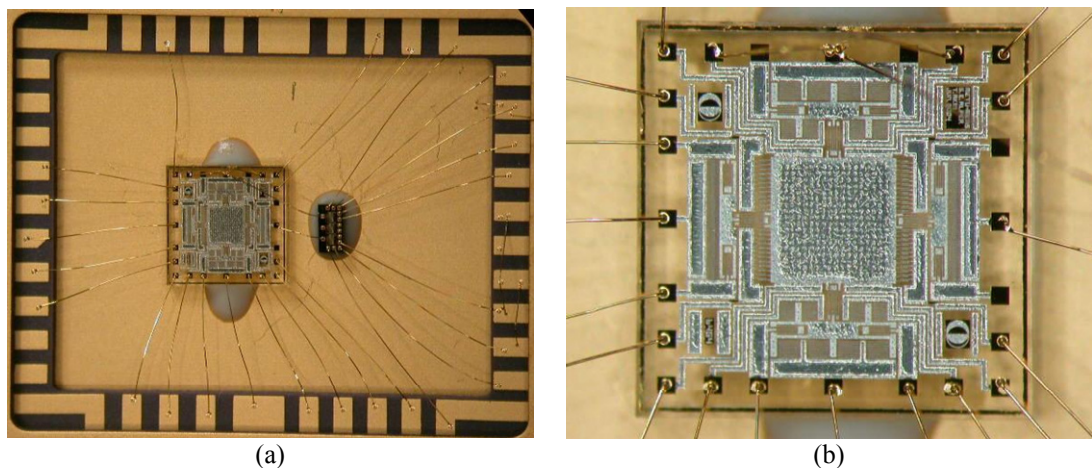
Figure 5.9: (a) The fabricated ARS-NE gyroscope hybrid-connected to the UGB capacitive interface circuit inside a 40-pin DIL package. (b) Close-up view of the fabricated gyroscope.
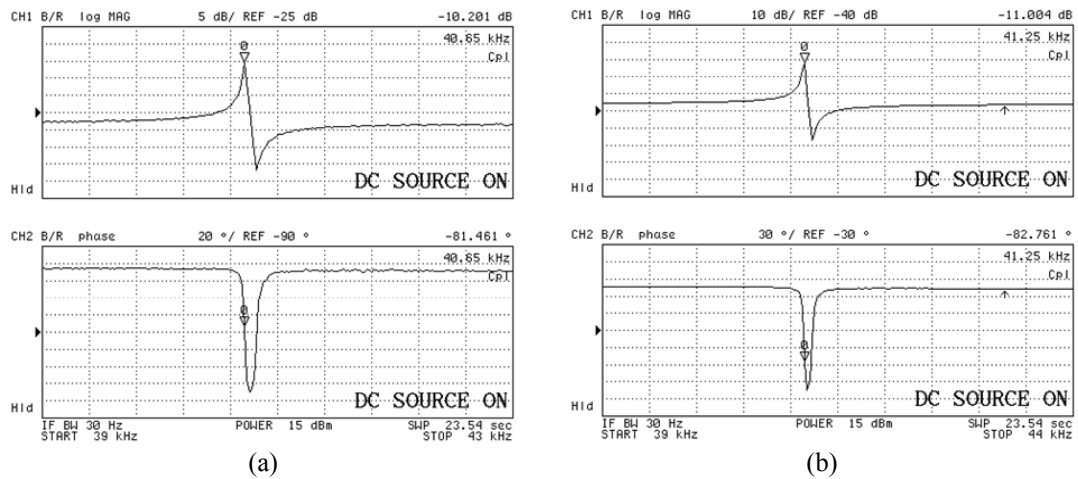
CH1 A/R log MAG   10 dB/ REF -70 dB   -33.4 dB
                                                    4,045 kHz
                                                    Cpl
                              DC SOURCE ON
Hld

CH2 A/R phase   50 °/ REF 0 °   -115.16 °
                                                    4,045 kHz
                                                    Cpl
                              DC SOURCE ON
Hld   IF BW 30 Hz   POWER 0 dBm   SWP 23.54 sec
      CENTER 4 kHz   SPAN 1 kHz
                              (a)

CH1 A/R log MAG   5 dB/ REF -25 dB   -12.238 dB
                                                    3,975 kHz
                                                    Cpl
                              DC SOURCE ON
Hld

CH2 A/R phase   50 °/ REF 0 °   -91.48 °
                                                    3,975 kHz
                                                    Cpl
                              DC SOURCE ON
Hld   IF BW 30 Hz   POWER 0 dBm   SWP 23.54 sec
      CENTER 4 kHz   SPAN 1 kHz
                              (b)
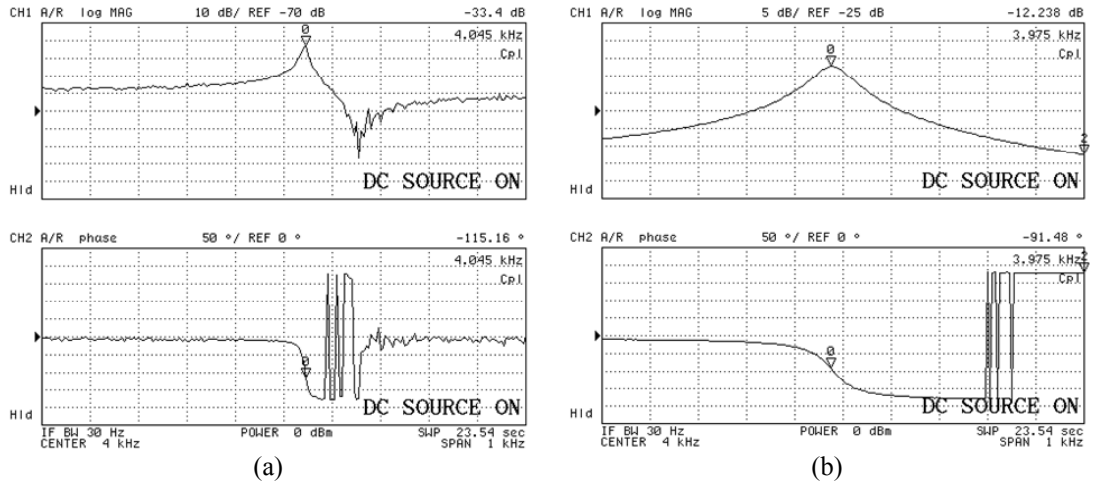
Figure 5.10: The resonance frequency measurements for (a) the drive and (b) the sense modes of the fabricated ARS-NE gyroscope, connected to the fabricated UGB capacitive interface circuit.

Figure 5.11 demonstrates the effective frequency tuning for the sense-mode of the ARS-NE gyroscope. The sense-mode resonance frequency of the gyroscope can be reduced from 4.25kHz@5^{V}DC down to 3.58kHz@20^{V}DC by negative electrostatic spring constant. The total electrostatic spring constant of the fabricated gyroscope is found to be -(0.1016)V^2, whereas the expected spring constant is -(0.1006)V^2 for 3μm capacitive gaps and -(0.1739)V^2 for 2.5μm capacitive gaps. The measured electrostatic spring constant is only 60% of that for the fabricated 2.5μm capacitive gaps. This result also matches with the measured ∂C/∂x values for the fabricated gyroscope, which are smaller than the expected values possibly due to reduced overlap area.

Figure 5.12 shows the drive and the sense mode resonance measurements of the fabricated ARS-NE gyroscope prototype at vacuum under 50mTorr. The quality factors of the drive and the sense modes exceed 850 and 550, respectively, at vacuum. The measured quality factors are limited by the mechanical properties of the electroformed nickel structural material as well as the adhesion of the anchors to the substrate.

Table 5.2 presents a comparison of the designed and the measured parameters for the fabricated ARS-NE gyroscope. The capacitive gaps are observed to shrink down

to 2.5µm, while expecting 3µm. This result sounds a more sensitive gyroscope, with increased sensor capacitances, capacitance gradients, and electrostatic springs. The sensor capacitances are measured to be increased as expected; however, the same effect could not be observed for the capacitive gradients and the electrostatic springs. The reason is believed to be due to the offset between the comb fingers of stationary and movable electrodes, which arise from the buckling of the structural layer as a result of the stress-gradient of electroformed nickel.

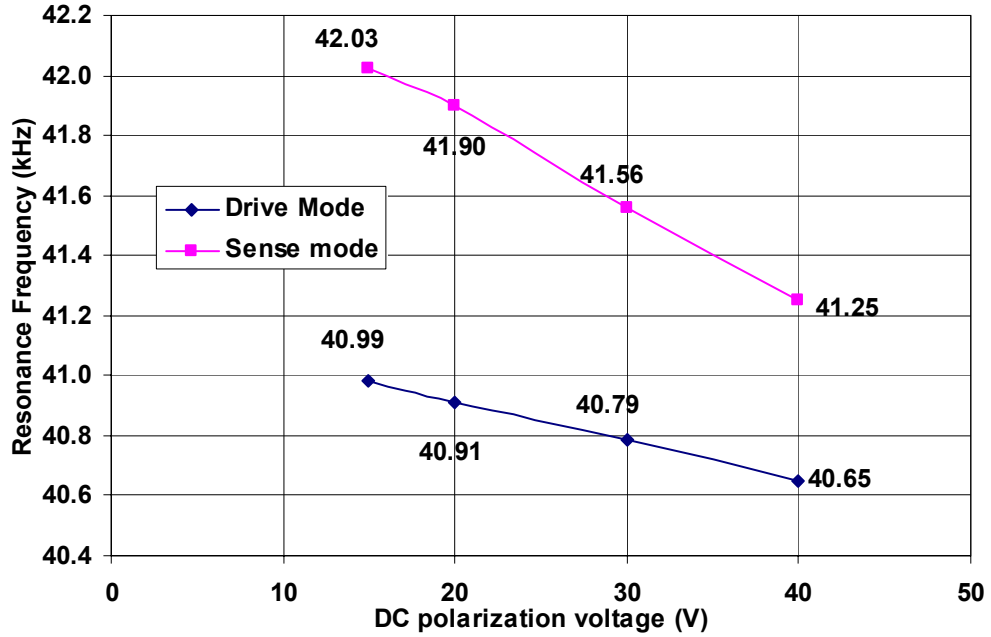**Figure 5.11:** Measured resonance frequencies of the drive and the sense modes of the fabricated ARS-NE gyroscope, at different DC polarization voltages applied to the proof mass.

Figure 5.12: (a) The drive and (b) the sense mode resonance measurements of the fabricated ARS-NE gyroscope prototype at vacuum under 50mTorr.

205

Although there is considerable difference between the designed and the measured values of few electrical parameters, most of the remaining parameters of the gyroscope are successfully predicted prior to fabrication, such as the spring constants, resonance frequencies, and the voltage required for matching the drive and the sense mode resonance frequencies. The insulating substrate of the nickel gyroscope yield very small parasitic capacitance as in the case of ARS-DWSM, limited by the hybrid wirebonding.

Table 5.2: Comparison of the designed and the measured parameters for the fabricated ARS-NE gyroscope.

Parameter	Designed		Measured	
	Drive	Sense	Drive	Sense
Capacitive gap, μm	3	3	2.5	2.5
Capacitive anti-gap, μm	N/A	8	N/A	8.3
Capacitance, fF	352	381	405	455*
$\partial C/\partial x$, F/m	$(8.88) \times 10^{-9}$	$(9.00) \times 10^{-8}$	$(6.15) \times 10^{-9}$	$(5.9) \times 10^{-8}$
$\partial^2 C/\partial x^2$, F/m^2	N/A	-0.1006	N/A	-0.1016
Mechanical spring constant, N/m	146	169	111	136.6**
Average beam width, μm	4	4	3.65	3.76
Mechanical resonance frequency, Hz	4,678	4,823	4,090	4,336***
Parasitic capacitance, fF	<500****	<500****	224	79
Voltage required for frequency matching, ^{V}DC	N/A	9.8	N/A	12

* Result exclude the anti-gap capacitance, which is theoretically evaluated about 108fF regarding the measured anti-gap of the fabricated gyroscope.
** Excludes the measured electrostatic spring constant.
*** Includes only the extracted mechanical spring constant.
**** A maximum of 0.5pF parasitic capacitance is expected for hybrid wirebonding.

The sensitivity of the nickel gyroscope is measured to improve at vacuum by an order of magnitude, due to the increase of the mechanical quality factor of the sense mode. Still, the quality factor of nickel is found to be much smaller than that measured for the silicon ARS-DWSM gyroscope, due to the higher mechanical losses for the structural nickel. Another problem observed during the preliminary characterization of the ARS-NE gyroscope is the reliability of nickel structural material. The mechanical resonance frequencies of the fabricated nickel gyroscope are observed to be very sensitive to the variations in the ambient temperature, which may cause permanent changes in the mechanical properties of the structure. Similar situation is also encountered during the vacuum tests, for which the resonance

frequencies of the gyroscope are observed to be unstable in time possibly due to the local heating of the flexing beams.

5.3 ARS-SOI Prototype Characterization

Figure 5.13 shows the measured electrode capacitances of the fabricated ARS-SOI gyroscope prototype. The conductive silicon substrate of the fabricated gyroscope is grounded prior to the tests in order to minimize the effects of parasitic stray capacitances. The drive and the sense electrode capacitances are then measured to be 991fF and 1685fF, respectively. The measurement associated with the drive electrode is observed to be affected from the parasitic capacitances at frequencies lower than 50kHz, even though the substrate is grounded. These capacitances are close to the expected capacitances of 1036fF and 1792fF, respectively, calculated for 2μm capacitive gaps, excluding anti-gap capacitances, and including electrostatic fringe-field effects. The fabricated capacitive gaps are measured to be 2.4μm for the varying-overlap-area type drive electrode, and 2.7μm with 6.3μm anti-gap for the varying-gap type sense electrode. The theoretical capacitances for the fabricated capacitive gaps are calculated to be 863fF and 1774fF, for the drive and the sense electrodes, respectively, assuming a simulated fringe-field correction factor of 1.1 for the anti-gap capacitance. As a result, the measured and expected capacitances are close to each other, and agree with the theoretically expected values. The different variation of the capacitive gap spacing for the drive and the sense electrodes is primarily due to the dependence of the initial etch undercut of DRIE to the etch pattern geometry.

Figure 5.14 shows the resonance tests for the drive and the sense modes of the fabricated ARS-SOI gyroscope measured with AGILENT 4395A network analyzer and Karl Suss probe station. The measurement is performed by applying 9^VDC to the proof mass. The resonance frequencies of the drive and the sense modes of the gyroscope are measured to be 5275Hz and 5250Hz, respectively, for 9^VDC proof mass voltage. The measured frequencies are close to the expected frequencies of 5424Hz and 5061Hz@9^VDC, assuming a capacitive gap spacing of 2μm. Note that,

the frequencies of the drive and the sense mode frequencies are estimated to be matching at 7.3^VDC, during the design. The mechanical spring constants of the gyroscope is determined from the measurements as 130.5N/m and 161N/m, by substracting the expected electrostatic spring constant for the sense mode with the measured capacitive gap spacing of 2.7μm and 9^VDC polarization voltage. These mechanical spring constants also agree with the expected values of 138N/m and 185N/m.
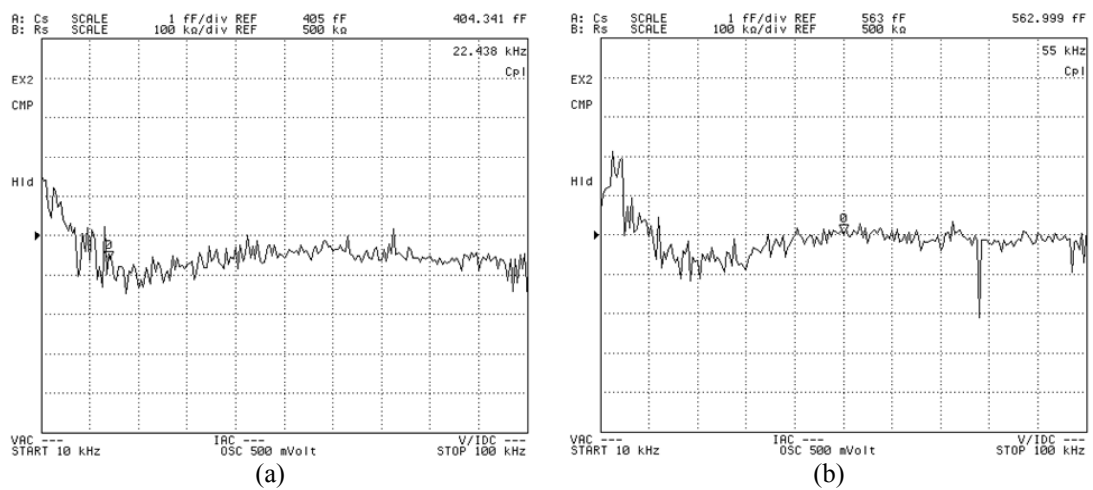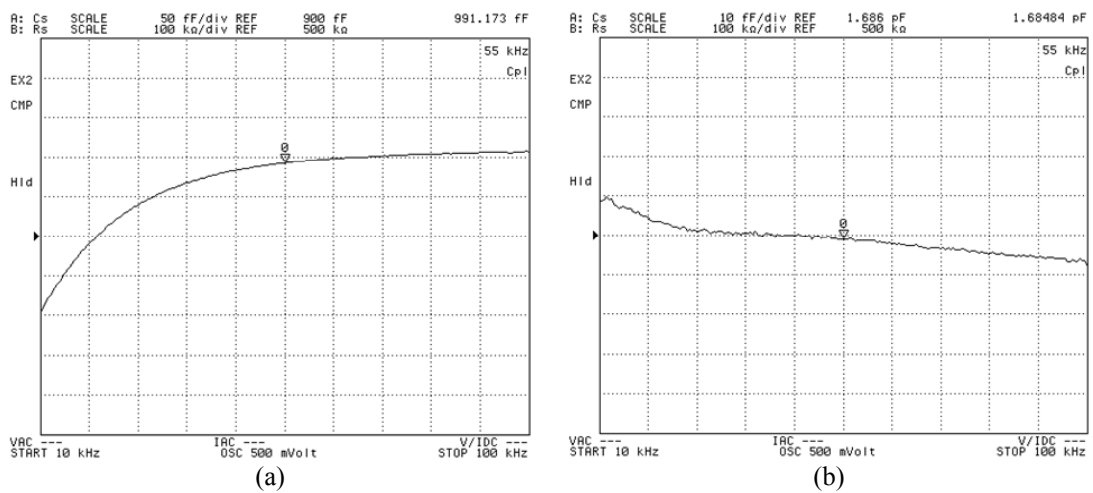

Figure 5.13: The measured capacitances of (a) the drive-mode and (b) the sense-mode electrode of the fabricated ARS-SOI prototype

Figure 5.14: The resonance frequencies of (a) the drive-mode and (b) the sense-mode of the fabricated ARS-SOI prototype, measured with a resistive probe, without using capacitive interface circuit.

The mechanical quality factors of the gyroscope are determined to be 462 and 11 at atmospheric pressure, respectively, for the drive and the sense modes of the fabricated gyroscope. Capacitance gradients, $\partial C/\partial x$, for the drive and the sense modes of the fabricated gyroscope are then extracted as 3.54×10^{-8}F/m and 3.87×10^{-7}F/m, using Equation 5.1. The measured $\partial C/\partial x$ values are higher than expected value for the drive mode, which is primarily due to positive disturbance in the measured gain as a result of the excessive stray capacitances through the substrate. Remembering the stray capacitance simulations of Figure 4.16 in Chapter 4, a high electrical coupling through a large stray capacitance may cause the level of the mechanical resonance peak being increased by more than 10dB especially for the case when the stray capacitance is much higher than the equivalent lumped capacitance of the resonator under test, which is valid for the drive-mode of ARS-SOI. Therefore, it can be stated that the probe measurements must not be relied if the resonance peak is very small, as in the measurement of Figure 5.14a. The expected $\partial C/\partial x$ of the drive mode for 2.4μm capacitive gap and including electrostatic fringe-field correction must be no greater than 1.79×10^{-8}F/m, which should result in a resonance gain 6dB smaller than the measured value in Figure 5.14a. This discussion also matches with the simulations of Figure 4.16 of Chapter 4, and as a result, the $\partial C/\partial x$ parameter of the fabricated gyroscope is estimated from the measured capacitive gap value, instead of the probe measurements of Figure 5.14. For the probe measurements of the sense mode resonance, however, there is no conflict between the measured and the expected result because of the fact that the stray capacitance is possibly smaller than or in the same order with the equivalent lumped capacitance of the sense mode resonator. The measured value of 3.87×10^{-7}F/m for the sense mode with 2.7μm capacitive gaps is smaller than the expected value of 6.72×10^{-7}F/m for 2μm capacitive gaps, which agree with the theory stating that the expected value should be about 3.69×10^{-7}F/m for 2.7μm capacitive gaps.

Figure 5.15 shows the fabricated SOI gyroscope hybrid-connected to the fabricated UGB capacitive interface circuit, in a 40-pin DIL package. Figure 5.16 shows the resonance tests for the drive and the sense modes of the fabricated ARS-SOI

gyroscope measured with AGILENT 4395A network analyzer and UGB capacitive interface circuit, measured at 11^VDC potential applied to the proof mass. Using the parameters measured from the probe tests and using $\partial C/\partial x$ values of 1.79×10^{-8}F/m for the drive-mode and 3.87×10^{-7}F/m for the sense-mode, the total effective capacitance at the output of the gyroscope is extracted to be 4.16pF and 4.56pF, respectively. Removing the measured sensor capacitance values from the measured total capacitance leaves 3.17pF and 2.87pF, as the parasitic capacitance at the high-impedance output nodes of the drive and the sense modes, respectively. Clearly, the measured parasitic capacitances are quite larger than the ones measured for ARS-DWSM and ARS-NE prototypes, which are implemented on insulating glass substrates. However, the conductive silicon substrate of the fabricated ARS-SOI prototype adds a parasitic capacitance about an order of magnitude greater than the parasitic capacitance expected from the hybrid wirebonding. The measured parasitic capacitances for the drive and the sense electrodes are proportional to the total anchor areas of the electrodes, where the anchor area of the drive-mode is greater than that of the sense mode as shown in the layout of Figure 3.14 in Chapter 3.

(a)   (b)
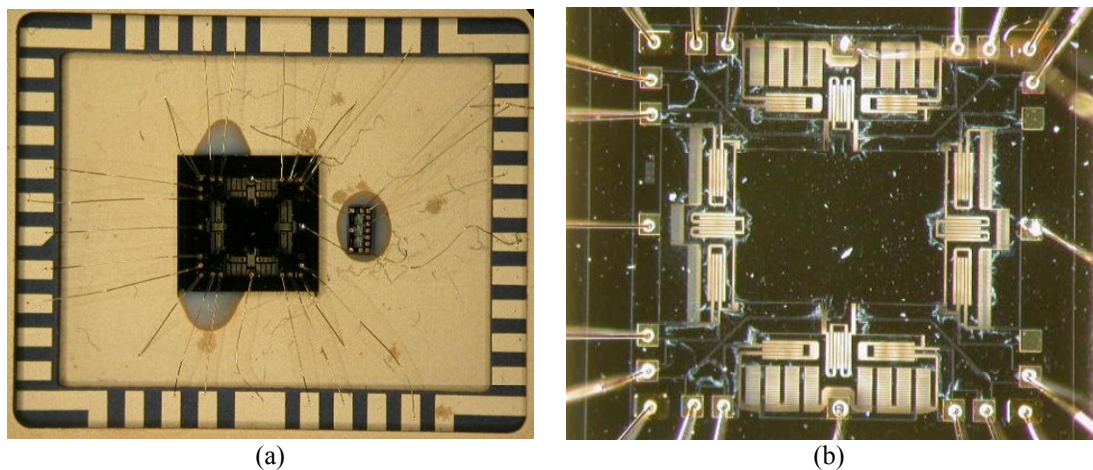
Figure 5.15: (a) The fabricated ARS-SOI gyroscope hybrid-connected to the UGB capacitive interface circuit inside a 40-pin DIL package. (b) Close-up view of the fabricated gyroscope.

Figure 5.17 shows the frequency-tuning characteristics of the fabricated ARS-SOI gyroscope measured after hybrid connection to the capacitive interface circuit. The sense-mode resonance frequency of the gyroscope can be reduced from 5.55kHz@5^VDC down to 4.72kHz@13^VDC by negative electrostatic spring constant.

The voltage at which the resonance frequency of the drive and the sense modes are matched is in between 8^VDC and 9^VDC. From the measurements, the total electrostatic spring constant of the fabricated gyroscope is extracted to be $-(0.2965)V^2$ for the fabricated sense electrode capacitive gap spacing of 2.7μm, whereas the expected spring constant is $-(0.6980)V^2$ for 2μm capacitive gaps and $-(0.2837)V^2$ for 2.7μm capacitive gaps. The measured electrostatic spring constant closely matches with the theoretically expected spring constant for the fabricated 2.7μm capacitive gaps.
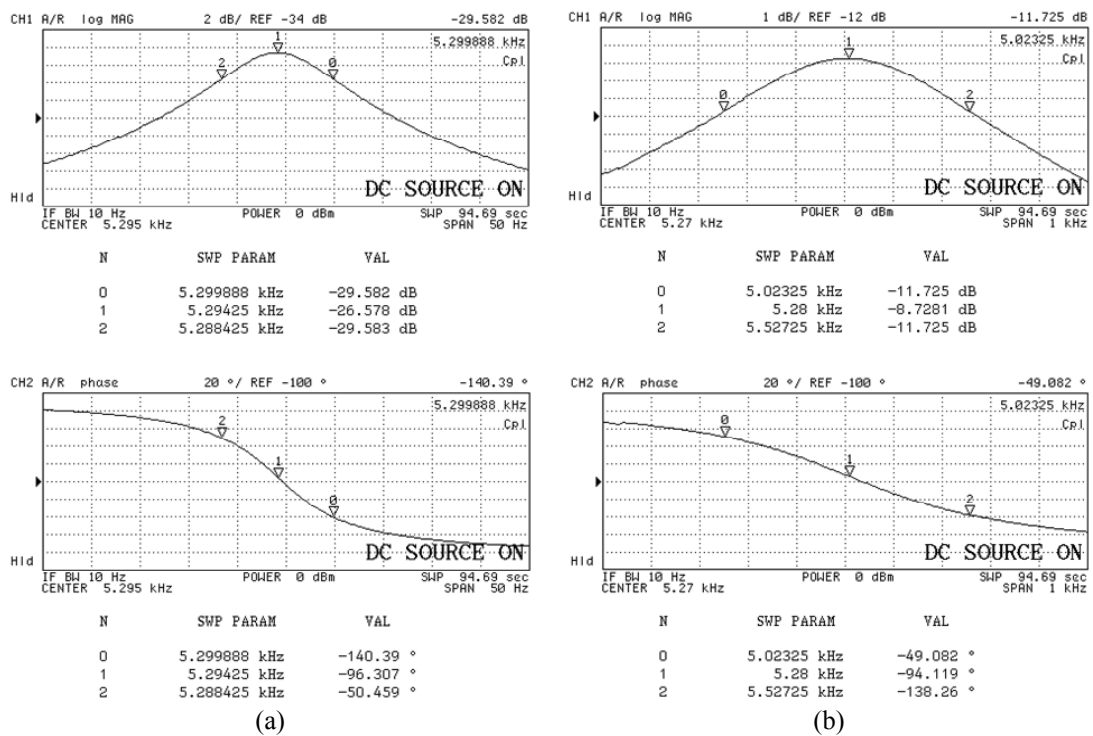
Figure 5.16: The resonance frequencies of (a) the drive-mode and (b) the sense-mode of the fabricated ARS-SOI prototype hybrid connected to the capacitive interface circuit.

Figure 5.18 shows the drive and the sense mode resonance measurements of the fabricated ARS-SOI gyroscope prototype at vacuum under 50mTorr. The quality factors of the drive and the sense modes are over 5000 and 700, respectively, at vacuum. The lower quality factor of the sense mode is expected to be due to the soft anchor of the sense electrode.

Table 5.3 presents a comparison of the designed and the measured parameters for the fabricated ARS-SOI gyroscope. The capacitive gaps are enlarged during

fabrication from the design value of 2μm, reaching to 2.4μm for the drive electrode and 2.7μm for the sense electrode. The capacitances, capacitance gradients, and the electrostatic springs extracted from the measurements agree well with the theory and close to the design values. In addition, the measured mechanical resonance frequencies show that the beam widths slightly changed during fabrication, typical for any micromachining process. The voltage for matching the resonance frequencies of the drive and the sense modes is only 1.5^V above the design value, which is basically due to the enlarged gaps and reduced electrostatic spring constants. The most important point about the preliminary characterization is the large parasitic capacitances at the high-impedance node connected to the capacitive interface circuit. This is an expected result due to the conductive silicon substrate under the structural silicon. The measured parasitic capacitances fall in the range of expected parasitic capacitances from the pads and the anchors to the silicon substrate, dominating the parasitic capacitances associated with hybrid wirebonding. The measured parasitic capacitance associated with the drive electrode is only 1/3 of the expected value, because of the undercut caused by the backside DRIE during the fabrication process, significantly reducing the effective anchor area for the drive electrode.
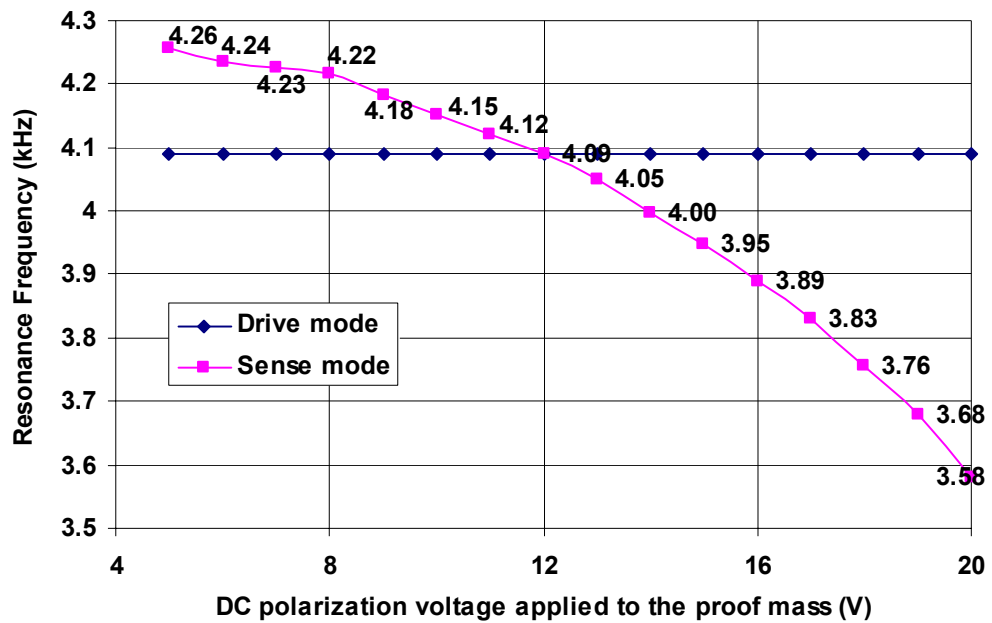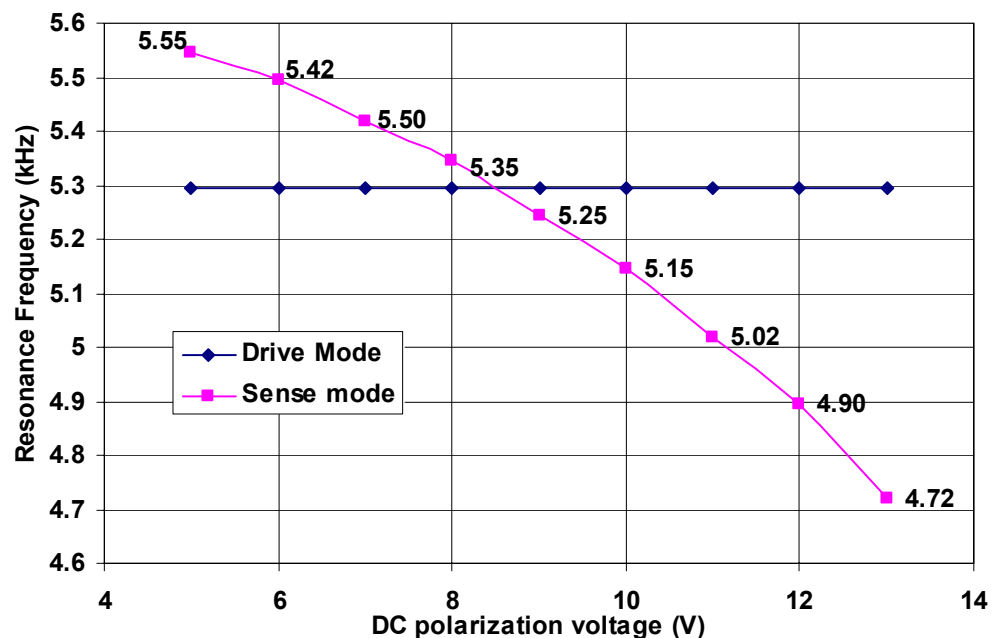

Figure 5.17: Measured resonance frequencies of the drive and the sense modes of the fabricated ARS-SOI gyroscope, at different DC polarization voltages applied to the proof mass.
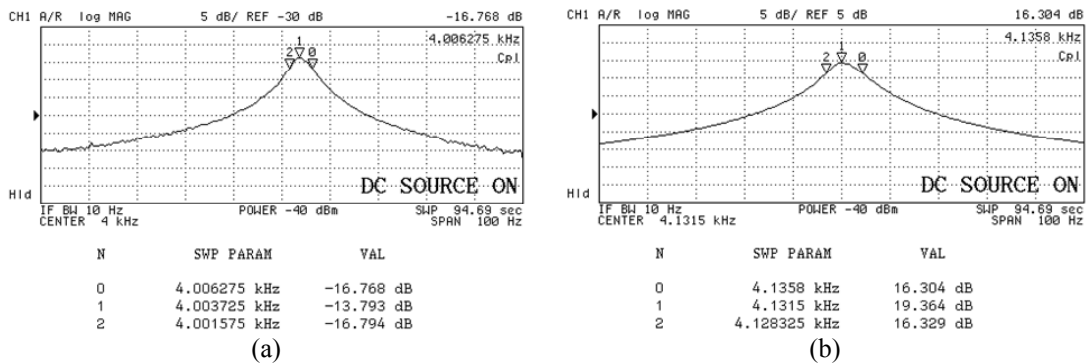
212
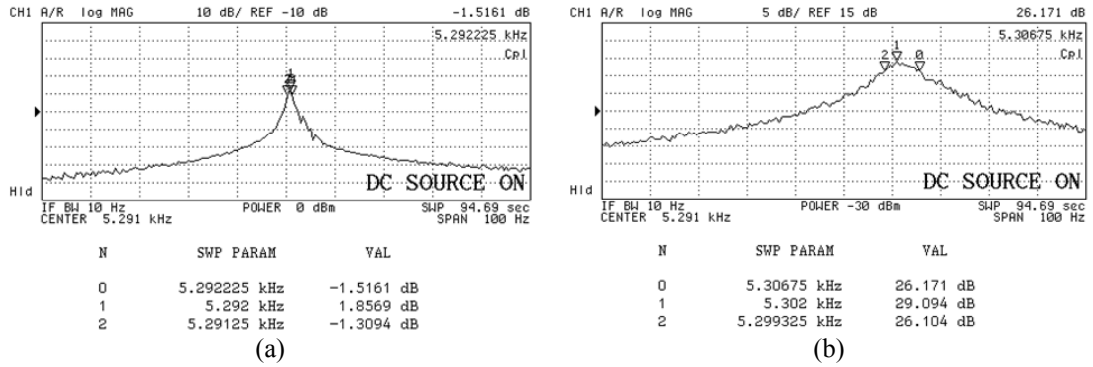
Figure 5.18: (a) The drive and (b) the sense mode resonance measurements of the fabricated ARS-SOI gyroscope prototype at vacuum under 50mTorr.

Table 5.3: Comparison of the designed and the measured parameters for the fabricated ARS-SOI gyroscope.

Parameter	Designed		Measured	
	Drive	**Sense**	**Drive**	**Sense**
Capacitive gap, µm	2	2	2.4	2.7
Capacitive anti-gap, µm	N/A	6	N/A	6.3
Capacitance, fF	1036	1792	991	1261*
$\partial C/\partial x$, F/m	$(2.58)\times10^{-9}$	$(6.72)\times10^{-7}$	$(1.79)\times10^{-8}$	$(3.87)\times10^{-7}$
$\partial^2 C/\partial x^2$, F/m^2	N/A	-0.6980	N/A	-0.2965
Mechanical spring constant, N/m	138	185	131	161**
Average beam width, µm	6	6	5.9	5.7
Mechanical resonance frequency, Hz	5,424	6,074	5,275	5,667***
Parasitic capacitance, pF	<10.7****	<3.2****	3.17	2.87
Voltage required for frequency matching, V_{DC}	N/A	7.3	N/A	9

* Result exclude the anti-gap capacitance, which is theoretically evaluated about 108fF regarding the measured anti-gap of the fabricated gyroscope.
** Excludes the measured electrostatic spring constant.
*** Includes only the extracted mechanical spring constant.
**** The parasitic capacitance is estimated by incuding the total anchor and pad area associated with each electrode and adding a 0.5pF wirebonding capacitance.

5.4 ARS-SOG Prototype Characterization

Figure 5.19 shows the test results for determining the electrode capacitances of the fabricated ARS-SOG gyroscope prototype, which are measured as 1.2pF and 12.9pF for the drive and the sense electrodes, respectively. The huge capacitance of the sense electrode is basically due to the high aspect ratio of the fabrication process and the large number of varying-gap type sense combs. Still, the measured capacitances

are slightly smaller than the expected capacitances of 1.37pF for the drive electrode, 12.1pF for the sense electrode capacitive gap, and 4.5pF for the sense electrode anti-gap capacitance, using 5μm capacitive gap, 11μm anti-gap, and electrostatic fringe-field correction factor of 1.3 for the capacitive gap and 1.05 for the anti-gap. The capacitive gaps of the fabricated gyroscope are measured to be 5.3μm for the varying-overlap-area type drive electrode, 5.6μm for the varying-gap type sense electrode, and 10.4μm for the anti-gap, through SEM inspection. The similar effect of DRIE encountered in the SOI process again cause different variations in the capacitive gaps of the fabricated gyroscope. The theoretical capacitances for the fabricated capacitive gaps are then calculated as 1.29pF for the drive electrode, 10.8pF for the sense electrode capacitive gap, and 4.44pF for the sense electrode anti-gap, which are close to the measured capacitances. The mismatch between the expected and the measured sense capacitances can be either due to the simulated fringe-field correction factors used in the design process or due to a measurement calibration error for the sense electrodes surrounded by the conductive silicon dicing street.
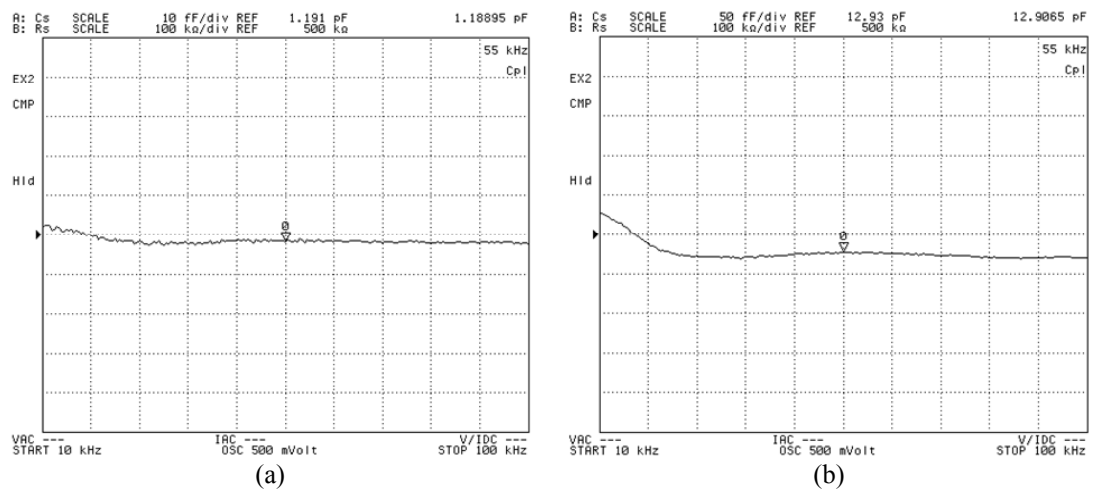
Figure 5.19: The measured capacitances of (a) the drive-mode and (b) the sense-mode electrode of the fabricated ARS-SOG prototype.

Figure 5.20 shows the resonance tests for the drive and the sense modes of the fabricated ARS-SOG gyroscope measured with AGILENT 4395A network analyzer and Karl Suss probe station. The resonance frequencies of the drive and the sense modes of the gyroscope are measured to be 2064Hz and 2020Hz, respectively, for

16^{V}DC proof mass voltage. The measured frequencies are much smaller than the expected frequencies of 3644Hz@28.8^{V}DC, assuming a capacitive gap spacing of 5µm. The main reason for reduced resonance frequencies is the narrowing of the widths of the fabricated beams, due to the lithography tolerance and DRIE undercut. The mechanical spring constants extracted from the measured resonance frequencies are 135.1N/m and 206.2N/m@16^{V}DC, respectively. The mechanical spring constant of the sense mode, excluding the electrostatic spring calculated for 5.6µm capacitive gaps and 16^{V}DC, is found as 341N/m. Comparing the measured mechanical spring constants with the design values of 421N/m and 1284N/m, the average beam width for both the drive and the sense modes are found as 2.7µm, respectively, instead of the 4µm design value. Such a large variation in the beam width cause significant shifts in the mechanical resonance frequencies, as measured. However, the gyroscope is still operational with a frequency matching voltage of 16^{V}DC instead of 28.8^{V}DC, due to the reduced mechanical stiffness.
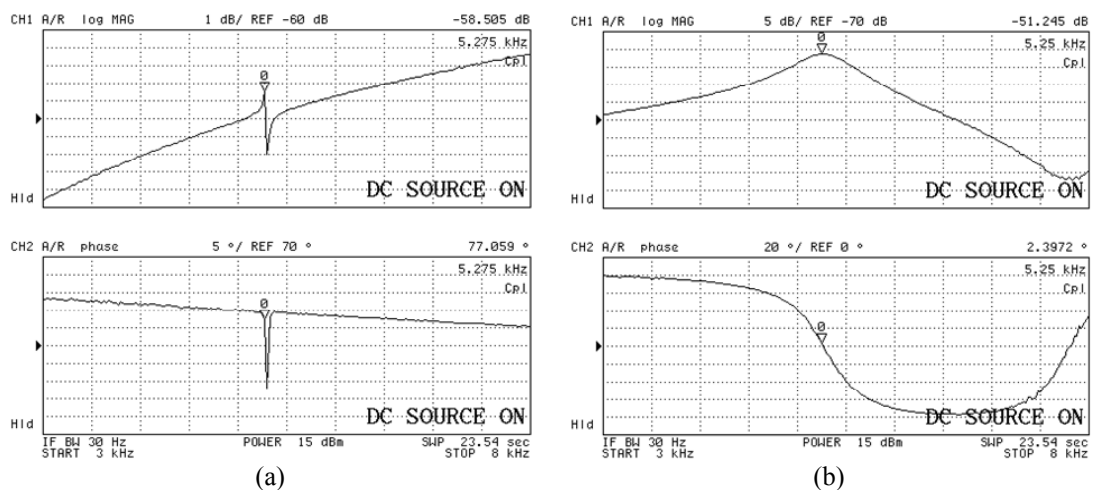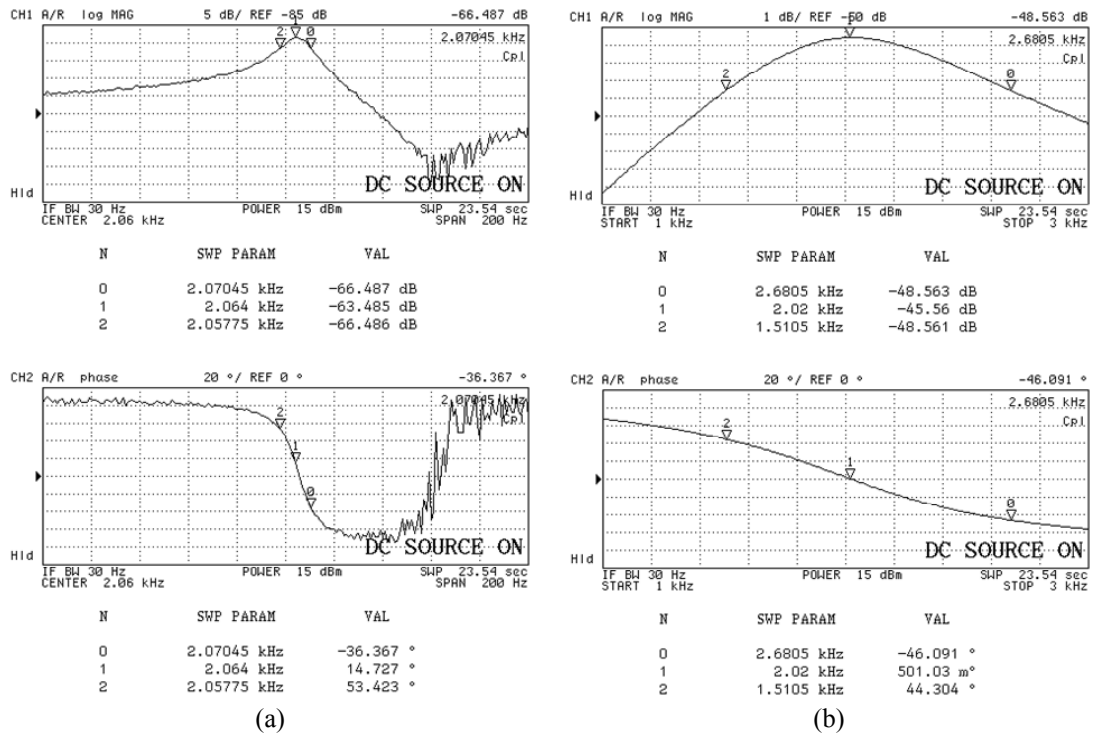
Figure 5.20: The resonance frequencies of (a) the drive-mode and (b) the sense-mode of the fabricated ARS-SOI prototype, measured with a resistive probe, without using capacitive interface circuit.

215

The mechanical quality factors of the gyroscope are determined to be 163 and 1.7 at atmospheric pressure, respectively, for the drive and the sense modes of the fabricated gyroscope. The large etch holes on the perforated masses and the high aspect ratio sense fingers result in quality factors much smaller than the previous prototypes characterized in this chapter.

Capacitance gradients, $\partial C/\partial x$, for the drive and the sense modes of the fabricated ARS-SOG gyroscope are extracted as 4.02×10^{-8} F/m and 1.4×10^{-6} F/m, using Equation 5.1. These values are close to but smaller than the design values of 4.21×10^{-8} F/m and 1.95×10^{-6} F/m, respectively, calculated for 5μm capacitive gaps. Note that, the $\partial C/\partial x$ parameter of the fabricated ARS-SOG is about 3 times greater than those of the other prototypes developed in this research. This is an expected result due to the high-aspect-ratio achieved in the SOG micromachining process.

Figure 5.21 shows two of the fabricated SOG gyroscopes hybrid-connected to the fabricated UGB capacitive interface circuits, in a 40-pin DIL package. Figure 5.22 shows the resonance tests for the drive and the sense modes of the fabricated ARS-SOG gyroscope measured with AGILENT 4395A network analyzer and UGB capacitive interface circuit, measured at 15^VDC potential applied to the proof mass. Using the parameters measured from the probe tests, the total effective capacitance at the output of the gyroscope is extracted to be 2.3pF and 16.5pF, respectively. Removing the measured sensor capacitance values from the measured total capacitance leaves 1.1pF and 3.6pF, as the parasitic capacitance at the high-impedance output nodes of the drive and the sense modes, respectively. The source of this high parasitic capacitance is believed to be due to the structure of the stationary electrodes, which are completely surrounded by either the movable silicon structures, or by the silicon dicing street surrounding the chip-frame. Obviously, extraction of the parasitic capacitances highly depend on the accuracy of the sensor capacitance measurements, which should take into account all available capacitive paths for the capacitive electrodes under test. Finding a more accurate method for measuring the sensor capacitances would improve the accuracy of the parasitic capacitance estimation. Observing the phase of the measurement in Figure 5.22b,

the impedance at the gyroscope output is not purely capacitive, which can be due to resistive behavior of the minimum-size sub-threshold biasing transistor at the high-impedance node. If this is so, the overall gain of the resonator system would be reduced, which may result in a higher estimate for the total capacitance at the high-impedance node. Future research should consider the effectiveness of the UGB capacitive interface circuit in buffering the high-impedance output of the gyroscopes with sense capacitances larger than 10pF.

(a)   (b)
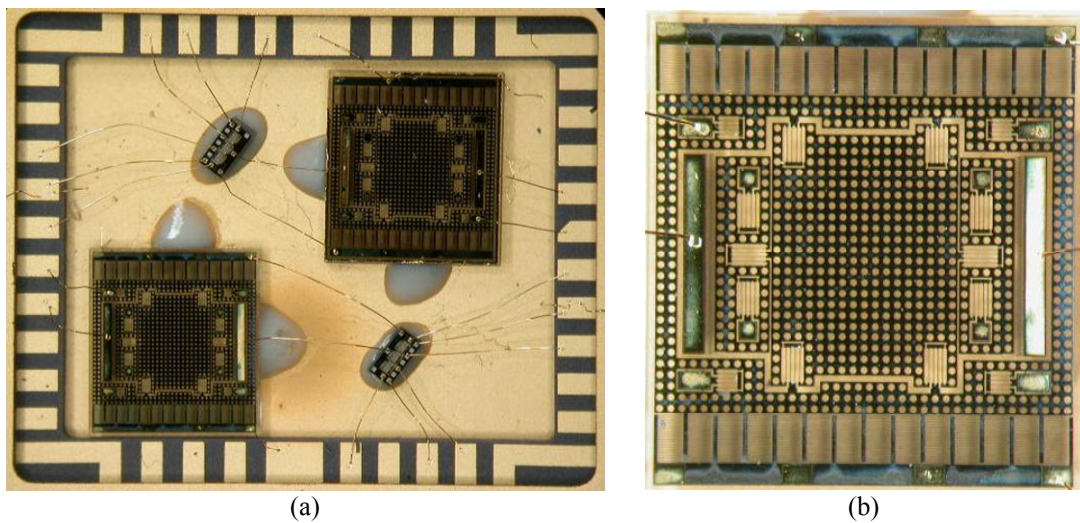
Figure 5.21: (a) Two of the fabricated ARS-SOG gyroscopes hybrid-connected to the UGB capacitive interface circuits inside a 40-pin DIL package. (b) Close-up view of the fabricated gyroscope.

Figure 5.23 shows the frequency-tuning characteristics of the fabricated ARS-SOG gyroscope. The sense-mode resonance frequency of the gyroscope can be reduced from 2.45kHz@5$^{\text{V}}$DC down to 2.02kHz@16$^{\text{V}}$DC by negative electrostatic springs. The total electrostatic spring constant of the fabricated gyroscope is measured to be -(0.42)V^2 for the fabricated sense electrode capacitive gap spacing of 5.6μm, whereas the expected spring constant is -(0.74)V^2 for 5μm capacitive gaps and -(0.53)V^2 for 5.6μm capacitive gaps. The measured electrostatic spring constant is quite close to the theoretically expected spring constant for the fabricated 5.6μm capacitive gaps.

Figure 5.24 shows the results of the drive and the sense mode resonance measurements of the fabricated ARS-SOI gyroscope prototype, at vacuum under

50mTorr. The quality factors of the drive and the sense modes are measured as 9750 and 24, respectively, at vacuum. The low quality factor of the sense mode is basically due to the small stiffness of the fabricated anchors, as a result of low-temperature anodic bonding during the fabrication process.
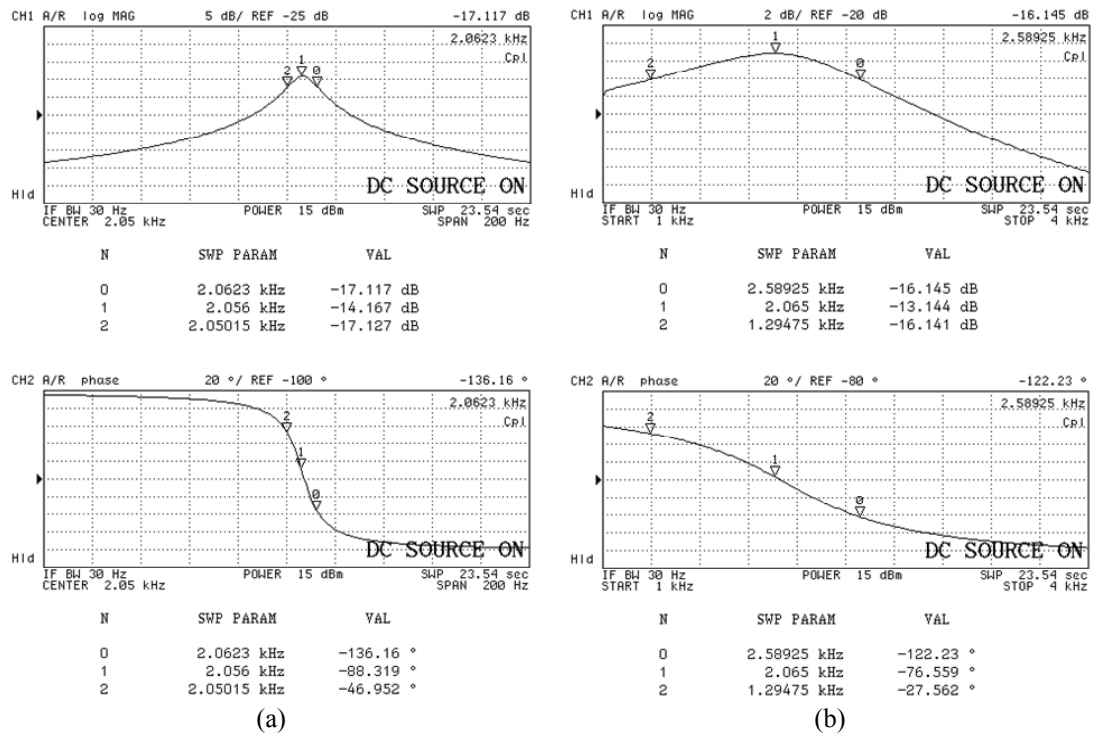
Figure 5.22: The resonance frequencies of (a) the drive-mode and (b) the sense-mode of the fabricated ARS-SOG prototype hybrid connected to the capacitive interface circuit.

Table 5.4 presents a comparison of the designed and the measured parameters for the fabricated ARS-SOG gyroscope. The capacitive gaps are enlarged during fabrication from the design value of 5μm, reaching to 5.3μm for the drive electrode and 5.6μm for the sense electrode. The capacitances, capacitance gradients, and the electrostatic springs extracted from the measurements agree well with the theory and close to the design values, as in the ARS-SOI characterization. The measured mechanical resonance frequencies show that the beam widths are significantly reduced during fabrication, due to the lithography tolerances and the DRIE etch undercut. The voltage for matching the resonance frequencies of the drive and the sense modes is found to be 16^V, much smaller than the design value, which is basically due to the decreased mechanical stiffness of the flexure beams.

218
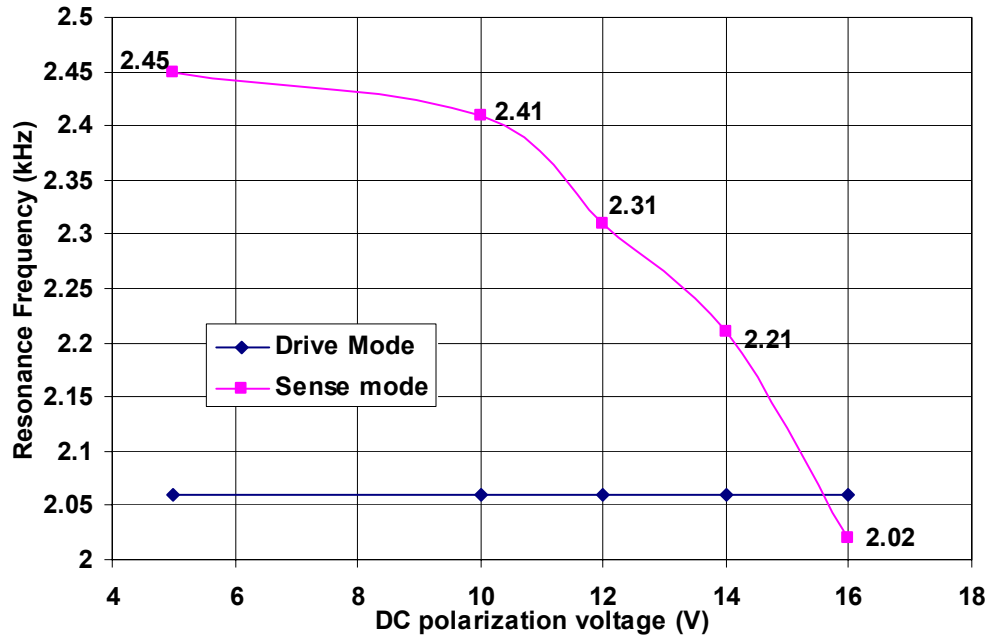
Figure 5.23: Measured resonance frequencies of the drive and the sense modes of the fabricated ARS-SOG gyroscope, at different DC polarization voltages applied to the proof mass.
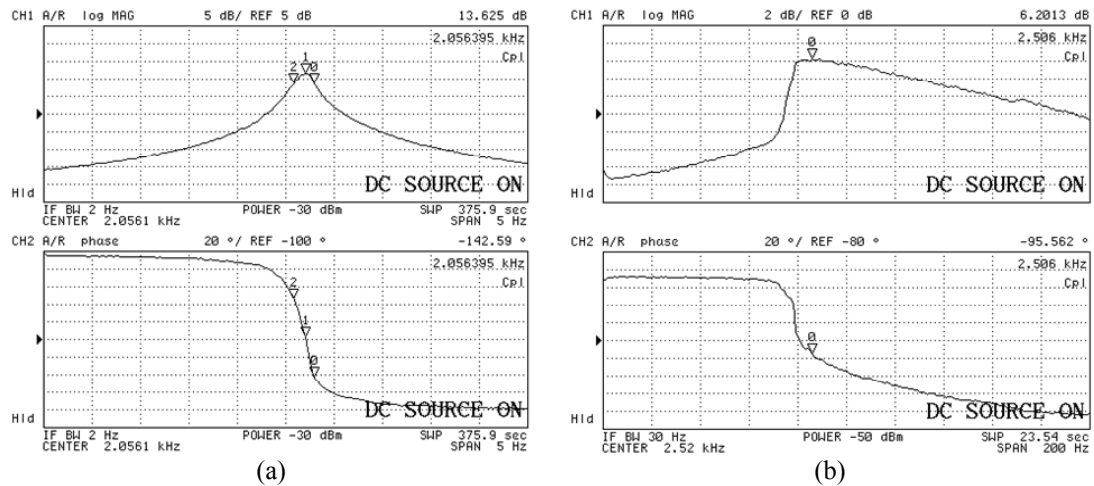
Figure 5.24: (a) The drive and (b) the sense mode resonance measurements of the fabricated ARS-SOG gyroscope prototype at vacuum under 50mTorr.

The parasitic capacitances at the high-impedance node of ARS-SOG connected to the capacitive interface circuit are measured to be higher than expected, within the range of 1 to 4pF even though the gyroscope is fabricated on insulating substrate. The sources of the high parasitic capacitances are possibly the silicon conductors surrounding the stationary drive and sense electrodes. However, the performance of

the UGB capacitive interface circuit for buffering the high-impedance outputs of large-capacitance gyroscope must also be questioned. Especially, the effect of the minimum-size sub-threshold biasing transistor scheme on determining the overall gain of the system must be carefully assessed. Future designs should take care of these facts.

Table 5.4: Comparison of the designed and the measured parameters for the fabricated ARS-SOG gyroscope.

Parameter	Designed		Measured	
	Drive	**Sense**	**Drive**	**Sense**
Capacitive gap, µm	5	5	5.3	5.6
Capacitive anti-gap, µm	N/A	11	N/A	10.6
Capacitance, pF	1.37	12.1	1.2	9.1*
$\partial C/\partial x$, F/m	$(4.21)\times10^{-8}$	$(1.95)\times10^{-6}$	$(4.02)\times10^{-8}$	$(1.40)\times10^{-6}$
$\partial^2 C/\partial x^2$, F/m	N/A	-0.74	N/A	-0.42
Mechanical spring constant, N/m	421	1284	135	341**
Average beam width, µm	4	4	2.7	2.7
Mechanical resonance frequency, Hz	3,644	5,041	2,064	2,598***
Parasitic capacitance, pF	<0.5****	<0.5****	1.1	3.6
Voltage required for frequency matching, ^VDC	N/A	28.8	N/A	16

* Result exclude the anti-gap capacitance, which is theoretically evaluated about 4.4pF regarding the measured anti-gap of the fabricated gyroscope.
** Excludes the measured electrostatic spring constant.
*** Includes only the extracted mechanical spring constant.
**** The parasitic capacitance expects a 0.5pF wirebonding capacitance.

A final word on the preliminary characterization of the ARS-SOG shows the importance of the fabrication process on the developed prototypes. Figure 5.25 shows the measured mechanical cross-coupling for two identical ARS-SOG prototypes, fabricated with the two-mask simple SOG process and with the four-mask advanced SOG process with metal etch-stop layer, respectively. The first prototype has comb fingers and beams with significant notching at the bottom as shown in Figure 3.19 in Chapter 3, while the second prototype has no destruction due to the robustness of the advanced SOG process against notching. A frequency-sweeping sine wave is applied to the drive-modes of the prototypes and the resulting sense-mode output is monitored. The effect of the drive-mode resonance is easily monitored as a spurious peak at the sense-mode output of the first prototype having DRIE-notching at the bottom, while no significant peak is observed at the sense-

mode output of the second prototype fabricated in the advanced SOG process. The mechanical coupling from the drive-mode to the sense-mode is found to be larger than 10,000ppm for the first prototype, while it is less than 250ppm for the second prototype, as predicted by the simulation of Figure 3.28 in Chapter 3.

(a)   (b)
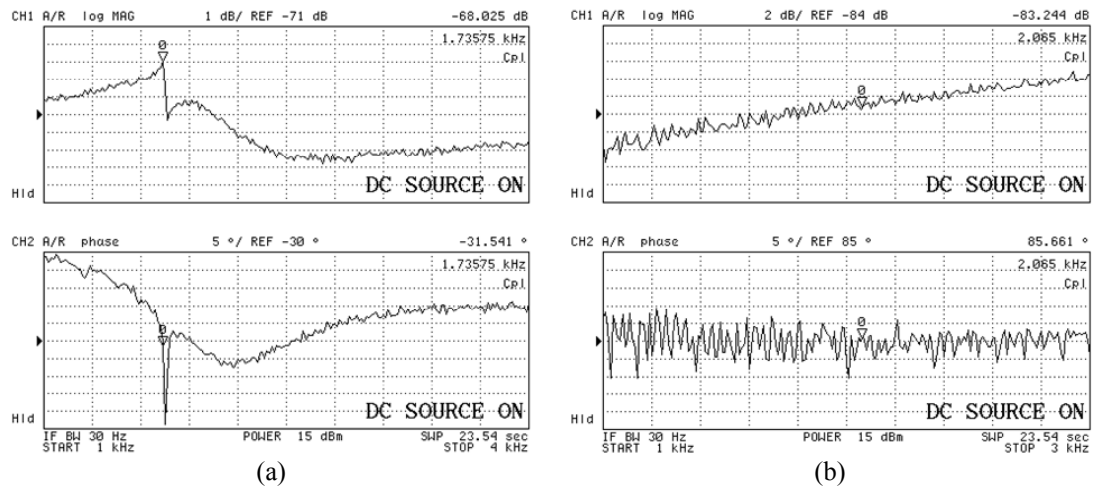
Figure 5.25: The measured mechanical cross-coupling for two identical ARS-SOG prototypes, fabricated with the two-mask simple SOG process and with the four-mask advanced SOG process with metal etch-stop layer, respectively. Quadrature coupling is (a) greater than 10,000ppm for the first-prototype having DRIE-notch-destruction at the bottom, causing a spurious peak at the sense-mode output, and (b) less than 250ppm for the second-prototype without any notching-destruction.

5.5 Summary and Discussion of the Results

This chapter presented the results of the preliminary characterizations performed for the fabricated gyroscopes as well as for the hybrid-connected gyroscope/interface assemblies. The characterization starts by measuring the sensor capacitances using a precision impedance analyzer and a micromanipulator probe station. The results of the capacitance measurements are then compared with the designed values and the expected values regarding the SEM inspection of the capacitive gaps with SEM. Next, the resonance frequencies of the fabricated gyroscopes are measured by a network analyzer and probe station. Resonance frequencies, spring constants, beam widths, and the quality factors of the fabricated gyroscope is extracted from the measured results. The known impedance of the measurement probes are used to extract the capacitance gradient, $\partial C/\partial x$, of the fabricated gyroscopes. Following that,

the gyroscope is hybrid-connected to the fabricated UGB capacitive interface circuit chip, inside 40-pin DIL IC test package. The improvements expected from the designed capacitive interface circuit are verified, while the total parasitic capacitance at the high-impedance output of the gyroscope is evaluated. In addition to these tests, the frequency tuning characteristics of the gyroscope are measured and the voltages required for matching the resonance frequencies of the drive and the sense modes are determined for the fabricated gyroscopes. Finally, the resonance characteristics of the fabricated gyroscopes are measured at vacuum, in order to determine the quality factors when the viscous air damping effect is removed from the ambient. This measurement gives an idea about the material damping and stiffness of the anchors, and provides a way to estimate the performance of the gyroscope when operated at vacuum.

The results of the preliminary characterization allow determination of the electromechanical model parameters of the fabricated gyroscopes, and evaluation of the design process, the fabrication process, and the capacitive interface circuit. The information collected from the preliminary characterization is then used to construct the electronic control loops for the fabricated gyroscopes, building an angular-rate sensor. In addition, the measured data from the fabricated gyroscope prototypes allows predicting the rate sensitivities of the fabricated angular rate sensors, both at atmosphere and at vacuum.

For the ARS-DWSM gyroscope prototype; the sensor capacitances, capacitance gradients, resonance frequencies, and the parasitic capacitances are measured to be very close to the expected values. The enlarged capacitive gaps during DRIE of silicon resulted slight variations between the designed and measured electrical parameters of the fabricated gyroscope. The parasitic capacitances are only limited by the hybrid wirebonding, and are measured to be less than 200fF due to the use of insulating substrate. The resonance frequencies of the drive and the sense modes are again observed to be mismatched by less than 1.5%, primarily due to a non-uniform mass distribution along the drive and the sense modes as a result of remained undoped silicon on the suspended mass. Theoretically, the complete symmetric

structure of the ARS-DWSM gyroscope has no frequency-tuning ability, due to its linear-force varying-overlap-area type drive and sense electrodes. Still, it has been found that the nonlinear electrostatic fringe fields are able to shift the frequencies slightly, which may be used to tune the resonance frequencies for a larger-area smaller-frequency gyroscope. Finally, the p^{++}-doped single-crystal silicon structural layer of the gyroscope demonstrated a quality factor above 10,000 at a vacuum level of less than 50mTorr. The characterization of the fabricated ARS-DWSM gyroscope verifies that it is possible to develop high-sensitivity gyroscopes with a precisely-controlled DWSM fabrication process with great accuracy between the designed and measured parameters.

For the ARS-NE gyroscope prototype; the measured sensor capacitances are close to the design values and agree well with the theoretically expected values estimated by taking into account the fabricated values of the capacitive gaps. The measured sense electrode capacitance also includes the physical anti-gap capacitance, as expected for the varying-gap type sense electrodes. In addition, the 18μm-thick nickel-electroformed, long interconnect lines on the chip surface add introduce considerable errors to the measured sensor capacitances, especially for small-capacitance electrodes. The measured resonance frequencies of the nickel gyroscope are again close to the expected values, due to the accurate estimation of fabrication tolerances during the design. The accuracy of the design, is however, limited by the buckling of the structural layer due to residual stress gradient of electroformed nickel. The buckling increase the fringe-field capacitances, however, reduces the capacitance gradient and the electrostatic spring constant of the sensor due to reduced capacitive overlap area. Another problem observed with the fabricated ARS-NE is the permanent shift in the mechanical properties of nickel, introduced during sample-heating before hybrid wirebonding to the capacitive interface circuit. On the other hand, the parasitic capacitances associated with the nickel gyroscope on insulating substrate are found to be similar to that of the ARS-DWSM. Next, the voltage required for matching the resonance frequencies of the drive and the sense modes is measured to be slightly higher than expected, due to the reduced electrostatic spring constant. Finally, the quality factors of nickel are

determined to be below 1,000 at vacuum, limited by the quality of electrodeposited nickel. The characterization results of the fabricated ARS-NE gyroscope mostly agree with the predicted parameters, however, the disturbances caused by the low-cost but also low-precision fabrication process reduce the accuracy of the design.

For the ARS-SOI gyroscope prototype; the sensor capacitances and the resonance frequencies are measured to be very close to the expected values, as in ARS-DWSM prototype. It is observed that, the large parasitic capacitances introduce significant errors to the measured capacitance gradients of especially the drive mode, as simulated in Chapter 4. Therefore, capacitance gradient of the drive mode is estimated from the measured capacitive gaps, and verified to agree with the remaining measurements. The electrostatic springs and frequency-tuning voltages of the fabricated gyroscope are accurately matching with the expected results regarding the fabricated capacitive gaps. The parasitic capacitance of the SOI substrate is pretty high, exceeding the sensor capacitances and introducing high electrical-coupling between the modes. An SOI substrate with a thicker insulating layer may help for reducing the parasitics. Finally, the gyroscope demonstrates high quality factors for the drive-mode at vacuum, but the quality factors for the sense mode is smaller due to excessive undercut of the anchor regions, causing a significant reduction in the anchor stiffness. Still, this problem can be solved by improving the control of backside trench etching step during the fabrication process. The characterization results of the fabricated ARS-SOI gyroscope almost completely agree with the theory, including the amount of large parasitic capacitances, which is the primary limitation of the SOI micromachining process.

For the ARS-SOG gyroscope prototype; the sensor capacitances are measured to be matching with the expected values, with a slight mismatch possibly related to the electrostatic fringe-field correction factors. The lithography and the DRIE tolerances caused an undercut for the flexure beams 60% higher than expected, during the thorough etching of 100μm-thick silicon. The result is a significant reduction in the resonance frequencies, which makes the device more sensitive to external acceleration signals. Still, the measured electrical parameters of the

gyroscope match with the theoretically expected values, except the high parasitic capacitances. The parasitic capacitances are estimated to be in the range of 1-4pF and higher for the sense mode output. The large silicon-volumes of the movable mass surrounding the stationary output electrodes of the gyroscope are the first suspect for these high parasitic capacitances. However, the accuracy of this measurement also needs further investigation due to the unpredicted behavior of the minimum-size sub-threshold biasing transistor of the UGB capacitive interface circuit connected to the sense electrode. The quality factors of the drive and the sense modes of the fabricated ARS-SOG gyroscope are found to be about 10,000 and 25, respectively. The huge difference between the measured quality factors is basically due to the soft anchors and pliant comb fingers of the stationary sense electrode. The soft anchors are observed to be due to the insufficient anodic bond strength, due to the low-temperature bonding recipe for preventing silicon-gold eutectic diffusion during the fabrication process. Still, the characterization results of the fabricated ARS-SOG gyroscope demonstrates the most-sensitive gyroscope prototype among the other prototypes developed in this research, owing to the dedicated structure of the designed prototype and the high-aspect ratio of the SOG micromachining process. Solving the problems associated with the fabrication process and developing an advanced capacitive interface circuit would yield a very-sensitive micromachined angular rate sensor from the ARS-SOG gyroscope prototype.

CHAPTER 6

ELECTRONIC FEEDBACK AND CONTROL CIRCUITS

This chapter presents the electronic feedback and control circuits required for constructing a complete angular rate sensor system powered from a single DC power supply and providing a DC output voltage proportional to the applied angular rate input. The functions of these circuits are to find and lock onto the mechanical resonance frequency of the drive-mode for generating sustained oscillations, and phase-sensitive detection of the output signal generated along the sense-mode. Two different closed-loop actuation mechanisms are investigated for the drive-mode electronics. The first mechanism uses an unstable positive feedback loop through a simple oscillator circuit, whereas the second mechanism employs a dedicated circuit with a stable feedback loop, allowing fine-adjustment of the oscillation amplitude. Similarly, two different phase-sensitive detection mechanisms are investigated for the sense-mode electronics; 1) the open-loop rate sensing and 2) the closed-loop rate sensing with electrostatic force-feedback. The operation of the developed actuation and detection circuits are verified by simulations before connecting them to the fabricated gyroscopes.

Section 6.1 describes the closed-loop actuation mechanisms designed for the drive-mode resonator of the fabricated micromachined vibratory gyroscopes. Section 6.2 describes the open-loop and closed-loop detection mechanisms designed for the sense-mode of the fabricated gyroscopes. Section 6.3 summarizes the chapter.

6.1 Drive-Mode Electronics

The major concern of the drive-mode electronics is the generation and control of the drive-mode oscillations in a micromachined vibratory gyroscope. Two different approaches are investigated for the generation of drive-mode oscillations, which are described in Sections 6.1.1 and 6.1.2.

6.1.1 Self-Resonance Excitation

The first and the simplest approach for generating the drive-mode oscillations is to use the drive-mode resonator as a high-Q oscillator, whose output is processed and fed-back to its input, constructing an unstable positive-feedback loop. Figure 6.1 shows the well-known topology of a simple positive feedback loop. The closed-loop gain of the system in Figure 6.1 is given as

$$\frac{V_{out}(j\omega)}{V_{in}(j\omega)} = \frac{A(j\omega)}{1 - \underbrace{A(j\omega) \cdot H(j\omega)}_{Loop\,Gain}} \tag{6.1}$$

where $A(j\omega)$ is the open-loop gain of the feed-forward network and $H(j\omega)$ is the gain of the feedback network. The conditions for starting unstable oscillations inside the loop are expressed by

$$\mathrm{Re}\{A(j\omega) \cdot H(j\omega)\} > 1 \tag{6.2a}$$

$$\mathrm{Im}\{A(j\omega) \cdot H(j\omega)\} = 0 \tag{6.2b}$$

vanishing the denominator of the closed-loop gain expressed in Equation 6.1.
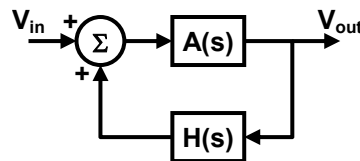
Figure 6.1: The topology of a simple positive feedback loop.

Figure 6.2 shows the electronics required for constructing the simple positive-feedback loop, in order to construct a self-resonance excitation of the fabricated gyroscopes. The loop includes the second-order model of a rate sensor, an AC coupler, a phase shifter, and a final gain stage. The second-order model of the rate sensor includes the drive-mode resonator of the gyroscope and the capacitive interface circuit hybrid-connected to the gyroscope output. The output of the capacitive interface circuit is filtered through an AC coupler, in order to remove any DC offset coming from the interface circuit. The phase-shifter generates the correct phase for electrostatic actuation to be supplied to the gyroscope input. The final gain stage is necessary to satisfy the overall gain of the system is above unity, so as to cause an amplitude build-up as a result of positive feedback. The amplitude would be limited by the voltage swings determined by the supply voltages of the electronic components constructing the self-resonance loop. The feedback loop of Figure 6.2 propose a simple method to generate self-oscillations along the drive-mode of the gyroscope, the frequency of which is determined by the mechanical resonance frequency of the gyroscope, provided that the phase of the signals are carefully controlled inside the loop.
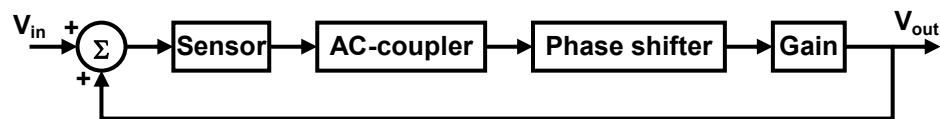
Figure 6.2: The sample self-resonance loop of the gyroscope together with the necessary electronic blocks.

The control of the signal phase inside the loop is very important for starting the self-resonance oscillations. Table 6.1 provides a fast look-up reference for checking the phase of the signals for a gyroscope/interface assembly, depending on the frequency matching of the gyroscope and the impedance at the output of the resonator associated with either the drive or the sense mode.

The loop gain of the system in Figure 6.2 is provided in Equation 6.3 below, for the case that the output impedance seen by the drive-mode resonator is capacitive, which is valid for the angular rate sensors developed in this research.

$$Loop\ Gain = \underbrace{\frac{K_D}{s^2 + \dfrac{\omega_D}{Q_D} \cdot s + \omega_D^2}}_{Sensor} \cdot \underbrace{\frac{s}{s + \dfrac{1}{\tau_{AC}}}}_{AC-Coupler} \cdot \underbrace{\left(-\frac{1}{s \cdot \tau_{PS}}\right)}_{Phase-shifter} \cdot \underbrace{K_{final}}_{Amplifier} \quad (6.3a)$$

$$K_D = \frac{V_{PM}^2}{m_D \cdot C_{in,D}} \cdot \left(\frac{\partial C}{\partial x}\right)_D^2 \quad (6.3a)$$

where the subscript "$_D$" denotes the drive-mode resonator, τ_{AC} and τ_{PS} are the time-constants for the AC-coupler and phase shifter circuits, respectively, and K_{final} is the gain of the final amplifier stage. After simplifying Equation 6.3 and re-arranging the terms yield

$$Loop\ Gain = \frac{\left(K_D \cdot K_{final}\right)/\tau_{PS}}{\left(\dfrac{\omega^2 \cdot \omega_D}{Q_D} + \dfrac{\omega^2 - \omega_D^2}{\tau_{AC}}\right) + j\left(\omega^3 - \omega \cdot \omega_D^2 - \dfrac{\omega \cdot \omega_D}{Q_D \cdot \tau_{AC}}\right)} \quad (6.4)$$

Equating the imaginary part of Equation 6.4 to zero gives

$$\omega = \sqrt{\omega_D^2 + \frac{\omega_D}{Q_D \cdot \tau_{AC}}} \quad (6.5)$$

which states that the resonance frequency of the closed-loop system in Figure 6.2 is determined by the mechanical resonance frequency of the drive-mode of the gyroscope, the mechanical quality factor of the drive-mode and the time-constant of the AC-coupler. If the quality factor of the drive-mode resonator is greater than 100 and the corner-frequency (-3dB) of the AC-coupler is smaller than $(0.1)\omega_D$, the resonance frequency of the loop would be only 0.05% higher than the mechanical resonance frequency of the drive-mode resonator. Increasing the quality factor of the drive-mode and decreasing the corner frequency of the AC-coupler will reduce the error between the mechanical resonance frequency and the frequency at which the self-resonance loop is locked. The analysis, however, is not complete since the self-resonance loop will lock onto the resonance frequency in Equation 6.5 if the

real part of the loop gain is greater than unity. The minimum gain required for starting the self-oscillations is then expressed as

$$K_{final} > \frac{\left(\omega_D^2 \cdot \tau_{AC}^2 + 1\right) \cdot \omega_D \cdot \tau_{PS}}{K_D \cdot Q_D \cdot \tau_{AC}^2}$$

(6.6)

Table 6.1: Look-up reference for checking the phase of the signals for a gyroscope/interface assembly, depending on the frequency matching of the gyroscope and the impedance at the output of the resonator associated with either the drive or the sense mode. The reference value for the given phases is the drive-mode input signal, $V_{drive\text{-}in}$, which starts the oscillations of the drive-mode.

Mode-matching	Interface type	X_{drive}	$V_{drive,out}$	Y_{sense}	$V_{sense,out}$
Matched	Capacitive	+90° *	+90°	±90°	±90°
	Resistive		In-phase		0° or 180°
Mismatched	Capacitive		+90°	0° or 180°	0° or 180°
	Resistive		In-phase		±90°

* Drive-mode is assumed to be at resonance during operation of the gyroscope.

Figure 6.3 shows the sample SIMULINK model constructed for the drive-mode resonator of the fabricated ARS-SOI gyroscope prototype and the result of transient simulations showing that the system will start self-oscillations. The simulation use the results of the preliminary characterization on the fabricated gyroscope, presented in the previous chapter. Gyroscope input is triggered with a 1msec-duration 1Vpeak pulse, after which the self-oscillations are started at the resonance frequency of the sensor. The amplitude of oscillations builds up with positive feedback until reaching to ±5V power supply limit. Then, the gyroscope is driven by the square wave input signal at the drive-mode resonance frequency. The high-Q drive-mode resonator filters out the harmonics of the input square wave and outputs an almost pure sinusoidal signal. Note that there is a 90° phase lag at the output signal, due to the interface circuit with capacitive input impedance. The start-up period of the self-resonance is close to 0.4sec for the given system, after which the gyroscope is ready for angular rate measurement.
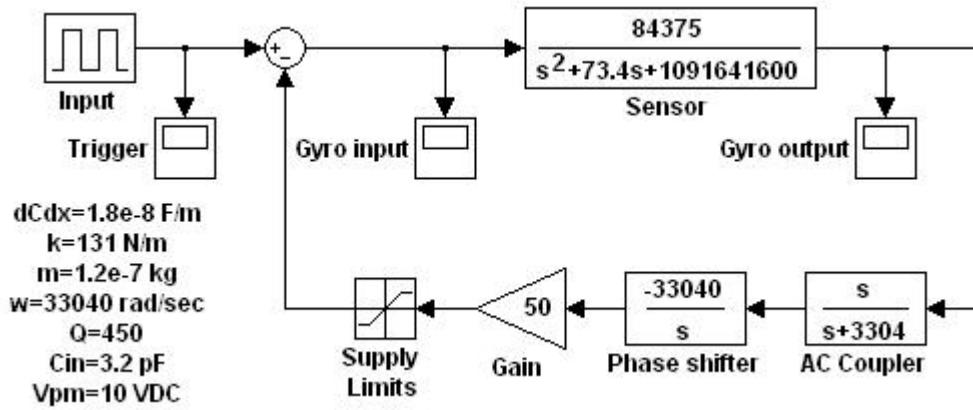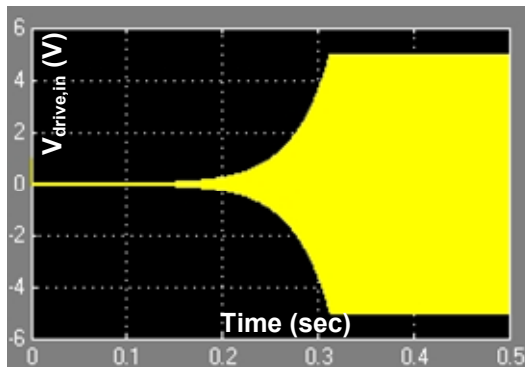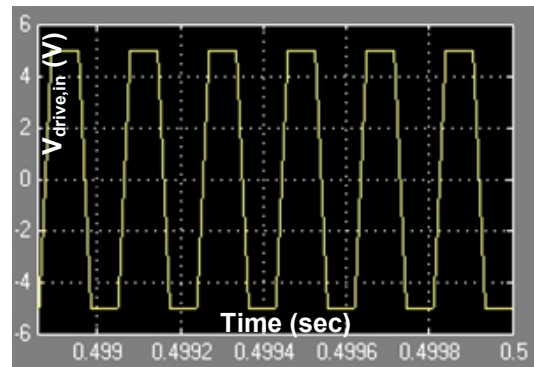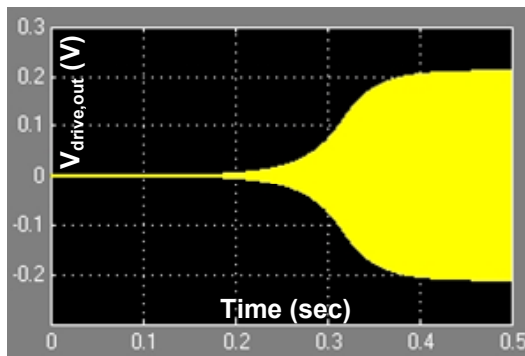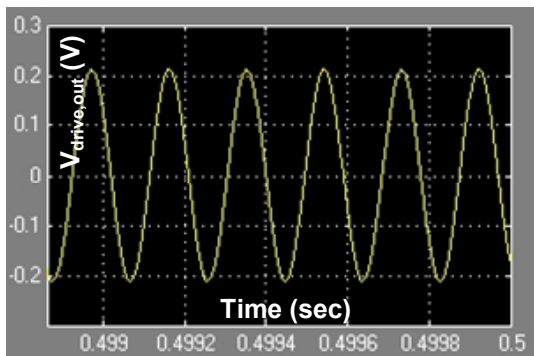
Figure 6.3: (a) Sample SIMULINK model constructed for self-resonance excitation of the ARS-SOI prototype. (b) Amplitude build-up at the input of the gyroscope. (c) Amplitude-limited input actuation signal at steady-state. (d) Amplitude build-up at the output of the gyroscope. (e) Sinusoidal output signal from the gyroscope at steady-state.

In conclusion, the self-resonance excitation of the drive-mode can be easily achieved by using a simple positive feedback loop, with proper tuning of the signal gain and phase inside the loop. The major disadvantage of the self-resonance excitation is the lack of vibration amplitude control. Although the amplitude of the input excitation

231

signal is limited, the amplitude of the physical vibrations will be determined by the mechanical quality factor of the sensor, since there is no feedback control on the amplitude of the output signal generated by the gyroscope. This would create problems for vacuum operation, in which the quality factors may increase significantly.

6.1.2 Self-Resonance with Amplitude Control

The lack of amplitude control in the simple self-resonance excitation through an unstable positive-feedback loop limits its use against variations in the quality factor of the system. The temperature-dependent variations in the quality factors of the resonators operated at vacuum may cause unstable oscillation amplitudes, which disturb the linearity and the scale factor of the gyroscope. The preferred solution is to remove the dependency of the vibration amplitude to the variations in the mechanical quality factor of the fabricated gyroscope, at least to some extent. This can be achieved by controlling the output signal from the gyroscope, which depends on the displacement amplitude of the resonator as well as a number of very stable parameters such as the DC polarization voltage, $\partial C/\partial x$ parameter, the mechanical resonance frequency, and the input impedance of the capacitive interface circuit. Therefore, the voltage at the output of the capacitive interface circuit is an accurate measure of the resonator displacement. Monitoring this voltage and keeping it constant by a proper closed-loop feedback configuration would result in vibration amplitude stable at the set value. However, this technique requires a stable closed-loop feedback configuration and cannot be adapted to the unstable self-resonance loop of Section 6.1.1. Instead, two different feedback loops are employed in the self-resonance excitation with amplitude control; the first loop finds and lock onto the resonance frequency of the drive-mode resonator whereas the second loop keeps the amplitude of vibrations stable. These loops are described in separate subsections below.

232

6.1.2.1 Frequency-Lock Loop Design

The loop that finds the resonance frequency of the drive-mode resonator and locks on it is based on a phase-locked loop (PLL) including a voltage-controlled-oscillator (VCO). Figure 6.4 shows the structure of the resonance-frequency-locking loop. The loop compares the phase of the input signal supplied from the gyroscope and the self-oscillation frequency of the VCO, and forces the phase of the VCO frequency track the frequency of the input signal by using closed-loop stable feedback mechanism. The loop consists of a phase-detector as a multiplier, a proportional-integral (PI) controller as an error amplifier, and a VCO.
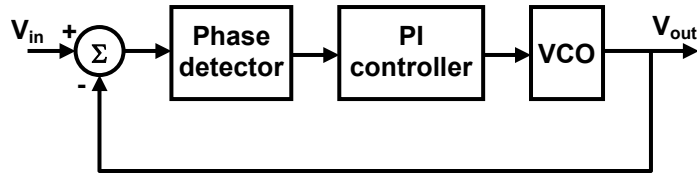
Figure 6.4: The structure of the resonance-frequency-locking loop.

The loop gain of the system in Figure 6.4 is given as

$$Loop\ Gain = \underbrace{K_{PD}}_{\substack{Phase \\ detector}} \cdot \underbrace{\left(\frac{\tau_2 \cdot s + 1}{\tau_1 \cdot s}\right)}_{PI\ controller} \cdot \underbrace{\frac{K_{VCO}}{s}}_{VCO} \qquad (6.7)$$

where the K_{PD} and K_{VCO} denote the gains of the phase-detector and the VCO, respectively. The characteristic equation of the feedback system in Figure 6.4 is used to determine the response time and the stability of the loop.

$$s^2 + \underbrace{\frac{\tau_2 \cdot K_{PD} \cdot K_{VCO}}{\tau_1}}_{2 \cdot \xi_n \cdot \omega_n} \cdot s + \underbrace{\frac{K_{PD} \cdot K_{VCO}}{\tau_1}}_{\omega_n^2} = 0 \qquad (6.7)$$

The resonance frequency and the damping factor of the second-order characteristic equation above is given by,

233

$$\omega_n = \sqrt{\frac{K_{PD} \cdot K_{VCO}}{\tau_1}} \tag{6.8a}$$

$$\xi_n = \frac{\tau_2 \cdot \omega_n}{2} \tag{6.8b}$$

Figure 6.5 shows a series of step-response curves given for a second-order system having a characteristic equation with the form in Equation 6.7. The damping factor of the system determines the percent overshoot of the step response applied to the system, and is selected as 0.8 for keeping the overshoot smaller than 20%. Then, the normalized settling time, $\omega_n t_s$, required for the output to be within 5% of its steady-state value must be greater than 5. The settling time, t_s, is selected to be an order of magnitude smaller than the response time of the gyroscope, so that the PLL can easily track the changes in the resonance frequency of the drive-mode. The response time of the drive-mode resonator is given as

$$t_{response} \approx \frac{1}{BW_D} = \frac{2 \cdot Q_D}{f_D} \tag{6.9}$$

where BW_D, Q_D and f_D are the bandwidth in Hz, the mechanical quality factor and the resonance frequency in Hz for the drive-mode resonator. After selecting the settling time of the loop, the parameters ω_n, τ_1, and τ_2 are determined, finalizing the construction of the loop.

Figure 6.6 shows a sample frequency-lock loop constructed in SIMULINK for the drive-mode resonator of the fabricated ARS-SOI gyroscope through a commercially available CD4046BC micropower PLL IC [111]. The measured values of 450 and 5275Hz are used as the quality factor and the resonance frequency of the drive-mode resonator. The response time of the gyroscope is then found as approximately 170msec. The settling time of the feedback loop is then selected to be 17msec, an order of magnitude smaller than the resonator's response time. The damping factor of the feedback loop is selected as 0.8 for keeping the overshoot below 20% for a step input, and the normalized time of 5 is selected for $\omega_n t_s$, for a steady-state error

less than 5%, yielding 295rad/sec for the natural frequency of the feedback loop. K_{VCO} is determined from the approximate equation of

$$K_{VCO} = \frac{2 \cdot \pi \cdot (f_{max} - f_{min})}{V_{DD} - 2^{V}} \tag{6.10}$$

where f_{max} and f_{min} denote the frequency range for which the constructed loop track the resonance frequency. This range is selected large enough to ensure tracking the possible variations in the resonance frequency, and small enough to prevent locking on the resonance frequency of an higher-order mode. A range of 2kHz up to 8kHz is selected for ARS-SOI prototype. The power supply, V_{DD}, of the VCO is selected as 5^{V}, although larger supplies are available. The VCO gain is then found as 12566 rad/V. Similarly, the phase detector gain, K_{PD}, of the 4046 series VCO is given as 0.4V/rad, for the 0°-locking VCO output and for a supply voltage of 5^{V} [112]. The time constants τ_1 and τ_2 of the PI controller are then determined as 57.8msec and 5.4msec, respectively.
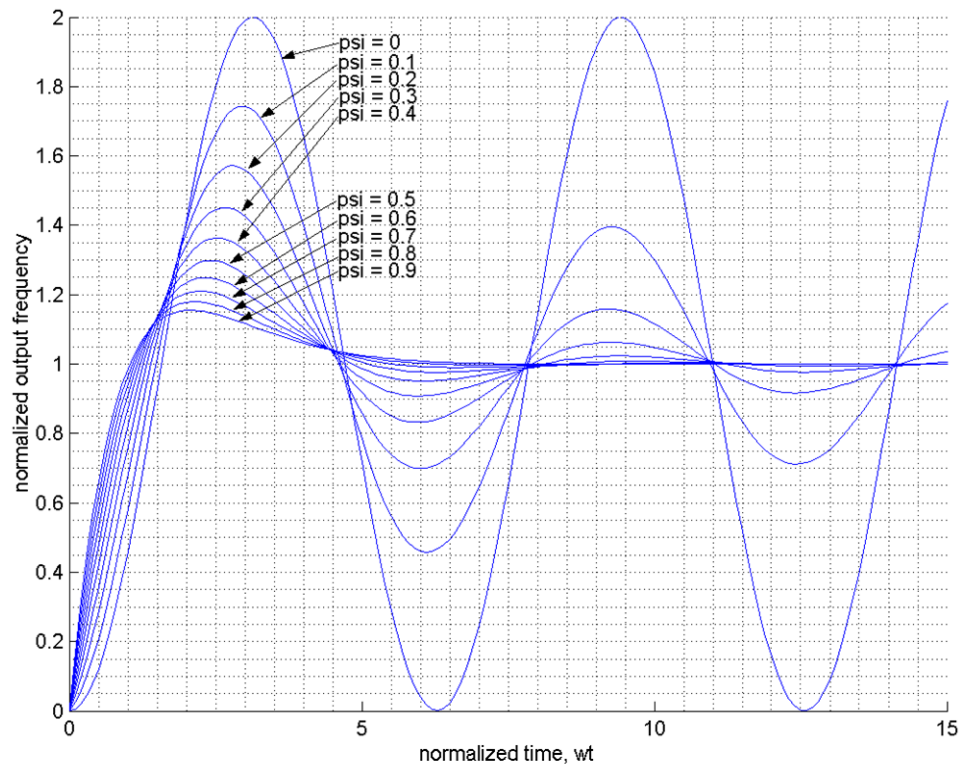
Figure 6.5: The step-response curves given for a second-order system for different damping factors.
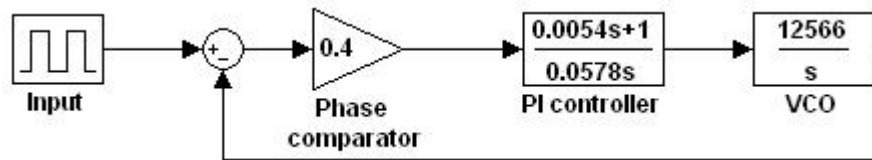
Figure 6.6: Sample frequency-lock loop constructed in SIMULINK for the drive-mode resonator of the fabricated ARS-SOI gyroscope, designed for a CD4046BC PLL IC.

Figure 6.7 shows the simulated step-response of the PLL constructed for the fabricated ARS-SOI gyroscope. The simulation shows that the PLL locks onto the input phase within a period of less than 20msec with an overshoot less than 20%, which agree with the calculated results.
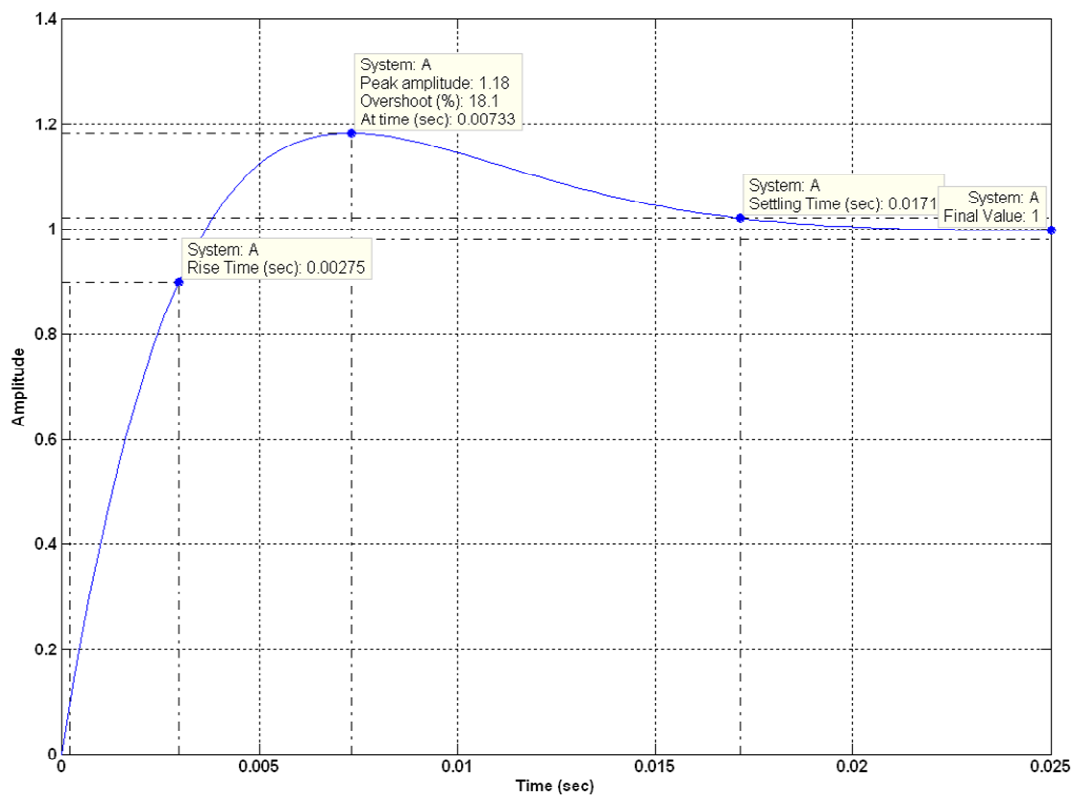
Figure 6.7: The simulated step-response of the PLL constructed for the fabricated ARS-SOI gyroscope.

6.1.2.2 Automatic Gain Control Loop

Once the frequency-lock loop detects the resonance frequency of the drive-mode resonator, its output is then used to construct the automatic gain control (AGC) loop.

236

Figure 6.8 shows the typical structure of the AGC loop. A first-order sensor model is used in the loop in order to keep the loop as a second-order system for simplifying the analysis. The first-order sensor model describes the behavior of the resonator in response to possible amplitude variations <u>at resonance</u>. Therefore, the gyroscope is assumed to be at resonance for the analysis, and the AGC loop is designed for stabilization of the vibration amplitude at resonance. The first-order approximate resonator model at resonance is given as

$$\frac{A}{1 + s \cdot t_{response}} \qquad (6.11)$$

where A is the gain of the resonator at resonance and must be evaluated using the gain expressions of Equations 5.1 or 5.2 in Chapter 5, depending on the type of the interface circuit. The response time, $t_{response}$, is given in Equation 6.9, evaluated from the slowly-varying envelope approximation for the amplitude variations in the second-order system. Note that AC-coupler is not included in the loop, since it complicates the analysis significantly, although has minimal effect on the results.
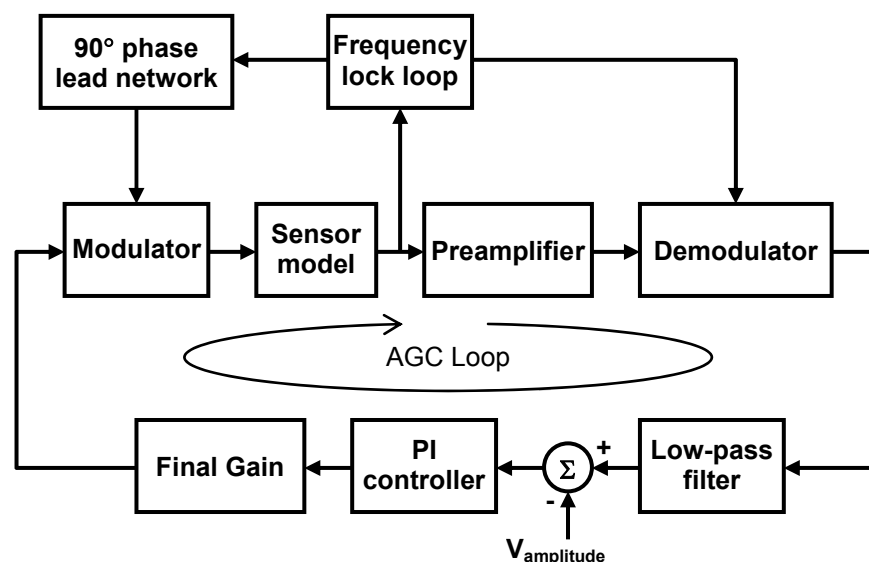
Figure 6.8: The typical structure of the automatic gain control (AGC) loop.

The output of the resonator model in Figure 6.8 is amplified, demodulated to baseband, filtered, and compared with an external DC voltage through a PI

controller. The external DC voltage is proportional to the amplitude of vibrations, and is used to set a constant vibration amplitude for the resonator. The output of the PI controller is modulated back to the resonance frequency of the resonator and applied to the input of the resonator. The closed-loop feedback keeps the amplitude of the resonator output close to the externally applied voltage, provided that the loop parameters are correctly determined.

The loop gain of the system in Figure 6.8 is given as

$$Loop \; Gain = \underbrace{\frac{A}{1 + s \cdot t_{response}}}_{Sensor} \cdot \underbrace{K_P}_{Preamplifier} \cdot \underbrace{K_D}_{Demodulator} \cdot \underbrace{\left(\frac{\tau_2 \cdot s + 1}{\tau_1 \cdot s}\right)}_{PI \; controller} \cdot \underbrace{K_F}_{Final \; gain} \cdot \underbrace{K_M}_{Modulator} \quad (6.12)$$

where K_P, K_D, K_F, and K_M, are the gains associated with the preamplifier, demodulator, final gain stage, and the modulator, respectively. The transfer function of the LPF is not included in the loop gain expression, since it does not affect the results of analysis provided that the corner frequency of the LPF is sufficiently higher than resonance frequency of the AGC loop. The resonance frequency and the damping factor of the second-order characteristic equation for the system above is given by,

$$\omega_n = \sqrt{\frac{A \cdot K_P \cdot K_D \cdot K_F \cdot K_M}{\tau_1 \cdot t_{response}}} \quad (6.13a)$$

$$\xi_n = \frac{1}{2 \cdot \omega_n \cdot t_{response}} \cdot \left(1 + \frac{\tau_2 \cdot A \cdot K_P \cdot K_D \cdot K_F \cdot K_M}{\tau_1}\right) \quad (6.13b)$$

Note that $t_{response}$, A, K_D, and K_M are defined by either the sensor or the modulator/demodulator IC, and are constant. It is possible to put two restrictions in the above equations for ω_n and ξ_n, however, there are four unknowns as τ_1, τ_2, K_P, and K_F. The values of K_P and K_F are determined based on the signal swing restrictions due to the power supplies of the components inside the loop. Figure 6.9 shows the SIMULINK model constructed for the ARS-SOI gyroscope prototype.

The constructed loop uses the second-order transfer function of the gyroscope instead of the first-order approximate transfer function used in the design step, and it also includes the LPF for accurate evaluation of the complete system. A low-cost analog multiplier IC is used for demodulation/modulation purposes [113]. Figure 6.10 shows the result of the simulation for the constructed AGC loop, with the initial vibration amplitude set to 4μm followed by a transition to 8μm at t=2.5sec. The AGC loop tracks the variations in the externally applied amplitude set voltage, and settles in about 2sec. Note that error voltage is minimized after each transition, and the amplified error voltage is proportional to the desired vibration amplitude.
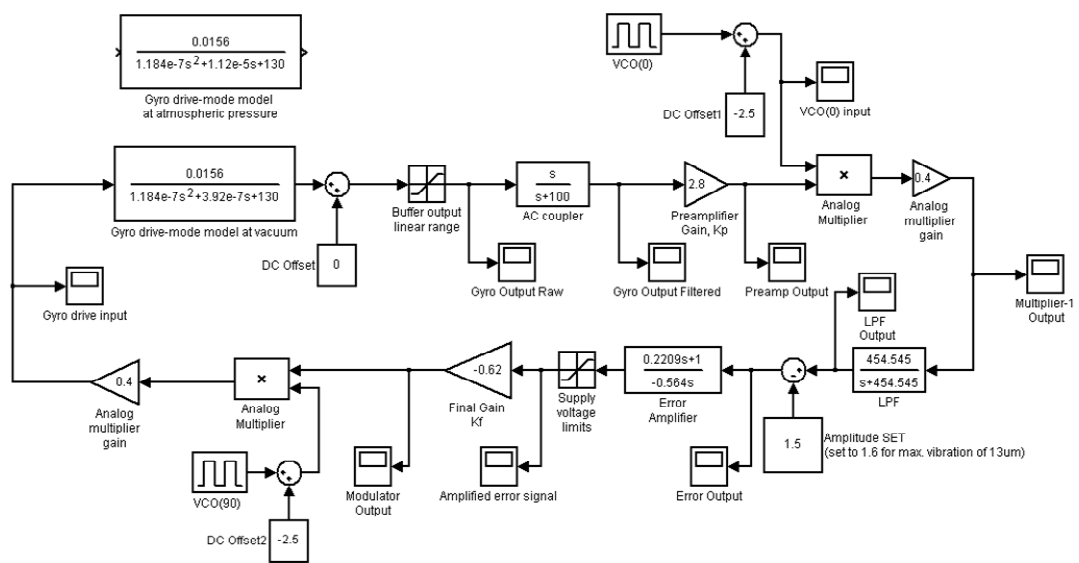
Figure 6.9: Sample AGC loop constructed in SIMULINK for the drive-mode resonator of the fabricated ARS-SOI gyroscope. VCO signals are fed from the frequency-lock loop not shown in the model.

6.2 Sense-Mode Electronics

The sense-mode output of the gyroscope in response to an applied angular rate input is an amplitude-modulated signal, at the drive-mode resonance frequency. This is simply due to the fact that the frequency of the rate-induced Coriolis force is identical to that of the drive-mode resonance. Therefore, the amplitude-modulated output of the sense-mode is first demodulated to the base-band and filtered through a LPF, being converted to a DC output proportional to the applied rate input. This

239

approach is simply the open-loop rate sensing, for which the sense-mode displacement is converted to an equivalent output voltage. Another approach is to operate the sense-mode with closed-loop feedback, for which the sense-mode displacement is electrostatically damped to zero-displacement, while the voltage required to generate the necessary damping is monitored. These two different approaches are described in Sections 6.2.1 and 6.2.2.
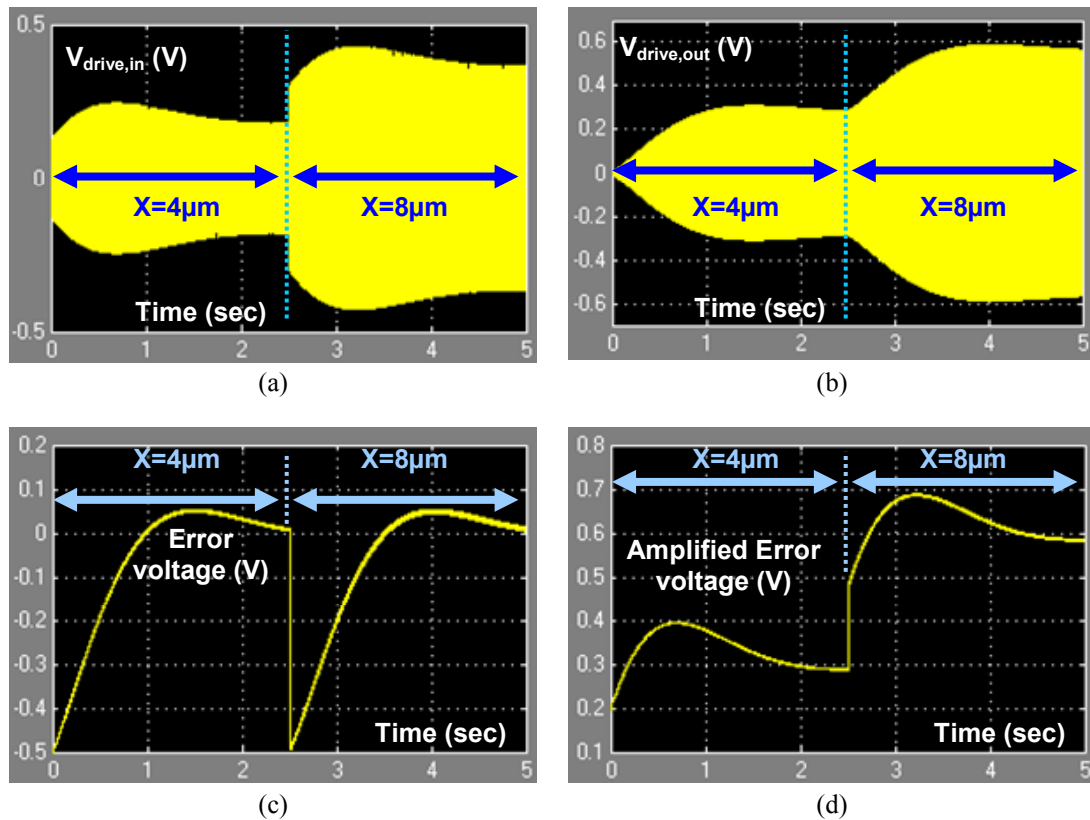
Figure 6.10: Simulation results for the AGC loop constructed in SIMULINK for the drive-mode resonator of ARS-SOI gyroscope, for three different amplitude set inputs applied at t=0 and t=2.5sec. (a) Drive-mode input signal. (b) Drive-mode output signal. (c) Error voltage at the input of the error amplifier (PI controller). (d) Amplified error signal at the output of the PI controller.

6.2.1 Open-Loop Rate Sensing

The open-loop rate sensing is a straightforward approach for converting the modulated output signal of the sense-mode to a DC voltage. Figure 6.11 shows the circuit blocks necessary for this conversion. The phases of the sense-mode output signal and the demodulating carrier must be matching, otherwise generating an

offset due to the quadrature signal at the sense-mode output. If the resonance frequencies of the drive and the sense modes are matched, then the demodulating carrier must be in-phase with the drive-mode output signal, otherwise, the carrier must be in-phase with the drive-mode input signal.
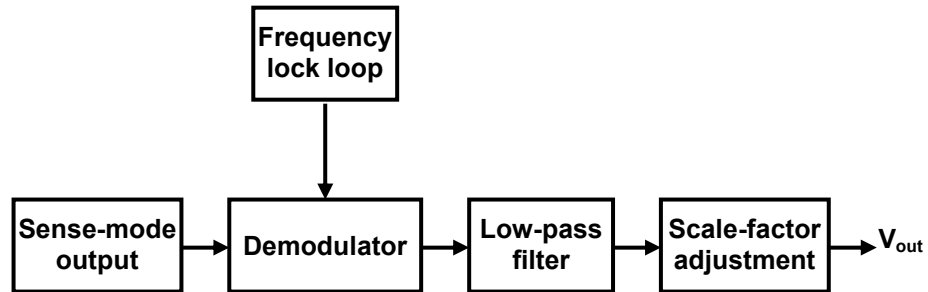
Figure 6.11: Illustration of open-loop rate sensing.

Figure 6.12 shows the SIMULINK model constructed for the open-loop rate sensing through the sense-mode output of the fabricated ARS-SOI gyroscope prototype operating at atmospheric pressure, including a quadrature signal of 200deg/sec, while the mechanical sensitivity of the gyroscope is set as 100μV/(deg/sec). Figure 6.13a shows that 15mV DC output voltage is generated for 1deg/sec rate input and 200deg/sec quadrature signal, with there is no phase error between the gyroscope output signals and the demodulating carrier. Figure 6.13b shows the case for zero rate input but there is a 1° phase error between the gyroscope output and the demodulating carrier. Such a phase error would result in a 3.5 deg/sec output offset due to the quadrature signal, in the absence of any angular rate input.
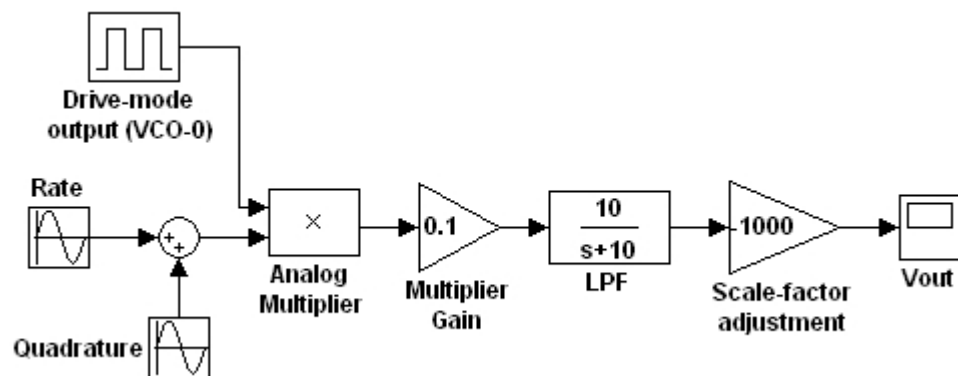
Figure 6.12: The SIMULINK model constructed for the open-loop rate sensing through the sense-mode output of the fabricated ARS-SOI gyroscope prototype operating at atmospheric pressure.

241
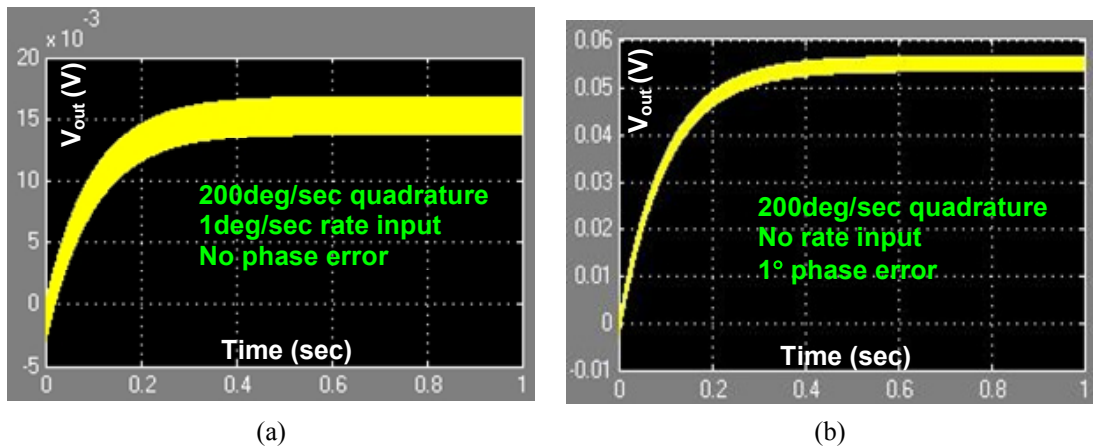
Figure 6.13: Simulation results for the open-loop rate sensing. (a) Electronics generate 15mV DC output for 1deg/sec angular rate input, and effectively suppress the 200deg/sec quadrature signal. (b) Only 1° phase error between the demodulating carrier and the sense-mode output results in a 55mV (3.5deg/sec) DC offset at the output in the absence of any angular rate.

The simple architecture of open-loop rate sensing works well for rate-sensing at atmospheric pressure, with the sense-mode quality factors smaller than 10. However, if the gyroscope is operated at vacuum, where the quality factors exceed 1000, the resulting sense-mode displacement may result in nonlinear output response, limited dynamic range, and disturbance in mode-matching. Therefore, usually a closed-loop rate sensing mechanism with electrostatic force-feedback is necessary to control the sense-mode displacement for vacuum operation.

6.2.2 Closed-Loop Rate Sensing

The displacement of the sense-mode of the gyroscope is limited at atmospheric pressure, where quality factor of the sense mode is typically low and the resulting sense-mode displacement is small. The small quality factor of the sense-mode allows easy matching for the resonance frequencies of the drive and the sense modes at atmospheric pressure. Also, the large bandwidth of the sense mode resonator reduces the response time of the sense output to a few msec. On the other hand, if the gyroscope is operated at vacuum with a high sense-mode quality factor, the bandwidth of the sense mode resonance would be quite narrow, being less than a few Hz. Tuning the resonance frequency of the sense-mode to that of the drive-

mode, with both resonances having such small bandwidths is quite difficult. In addition, the response time of the gyroscope may reach few seconds, due to reduced damping at vacuum. The narrow bandwidth of the sense-mode at vacuum also limits the use of the sensor for time-varying angular rates with frequencies smaller than the response bandwidth of the sense-mode at vacuum, which is not sufficient for many applications. In order to overcome these problems for rate sensing at vacuum, it is possible to construct a closed-loop rate sensing architecture for the sense mode, using electrostatic force-feedback.

Figure 6.14 shows the basic structure of the force-feedback loop (FFL) for a vibratory gyroscope with the drive and the sense mode resonance frequencies are matched. The modulator/demodulator connections must be switched for the case when the frequencies are mismatched. The sensor model in Figure 6.14 must be constructed from the transfer function of the sense-mode resonator, with the electrostatic feedback electrode as the input. The Coriolis-induced angular rate input and the quadrature signal must are converted to an equivalent time-varying voltage, $V_{Coriolis-equivalent}$, and inserted into the loop. This conversion is performed by equating the Coriolis force expression in Equation 2.11b to the first-harmonic of the electrostatic force expression in Equation 2.38, from Chapter 2.

$$\underbrace{2 \cdot A_g \cdot m_{PM} \cdot \Omega_{in} \cdot \omega_D \cdot X_D}_{\text{Coriolis Force Acting Along the Sense Mode}} = \underbrace{V_{Coriolis-equivalent} \cdot V_{PM} \cdot \left(\frac{\partial C}{\partial x} \right)_{FF}}_{\text{Electrostatic Force Across FF Electrode}} \qquad (6.14)$$

where subscript "FF" denotes the force-feedback electrode and $V_{Coriolis-equivalent}$ is a fictitious time-varying voltage applied across the force-feedback electrode of the sense-mode, generating a force equivalent to the applied Coriolis force. Expressing this equivalent voltage in terms of the other terms yield,

$$V_{Coriolis-equivalent} = \frac{2 \cdot A_g \cdot m_{PM} \cdot \Omega_{in} \cdot \omega_D \cdot X_D}{V_{PM} \cdot \left(\frac{\partial C}{\partial x} \right)_{FF}} \qquad (6.15)$$

243

The remaining analysis of the loop is similar to that of the AGC loop, except the desired vibration amplitude is set to 0, by assigning 0^V DC to the $V_{amplitude}$ input of the AGC loop. If there is any displacement caused by the Coriolis force, the loop force this displacement to zero by an electrostatic force of equal-magnitude and opposite-sign applied to the force-feedback electrode of the gyroscope. Therefore, the sense-mode of the gyroscope is electrostatically forced to stay its zero-position, while the voltage required for generating the necessary electrostatic force, V_{out}, is monitored as the output proportional to the applied angular rate input.

The closed-loop rate sensing using electrostatic force-feedback acts as an electrostatic damper, increasing the response bandwidth of the sense-mode. The response bandwidth of the gyroscope is roughly increased by factor of the total gain of the preamplifier and the final gain stages in the FF loop. The cost of increasing the bandwidth is a reduction in the overall SNR of the rate sensor due to the noise introduced by the amplifier stages in the loop.

Figure 6.15 shows the SIMULINK model constructed as the force-feedback loop for the fabricated ARS-SOI gyroscope. Similar to the AGC loop, the complete second-order sensor model is used for accurate estimation of the loop response. Figure 6.16 shows the results of simulations for the constructed FF loop, where input angular rates of 10, 20, 30, and 40deg/sec are applied to the gyroscope at t=1, 2, 3, and 4 seconds, respectively. Note that, the feedback signal amplitude is increased for keeping the sense-mode stationary, while the sense-mode output turns back to its zero-rate value within 1sec. The error voltage is minimized in the loop each time a different angular rate input is applied, and the loop amplifies the error voltage to a value proportional to the applied angular rate input.

It is verified by the simulations that the response bandwidth of the gyroscope is extended from 1Hz at vacuum up to more than 60Hz, by using the designed FF loop.
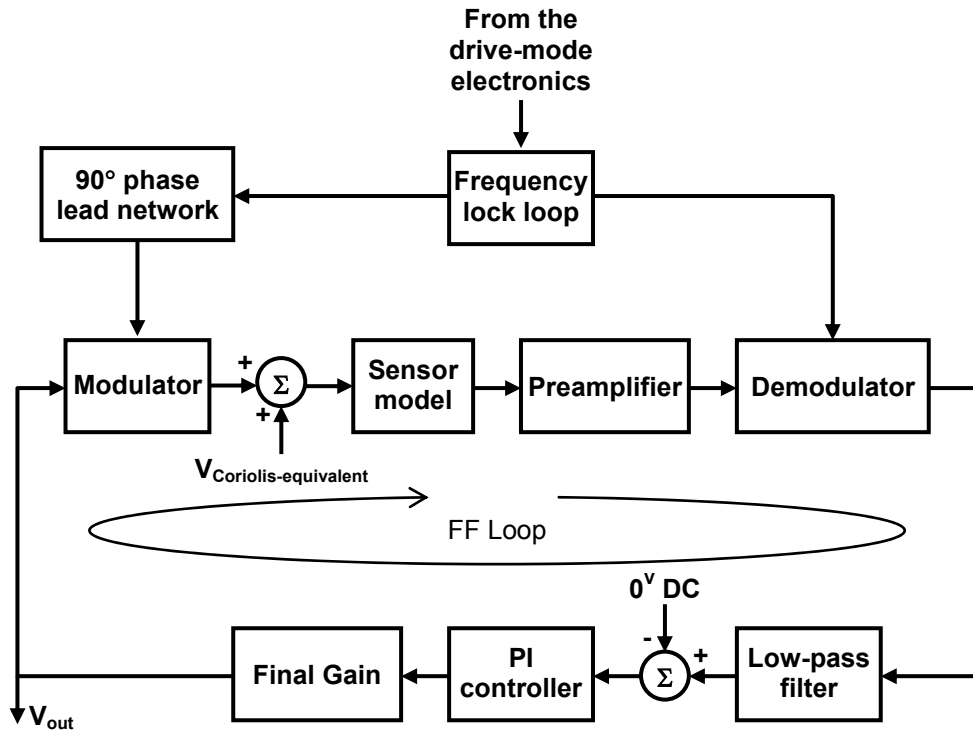
Figure 6.14: The basic structure of the force-feedback loop (FFL) for a vibratory gyroscope with the drive and the sense mode resonance frequencies are matched.
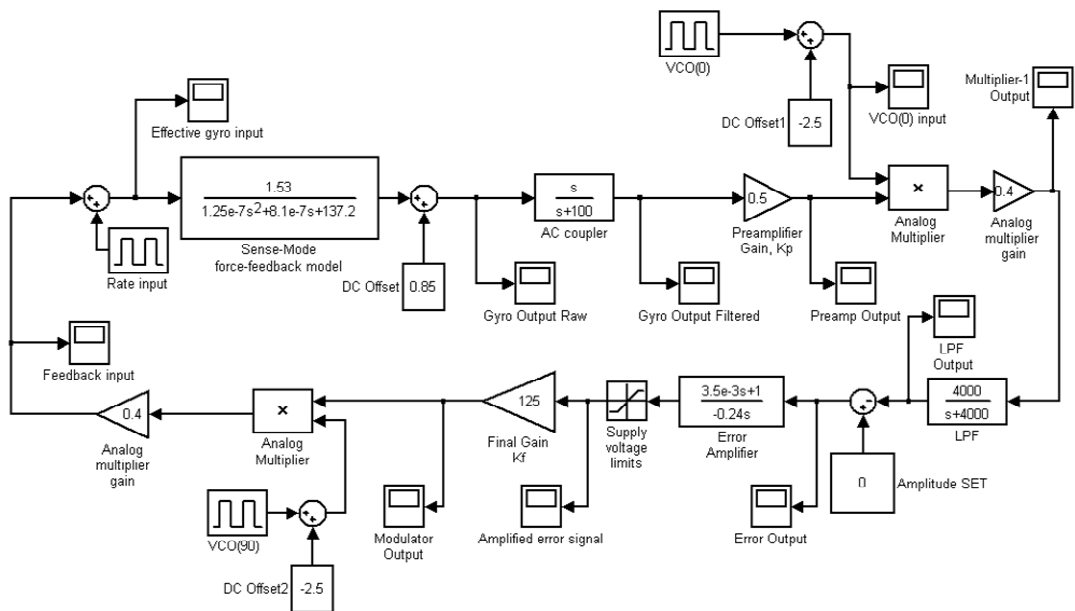
Figure 6.15: The SIMULINK model constructed as the force-feedback loop for the fabricated ARS-SOI gyroscope. VCO signals are fed from the frequency-lock loop not shown in the model.
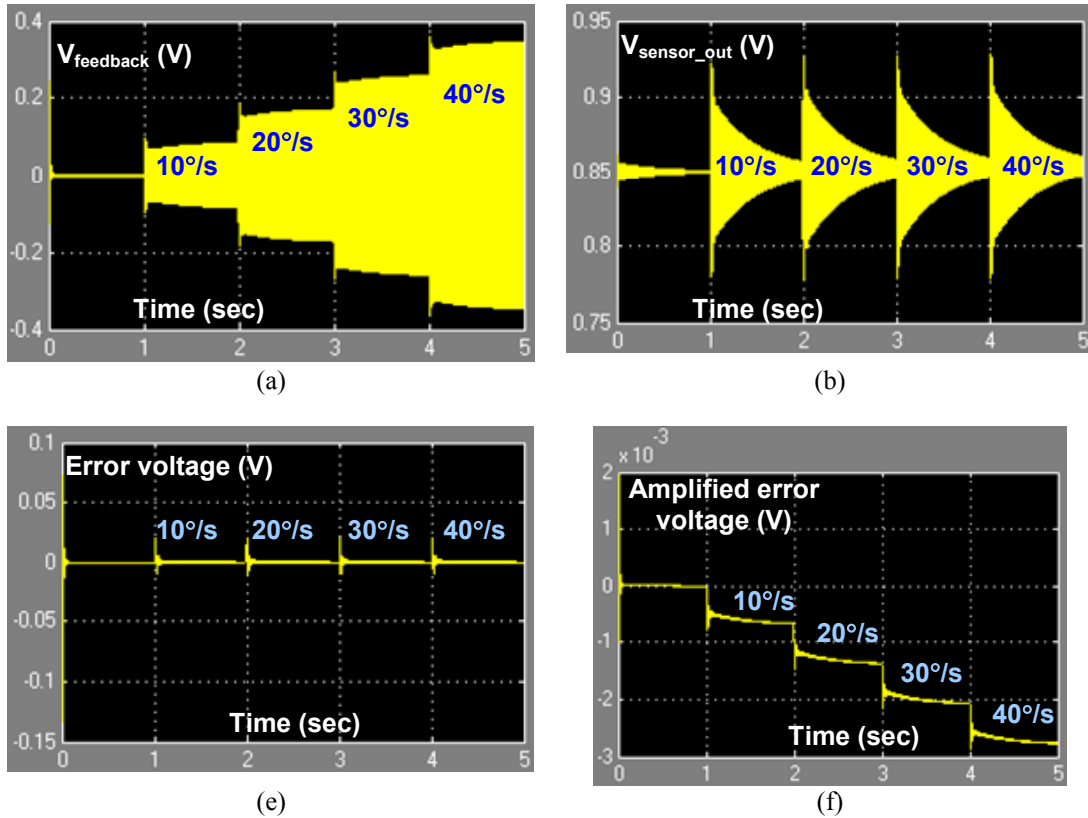
Figure 6.16: The results of simulations for the constructed FF loop, where input angular rates of 10, 20, 30, and 40deg/sec are applied to the gyroscope at t=1, 2, 3, and 4 seconds, respectively. (a) Electrostatic feedback signal. (b) Sensor output signal proportional to the sense-mode displacement. (c) Error voltage at the input of the error amplifier. (d) Amplified error signal at the output of the PI controller.

6.3 Summary and Discussion

The electronic circuit blocks necessary for constructing a complete angular rate sensor system, powered from a single DC power supply, are presented. First of all, it is necessary to generate oscillations for the drive-mode of the gyroscope in order to start angular rate measurement. This can simply achieved by using a closed-loop positive-feedback, similar to constructing an RLC oscillator circuit. The frequency of oscillations in the feedback loop is determined by the drive-mode resonator of the gyroscope and is very close to the mechanical resonance frequency of the drive-mode resonator, provided that the mechanical quality factor of the resonator is sufficiently high. This method works well for constructing self-resonance of the drive-mode resonator, however, the amplitude of oscillations highly depends on the variations in the quality factor and also they are limited by the allowable voltage

swing inside the loop. Therefore, self-resonance excitation with positive-feedback may have problems for vacuum operation, for which the mechanical quality factors are improved by more than an order of magnitude for the fabricated gyroscopes. The high-quality factor without any vibration amplitude control may result in destruction of the resonator at vacuum. For this reason, a closed-loop stable feedback control mechanism is also studied for generating self-resonance at vacuum. The operation of this improved loop depends on the coordination between a PLL-based frequency-locking loop and an automatic gain control loop.

The second part of the electronics control targets the sense-mode output of the gyroscope. Although the micromachined gyroscope combined with the capacitive interface circuit is enough to make an angular rate measurement, the raw output of the capacitive interface circuit is simply an amplitude-modulated signal, with a modulation frequency equal to the resonance frequency of the drive-mode resonator. The straightforward method of open-loop rate sensing requires the demodulation of the sense-mode output to the base-band using a proper carrier signal, generated from the drive-mode resonator electronics. Phase-sensitive detection suppress the quadrature signal, which can be several orders of magnitude larger than the Coriolis rate signal, provided that the phase of the Coriolis output and the demodulating carrier closely match. Open-loop rate sensing is a simple and straightforward method for gyroscopes operating at atmospheric pressure, for which the quality factor of the sense-mode is already small and the response bandwidth is large. However, the quality factor of the sense-mode increase at vacuum and may result in a response bandwidth smaller than few Hz, which is not sufficient for many practical applications. For this reason, the closed-loop rate sensing with electrostatic force-feedback is investigated for vacuum operation of the fabricated gyroscopes. In this approach, the sense-mode displacement is suppressed by an electrostatic damper controlled by closed-loop feedback. The voltage required to generate the necessary electrostatic force is then proportional to the applied angular rate input, and this voltage is monitored as output. The response bandwidth of the sense-mode can be extended by increasing the gain of the force-feedback loop, at the cost of reduced mechanical sensitivity. The closed-loop rate sensing requires force-feedback

electrodes and a small quadrature signal for proper realization, as well as an accurate phase control as in the case of open-loop rate sensing.

The behavior of the drive-mode excitation and the sense-mode rate-detection electronics are simulated using SIMULINK and the sensor models constructed from the results of preliminary characterizations of the fabricated gyroscopes, presented in the previous chapter. The simulations performed on the ARS-SOI gyroscope verify the concepts of the investigated feedback and control electronics for excitation and sensing of the fabricated gyroscopes. The electronics presented in this chapter are then applied to the fabricated gyroscopes for constructing the top-level angular rate sensors.

CHAPTER 7

TEST RESULTS OF THE FABRICATED GYROSCOPES

This chapter reports the results of the final tests performed on the angular-rate sensors developed in this research. These sensors are constructed from four different gyroscope prototypes developed in different micromachining technologies discussed in Chapter 3, which are then hybrid-connected to the capacitive interface circuit and the feedback/control electronics described in Chapters 4 and 6, respectively. The performed tests yield the angular rate sensitivity, noise-equivalent rate, quadrature error, scale-factor, linearity, and the bias instability of each fabricated gyroscope. The performance demonstrated by each gyroscope is compared with the expected results, and the factors limiting the overall performance are briefly assessed. The operation bandwidth, g-sensitivity, and the power dissipation of the fabricated gyroscope prototypes are also discussed at the end of the chapter.

Sections 7.1, 7.2, 7.3, and 7.4 presents the results of the tests of the fabricated ARS-DWSM, ARS-NE, ARS-SOI, and ARS-SOG gyroscope prototypes hybrid-connected to the fabricated UGB capacitive interface circuit and combined with the electronic feedback and control circuits. Section 7.5 summarizes the tests, compares the performances of the gyroscopes fabricated in each micromachining process, and discuss the performance limitations of each gyroscope.

7.1 ARS-DWSM Gyroscope

The fabricated ARS-DWSM gyroscope prototype has the simplest sensor architecture among the other three prototypes developed in this research. The simple geometry is a result of the inherent symmetry of the sensor, for which the drive and the sense modes are identical in all aspects. However, the complexity of the control of the dissolved wafer micromachining process at METU-MET facility prevented more than a single fabrication attempt. Therefore, the results reported in this section belong to the first and the last fabricated ARS-DWSM prototype in this research.

The drive-mode of the ARS-DWSM gyroscope is easily entered resonance with the use of positive-feedback self-resonance loop described in Chapter 6. The vibration amplitude of the drive-mode is limited below 2µm, for keeping the drive-mode oscillations linear, over which the clamped-guided type flexures of the gyroscope has force-deflection characteristics with nonlinearity above 5%. The power supplies of the self-resonance electronics are set to $\pm5^V$, while the gain stage in the self-resonance loop is set to a gain of 20, providing a loop gain slightly above unity.

The complete symmetry along the drive and the sense modes of the gyroscope with linear varying-overlap-area type comb fingers limits the use of electrostatic springs, preventing the post-fabrication tuning of the resonance frequencies of the gyroscope. Therefore, the rate sensitivity of the gyroscope is measured with mismatched resonance frequencies. The angular rate measurements are performed without using any special phase-sensitive detection schemes described in the previous chapter, because of the fact that the large stray capacitances and resulting electrical cross-talk disturb the phase of the gyroscope output signals.

Figure 7.1 shows the output of the sense-mode capacitive interface circuit measured with Agilent 4395A spectrum analyzer, after the self-resonance excitation of the drive-mode, and with no angular-rate applied to the input. The major peak at the center corresponds to the quadrature error signal at the drive-mode resonance frequency, whereas the remaining peaks are the modulated components of the

electrical coupling from the 50Hz power line. The quadrature signal amplitude is measured to be 35.5mV-rms, which corresponds to a sense-mode displacement of 16.6nm, corresponding to 0.83% (8300ppm) of the drive-mode vibration amplitude. Such a quadrature signal is quite high and is a typical result of the non-uniform mass distribution caused by undoped silicon over the highly-doped structural layer.
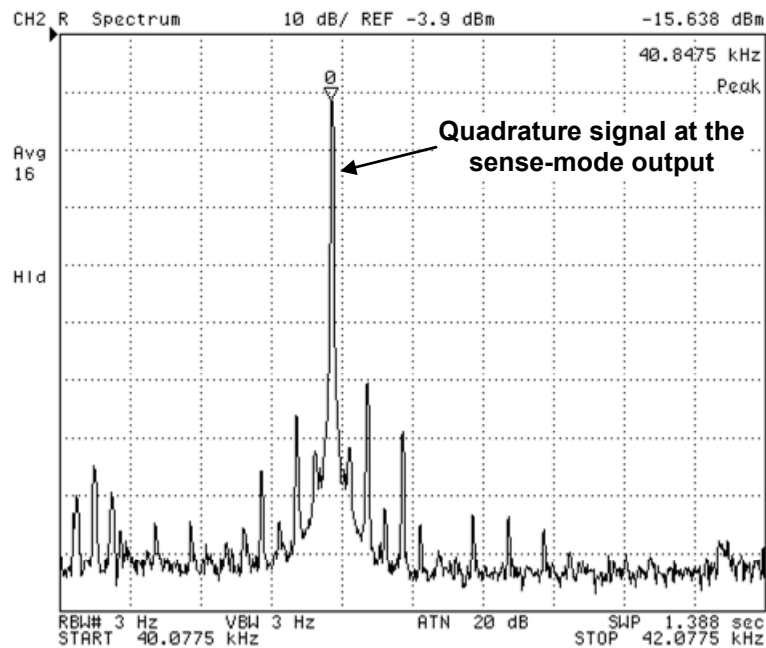
Figure 7.1: The output of the sense-mode capacitive interface circuit measured with Agilent 4395A spectrum analyzer, after the self-resonance excitation of the drive-mode, and with no angular-rate applied to the input. There is a large quadrature signal observed at the output of the sense-mode.

Rate sensitivity of the gyroscope is measured using Ideal Aerosmith 1280 single-axis rate table. Figure 7.2 shows the photographs of the gyroscope package mounted on the test PCB, the PCB mounted inside the chamber of the rate table, and the complete test setup showing the measurement equipments used during the tests. Figure 7.3 shows the measured outputs of the fabricated gyroscope, for constant angular rates of -300deg/sec and +300deg/sec. The level of the central peak is monitored at each measurement step, which provides the sum of the quadrature signal and the angular rate signal. Figure 7.4 shows the measured outputs versus the applied angular rate inputs within the measurement range of -300deg/sec up to +300deg/sec with 100deg/sec steps, together with the best-fit straight line describing the output response of the gyroscope. The slope of the best-fit line gives the scale

factor of the gyroscope as 24.9μV/(deg/sec), without using any amplification or demodulation stages. The R^2-nonlinearity of the scale-factor is 1.1%, mainly disturbed by the large quadrature signal and clamped-guided flexures. The quadrature signal in Figure 7.1 corresponds to more than 2000deg/sec, primarily due to the non-uniform mass distribution.

(a)

(b)

(c)

Figure 7.2: The photographs of (a) the gyroscope package mounted on the test PCB, (b) the PCB mounted inside the chamber of the rate table, and (c) the complete test setup showing the measurement equipments used during the tests.
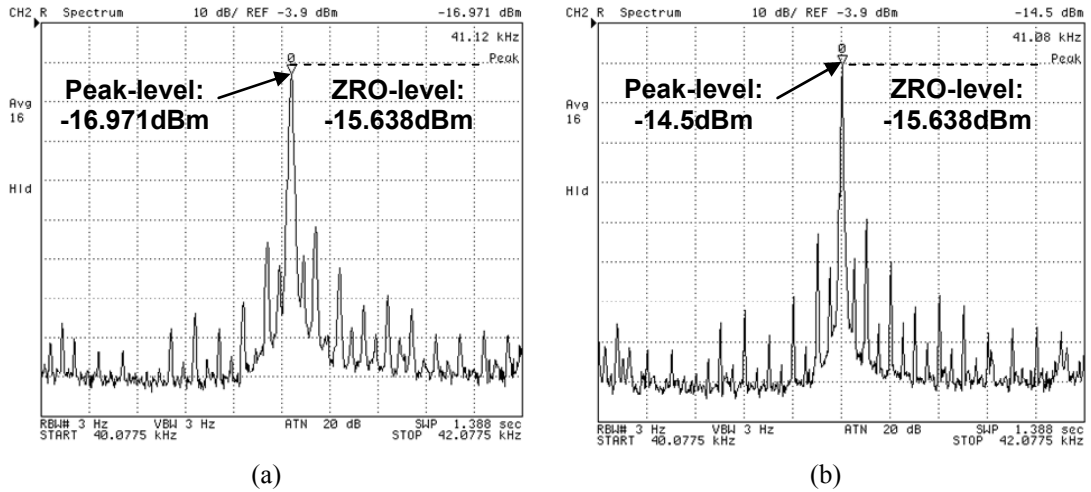
Figure 7.3: The measured outputs of the fabricated gyroscope, for constant angular rates of (a) -300deg/sec and (b) +300deg/sec. The level of the central peak is monitored at each measurement step, which provides the sum of the quadrature signal and the angular rate signal.
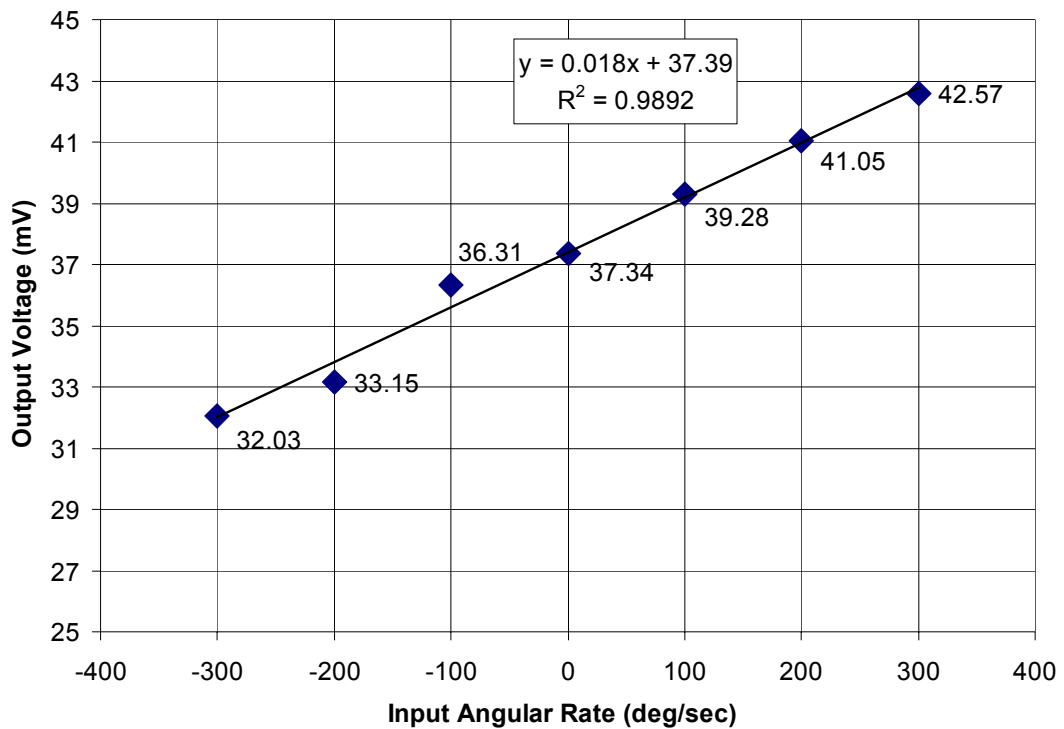
Figure 7.4: The measured outputs versus the applied angular rate inputs within the measurement range of -300deg/sec up to +300deg/sec with 100deg/sec steps, together with the best-fit straight line describing the output response of the gyroscope.

The noise at the output of the capacitive interface circuit is measured to be 2.4μV in 3Hz measurement bandwidth, corresponding to an rms-noise density of 1.39μV/Hz$^{1/2}$. The rms-noise-equivalent rate of the fabricated gyroscope is then

determined to be better than $0.06(\text{deg/sec})/\text{Hz}^{1/2}$. The sense-mode displacement estimated using Equation 2.21 of Chapter 2 is less than $0.09\text{Å}/(\text{deg/sec})$, for $2\mu\text{m}$ drive-mode vibration amplitude and for the measured resonance frequencies of the drive and the sense modes. The expected voltage output for this displacement is about $22.6\mu\text{V}$, slightly less than the measured value of $24.9\mu\text{V}$. As a result, the measured and the expected results closely agree with each other, verifying the theory. The difference is believed to be due to the electrostatic fringe-fields and the measurement error for the drive-mode vibration amplitude.

The gyroscope performance is not evaluated at vacuum due to the fact that, no significant improvements are expected at vacuum without matching the resonance frequencies of the drive and the sense modes of the fabricated gyroscope, which is not possible for the simple geometry of the current ARS-DWSM prototype.

The measured performance of the ARS-DWSM prototype is basically limited by the small sensor capacitances and the lack of matching the resonance frequencies of the drive and the sense modes of the fabricated gyroscope. Still, the performance of the fabricated gyroscope is found to be satisfactory for many rate-grade applications. Future research should consider more advanced gyroscope prototypes to be fabricated with the dissolved wafer silicon micromachining process, considering the fabrication results of the current ARS-DWSM prototype.

7.2 ARS-NE Gyroscope

The drive-mode oscillation of the ARS-NE gyroscope is also generated by the simple positive-feedback self-resonance loop described in Chapter 6. Figure 7.5 shows the measured drive-mode output of the fabricated gyroscope at self-resonance. The measured output voltage corresponds to drive-mode vibration amplitude of $9.1\mu\text{m}$ at resonance, by applying 10V DC to the proof mass and -50V DC to the actuation electrode of the drive-mode and using $\pm 10\text{V}$ supplies for the ICs inside the self-resonance loop. Applying negative bias to the drive-mode actuation electrode increase the drive-mode vibration amplitude to above $10\mu\text{m}$ at atmospheric pressure.

The estimated value of drive-mode vibration amplitude is 11.7µm, using the applied voltages and the preliminary characterization results. This value is slightly higher than the value of 9.1µm predicted from the output voltage of the capacitive interface circuit connected to the drive-mode output. In practice, the vibration amplitude predicted from the interface circuit output can be smaller than expected, since the output of the interface circuit starts saturating for peak-to-peak voltages above 1.5V. Saturation of the interface circuit causes a loading on the sensor, reducing the quality factor of the resonator. As a result, the vibration amplitude calculated from the theory with a high quality factor can be above the actual value. Therefore, the actual vibration amplitude of the drive-mode resonator is expected to be somewhere in between 9.1µm and 11.7µm, and possibly above 10µm.

Figure 7.5: The measured drive-mode output of the fabricated ARS-NE gyroscope at self-resonance.

Figure 7.6 shows the measured output of the fabricated nickel angular rate sensor prototype prior to demodulation, in response to a sinusoidal angular rate input of amplitude 2π deg/sec and frequency 10Hz. The two side-lobes in the figure

correspond to the rate outputs, separated from the quadrature signal (central peak) by a frequency equal to the frequency of the applied rate input. The mechanical sensitivity of the nickel gyroscope is determined to be 130μVrms/(deg/sec) or 180μV/(deg/sec). The quadrature error is determined to be about 30mVrms, corresponding to 230deg/sec with the measured mechanical sensitivity. The estimated sense-mode displacement is 6.1Å/(deg/sec), corresponding to an output voltage of 560μV-peak for 1deg/sec rate input, for matched-mode operation. This voltage corresponds to the sum of two side-lobes in the measurement and each side lobe is expected to be 280μV-peak or 185μV-rms, which is higher than the measured value of 180μV-peak. However, note that the estimated value assumes perfect matching of the resonance frequencies of the drive and the sense modes, whereas the response bandwidth of the sense-mode is characterized to be less than 80Hz for the fabricated nickel gyroscope. Therefore, the sense-mode response will drop if the resonance frequencies of the drive and the sense modes are not identically matched. The sense-mode response will drop by a factor of 0.707 for a frequency mismatch of about 40Hz, which is typical for the manual tuning by adjusting the DC voltage applied to the proof mass. Examining the measurement of Figure 7.6, the amplitudes of the two side lobes are different from each other, which are 145μV/(deg/sec) and 118μV/(deg/sec) for the left and right lobes, respectively. This simply states that the sense-mode resonance peak is slightly below the drive-mode resonance frequency, and located towards the left of it in the frequency domain, explaining the small difference between the expected and measured rate sensitivities.

Figure 7.7 shows the measured zero rate output of the gyroscope prior to demodulation. The rms noise floor is found to be $17.5 \mu V/Hz^{1/2}$, corresponding to the rms-noise-equivalent rate of $0.095 (deg/sec)/Hz^{1/2}$. The mechanical-thermal noise of the nickel gyroscope is estimated to be less than $4 (deg/hr)/Hz^{1/2}$, which is much smaller than the measured output noise. The main source of the output noise is expected to be due to rotational mode of the fabricated nickel gyroscope, whose frequency approach to the operational frequency of the gyroscope during the fabrication due to the narrowed beam widths. Another possible source is the

double-frequency motion of the sense electrodes, which may cause spurious vibration of the sense-frame even in the absence of an angular rate input.


```
CH1 A   Spectrum        12 dB/ REF 0 dBm            -17.383 dBm
                                  0    Quadrature      3.988065 kHz
                                  ▽      @ fD
                         1                2
                         ▽                ▽      Rate output
                                                @ fD±10Hz
      3
      ▽
                                              DC SOURCE ON
Hld
RBW# 1 Hz         VBW 1 Hz          ATN  20 dB      SWP  5.479 sec
CENTER  3.99338 kHz                                 SPAN  80 Hz

        N          SWP PARAM           VAL

        0        3.988065 kHz       -17.383 dBm
        1        3.977995 kHz        -47.83 dBm
        2        3.997762 kHz       -49.597 dBm
        3        3.958228 kHz        -80.97 dBm
```

Figure 7.6: The measured output of the fabricated nickel gyroscope prototype prior to demodulation, in response to a sinusoidal angular rate input of amplitude 2π deg/sec and frequency 10Hz.


```
CH1 A   Spectrum        13 dB/ REF 0 dBm             -17.44 dBm
                                  0                 3.987319 kHz
                                  ▽
      Noise floor
      < 17.6μVrms/Hz^{1/2}
      1
      ▽
                                              DC SOURCE ON
Hld
RBW# 1 Hz         VBW 1 Hz          ATN  20 dB      SWP  5.479 sec
CENTER  3.99338 kHz                                 SPAN  80 Hz

        N          SWP PARAM           VAL

        0        3.987319 kHz        -17.44 dBm
        1        3.965688 kHz       -82.115 dBm
```

Figure 7.7: The measured zero rate output of the gyroscope prior to demodulation. The rms noise floor is found to be $17.5\mu V/Hz^{1/2}$, corresponding to the rms-noise-equivalent rate of $0.095(\text{deg/sec})/Hz^{1/2}$.

257

The output of the ARS-NE is demodulated, 40dB-amplified, and filtered using an open-loop rate sensing scheme described in the previous chapter. Figure 7.8 shows the measured output of angular rate sensor in response to rate inputs from 0 to -100 and then to +100deg/sec with 10deg/sec steps. Figure 7.9 shows the output response of the nickel gyroscope with respect to the applied angular rate input in a range from -100deg/sec to +100deg/sec. The scale factor of the gyroscope is measured as 17.7mV/(deg/sec), in agreement with the 180μVpeak sensitivity at the raw output of the capacitive interface circuit prior to demodulation. The R^2-nonlinearity of the scale factor is measured to be 0.12%, owing to the linear drive-mode vibrations and stress-relieving flexure designs. The zero-rate output bias of the sensor is approximately 17deg/sec, limited by the quadrature signal at the output of the gyroscope due to mechanical and electrical crosstalk. Indeed, the raw quadrature signal can add to the offset by such an amount for a 4° phase error during demodulation. This is a typical result of slightly mismatched resonance frequencies for the drive and the sense modes.
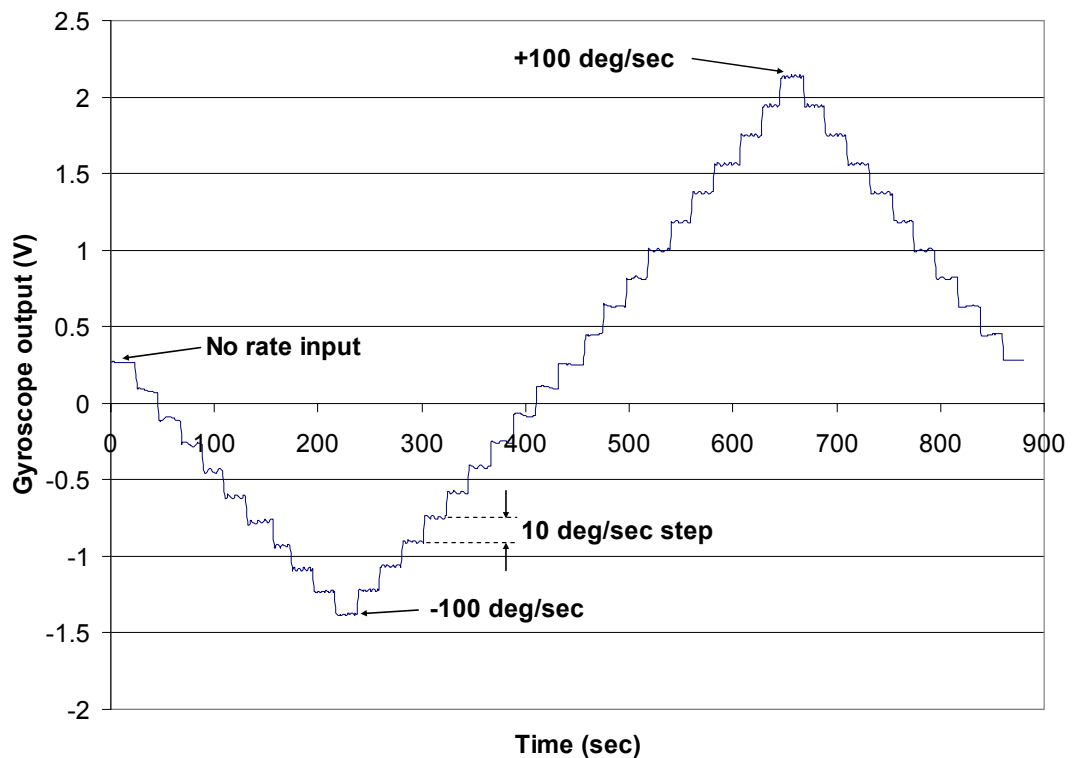
Figure 7.8: The measured output of the fabricated nickel gyroscope in response to rate inputs from 0 to -100 and then to +100deg/sec with 10deg/sec steps.

258

Figure 7.9: The output response of the fabricated nickel gyroscope with respect to the applied angular rate input in a range from -100deg/sec to +100deg/sec.

Figure 7.10 shows the random variation of the gyroscope output bias and noise for zero rate input. The short-term (100 seconds) bias stability is measured to be better than 0.1deg/sec. The bias is observed to be stable within 1deg/sec over 2 hours measurement period. The rms output noise of the sensor is measured to be 0.5deg/sec in 30Hz bandwidth, including noise contributions from the external signal processing electronics.

Following the rate tests at atmospheric pressure, the gyroscope is located inside the vacuum chamber of the rate table. However, the voltage required for matching the resonance frequencies of the drive and the sense modes are determined to be as large as 20V, instead of 12V determined during preliminary characterization. Therefore, it is concluded that permanent destruction occurred for the nickel gyroscope at vacuum, probably due to local overheating of the flexure beams, which cause permanent change in the mechanical properties of nickel structural material.

The measured performance of the ARS-NE prototype is limited by the high output noise. The source of this high noise is expected to be due to the rotational modes associated with the sense electrodes and the proof mass, whose frequencies shift down during fabrication. Therefore, the source of the noise should be mechanical rather than electronic, and can be highly suppressed by increasing the stiffness of the rotational modes for the future designs.
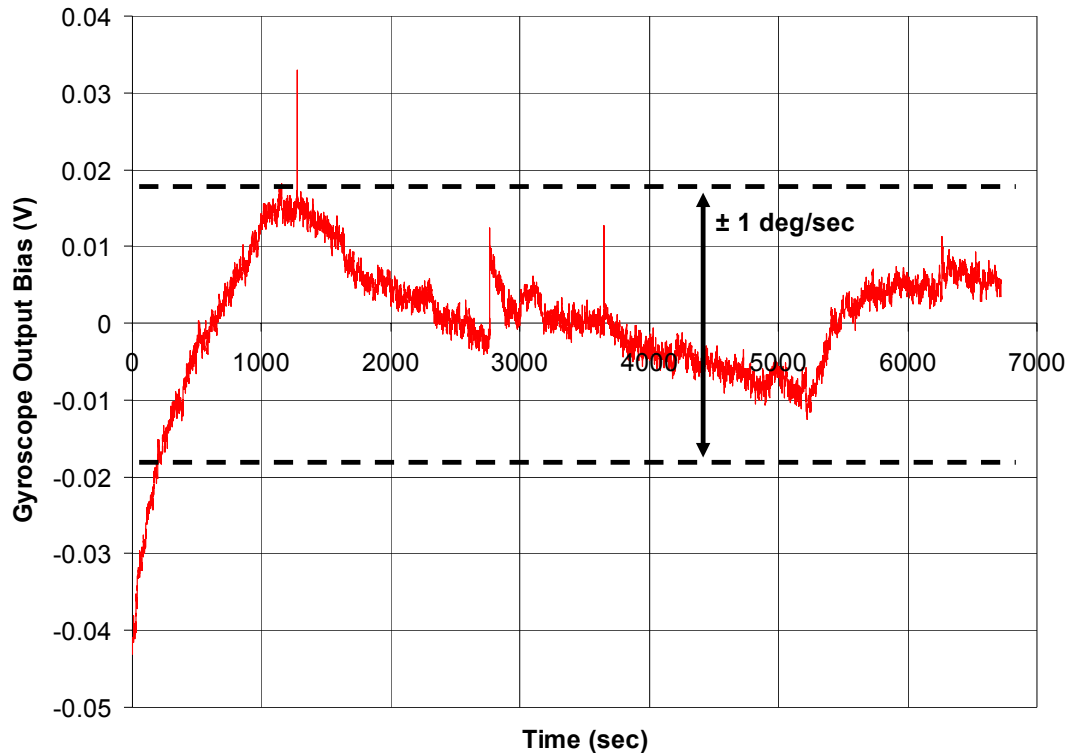
Figure 7.10: The random variation of the fabricated nickel gyroscope output bias and noise at zero rate input.

7.3 ARS-SOI Gyroscope

The drive-mode oscillation of the ARS-SOI gyroscope is generated by the simple positive-feedback self-resonance loop. Figure 7.11 shows the measured drive-mode output of the fabricated gyroscope at self-resonance. The drive-mode of the gyroscope is actuated by applying 11^VDC to the proof mass and using $\pm18^V$ power supplies for the self-resonance loop. The expected drive-mode vibration amplitude for the given actuation condition is 15.9μm, using the preliminary characterization

results of Chapter 5. The measured output of the drive-mode is a 0.9Vpeak sine wave, corresponding to displacement amplitude of 18.8μm, which is higher than the expected result. The mismatch is possibly due to the higher quality factor of the drive-mode, which may be underestimated during the preliminary characterization. The latter value is selected since the unity-gain buffer type capacitive interface circuit output provides a more reliable measure of the displacement, as it does not depend on the quality factor. The frequency of the self-resonance is 5296Hz, slightly above the measured resonance frequency of the drive-mode, possibly due to a small increase in the stiffness of the folded-flexure for large vibration amplitude.
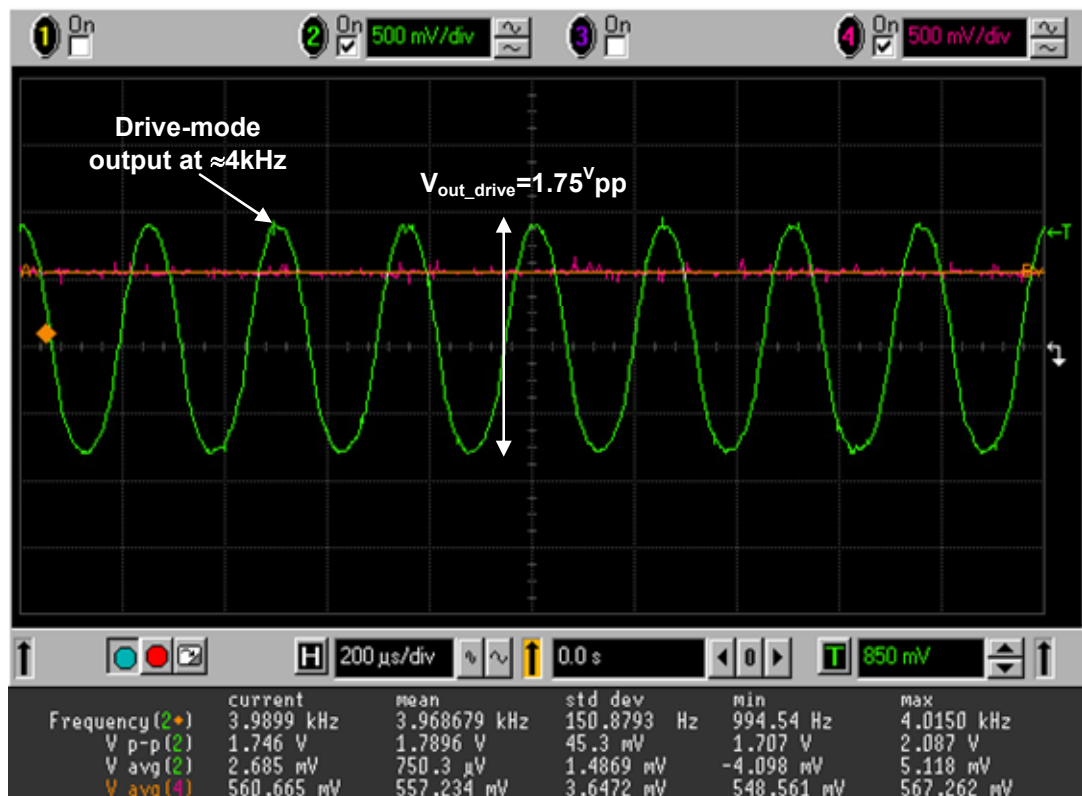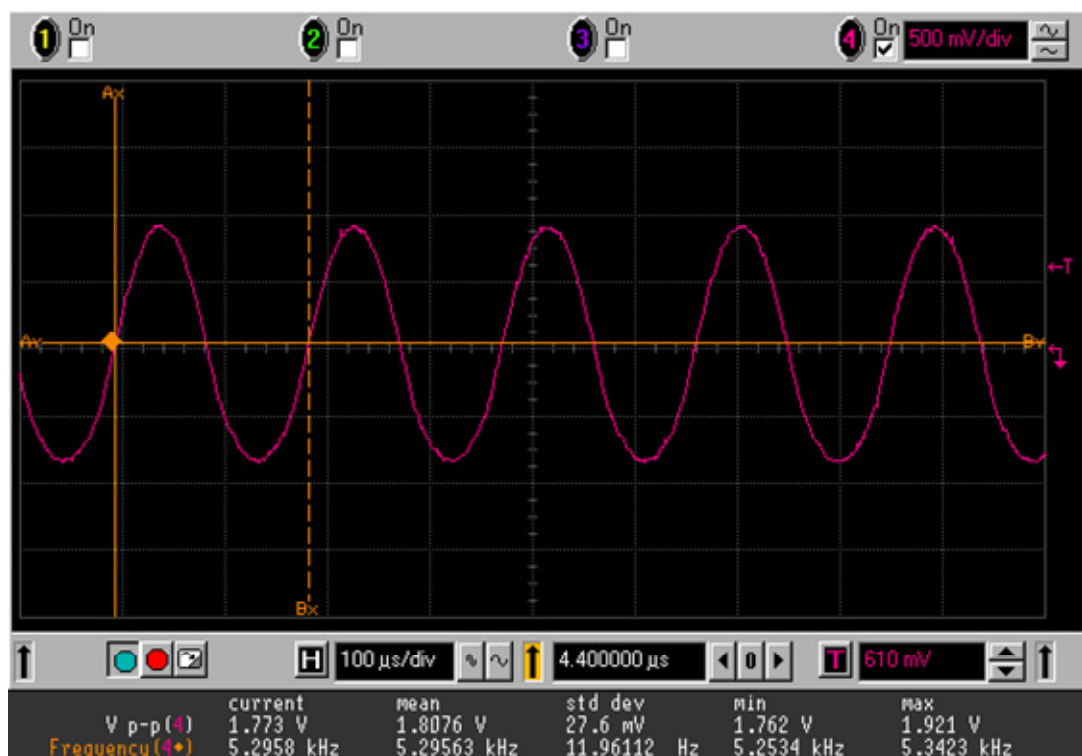

Figure 7.11: The measured drive-mode output of the fabricated ARS-SOI gyroscope at self-resonance.

Figure 7.12 shows the measured output of the fabricated SOI angular rate sensor prototype prior to demodulation, in response to a sinusoidal angular rate input of amplitude 10deg/sec and frequency 10Hz. The mechanical sensitivity of the SOI gyroscope is determined to be 51.8μVrms/(deg/sec) or 73.3μVpeak/(deg/sec). The estimated sense-mode displacement is 0.82Å/(deg/sec) for the ARS-SOI, calculated from the preliminary characterization results with the estimated drive-mode

vibration amplitude of 18.8μm. The expected sensitivity of the SOI gyroscope for the given sense-mode displacement is 84μVpeak/(deg/sec), which is slightly higher than the measured value. The small mismatch can be due to the frequency matching, the error in drive-mode displacement amplitude, or the error in angular gain of the gyroscope. The quadrature signal at the sense-mode output is about 5.9mVrms, corresponding to 115deg/sec using the measured mechanical sensitivity. The improved decoupling mechanism in the ARS-SOI gyroscope resulted in a quadrature error smaller than that in the ARS-NE gyroscope, as expected.


```
CH1 A  Spectrum        10 dB/ REF -20 dBm           -107.72 dBm
                                                   5.270373 kHz



HId
       RBW# 1 Hz      VBW 1 Hz        ATN  0 dB      SWP  5.476 sec
       CENTER  5.295 kHz                            SPAN   50 Hz


            N           SWP PARAM           VAL

            0          5.270373 kHz      -107.72  dBm
            1          5.294813 kHz      -31.531  dBm
            2          5.304515 kHz      -52.717  dBm
            3          5.284925 kHz      -52.835  dBm
```
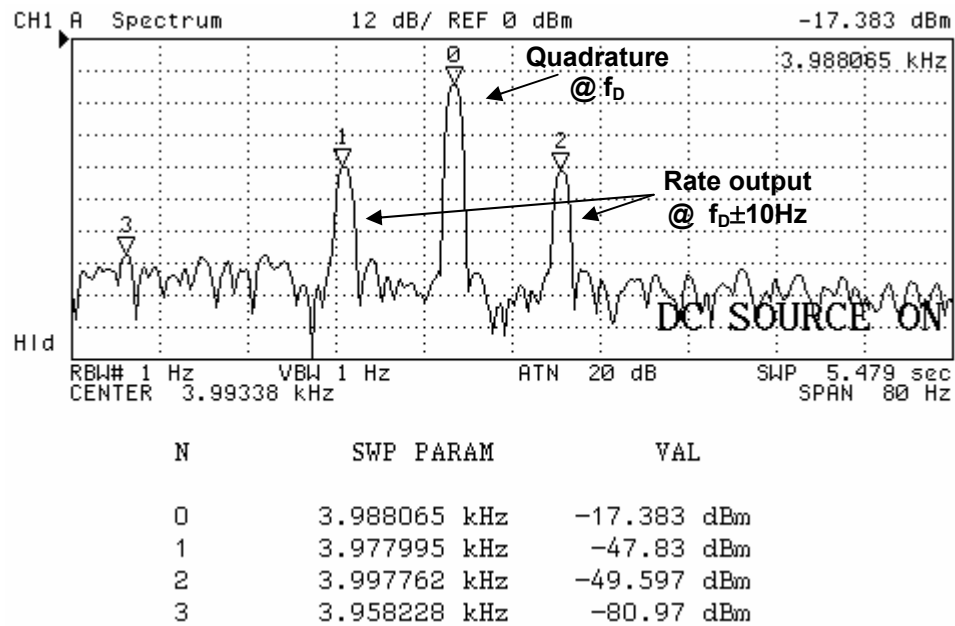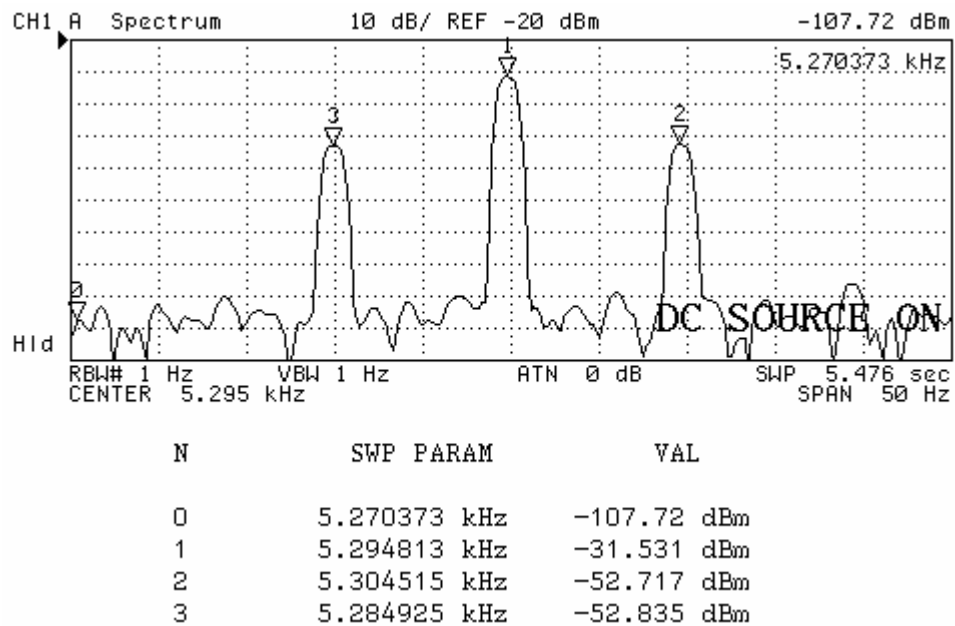
Figure 7.12: The measured output of the fabricated SOI gyroscope prototype prior to demodulation, in response to a sinusoidal angular rate input of amplitude 10deg/sec and frequency 10Hz.
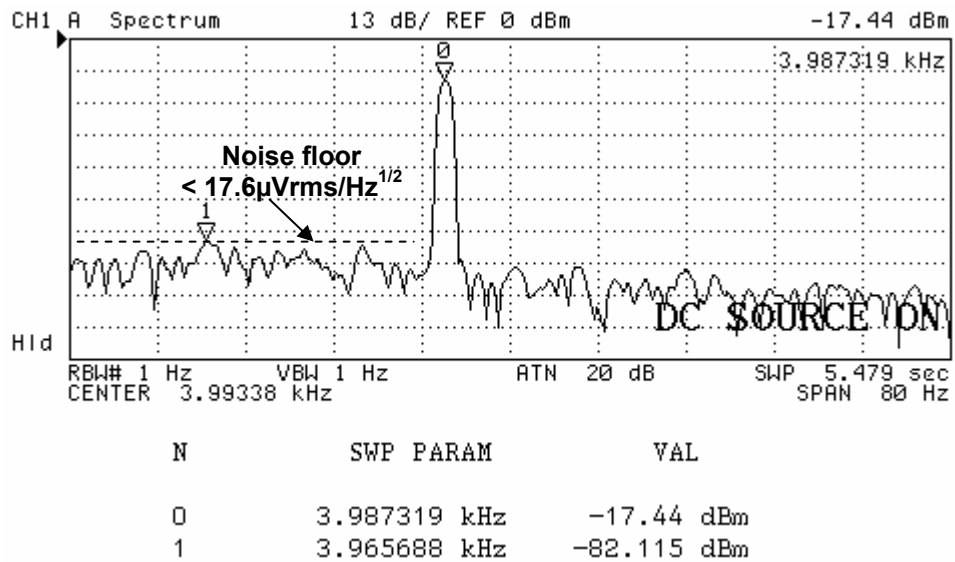
The measured noise floor of the gyroscope is below -100dBm (2.24μVrms) in 1Hz measurement bandwidth. Taking the ratio of the rms noise floor to the raw scale factor of the gyroscope, 73.3μVpeak/(deg/sec), yields an rms-noise-equivalent rate of 0.03(deg/sec)/Hz$^{1/2}$. The noise at the output of the fabricated ARS-SOI gyroscope is much smaller compared to that of ARS-NE gyroscope, however, is still higher than the expected noise taking into account the mechanical-thermal noise of the SOI gyroscope and the input-current noise of the capacitive interface circuit. Note that the measured noise above includes the mechanical noise from the vibrating rate table setup. Stopping the rate table during noise measurement yields a noise floor below

$1.9\mu\text{Vrms/Hz}^{1/2}$, corresponding to an rms-noise-equivalent rate of $0.025(\text{deg/sec})/\text{Hz}^{1/2}$. Clearly, the noise from the environment disturbs the measurement significantly and the future research must consider robust methods for the sensor noise measurements.

The output of the fabricated ARS-SOI gyroscope is demodulated, 40dB-amplified, and filtered using an open-loop rate sensing scheme similar to that used for ARS-NE. Figure 7.13 shows the output response of the SOI gyroscope with respect to the applied angular rate input in a range from -100deg/sec to +100deg/sec, using ±15V supplies in stead of ±18V supplies for the safe operation of the demodulator IC. The scale factor of the gyroscope is measured as 6mV/(deg/sec), in agreement with the $61\mu\text{Vpeak}$ sensitivity at the raw output of the capacitive interface circuit prior to demodulation, using ±15V supplies. The R^2-nonlinearity of the scale factor is measured to be 0.06%, better than the ARS-NE gyroscope. The zero-rate output bias of the sensor is approximately 37deg/sec, due to demodulation phase error.
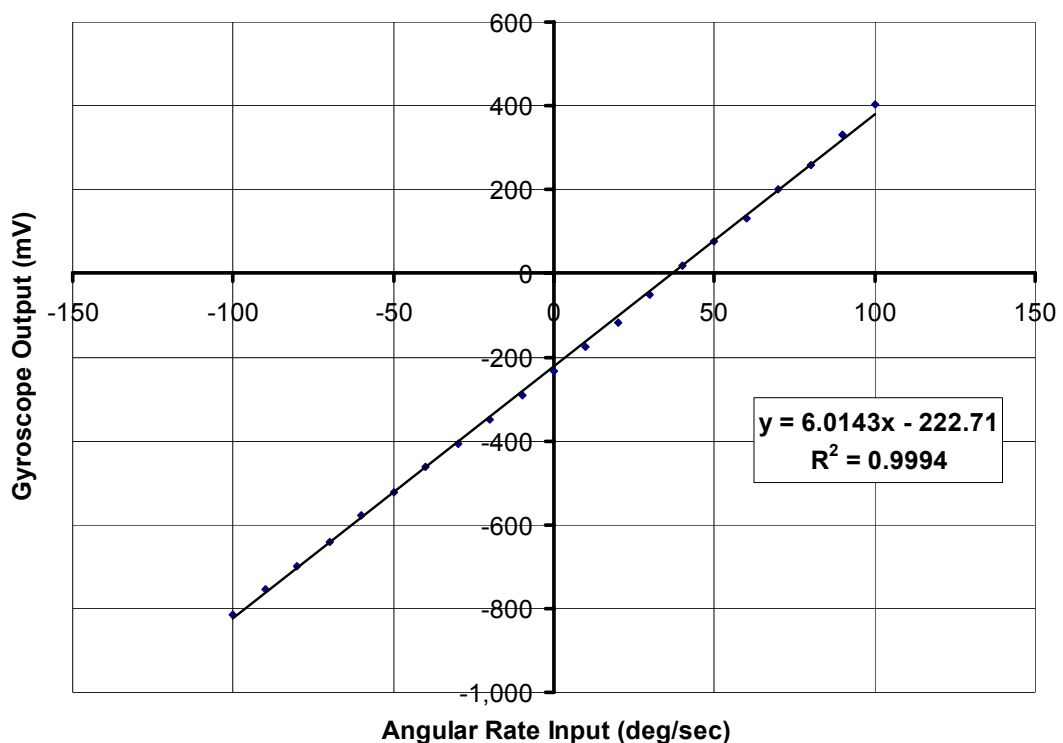
Figure 7.13: The output response of the fabricated SOI gyroscope with respect to the applied angular rate input in a range from -100deg/sec to +100deg/sec.
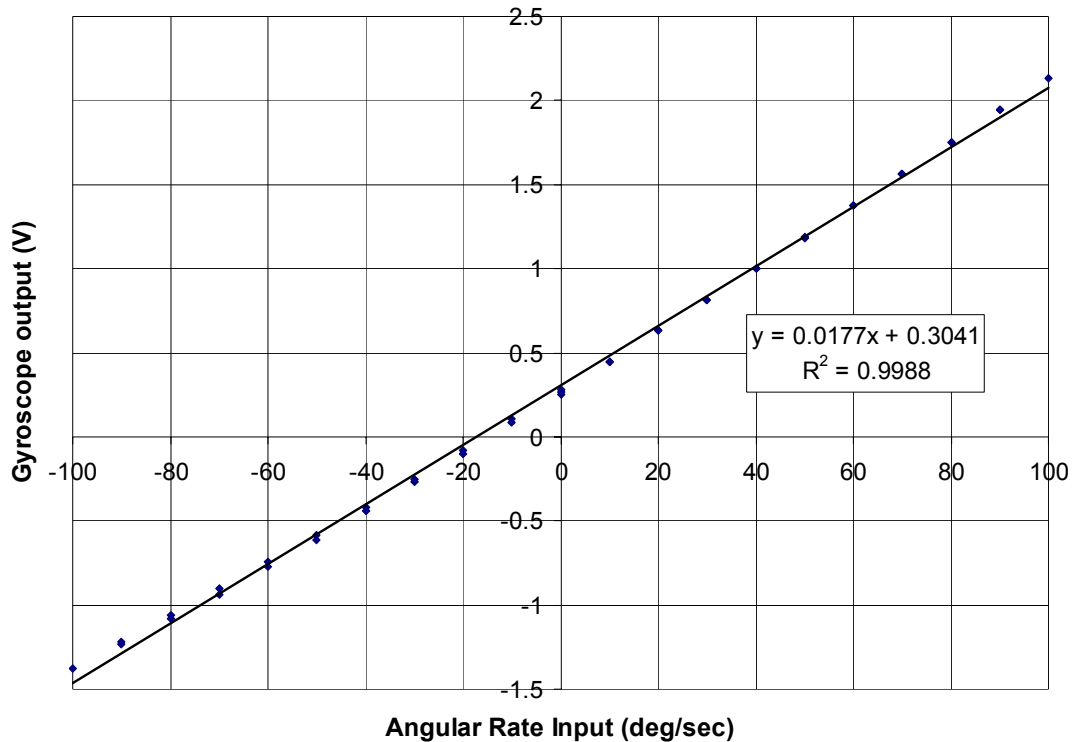
Figure 7.14 shows the random variation of the gyroscope output bias and noise for zero rate input. The bias of the gyroscope is measured to be unstable after 1 hours from the start-up, while it is more stable then. Still, the bias stability of the fabricated ARS-SOI gyroscope together with the demodulation electronics is over 1deg/sec, much higher than the expected. The instability of the bias may be due to the conductive silicon substrate of the gyroscope, which must be kept quiet during the measurement. However, the substrate contacts are not located optimally, and biased from the power supplies. The ripples in the power supplies or in the ground line of the measurement setup may affect the measurements, especially for conductive substrates. The fluctuations in the substrate bias affect the electrical-cross coupling, which cause variation of the phase error during demodulation, resulting in an unstable bias. The rms output noise of the sensor is measured to be 1deg/sec in 10Hz bandwidth, dominated by the unstable bias. Future designs must consider optimum biasing of the conductive SOI substrate, higher sensor capacitances dominating over the parasitic capacitances, and better demodulation schemes using balanced demodulators instead of simple analog multiplier IC.
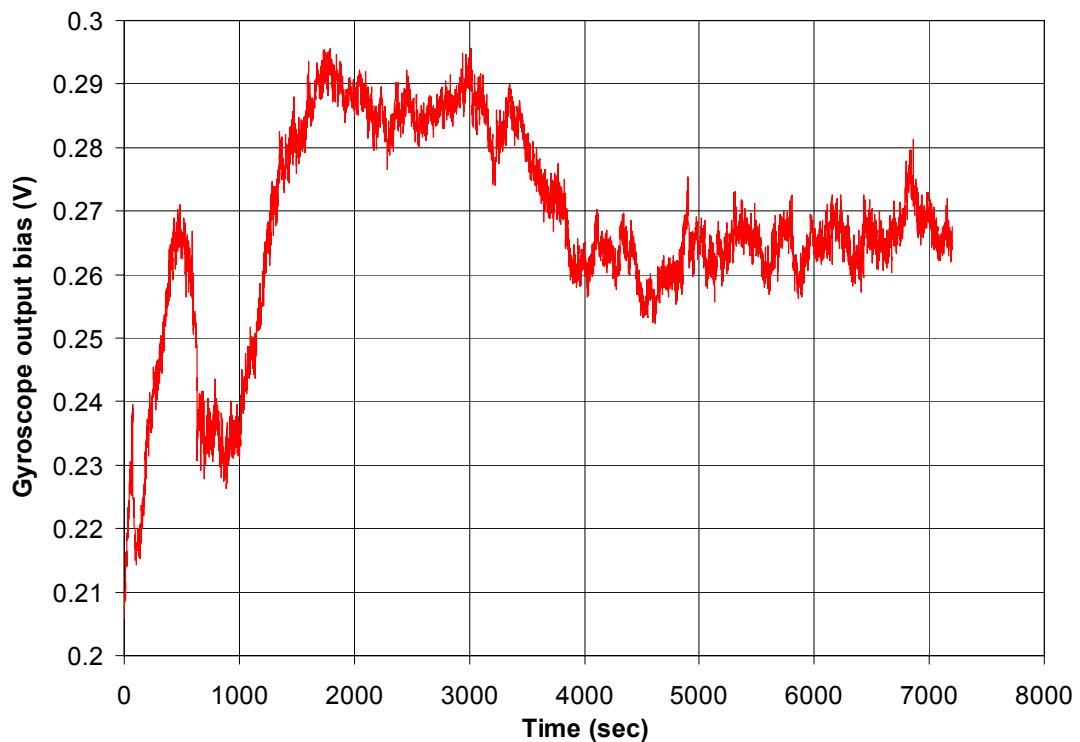
Figure 7.14: The random variation of the fabricated SOI gyroscope output bias and noise at zero rate input.

Completing the rate tests at atmospheric pressure, the gyroscope is also tested at vacuum. An automatic gain control scheme is necessary for the ARS-SOI gyroscope at vacuum, since the maximum allowable drive-mode vibrations (20µm) cannot saturate the capacitive interface, preventing the use of electronic damping for limiting the drive-mode vibrations at vacuum. Therefore, the drive-mode excitation of the gyroscope is performed by constructing a self-resonance loop with automatic gain control. Similarly, a force-feedback loop is also constructed for vacuum operation, since the sense-mode quality factors are measured to be higher than 700, limiting the sense-mode response bandwidth to few hertz. Figure 7.15 shows the frequency-locking loop, automatic gain control loop, and the force-feedback loop electronics, constructed on a single breadboard. Figure 7.16 shows the measured drive-mode output versus the applied amplitude tuning voltage in the self-resonance loop with amplitude control. The drive-mode vibration of the gyroscope can be tuned from 3.4µm up to 18.9µm, by varying the amplitude set signal from 0.2^VDC to 1.4^VDC, demonstrating the successful operation of the self-resonance loop with amplitude control.
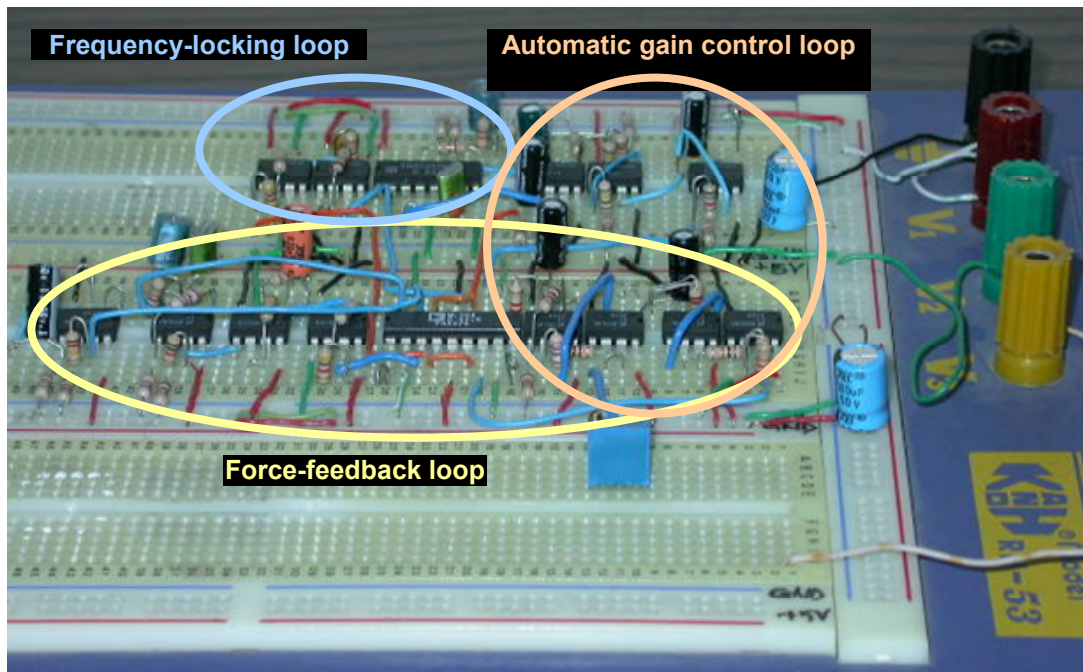
Figure 7.15: The frequency-locking loop, automatic gain control loop, and the force-feedback loop electronics, constructed on a single breadboard.
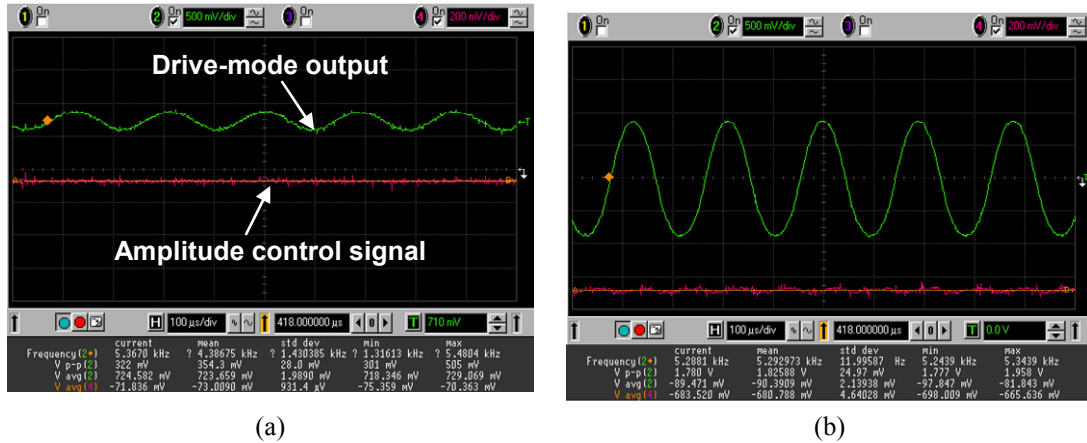
Figure 7.16: The measured drive-mode output versus the applied amplitude tuning voltage in the self-resonance loop with amplitude control. The drive-mode vibration of the gyroscope can be tuned from (a) 3.4μm up to (b) 18.9μm, by varying the amplitude set signal from (a) 0.2VDC to (b) 1.4VDC, demonstrating the successful operation of the self-resonance loop with amplitude control.

Figure 7.17 shows the measured sense-mode raw output of the ARS-SOI at vacuum, in response to a sinusoidal angular rate input of amplitude 2π deg/sec and frequency 10Hz. The rate sensitivity of the gyroscope is higher than 1.6mV/(deg/sec), with an rms-noise equivalent rate of $50(\text{deg/hr})/\text{Hz}^{1/2}$ (for the measured noise floor of $22.4\mu\text{Vrms}/\text{Hz}^{1/2}$), at vacuum. This measurement is performed using open-loop rate-sensing mechanism and by manual tuning of the resonance frequencies of the drive and the sense modes without any feedback control, and therefore is not stable in time. The gyroscope is then inserted in the constructed force-feedback loop for closed-loop stable rate sensing. Unfortunately, the large displacement due to the double-frequency motion of the sense electrodes saturates the force-feedback loop preventing closed-loop rate measurements.

The performance of the ARS-SOI prototype is limited by the substrate effects and the low-stiffness of the isolated sense electrodes against spurious vibrations along the sense axis, for large drive-mode vibration amplitudes. The angular rate sensitivity of the ARS-SOI is remarkable for operation at atmospheric pressure due to high sense-mode quality factor, and the performance approach to tactical-grade application limits at vacuum operation. However, the control electronics developed for the ARS-SOI must be improved for stable operation at vacuum and the isolated sense electrodes must be connected to each other as in the advanced symmetrical

266

and decoupled gyroscope ARS-SOG, which demonstrated the best performance among the other gyroscope prototypes developed in this research.
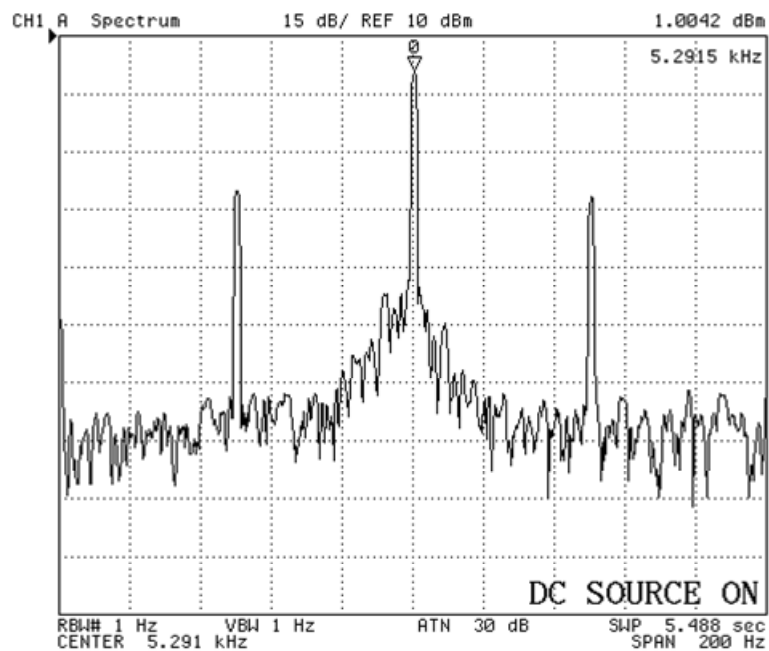
Figure 7.17: The measured sense-mode raw output of the ARS-SOI at vacuum, in response to a sinusoidal angular rate input of amplitude 2π deg/sec and frequency 10Hz.

7.4 ARS-SOG Gyroscope

The drive-mode oscillation of the ARS-SOG gyroscope is generated by the simple positive-feedback self-resonance loop, as for the other prototypes operated at atmospheric pressure. However, the large sensitivity of the ARS-SOG gyroscope due to the high-aspect-ratio capacitive gaps limits the use of the capacitive interface circuit output as a measure of the drive-mode vibration amplitude. The output of the capacitive interface circuit connected to the drive-mode resonator strongly saturates at -1.1V even for 3.8μm drive-mode vibration amplitude. Once the interface circuit saturates, it adds extra damping to the drive-mode resonator, reducing the overall quality factor of the drive-mode at atmosphere. As a result, estimating the drive-mode vibration amplitude is not straightforward if the interface circuit saturates. For this reason, the vibration amplitude of the ARS-SOG gyroscope is optically monitored under Karl Süss probe station, during self-resonance. Table 7.1 compares the optically measured drive-mode vibration amplitude with the expected

267

values for different input excitation voltages. Clearly, the optically measured vibration amplitudes are smaller than the expected values estimated using a constant quality factor of 170 for the drive-mode resonator. In addition, the drive-mode output buffer saturates for vibration amplitudes larger than 3.8μm and cannot be used as a measure. Once the buffer saturates, the optically measured vibration amplitude linearly increase with higher excitation signals, corresponding to a constant quality factor of 100 instead of 170 measured during preliminary characterization. This reduction can be either due to the loading of the saturated capacitive interface circuit or due to the excitation of the drive-mode slightly out-of-resonance due to a phase-error in the self-resonance loop. In any case, the optically-measured drive-mode vibration amplitudes are used for future references.

Table 7.1: Comparison of the optically measured drive-mode vibration amplitude with the expected values for different input excitation voltages for the fabricated ARS-SOG.

V_{PM}	V_{DD}/V_{SS}	$X_{expected}$ for Q_D=170	V_{out_drive} (peak)	$X_{measured}$ using V_{out_drive}	$X_{measured}$ using optical setup
15^V	$\pm 5^V$	3.4μm	0.58^V	2.2μm	2μm
	$\pm 10^V$	7.8μm	1^V (saturated)	3.8μm	4.8μm
	$\pm 15^V$	12.8μm	1.1^V (saturated)	4.2μm	7.5μm
	$\pm 18^V$	15.7μm	1.1^V (saturated)	4.2μm	8.8μm

The rate sensitivity of the ARS-SOG at atmospheric pressure is expected to be smaller than the other prototypes, mainly due to the very small quality factor of the sense mode of the SOG gyroscope ($Q_{S\_atmosphere}$=1.6). The expected displacement for a 1deg/sec rate input is 0.19Å, corresponding to a rate sensitivity smaller than 12μV/(deg/sec), for a proof mass voltage of 15V, drive-mode vibration amplitude of 8.8μm, and for the sense-mode angular gain of 0.46. Figure 7.18a shows the measured sense-mode raw output of the ARS-SOG at atmospheric pressure for the given conditions above except for a proof mass voltage of 19V, when a sinusoidal angular rate is applied with amplitude 2π deg/sec and frequency 10Hz. The measured rate sensitivity is 15.9μV/(deg/sec), in agreement with the expected value of 15.2μV/(deg/sec) for a proof mass voltage of 19V. Figure 7.18b shows the measured sense-mode raw output, when the rate table is stopped. The noise floor of the gyroscope is 1.4μVrms/Hz$^{1/2}$, corresponding to 0.09(deg/sec)/Hz$^{1/2}$ rms-noise-equivalent-rate at atmospheric pressure. The quadrature signal is less than

60deg/sec, best of the all other prototypes due to the advanced-decoupled structure of ARS-SOG. Still the quadrature signal at atmospheric pressure is dominated by electrical cross-coupling and is further reduced at vacuum operation, verified by the vacuum measurements presented later in this section.
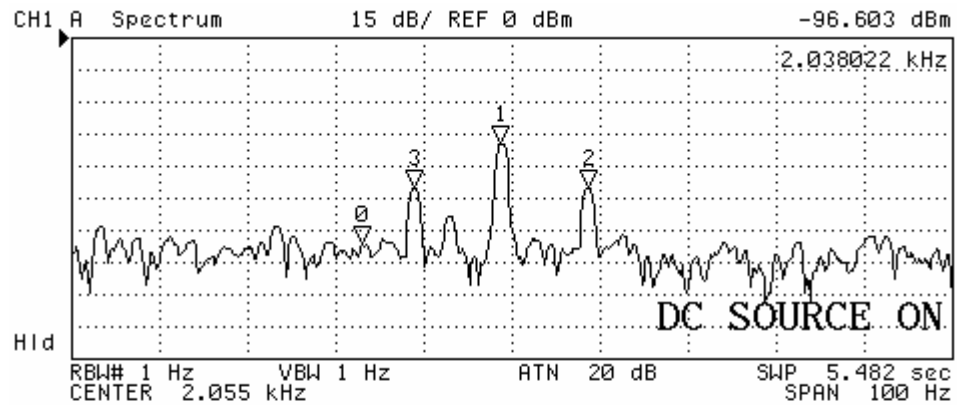
N	SWP PARAM	VAL
0	2.038022 kHz	−96.603 dBm
1	2.053694 kHz	−49.485 dBm
2	2.063582 kHz	−69.873 dBm
3	2.043806 kHz	−70.517 dBm

(a)
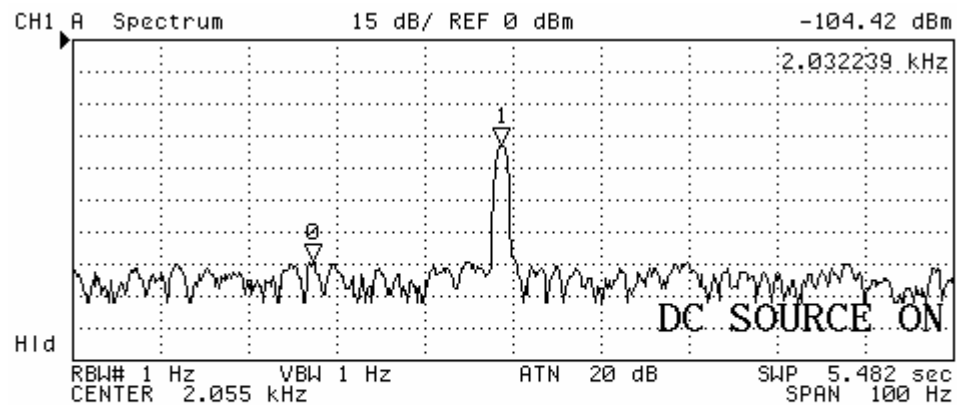
N	SWP PARAM	VAL
0	2.032239 kHz	−104.42 dBm
1	2.053694 kHz	−49.478 dBm

(b)

Figure 7.18: The measured sense-mode raw output of the ARS-SOG at atmospheric pressure, (a) when a sinusoidal angular rate is applied with amplitude 2π deg/sec and frequency 10Hz., and (b) when the rate table is stopped.

269

The output of the fabricated ARS-SOG gyroscope is demodulated, 40dB-amplified, and filtered using an open-loop rate sensing scheme. Figure 7.19 shows the output response of the ARS-SOG gyroscope with respect to the applied angular rate input in a range from -100deg/sec to +100deg/sec, measured at atmospheric pressure. The scale factor of the gyroscope is measured as only 0.8mV/(deg/sec), smaller than the expected value of 1.2mV/(deg/sec) for 15V proof mass voltage. The R^2-nonlinearity of the scale factor is measured to be 0.12%. The zero-rate output bias of the sensor is more than 700deg/sec, even larger than the quadrature signal. This result states that, additional offset comes from the demodulating electronics, adding on the raw output of the gyroscope, and appears as an output offset. Obviously, the variation of this offset coming from the electronics dominates the offset coming from the gyroscope, decreasing the reliability of the bias drift measurements for the fabricated gyroscopes.
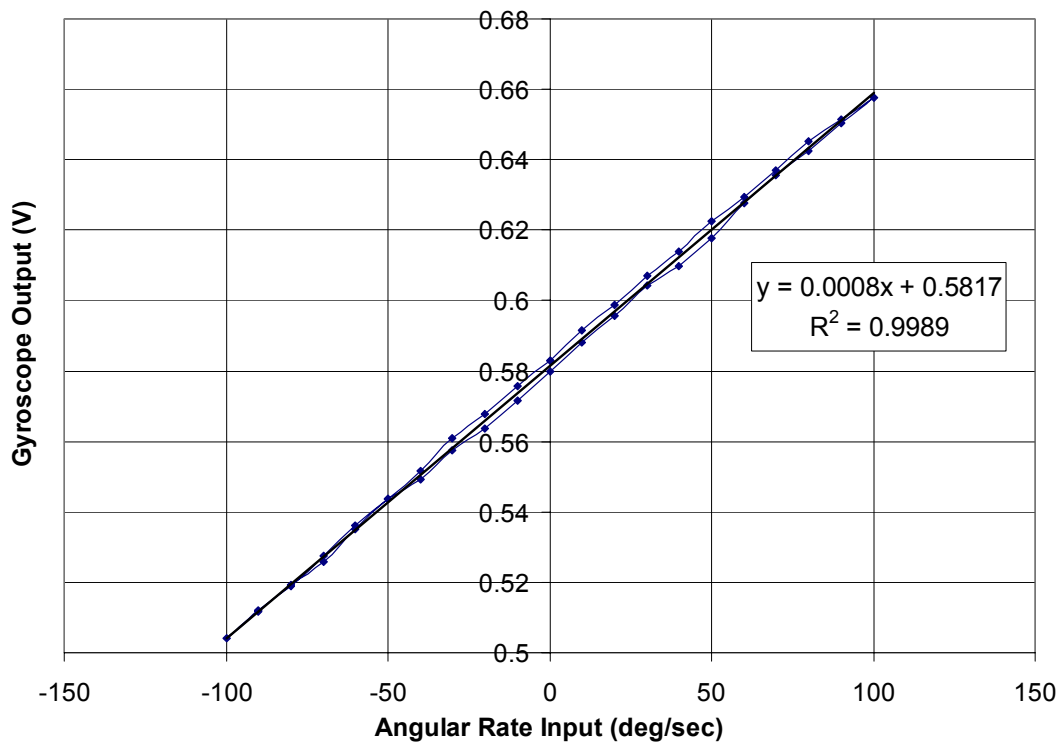
Figure 7.19: The output response of the ARS-SOG gyroscope with respect to the applied angular rate input in a range from -100deg/sec to +100deg/sec, measured at atmospheric pressure.

270

Figure 7.20 shows the variation of the output bias of the fabricated ARS-SOG gyroscope, measured at atmospheric pressure. The bias is stable within a 10deg/sec range, during 2 hours measurement period. Clearly, the instability is mostly due to the demodulating electronics, which is also responsible for most of the output bias. Future research should focus on better demodulating circuits, for increasing the stability and the reliability of the demodulated output.
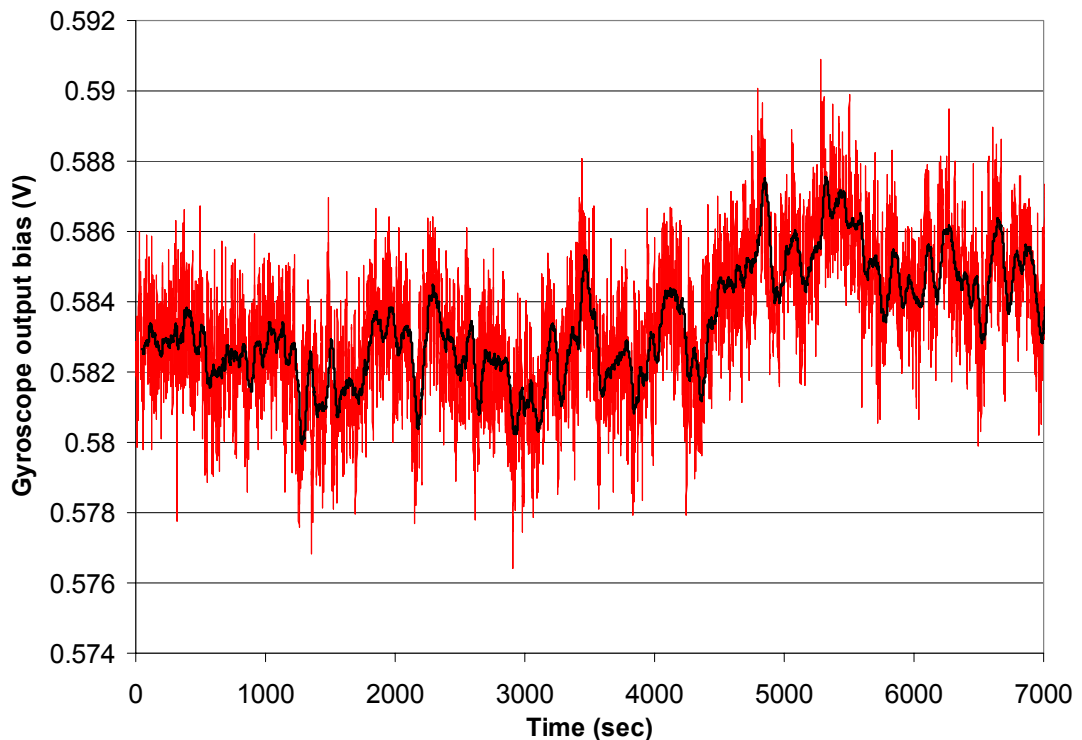
Figure 7.20: The variation of the output bias of the fabricated ARS-SOG gyroscope, measured at atmospheric pressure.

One of the most important features of the ARS-SOG gyroscope is its robustness against mechanical quadrature signals. The sense electrodes of ARS-SOG are connected by rigid trusses constructing a single sense-frame, increasing the stiffness of the sense electrodes against the spurious deflections caused by the large vibration amplitudes along the drive-mode. In addition, the flexures of the sense frame are located such that the sense frame is highly robust against rotary oscillations. Figure 7.21 shows the measured sense-mode outputs in response to 10μm drive-mode vibration amplitude for the fabricated SOG gyroscopes with and without the rigid-link connection between the sense electrodes. The quadrature coupling from

271

the drive-mode to the sense-mode is measured as 15000ppm for the gyroscope
without the rigid link between the sense electrodes, causing a spurious peak at the
sense-mode output; while it is less than 250ppm for the new gyroscope with the
single and rigid sense frame, verifying the improvement.

(a)

(b)
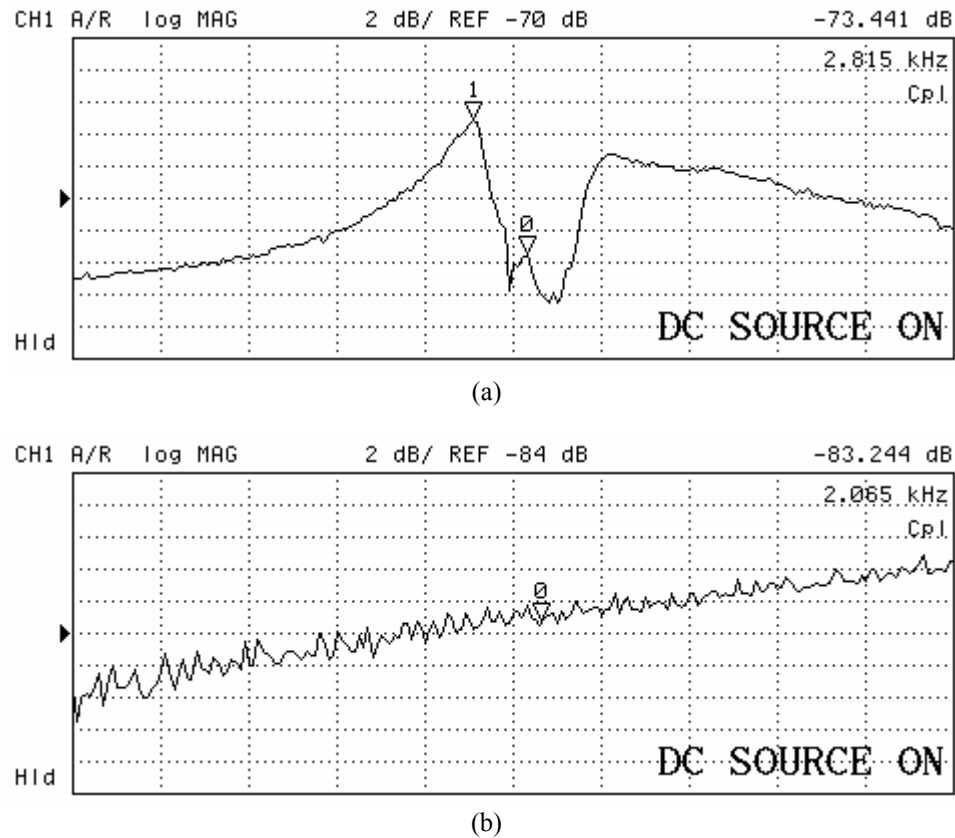
Figure 7.21: The measured sense-mode output in response to 10μm drive-mode vibration
amplitude. Quadrature coupling is (a) 15000ppm for the dual isolated sense frame,
causing a spurious peak at the sense-mode output, and (b) less than 250ppm for the
single and rigid sense-frame of the new gyroscope.

The performance of ARS-SOG gyroscope at atmospheric pressure is far from
demonstrating its limits. It is necessary to operate the gyroscope at vacuum, in order
to demonstrate its ultimate performance. Contrary to the ARS-SOI gyroscope, the
ARS-SOG gyroscope does not need special amplitude-control for preventing
overdrive-destruction as a result of the increased quality factor of the drive-mode at
vacuum. This is because, the capacitive interface circuit limits the vibration
amplitude of the ARS-SOG gyroscope, once it saturates. Figure 7.22 presents the
measured variation of the drive-mode quality factor as a function of the output

voltage of the capacitive interface circuit connected to the drive-mode resonator. The drive-mode quality factor reduces from 10,000 down to less than 1,000 as the output of the interface circuit increase from 0.07Vpeak up to more than 0.8Vpeak. As a result, the damping of the capacitive interface circuit is used for controlling the vibration amplitude of the drive-mode of the gyroscope. The amplitude of vibration at vacuum should not exceed the optically observed vibration amplitude at atmospheric pressure, since the capacitive interface circuit highly saturates already for 8.8μm vibration amplitude. Figure 7.23 shows the highly-saturated output of the capacitive interface circuit connected to the drive-mode resonator oscillating at vacuum, and the output of the sense-mode showing the small quadrature signal.
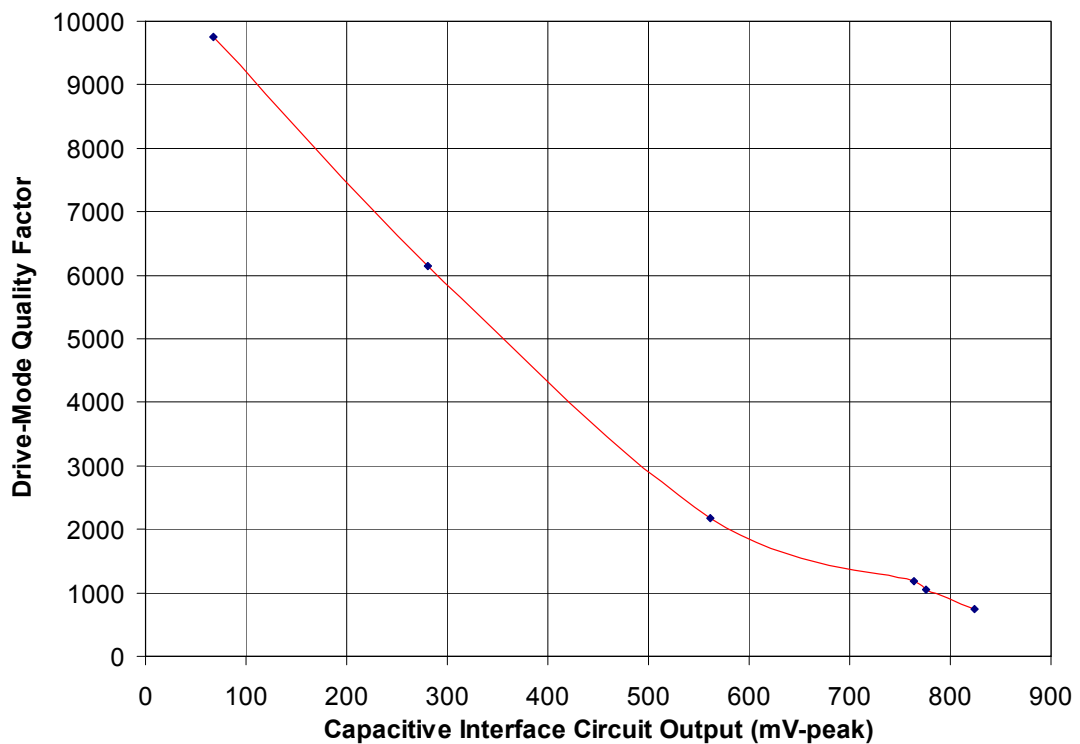
Figure 7.22: The measured variation of the drive-mode quality factor as a function of the output voltage of the capacitive interface circuit connected to the drive-mode resonator.

Figure 7.24a shows the measured sense-mode output of the gyroscope in response to a 2π deg/sec sinusoidal angular rate input at 10Hz, measured at vacuum. The gyroscope demonstrates a mechanical sensitivity of 900μV/(deg/sec), about 60 times higher than the sensitivity at atmospheric pressure. The result states that the

mechanical quality factor of the sense mode reaches to about 100 at vacuum, conflicting with the results of preliminary characterization, which is 24 at vacuum. However, examining Figure 5.24b of Chapter 5 shows a nonlinear response characteristics for the sense-mode resonance at vacuum, which may result in an underestimation of the quality factor based on the preliminary measurements. Finally, the quadrature signal is only 15deg/sec at vacuum, about 4 times smaller than the quadrature signal at atmospheric pressure, verifying the discussion for the quadrature signal at atmospheric pressure. Figure 7.24b shows the measured RMS noise floor of the gyroscope, which is less than $9\mu V/Hz^{1/2}$, corresponding to an rms-noise-equivalent rate better than 36deg/hr, when no angular rate is applied to the gyroscope and the servo of the rate table is off.
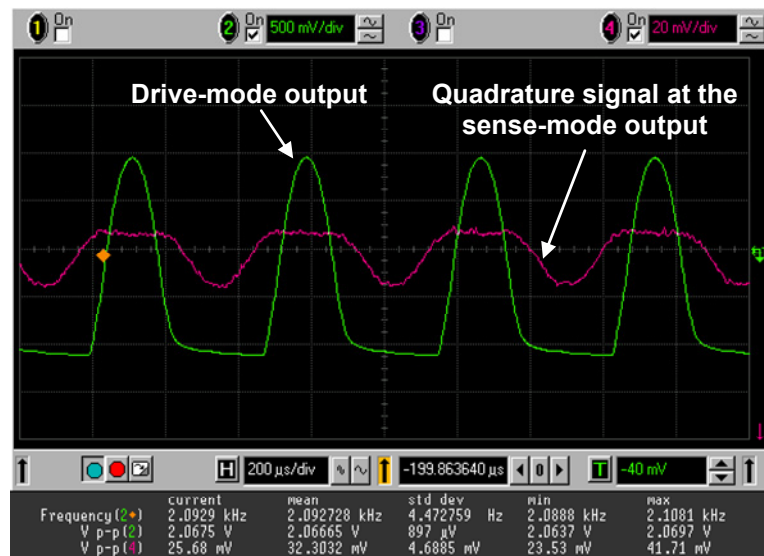
Figure 7.23: Highly-saturated output of the capacitive interface circuit connected to the drive-mode resonator oscillating at vacuum, and the output of the sense-mode showing the small quadrature signal

The low quality factor of the sense-mode at vacuum allows open-loop rate sensing, instead of closed-loop rate sensing. However, the primitive demodulation electronics prevent reliable scale-factor measurements for the ARS-SOG prototype at vacuum. The poor control of the signal phase for the very-sensitive output of the gyroscope cause a large instability of bias, disturbing the accurate measurement of the scale-factor. In addition, very small displacements due to axial and tangential accelerations resulting from the rotation of the rate table are also sensed by the

ARS-SOG at vacuum, which is another disturbance for the full characterization of the gyroscope at vacuum. Yet, the demonstrated performance of the ARS-SOG is remarkably close to the requirements of tactical-grade applications.
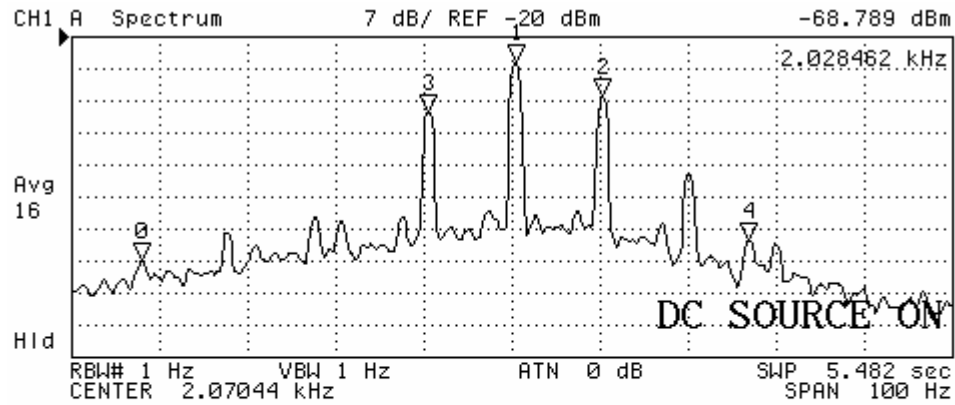
N	SWP PARAM	VAL
0	2.028462 kHz	−68.789 dBm
1	2.070813 kHz	−25.694 dBm
2	2.080701 kHz	−33.298 dBm
3	2.060925 kHz	−36.651 dBm
4	2.097306 kHz	−64.515 dBm

(a)
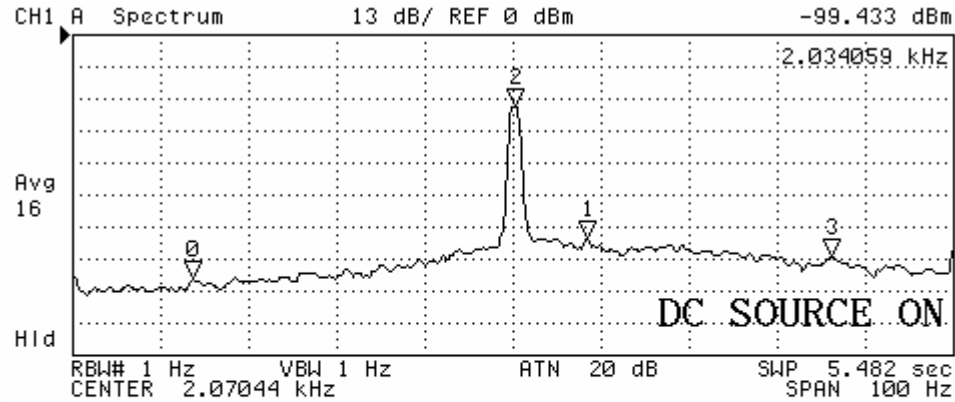
N	SWP PARAM	VAL
0	2.034059 kHz	−99.433 dBm
1	2.078836 kHz	−82.722 dBm
2	2.070627 kHz	−29.042 dBm
3	2.106634 kHz	−90.23 dBm

(b)

Figure 7.24: The measured sense-mode raw output of the ARS-SOG at 20mTorr vacuum, (a) when a sinusoidal angular rate is applied with amplitude 2π deg/sec and frequency 10Hz., and (b) when the rate table is stopped.

7.5 Summary of the Final Tests and Conclusions

This chapter presented the results of the final characterization tests performed on four different angular-rate sensors developed in this research study. Each sensor consists of a MEMS gyroscope hybrid-connected to the capacitive interface circuit and combined with the feedback and control electronics, all designed and developed within this research. The performed tests yield the angular rate sensitivity, rms noise-equivalent rate, quadrature output, scale-factor, linearity, and the bias instability of each fabricated gyroscope. The results verify that the developed symmetric and decoupled micromachined gyroscope structures have the potential of tactical-grade performance, provided that the gyroscope is operated at vacuum.

Table 7.2 summarizes the performance parameters of the fabricated gyroscopes, measured at atmospheric pressure. The vibration amplitude of the ARS-DWSM is kept small for the flexure beams show linear force-deflection behavior. The vibration amplitudes of the remaining structures have stress-relieving folded flexures, allowing large drive-mode vibration amplitudes.

The measured angular rate sensitivities are close to the expected values, based on the results of the preliminary characterization tests presented in Chapter 5. However, the output noise from the gyroscopes varies significantly for different prototypes, although identical capacitive interface circuits are used. In addition, the measured noise level is above $1\mu V_{rms}/Hz^{1/2}$ for all gyroscopes, much higher than the expected noise floor of the capacitive interface circuit ($<100nV/Hz^{1/2}$). The noise floors are possibly dominated by the mechanical noise from the gyroscope, rather than the electronic noise of the interface circuit. It is observed that the better the decoupling in the gyroscope (i.e., smaller the quadrature error), smaller the output noise, except the ARS-DWSM, which is operated with mismatched resonance frequencies and the large quadrature error for ARS-DWSM is mainly dominated by electrical cross-coupling. The quadrature errors, for the other three prototypes are better than 250deg/sec, with the ARS-SOG has the smallest coupling as expected. The noise-equivalent rates of the fabricated gyroscopes are determined from the ratio of the rms-noise floor to the angular rate sensitivity. ARS-SOI demonstrated the best

performance at atmospheric pressure, due to its low output noise. ARS-DWSM also yield a nice performance due to its small capacitive gaps, even though it is operated with mismatched resonance frequencies. The performance of ARS-NE and ARS-SOG are limited by the output mechanical noise and the low sense-mode quality factor, respectively.

The scale-factors of the gyroscopes are measured after demodulation, amplification, and low-pass filtering using low-cost hybrid electronics constructed on either PCB or on breadboard. Still the measured R^2-linearity values are all better than 1.1%, for the fabricated gyroscopes. The measured output bias of the fabricated gyroscopes are dominated by the phase-errors in the low-cost and high-offset demodulation electronics, which results in a significant amount of the quadrature error couple to the demodulated output. Therefore, the bias instability values in Table 7.2 do not reflect the actual bias drift of the fabricated gyroscopes, but are dominated by the drifts in the external electronics.

Table 7.2: The performance parameters of the fabricated gyroscopes, measured at atmospheric pressure.

Performance Parameter	ARS-DWSM	ARS-NE	ARS-SOI	ARS-SOG
Drive-mode vibration amplitude, μm	2	10.4	18.8	8.8
Angular rate sensitivity, μV/(deg/sec)	24.9	180	73.3	12
Noise floor, $\mu V_{rms}/Hz^{1/2}$	1.5	17.1	2.2	1.1
Noise equivalent rate, $(deg/sec)/Hz^{1/2}$	0.06	0.095	0.025	0.09
Quadrature output, deg/sec	2077	230	115	60
Scale-factor, mV/(deg/sec)	-	17.7	6	0.8
R^2-Linearity, %	1.1	0.12	0.06	0.12
Output bias, deg/sec	-	17	37	700
Bias instability, deg/sec	-	1	1.5	10

The measured noise-equivalent rates of the fabricated gyroscopes are better than $0.1(deg/sec)/Hz^{1/2}$, but far from tactical-grade performance. Therefore, the

gyroscopes are also tested in vacuum, for improving their angular rate sensitivity and improving the minimum detectable rate. However, no improvement is expected for the ARS-DWSM at vacuum due to its mismatched operation frequencies. Similarly, the large mechanical coupling in the ARS-NE gyroscope prevented it from entering into vacuum. Therefore, only ARS-SOI and ARS-SOG gyroscopes are tested at vacuum, because of their improved decoupling mechanisms and robustness to rotational vibrations. Table 7.3 summarizes the performance parameters of the fabricated SOI and SOG gyroscopes, measured at vacuum ambient below 50mTorr. The drive-mode vibration amplitude of the ARS-SOI is limited with the help of an automatic gain control loop, while the saturating capacitive interface circuit performed the similar limiting action for the ARS-SOG. The measured angular rate sensitivities are significantly improved at vacuum, due to the increase in the sense-mode quality factors. The measured noise-equivalent rates at vacuum are close to the tactical-grade limits for both prototypes, reaching to 36deg/hr for the ARS-SOG in 1Hz bandwidth. The improvement achieved by switching from the atmospheric pressure to vacuum ambient is higher for the ARS-SOG gyroscope, simply because of its advanced decoupling mechanism. The quadrature error of ARS-SOG is only 15deg/sec at vacuum without employing any quadrature cancellation electronics, about an order of magnitude smaller than that of ARS-SOI.

Table 7.3: The performance parameters of the fabricated gyroscopes, measured at vacuum ambient below 50 mTorr.

Performance Parameter	ARS-SOI	ARS-SOG
Drive-mode vibration amplitude, μm	>18	>9
Angular rate sensitivity, mV/(deg/sec)	1.6	0.9
Noise floor, $\mu V_{rms}/Hz^{1/2}$	22.2	9
Noise equivalent rate, $(deg/hr)/Hz^{1/2}$	50	36
Quadrature output, deg/sec	157	15

The results of the final tests provide different conclusions for each of the characterized gyroscopes, in terms of performance limitations. The limited frequency-matching ability and the small sensor size are the two major factors bounding the performance of ARS-DWSM. Still, it demonstrated a nice performance even at atmospheric pressure due to its small capacitive gaps. The

basic limiting factor for the ARS-NE is its susceptibility to rotational vibrations. Improving the mechanical design of the nickel gyroscope may yield a very sensitive gyroscope, even at atmospheric pressure, because of its large mechanical quality factors at atmospheric pressure. Similar discussion is valid for ARS-SOI prototype, while its decoupling is better than the nickel gyroscope due to precise silicon micromachining. However, the isolated dual sense-frame of the improved symmetrical and decoupled gyroscope is never as robust as the single and rigid sense-frame of the advanced design used for ARS-SOG. The ARS-SOG prototype demonstrated a performance very close to the tactical-grade applications, when operated at vacuum. The performance of ARS-SOG is currently limited by the large capacitive gaps, saturating capacitive interface circuit, low-quality demodulating electronics, and the lack of closed-loop electronics for keeping the drive and sense mode resonance frequencies identically matched. Decreasing the capacitive gaps of the gyroscope from 5µm to less than 3µm, using a capacitive interface circuit with a wider operation swing range, which allows larger drive-mode vibration amplitudes, employing a high-quality doubly-balanced demodulation scheme, and constructing closed-loop frequency-control electronics would improve the performance of the ARS-SOG towards better than 10deg/hr.

The operation bandwidths of the gyroscopes are currently defined by the mechanical quality factors of the gyroscopes, as open-loop rate sensing is employed. Control of the bandwidth is necessary especially at vacuum, where high quality factors shrink the bandwidths to less than few hertz, as observed for ARS-SOI. This must be achieved by using force-feedback electronics, which could not be operated with the ARS-SOI gyroscope due to the double-frequency motion of the sense electrodes saturating the feedback electronics. The second prototype characterized at vacuum is the ARS-SOG, whose sense-mode quality factor is already smaller than 100 at vacuum, due to soft anchors, and therefore no force-feedback mechanism is needed. Still, future research may investigate the closed-loop rate sensing for a better quality ARS-SOG prototype, with higher sense-mode quality factor.

The gyroscopes designed in this research are sensitive to external accelerations, as most of the single-mass vibratory gyroscopes are. The g-sensitivities of the current gyroscopes are left as a future research topic, after constructing a more reliable demodulation scheme for reading the outputs of the gyroscopes. The g-sensitivity of the current designs can be reduced by employing two identical gyroscopes with anti-phase drive-mode vibrations, as in tuning-fork designs.

Currently, the power dissipation of the fabricated gyroscope prototypes is determined by the external electronics used for actuating the drive-mode and detecting the rate-response, approaching to 1W from ±15V power supplies. The power consumption can be reduced by optimizing the minimum necessary circuit blocks for operating the gyroscope and by implementing the external electronics in a CMOS ASIC.

In conclusion, the MEMS gyroscopes developed in this research are all successfully characterized; and the results closely agree with the theory. The advanced symmetric and decoupled gyroscope prototype ARS-SOG demonstrated a performance very close to the tactical-grade requirements when operated at vacuum, and its performance is currently limited by the fabrication process and the electronics. Improving the fabrication process and the electronics would yield a gyroscope with an overall performance better than 10deg/hr.

CHAPTER 8

CONCLUSIONS AND FUTURE RESEARCH

The research presented in this dissertation involves the development of micromachined gyroscopes for tactical-grade applications. The gyroscopes are based on a symmetric and decoupled architecture, for a small mechanical cross-coupling and better frequency matching. Three different symmetric and decoupled MEMS gyroscopes are designed, fabricated, and characterized within the framework of this research, together with the CMOS capacitive interface circuit and external control electronics. Four different micromachining technologies are used for the fabrication of the designed gyroscopes, namely, the dissolved wafer silicon micromachining (DWSM), nickel electroforming (NE), silicon-on-insulator (SOI) micromachining, and silicon-on-glass (SOG) micromachining. The operations of the fabricated gyroscopes are verified through preliminary characterization steps, and their performances are evaluated by a series of angular rate measurements.

Based on the achievements and the results of this study, following conclusions can be drawn:

1. The electromechanical design of micromachined vibratory gyroscopes is investigated. Complete electromechanical models of the symmetric and decoupled vibratory gyroscopes are constructed. These models are then analyzed for understanding the effect of resonance frequency matching, electrostatic actuation, capacitive sensing, and electrostatic tuning. It is concluded that the frequency matching is inevitable for reaching

tactical-grade performance in vibratory gyroscopes. The actuation mechanism of the gyroscope should allow large drive-mode vibration amplitudes with the use of linear varying-overlap-area type comb electrodes and stress-relieving folded flexures. The sense mechanism of the gyroscope should have nonlinear varying-gap type comb electrodes for high sensitivity and for fine-tuning the resonance frequency of the sense-mode after fabrication using electrostatic springs. In addition, it is concluded that the drive and the sense modes of the gyroscope must be fully decoupled from the each other by restricting the drive and sense electrode motions to one degree-of-freedom, while a single proof mass with two degree-of-freedom is used for coupling the rate-induced Coriolis force to the sense-mode. The second order effects such as the quadrature error, frequency-doubling, and mechanical-thermal noise are also examined in detail.

2. Three new symmetric and decoupled gyroscope architectures are developed based on the theoretical investigations. The first and original structure has completely symmetric drive and sense modes for achieving identical resonance frequencies for the drive and the sense modes. It has linear comb electrodes for both the drive and the sense modes and has clamped-guided flexures for increased robustness against rotational vibrations. The second and improved gyroscope structure is optimized for large drive-mode vibration amplitudes using linear combs and folded flexures, and for high angular rate sensitivity using nonlinear combs. It also has post-process frequency-tuning capability. The third and advanced gyroscope structure has the advantages of the improved design with an increased robustness against double-frequency-motion and quadrature coupling using a single-rigid sense frame and increased stiffness against rotational vibrations.

3. The designed gyroscopes are fabricated in four different micromachining processes, including dissolved wafer silicon micromachining (DWSM), nickel electroforming (NE), silicon-on-insulator (SOI) micromachining, and silicon-on-glass (SOG) micromachining. The first and original symmetric

282

and decoupled gyroscope structure is fabricated in DWSM process (ARS-DWSM: Angular Rate Sensor fabricated in DWSM process), occupying an area of only 1.2x1.2mm^2, having a structural layer thickness of 12μm, and capacitive gaps of 1.5μm. The second and improved gyroscope structure is fabricated in both NE and SOI micromachining processes. The ARS-NE prototype occupies an area of 3.3x3.3mm^2, having a structural layer thickness of 18μm, and capacitive gaps of 2.5μm. ARS-SOI prototype, on the other hand, occupies an area of 3.6x3.8mm^2, having a structural layer thickness of 25μm, and capacitive gaps of 2.6μm. The third and advanced gyroscope structure is fabricated in SOG micromachining process. ARS-SOG prototype occupies an area of 4.2x4.6mm^2, having a structural layer thickness of 100μm, and capacitive gaps of 5.5μm. All of the fabrication processes are developed and optimized within the Class 100 and Class 1000 cleanroom environment of Middle East Technical University, Microelectronic Technologies (METU_MET) facility, except the SOI micromachining process conducted at SOIMUMPs of MEMSCAP and the DRIE step of the DWSM process conducted at The University of Michigan.

4. The problems associated with each fabrication process conducted at METU-MET are solved after a careful assessment of the source of the problem. The DWSM process is optimized for the highest available aspect ratio with minimum gap spacing. The NE process is optimized for low-stress electrodeposition of sacrificial copper and structural nickel layers, and for generating a high-aspect ratio plating mold. The designs sent to the SOIMUMPs process of MEMSCAP are optimized against uncontrolled process behaviors such as excessive trench undercut or fracture of slender structures. Finally, the SOG process is optimized for high-aspect ratio thorough etching of a 100μm-thick silicon substrate anodically bonded to a glass substrate, without any significant ion damage, sidewall destruction, or SOI notch effects.

5. A unity-gain buffer type capacitive interface circuit is designed for the gyroscopes developed in this research. The input impedance of the interface circuit is maximized for serving an effective buffer action at the high-impedance outputs of the gyroscopes. This is achieved by minimizing the capacitances and maximizing the biasing resistance at the input of the designed circuit. The input capacitance of the buffer circuit is designed to be lower than 20fF by bootstrapping, while the bias resistance is designed to be above 6Gohm by using a minimum size MOS transistor operating in the sub-threshold region. The noise of the interface circuit is estimated to be less than $70nV/Hz^{1/2}$. The design values are verified by simulations performed in SpectreS. The designed circuit is fabricated in the 0.6μm n-well CMOS process offered by XFAB. The fabricated interface circuit includes three measurement channels and occupies an area of only 0.7x1.3mm^2. The power dissipation of the fabricated 3-channel interface circuit is less than 3mW from ±2.5V supplies, excluding the on-chip amplification stages.

6. The fabricated gyroscope prototypes are hybrid-connected to the fabricated CMOS capacitive interface circuit inside 40-pin DIL package, and characterized. This preliminary characterization is found to be vital prior to the design of external control electronics, which require the exact mechanical model parameters of the fabricated gyroscopes. The preliminary characterization is also proven to be an efficient method for the evaluation of the fabrication process and the verification of the theory. The measured capacitances, capacitance gradients, and resonance frequencies are found to be closely matching with the expected results for all of the fabricated gyroscope prototypes. The fabrication tolerances are well-estimated prior to fabrication except for the SOG process, for which the pattern-dependent etching characteristics should be assessed further. The capacitance gradient of the fabricated gyroscopes, which is one of the major factors determining the sensitivity, are measured to be in the range of $8.4x10^{-9}$F/m to $1.4x10^{-6}$ F/m, better than many micromachined gyroscopes in the literature. The sense-mode resonance frequencies of the fabricated gyroscopes, except

ARS-DWSM, can be electrostatically tuned to the drive-mode frequency by DC polarization voltages less than 16V, within the practical power supply range. The quality factors of the fabricated gyroscopes reach to about 500 at atmospheric pressure, while this value exceeds 10,000 for the silicon gyroscopes at vacuum. The parasitic capacitance associated with the output of the gyroscopes is estimated to be as small as 120fF for the gyroscopes fabricated on insulating substrates. This value exceeds 3.5pF for the ARS-SOI gyroscope fabricated on a conductive substrate. In conclusion, most of the results obtained from the preliminary characterization closely agree with the theoretically expected values.

7. Electronic control and feedback circuits are developed based on the results of the preliminary characterization performed on the fabricated gyroscopes. Self-resonance excitations of the drive-mode with positive feedback and with automatic gain control are both investigated and applied to the fabricated gyroscopes. In addition, the open-loop and closed-loop rate sensing schemes are developed for the fabricated gyroscope prototypes. The operation of the constructed feedback loops and control electronics are verified with the help of SIMULINK behavioral models including the electromechanical models of the fabricated gyroscopes, prior to combining them with the gyroscopes. The designed automatic gain control loop has the ability of tuning the drive-mode vibration amplitude from 0 to 20μm, with a tuning voltage range of less than 2^V. Similarly, the closed-loop force-feedback scheme can null the sense-mode vibrations in response to angular rate inputs as large as 40deg/sec, with an equivalent electrostatic feedback force generated from a DC voltage less than 3^V.

8. The performances of the fabricated MEMS gyroscopes are evaluated after hybrid-connecting them to the capacitive interface circuit and combining with the constructed control/feedback electronics. A series of angular rate measurements are performed on the fabricated gyroscopes for determining their angular rate sensitivity, noise-equivalent rate, quadrature output,

scale-factor, linearity, bias, and bias instability. The ARS-SOI prototype demonstrated an angular rate sensitivity as high as 73µV/(deg/sec), with a noise equivalent rate of $0.025(\text{deg/sec})/\text{Hz}^{1/2}$, measured at atmospheric pressure. On the other hand, the ARS-DWSM prototype, besides its very small footprint and mismatched-mode operation, demonstrated a remarkable performance of $0.06(\text{deg/sec})/\text{Hz}^{1/2}$ at atmospheric pressure, owing to its small capacitive gaps. The performances of the ARS-NE and ARS-SOG prototypes are found to be about $0.1(\text{deg/sec})/\text{Hz}^{1/2}$ at atmospheric pressure, limited by the mechanical noise and the low sense-mode quality factor, respectively. The linearity of the fabricated gyroscopes are determined to be better than 1.1%, owing to linear drive-mode vibrations and stress-relieving flexures. The output bias values of the gyroscopes are observed to be dominated by the phase error introduced by low-cost and high-offset demodulation electronics, which must be improved in future research.

9. The ARS-SOI and ARS-SOG gyroscopes are also characterized at vacuum ambient, for determining their ultimate performance limits. The ARS-SOI and ARS-SOG gyroscopes demonstrated excellent angular rate sensitivities as high as 1.6mV/(deg/sec) and 0.9mV/(deg/sec), respectively, due to the improvement of the sense-mode mechanical quality factor at vacuum. The noise equivalent rates of the ARS-SOI and ARS-SOG gyroscopes are measured to be lower than $50(\text{deg/hr})/\text{Hz}^{1/2}$ and $36(\text{deg/hr})/\text{Hz}^{1/2}$, respectively, being close to the tactical-grade application limits. The performance of the ARS-SOG is better than ARS-SOI, due to its improved decoupling mechanism, which achieves a quadrature error as small as 15deg/sec without employing any quadrature cancellation electronics, which is one of the best values reported in the literature. Decreasing the capacitive gaps of the ARS-SOG gyroscope from 5µm to less than 3µm, increasing the drive-mode vibration amplitude from 9µm to above 15µm, employing a high-quality doubly-balanced demodulation scheme, and constructing closed-loop frequency-control electronics would improve the performance of the ARS-SOG towards better than 10deg/hr.

Figure 8.1 presents the improvement in the performance of the symmetric and decoupled gyroscopes developed at METU since year 2000, approaching to the tactical-grade limits.
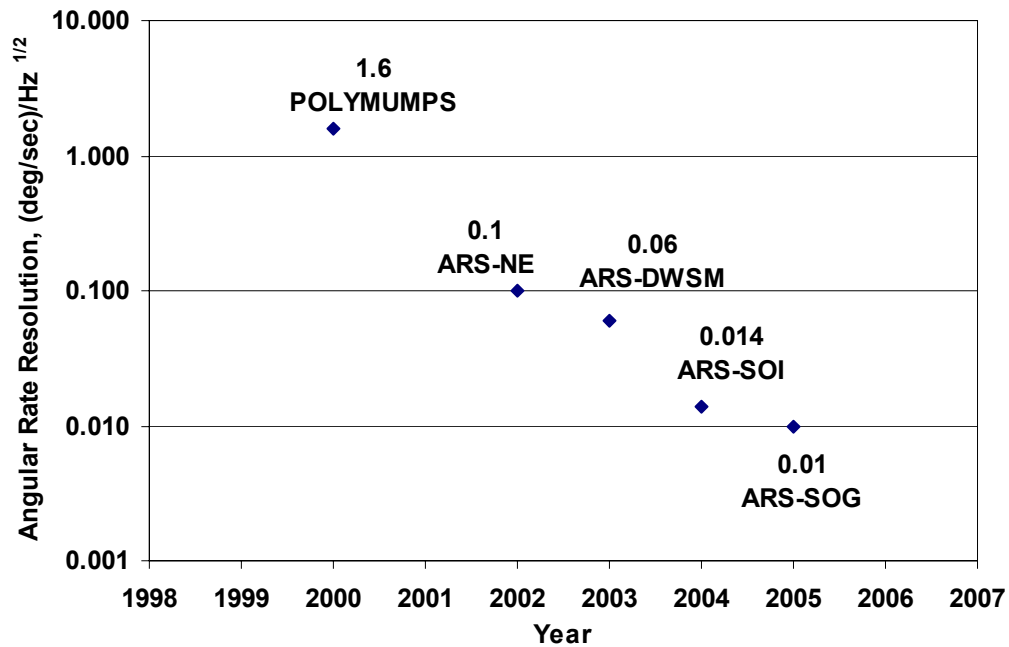
Figure 8.1: The improvement in the performance of the symmetric and decoupled gyroscopes developed at METU since year 2000.

Although all of the major research objectives have been achieved within this research, there are still some issues to be undertaken for improving the overall performance of the vibratory MEMS gyroscopes. Some of these issues are listed below:

1. Minimizing the capacitive gap spacing is essential for increasing the angular rate sensitivity of micromachined capacitive gyroscopes. Therefore, it is necessary to optimize the SOG process for reducing the minimum trench size below the current value of 5.5μm. Currently, the aspect ratio of the SOG process is close to 20 using DRIE, which can be increased above 30 approaching to the practical limits of DRIE. Such an improvement would roughly increase the angular rate sensitivity of the fabricated ARS-SOG prototype by a factor of about 3, provided that the structural layer thickness is still 100μm.

2. The future research must consider improvements in DWSM process or alternatives to it. This process allows capacitive gap spacing as small as 1µm, with a maximum structural layer thickness of 15µm. The angular rate sensitivity of a gyroscope, having identical layout with the current ARS-SOG prototype, and fabricated in such a DWSM process would approach to 1deg/hr, provided that the gyroscope is operated at vacuum and have similar mechanical quality factors to the ARS-SOG. Minimizing the capacitive gap to sub-micron dimensions using high-resolution stepper lithography while preserving the structural layer thickness would improve the sensitivity further below 1deg/hr.

3. Packaging the fabricated MEMS gyroscope in vacuum ambient is also vital for achieving tactical-grade performance. However, packaging each gyroscope in a hermetic vacuum seal would increase the cost of the sensors significantly. Future research should focus on wafer-level vacuum packaging of the current gyroscopes, minimizing the packaging costs.

4. The capacitive interface circuit must be improved in terms of input biasing and input voltage swing. The minimum-size subthreshold-MOS biasing transistor of the current circuit has problems while buffering large sensor capacitances. It is also observed to be very sensitive to ambient illumination. It is necessary to develop an improved capacitive interface circuit, with a more-stable and efficient biasing scheme with minimum noise. Finally, it is also important to develop differential readout schemes for tuning-fork gyroscope configuration, which contains two identical gyroscopes oscillated anti-phase along the drive-mode for suppressing common-mode acceleration signals and reducing g-sensitivity of the angular rate sensor.

5. The effects of the demodulating electronics on the bias and the drift should be investigated in detail and minimized. In addition, the external control and feedback electronics complementing the gyroscope/interface assemblies must be optimized in terms of reliable-operation, noise, and selected

components. It is necessary to use dedicated components in these circuits, achieving an accurate phase control throughout the feedback loops. In the long-term, the implementation of these electronic circuits in a single CMOS ASIC should be considered.

In conclusion, the major achievement of this research is the demonstration of the development of new and novel MEMS gyroscopes for tactical-grade applications. The measured performances of the fabricated gyroscopes together with the developed electronics show that the advanced symmetric and decoupled gyroscope structure has the potential of resolving angular rates smaller than 10deg/hr, sufficient for many tactical-grade applications. It is believed that, the results of this research would be helpful in the development of batch-producible high-performance MEMS gyroscopes for both industrial and military applications.

REFERENCES

[1]   N. Yazdi, F. Ayazi, and K. Najafi, "Micromachined Inertial Sensors," Proc. of the IEEE, Vol. 86, No. 8, pp. 1640-1659, August 1998.

[2]   Dr. J. Marek, "Microsystems for Automotive Applications," Proc. 13th Eur. Conf. Solid-State Transducers (Eurosensors XIII), The Hague, The Netherlands, September 1999, pp. 1-8.

[3]   H. Kuisma, "Inertial Sensors for Automotive Applications," Tech. Dig. 11th Int. Conf. Solid-State Sensors and Actuators (Transducers'01), Munich, Germany, June 2001, pp. 430-433.

[4]   S. Y. Bae, K. J. Hayworth, K. Y. Yee, K. Shcheglov, and D. V. Wiberg, "High Performance MEMS Micro-Gyroscope," Proc. SPIE-Int. Soc. Opt. Eng., Vol. 4755, pp. 316–324, 2002.

[5]   A. Gripton, "The Application and Future Development of a MEMS SiVS/spl reg/ for Commercial and Military Inertial Products," IEEE Position Location and Navigation Symp. (PLANS'02), Palm Springs, CA, April 2002, pp. 28-35.

[6]   A. M. Madni, L. E. Costlow, S. J. Knowles, "Common Design Techniques for BEI GyroChip Quartz Rate Sensors for Both Automotive and Aerospace/Defense Markets," IEEE Sensors, Vol. 3, No. 5, pp.569–578, October 2003.

[7]   D. Karnick, G. Ballas, L. Koland, M. Secord, T. Braman, and T. Kourepenis, "Honeywell Gun-Hard Inertial Measurement Unit (IMU) Development," IEEE Position Location and Navigation Symp. (PLANS'04), Monterey, CA, April 2004, pp. 49-55.

[8]   G. T. Schmidt, "INS/GPS Technology Trends," NATO RTO Sensors & Electronics Technology (RTO-SET) Panel: Symp. Emerging Military Capabilities Enabled by Advances in Navigation Sensors (SET'02), Istanbul, Turkey, October 2002.

[9]   A. M. Madni and R. D. Geddes, "A Micromachined Quartz Angular Rate Sensor for Automotive and Advanced Inertial Applications," Sensors Magazine, Vol. 16, No. 8, August 1999.

[10]   J. Krim, "Friction at the Nanoscale," Physics World, February 2005.

[11]   IEEE Standard for Inertial Sensors Terminology, Std 528-2001, November 2001.

[12]   T. B. Gabrielson, "Mechanical-Thermal Noise in Micromachined Sensors and Acoustic and Vibration Sensors," IEEE Trans. Electron. Devices, Vol. 40, No. 5, May 1993, pp.903-909.

[13]   H. R. Samuels and J. A. Farash, "Micromachined Device with Enhanced Dimensional Control," U.S. Patent 6 282 960, September 4, 2001.

[14]   A. Duwel, M. Weinstein, J. Gorman, J. Borenstein, and P. Ward, "Quality Factors of MEMS Gyros and the Role of Thermoelastic Damping," Proc. IEEE Micro Electro Mechanical Systems Workshop (MEMS'02), Las Vegas, CA, January 2002, pp. 214-219.

[15]   T. Veijola and M.Turowski, "Compact Damping Models for Laterally Moving Microstructures with Gas-Rarefaction Effects," J. Microelectromechanical Sys., Vol. 10, No. 2, June 2001, pp. 263-273.

[16]   B. E. Boser, "Electronics for Micromachined Inertial Sensors," Tech. Dig. 9th Int. Conf. Solid-State Sensors and Actuators (Transducers'97), Chicago, IL, June 1997, pp. 1169-1172.

[17]   P. Greiff, B. Boxenhorn, T. King, and L. Niles, "Silicon Monolithic Micromechanical Gyroscope," Tech. Dig. 6th Int. Conf. Solid-State Sensors and Actuators (Transducers'91), San Fransisco, NY, June 1991, pp. 966-968.

[18]   M. Niu, W. Xue, X. Wang, J. Xie, G. Yang, and W. Yang, "Design and Characteristics of Two-gimbals Micro-gyroscopes Fabricated with Quasi-LIGA Process," Tech. Dig. 9th Int. Conf. Solid-State Sensors and Actuators (Transducers'97), Chicago, IL, June 1997, pp. 891-894.

[19]   K. Maenaka, N. Sawai, S. Ioku, H. Sugimoto, H. Suzuki, T. Fujita, and Y. Takayama, "MEMS Gyroscope with Double Gimbal Structure," Tech. Dig. 12th Int. Conf. Solid-State Sensors and Actuators (Transducers'03), Boston, MA, June 2003, pp. 163-166.

[20]   T. Tsuchiya, Y. Kageyama, H. Funabashi, and J. Sakata, "Vibrating Gyroscope Consisting of Three Layers of Polysilicon Thin Films," Tech. Dig. 10th Int. Conf. Solid-State Sensors and Actuators (Transducers'99), Sendai, Japan, June 1999, pp. 976-979.

[21]   T. Tsuchiya, Y. Kageyama, H. Funabashi, and J. Sakata, "Polysilicon Vibrating Gyroscope Vacuum-Encapsulated in an On-Chip Micro Chamber," Sensors Actuators A, vol. 90, pp. 49-55, May 2001.

[22] H. Yang, M. Bao, H. Yin, and S. Shen, "A Novel Bulk Micromachined Gyroscope Based on a Rectangular Beam-Mass Gyroscope," Sensors Actuators A, vol. 96/2-3, pp. 145-151, February 2002.

[23] R. Voss, K. Bauer, W. Ficker, T. Gleissner, W. Kupke, M. Rose, S. Sassen, J. Schalk, H. Seidel, and E. Stenzel, "Silicon Angular Rate Sensor for Automotive Applications with Piezoelectric Drive and Piezoresistive Read-out," Tech. Dig. 9th Int. Conf. Solid-State Sensors and Actuators (Transducers'97), Chicago, IL, June 1997, pp. 879-882.

[24] M. Lutz, W. Golderer, J. Gerstenmeier, J. Marek, B. Maihofer, S. Mahler, H. Munzel and U. Bischof, "A Precision Yaw Rate Sensor in Silicon Micromachining," Tech. Dig. 9th Int. Conf. Solid-State Sensors and Actuators (Transducers'97), Chicago, IL, June 1997, pp. 847-850.

[25] K. Funk, H. Emmerich, A. Schilp, M. Offenberg, R. Neul, and F. Larmer, "A Surface Micromachined Silicon Gyroscope Using a Thick Polysilicon Layer," Proc. IEEE Micro Electro Mechanical Systems Workshop (MEMS'99), Orlando, FL, January 1999, pp. 57-60.

[26] Y. Yahong, G. Zhongyu, Z. Rong, D. Yuqian, and C. Zhiyong, "A Silicon Wafer Dissolved Vibrating Gyroscope," Proc. IEEE Instrumentation and Measurement Technology Conf. (IMTC'98), St. Paul, MN, May 1998, pp. 1133-1136.

[27] J. Bernstein, S. Cho, A. T. King, A. Kourepenis, P. Maciel, and M. Weinberg, "A Micromachined Comb-Drive Tuning Fork Rate Gyroscope," Proc. of IEEE Micro Electro Mechanical Systems Workshop (MEMS'93), Fort Lauderdale, FL, February 1993, pp. 143-148.

[28] M. Weinberg, J. Connely, A. Kourepenis, and D. Sargent, "Microelectromechanical Instrument and Systems Development at the Charles Stark Draper Laboratory," AIAA/IEEE Digital Avionics Systems Conf., October 1997, pp. 8.5.33-8.5.40.

[29] M. Fujiyoshi, Y. Nonomura, Y. Omura, K. Tsukada, S. Matsushige, and N. Kurata, "Modeling and Vibration Analysis of a Quartz Yaw Rate Sensor to Reduce Mechanical Coupling," Proc. Int. Symp. on Micromechatronics and Human Science (MHS'01), Nagoya, Japan, September 2001, pp. 105-108.

[30] K. Schumacher, O. Kromer, U. Wallrabe, J. Mohr, and V. Saile, "Micromechanical LIGA-Gyroscope," Tech. Dig. 10th Int. Conf. Solid-State Sensors and Actuators (Transducers'99), Sendai, Japan, June 1999, pp. 1574-1577.

[31] M. W. Putty, "A Micromachined Vibrating Ring Gyroscope," Ph.D. Dissertation, The University of Michigan, 1995.

[32] S. Chang, M. Chia, P. Castillo-Borelley, W. Hidgon, Q. Jiang, J. Johnson, L. Obedier, M. Putty, Q. Shi, D. Sparks, and S. Zarabadi, "An Electroformed

CMOS Integrated Angular Rate Sensor," Sensors Actuators A, vol. 66, pp. 138-143, April 1998.

[33] F. Ayazi and K. Najafi, "A HARPSS Polysilicon Vibrating Ring Gyroscope," J. Microelectromechanical Sys., Vol. 10, No. 2, pp. 169-179, June 2001.

[34] G. He and K. Najafi, "A Single-Crystal Silicon Vibrating Ring Gyroscope," Proc. IEEE Micro Electro Mechanical Systems Workshop (MEMS'02), Las Vegas, CA, January 2002, pp. 718-721.

[35] M. F. Zaman, A. Sharma, B. V. Amini, and F. Ayazi, "The Resonating Star Gyroscope," Proc. IEEE Micro Electro Mechanical Systems Workshop (MEMS'05), Miami, FL, January 2005, pp. 355-358.

[36] B. J. Gallacher, J.. S.. Burdess, A. J. Harris, and M. E. McNea, "Principles of a Three-Axis Vibrating Gyroscope," IEEE Trans. on Aerospace and Electronic Systems, Vol. 37, No. 4, pp. 1333-1343, October 2001.

[37] X. Huikai and G. K. Fedder, "A CMOS-MEMS Lateral-Axis Gyroscope," in Proc. IEEE Micro Electro Mechanical Systems Workshop (MEMS'01), Interlaken, Switzerland, January 2001, pp. 162-165.

[38] H. Luo, X. Zhu, H. Lakdawala, L. R. Carley, and G. Fedder, "A Copper CMOS-MEMS Z-Axis Gyroscope," in Proc. IEEE Micro Electro Mechanical Systems Workshop (MEMS'02), Las Vegas, CA, January 2002, pp. 631-634.

[39] J. A. Geen, S. J. Sherman, J. F. Chang, and S. R. Lewis, "Single-Chip Surface Micromachined Intergated Gyroscope with 50/spl deg//h Allan Deviation," J. Solid State Cct., Vol. 37, No. 12, pp. 1860-1866, December 2002.

[40] X. Huikai and G. K. Fedder, "A DRIE CMOS-MEMS Gyroscope," IEEE Sensors, Vol. 2, pp. 1413-1418, June 2002.

[41] X. Huikai and G. K. Fedder, "Fabrication, Characterization, and Analysis of a DRIE CMOS-MEMS Gyroscope," IEEE Sensors, Vol. 3, No. 5, pp. 622-631, October 2003.

[42] S. A. Bhave, J. I. Seeger, J. Xuesong, B. E. Boser, R. T. Howe, J. Yasaitis, "An Integrated, Vertical-Drive In-Plane-Sense Microgyroscope," Tech. Dig. 12th Int. Conf. Solid-State Sensors and Actuators (Transducers'03), Boston, MA, June 2003, pp. 171-174.

[43] Y. Guizhen, Z. Yong, W. Chengwei, Z. Rong, C. Zhiyong, L. Xuesong, and Y. Y. Wang, "Integrated Bulk-Micromachined Gyroscope Using Deep Trench Isolation Technology," Proc. IEEE Micro Electro Mechanical Systems Workshop (MEMS'04), Maastricht, Holland, January 2004, pp. 605-608.

[44]   S. S. Baek, Y. S. Oh, B. J. Ha, S. D. An, B. H. An, H. Song, and C. M. Song, "A Symmetrical Z-Axis Gyroscope with a High Aspect Ratio Using Simple and New Process," Proc. IEEE Micro Electro Mechanical Systems Workshop (MEMS'99), Orlando, FL, January 1999, pp. 612-617.

[45]   Z. Li, Z. Yang, Z. Xiao, Y. Hao, T. Li, G. Wu, and Y. Wang, "A Bulk Micromachined Vibratory Lateral Gyroscope Fabricated with Wafer Bonding and Deep Trench Etching," Tech. Dig. 10th Int. Conf. Solid-State Sensors and Actuators (Transducers'99), Sendai, Japan, June 1999, pp. 1594-1597.

[46]   Y. Mochida, M. Tamura, and K. Ohwada, "A Micromachined Vibrating Rate Gyroscope with Independent Beams for the Drive and Detection Modes," Sensors Actuators A, Vo. 80, pp. 170-178, 2000.

[47]   H. Kawai, K.-I. Atsuchi, M. Tamura, and K. Ohwada, "High-Resolution Microgyroscope Using Vibratory Motion Adjustment Technology," Sensors Actuators A, Vol. 90/1-2, pp. 153-159, May 2001.

[48]   H. Sato ,T. Fukuda, F. Arai, K. Itoigawa, and Y. Tsukahara, "Suppression of Mechanical Coupling for Parallel Beam Gyroscope," Proc. IEEE Int. Conf. on Robotics and Automation (ICRA'00), San Fransisco, CA, April 2000, Vol. 4, pp. 3939-3944.

[49]   J. W. Song, J. G. Lee, T. Kang, and S. Sung, "Design and Performance Test of an In-plane Gimbaled Silicon Gyroscope," Proc. IEEE National Aerospace and Electronics Conference (NAECON'00), Dayton, OH, October 2000, pp. 339-345.

[50]   B. L. Lee, S. W. Lee, K. D. Jung, J. H. Choi, T. R. Chung, and Y. C. Cho, "A Decoupled Vibratory Gyroscope Using a Mixed Micromachining Technology," Proc. IEEE Int. Conf. on Robotics&Automation (ICRA'01), Seoul, Korea, May 2001, pp. 3412-3416.

[51]   W. Geiger, W. U. Butt, A. Gaiβer, J. Frech, M. Braxmaier, T. Link, A. Kohne, P. Nommensen, H. Sandmaier, and W. Lang, "Decoupled Microgyros and the Design Principle DAVED," Sensors Actuators A, vol. 95, pp. 239-249, 2002.

[52]   M. Palaniapan, R. T. Howe, and J. Yasaitis, "Performance Comparison of Integrated Z-Axis Frame Microgyroscopes," Proc. IEEE Micro Electro Mechanical Systems Workshop (MEMS'03), Kyoto, Japan, January 2003, pp. 482-485.

[53]   M.Kranz, S. Burgett, T. Hudson, M. Buncick, P. Ruffin, P. Ashley, and J. McKee, "Performance of a Silicon-on-Insulator MEMS Gyroscope with Digital Force Feedback," IEEE Position Location and Navigation Symp. (PLANS'04), Monterey, CA, April 2004, pp. 7-14.

[54]   C. Acar and A. Shkel, "Distributed-Mass Micromachined Gyroscopes: Demonstration of Drive-Mode Bandwidth Enhancement," Proc. Electronic Components and Technology Conf. (ECTC'04), Las Vegas, CA, June 2004, pp. 874-882.

[55]   C. Acar and A. M. Shkel, "Structurally Decoupled Micromachined Gyroscopes with Post-Release Capacitance Enhancement," J. Micromech. Microeng., Vol. 15, pp. 1092-1101, 2005.

[56]   N. Hedenstierna, S. Habibi, S. M. Nilsen, T. Kvisterϕy, and G. U. Jensen, "Bulk Micromachined Angular Rate Sensor Based on the Butterfly-Gyro Structure," Tech. Dig. IEEE Micro Electro Mechanical Systems Conf. (MEMS'01), Interlaken, Switzerland, January 2001, pp. 178-181.

[57]   H. T. Lim, J. W. Song, J. G. Lee, and Y. K. Kim, "A Few deg/hr Resolvable Low Noise Lateral Microgyroscope," Proc. IEEE Micro Electro Mechanical Systems Workshop (MEMS'02), Las Vegas, CA, January 2002, pp. 627-630.

[58]   J.-Y. Lee, S.-H. Jeon, H.-K. Jung, H.-K. Chang, and Y.-K. Kim, "Vacuum Packaged Low Noise Gyroscope with Sub mdeg/s/√Hz Resolution," Proc. IEEE Micro Electro Mechanical Systems Workshop (MEMS'05), Miami, FL, January 2005, pp. 359-362.

[59]   S. Lee, S. Park, J. Kim, S. Lee, and Dong-il (Dan) Cho, "Surface/Bulk Micromachined Single-Crystalline-Silicon Micro-Gyroscope," J. Microelectromechanical Sys., Vol. 9, No. 4, pp. 557-567, December 2000.

[60]   K. Jongpal, P. Sangiun, K. Donghun, K. Hyougho, and D. C. Dong-il, " A Planar, X-Axis, Single-Crystalline Silicon Gyroscope Fabricated Using the Extended SBM Process," Proc. IEEE Micro Electro Mechanical Systems Workshop (MEMS'04), Maastricht, Holland, January 2004, pp. 556-559.

[61]   A. Sharma, F. M. Zaman, B. V. Amini, F. Ayazi, "A High-Q In-Plane SOI Tuning Fork Gyroscope," Proc. IEEE Sensors Conf., Vienna, Austria, October 2004, pp. 467-470.

[62]   S. Kim, B. Lee, J. Lee, and K. Chun, "A Gyroscope Array with Linked-Beam Structure," Tech. Dig. IEEE Micro Electro Mechanical Systems Conf. (MEMS'01), Interlaken, Switzerland, January 2001, pp. 30-33.

[63]   W. C. Tang, "Micromechanical Devices at JPL for Space Exploration," Proc. IEEE Aerospace Conf., Aspen, CO, March 1998, pp. 461-470.

[64]   T. Juneau, A. P. Pisano, and J. H. Smith, "Dual Axis Operation of a Micromachined Rate Gyroscope," Tech. Dig. 9th Int. Conf. Solid-State Sensors and Actuators (Tranducers'97), Chicago, IL, June 1997, pp. 883-886.

[65]   B. Xiong, L. Che, and Y. Wang, "A Novel Bulk Micromachined Gyroscope with Slots Structure Working at Atmosphere," Sensors Actuators A, Vol. 107/2, pp. 137-145, October 2003.

[66]   D. Piyabongkarn, R. Rajamani, and M. Greminger, "The Development of a MEMS Gyroscope for Absolute Angle Measurement," IEEE Trans. Control Systems Tech., Vol. 13, No. 2, pp. 185-195, March 2005.

[67]   F. Gretillat, M.-A. Gretillat, and N. F. de Rooij, "Improved Design of a Silicon Micromachined Gyroscope with Piezoresistive Detection and Electromagnetic Actuation," J. Microelectromechanical Sys., Vol. 8, No. 3, pp. 243-250, September 1999.

[68]   S. Nakano, T. Toriyama, and S. Sugiyama, "Sensitivity Analysis for a Piezoresistive Rotary Movement Micro Gyroscope," Proc. Int. Symp. on Micromechatronics and Human Science (MHS'01), Nagoya, Japan, September 2001, pp. 87-92.

[69]   O. Degani, D. J. Seter, E. Socher, S. Kaldor, and Y. Nemirovsky, "Optimal Design and Noise Consideration of Micromachined Vibrating Rate Gyroscope with Modulated Integrative Differential Optical Sensing," J. Microelectromechanical Sys., Vol. 7, No. 3, pp. 329-338, September 1998.

[70]   S. Zhaohui, C. Xuemeng, H. Shusen, W. Yuelin, J. Jiwei, and L. Xinxin, "A High-Sensitivity Piezoresistive Gyroscope with Torsional Actuation and Axially-Stressed Detection," Proc. IEEE Sensors Conf., Toronto, Canada, October 2003 pp. 457-460.

[71]   A. A. Seshia, R. T. Howe, and S. Montague, "An Integrated Microelectromechanical Resonant Output Gyroscope," Proc. IEEE Micro Electro Mechanical Systems Workshop (MEMS'02), Las Vegas, CA, January 2002, pp. 722-726.

[72]   O. Bel, R. Bourquin, and A. Jeanrov, "Two-Axes Quartz Angular Rate Sensor," IEEE Int. Freq. Control Symp. And PDA Exhibit., New Orleans, LA, May 2002, pp. 214-219.

[73]   C. R. Dauwalter and J. C. Ha, "Magnetically Suspended MEMS Spinning Wheel Gyro," IEEE Aerospace and Electronic Systems Magazine, Vol. 20, No. 2, pp. 21-26, February 2005.

[74]   T. Shiozawa,, V. T. Dau, D. V. Dao, H. Kumagai, and S. Sugiyama, "A Dual-Axis Thermal Convective Silicon Gyroscope," Proc. Int. Symp. Micro-Nanomechatronics for Information-Based Society and Micro-Nanomechatronics and Human Science (MHS'04), Nagoya, Japan, November 2004, pp. 277-282.

[75]   J. Zhou, G. Yan, Y. Zhu, Z. Xiao, and J. Fan, "Design and Fabrication of a Microfluid Angular Rate Sensor," in Proc. IEEE Micro Electro Mechanical Systems Workshop (MEMS'05), Miami, FL, January 2005, pp. 363-366.

[76] S. E. Alper, "Silicon Surface Micromachined Gyroscope Using MEMS Technology," M.Sc. Thesis, Middle East Technical University, 2000.

[77] S. E. Alper and T. Akin, "A Planar Gyroscope Using a Standard Surface Micromachining Process," The 14th European Conf. on Solid-State Transducers (Eurosensors XIV), Copenhagen, Denmark, August 2000, pp. 387-390.

[78] S. E. Alper and T. Akin, "A Symmetric Surface Micromachined Gyroscope with Decoupled Oscillation Modes," The 11th Int. Conf. Solid-State Sensors and Actuators and 15th European Conf. on Solid-State Transducers (Transducers'01, Eurosensors XV), Munich, Germany, June 2001, pp. 456-459.

[79] S. E. Alper and T. Akin, "A Symmetric Surface Micromachined Gyroscope with Decoupled Oscillation Modes," Sensors and Actuators A, Vol. 97-98C, pp. 337-348, April 2002.

[80] S. E. Alper and T. Akin, "A Symmetrical and Decoupled Microgyroscope with Electroforming Process on Insulating Substrate," The 16th European Conf. on Solid-State Transducers (Eurosensors XVI), Prague, Czech Republic, September 2002, pp. 814-817.

[81] S. E. Alper and T. Akin, "A Symmetrical and Decoupled Nickel Microgyroscope on Insulating Substrate," The 17th European Conf. on Solid-State Transducers (Eurosensors XVII), Guimaraes, Portugal, September 2003, pp. 24-27.

[82] S. E. Alper and T. Akin, "A Symmetrical and Decoupled Nickel Microgyroscope on Insulating Substrate," Sensors and Actuators A, Vol. 115, pp. 336-350, September 2004.

[83] S. E. Alper and T. Akin, "A Single-Crystal Silicon Symmetrical and Decoupled Gyroscope on Insulating Substrate," The 12th Int. Conf. on Solid-State Sensors and Actuators (Transducers'03), Boston, MA, June 2003, pp. 1399-1402.

[84] S. E. Alper and T. Akin, "A Single-Crystal Silicon Symmetrical and Decoupled MEMS Gyroscope on an Insulating Substrate," J. Microelectromechanical Systems, Vol. 14, No. 4, pp. 707-717, August 2005.

[85] S. E. Alper and T. Akin, "A Low-Cost Rate-Grade Nickel Microgyroscope," The 19th European Conf. on Solid-State Transducers (Eurosensors XIX), Barcelona, Spain, September 2005, (accepted for publication).

[86] R. J. Roark and W. C. Young, *Formulas for Stress and Strain*, McGraw-Hill, 1983.

[87] S. D. Senturia, Microsystem Design, *Kluwer Academic Publishing*, 2001.

[88]   W. C.-K. Tang, "Electrostatic Comb Drive for Resonant Sensor and Actuator Applications," Ph.D. Dissertation, The University of California at Berkeley, 1990.

[89]   G. K. Fedder, "Simulation of Microelectromechanical Systems," Ph.D. Dissertation, The University of California at Berkeley, 1995.

[90]   CoventorWare MEMS Design and Analysis Supplemental Tutorials and Reference Guide, pp. M6_44-M6_51, 2001.

[91]   M. J. Silver, L. D. Peterson, and R. S. Erwin, "Predictive Thermoelastic Damping in Beams using Finite Element Techniques," AIAA-2002-1729 Proc. of the 43rd Structures, Structural Dynamics and Materials Conf., Denver, CO, April 2002, pp. 1-10.

[92]   D. S. Bindel and S. Govindjee, "Elastic PMLs for Resonator Anchor Loss Simulation," Technical Report, UCB/SEMM-2005/01, 2005, pp. 1-23.

[93]   C. T.-C. Nguyen, "Micromechanical Signal Processors," Ph.D. Dissertation, The University of California at Berkeley, 1994.

[94]   W. C. Tang, M. G. Lim, and R. T. Howe, "Electrostatic Comb Drive Levitation and Control Method," J. Microelectromech. Syst., Vol. 1, No. 4, pp. 170-178, December 1992.

[95]   R. Legtenberg, A. W. Groeneveld, and M. Elwenspoek, "Comb-Drive Actuators for Large Displacements," J. Micromech. Microeng., Vol. 6, No. 3, pp. 320-329, September 1996.

[96]   W. A. Clark, "Micromachined Vibratory Rate Gyroscopes," Ph.D. Dissertation, The University of California at Berkeley, 1997.

[97]   Y. B. Gianchandani and K. Najafi, "A Bulk Silicon Dissolved Wafer Process for Microelectromechanical Systems," J. Microelectromechanical Sys., Vol. 1, No. 2, June 1992, pp. 77-85.

[98]   M. J. Madou, *Fundamentals of Microfabrication*, CRC Press, 2002.

[99]   F. Lowenheim, *Modern Electroplating*, Wiley, 1974.

[100]   L. J. Durney, *Electroplating Engineering Handbook*, Van Nostrand Reinhold, New York, 1984.

[101]   S. A. Watson, "Nickel Sulphamate Solutions," Nickel Institute Series, December 1990, pp. 1-5.

[102]   I.V. Kadija, "A Novel Wet Processing Technology," Proc. of the Symp. on High Rate Metal Dissolution Processes, The Electrochemical Society, Vol. 95-19, pp. 1-14.

[103] K. Miller, A. Cowen, G. Hames, and B. Hardy, *SOIMUMPs Design Handbook*, MEMSCAP, 2004.

[104] J. Chae, H. Kulah, and K. Najafi, "A Hybrid Silicon-on-Glass (SOG) Lateral Micro-Accelerometer with CMOS Readout Circuitry," in Proc. IEEE Micro Electro Mechanical Systems Workshop (MEMS'02), Las Vegas, CA, January 2002, pp. 623-626.

[105] J. Kiimahaki and S. Franssila, "Pattern Shape Effects and Artefacts in Deep Silicon Etching," J. Vac. Sci. Technol. A, Vol. 17, No. 4, pp. 2280-2285, July/August 1999.

[106] J. C. Arnold and H. H. Sawin, "Charging of Pattern Features During Plasma Etching," J. Appl. Phys. Vol. 70, No. 10, pp. 5314-5317, November 1991.

[107] G. S. Hwang and K. P. Giapis, "Aspect-Ratio-Dependent Charging in High-Density Plasmas," J. Appl. Phys. Vol. 82, No. 2, pp. 566-571, July 1997.

[108] T. Kinoshita, M. Hane, and J. P. McVittie, "Notching as an Example of Charging in Uniform High Density Plasmas," J. Vac. Sci. Technol. B, Vol. 14, No.1, pp. 560-565, January/February 1996.

[109] M. Chabloz, J. Jiao, Y. Yoshida, T. Matsuura, and K. Tsutsumi, "A Method to Evade Microloading Effect in Deep Reactive Ion Etching for Anodically Bonded Glass-Silicon Structures," Proc. IEEE Micro Electro Mechanical Systems Workshop (MEMS'00), Miyazaki, Japan, January 2000, pp. 283-287.

[110] C.-H. Kim, J. Park, N. Park, and Y.-K. Kim, "MEMS Fiber-Optic Variable Optical Attenuator Using Collimating Lensed Fiber," IEEE/LEOS Int. Conf. on Optical MEMS, Waikoloa, HI, August 2003, pp. 145-146.

[111] Fairchild Semiconductor, CD04046BC Micropower Phase-Locked Loop Datasheet, 1999.

[112] ON Semiconductor, MC14046 Phase Locked Loop Datasheet, 2001.

[113] Analog Devices, AD633 Low-Cost Analog Multiplier Datasheet, 2002.

CURRICULUM VITAE

PERSONAL INFORMATION

Surname, Name: Alper, Said Emre

Nationality: Turkish (TC)

Date and Place of Birth: 2 October 1976 , Ankara

Marital Status: Married

Phone: +90 312 210 44 09

Fax: +90 312 210 12 61

email: said@metu.edu.tr

EDUCATION

Degree	Institution	Year of Graduation
M.Sc.	METU Electrical and Electronics Engineering	2000
B.Sc.	METU Electrical and Electronics Engineering	1998
High School	Gazi Anadolu High School, Ankara	1994

WORK EXPERIENCE

Year	Place	Enrollment
1998-Present	METU Electrical and Electronics Engineering	Research Assistant
1997 July	GATA Biomedical Center	Summer Practice
1996 August	ASELSAN	Summer Practice

FOREIGN LANGUAGES

Advanced English

INTERNATIONAL CONFERENCE PUBLICATIONS

[1] S. E. Alper and T. Akin, "A Planar Gyroscope Using a Standard Surface Micromachining Process," The 14th European Conf. on Solid-State Transducers (Eurosensors XIV), Copenhagen, Denmark, August 2000, pp. 387-390.

[2] S. E. Alper and T. Akin, "A Symmetric Surface Micromachined Gyroscope with Decoupled Oscillation Modes," The 11th Int. Conf. Solid-State Sensors and Actuators (Transducers'01, Eurosensors XV), Munich, Germany, June 2001, pp. 456-459.

[3] S. E. Alper and T. Akin, "A Symmetrical and Decoupled Microgyroscope with Electroforming Process on Insulating Substrate," The 16th European Conf. on Solid-State Transducers (Eurosensors XVI), Prague, Czech Republic, September 2002, pp. 814-817.

[4] S. E. Alper and T. Akin, "Optimum Designs for High-Performance Micromachined Gyroscopes," NATO RTO Sensors & Electronics Technology (RTO-SET) Panel: Symposium on Emerging Military Capabilities Enabled by Advances in Navigation Sensors (SET'02), Istanbul, Turkey, October 2002.

[5] S. E. Alper and T. Akin, "A Single-Crystal Silicon Symmetrical and Decoupled Gyroscope on Insulating Substrate," The 12th Int. Conf. on Solid-State Sensors and Actuators (Transudcers'03), Boston, Massachusetts, June 2003, pp. 1399-1402.

[6] S. E. Alper and T. Akin, "A Symmetrical and Decoupled Nickel Microgyroscope on Insulating Substrate," The 17th European Conf. on Solid-State Transducers (Eurosensors XVII), Guimaraes, Portugal, September 2003, pp. 24-27.

[7] S. E. Alper and T. Akin, "A Low-Cost Rate-Grade Nickel Microgyroscope," The 19th European Conf. on Solid-State Transducers (Eurosensors XIX), Barcelona, Spain, September 2005, (accepted for publication).

INTERNATIONAL JOURNAL PUBLICATIONS

[1] S. E. Alper and T. Akin, "A Symmetric Surface Micromachined Gyroscope with Decoupled Oscillation Modes," Sensors and Actuators Journal A, Vol. 97-98C, pp. 337-348, April 2002.

[2] S. E. Alper and T. Akin, "A Symmetrical and Decoupled Nickel Microgyroscope on Insulating Substrate," Sensors Actuators A, Vol. 115/2-3, pp. 336-350, September 2004.

[3] S. E. Alper and T. Akin, "A Single-Crystal Silicon Symmetrical and Decoupled Gyroscope on Insulating Substrate," IEEE Journal of Microelectromechanical Systems, Vol. 14, No. 4, pp. 707-717, August 2005.